TARGETING ENDOPLASMIC RETICULUM STRESS AS A THERAPEUTIC STRATEGY IN CANCER

A THESIS

SUBMITTED TO PARTIAL FULFILMENT OF THE DEGREE

OF

DOCTOR OF PHILOSOPHY

IN CHEMISTRY

BY

SHALINI PANDEY

ID: 20142016

UNDER THE GUIDANCE OF

DR. NIRMALYA BALLAV

&

DR. SUDIPTA BASU

AT

INDIAN INSTITUTE OF SCIENCE EDUCATION AND RESEARCH, PUNE

2021

CERTIFICATE

Certified that the work incorporated in the thesis entitled ***"Targeting Endoplasmic Reticulum Stress as a Therapeutic Strategy in Cancer"*** submitted by **Ms. Shalini Pandey** was carried out by the candidate, under my supervision. The work presented here or any part of it has not been included in any other thesis submitted previously for the award of any degree or diploma from any other University or institution.

Date: 19/01/2021

Dr. Nirmalya Ballav
(Supervisor)

Dr. Sudipta Basu
(Co-Supervisor)

DECLARATION

I declare that this written submission represents my ideas in my own words and where others' ideas have been included, I have adequately cited and referenced the original sources. I also declare that I have adhered to all principles of academic honesty and integrity and have not misrepresented or fabricated or falsified any idea/data/fact/source in my submission. I understand that violation of the above will be cause for disciplinary action by the Institute and can also evoke penal action from the sources which have thus not been properly cited or from whom proper permission has not been taken when needed.

Date:18/01/2021 **Shalini Pandey**

ID 20142016

ACKNOWLEDGEMENTS

Foremost, I express my heartfelt gratitude towards my thesis supervisor Dr. Nirmalya Ballav for being so supportive throughout. I will always be indebted to him for all the help, advice, suggestions, encouragement and the freedom he provided to pursue my research. I am thankful to him for always providing a helping hand in the most stressed times during my PhD.

Next, I extend my gratitude towards my co-supervisor Dr. Sudipta Basu for his encouragement, motivation, independence, guidance and support and of course the lab facilities. I shall be always thankful to him for bearing me, my doubts and anxieties and dealing with them patiently. I am grateful to him for instilling that sense of self dependence in me.

Besides my advisors, I am thankful to Dr. Jayant. B. Udgaonkar, Director IISER Pune and Dr. K.N. Ganesh, former director IISER Pune for providing an excellent infrastructure and facilities. I am also thankful to my RAC members, Dr. H.N. Gopi and Dr. D.S. Reddy for the guidance and suggestions they provided during the RAC meetings. I also thank all the technicians at IISER Pune Anil, Mahesh, Sandeep, Megha, Suresh, Yatish and Dnyaneshwar for their assistance. I am also thankful to Tushar Sir for all the administrative help. I extend my sincere thanks to Dr. Mayurika Lahiri, Deapartment of Biological Sciences at IISER Pune for allowing me to work in her lab and use the facilities there. A special thanks to Abhijith K, Vaishali Chakravarty, Rupa, Aishwarya, Rintu and of course my favourite Virender Sharma for teaching me the techniques and helping me in my experiments.

I take this opportunity to thank all my labmates for being there for me. A special mention goes to Chandramouli with whom I first worked when I joined the lab. Also, I am thankful to Sohan and Aditi for their help, suggestions and the fruitful discussions apart from all the gossip mongering. I will miss the BTS discussion I had with Aditi and the intense political discussions with Sohan. I also thank Aman for helping me and being a great host while my stay at IIT Gandhinagar. I am also thankful to Sai, Sadhana and Ankur for being the best juniors and letting me feel those senior vibes. I will also be thankful to Dr. S.G. Srivatsan, Dr. Pramod Pillai and Dr. Anirban Hazra for letting me rotate in their labs during my course. A special thanks to Ashok and Soumendu for being so supportive during that phase.

I am thankful to my friends at IISER Pune for providing me those stress free moments. I am thankful to Dr. Argha Banerjee for those unplanned trips, those funny chai sessions and being a great host for several dinners. Thank you for inspiring me to be a better version of myself each day. I am thankful to Anna of Shivsagar cafeteria for being that gentle soul he is and I

will miss him and his chai for sure. I also thank Prachi, Dibyata, Navita and all the members of Dr. Surjeet Singh's lab for diligently waiting for me for the evening snacks and providing me that lab vibe which I missed after my seniors left. I am thankful to my friend Deepak or rather Sharma as I would call him for his rather funny teachings of simple living and high thinking while being crazy for brands at the same time. I am thankful to my friend Mayur for introducing me to Baba Sehgal's world of music. My gratitude to my friends won't be complete if I don't thank Kumar Saurabh, my best friend at IISER Pune for always being there for me unconditionally, helping me handle my emotions, being there for me in my hardest times, irritating me to the core so that I rediscover my patience level every day and of course for respecting the foodie in me by preparing the delicacies. I will always miss and reminisce the times I spent exploring the food outlets in Pune with him. I will miss the times I spent with Sharma, Saurabh and Mayur listening to their stupid talks including their dumb childhood stories and of course their ganging up against me. I also take this opportunity to thank Saurabh's family especially his father for always being so homely to all our friends. His home was our go to place whenever we missed the home-made food and vibes and I will be thankful for that too because yes food is important.

I take this opportunity to thank teachers from my school and college especially Mrs. Shakuntala Semwal and Prof. Geeta Joshi for motivating me. I will be thankful to my late grandfather at Pune for making me feel so homely during my initial five years in Pune and I will miss him. I thank my grandmother too for her care and affection. I take the opportunity to thank the most important people in my life without whose support I would not have dared to pursue research. I thank my brother Saurabh Pandey for being my friend, support and guide. Thank you for being younger to me but taking up the role of an elder brother in all adversities of life I have faced. Thank you for believing in me and my capabilities and listening to all my research related problems even when you did not understand a word. I am thankful to my mother for all the love and sacrifices, for being my biggest critic and pushing me beyond my limits always and for being the strongest lady I know. I wish to thank my late father for being my first teacher and friend, for all the sacrifices he made and for all the love and encouragement he gave me all through my life. I miss you Papa and I will be forever indebted to you. I will never be able to come in terms with the fact that you left me few months before my thesis defense. It is because of fathers like you that daughters like me dare to dream.

Finally I thank each and every one who has been part of journey at IISER Pune. Each one I met here taught me some bitter sweet lessons for my life ahead.

Dedicated

To the loving memory of my dearest Papa

ABSTRACT

Endoplasmic Reticulum (ER) is a vital organelle involved in the synthesis and folding of proteins. Upon excessive cellular demands, this machinery escalates its production resulting in accumulation of several unfolded and misfolded proteins inside ER lumen. This condition is termed as Endoplasmic Reticulum Stress. To overcome this, a cytoprotective mechanism known as Unfolded Protein Response (UPR) is launched by the cell. However, upon prolonged ER stress, it morphs into terminal UPR and cells undergo apoptosis. Baseline activity level of ER stress response system is elevated in cancer cells than normal cells. ER stress is now found to be closely associated with several hallmarks of cancer and therefore it bears the potential to emerge as the new Achilles' heel in cancer. However, there are two specific challenges: ***(a) development of sub-cellular ER targeting tools and (b) development of ER stress inducers.*** To address these, we have engineered ER specific nanoparticles and spatially targeted anti-apoptotic Bcl-2 present there to induce ER stress in HeLa cells. Cellular internalization studies revealed that these nanoparticles internalized into the ER. Western blot analysis and cell viability studies revealed that ER stress induction was followed by autophagy. We then studied the location-function-relationship of Bcl-2 on ER and mitochondria. Subsequently, we explored graphene oxide (GO) and doxorubicin and cisplatin as ER stress inducers to engineer ER-GO-NPs. Fluorescence confocal microscopy revealed that these ER targeting GO-NPs successfully localized into ER in HeLa cervical cancer cells. Concomitant increase in ER stress marker CHOP indicated that these nanoparticles successfully induced ER stress and induced autophagy in HeLa cells. Combinatorial treatment with chloroquine (autophagy inhibitor) further improved the cell killing ability of the ER targeted nanoparticles. These ER-GO-NPs exhibited excellent cell killing ability over other cancer cell lines as well. Finally, to develop novel small molecule-based ER stress inducers, we synthesised a library of sulfonohydrazide-hydrazone based molecules and screened them against HeLa cell lines. Four molecules were identified as novel potential ER stress inducers, one of them being fluorescent. Further studies with the fluorescent derivative revealed its localization in ER within 3 h. Cell viability studies, immunofluorescence and western blot assays revealed that the fluorescent molecule induced ER stress in HeLa cells that was accompanied by autophagy induction. We anticipate that here presented approaches can serve as a tool to exploit ER stress as an alternative in future cancer therapy.

CONTENTS

SYNOPSIS

Endoplasmic reticulum (ER) is an important organelle found in the eukaryotic cells. It performs multitude of subcellular functions like synthesis and proper folding of proteins, lipid biogenesis and maintaining calcium homeostasis. Despite performing these crucial roles, the organelle has been largely unexplored. Endoplasmic reticulum can be regarded as the protein factory of the cell as it is the site where majority of proteins mature. Upon increased cellular demands, this factory escalates its production rate. However, this increased production comes with the price of accumulation of unfolded ad misfolded proteins in ER lumen leading to a condition called Endoplasmic Reticulum Stress (ER Stress). This stress if not mitigated can lead to cell death. In order to relieve the cells from this stress, the organelle launches an adaptive program termed as Unfolded Protein Response (UPR) with the primary aim of resolving the cellular stress. But, if the stress is intensified and cannot be resolved then this very adaptive program turns destructive and lead to cell death. Recently, ER stress and UPR have discovered to be linked with cancer and its hallmarks. ER stress thus can emerge as the new Achilles heel in cancer therapy. However, targeting ER stress is a daunting task due to limited availability of bio tools. Though significant progress has been made in exploiting the potential of ER stress and UPR as a promising strategy in cancer therapy (***Chapter 1***), a lot remains to be explored. In this thesis, we have tried to address these challenges by amalgamating the principles of organic synthesis, nanotechnology and chemical biology.

In ***Chapter 2***, we have engineered lipid based ER specific nanoplatforms that selectively accumulate in the subcellular ER of HeLa cells. These nanoparticles encaplsulated obatoclax a pan BCL-2 inhibitor. Upon their accumulation in ER, the ER specific nanoparticles (ER-Obt-NP) successfully inhibited the associated Bcl-2 protein and induces ER stress mediated apoptosis. We further observed that inhibition of ER associated Bcl-2 lead to induction of autophagy that enabled cell survival. Simultaneous inhibition of autophagy and Bcl-2 lead to improved efficacy of ER-Obt-NPs. We then studied the location-function relationship of Bcl-2 at ER and mitochondria. To accomplish that, we engineered mitochondria specific lipidic nanoparticles encapsulating obatoclax (Mito-Obt-NP) that selectively accumulated in mitochondria of HeLa cells and induced apoptosis. Interestingly, apoptosis induced in case of Mito-Obt-NPs was greater than ER-Obt-NPs. We thus established that mitochondrial Bcl-2 is more apt as a target in cancer therapy than its counterpart in ER.

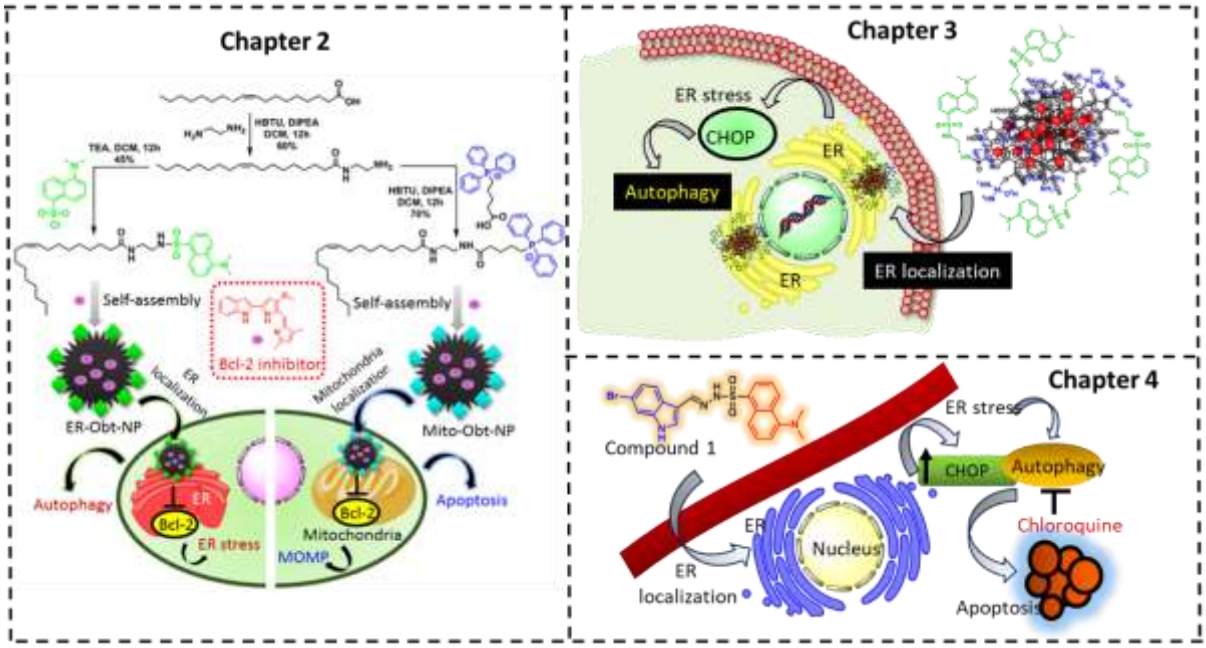

Scheme: Chemical tools to induce ER stress in Cancer Cells.

Graphene Oxide (GO) has revolutionized the field of cancer therapy due to its biocompatible and biodegradable properties. GO and GO based platforms are extensively being used as drug carriers to treat several malignancies. In our previous study, we had observed the self-assembly of GO sheets into 3D spherical nanoparticles of sub 200 nm diameter in presence of cisplatin. In ***Chapter 3,*** we have utilised this approach to engineer ER specific GO based nanoparticles encompassing two popular chemotherapeutic drugs, doxorubicin and cisplatin (ER-GO-NPs). These nanoparticles escaped the lysosomal pathway to localize in the ER and induced ER stress mediated apoptosis in HeLa cells. Furthermore, we observed induction of autophagy as an adaptive response to the induced ER stress. Combinatorial treatment of HeLa cells with ER-GO-NPs and chloroquine improved the cell killing efficacy of these nanoparticles. Interestingly, the nanoparticles exhibited remarkable efficacy over other cancer cell lines like MCF-7, A549 and MDA-MB-231.

Lastly, in ***Chapter 4*** we have used a concise and robust synthesis strategy to develop a library of 66 novel small molecules based on sulfonohydrazide- hydrazone based scaffold. Out of these, 4 molecules were identified as the potential ER stress inducers. Further studies with the lead molecule demonstrated its localization in ER within 6 h and induction of ER stress. The lipid accumulation in the HeLa cells and combinatorial treatment with 4- phenyl butyric acid established that the apoptosis induced by the molecule was indeed ER stress mediated. ER stress induction also lead to triggering of autophagy. Cotreatment of HeLa cells with the

molecule and chloroquine improved the apoptotic outcome. Interestingly the compound exhibited three fold high IC_{50} in the non-cancerous HEK-239 cell line. We also screened other cancer cell lines like MCF-7, A549 and MDA-MB-231 against the lead molecule. The molecule was found efficient over these cell lines as well.

We envision that the nanoplatforms and small molecules we presented here can be utilised in deciphering the location-function relationship of proteins at ER and mitochondria as well as in impairing multiple targets in ER and exploring ER biology for an improved cancer therapy.

LIST OF PUBLICATIONS

1. Spatial targeting of Bcl-2 on endoplasmic reticulum and mitochondria in cancer cells by lipid nanoparticles **S. Pandey**, S. Patil, N. Ballav, S. Basu*** *J. Mater. Chem. B,* 2020, 8, 4259-4266.**

2. Inducing Endoplasmic Reticulum Stress in Cancer Cells by Graphene Oxide-Based Nanoparticles **S. Pandey**, A. Nandi, S. Basu*, N. Ballav* ***Nanoscale Adv.,* 2020, 2, 4887-4894.**

3. Small Molecules as ER stress Inducers in Cancer Cells **S. Pandey**, V.K. Sharma, M. Lahiri, S. Basu* ***(Manuscript Under Revision)***

4. Hydrazide–Hydrazone Small Molecules as AIEgens: Illuminating Mitochondria in Cancer Cells S. Patil, **S. Pandey**, A. Singh, M. Radhakrishna, S. Basu* ***Chem. Eur. J.*, 2019, 25, 8229-8235.**

Chapter 1

Introduction

1.1 Endoplasmic Reticulum

Endoplasmic Reticulum (ER) is one of the vital organelles found in the eukaryotic cells.[1] Porter et.al. for the first time in 1945 using electron microscopy described ER as a membrane network of tubules and flattened sacs.[2] ER occupies almost 50% of the cytoplasm and is in contact with several important subcellular organelles like mitochondria and nucleus. [3-6] ER performs a plethora of essential subcellular functions. It is the central player in protein biogenesis and is involved in the synthesis, folding and post-translational modification of proteins. About one- third of all the cellular proteins are produced and modified in ER before they traverse to their final cellular or extracellular locations.[7-13] Certain molecular machines which consists of chaperones, foldases and quality control proteins are also found compartmentalized in the ER. These machines assist in the productive folding of the newly synthesized nascent proteins and modify them to their exportable forms. Apart from this, ER has a crucial role to play in lipid biosynthesis, maintaining calcium homeostasis, detoxification and regulating intracellular signalling pathways. [13-19] It is noteworthy, that in the due course of the process of protein synthesis in this machinery, a significant proportion of unfolded and misfolded proteins also exists. These proteins fail the ER quality control criteria and so they are addressed to the ER-associated degradation (ERAD) system which then guides these proteins to the cytosol for ubiquitinylation and proteasomal degradation.[20-22] Thus, not only ER is concerned with the biogenesis of proteins but also with the disposing off of the misfolded proteins. Apart from these, ER is also involved in the major cross talks with nucleus and mitochondria.[23,24] The regions of ER- mitochondria contact are of special importance. These are termed as mitochondria- associated membranes (MAMs) and are known to play crucial role in calcium homeostasis.[25-28]

1.1.1 Endoplasmic Reticulum Stress

Oxidative environment in the ER lumen is essential for optimum protein folding.[29,30] ER homeostasis is influenced by a multitude of cellular and extracellular parameters. Cellular stress like reduced glucose availability (hyperglycemia), limited oxygen supply (hypoxia) or changes in the cellular microenvironment like pH, hyperthermia or imbalance in calcium levels can disturb the ER homeostasis (Fig. 1.1).[31-33] Once the ER homeostasis gets perturbed it disrupts the protein translation machinery.[34] Under such conditions, to cope up with the increased cellular demands the protein synthesis gets escalated. As a result, several

unfolded and misfolded proteins that fail to comply with the ER protein quality control criteria start accumulating inside the ER lumen giving rise to a condition termed as Endoplasmic Reticulum Stress (ER stress).[32,35,36]

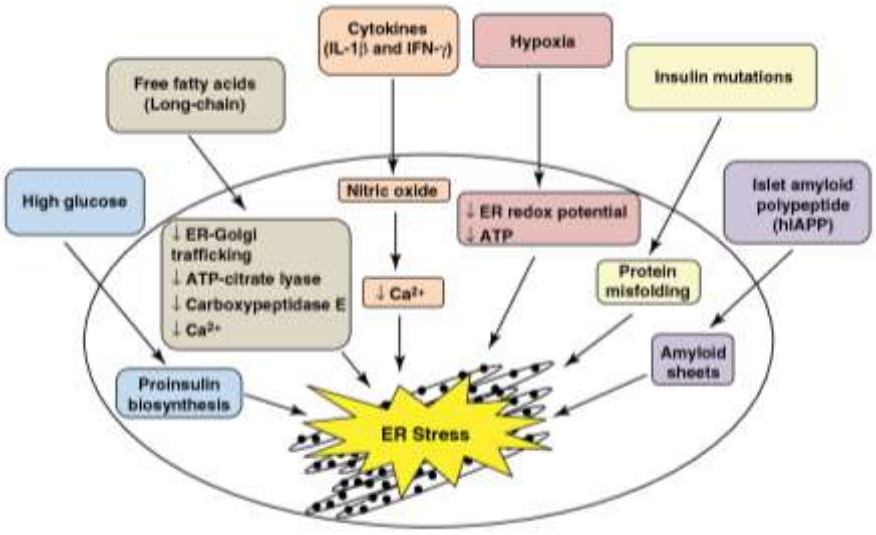

Figure 1.1: Causes of ER Stress. (Adapted from *Trends Endrocrinol. Metab.* **2011**, *22***,** 266-274**)**[33]

1.1.2 Unfolded Protein Response

Accumulation of these unfolded and misfolded proteins in the ER lumen presents a serious challenge to cell survival. To combat this situation, an adaptive response is launched by the cell to get rid of this baggage of unwanted proteins. This adaptive response is termed as Unfolded Protein Response (UPR) and it aims at restoring the fine-tuned balance of ER. Unfolded Protein Response operates through three distinct signalling pathways that are governed by pancreatic ER kinase- like ER kinase (PERK), Inositol - requiring enzyme 1α (IRE-1α), and activating transcription factor 6 (ATF6). These three different pathways work together to re-establish ER balance. [37-41] UPR is launched by the cell with the aim of restoring normalcy in ER functions by relieving it of the stress. This is achieved via blocking of further protein synthesis and increasing the production of chaperones that assist in protein folding. Glucose Regulated Protein 78 (GRP78) is an ER chaperone that plays an important role in UPR cascading pathway. Upon sensing the unfolded and misfolded proteins in the ER lumen, GRP78 dissociates from the three ER stress sensors: PERK, IRE-1α and ATF6. This triggers a series of events downstream the pathway (Fig. 1.2).[41-43]

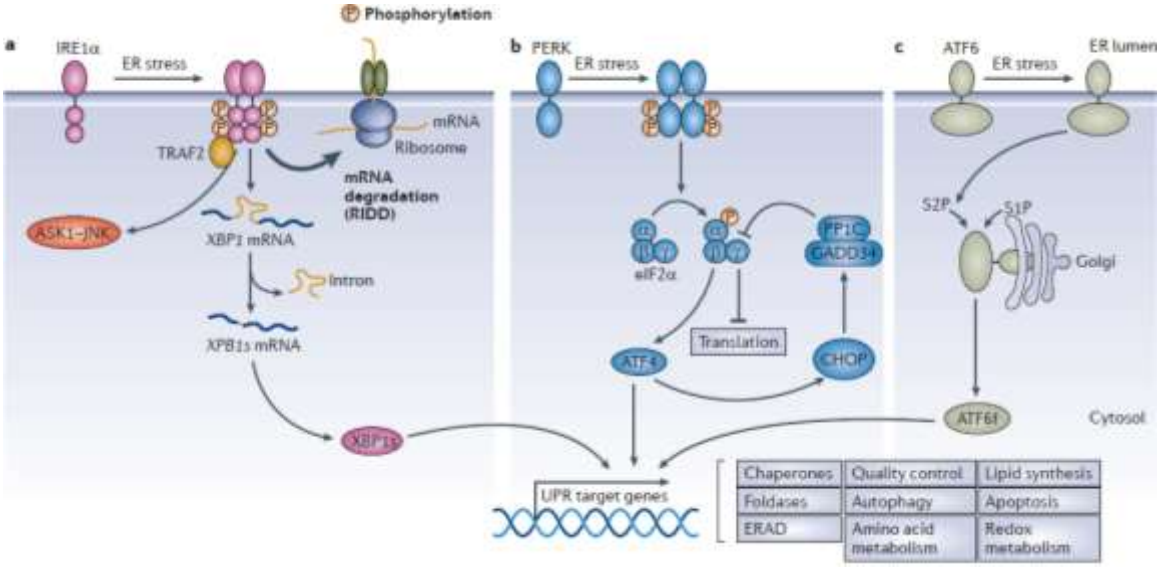

Figure 1.2: Mechanism of UPR. (Adapted from *Nat. Rev. Drug Discov*, **2013**, *12*, 703-719)[41]

Upon dissociation of GRP78, PERK homo- dimerizes and auto-phosphorylates, which in then followed by the phosphorylation of eukaryotic initiation factor-2α (eIF-2α). This decreases the influx of proteins in the ER lumen thereby limiting the load of accumulated proteins. Simultaneously, phosphorylation of eIF-2 α also results in activating transcription factor 4 (ATF 4) which activates genes responsible for protein metabolism.[44]

Dissociation of GRP78 from ER- membrane bound IRE-1α also results in its homo-dimerization and auto-phosphorylation. This activates IRE-1α which then assists the splicing of 26- base fragment of an mRNA that encodes for X-box binding protein 1 (XBP-1) resulting in spliced X- box binding protein (XBP-1s). The XBP-1s formed regulates the expression of various genes that are involved in ERAD and protein folding. Under ER stress condition, the ER membrane expands in order to contain the accumulated proteins in its lumen. XBP-1s also monitors the synthesis of phospholipids that are essential for the expansion of ER membrane. IRE- 1α arm of the UPR thus ensures to maintain ER folding capacity at par with the protein folding demands.[45-47]

ATF6, upon dissociation of GRP78 from its membrane, translocate to Golgi apparatus where it gets cleaved by site-1 protease (S1P) and site-2 protease (S2P). This S1P and S2P mediated proteolysis activates ATF6 which then migrates to the nucleus and regulate prominent ER chaperones like GRP94 and GRP78 and X-box binding proteins and protein disulphide isomerase (PDI) to enable protein folding and secretion.[48,49] The three branches

of UPR pathway thus work in coordination to resolve the ER stress by limiting the stock of accumulated unfolded proteins, enhancing protein folding capacity by regulating genes responsible for the same and directing the protein load beyond repair to the ERAD pathway, thus relieving cells from the burden of unfolded and misfolded proteins in ER lumen.

1.1.3 UPR and Cell Fate

Initially, UPR originates as an adaptive mechanism of the cell. However, the outcome of the UPR pathway depends upon the severity and duration of ER stress (Fig. 1.3). If the ER stress is excessive and cannot be resolved or if the UPR exists for a prolonged period of time but fails to restore the normalcy then under such conditions the proapoptotic module of the UPR gets activated and the cell is pushed towards apoptosis. UPR thus can evolve from its pro-survival form to proapoptotic form depending upon the cellular conditions.[50-52, 84]The proapoptotic arm of UPR is led by CHOP, the master regulator of ER assisted apoptosis, encoded by ATF4. Excessively high levels of CHOP can tip the balance off towards apoptosis to eliminate the stressed cells. UPR therefore serves two opposing functions: to mitigate the ER stress and support cell survival and ensure systematic destruction of cells when the ER stress threatens the existence of the organism as a whole.[53-55] However the mechanisms via which UPR performs these functions are still not completely understood.

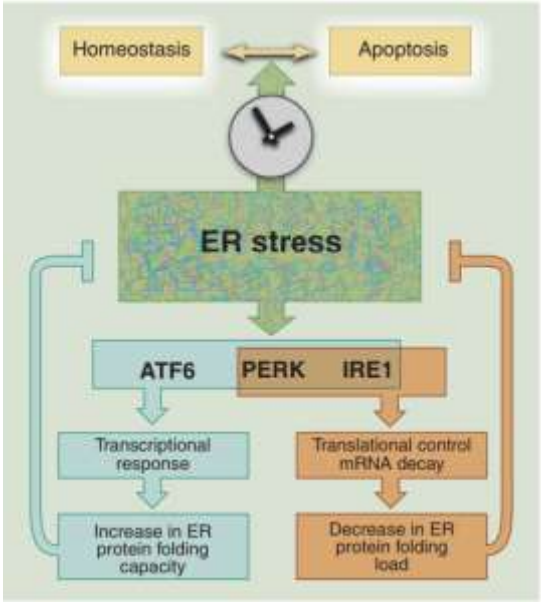

Figure 1.3: Outcome of ER stress (Adapted from *Science*, **2011,** *334*, 1081).[52]

1.1.4 ER stress and Autophagy

Additionally, it is now becoming quite evident that ER stress can also trigger onset of autophagy.[55-57] Activation of autophagy upon ER stress induction comes as no surprise since ER is known to have physical contact sites with endosomes, lysosomes and mitochondria. Omegasome is a specialized ER structure that form contact sites with phagophore which later matures into autophagasomes.[58,59] ER therefore, in coordination with other organelles governs the execution of autophagy. Autophagy is an intrinsic cytoprotective mechanism.[60] The word autophagy implies self-eating (auto: self, phagy: eating). It enables cells to endure detrimental conditions of low nutrient supply and other cellular insults by generating energy via recycling of cell's very own components. Of late, autophagy has begun to be recognized as an important player in life and death decision making of ER stress response system. Recent studies have demonstrated that ER stress and autophagy bear a reciprocal relationship to each other i.e. ER stress can trigger autophagy and blocking the autophagy can result in intensified ER stress.[32]

1.2 ER Stress, UPR and Cancer

ER coordinates with several other cell organelles and controls the major physiological processes in the cell. It is the hub of various signalling pathways and therefore ER stress finds its implications in the development of several human diseases. ER stress and UPR have begun to be recognized associated with a diverse range of diseases including diabetes, neurodegenerative disorders like Alzheimer's and Parkinson disease, cardiovascular diseases, cancer and autoimmunity.[61,62] Cancer, being the second leading cause of the death worldwide, becomes really important in this regard. Despite witnessing colossal advancements in the field of medicine, cancer still remains one of the deadly causes claiming 9.6 million lives worldwide.[63] Cancer cells continuously divide and proliferate and therefore conditions like limited nutrient and oxygen supply pose a serious challenge to tumor progression. To satisfy the demand of growing cells of surplus nutrients, an increased load is exerted by the cancer cells on the protein factory i.e. ER. As a result, cancer cells are subjected to high levels of ER stress. To combat the intrinsic perturbations that they experience, elevated levels of UPR are demonstrated in order to enhance protein folding and restore balance in ER functions. UPR thus acts as an adaptive mechanism that

enables cancer cells to acquire several characteristics to endure and survive the stress conditions. Lately, evidences have emerged that link UPR to many hallmarks of cancer including cell proliferation, invasion, angiogenesis, cell dormancy and cell death resistance. At least one of the three arms of UPR has been found to be elevated in cancer cells (Figure 1.4).[37] For example, PERK signalling pathway is illustrated to be involved in the initiation and progression of tumor types. PERK is also shown to negatively regulate the expression levels of cyclin D1 and induce cell cycle arrest in G1 phase leading to dormancy in tumors.[64] Likewise, the IRE- 1α branch of the UPR is believed to be implicated in tumor progression. Recently, it has been demonstrated in a glioblastoma model that this arm of UPR signalling pathway is crucial for tumor growth, angiogenesis and invasion.[65,66] Moreover, this IRE- 1α signalling axis is considered as potential cancer driver when mutated and is also linked to metastasis and chemotherapy resistance in cancer cells.[67] In fact, tumor dormancy has also been associated with their enhanced ATF6 levels. Dormant cells reactivate into full-fledged cancer tumor once they are in the optimum environmental conditions. These recurrent tumors exhibit high levels of ATF6. In human squamous carcinoma models, ATF6 is found active in the dormant cells.[68-70] These findings suggest that UPR is also one among the underlying causes of cancer recurrences. Thus, UPR and cancer progression are closely associated.

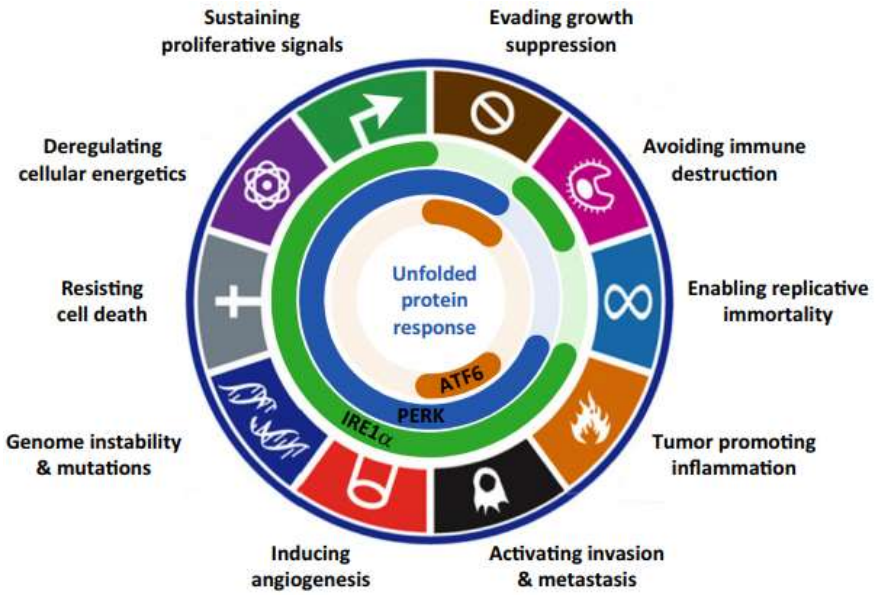

Figure 1.4: UPR and Hallmarks of Cancer (Adapted from *Trends Cancer* **2016**, *2*, 941-953)

However, there is another side to the coin too. Under circumstances when the ER stress cannot be subdued, its terminal arm dominates and proapoptotic effect of CHOP-the master regulator of ER associated apoptosis emerges. CHOP launches an apoptosis program wherein the proapoptotic BH3 proteins are enhanced and anti-apoptotic Bcl-2 proteins are repressed. In fact, ER stress has been deciphered in inducing apoptosis in B cell chronic lymphocytic lymphoma.[71] Additionally, recent studies have shown that inflammatory responses induced as an outcome of ER stress can inhibit tumor growth. Thus depending upon the intensity and the duration of ER stress, the UPR can morph itself from pro-survival to terminal. However, the mechanisms involved in this transition are not yet completely understood.[52]

1.3 ER stress as a Target in Cancer Therapy.

A remarkable point to be noted is that contrary to normal cells, majority of cancer types exhibit chronically elevated ER stress levels.[72] For example, overexpressed levels of GRP78 in cancer cells enable them to grow and survive in their sub optimal microenvironments and bestows them chemoresistance. These elevated levels of GRP78 in cancer cells represents a "chronic ER stress" condition which is opposite to the "no ER stress" condition of the normal cells.[32] Thus, while a large window is available for the normal cells to accommodate excess ER stress, the margin for already stressed cancer cells remains very small. As a result, cancer cells will reach the threshold value of ER stress easily and apoptosis will be triggered.[73] This very fact can be utilized in generating opportunities of therapeutic intervention specifically aimed at this stress response system. ER stress and UPR thus undoubtedly has the potential to emerge as the new Achilles heel in cancer therapy.[74]

Role of UPR in cancer prognosis has been suggested since mid-1990s but it was in 2004 when Ma and Henderson formally proposed it. With ER stress earning recognition of being associated with cancer and with new molecular mechanisms underlying their relationship being deciphered, new targets for drug development and new strategies of targeting ER signalling pathway have started emerging and the field has already witnessed some exciting developments.[41] For instance, KDEL peptide sequence is believed to be an ER localization signal and mediate protein trafficking to ER. Using this to their advantage Acharya et.al. reported the development of gold nanoparticles conjugated to KDEL peptide for siRNA delivery to ER. This was proven to be an efficient strategy in transfecting differentiated

myotubes.[75] On similar lines, Feng et.al. developed supramolecular self-assemblies of short peptides that specifically target ER and induce cell death in cancer cells selectively. These enzymatically prepared self-assemblies disrupted the plasma membrane, accumulated in ER and induced apoptosis via ER stress.[76] Ghosh et. al have also engineered supramolecular assembled hexameric rosette structure from a trisubstituted triazine and 5- fluorouracil molecules. These self-assembled nanostructures specifically target the ER of HeLa cervical cancer cells and induce ER stress mediated cell death.[77]

Nanotechnology is also being implored to develop ER targeting tools. Cancer therapy has already witnessed a paradigm shift due to the development of several nanomaterials for its diagnosis, drug-delivery and treatment. ER targeting is also witnessing new advancements with advent of lipid and polymer based nanotools.[78] Wang et.al. engineered PEGylated phospholipid micelles and employed them to induce ER dependent apoptosis in cancer cells but not in normal cells.[79] Sneh-Edri et. al. has reported PLGA based polymeric nanoparticles that are targeted to ER.[80] Small molecule-based approach to target and understand ER physiology are also emerging. For instance, Zhang et.al. developed ER targeted ratiometric probe for sensing hydrogen sulphide in living cells. This probe can provide insights in understanding physiological role of H_2S in ER and ER-related diseases.[81] Similarly, zinc ions are crucial for normal functioning of ER. Watkinson et.al. have synthesised ER localized fluorescent Zn^{2+} probes. These probes have been useful to detect mobile Zn^{2+} changes upon ER stress induction by tunicamycin and thapsigargin.[82] Such probes can provide a better understanding of mechanisms involved in progression of ER associated diseases.

Exploiting UPR in cancer therapy via development of ER stress inducers and UPR inhibitors is promising as the ER signalling pathway provides ample opportunities for the same. Thapsigargin is already established as an ER stress inducer. ERAD pathway clears the unwanted protein load and is activated in cancer cells so developing proteasome inhibitors seems to be a favourable strategy as proteasome activation is the main pathway for ERAD. Bortezomib is the first proteasome inhibitor approved for the treatment of multiple myeloma (MM). It is believed to induce caspase mediated apoptosis via intrinsic mitochondrial pathway and extrinsic death receptor pathway and interestingly, ER stress activates both of these. [32,41,73.]

Another interesting approach to manipulate ER stress is by modulating its markers or one or more arms of the UPR pathway. Cancer cells exhibit resistance to chemotherapy which is attributed to elevated levels of GRP78: a key ER stress marker. Knockdown of GRP78 increases the sensitivity of cancer cells against existing therapeutics and so developing GRP78 inhibitors is an attractive strategy.71 Epigallocatechin gallate, for example is an inhibitor of ATP domain of GRP78 that blocks its UPR prosurvival feature and sensitize glioma cells against chemotherapeutic agents.[71] Very recently, Rocchi et.al. developed small molecule that target GRP78 and enable melanoma cells to overcome resistance to BRAF inhibitors and showed anticancer activity.[83] Additionally, combination therapy for inhibiting GRP78 and regulating tumor growth is also promising.[73] Apart from GRP78, the three branches of UPR also seem to be an alluring target for developing ER stress inducers.[39,41] A decent progress is made in this context with the identification of several molecules as inhibitors of mediators of UPR signalling pathway (Fig. 1.5).[41] In conclusion, a good start has been made in the direction of targeting ER proteostasis in cancer by blocking one or more aspects of UPR.

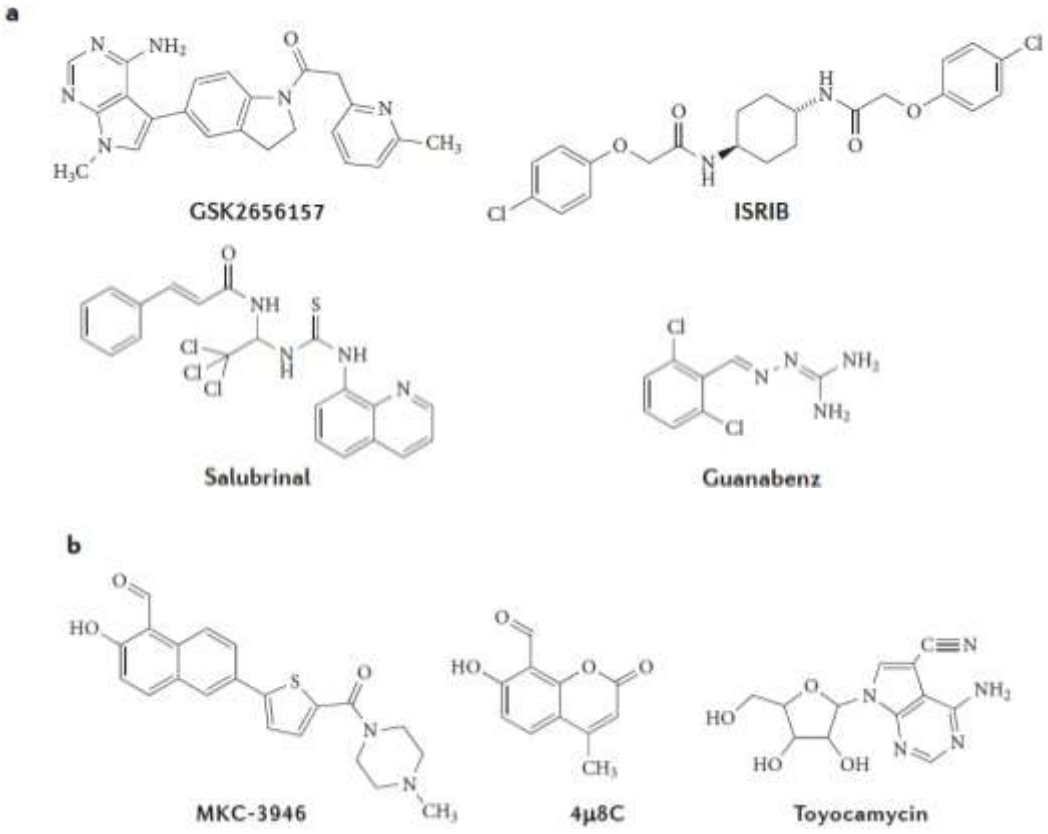

Figure 1.5: Pharmacological Modulators of (a) PERK signalling pathway (b) IRE-1α pathway. (Adapted from *Nat. Rev. Drug Discov*, **2013**, *12*, 703-719).[41]

While discussing the therapeutic potential of ER stress in cancer, simultaneously targeting autophagy deserves a mention. As elaborated in the chapter earlier, Autophagy like ER stress follows the yin-yang principle. Since it is both cytoprotective as well as destructive, initially this dual behaviour generated a lot of confusion in the community and still the process to exploit it for therapeutic benefit is not clear. But as they are inter-related simultaneously targeting both, ER stress and autophagy seems a promising strategy for improved therapeutic outcomes.[84]

1.4 Aim of thesis

Despite significant progress made in exploiting ER stress as a therapeutic target in cancer, the field is still in its infancy due to limited chemical tools. The main challenges that need to be addressed in this context are (i) development of subcellular ER targeting tools (ii) development of ER stress inducers.

To address these challenges, first we developed a novel lipid based nanoplatform to specifically target ER in cancer cells. We engineered oleic acid-based nanoparticles encapsulating obatoclax, a Bcl-2 inhibitor to spatially target the anti-apoptotic Bcl-2 at ER in HeLa cervical cancer cells. These nanoparticles successfully inhibited Bcl-2 and induced ER stress mediated apoptosis as well as autophagy in HeLa cells. Combinatorial treatment with chloroquine, an autophagy inhibitor significantly enhanced the efficacy of the nanoparticles. We also utilized these lipid based nanotools to study the location-function relationship of Bcl-2 at ER and mitochondria.

Subsequently, we developed an easy and robust synthesis of GO- based nanoplatform for selective targeting of ER in cancer cells. We capitalized upon the well-established chemotherapeutic drugs, doxorubicin and cisplatin that are already in clinics to treat several malignancies and engineered ER-GO-NPs. These nanoparticles were found to selectively accumulate in the subcellular ER of HeLa cells and induce ER stress mediated apoptosis along with induction of autophagy. Concomitant inhibition of autophagy improved the cell killing ability of these nanoparticles. Furthermore, the nanoparticles showed remarkable cell killing efficacy in different cancer cell lines including the drug resistant MDA-MB-231 breast cancer cells.

Finally, using a concise and robust synthetic scheme, we have developed a library of small molecules comprising of 66 molecules based on sulfonohydrazide-hydrazone based scaffold. The molecules were screened against HeLa cells at a concentration of 30 μM and

four molecules were identified as potential ER stress inducers. One of the hit molecules was fluorescent and therefore was explored for further studies. Confocal microscopy established that the molecule accumulated in the ER of HeLa cells within 6 h. Immunofluorescence and gel electrophoresis successfully demonstrated the onset of ER stress mediated apoptosis in HeLa cells along with autophagy upon treatment with the small molecule. Furthermore, the small molecule demonstrated improved therapeutic outcome upon co-treatment of cells with chloroquine and was effective on different cancer cell lines as well. We anticipate that these small molecules will be beneficial in understanding ER biology and development of future ER targeted therapeutics.

In summary, this thesis aims at design, development and validation of ER targeted nanoplatforms and small molecules to induce ER stress mediated apoptosis in cancer cells.

REFERENCES

1. D. S. Schwarz and M. D. Blower. The endoplasmic reticulum: structure, function and response to cellular signaling. *Cell Mol Life Sci*. **2016**, *73*, 79-94.
2. K. R. Porter, A. Claude and E. F. Fullam. 1945. A study of tissue culture cells by electron microscopy: methods and preliminary observations. *J Exp Med*, **81**, 233‑ 246.
3. M. J. Phillips and G. K Voeltz. Structure and function of ER membrane contact sites with other organelles. *Nat Rev Mol Cell Biol.,* **2016**, *17*, 69-82.
4. A. R. English and G. K. Voeltz. Endoplasmic reticulum structure and interconnections with other organelles. *Cold Spring Harb Perspect Biol*. **2013**, *5*, a013227.
5. Y. Wu, C. Whiteus, C. S. Xu, K. J. Hayworth, R. J. Weinberg, H. F. Hess, and P. De Camilli. Contacts between the endoplasmic reticulum and other membranes in neurons. *Proc. Natl. Acad. Sci. U.S.A.*, **2017**, *114*, E4859–E4867.
6. P. Pizzo and T. Pozzan. Mitochondria–endoplasmic reticulum choreography: structure and signaling dynamics. *Trends Cell Biol.*, **2007**, *17*, 511-517.
7. I. Kim, W. Xu and J. C. Reed. Cell death and endoplasmic reticulum stress: disease relevance and therapeutic opportunities. *Nat. Rev. Drug Discovery*, **2008**, *7*, 1013-1030.
8. Y. Ma and L. M. Hendershot. ER chaperone functions during normal and stress conditions *J. Chem. Neuroanat.*, **2004**, *28*, 51-65.

9. T. Anelli and R. Sitia. Protein quality control in the early secretory pathway. *EMBO J.*, **2008**, *27*, 315-327.
10. M. D. Shoulders, L. M. Ryno, J. C. Genereux, J. J. Moresco, P. G. Tu, C. Wu, J. R. Yates, Al. Su, J. W. Kelly and R. L. Wiseman. Stress-Independent Activation of XBP1s and/or ATF6 Reveals Three Functionally Diverse ER Proteostasis Environment. *Cell Rep.*, **2013**, *3*, 1279-1292.
11. R. Bravo-Sagua, A. E. Rodriguez, J. Kuzmicic, T. Gutierrez, C., Lopez-Crisosto, C. Quiroga, J. Díaz-Elizondo, M. Chiong, T. G. Gillette, B. A. Rothermel, and S. Lavandero. Cell death and survival through the endoplasmic reticulum-mitochondrial axis. *Curr Mol Med*., **2013**, *13*, 317-329.
12. K. Mori. Tripartite Management Minireview of Unfolded Proteins in the Endoplasmic Reticulum. *Cell*, **2000,** *101***,** 451-454.
13. C. Hetz. The unfolded protein response: controlling cell fate decisions under ER stress and beyond. *Nat. Rev. Mol. Cell Biol.*, **2012**, *13*, 89-102.
14. G. Jansen, P. Määttänen, A. Y. Denisov, L. Scarffe, B. Schade, H. Balghi, K. Dejgaard, L. Y. Chen, W. J. Muller, K. Gehring and D. Y. Thomas. An Interaction Map of Endoplasmic Reticulum Chaperones and Foldases. *Mol. Cell. Proteom*. **2012**, *11*, 710-723.
15. D. N. Hebert and M. Molinari. In and Out of the ER: Protein Folding, Quality Control, Degradation, and Related Human Diseases. *Physiol. Rev.*, **2007**, *87*, 1377-1408.
16. I. Braakman and D. N. Hebert. Protein folding in the endoplasmic reticulum. *Cold Spring Harb Perspect Biol*. **2013**, *5*, a013201.
17. A. Ciechanover and Y.T. Kwon. Protein Quality Control by Molecular Chaperones in Neurodegeneration. *Front. Neurosci.*, **2017,** *11*, 185.
18. J. Buchner. Molecular chaperones and protein quality control: an introduction to the JBC Reviews thematic series. *J. Biol. Chem.*, **2019**, *294*, 2074-2075.
19. R. V. Rao and D. E. Bredesen. Misfolded proteins, endoplasmic reticulum stress and neurodegeneration. *Curr Opin Cell Biol*. **2004**, *16*, 653-662.
20. L. Qi, B. Tsai and P. Arvan. New Insights into the Physiological Role of Endoplasmic Reticulum-Associated Degradation. *Trends Cell Biol*. **2017**, *27*, 430-440.
21. J. A. Olzmann, R. R. Kopito and J. C. Christianson. The mammalian endoplasmic reticulum-associated degradation system. *Cold Spring Harb Perspect Biol*. **2013**, *5*, a013185.
22. B. Meusser, C. Hirsch, E. Jarosch, and T. Sommer. ERAD: the long road to destruction. *Nat Cell Biol.*, **2005**, *7*, 766–772.

23. J. Häcki, L. Egger, L. Monney, S. Conus, T. Rossé, I. Fellay and C. Borner. Apoptotic crosstalk between the endoplasmic reticulum and mitochondria controlled by Bcl-2. *Oncogene*. **2000**, *19*, 2286-2295.
24. V. P. Nakka, P. Prakash-Babu and R. Vemuganti. Crosstalk Between Endoplasmic Reticulum Stress, Oxidative Stress, and Autophagy: Potential Therapeutic Targets for Acute CNS Injuries. *Mol Neurobiol.*, **2016**, *53*, 532-544.
25. M. Perrone, N. Caroccia, I. Genovese, S. Missiroli, L. Modesti, G. Pedriali, B. Vezzani, V. A. M. Vitto, M. Antenori, M. Lebiedzinska-Arciszewska, M. R. Wieckowski, C. Giorgi and P. Pinton. The role of mitochondria-associated membranes in cellular homeostasis and diseases. *Int. Rev. Cell Mol. Bio.*, **2020**, *350*, 119-196,
26. S. Patergnani, J. M. Suski, C. Agnoletto, A. Bononi, M. Bonora, E. De Marchi, C. Giorgi, S. Marchi, S. Missiroli, F. Poletti, A. Rimessi, J. Duszynski, M. R. Wieckowski and P. Pinton. Calcium signaling around Mitochondria Associated Membranes (MAMs). *Cell Commun Signal.*, **2011**, *9*, 19.
27. G. Morciano, S. Marchi, C. Morganti, L. Sbano, M. Bittremieux, M. Kerkhofs, M. Corricelli, A. Danese, A. Karkucinska-Wieckowska, M. R. Wieckowski, G. Bultynck, C. Giorgi and P. Pinton. Role of Mitochondria-Associated ER Membranes in Calcium Regulation in Cancer-Specific Settings. *Neoplasia*, **2018**, *20*, 510-523.
28. A. P. Arruda and G. S. Hotamisligil. Calcium Homeostasis and Organelle Function in the Pathogenesis of Obesity and Diabetes. *Cell Metab*., **2015,** *22*, 381-397.
29. M. Mullick and S. Nayak. Comprehending the Unfolded Protein Response as a Conduit for Improved Mesenchymal Stem Cell-Based Therapeutics. *Regen. Eng. Transl. Med.* **2020**, *6*, 179-188.
30. B. P. Tu, S. C. Ho-Schleyer, K. J. Travers and J. S. Weissman. Biochemical basis of oxidative protein folding in the endoplasmic reticulum. *Science*, **2000**, *290*, 1571-1574.
31. S. Chipurupalli, E. Kannan, V. Tergaonkar, R. D'Andrea and N. Robinson. Hypoxia Induced ER Stress Response as an Adaptive Mechanism in Cancer. *Int J Mol Sci*., **2019**, *20*, 749.
32. A. H. Schönthal. Endoplasmic reticulum stress: its role in disease and novel prospects for therapy. *Scientifica*, **2012**, *2012*, 857516.
33. S. G. Fonseca, J. Gromada, and F. Urano. Endoplasmic reticulum stress and pancreatic β-cell death. *Trends Endrocrinol. Metab.*, **2011**, *22*, 266-274.

34. J. Mandl, T. Mészáros, G. Bánhegyi and M. Csala. Endoplasmic Reticulum Stress: Control in Protein, Lipid, and Signal Homeostasis, *Mol. Endocrinol.*, **2013**, *27*, 384-393.
35. F. Navid and R. Colbert. Causes and consequences of endoplasmic reticulum stress in rheumatic disease. *Nat Rev Rheumatol*, **2017**,*13*, 25-40.
36. A. S. Lee and L. M. Hendershot. ER stress and cancer. *Cancer Biol Ther.*, **2006**, *5*, 721-722.
37. H. Urra, E. Dufey, T. Avril, E. Chevet and C. Hetz. Endoplasmic Reticulum Stress and Hallmarks of Cancer. *Trends Cancer* **2016**, *2*, 941-953.
38. M. Wang and R. J. Kaufman. Protein misfolding in the endoplasmic reticulum as a conduit to human disease. *Nature*, **2016**, *529*, 326-335.
39. D. Maly and F. R. Papa. Druggable sensors of the unfolded protein response. *Nat. Chem. Biol.*, **2014**, *10*, 892-901.
40. K. Raina, D. J. Noblin, Y. V. Serebrenik, A. Adams, C. Zhao and C. M. Crews. Targeted protein destabilization reveals an estrogen-mediated ER stress response. *Nat. Chem. Biol.*, **2014**, *10*, 957-962.
41. C. Hetz, E. Chevet and H. P. Harding. Targeting the unfolded protein response in disease. *Nat Rev Drug Discov.*, **2013**, *12*, 703-719.
42. M. Wang, S. Wey, Y. Zhang, R. Ye and A. S. Lee. Role of the unfolded protein response regulator GRP78/BiP in development, cancer, and neurological disorders. *Antioxid Redox Signal*., **2009**,*11*, 2307-2316.
43. G. Zhu and A. S. Lee. Role of the unfolded protein response, GRP78 and GRP94 in organ homeostasis. *J Cell Physiol*. **2015**, *230*,1413-1420.
44. D. R. Fels and C. Koumenis. The PERK/eIF2alpha/ATF4 module of the UPR in hypoxia resistance and tumor growth. *Cancer Biol Ther.*, **2006**, *5*, 723-728.
45. V. M. Parmar and M. Schroder. Sensing endoplasmic reticulum stress. *Adv. Exp. Med. Biol.*, 2012, 738, 153-168.
46. I. Braakman and N. J. Bulleid. Protein folding and modification in the mammalian endoplasmic reticulum. *Annu. Rev. Biochem.*, **2011**, *80*, 71-99.
47. R. Jäger, M. J. Bertrand, A. M. Gorman, P. Vandenabeele and A. Samali. The unfolded protein response at the crossroads of cellular life and death during endoplasmic reticulum stress. *Biol. Cell*, **2012**, *104*, 259-270.

48. Y. Adachi, K. Yamamoto, T. Okada, H. Yoshida, A. Harada, and K. Mori. ATF6 is a transcription factor specializing in the regulation of quality control proteins in the endoplasmic reticulum. *Cell Struct Funct.*, **2008**, *33*, 75-89.
49. H. Yoshida, T. Matsui, A. Yamamoto, T. Okada, and K. Mori. XBP1 mRNA is induced by ATF6 and spliced by IRE1 in response to ER stress to produce a highly active transcription factor. *Cell*, **2001**, *107*, 881-891.
50. C. Hetz. The unfolded protein response: controlling cell fate decisions under ER stress and beyond. *Nat. Rev. Mol. Cell Biol.*, **2012**, *13*, 89-102.
51. C. Xu, B. Bailly-Maitre and J. C. Reed. Endoplasmic reticulum stress: cell life and death decisions. *J Clin Invest*. **2005**,*115*, 2656-2664.
52. P. Walter and D. Ron. The Unfolded Protein Response: From Stress Pathway to Homeostatic Regulation. *Science*, **2011,** *334*, 108.
53. H. Nishitoh. CHOP is a multifunctional transcription factor in the ER stress response. *J. Biochem.*, **2012**, *151*, 217-219.
54. K. D. McCullough, J. L. Martindale, L. O. Klotz, T. Y. Aw, and N. J. Holbrook. Gadd153 sensitizes cells to endoplasmic reticulum stress by down-regulating Bc12 and perturbing the cellular redox state. *Mol. Cell Biol.*, **2001**, *21*, 1249-1259.
55. H. Puthalakath, L. A. O'Reilly, P. Gunn, L. Lee, P. N. Kelly, N. D. Huntington, P. D. Hughes, E. M. Michalak, J. McKimm-Breschkin, N. Motoyama, T. Gotoh, S. Akira, P. Bouillet and A. Strasser. ER stress triggers apoptosis by activating BH3-only protein Bim. *Cell*, **2007**, *129*, 1337-1349.
56. M. Ogata, S. I. Hino, A. Saito, K. Morikawa, S. Kondo, S. Kanemoto, T. Murakami, M. Taniguchi, I. Tanii, K. Yoshinaga, S. Shiosaka, J. A. Hammarback, F. Urano and K. Imaizumi. Autophagy is activated for cell survival after endoplasmic reticulum stress. *Mol. Cell.Biol.*, **2006**, *26*, 9220-9231.
57. T. Yorimitsu, U. Nair, Z. Yang, and D. J. Klionsky. Endoplasmic reticulum stress triggers autophagy. *J. Biol. Chem.*, **2006**, *281*, 30299-30304.
58. M. Hayashi-Nishino, N. Fujita, T. Noda, A. Yamaguchi, T. Yoshimori and A. Yamamoto. Electron tomography reveals the endoplasmic reticulum as a membrane source for autophagosome formation. *Autophagy*, **2010**, *6*, 301-303.
59. T. Uemura, M. Yamamoto, A. Kametaka, Y. S. Sou, A. Yabashi, A. Yamada, H. Annoh, S. Kametaka, M. Komatsu and S. Waguri. A cluster of thin tubular structures mediates transformation of the endoplasmic reticulum to autophagic isolation membrane. *Mol. Cell Biol.*, **2014**, *34*, 1695–1706.

60. I. Dikic and Z. Elazar. Mechanism and medical implications of mammalian autophagy. *Nat Rev Mol Cell Biol.* **2018**, *19*, 349-364.
61. H. Yoshida. ER stress and diseases. *FEBS J.*, **2007**, *274*, 630-658.
62. M. Kaneko, K. Imaizumi, A. Saito, S. Kanemoto, R. Asada, K. Matsuhisa and Y. Ohtake. ER Stress and Disease: Toward Prevention and Treatment. *Biol Pharm Bull.*, **2017**, *40*, 1337-1343.
63. F. Bray, J. Ferlay, I. Soerjomataram, R. L. Siegel, L. A. Torre and A. Jemal. Global cancer statistics 2018: GLOBOCAN estimates of incidence and mortality worldwide for 36 cancers in 185 countries. *CA Cancer J Clin.* **2018**, *68*, 394-424.
64. J. W. Brewer and J. A. Diehl. PERK mediates cell-cycle exit during the mammalian unfolded protein response. *Proc. Natl. Acad. Sci. U.S.A.*, **2000**, *97*, 12625-12630.
65. G. Auf, A. Jabouille, S. Guérit, R. Pineau, M. Delugin, M. Bouchecareilh, N. Magnin, A. Favereaux, M. Maitre, T. Gaiser, A. von Deimling, M. Czabanka, P. Vajkoczy, E. Chevet, A. Bikfalvi, and M. Moenner. Inositol-requiring enzyme 1alpha is a key regulator of angiogenesis and invasion in malignant glioma *Proc. Natl. Acad. Sci. U.S.A.*, **2010**, *107*, 15553-15558.
66. N. Dejeans, O. Pluquet, S. Lhomond, F. Grise, M. Bouchecareilh, A. Juin, M. Meynard-Cadars, A. Bidaud-Meynard, C. Gentil, V. Moreau, F. Saltel and E. Chevet. Autocrine control of glioma cells adhesion and migration through IRE1alpha-mediated cleavage of SPARC mRNA. *J. Cell Sci*. **2012**, *125*, 4278-4287.
67. A. N. Shajahan, R. B. Riggins and R. Clarke. The role of X-box binding protein-1 in tumorigenicity. *Drug News Perspect*. **2009**, *22*, 241-246.
68. M. A. Ginos, G. P. Page, B. S. Michalowicz, K. J Patel, S. E Volker, S. E Pambuccian, F. G Ondrey, G. L. Adams and P. M Gaffney. Identification of a gene expression signature associated with recurrent disease in squamous cell carcinoma of the head and neck. *Cancer Res.* **2004**, *64*, 55-63.
69. S. Ramaswamy, P. Tamayo, R. Rifkin, S. Mukherjee, C. H. Yeang, M. Angelo, C. Ladd, M. Reich, E. Latulippe, J. P. Mesirov, T. Poggio, W. Gerald, M. Loda, E. S. Lander and T. R. Golub. Multiclass cancer diagnosis using tumor gene expression signatures. *Proc. Natl. Acad. Sci. U.S.A.* **2001**, *98*, 15149-15154.
70. D. M. Schewe and J. A. Aguirre-Ghiso. ATF6alpha–Rheb– mTOR signaling promotes survival of dormant tumor cells in vivo. *Proc. Natl. Acad. Sci. U.S.A.* **2008**, *105*, 10519-10524.

71. Y. Li, Y. Guo, J. Tang, J. Jiang and Z. Chen. New insights into the roles of CHOP-induced apoptosis in ER stress, *Acta Biochimica et Biophysica Sinica*, **2014**, *46*, 629-640.
72. A. D. Garg, H. Maes, A. R. van Vliet and P. Agostinis. Targeting the hallmarks of cancer with therapy-induced endoplasmic reticulum (ER) stress. *Mol. Cell. Oncol.*, **2015**, *2*, e975089.Scho
73. R. K. Yadav, S. W. Chae, H. R. Kim and H. J. Chae. ER stress and cancer. *J Cancer Prev*, **2014**, *19*, 75-88.
74. L. Vincenz, R. Jäger, M. O'Dwyer and A. Samali. Endoplasmic reticulum stress and the unfolded protein response: targeting the Achilles heel of multiple myeloma. *Mol Cancer Ther.* **2013**, *12*, 831-843.
75. S. Acharya and R. A. Hill. High efficacy gold-KDEL peptide-siRNA nanoconstruct-mediated transfection in C2C12 myoblasts and myotubes. *Nanomedicine*, **2014**, *10*, 329-37.
76. Z. Feng, H. Wang, S. Wang, Q. Zhang, X. Zhang, A. A. Rodal and B. Xu. Enzymatic Assemblies Disrupt the Membrane and Target Endoplasmic Reticulum for Selective Cancer Cell Death. *J. Am. Chem. Soc.*, 2018, *140*, 9566-9573.
77. C. Ghosh, A. Nandi and S. Basu. Supramolecular self-assembly of triazine-based small molecules: targeting the endoplasmic reticulum in cancer cells. *Nanoscale*, **2019**,*11*, 3326-3335.
78. Y. Cao, J. Long, L. Liu, T. He, L. Jiang, C. Zhao and Z. Li. A review of endoplasmic reticulum (ER) stress and nanoparticle (NP) exposure. *Life Sci.* **2017**, *186*, 33-42.
79. J. Wang, X. Fang and W. Liang. Pegylated phospholipid micelles induce endoplasmic reticulum-dependent apoptosis of cancer cells but not normal cells. *ACS Nano* **2012**, *6*, 5018-5030.
80. H. Sneh-Edri, D. Likhtenshtein and D. Stepensky. Intracellular targeting of PLGA nanoparticles encapsulating antigenic peptide to the endoplasmic reticulum of dendritic cells and its effect on antigen cross-presentation in vitro. *Mol. Pharmaceutics* **2011**, *8*, 1266-1275.
81. W. Shu, S. Zang, C. Wang, M. Gao, J. Jing and X. Zhang. An Endoplasmic Reticulum-Targeted Ratiometric Fluorescent Probe for the Sensing of Hydrogen Sulfide in Living Cells and Zebrafish. *Anal. Chem.* **2020**, *92*, 9982-9988.

82. L. Fang, G. Trigiante, R. Crespo-Otero, C. S. Hawes, M. P. Philpott, C. R. Jones and M. Watkinson. Endoplasmic reticulum targeting fluorescent probes to image mobile Zn^{2+}. *Chem. Sci.*, **2019**, *10*, 10881-10887.
83. M. Cerezo, A. Lehraiki, A. Millet, F. Rouaud, M. Plaisant, E. Jaune, T. Botton, C. Ronco, P. Abbe, H. Amdouni, T. Passeron, V. Hofman, B. Mograbi, A. S. Dabert-Gay, D. Debayle, D. Alcor, N. Rabhi, J. S. Annicotte, L. Héliot, M. Gonzalez-Pisfil, C. Robert, S. Moréra, A. Vigouroux, P. Gual, M. M. U. Ali, C. Bertolotto, P. Hofman, R. Ballotti, R. Benhida and S. Rocchi. Compounds Triggering ER Stress Exert Anti-Melanoma Effects and Overcome BRAF Inhibitor Resistance. *Cancer Cell*. **2016**, *29*, 805-819.
84. A. H. Schönthal. Endoplasmic reticulum stress and autophagy as targets for cancer therapy. *Cancer Lett,* **2009,** *275*, 163-169.

Chapter 2
Spatial Targeting of Spatial targeting of Bcl-2 on Endoplasmic Reticulum and Mitochondria in Cancer Cells by lipid nanoparticles

This chapter has been published as

Shalini Pandey, Sohan Patil, Nirmalya Ballav and Sudipta Basu. Spatial targeting of Bcl-2 on endoplasmic reticulum and mitochondria in cancer cells by lipid nanoparticles. *J. Mater. Chem. B*, **2020,** 8, 4259-4266

2.1 Abstract

The presence of the same proteins at different sub-cellular locations with completely different functions adds to the complexity of signalling pathways in cancer. Subsequently, it becomes indispensable to understand the diverse critical roles of these proteins based on their spatial distribution for the development of improved cancer therapeutics. To address this, in this work, we report the development of endoplasmic reticulum (ER) and mitochondria targeted nanoscale particles to spatially impair anti-apoptotic Bcl-2 protein in these organelles in HeLa cervical cancer cells. Confocal microscopy and gel electrophoresis confirmed that these nanoparticles selectively home into ER and mitochondria and inhibited Bcl-2 localized there. Interestingly, Bcl-2 inhibition in ER induced ER stress leading to autophagy, whereas inhibition of Bcl-2 in mitochondria leads to mitochondrial damage and programmed cell death (apoptosis) in HeLa cells. These nanoscale platforms can be further explored as chemical biology tools to decipher the location–function relationship of proteins towards next generation cancer therapeutics.

2.2 Introduction

Cancer is a dynamic disease and is regarded as the second leading cause of death globally.[1–3] Despite the rapid advances made in the field of cancer biology and its therapeutic development, carcinogenesis still remains a very complex phenomenon, which can be attributed to the intricate cellular signalling networks involved in the process.[4,5] A plethora of proteins constitute the architecture of these pathways. These signalling proteins that serve as nodes to generate different responses in the cell have been explored as the potential targets for cancer therapy.[6–8] Increasing evidence suggests that the spatial location of these signalling proteins is crucial in deciding and regulating the outcome of the signalling pathway and thus the cellular behaviour.[8,9] For instance, Park and co-workers showed that apoptozole, an inhibitor of Hsp 70, induced cell death *via* distinctly different pathways depending upon its localization in the lysosomes or mitochondria.[10] Apoptozole localized in lysosomes induced apoptosis and disrupted autophagy. On the other hand, apoptosis was induced without affecting autophagy when it localized into the mitochondria of cancer cells. Thus, it becomes imperative to understand the behaviour at their spatial localization for a better understanding of the outputs of the signalling pathway. Not only will it lead to exploring their individual potential as a

therapeutic target but it will also lead to the development of novel rational strategies for cancer therapy and improving the efficacy of the existing ones.

The Bcl-2 family is one such family of spatially different proteins that has garnered a lot of attention as a potential target in cancer treatment.[11,12] These gatekeepers of apoptosis have diverse intracellular locations and are found residing in cytosol, endoplasmic reticulum, mitochondria and nucleus.[12–15] The functions of Bcl-2 localized at the endoplasmic reticulum (ER) and mitochondria are entirely different. Bcl-2 in ER is known to mitigate ER stress, which leads to the unfolded protein response (UPR).[16,17] However, Bcl-2 in mitochondria initiates apoptosis by permeabilization of mitochondrial outer membrane (MOMP) followed by cytochrome *c* release.[18–21] Evasion of apoptosis is one of the critical hallmarks of cancer and it is not surprising that increased levels of pro-survival proteins are a common phenomenon in many cancer types.[22–26] Deregulation of the Bcl-2 proteins has thus paved the way for the development of pro-survival Bcl-2 inhibitors.[27] Hence, spatial targeting of pro-survival Bcl-2 proteins in different sub-cellular locations can give rise to different therapeutic outcomes towards cancer therapeutics. However, developing the chemical tools to target diverse organelles in cellular milieu is highly challenging and less explored until now.

Genetic tags with small molecule dyes, fluorescent proteins and quantum dots have been developed for the spatial targeting of proteins. However, the significant limitations associated with them are the lack of specificity, high background staining, restrictions in the usage of targeting in live cells and the exorbitant cost associated with their development.[28] Hence, there is a severe need to develop cost-effective, easily synthesizable chemical probes that can localize into the specific organelles having our protein of interest. Spatial targeting will be beneficial in understanding the importance of the spatial location of the protein for future cancer therapeutics. To address this, herein, we have amalgamated the principles of synthetic chemistry and nanoparticle engineering to selectively target the anti-apoptotic Bcl-2 at the endoplasmic reticulum (ER) and mitochondria respectively in cancer cells. We have developed ER and mitochondria specific oleic acid-based lipophilic molecules and engineered self-assembled spherical nanoparticles containing Obatoclax, a pan-Bcl-2 inhibitor. These nanoparticles internalized specifically into mitochondria and ER through lysosomes in HeLa cervical cancer cells within 3 h and 6 h, respectively, generated reactive oxygen species (ROS) and inhibited Bcl-2 in the respective organelles. The ER targeted nanoparticles (ER-Obt-NPs) induced ER stress followed by triggering early and late apoptosis. This ER stress induction led to autophagy, which can be inhibited by a combination treatment with chloroquine (autophagy

inhibitor). In contrast, mitochondria targeted nanoparticles (Mito-Obt-NPs) inhibited anti-apoptotic Bcl-2/Bcl-xL and led to a high amount of late apoptosis through caspase-3/9 cleavage in HeLa cells. We have thus shown that nanoparticle-mediated spatial targeting of Bcl-2 produces different outcomes in cancer cells. Furthermore, the localization of the inhibitor in the correct organelle resulted in its improved efficacy. We anticipate that this approach can be explored to study the therapeutic potential of various spatially and functionally different proteins residing in different organelles in cancer cells.

2.3 Results and Discussion

2.3.1 Engineering Nanoparticles for Spatial Targeting of Endoplasmic Reticulum and Mitochondria. To selectively target the nanoparticles for ER, we took advantage of the lipid flux present there. Lipophilic molecules are known to home into ER, so we chose the biocompatible oleic acid (1) (Scheme 1a).[29] We reacted ethylenediamine with oleic acid in presence of O-(benzotriazol-1-yl)- *N,N,N′,N′*-tetramethyluronium hexafluorophosphate (HBTU) and diisopropyl ethylamine (DIPEA) as coupling agents to synthesize oleic acid-ethylenediamine conjugate (2) in 60% yield.[30] We further reacted dansyl chloride (3) with compound **2** to obtain an oleic acid-ethylenediamine-dansyl conjugate (4) in 45% yield. Sulphonamide linkage in the probe (4) aided its binding to the sulphonamide receptors present in the ER.[31–34] On the other hand, mitochondrial membrane is known to have a large negative membrane potential, which allows positively charged lipophilic cations to easily pass through it and accumulate in the mitochondrial matrix.[35,36] Hence, we reacted (4-carboxybutyl) triphenylphosphonium bromide (5) with conjugate 2 in the presence of HBTU and DIPEA as coupling agents to obtain the oleic acid-ethylenediamine-TPP conjugate (6) in 70% yield (Scheme 1).[37] We characterized all the compounds using $^{1}H/^{13}C$ NMR and MALDI-TOF spectra (Appendix-A; Figure A1-6). We also characterized compound 6 using ^{31}P NMR spectroscopy (Appendix-A; Figure A7).

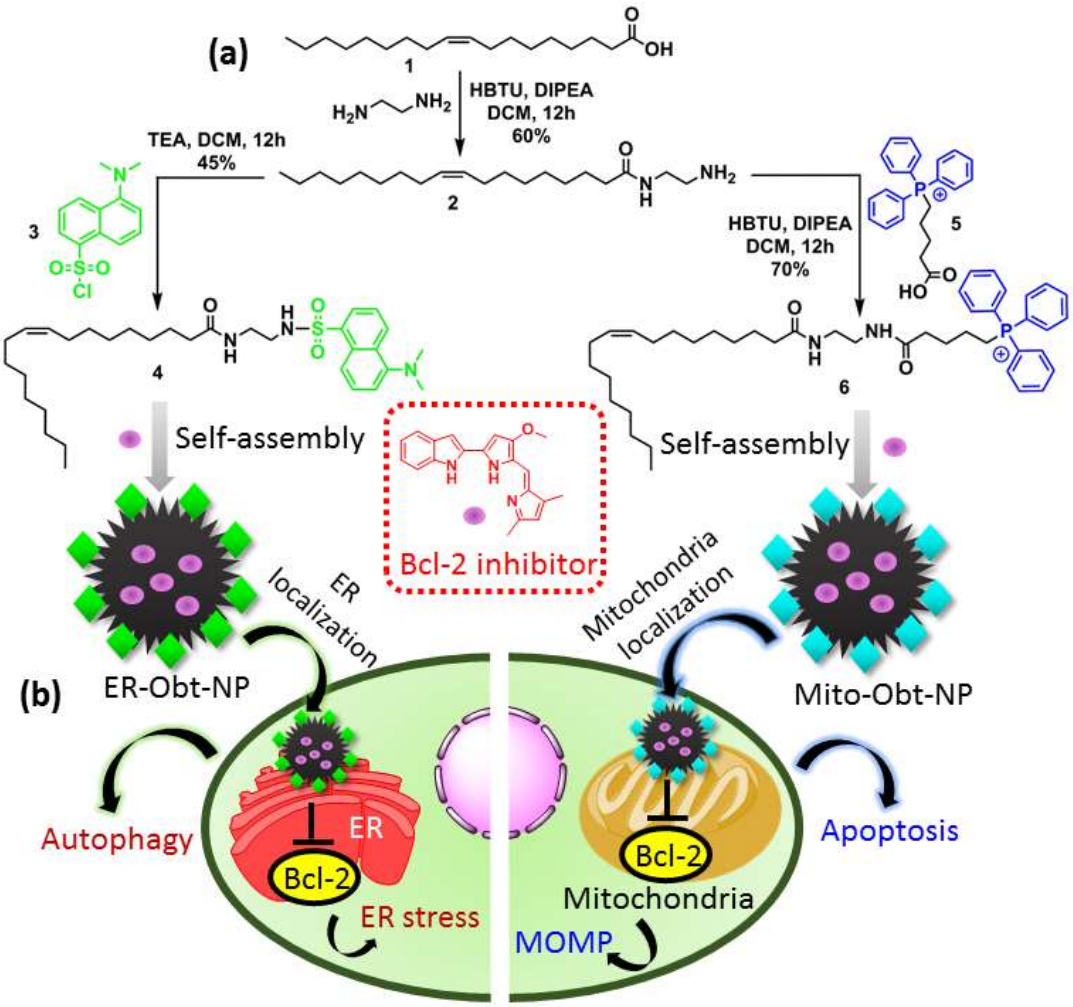

Scheme 2.1: (a) Synthetic scheme of oleic acid-dansyl and oleic acid-TPP conjugates and ER-Obt-NPs and Mito-Obt-NPs. (b) Schematic representation of mechanism of action of ER-Obt-NPs and Mito-Obt-NPs in HeLa cervical cancer cells.

We then engineered ER and mitochondria targeted, obatoclax loaded nanoparticles from conjugates 4 and 6 respectively, by thin lipid film hydration-extrusion technique.[38] Obatoclax, a small molecule, acted as the Bcl-2 inhibitor and also enabled monitoring of the subcellular localization of the nanoparticles due to its intrinsic red fluorescence.[39] Dynamic light scattering revealed the hydrodynamic diameter of ER-Obt-NPs and Mito-Obt-NPs to be 89 nm and 136 nm, respectively (Fig. 2.1a and b) with a polydispersity index (PDI) of 0.151 and 0.385, respectively. This suggested that the nanoparticles were monodispersed and within the suitable size range of sub-200 nm to home into the tumor tissues by the enhanced permeability and retention (EPR) effect.[40] The surface charge of Mito-Obt-NPs was evaluated by zeta potential analysis and found to be +29.8 mV (Fig. 2.1c), which was suitable for mitochondria localization.[41] Interestingly, we also found the zeta potential of ER-Obt-NPs to be +10.4 mV

(Fig. 2.1d). Although the same lipid was used to synthesize both the nanoparticles, the difference in size could be attributed to a huge difference in the steric bulk of the TPP moiety compared to the dansyl moiety, which increases the size of Mito-ER-NPs compared to ER-Obt-NPs. Moreover, the dansyl moiety can be involved in π–π stacking interaction leading to a more compact and smaller size of ER-Obt-NPs compared to Mito-Obt-NPs. FESEM and AFM images also confirmed the spherical morphology of the nanoparticles (Fig. 2.1e-h).

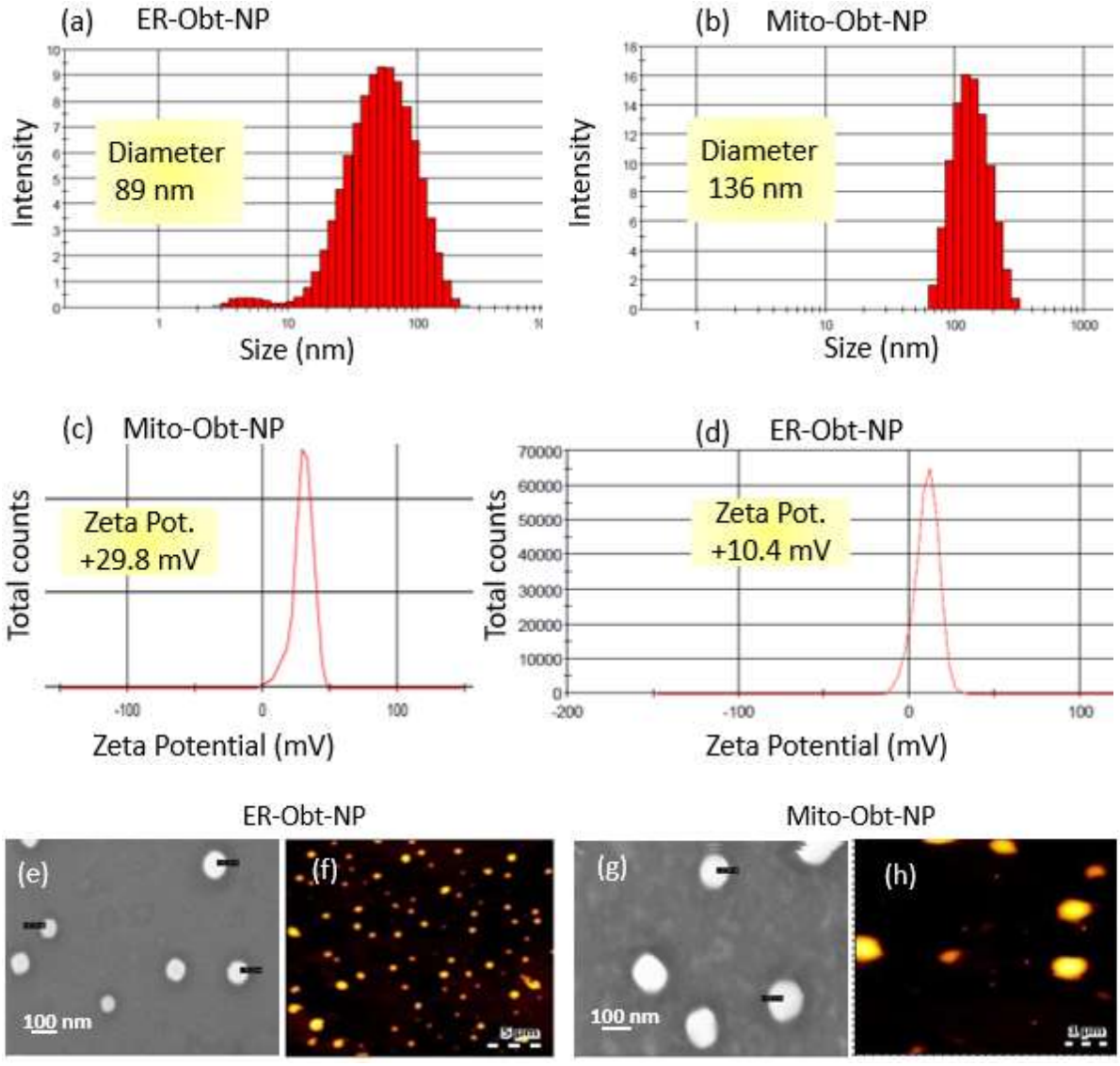

Figure 2.1: (a, b) Hydrodynamic diameter of ER-Obt-NPs and Mito-Obt-NPs from DLS. (c, d) Zeta potential of Mito-Obt-NPs and ER-Obt-NPs by DLS. (e, g) FESEM images of ER-Obt-NPs and Mito-Obt-NPs. (f, h) AFM images of ER-Obt-NPs and Mito-Obt-NPs.

Loading of obatoclax was evaluated by UV-Vis spectroscopy at the characteristic λ_{max} = 488 nm. The loading was estimated to be 785 μM (loading efficiency = 54.1%) and 500 μM (loading efficiency = 34.4%) for ER-Obt-NPs and Mito-Obt-NPs, respectively (Fig. 2.2a). Further, the weight% of obatoclax in the solid lipid particles was calculated to be 30.3% and 59.2% in Mito-Obt-NPs and ER-Obt-NPs, respectively. We also evaluated the stability of the nanoparticles at 37 °C in PBS for 6 days by using DLS, which clearly showed marginal changes in hydrodynamic diameter (Fig. 2.2b). To understand the stability in biological fluid, we incubated both the nanoparticles in DMEM cell culture media with 10% Fetal Bovine Serum (FBS) at 37 °C for 6 days and evaluated the hydrodynamic diameter. We observed that the size of ER-Obt-NPs increased from 88.9 nm to 168.7 nm on day 4. However, the size dramatically reduced to 123.5 nm on day 6 (Fig. 2.2c). On the other hand, the size of Mito-Obt-NPs changed marginally from 137.8 nm to 134.0 nm over 4 days. Again, the size of Mito-Obt-NPs on day 6 reduced to 97.6 nm (Fig. 2.2c). This stability assay demonstrated that both the nanoparticles are stable in cellular milieu for 4 days. This experiment confirmed that the nanoparticles retained their sub-200 nm size for over a week in a physiological medium and for 4 days in biological medium.

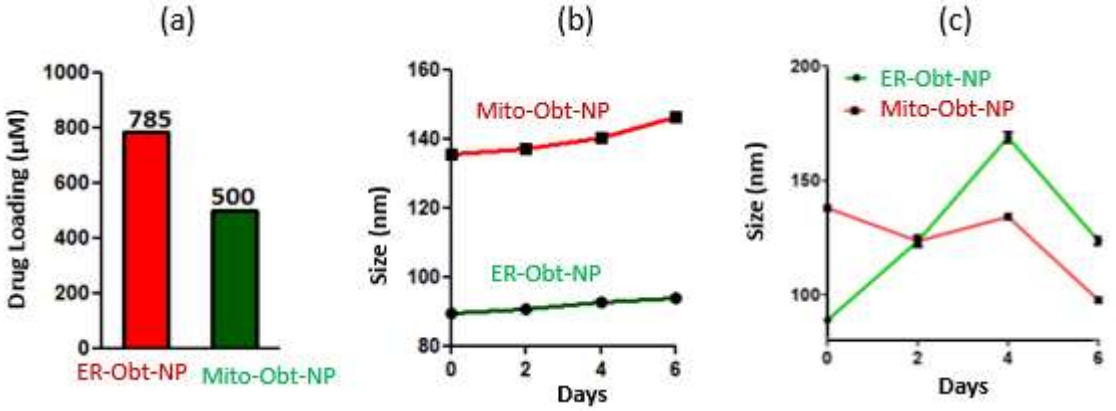

Figure 2.2: (a) Drug loading of ER-Obt-NP and Mito-Obt-NP calculated at λmax= 488 nm using UV-Vis spectroscopy. (b,c) Stability of the nanoparticles in PBS and in DMEM cell culture media with 10% FBS at 37ºC respectively.

2.3.2 Subcellular Localization of Nanoparticles. We first evaluated the localization of the organelles targeted nanoparticles in HeLa cervical cancer cells by fluorescence confocal microscopy. We incubated the HeLa cells with the red fluorescent ER-Obt-NPs in a time-dependent manner (3 h, 6 h and 24 h) and co-stained ER with ER-Tracker Green dye followed

by visualization by confocal microscopy. Live cell images revealed that the ER-Obt-NPs began to accumulate into the ER within 3 h and retained there for 24 h (Fig. 2.3). Confocal image-based quantification using Pearson's and Mander's coefficient confirmed that ER-Obt-NPs localised into ER with 0.71, 0.83 and 1.0 of Mander's coefficients (M2) for 3 h, 6 h and 24 h time points respectively (Table A1, Appendix-A). These confocal images evidently showed that the ER targeted nanoparticles home into the ER in a time-dependent manner.

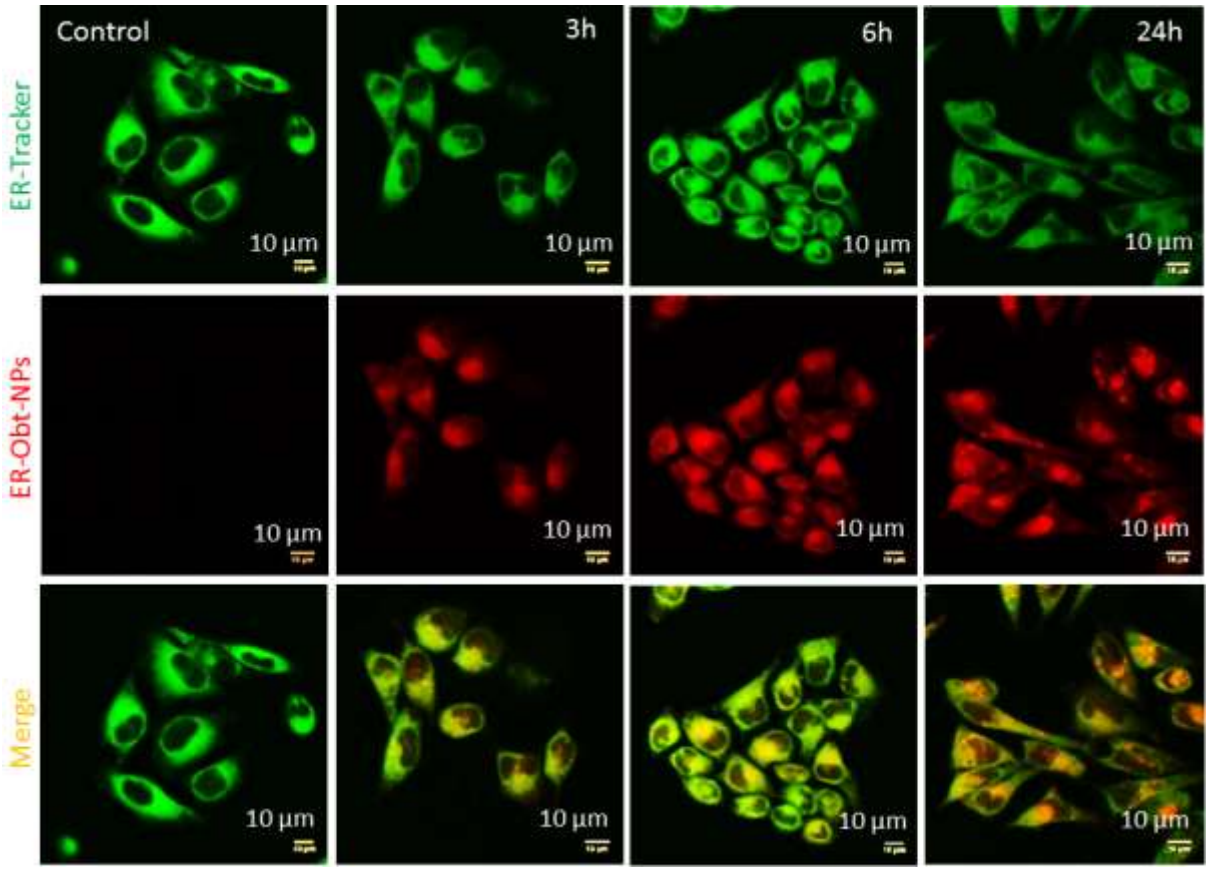

Figure 2.3: Confocal microscopy images of HeLa cells treated with red fluorescent ER-Obt-NPs at 3 h, 6 h and 24 h. ER were stained with green fluorescent ER Tracker Green. Scale bar =10 µm.

We further evaluated the cellular uptake mechanism of ER-ObtNPs in HeLa cervical cancer cells using confocal microscopy. We hypothesised that ER-Obt-NPs would internalize in the lysosomes first. To substantiate this hypothesis, we stained the lysosomes with Lyso-Tracker Green DND-26 and counter stained the nuclei with Hoechst 33342 (blue) dye. We incubated the HeLa cells with ER-Obt-NPs at different time points 1 h, 3 h and 6 h and visualized the cells under fluorescence confocal microscopy. Merging of red and green images leading to yellow colour in confocal images confirmed that the nanoparticles localized into the lysosomes

within 1 h (Fig. 2.4). Further quantification revealed the change in Mander's coefficients (M2) from 0.57 to 0.72 to 0.67 at 1h, 3h and 6h respectively (Table A2, Appendix-A). This confocal imaging indicated that ER-ObtNPs internalized into lysosome slowly within 1 h and escaped from the lysosomes over a period of 6 h. This confocal microscopy confirmed that ER-Obt-NPs localized into the lysosomes within 1 h and escaped to further localize into ER within 6 h and remained there for 24 h.

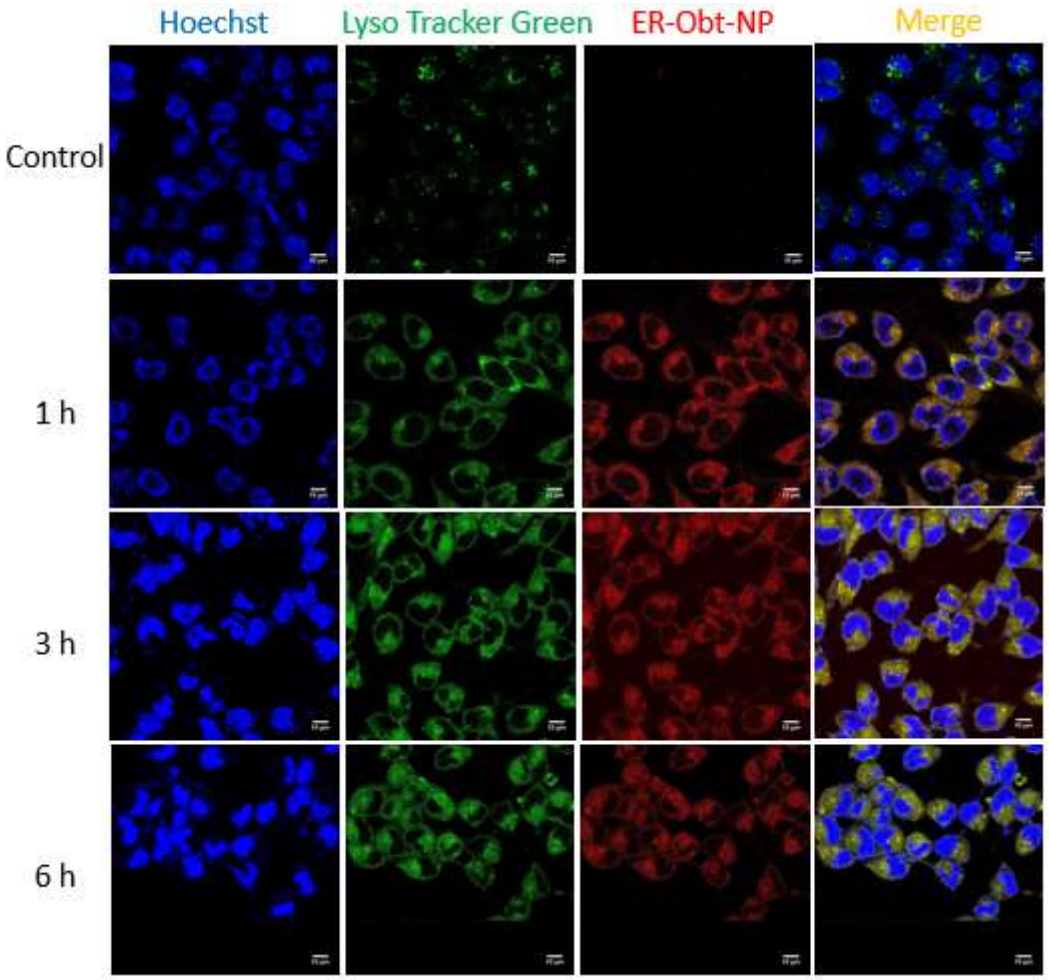

Figure 2.4: Confocal microscopy images of HeLa cells treated with red fluorescent ER-Obt-NPs at 1 h, 3 h and 6 h. Lysosomes were stained with LysoTracker Green. Scale bar = 10 μm.

To evaluate the trafficking of Mito-Obt-NPs, we incubated the HeLa cells with the nanoparticles for 3 h, 6 h and 24 h and costained mitochondria with MitoTracker Green dye followed by imaging through confocal microscopy. The merging of green and red fluorescence to yield yellow fluorescence signals in confocal images confirmed that the Mito-Obt-NPs homed into mitochondria within 3 h and retained there for 6 h with less intensity at 24 h (Fig.

2.5). The confocal microscopy-based quantification also corroborated that the Mito-Obt-NPs localized in the mitochondria with 0.93, 0.86 and 0.47 Mander's coefficients at 3 h, 6 h and 24 h respectively (Table A3, Appendix-A). In our previous study, we have shown that mitochondria-targeted nanoparticles after cellular uptake would localize in the lysosomes within 1 h but after 6 h managed to escape the lysosomes and localized into mitochondria.[41] Hence, these confocal microscopy studies demonstrated that both the nanoparticles home into their desired organelles in a time dependent manner and retained there for 24 h.

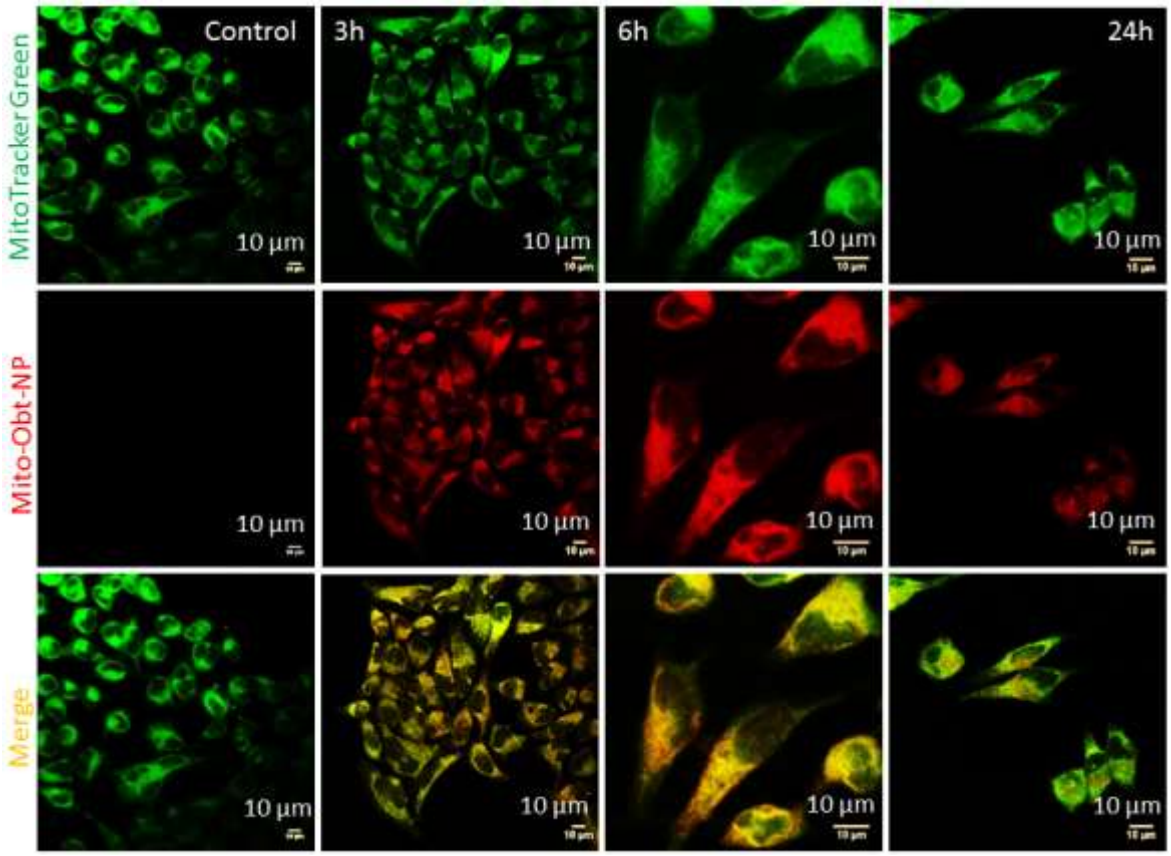

Figure 2.5: Confocal microscopy images of HeLa cells treated with red fluorescent Mito-Obt-NPs at 3 h, 6 h and 24 h. Mitochondria were stained with green fluorescent MitoTracker Green. Scale bar = 10 µm.

We have now observed that the ER-Obt-NPs first localized into acidic lysosomes. Also, our previous study showed that TPP coated nanoparticles localized into lysosome before homing into mitochondria. Hence, we evaluated the release of obatoclax from both the nanoparticles at pH = 5.5 to mimic lysosome environment. We incubated both the nanoparticles in pH = 5.5 buffer in a time-dependent manner and quantified the amount of free obatoclax released by dialysis method using UV-Vis spectroscopy at λ_{max} = 488 nm. We observed that at pH = 5.5 only 7.2% and 17.0% of obatoclax was released from ERObt-NPs and Mito-Obt-NPs even

after 72 h (Fig. 2.6a). As a control experiment, we also assessed the release of obatoclax at physiological pH = 7.4. Interestingly, both the nanoparticles released nearly 41.2% of obatoclax after 72h at pH = 7.4 (Fig. 2.6b). This data is accordance with our previous observation.[41] However, the exact mechanism of obatoclax release is still elusive. Hence, from this release study, it was obvious that very less amount of obatoclax was released from both the nanoparticle in lysosomes even after 3 days.

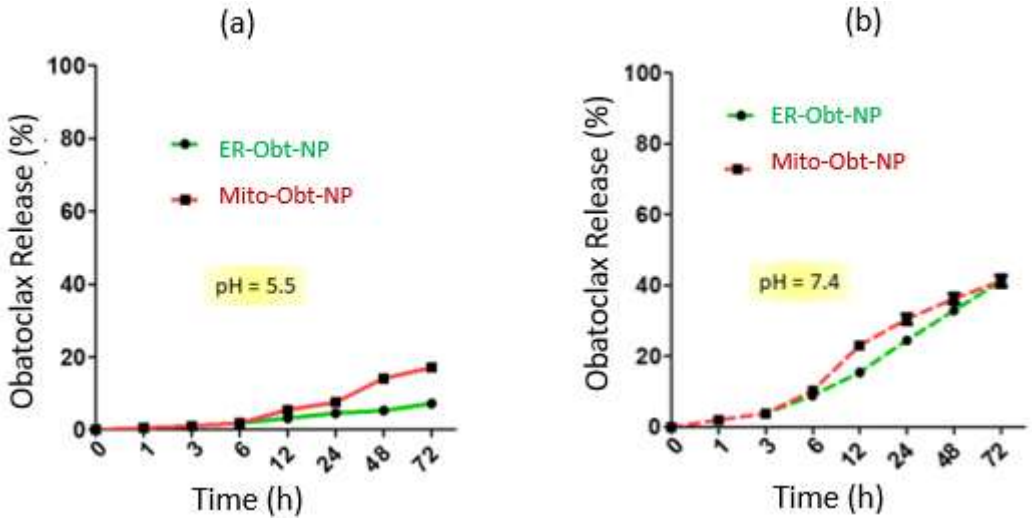

Figure 2.6: (a,b) Release of obatoclax from ER-Obt-NPs and Mito-Obt-NPs at pH = 5.5 and pH = 7.4 over 72h respectively.

2.3.3 Induction of ER stress and autophagy. Once ER-Obt-NPs internalized in the ER of the HeLa cervical cancer cells they are expected to release their payload (obatoclax) and inhibit the Bcl-2 homologue. We evaluated the expression of Bcl-2 protein by western blot analysis. The western blot image showed a reduction of the expression of Bcl-2 compared to non-treated control cells (Fig. 2.7a, b). Inhibition of the antiapoptotic Bcl-2 at ER is expected to induce ER stress in the cells. So we evaluated the expression of ER stress-related proteins by Western blot analysis. We observed an increment in the expression of ER stress markers IRE1-α and CHOP which indicated the onset of ER-associated stress and apoptosis (Fig. 2.7a).[42-44] Quantification from the Western blot also revealed that ER-Obt-NPs increased the expression of IRE1-α and CHOP by 4.2 and 2.7 folds respectively compared to the control cells (Fig. 2.7c and d).

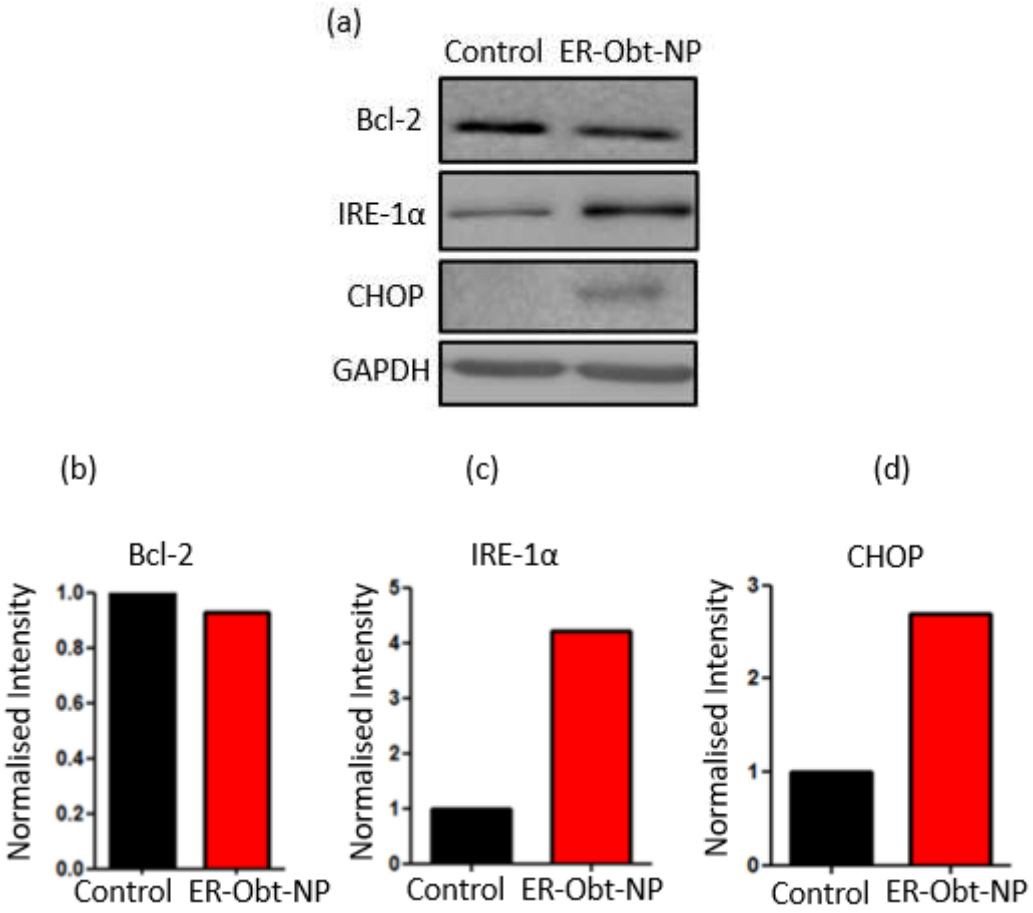

Figure 2.7: (a) Western blot images showing the expression of Bcl-2, IRE-1α and CHOP after treatment of HeLa cells with ER-Obt-NPs. (b) Quantification of (a) Bcl-2 (b) IRE1-α (c) CHOP from western blot analysis.

An increase in ER stress leads to the generation of the reactive oxygen species (ROS).[45] We evaluated the ROS generation by 2,7-dichlorodihydrofluorescein (H2DCFDA) assay.[46] HeLa cells were treated with ER-Obt-NPs followed by incubation with H2DCFDA. We then visualized the cells by confocal microscopy. Control cells hardly generated any green fluorescence signal indicating negligible ROS generation. However, cells treated with the ER-Obt-NPs showed a remarkable increment in the green fluorescence signal (4-fold) confirming the generation of subcellular ROS (Fig. 2.8a and b). Inhibition of the anti-apoptotic Bcl-2 should induce programmed cell death. So we evaluated the apoptosis induced by ER-Obt-NPs by flow cytometry analysis. We treated HeLa cells with 10 μM concentration of the ER-Obt-NPs and stained the apoptotic cells and the necrotic cells with APC labelled Annexin V and 7-AAD respectively followed by flow cytometric analysis to count cells at different stages. We observed that after 24 h ER-Obt-NPs were able to induce 28% cells into early and 52% cells

into late apoptosis compared to only 1.25% and 0.18% cells into early and late apoptotic stages in control cells (Fig. 2.8c).

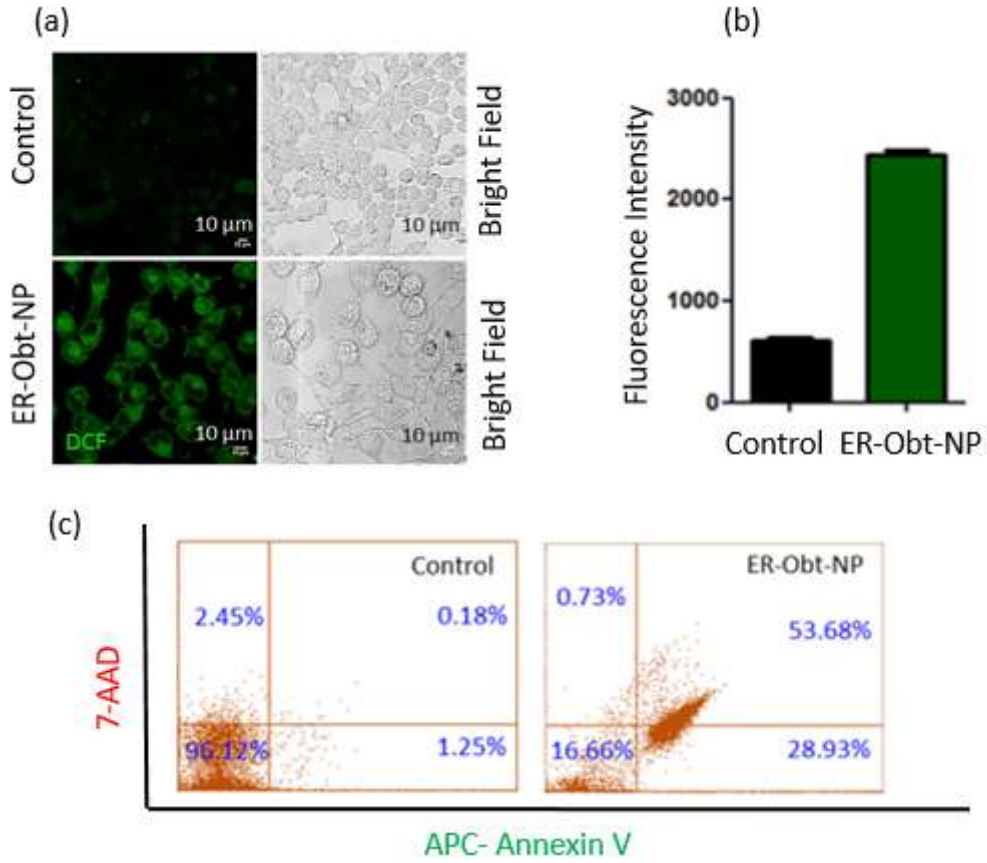

Figure 2.8: (a) Confocal images showing the ROS generation (b) Confocal microscopy-based quantification of green fluorescence intensity after incubation with H2DCFDA in ER-Obt-NPs treated HeLa cells. (c) Flow cytometry to show the induction of apoptosis by staining by APC-Annexin V and 7-AAD.

We also evaluated the cell killing efficacy of the ER-Obt-NPs by cell viability assay. We treated HeLa cervical cancer cells with the ER-Obt-NPs in a dose-dependent manner for 48 h and estimated the cell viability by MTT assay. The nanoparticles exhibited an IC_{50} of about 20 µM which was comparable with the IC_{50} of free Obatoclax (Fig. 2.9a). We also evaluated the toxicity of oleic acid and oleic acid-dansyl conjugate (4) in HeLa cells in a dose-dependent manner by MTT assay. We observed absolutely no toxicity for oleic acid even at 50 µM concentration (Fig. 2.9b). Conjugate 4 also showed negligible toxicity with 66.0% cell viability at 50 µM (Fig. 2.9c).

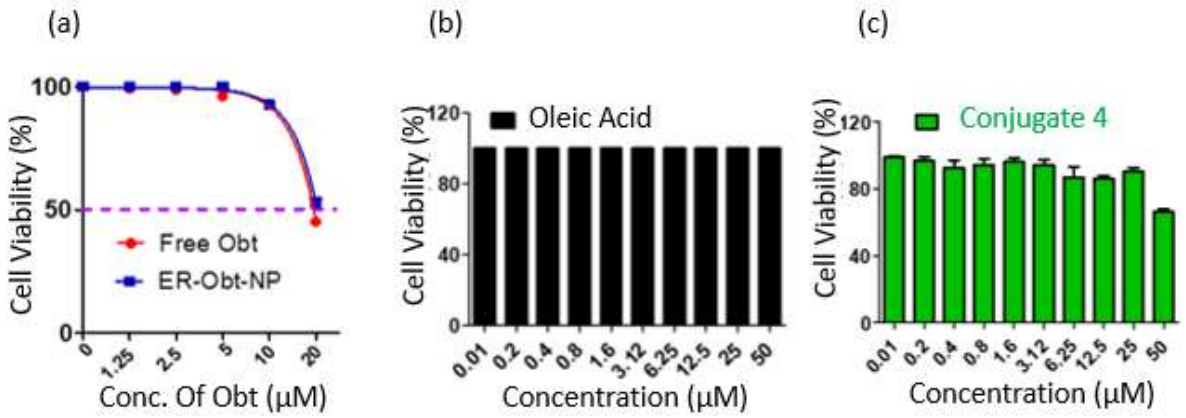

Figure 2.9: (a) Dose-dependent viability of HeLa cells after treatment with ER-Obt-NPs at 48 h post-incubation.(b, c) Viability of HeLa cells after treatment with oleic acid and oleic acid-dansyl conjugate (4) in a dose dependent manner over 48h, determined by MTT assay.

Since anti-apoptotic Bcl-2 is known to be one of the key proteins associated with autophagy, we expected the inhibition of Bcl-2 in ER would trigger autophagy.[47] We also anticipated autophagy. a reason for the reduced cell death in case of ER-Obt-NPs.[48,49] Hence, we evaluated the expression of the autophagy related protein LC3B by gel electrophoresis in HeLa cells.[50] From the gel images, we found that the expression of LC3B significantly increased (9.3 folds) after treatment with ER-Obt-NPs for 24 h compared to control cells (Fig. 2.10a and c). Increased expression of LC3B confirmed the onset of autophagy after inhibition of Bcl-2 at ER. To further confirm our hypothesis, we treated the HeLa cervical cancer cells with the ER-Obt-NPs followed by the treatment with chloroquine (an autophagy inhibitor) for 24 h and then evaluated the expression of the LC3B proteins.[51] As expected, co-treatment with autophagy inhibitor reduced the expression of LC3B proteins (4.8 folds) compared to control cells, which is 2 times less compared to the ER-Obt-NPs treatment alone (Fig. 2.10b and e). We also observed a concomitant increment (7.2 folds) in the expression levels of ER stress associated apoptosis marker CHOP compared to control cells (Fig. 2.10b and d). We also evaluated the generation of ROS by H2DCFA assay. We treated HeLa cells with the combination of ER-Obt-NPs and chloroquine for 24 h and visualized the green fluorescent DCF by confocal microscopy. The fluorescence microscopy image showed that combination treatment with ER-Obt-NPs and chloroquine remarkably increased the green fluorescence into the cells (14 folds) compared to the control cells (Fig. 2.11a and b).

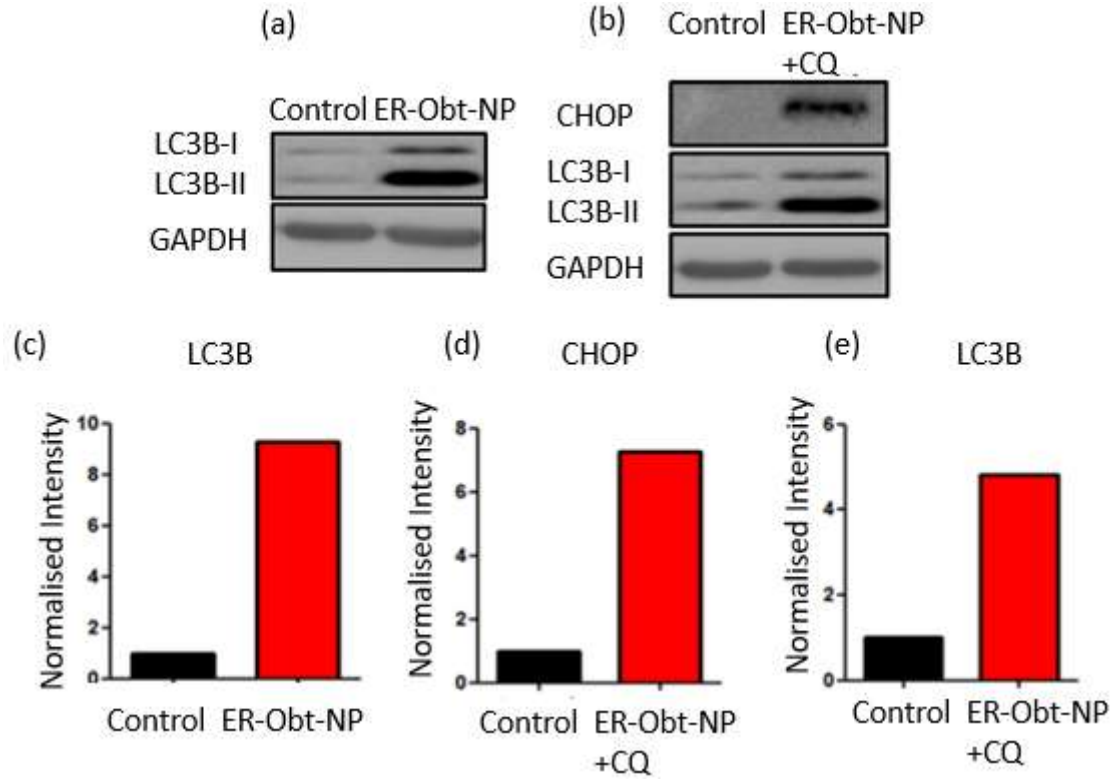

Figure 2.10: Western blot analysis showing the expression of LC3B and CHOP in HeLa cells after treatment with (a) ER-Obt-NPs and (b) combination of ER-Obt-NPs and chloroquine at 24 h. Quantification of (c) LC3B from western blot analysis after treatment with ER-Obt-NPs for 24 h in HeLa cells. (d) CHOP and (e) LC3B from western blot analysis after treatment of HeLa cells with ER-Obt-NPs and chloroquine.

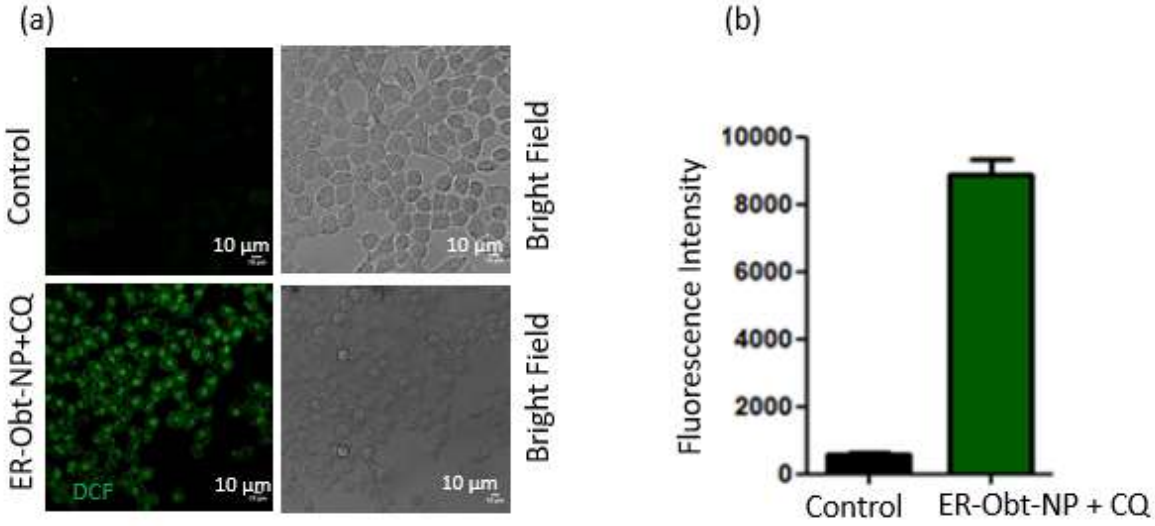

Figure 2.11: (a) Confocal microscopy images of HeLa cells (b) quantification of green fluorescence intensity after treatment with ER-Obt-NPs and chloroquine combination.

To further substantiate the effect of autophagy inhibition and induction of apoptosis, we performed the flow cytometry analysis. We treated HeLa cervical cancer cells with ER-Obt-NPs along with 50 µM chloroquine for 24 h. Flow cytometry analysis revealed 7% and 84% cells in early and late apoptotic stages respectively (Fig. 2.12a) much higher compared to the ER-Obt-NP treatment alone. We also treated the HeLa cervical cancer cells with ER-Obt-NPs along with 50 µM chloroquine and estimated the cell viability by MTT assay. The combination treatment exhibited an IC_{50} of 15 µM which is much lower compared to the ER-Obt-NPs treatment alone (Fig. 2.12b). Thus inhibition of autophagy resulted in improved efficacy of the ER-Obt-NPs. These experiments showed that ER-Obt-NPs inhibited Bcl-2 in ER and induced ER stress leading to autophagy which can be suppressed by combination treatment with autophagy inhibitor chloroquine.

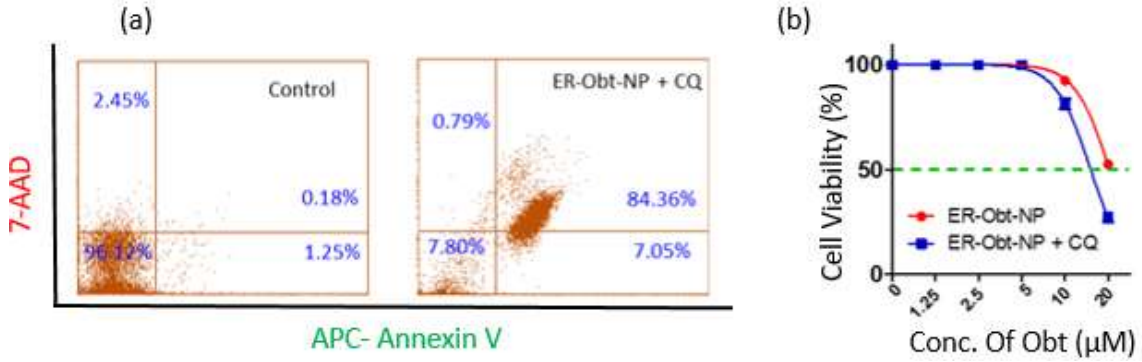

Figure 2.12: (a) Flow cytometry analysis of HeLa cells after treatment with the combination of ER-Obt-NPs and chloroquine for 24 h (b) Dose-dependent viability of HeLa cells after treatment with ER-Obt-NPs and combination with chloroquine at 48 h post-incubation.

2.3.4 Mitochondrial damage and apoptosis. After internalizing in the mitochondria of the HeLa cervical cancer cells we expected the Mito-Obt-NPs to release their payload and inhibit the mitochondrial Bcl-2. So we evaluated the expression level of anti-apoptotic Bcl-2 by gel electrophoresis. HeLa cells were treated with the Mito-Obt-NPs for 24 h and the cellular proteins were then subjected to western blot analysis. We found that treatment with Mito-Obt-NPs resulted in reduced expression levels of Bcl-2 protein by 1.6 folds compared to control cells (Fig. 2.13a and b). Furthermore a concomitant 1.3 folds decrease in the levels of Bcl-xL, another anti-apoptotic protein was also observed (Fig. 2.13a and c). Once the mitochondrial Bcl-2 is impaired, activation of the caspase cascade would induce apoptosis. We evaluated the cleavage of initiator caspase-9 and executioner caspase-3 as apoptotic markers.[52,53] We treated HeLa cells with Mito-Obt-NPs for 24 h and evaluated the expression of caspase-9 and caspase-

3 by Western blot analysis. The gel images and quantification showed that Mito-Obt-NPs reduced the expression of caspase3 and caspase-9 by 1.3 folds and 2.1 folds respectively (Fig. 2.13a, d and e).

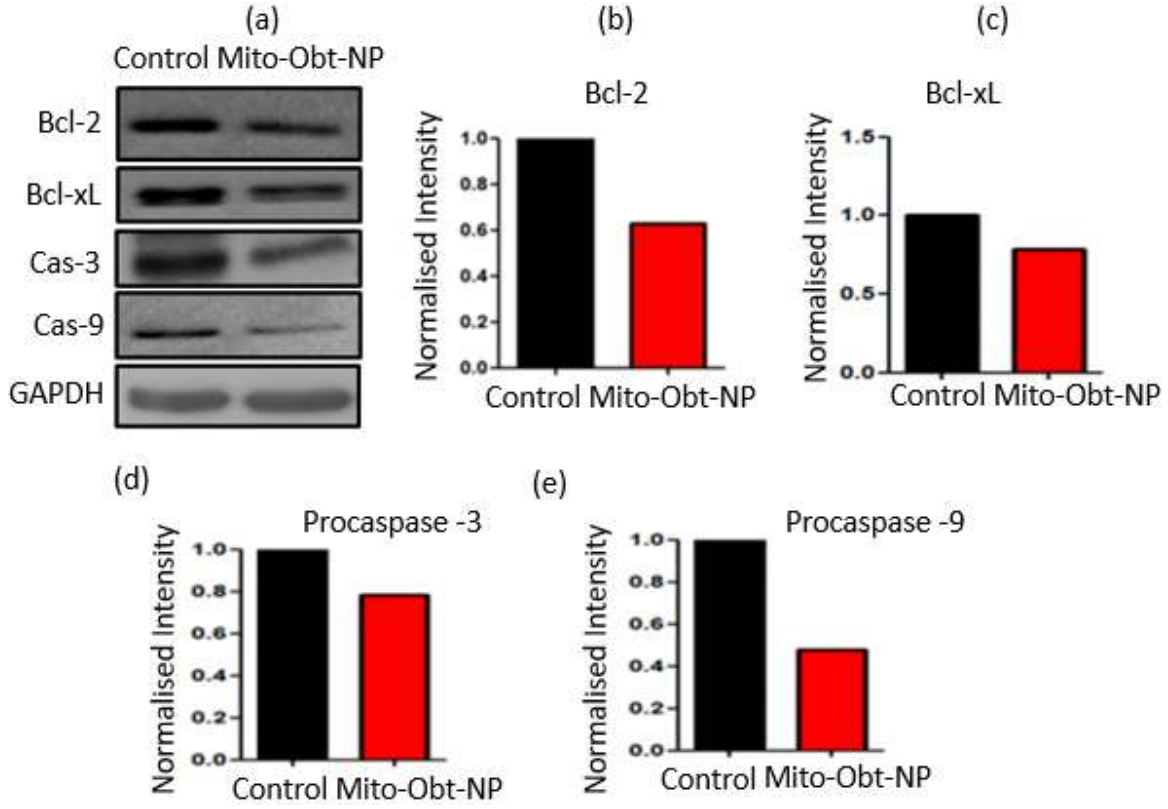

Figure 2.13: (a) Western blot images showing the expression of Bcl-2, Bcl- xL, Procaspase-3 and Procasspase-9 after treatment of HeLa cells with Mito-Obt-NPs. (b) Quantification of (b) Bcl-2 (c) Bcl- xL (d) Procasspase-3 and (e) Procasspase-9 from western blot analysis.

Impairment of mitochondrial Bcl-2 by Mito-Obt-NPs will lead to generation of ROS. We treated HeLa cells with Mito-Obt-NPs for 24 h followed by incubation with H2DCFDA to evaluate the ROS generation. Cells were then visualized with confocal microscopy. A remarkable increment (300 folds) in the green fluorescence was observed in case of the cells treated with Mito-Obt-NPs as compared to the control cells (Fig. 2.14a and c) which indicated the generation of ROS after treatment with nanoparticle. Once the mitochondrial Bcl-2 is impaired by the Mito-Obt-NPs, they should also induce damage to the mitochondria of the HeLa cells and opening of the mitochondrial permeability transition pore (MPTP) resulting in the reduction of mitochondria membrane potential ($\Delta\Psi m$) followed by rupturing of outer membrane.[54] We estimated the MPTP formation by Calcein-AM assay.[55] We treated HeLa cells with Mito-Obt-NPs for 24 h followed by incubation with Calcein-AM and $CoCl_2$. The

live HeLa cells were then visualized by confocal microscopy wherein the cells treated with Mito-Obt-NPs exhibited an enhancement in the green fluorescence intensity (17 folds) as compared to the control cells that hardly showed any green fluorescent signals (Fig. 2.14b and d).

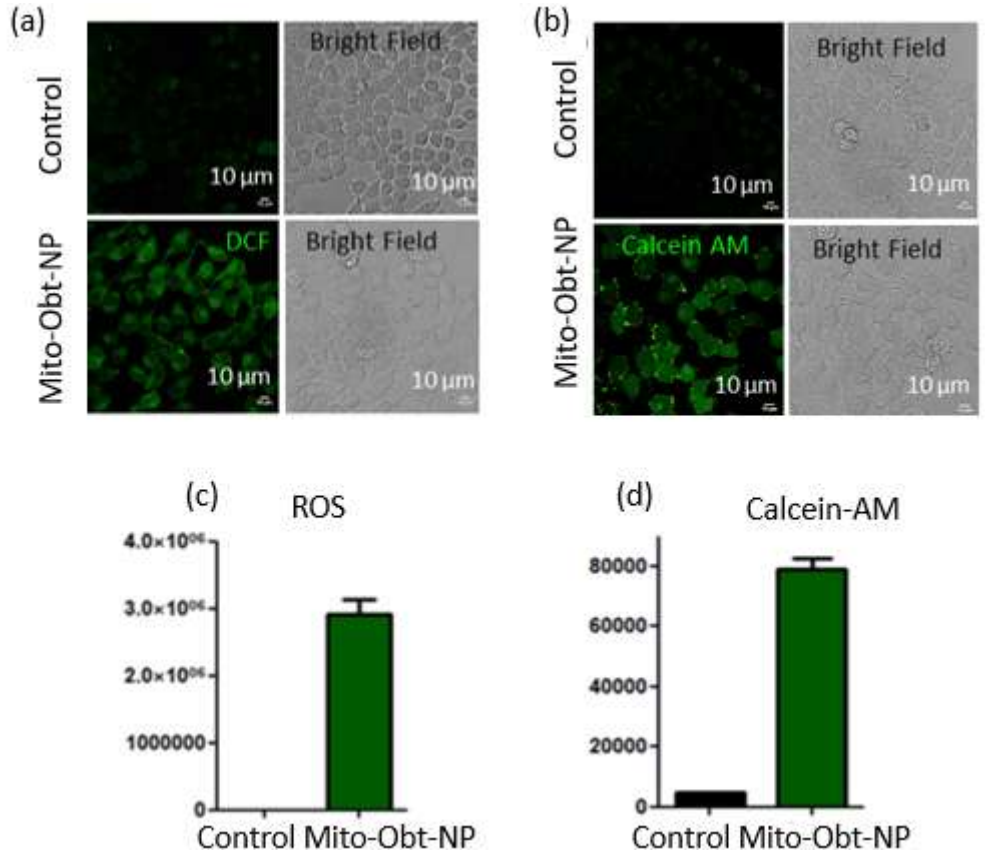

Figure 2.14: (a, b) Confocal microscopy images to show ROS generation and MPTP formation respectively. Quantification of green fluorescence intensity after incubation with (c) H2DCFDA and (b) Calcein-AM in Mito-Obt-NPs treated NPs in HeLa cells.

Mitochondrial damage through MPTP formation and inhibition of the anti-apoptotic Bcl-2 and Bcl-xL proteins would trigger programmed cell death or apoptosis. We quantified the induction of apoptosis by flow cytometry analysis by treating HeLa cells with Mito-Obt-NP at a concentration of around 10 µM for 24 h followed by co-staining the cells with APC- Annexin V and 7-AAD. Cells were then sorted with flow cytometry which demonstrated 0.03% cells into early and 99.4%cells into late apoptosis respectively (Fig. 2.15a) compared to only 2.3% cells in late apoptosis in non-treated cells. Although cationic nanoparticles were reported to induce necrosis in cancer cells, we observed late apoptosis with our cationic Mito-Obt-NPs which was in accordance with our previous observations.[41, 56] We finally validated the cell killing efficacy of the Mito-Obt-NPs by cell viability assay. We treated HeLa cells with the

Mito-Obt-NPs in a dose-dependent manner for 48 h and calculated the cell viability by MTT assay. Mito-Obt-NPs exhibited much lower IC_{50} = 7 µM compared to IC_{50} = 20 µM for free obatoclax indicating improved efficacy in killing HeLa cells than the free drug (Fig. 2.15b). As a control, we also evaluated the toxicity of oleic acid-TPP conjugate (6) in HeLa cells in a dose-dependent manner at 48h by MTT assay, which showed only 57.6% cell viability at very high concentration of 50 µM (Fig. 2.15c). These experiments confirmed that Mito-Obt-NPs inhibited Bcl2 in mitochondria to induce late apoptosis leading to improved HeLa cell death compared to free Bcl-2 inhibitor. Our studies at the same time revealed the difference in the functionality of Bcl-2 protein in different locations. We found that in HeLa cells mitochondria-targeted nanoparticles exhibited much better induction of apoptosis as compared to the ER-Obt-NPs. In fact, inhibiting the Bcl-2 at mitochondria was 2 times more efficacious compared to its homologue at ER. This observation was in complete correlation with the results of cell viability assay which further corroborating the mitochondrial Bcl-2 as an effective target than Bcl-2 at ER. We anticipate autophagy a reason for the reduced cell death in case of ER-Obt-NPs as the nanoparticles exhibited better efficacy and improved IC_{50} when the autophagy was suppressed. Thus, mitochondrial Bcl-2 seems to be more apt as a target than its homologue at ER for cancer therapeutics.

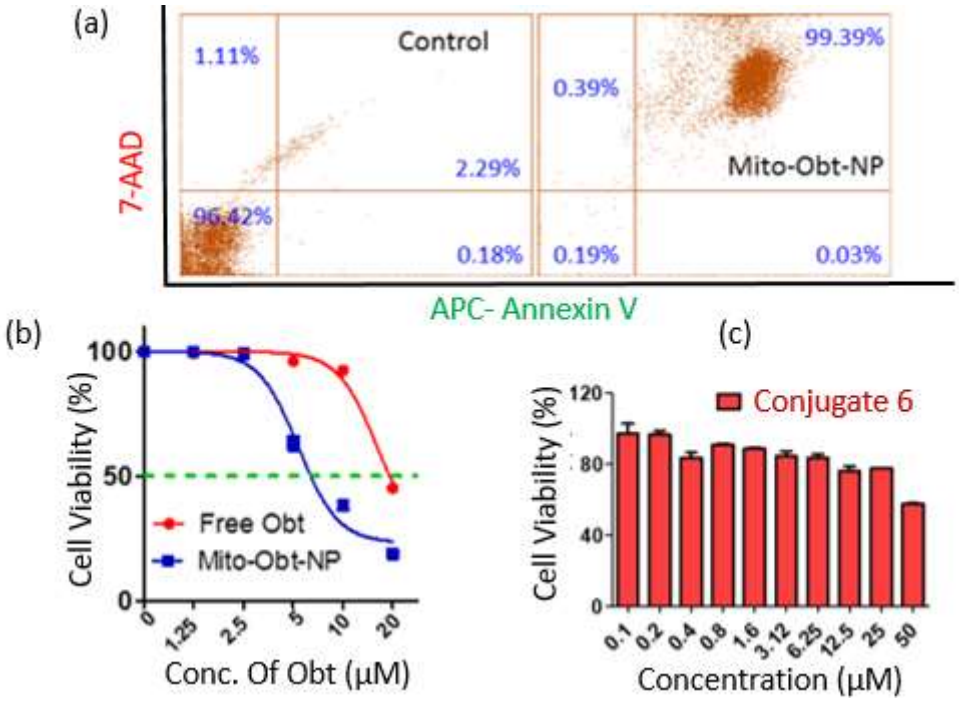

Figure 2.15: (a) Flow cytometry analysis after staining with APC-Annexin V and 7-AAD.Dose-dependent viability of HeLa cells after treatment with (b) Mito-Obt-NPs and (c) OA-TPP conjugate at 48 h post-incubation.

2.4 Materials and Methods

2.4.1 Materials: All the chemicals were purchased from commercial suppliers unless otherwise noted. Obatoclax mesylate was purchased from Selleck Chemicals. Reactions were performed in the oven-dried glassware with or without inert gas. Analytical thin-layer chromatography (TLC) was performed using pre-coated silica gel aluminium sheets 60 F254 bought from EMD Millipore Laboratories. Compounds were purified by column chromatography using silica gel 100-200 mesh as the stationary phase. 1H, 13C, 31P spectra were recorded on a Bruker Avance III HD Ascend 9.4 Tesla/400 MHz with autosampler and/or Jeol 9.4 Tesla/400 MHz with autosampler spectrometer. Chemical shifts are mentioned in parts per million (ppm) and referred to residual protons on the corresponding deuterated solvent. UV- Visible spectra was recorded on Shimadzu. DMEM media and 3-(4, 5-dimethylthiazol-2-yl)-2, 5- diphenyltetrazolium bromide (MTT) was purchased from HiMedia. Nunc® Lab-Tek® II chambered coverglass, and Sodium dodecyl sulfate (SDS) was purchased from Sigma-Aldrich. MitoTracker® Green, ER Tracker Green and LysoTracker Green DND-26 were purchased from Invitrogen. AnnexinV- APC and 7-AAD staining Kit was purchased from Biolegend. Flow Cytometry analysis was recorded on BD- Accuri. Western blot analysis was performed on Las ImageQuant 400.

2.4.2 Synthesis of N-(2-aminoethyl)oleamide (2). Ethylene diamine was conjugated to oleic acid via amide coupling according to the reported procedure[30].

2.4.3 Synthesis of N-(2-((5-dimethylaminonapthalene)-1-sulfonamido)ethyl)oleamide (4). To a solution of N-(2-aminoethyl)oleamide (1 eq.) in DCM was added dansyl chloride (1 eq.) and trimethylamine (2.2 eq.). The reaction mixture was allowed to stir overnight under nitrogen atmosphere. Progress of the reaction was monitored through TLC. On completion, the reaction mixture was diluted with DCM and washed with brine. Organic layer was collected, dried over sodium sulphate and evaporated. Residue obtained was purified by column chromatography (35% ethyl acetate in hexane) in 45% yield.

^{1}H NMR (400 MHz, $CDCl_3$): δ=8.56 (d, *J* = 8 Hz, 1H), 8.22 (dd, J = 2Hz, 4 Hz, 2H), 7.58 (m, 2H), 7.20 (d, *J* = 8 Hz, 1H), 5.82 (m, 1H), 5.5 (s, 1H), 5.35 (m, 2H), 3.29-3.26 (m, 2H), 3.02 (q, *J* = 4 Hz, 8Hz, 2H), 2.89 (q, J = 4 Hz, 8 Hz, 6H), 2.00 (m, 6H), 1.41-1.25 (m, 22H), 2H), 0.86 (m , 3H).

^{13}C NMR (100 MHz, $CDCl_3$): δ 174.33, 152.28, 139.42, 134.48, 130.82, 130.15, 130.09, 129.89, 129.64, 128.72, 123.33, 118.72, 115.42, 114.21, 77.16, 45.56, 32.08, 32.06, 30.39, 29.85, 29.81, 29.68, 29.47, 29.40, 29.31, 27.39, 27.35, 25.66, 22.84, 14.27

2.4.4 Synthesis of (5-((2-oleamidoethyl)amino)-5-oxopentyl) triphenylphosphonium bromide (6). To a solution of N-(2-aminoethyl)oleamide (1 eq.) at 0^{o}C in DCM under nitrogen atmosphere was added HBTU and DIPEA. The reaction mixture was allowed to stir for 15 minutes and then (4-carboxybutyl)triphenylphosphonium bromide (1.2 eq.) was added. Reaction was then allowed to stir overnight. Progress of the reaction was monitored through TLC. On completion, the reaction mixture was diluted with DCM and washed with brine. Organic layer was collected, dried over sodium sulphate and evaporated. A sticky residue was obtained which was further washed with pentane to get the pure compound in 75% yield.

^{1}H NMR (400 MHz, $CDCl_3$): δ 7.71 (t, *J* = 32.2 Hz, 15H), 6.92 (s, 1H), 6.73 (s, 1H), 5.31 (t, *J* = 5.4 Hz, 2H), 3.27 (s, 3H), 3.17 (s, 2H), 2.88 (d, *J* = 66.7 Hz, 2H), 2.31 (s, 2H), 2.16 (t, *J* = 7.1 Hz, 2H), 2.03 – 1.93 (m, 4H), 1.87 (s, 2H), 1.69 (s, 2H), 1.55 (s, 2H), 1.25 (s, 22H), 0.86 (t, *J* = 6.8 Hz, 3H).

^{13}C NMR (100 MHz, $CDCl_3$): δ 174.33, 173.17, 135.43, 133.45, 133.36, 130.79, 130.67, 129.95, 118.32, 117.40, 39.81, 39.63, 36.49, 34.43, 31.97, 29.85, 29.60, 29.39, 29.24, 27.30, 26.09, 25.93, 25.84, 22.75, 21.64, 21.54, 21.50, 14.20.

^{31}P NMR (162 MHz, $CDCl_3$): δ 24.4

2.4.5 Synthesis of nanoparticles. Endoplasmic reticulum targeted (ER-obt-NPs) and mitochondria targeted nanoparticles (Mito-obt-NPs) were synthesised from the conjugates **4** and **6** according to the previously reported procedure[1].

2.4.6 Determination of shape, size and morphology. The shape, size and morphology of the nanoparticles was determined using light scattering and electron microscopy techniques like field-emission scanning electron microscopy (FESEM) and atomic force microscopy (AFM). Samples were prepared according to the previously reported procedures.

2.4.7 Quantification of drug loading in the nanoparticles. Loading of obatoclax in the nanoparticles was determined at λ_{max}= 488 nm by UV-Vis spectroscopy using the previously reported method.

$$\text{Drug Loading Efficiency (\%)} = \frac{Amount\ of\ drug\ loaded\ in\ nanoparticle}{Amount\ of\ drug\ used} X\ 100$$

$$\text{Weight \% of Obatoclax} = \frac{Weight\ of\ obatoclax\ in\ nanoparticles}{Weight\ of\ solid\ nanoparticles} X\ 100$$

2.4.8 Cell Viability assay. 100 µL of 5000 cells in DMEM media were seeded per well in 96-well microtiter plate and incubated for 16 h in a 5% CO_2 incubator at 37ºC. Cells were treated with different concentrations of the nanoparticles and incubated for 24 h and 48 h. After the said time points, media was removed and 100 µL of MTT in DMEM (0.5 mg/mL) was added. After 4 h, 50 µL of solubilisation buffer (10%SDS in 0.01 N HCl) was added to dissolve the formazan crystals and left for incubation overnight. Absorbance was then recorded at 570 nm on Perkin Elmer Ensight. The assay was performed in triplicate of triplicates (n=3).

2.4.9 Cellular Internalization. 2 x 10^4 cells were seeded in a 8-well LabTek chamber. Cells were incubated with the ER and mitochondria targeted nanoparticles for the mentioned time points. Cells were washed with cold PBS and costained with ER Tracker Green and MitoTracker green respectively and incubated for 20 mins. Cells were then washed and visualised using CLSM, Zeiss LSM 700. Similar method was adopted for monitoring the localization of nanoparticles in lysosomes using LysoTracker Green DND-26. (n=2)

2.4.10 DCFH-DA assay. 2 x 10^4 cells were seeded in a 8-well LabTek slide. Cells were treated with the nanoparticles for 24 h. Post incubation cells were treated with DCFH-DA for 15 min. Cells were then washed thrice and visualized by CLSM. (n=2)

2.4.11 Calcein AM assay. 2 x 10^4 cells were seeded in a LabTek slide (8-well). Cells were treated with the nanoparticles. Post 24 h incubation calcein AM (1 µM) and 1mM $CoCl_2$ were added into the cells followed by imaging by CLSM.

2.4.12 Flow Cytometry analysis. 2 x 10^6 cells were seeded in a 6-well plate and treated with the nanoparticles for 24 h. The cells were then trypsinized and washed with PBS. Suspended cells were then incubated with APC Annexin V and 7-AAD according to the manufacturer's protocol. Apoptotic and necrotic cells were then quantified using BD Accuri C6 flow cytometer (n=2).

2.4.13 Western Blot analysis. 1x 10^6 cells were seeded in a 6-well plate and treated with the nanoparticles for 24 h. Cells were then lysed. SDS-PAGE was used to separate the different proteins (n=2).

2.5 Conclusion

In conclusion, we chemically synthesized ER and mitochondria specific oleic acid based probes and engineered obatoclax loaded nano-scale particles that selectively localized into ER and mitochondria respectively and inhibited Bcl-2 at those organelles. Interestingly, inhibition of Bcl-2 in ER lead to ER stress and autophagy in HeLa cervical cancer cells. On the other hand, inhibition of Bcl-2 in mitochondria triggered mitochondrial outer membrane permeabilization leading to late apoptosis. This study revealed that inhibiting Bcl-2 at mitochondria was more prone to induce apoptosis than its spatial counterpart at ER since the autophagy induction leads to reduced cell killing. Thus, our approach established Bcl-2 at mitochondria as a more promising target for the Bcl-2 inhibitors than Bcl-2 located at ER. This study confirmed that it is really essential to understand the disparity in the function and behaviour of protein homologues at different spatial locations. Equally important is to ensure that small molecule drugs or inhibitors localize in the correct organelle after it crosses the plasma membrane in order to achieve maximum efficacy. This novel nano-platform can be extended to understand the location-function-relationship of other therapeutically important proteins located at the mitochondria and the endoplasmic reticulum. Not only will it lead to the development of better therapeutics but, it will also potentially contribute in understanding their cross-talk. Thus, in this chapter we have established that the therapeutic efficacy of mitochondrial Bcl-2 is more as compared to Bcl-2 at ER and therefore, to realize the maximum therapeutic potential of Bcl-2 inhibitors they should be directed to inhibit the protein at mitochondria than at ER.

2.6 Appendix- A

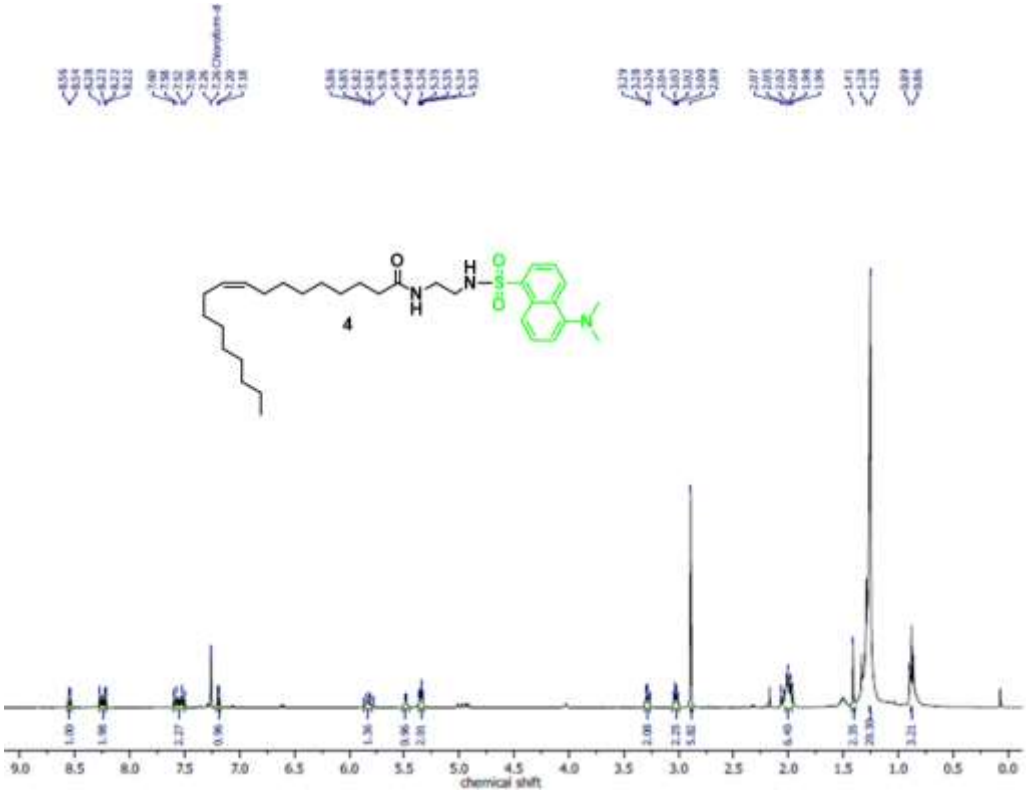

Figure A1: ^{1}H NMR spectrum of compound 4 in $CDCl_3$ at 400 MHz.

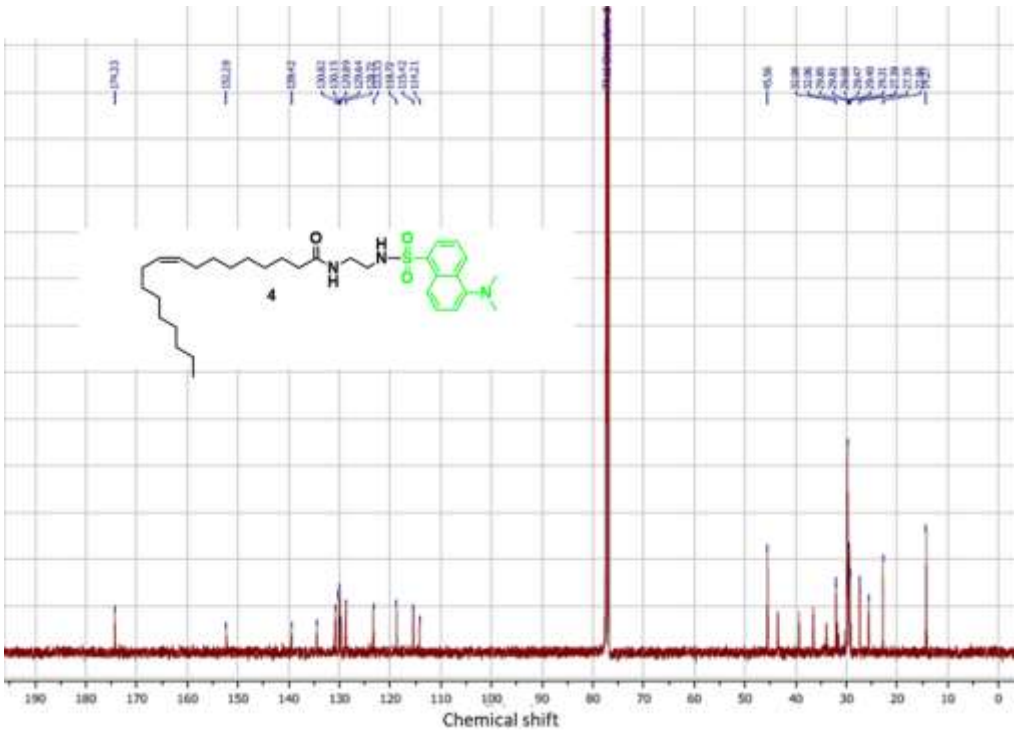

Figure A2: ^{13}C NMR spectrum of compound 4 in $CDCl_3$ at 100 MHz.

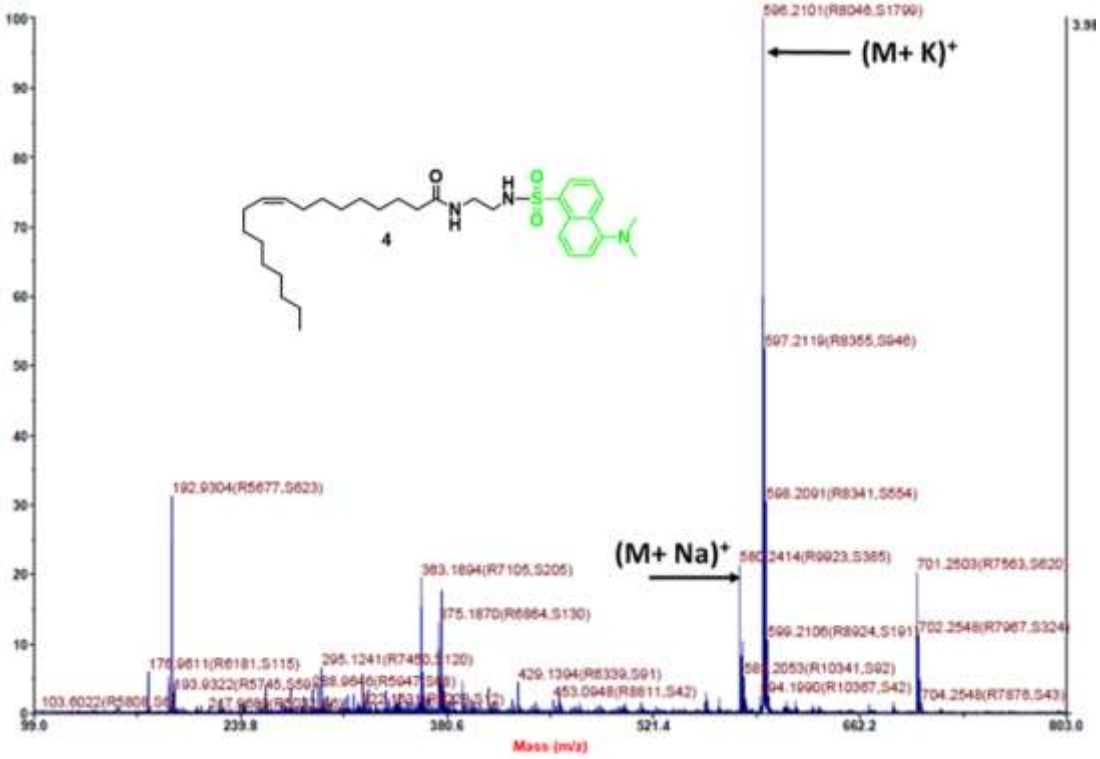

Figure A3: MALDI- TOF spectrum of Compound 4.

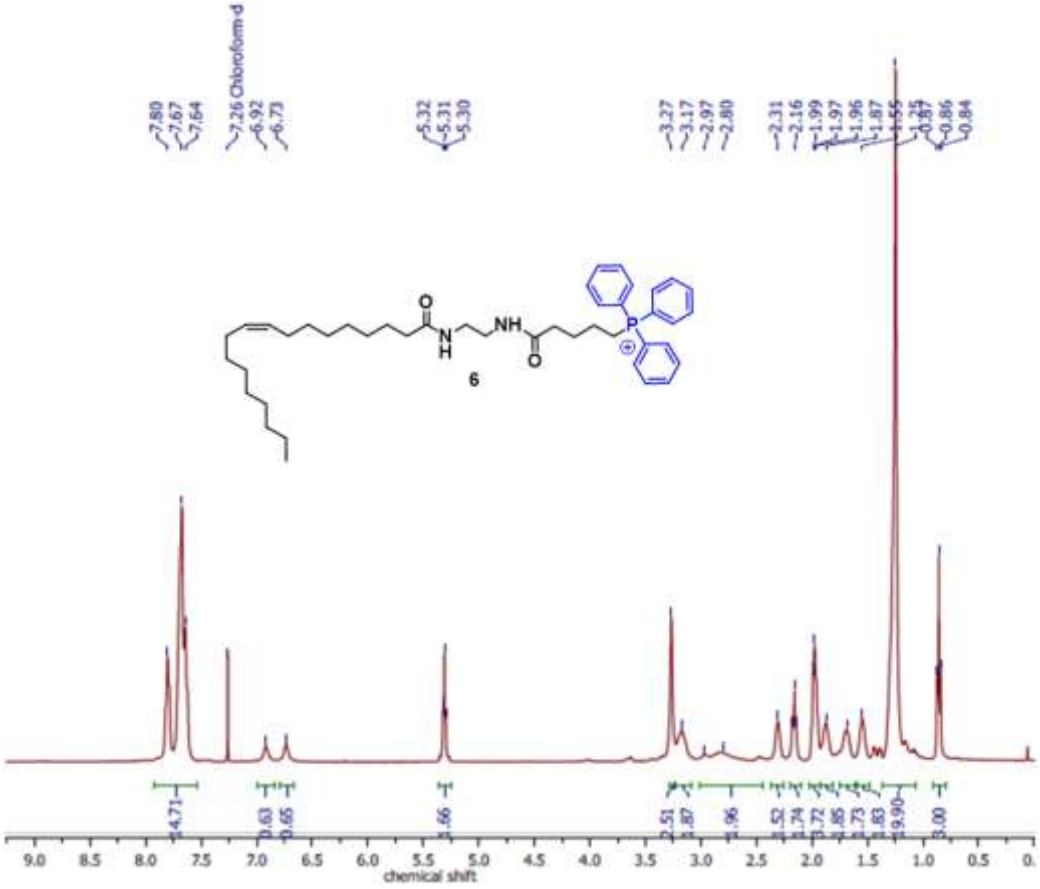

Figure A4: ^{1}H NMR spectrum of compound 6 in $CDCl_3$ at 400 MHz.

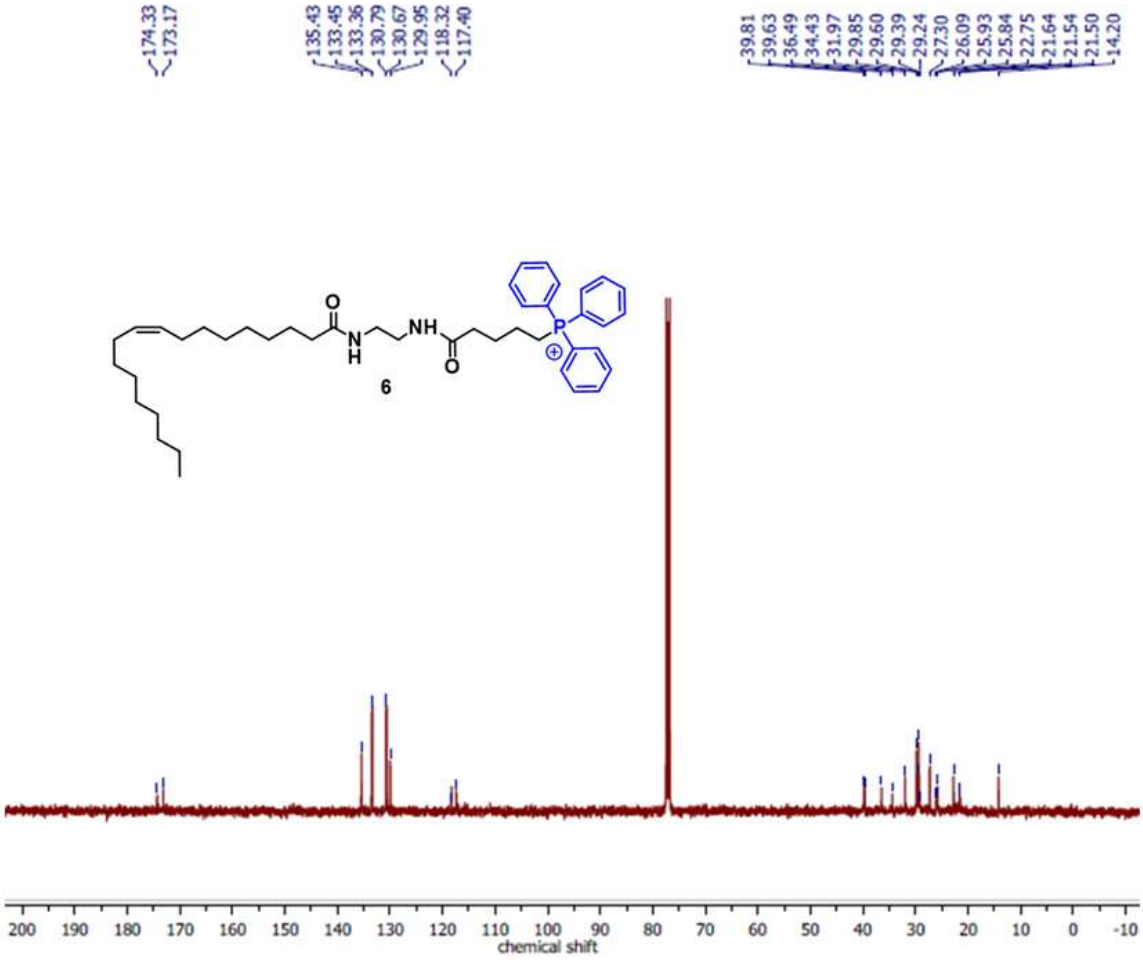

Figure A5: ^{13}C NMR spectrum of compound 6 in $CDCl_3$ at 100 MHz.

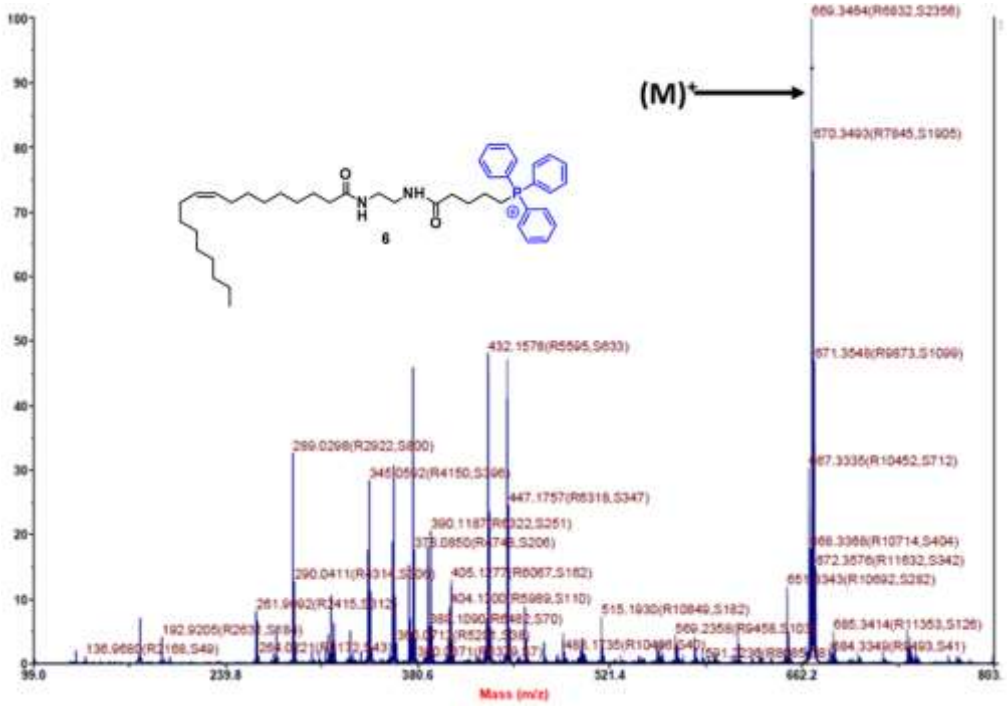

Figure A6: MALDI- TOF spectrum of compound 6.

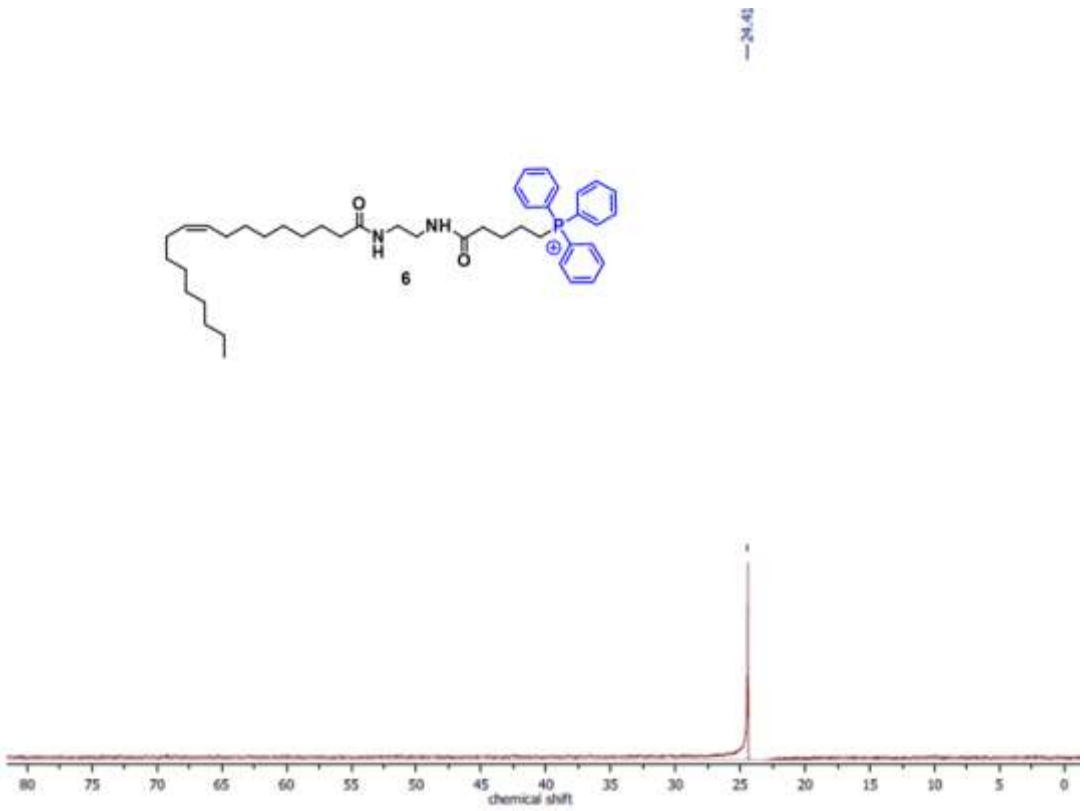

Figure A7: ^{31}P NMR spectrum of compound 6 in $CDCl_3$.

Treatment Time		3 h	6 h	24 h
Image Channels		C1 (green) C3 (red)	C1 (green) C3 (red)	C1 (green) C3 (red)
Pearsons' Correlation Coeffecient		0.937	0.964	0.906
Manders Coeffecients	M1 (fraction of C1 overlapping C3)	0.824	0.9182	0.913
	M2 (fraction of C3 overlapping C1)	0.7084	0.8284	1.00

Table A1: Quantification of co-localization of ER-Obt-NPs in ER of HeLa cells at 3 h, 6 h and 24 h from CLSM.

Treatment Time		1 h	3 h	6 h
Image Channels		C2 (green) C3 (red)	C2 (green) C3 (red)	C2 (green) C3 (red)
Pearsons' Correlation Coeffecient		0.2253	0.2381	0.1574
Manders Coeffecients	M1 (fraction of C2 overlapping C3)	0.363	0.5237	0.5331
	M2 (fraction of C3 overlapping C2)	0.5787	0.7227	0.6743

Table A2: Quantification of co-localization of ER-Obt-NPs in lysosomes of HeLa cells at 1 h, 3 h and 6 h from CLSM.

Treatment Time		3 h	6 h	24 h
Image Channels		C1 (green) C2 (red)	C1 (green) C2 (red)	C1 (green) C2 (red)
Pearsons' Correlation Coeffecient		0.8097	0.7663	0.7214
Manders Coeffecients	M1 (fraction of C1 overlapping C3)	0.949	0.891	0.8403
	M2 (fraction of C3 overlapping C1)	0.9292	0.8619	0.4751

Table A3: Quantification of co-localization of Mito-Obt-NPs in mitochondria of HeLa cells at 3 h and 6 h and 24 h from CLSM.

2.7 References

1. F. Grizzi and M. Chiriva-Internati, Cancer: looking for simplicity and finding complexity. *Cancer Cell Int.*, **2006**, *6*, 1–7.

2. H. Rubin. Cancer as a Dynamic Developmental Disorder. *Cancer Res.*, **1985**, *45*, 2935–2942.

3. H. Nagai and Y. H. Kim. Cancer prevention from the perspective of global cancer burden patterns**.** *J. Thorac. Dis.*, **2017**, *9*, 448–451.

4. C. Sonnenschein, A. M. Soto and B. Ma. THEORIES of CARCINOGENESIS: An Emerging Perspective. *Semin. Cancer Biol.*, **2009**, *18*, 372–377.

5. R. Sever and J. S. Brugge. Signal Transduction in Cancer. *Cold Spring Harb Perspect Med.*, **2015**, *5*, a006098.

6. G. S. Martin. Cell Signalling and Cancer. *Cancer Cell*, **2003**, *4*, 167–174.

7. J. S. Logue and D. K. Morrison. Complexity in the signaling network:insights from the use of targeted inhibitors in cancer therapy *Genes Dev.*, **2012**, *26*, 641– 650.

8. K. Inder, A. Harding, S. J. Plowman, M. R. Philips, R. G. Parton and J. F. Hancock. Activation of the MAPK Module from Different SpatialLocations Generates Distinct System Outputs. *Mol. Biol. Cell*, **2008**, *19*, 4776–4784.

9. L. H. Loo, D. Laksameethanasan and Y. L. Tung. Quantitative Protein Localization Signatures Reveal an Association between Spatial and Functional Divergences of Proteins. *PLoS Comput. Biol.*, **2014**, *10*, e1003504.

10. S. H. Park, K. H. Baek, I. Shin and I. Shin. Subcellular Hsp70 Inhibitors Promote Cancer Cell Death via Different Mechanisms. *Cell Chem. Biol.*, **2018**, 25, 1242-1254.

11. A. N. Hata, J. A. Engelman and A. C. Faber. The BCL2 Family: Key Mediators of the Apoptotic Response to Targeted Anticancer Therapeutics. *Cancer Discov*, **2015**, *5*, 475–487.

12. K. W. Yip and J. C. Reed. Bcl-2 family proteins and cancer. *Oncogene*, **2008**, *27*, 6398–6406.

13. N. Popgeorgiev, L. Jabbour and G. Gillet. Subcellular Localization and Dynamics of the Bcl-2 Family of Proteins. *Front. Cell Dev. Biol.*, **2018**, *6*, 1–11.

14. Y. Akao, Y. Otsuki, S. Kataoka and Y. Ito, and Y. Tsujimoto. Multiple Subcellular Localization of bcl-2: Detection in Nuclear Outer Membrane, Endoplasmic Reticulum Membrane, and Mitochondrial Membranes. *Cancer Res.*, **1994**, *54*, 2468–2471.

15. V. Kirkin, S. Joos and M. Zörnig. The role of Bcl-2 family members in tumorigenesis *Biochim. Biophys. Acta*, **2004**, *1644*, 229–249.

16. P. Pihán, A. Carreras-Sureda and C. Hetz. BCL-2 family: integrating stress responses at the ER to control cell demise. *Cell Death Differ.*, **2017**, *24*, 1478–1487.

17. R. Clarke, K. L. Cook, R. Hu, C. O. B. Facey, I. Tavassoly, J. L. Schwartz, W. T. Baumann, J. J. Tyson, J. Xuan, Y. Wang, A. Wärri and A. N. Shajahan. Endoplasmic Reticulum Stress, the Unfolded Protein Response, Autophagy, and the Integrated Regulation of Breast Cancer Cell Fate. *Cancer Res.*, **2012**, *72*, 1321–1331.

18. J. E. Chipuk and D. R. Green. How do BCL-2 proteins induce mitochondrial outer membrane permeabilization? *Trends Cell Biol.*, **2008**, *18*, 157–164.

19. J. Kale, E. J. Osterlund and D. W. Andrews. BCL-2 family proteins: changing partners in the dance towards death *Cell Death Differ.*, **2018**, *25*, 65–80.

20. J. Lindsay, M. D. Esposti and A. P. Gilmore. Bcl-2 proteins and mitochondria-Specificity in membrane targeting for death. *Biochim. Biophys. Acta*, **2011**, *1813*, 532-539.

21. J. K. Brunelle and A. Letai. Control of mitochondrial apoptosis by the Bcl-2 family *J. Cell Sci.*, **2009**, *122*, 437–441.

22. D. Hanahan and R. A. Weinberg. The Hallmarks of Cancer. *Cell*, **2000**, *100*, 57-70.

23. A. Slomp and V. Peperzak. Role and Regulation of Pro-survival BCL-2 Proteins in Multiple Myeloma. *Front. Oncol.*, **2018**, *8*, 1-9.

24. L. Coultas and A. Strasser. The role of the Bcl-2 protein family in cancer. *Semin. Cancer Biol.*, **2003**, *13*, 115–123.

25. P. N. Kelly and A. Strasser. The role of Bcl-2 and its pro-survival relatives in tumourigenesis and cancer therapy. *Cell Death Differ.*, **2011**, *18*, 1414–1424.

26. A. Sharma, L. H. Boise and M. Shanmugam. Cancer Metabolism and the Evasion of Apoptotic Cell Death *Cancers*, **2019**, *11*, 1–20.

27. M. Vogler, D. Dinsdale, M. J. S. Dyer and G. M. Cohen. Bcl-2 inhibitors: small molecules

with a big impact on cancer therapy. *Cell Death Differ.*, **2009**, *16*, 360–367.

28. B. N. G. Giepmans, S. R. Adams, M. H. Ellisman and R. Y. Tsien. The Fluorescent Toolbox for Assessing Protein Location and Function. *Science*, **2006**, *312*, 217–224.

29. J. Wang, X. Fang and W. Liang. Pegylated Phospholipid Micelles Induce Endoplasmic Reticulum-Dependent Apoptosis of Cancer Cells but not Normal Cells. *ACS Nano*, **2012**, *6*, 5018–5030.

30. S. Palvai, P. More, N. Mapara, J. Nagraj, R. Chowdhury and S. Basu. Self-Assembled Oleic Acid Nanoparticle Mediated Inhibition of Mitogen-Activated Protein Kinase Signaling in Combination with DNA Damage in Cancer Cells. *ChemNanoMat*, **2016**, *2*, 201–211.

31. H. Xiao, P. Li, X. Hu, X. Shi, W. Zhang and B. Tang. Simultaneous fluorescence imaging of hydrogen peroxide in mitochondria and endoplasmic reticulum during apoptosis. *Chem. Sci.*, **2016**, *7*, 6153–6159.

32. H. Xiao, C. Wu, P. Li, W. Gao, W. Zhang, W. Zhang, L. Tong and B. Tang. Ratiometric photoacoustic imaging of endoplasmic reticulum polarity in injured liver tissues of diabetic mice. *Chem. Sci.*, **2017**, *8*, 7025–7030.

33. C. Ghosh, A. Nandi and S. Basu. Supramolecular self-assembly of triazine-based small molecule: targeting endoplasmic reticulum in cancer cells. *Nanoscale*, **2019**, *11*, 3326-3335.

34. C. Ghosh, A. Nandi and S. Basu. Lipid Nanoparticle-Mediated Induction of Endoplasmic Reticulum Stress in Cancer Cells. *ACS Appl. Bio Mater.*,**2019**, *2*, 3992-4001.

35. D. E. Robertson and H. Rottenberg. Membrane Potential and Surface Potential Mitochondria. *J. Biol. Chem.*, **1983**, *258*, 11039–11048.

36. M. P. Murphy. Targeting lipophilic cations to mitochondria. *Biochim. Biophys. Acta*, **2008**, 1777, 1028–1031.

37. M. Han, M. R. Vakili, H. Soleymani Abyaneh, O. Molavi, R. Lai and A. Lavasanifar. Mitochondrial Delivery of Doxorubicin via Triphenylphosphine Modification for Overcoming Drug Resistance in MDA-MB-435/DOX Cells *Mol. Pharm.*, **2014**, *11*, 2640–2649.

38. P. Sengupta, S. Basu, S. Soni, A. Pandey, B. Roy, M. S. Oh, K. T. Chin, A. S. Paraskar, S. Sarangi, Y. Connor, V. S. Sabbisetti, J. Kopparam, A. Kulkarni, K. Muto, C. Amarasiriwardena, I. Jayawardene, N. Lupoli, D. M. Dinulescu, J. V. Bonventre, R. A.

Mashelkar and S. Sengupta. Cholesterol-tethered platinum II-based supramolecular nanoparticle increases antitumor efficacy and reduces nephrotoxicity. *Proc. Natl. Acad. Sci. U. S. A.*, **2012**, *109*, 11294–11299.

39. M. Nguyen, R. C. Marcellus, A. Roulston, M. Watson, L. Serfass, S. R. Murthy Madiraju, D. Goulet, J. Viallet, L. Bélec, X. Billot, S. Acoca, E. Purisima, A. Wiegmans, L. Cluse, R. W. Johnstone, P. Beauparlant and G. C. Shore. Small molecule obatoclax (GX15-070) antagonizes MCL-1 and overcomes MCL-1-mediated resistance to apoptosis. *Proc. Natl. Acad. Sci. U. S. A.*, **2007**, *104*, 19512–19517.

40. J. Wang, W. Mao, L. L. Lock, J. Tang, M. Sui, W. Sun, H. Cui, D. Xu and Y. Shen. The Role of Micelle Size in Tumor Accumulation, Penetration, and Treatment. *ACS Nano*, **2015**, *9*, 7195–7206.

41. A. Mallick, P. More, M. M. K. Syed and S. Basu. Nanoparticle-Mediated Mitochondrial Damage Induces Apoptosis in Cancer. *ACS Appl. Mater. Interfaces*, **2016**, *8*, 13218–13231.

42. Y. Chen and F. Brandizzi. IRE1: ER stress sensor and cell fate executor *Trends Cell Biol.*, **2013**, *23*, 1–9.

43. S. Oyadomari and M. Mori. Roles of CHOP/GADD153 in endoplasmic reticulum stress *Cell Death Differ.*, **2004**, *11*, 381–389.

44. H. Nishitoh. CHOP is a multifunctional transcription factor in the ER stress response. *J. Biochem.*, **2012**, *151*, 217–219.

45. H. M. A. Zeeshan, G. H. Lee, H. R. Kim and H. J. Chae. Endoplasmic Reticulum Stress and Associated ROS. *Int. J. Mol. Sci.*, **2016**, *17*, 1–20.

46. D. Wu and P. Yotnda. Production and Detection of Reactive Oxygen Species (ROS) in Cancers *J. Visualized Exp.*, **2011**, e3357.

47. R. T. Marquez and L. Xu. Bcl-2: Beclin 1 complex: multiple, mechanisms regulating autophagy/apoptosis toggle switch. *Am. J. Cancer Res.*, **2012**, *2*, 214–21.

48. V. Sica, L. Galluzzi, J. M. Bravo-San Pedro, V. Izzo, M. C. Maiuri and G. Kroemer. Organelle-Specific Initiation of Autophagy*Mol. Cell*, **2015**, *59*, 522–539.

49. M. Ogata, A. Saito, K. Morikawa, S. Kondo, S. Kanemoto, T. Murakami, M. Taniguchi, I. Tanii, K. Yoshinaga, S. Shiosaka, J. A. Hammarback, F. Urano and K. Imaizumi. Autophagy

Is Activated for Cell Survival after Endoplasmic Reticulum Stress. *Mol. Cell Biol.*, **2006**, *26*, 9220–9231.

50. I. Tanida, T. Ueno and E. Kominami. LC3 and Autophagy. *Methods Mol. Biol.*, **2008**, *445*, 77–88.

51. M. Mauthe, I. Orhon, C. Rocchi, X. Zhou, M. Luhr, K. J. Hijlkema, R. P. Coppes, N. Engedal, M. Mari and F. Reggiori. Chloroquine inhibits autophagic flux by decreasing autophagosome-lysosome fusion *Autophagy*, **2018**, *14*, 1435–1455.

52. A. G. Porter and R. U. Jänicke. Emerging roles of caspase-3 in apoptosis. *Cell Death Differ.*, **1999**, *6*, 99–104.

53. G. Mariño, M. Niso-santano, E. H. Baehrecke and G. Kroemer. Self-consumption: the interplay of autophagy and apoptosis *Nat. Rev. Mol. Cell Biol.*, **2014**, *15*, 81–94.

54. S. W. G. Tait and D. R. Green. Mitochondria and cell death: outer membrane permeabilization and beyond. *Nat. Rev. Mol. Cell Biol.*, **2010**, *11*, 621–632.

55. V. Petronilli, G. Miotto, M. Canton, M. Brini, R. Colonna, P. Bernardi and F. Di Lisa. Transient and Long-Lasting Openings of the Mitochondrial Permeability Transition Pore Can Be Monitored Directly in Intact Cells by Changes in Mitochondrial Calcein Fluorescence *Biophys. J.*, **1999**, *76*, 725–734.

56. M. An, C. Yu, J. Xi, J. Reyes, G. Mao, W. Wei and H. Liu. Induction of necrotic cell death and activation of STING in the tumor microenvironment via cationic silica nanoparticles leading to enhanced antitumor immunity. *Nanoscale*, **2018**, *10*, 9311-9319.

Chapter 3

Inducing Endoplasmic Reticulum Stress in Cancer Cells using Graphene Oxide-based Nanoparticles

This chapter has been published as:

Shalini Pandey, Aditi Nandi, Sudipta Basu and Nirmalya Ballav. Inducing endoplasmic reticulum stress in cancer cells using graphene oxide-based nanoparticles. *Nanoscale Adv.*, **2020**, 2, 4887-4894

3.1 Abstract

The endoplasmic reticulum is one of the vital organelles primarily involved in protein synthesis, folding, and transport and lipid biosynthesis. However, in cancer cells its functions are dysregulated leading to ER stress. ER stress is now found to be closely associated with hallmarks of cancer and has subsequently emerged as an alluring target in cancer therapy. However, specific targeting of the ER in a cancer cell milieu remains a challenge. To address this, in this report we have engineered ER-targeted self-assembled 3D spherical graphene oxide nanoparticles (ER-GO-NPs) encompassing dual ER stress inducers, doxorubicin and cisplatin. DLS, FESEM and AFM techniques revealed that the nanoparticles were spherical in shape with a sub 200 nm diameter. Confocal microscopy confirmed the specific homing of these ER-GO-NPs into the subcellular ER within 3 h. A combination of gel electrophoresis, confocal microscopy and flow cytometry studies revealed that these ER-GO-NPs induced ER stress mediated apoptosis in HeLa cells. Interestingly, the nanoparticles also activated autophagy which was inhibited through the cocktail treatment with ER-GO-NPs and chloroquine (CQ). At the same time these ER-GO-NPs were found to be efficient in prompting ER stress associated apoptosis in breast, lung and drug resistant triple negative breast cancer cell lines as well. We envision that these ER specific self-assembled graphene oxide nanoparticles can serve as a platform to exploit ER stress and its associated unfolded protein response (UPR) as a target resulting in promising therapeutic outcomes in cancer therapy.

3.2 Introduction

Cancer cells endure both oncogenic and environmental stresses while they relentlessly proliferate. These stresses act as potential growth inhibiting factors for tumorigenesis.[1–3] To counter them, cancer cells exploit an innate adaptive mechanism of the unfolded protein response (UPR) launched by the endoplasmic reticulum (ER) of cells.[4,5] The ER is a major regulator of various metabolic processes including protein synthesis and folding.[6,7] A high proliferation rate of cancer cells requires increased protein demands leading to ER stress, a condition characterized by accumulation of unfolded or misfolded proteins in the ER lumen.[8,9] In response to such stresses, the cytoprotective UPR mechanism is triggered and cells work in a coordinated fashion to establish ER homeostasis.[9–11]

The baseline activity level of the ER stress response system in normal and cancer cells differs.[12] Cancer cells display chronically elevated ER stress levels hinting that they are already

struggling to survive. The burden on the ER stress response system when aggravated would lose its pro-survival feature. On the other hand, its proapoptotic module is triggered.[13] The persistent activity of chronic ER stress in tumor cells may constitute an Achilles heel and provide a window of opportunity for development of therapeutic regimens. Growing interest in the UPR as a therapeutic target in cancer has led to the development of several pharmacological agents that induce cancer cell death by impairing the UPR.[14–16] Bortezomib, 17-AAG, and brefeldin-A are to name a few that have recently been added to the list of promising UPR inhibitors.[17,18] Interestingly, several in-clinic chemotherapeutics such as doxorubicin and cisplatin have been explored to establish new targets in the ER. Doxorubicin has been shown to inhibit the IRE1-α arm of the UPR.[19] On the other hand, cisplatin binds to proteins such as calreticulin and protein disulphide isomerase (PDI) residing in the ER and induces stress.[20–23] In fact, various cancer cell lines have shown increased sensitivity to cisplatin when it is used in combination with other ER stress inducers.[16] However, doxorubicin and cisplatin exert off-target cytotoxicity especially damaging topoisomerases and nuclear DNA respectively.[24,25] Hence selectively delivering these stress inducers directly into the subcellular ER in cancer cells is a daunting task due to limited chemical tools present.

In recent years, nanoscale materials have been used to address this challenge. Lipidic and polymeric nanoparticles, small molecule based supramolecular self-assemblies have been developed to specifically navigate to the ER, induce stress and impair the UPR.[26,27] Graphene oxide (GO) based nanoplatforms have also emerged as a promising candidate owing to the panoply of features they possess.[28,29] Apart from being biocompatible and biodegradable, their unique aromatic π–π system and surface modalities present allow for stacking of drugs and conjugation of targeting moieties.[30–33] Nonetheless, there is a serious lack of effective nanoscale tools for impairment of the adaptive UPR and induction of ER stress mediated apoptosis in cancer cells.

To address this, in this manuscript we report easy and robust engineering of self-assembled graphene oxide nanoparticles (ER-GO-NPs), decorated with dansyl groups (for ER localization), encompassing ER stress inducers (doxorubicin and cisplatin) (Scheme 3.1a). These ER-GO-NPs were spherical in shape with a sub-200 nm diameter confirmed by light scattering (DLS) and electron microscopy (SEM and AFM). These ER-GO-NPs specifically localized into the subcellular ER of HeLa cervical cancer cells within 3 h and released their payload causing UPR impairment as visualised by confocal laser scanning microscopy (CLSM) and gel electrophoresis (Scheme 3.1b). This nanoparticle-mediated ER stress led to

the activation of autophagy which was inhibited by autophagy inhibitor chloroquine in a combination treatment.

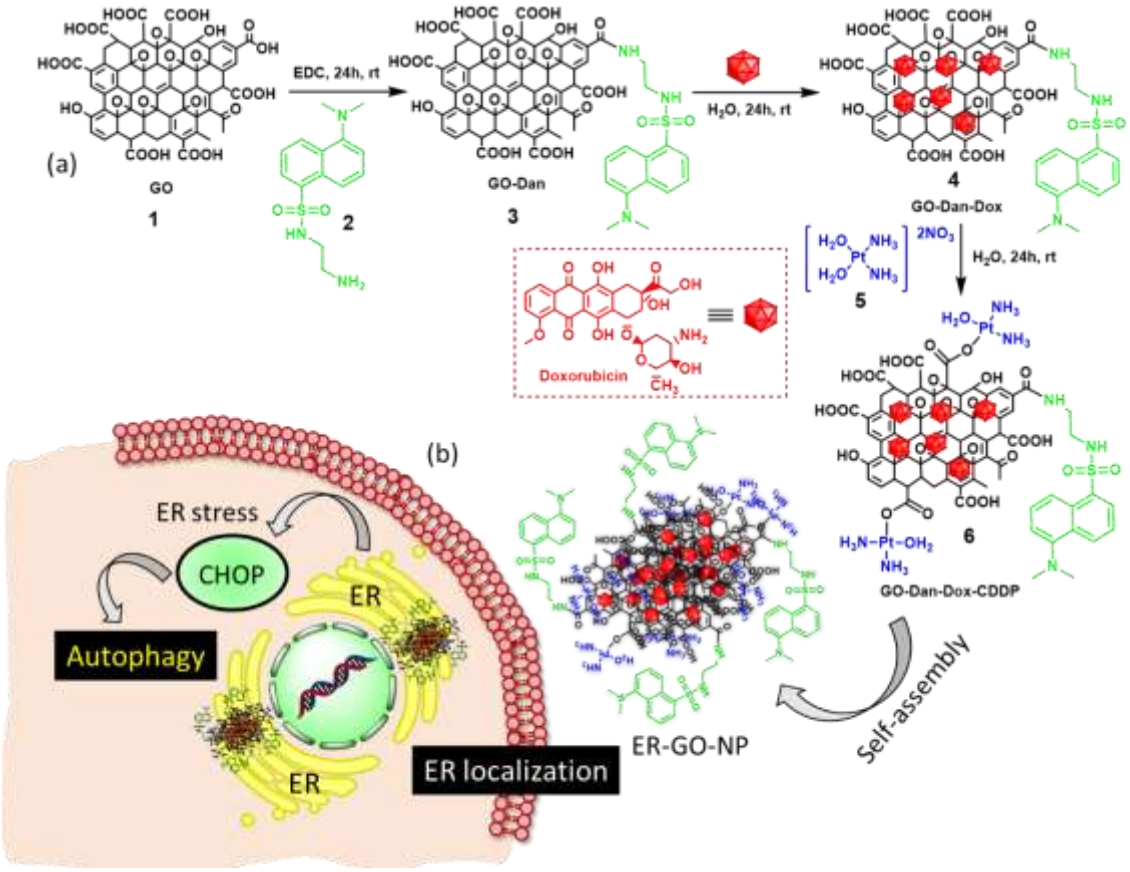

Scheme 3.1: (a) Synthetic scheme for engineering ER targeted GO-nanoparticles (ER-GO-NPs). (b) Schematic representation of ER stress induction of ER-GO-NPs in cancer cells leading to autophagy and apoptosis.

3.3 Results and Discussion

3.3.1 Engineering ER specific GO-based nanoparticles. To specifically navigate the GO-based NPs to the subcellular ER, we planned to conjugate the dansyl moiety to the GO surface *via* the ethylene diamine linker. We have chosen the dansyl moiety for ER targeting (a) as it has the necessary sulfonamide functionality to interact with the sulphonamide receptors present on the ER surface and (b) due to its fluorescent nature for sub-cellular ER trafficking of the nanoparticles in cancer cells.[26,27,35-37] We have capitalized upon the combination of doxorubicin and cisplatin, clinically used to treat several malignancies, to inhibit the UPR in cancer cells. Moreover, fluorescent Dox will also help us to visualize the localization of the nanoparticles into the sub-cellular ER through fluorescence microscopy. The dansyl moiety

was conjugated to the free carboxylic acid (–COOH) groups of 2D GO sheets (**1**) using the ethylene diamine linker *via* amide coupling by reacting GO and the dansyl ethylene diamine conjugate (**2**) in a 1: 5 weight ratio in the presence of EDC as a coupling reagent in water for 24 h to obtain the GO–dansyl conjugate (GO–Dan) (**3**) (Scheme 3.1a). Doxorubicin was then stacked onto the two-dimensional GO–Dan (**3**) surface by aromatic π–π interactions by incubating Dox and GO–Dan in a 1: 1 weight ratio in water for 24 h to obtain GO–Dan–Dox (**4**). The presence of the dansyl moiety and Dox over GO was confirmed by UV-Vis spectroscopy (Fig. 3.1a and b). The characteristic peaks at λ_{max} = 350 nm and λ_{max} = 480 nm validated the presence of dansyl and doxorubicin respectively. Furthermore, stacking of Dox on GO–Dan–Dox (**4**) was confirmed by fluorescence microscopy. Drastic reduction in the fluorescence emission intensity of Dox stacked on GO compared to free Dox at λ_{max} = 590 nm confirmed the incorporation of doxorubicin over the GO surface (Fig. 3.1c). GO–Dan–Dox (**4**) was further reacted with $[(OH_2)_2Pt(NH_3)_2]^{2+}$ in a 1 : 5 ratio in water for another 24 h followed by dialysis to afford the GO–Dan–Dox–CDDP conjugate (**6**). Conjugate **6** was found to hierarchically self-assemble into spherical nanoparticles (ER-GO-NPs) which was in complete agreement with our previous study wherein we had observed the graphene oxide sheets to self assemble into spherical nanoparticles in presence of cisplatin.[33,34]

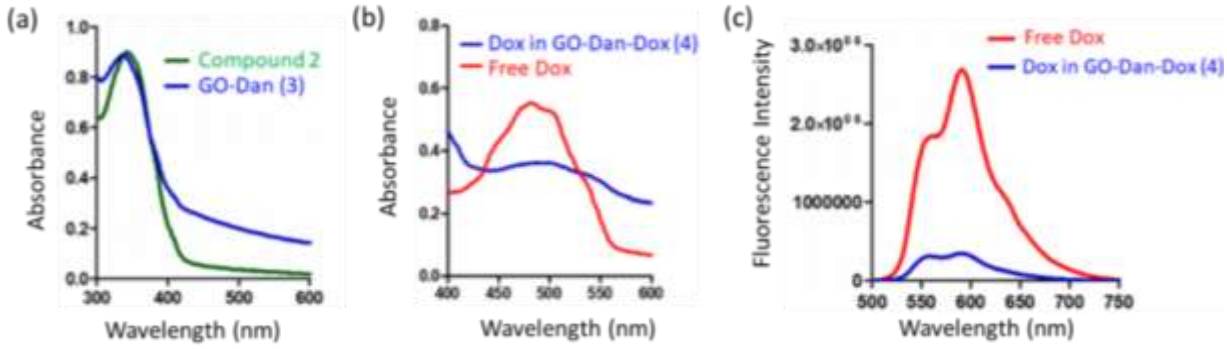

Figure 3.1: (a, b) UV-Vis spectra confirming the presence of dansyl and dox. (c) Fluorescence emission spectra exhibiting the stacking of dox on GO surface.

The hydrodynamic diameter of the ER-GO-NPs was found to be 145 nm by dynamic light scattering (DLS) (Fig. 3.2a). The spherical morphology of ER-GO-NPs was visualized by field emission-scanning electron microscopy (FESEM) and atomic force microscopy (AFM) (Fig. 3.2b and c). These shape and size are suitable for the accumulation of ER-GO-NPs into tumor tissues through the enhanced permeability and retention (EPR) effect.[38,39] The presence of cisplatin in ER-GO-NPs was confirmed by elemental mapping of Pt using FESEM based energy dispersive X-ray spectroscopy (EDAX) (Fig. 3.2e). The characteristic D and G bands

in the single particle Raman spectra confirmed the presence of GO in ER-GO-NPs (Fig. 3.2d). We finally evaluated the loading of doxorubicin and cisplatin in ER-GO-NPs using UV-Vis spectroscopy. It was estimated that the ER-GO-NPs contained 196 μg mL^{-1} and 100 μg mL^{-1} doxorubicin and cisplatin with 78% and 80% drug loading efficiency respectively (Fig. 3.2f).

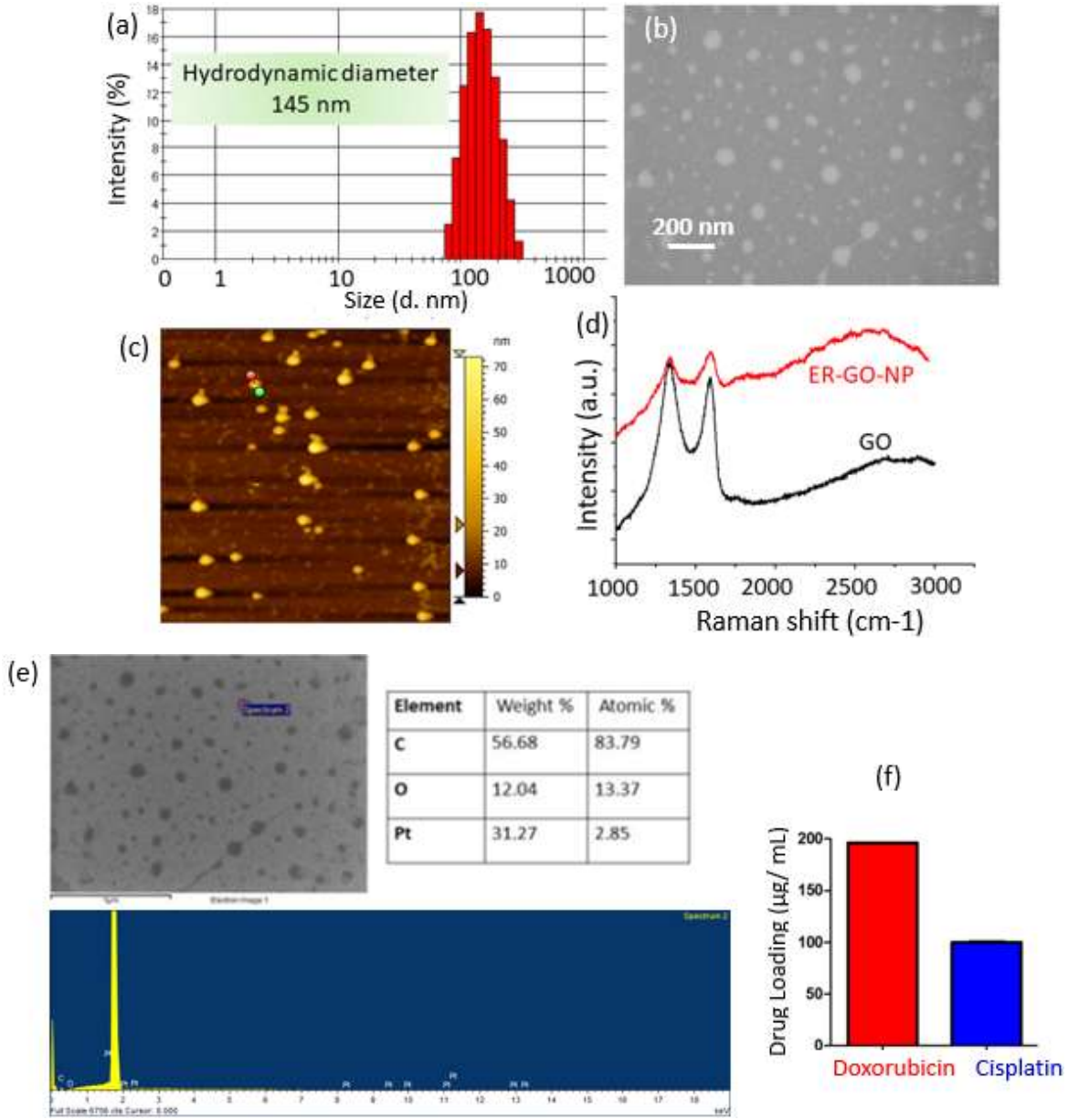

Figure 3.2: (a-c) DLS, FESEM and AFM images of ER-GO-NPs. (d) Single particle Raman spectra of ER-GO-NPs to show the presence of GO. (e) EDAX of ER-GO-NPs from FESEM confirming the presence of cisplatin. (f) Drug loading of dox and cisplatin in ER-GO-NPs.

3.3.2 ER homing. We hypothesized that the dansyl group will facilitate the internalization of the ER-GO-NPs into sub-cellular ER due to the presence of sulphonamide receptors. To validate our hypothesis, we treated HeLa cervical cancer cell with ER-GO-NPs at different time points (3 h, 6 h, 12 h and 24 h) and co-stained them with ER-Tracker Green. We then visualised the live cells using confocal laser scanning microscopy (CLSM). The fluorescence microscopy images revealed that the ER-GO-NPs started internalizing in the ER within 3 h and the accumulation gradually increased with time (Fig. 3.3). Further quantification by CLSM using Pearson's and Mander's coefficients confirmed that the ER-GO-NPs localized into ER with Pearson's coefficient of 0.72 and 0.86 and Mander's coefficients of 0.92 and 0.97 at 3 h and 6 h respectively (Table B1, Appendix-B). Confocal images of incubation at higher time points (12 h and 24 h) revealed that the ER-GO-NPs retained in the ER with Pearson's coefficient of 0.73 and 0.86 and Mander's coefficients of 0.972 and 0.97 respectively.

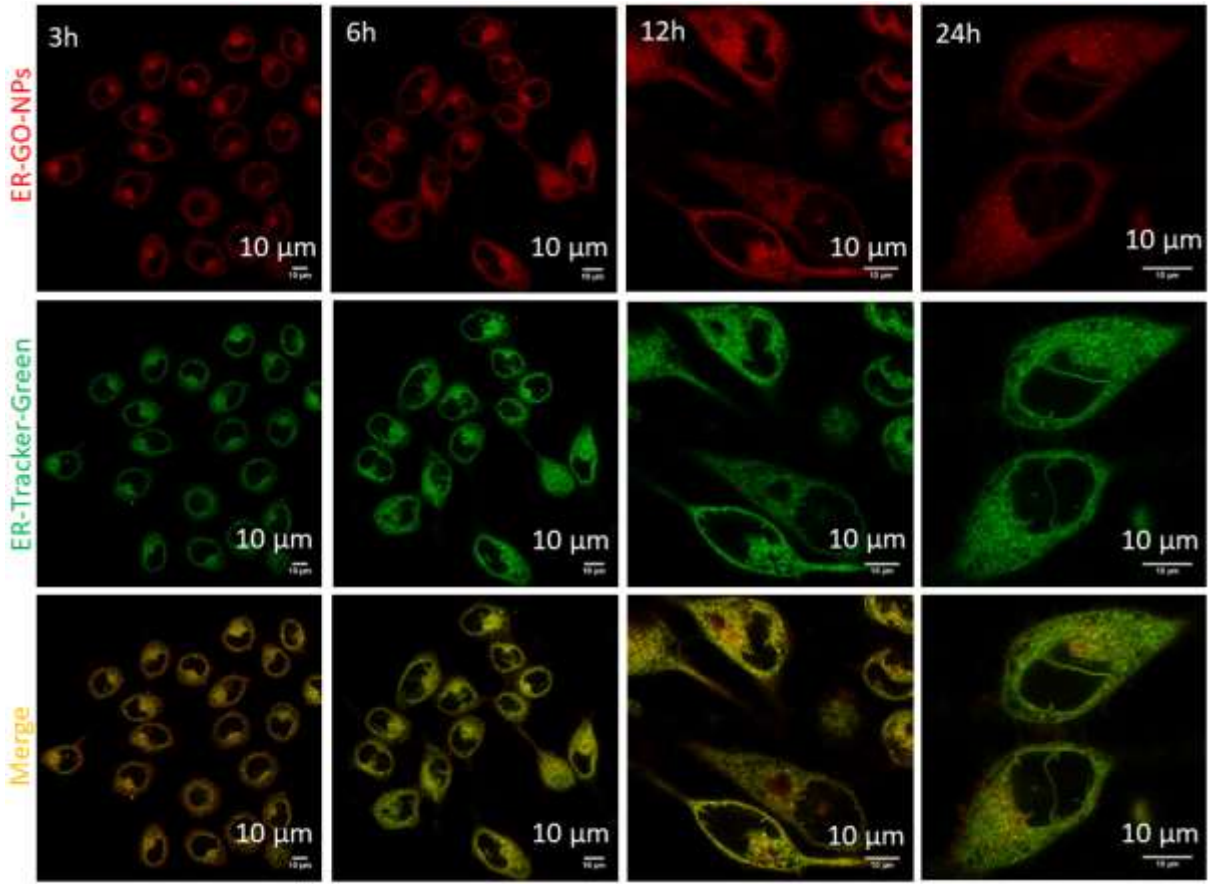

Figure 3.3: Confocal laser scanning microscopy images of HeLa cells treated with ER-GO-NPs (red fluorescent) at 3 h, 6 h, 12 h and 24 h. The cells were counter stained with ER-Tracker-Green dye. Scale bar = 10 µm.

To evaluate the specific localization of ER-GO-NPs into ER compared to the other organelles, we also visualized the localization of ER-GO-NPs in mitochondria. We treated the HeLa cells with ER-GO-NPs for 12 h and 24 h followed by staining mitochondria with MitoTracker Deep Red dye. The cells were then visualized under confocal microscopy. From the confocal images, we can clearly observe that even at 12 h and 24 h, very low yellow regions were visible by overlapping green and red fluorescence from ER-GO-NPs and MitoTracker Deep Red respectively (Fig. 3.4). We also confirmed the lower accumulation of ER-GO-NPs into mitochondria at 12 h and 24 h from the lower value of Pearson's and Mander's coefficients (Table B2, Appendix-B).

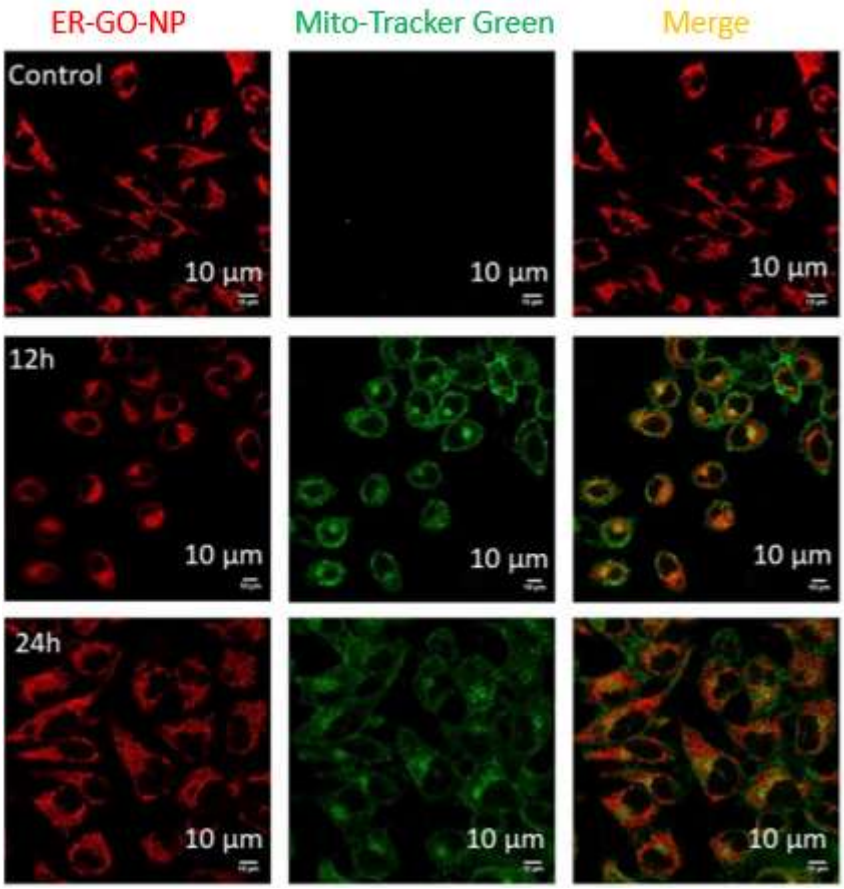

Figure 3.4: Confocal laser scanning microscopy images of HeLa cells treated with ER-GO-NPs (red fluorescent) at 12 h and 24 h post incubation. Mitochondria were counter stained with red fluorescent Mito Tracker Deep Red. Scale bar = 10 µm.

Our previous experience showed that GO nanoparticles initially localize into lysosomes in the cancer cells through a clathrin mediated endocytosis.[34,40] To evaluate the homing into lysosomal compartments, we treated HeLa cells with ER-GO-NPs at 1 h, 3 h and 6 h time points and co-stained the lysosomes with Lyso Tracker Green dye. The ER-GO-NPs showed

inherent red fluorescence due to the presence of doxorubicin. We visualized the cells under confocal microscopy. We observed considerable number of yellow signals at 3 h (Fig. 3.5) which showed that the ER-GO-NPs localized into lysosomes within 3 h. However, at 6 h, we hardly visualized any colocalization. This observation was also confirmed from high value of Pearson's and Mander's coefficients at 3 h with very low value at both 1 h and 6 h time points (Table B3, Appendix-B). It was previously observed that dansyl-coated nanoparticles showed positive surface charge in acidic milieu (in lysosome) which we expected to be the reason behind the quick escape of dansyl-coated ER-GO-NPs from lysosomes through electrostatic repulsion.[26] Furthermore, from our earlier report, we found out that doxorubicin and cisplatin loaded self-assembled GO nanoparticles released less than 10% of their payload in acidic medium of pH = 5.5 at 6 h.[34] This observation clearly indicated that ER-GO-NPs would lose minimum amount of ER stress inducers in lysosomes due to their quick escape from lysosomes within 3 h. Hence, from these confocal microscopy studies, it was evident that ER-GO-NPs homed into ER within 3 h and hardly localized into mitochondria. These ER-GO-NPs localized initially into lysosomes within 3 h, but slowly escaped them to home into ER.

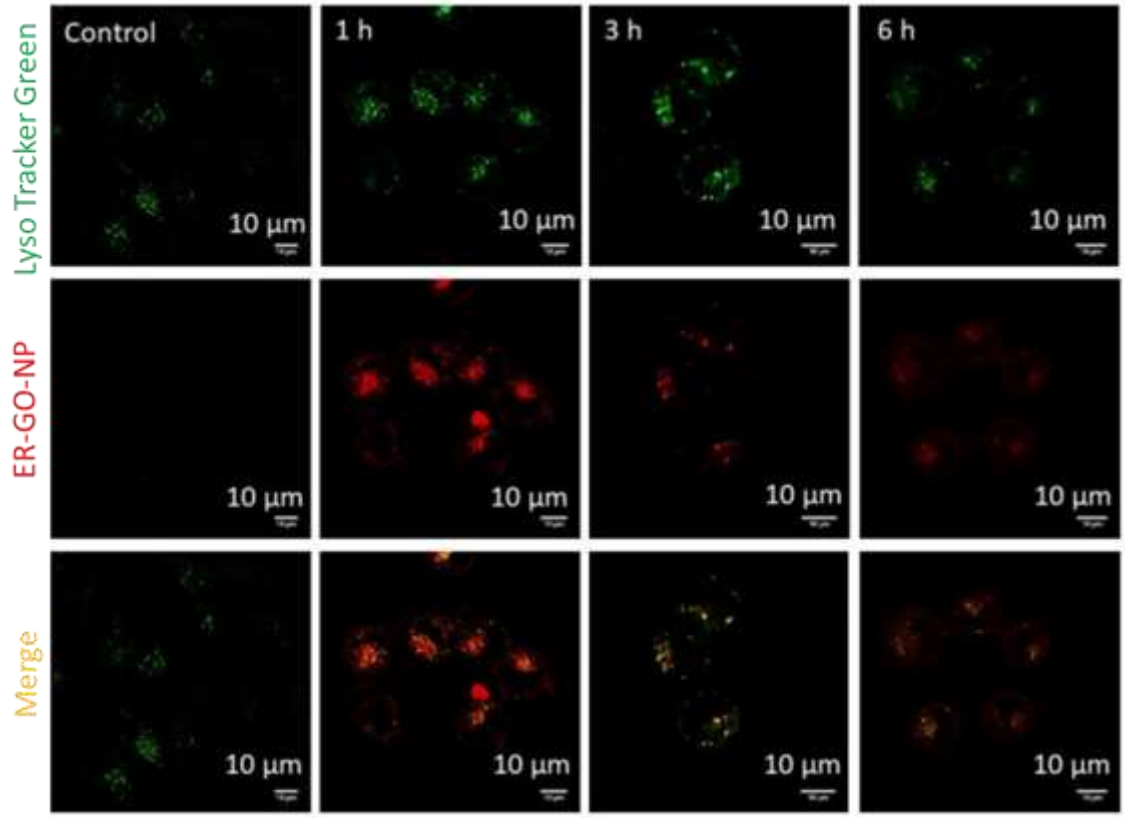

Figure 3.5: Confocal laser scanning microscopy images of HeLa cells treated with ER-GO-NPs (red fluorescent) at 1 h, 3 h and 6 h post incubation. Lysosomes were stained with Lyso Tracker Green DND-26 (green fluorescent). Scale bar = 10 µm.

3.3.3 Induction of ER stress and DNA damage. Once internalized into the ER of the HeLa cells, we anticipate that the carboxylesterases present in ER[41] will cleave the coordinate bond between Pt and carboxylic acid of GO to release cisplatin followed by disintegration of the self-assembled ER-GO-NPs. This carboxylesterase mediated fragmentation of the nanoparticle will also release GO-stacked doxorubicin.[34] This simultaneous release of cisplatin and doxorubicin would further induce ER stress impairing UPR. Onset of ER stress leads to increased expression of CHOP, a marker for ER stress induced apoptosis.[42,43] We visualized the increment in CHOP expression by immunofluorescence assay. We incubated HeLa cells with ER-GO-NPs for 24 h followed by treatment with CHOP specific primary antibody. The primary antibody was further detected by an Alexa Fluor 594 tagged secondary antibody (red fluorescent). Nucleus of the cells were stained with blue fluorescent DAPI and then visualized using confocal microscopy. Confocal images showed that cells treated with ER-GO-NPs showed a significant increase in red fluorescence intensity as compared to control (Fig. 3.6a). Confocal microscopy-based quantification showed that ER-GO-NP treatment increased the expression of CHOP by 3.8 folds compared to the control non-treated cells (Fig. 3.6b). Induction of ER stress leads to increase in levels of CHOP as well as its accumulation in nucleus. The overlap of red fluorescent signals with blue fluorescent signals of DAPI leading to purple fluorescence confirmed that CHOP accumulated in the nucleus upon ER stress induction by ER-GO-NPs, which was absent in the control cells.

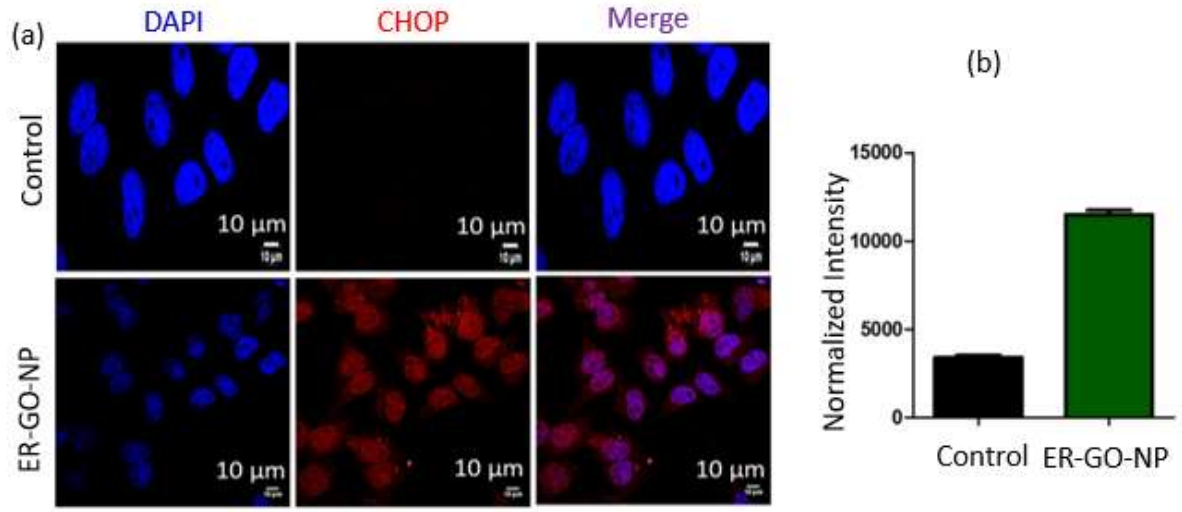

Figure 3.6: (a) Fluorescence confocal images of HeLa cells treated with ER-GO-NPs for 24 h followed by treatment with CHOP-primary antibody and Alexa Fluor 594-tagged secondary

antibody (Red). Nuclei were stained with DAPI (Blue). Scale bar = 10 μm. (b) Quantification of CHOP from confocal microscopy.

We also evaluated the expression of CHOP by gel electrophoresis. We treated HeLa cells with ER-GO-NPs for 24 h followed by their lysis and then separated the proteins to perform Western blot analysis. We observed an increment of CHOP expression by 1.6 folds compared to the non-nanoparticle treated control cells (Fig. 3.7a and c). We expected this lower increment in CHOP expression as doxorubicin inhibits XBP1 protein which prevents upregulation of CHOP.[44] To further estimate the ER stress, we evaluated the expression level of GRP78, one of the key markers for triggering of ER stress induction by Western blot analysis.[45-47] It was observed that while control cells hardly showed any expression of GRP78, the ER GO-NP treated cells showed increased levels of GRP78 (1.5 folds) indicating the onset of ER stress (Fig. 3.7b and d).

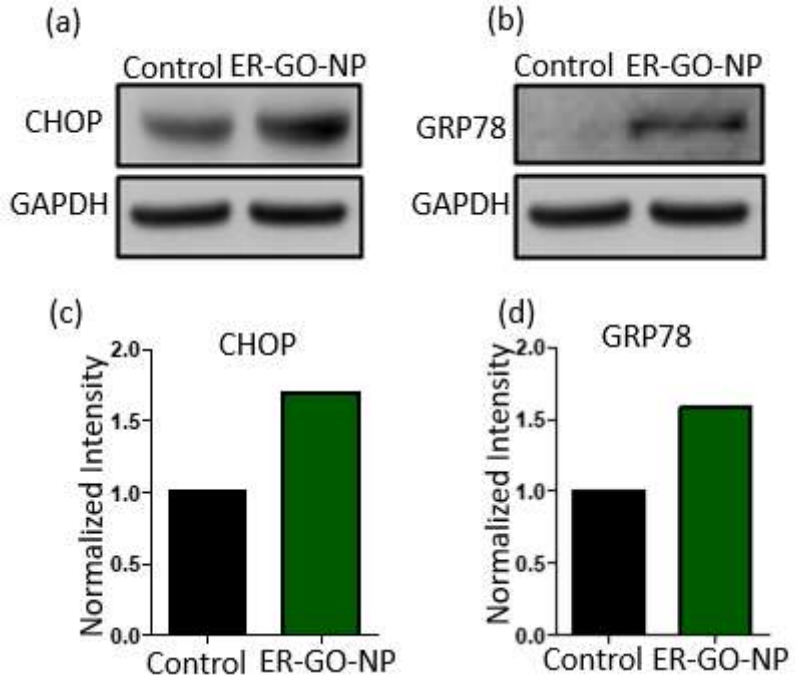

Figure 3.7: (a,b) Western blot images of HeLa cells after treatment with ER-GO-NPs for 24 h to evaluate the expression of CHOP and GRP78 as ER stress markers respectively. (c,d) Quantification of CHOP and GRP78 from western blot analysis.

The protooncogene CHOP also known as growth arrest and DNA damage 153 (GADD 153) encodes for DNA damage as well.[48, 49] Therefore, we expect that induction of ER stress by ER-GO-NPs will lead to damage of nuclear DNA. We validated the DNA damage by ER-GO-NPs by immunofluorescence assay. We incubated HeLa cells with ER-GO-NPs for 24 h and then treated the cells with γH2AX specific primary antibody followed by Alexa Fluor 594 tagged

secondary antibody (red fluorescence). We also stained the nucleus of the HeLa cells with blue fluorescent DAPI. We then visualized cells by confocal microscopy and observed an enhanced red fluorescence in treated cells as compared to control (Fig. 3.8a). Furthermore, purple fluorescence observed due to the overlap of red and blue fluorescence signals confirmed that the ER GO-NPs damaged nuclear DNA. We also evaluated the ER-GO-NP-mediated DNA damage by Western blot analysis. We treated HeLa cells with ER-GO-NPs for 24 h, extracted the proteins and performed the gel electrophoresis. From the Western blot image, it was clear that control cells showed negligible expression of γH2AX. However, the ER-GO-NP treated cells showed a significant increase (3 folds) in the expression of γH2AX (Fig. 3.8b and c). These confocal imaging and Western blot analysis revealed that ER-GO-NPs induced ER stress and DNA damage in HeLa cells.

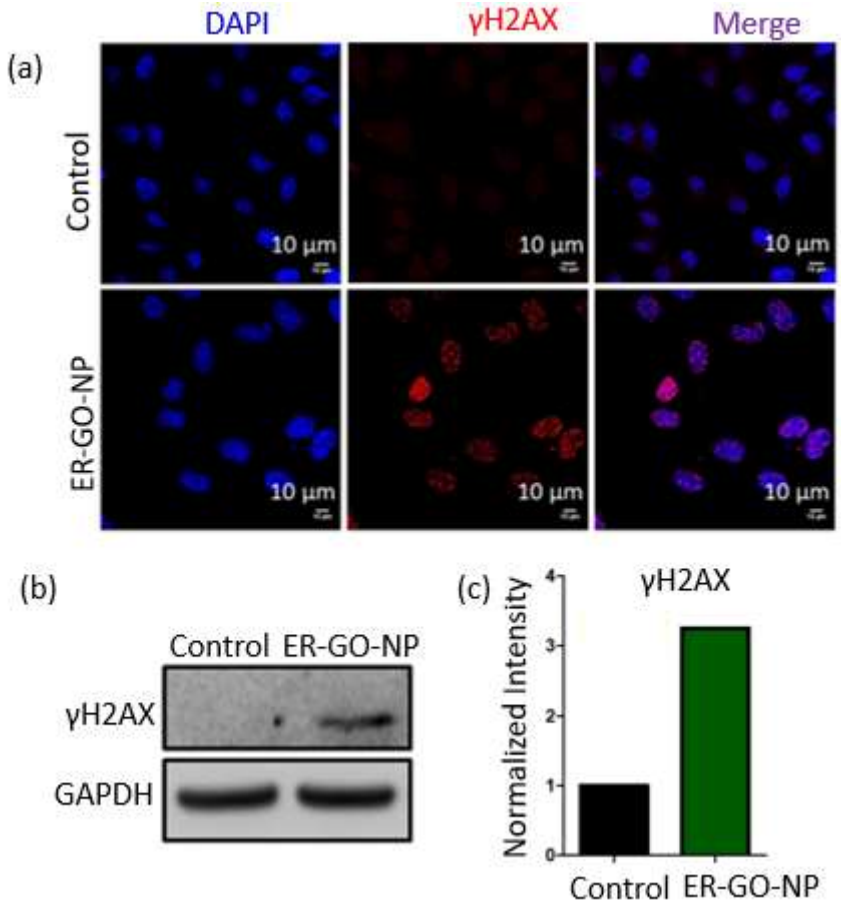

Figure 3.8: (a) Confocal images of the HeLa cells treated with ER-GO-NPs for 24 h and stained with γH2AX selective primary antibody followed by Alexa Fluor 594-tagged secondary antibody (Red). Nucleus were stained with DAPI (Blue). Scale bar = 10 μm. (b) Western blot analysis after treating HeLa cells with ER-GO-NPs for 24 h to show the expression of γH2AX as DNA damage marker. (c) Quantification of γH2AX from western blot analysis.

3.3.4 Autophagy induction. ER stress is also a potent trigger for autophagy, a self-degradative process with adaptive functions.[50, 51] To validate if autophagy was activated upon treatment with ER-GO-NPs, we evaluated the expression level of LC3B as an autophagy marker.[52] We validated the expression of LC3B using immunofluorescence assay. HeLa cells were treated with ER-GO-NPs for 24 h, incubated with LC3B primary antibody followed by secondary antibody tagged with Alexa Fluor 488 dye (green). We stained the nucleus with DAPI (blue). We observed formation of puncta (autophagosomes) in the ER-GO-NP treated cells as compared to control cells (Fig. 3.9a). This formation of autophagosomes is a hallmark of autophagy.[53]We further validated the expression of LC3B by Western blot analysis. We treated HeLa cells with ER-GO-NPs for 24 h and the cellular proteins were subjected to the gel electrophoresis. From the Western blot image, we observed that ER-GO-NPs increased the expression of LC3B in HeLa cells compared to the control cells (Fig. 3.9b). Further quantification also confirmed that ER-GO-NPs increased the expression of LC3B by 11 folds compared to control cells (Fig. 3.9c).

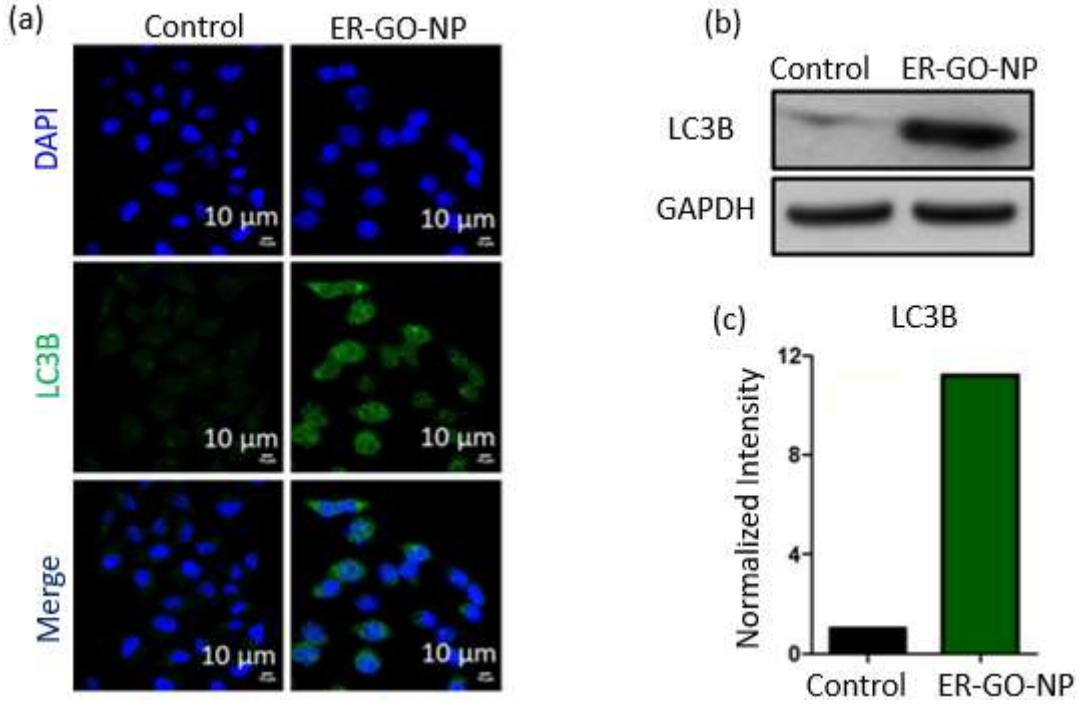

Figure 3.9: (a) Confocal images of HeLa cells after treatment with ER-GO-NPs for 24 h and stained with primary antibody specific for LC3B, followed by Alexa Fluor 488 tagged secondary antibody (green). (b) Western blot analysis of LC3B after incubation of HeLa cells with ER-GO-NPs for 24 h. (c) Quantification of LC3B from western blot analysis.

We also evaluated the level of Beclin, another autophagy marker via immunofluorescence assay.[54] We incubated HeLa cells with ER-GO-NPs for 24 h. We then treated HeLa cells with Beclin specific primary antibody followed by incubation with Alexa Fluor 594 tagged secondary antibody (red). We also counter stained the nucleus of the cells with DAPI (blue). We then visualized the cells using confocal microscopy. Increased red fluorescence in treated cells as compared to control indicate that Beclin expression has indeed increased to trigger autophagy (Fig. 3.10). These immunofluorescence assays and Western blot analysis thus showed that ER-GO-NPs induced ER stress in HeLa cells. Prolonged ER stress triggered autophagy as an adaptive response to it. Interestingly, to induce autophagy the ER-GO-NPs needed to escape the lysosomes quickly and localize into ER to trigger ER stress. As prolonged lysosomal homing of ER-GO-NPs would release the ER stress inducers prematurely into the cytosol leading to non-specific effects in other organelles like nucleus towards direct apoptosis. We anticipate that this induction of autophagy could be specific degradation of endoplasmic reticulum through ER-phagy which is currently an elusive field of study.[55, 56]

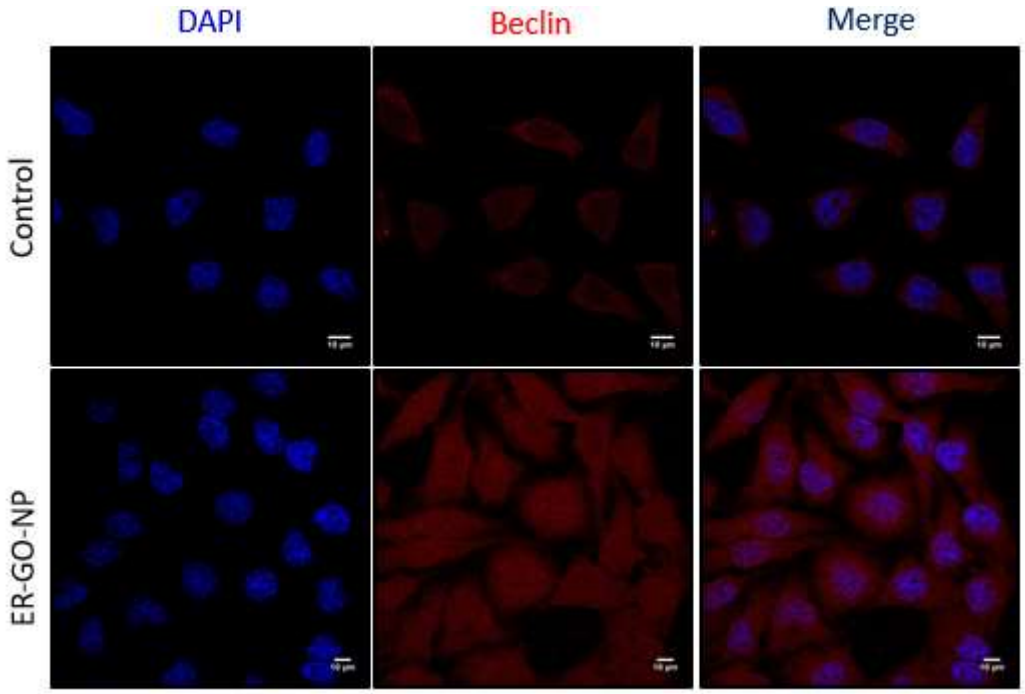

Figure 3.10: Confocal images of the HeLa cells after treatment with ER-GO-NPs for 24 h. The cells were stained with primary antibody specific for Beclin followed by Alexa Fluor 594 tagged secondary antibody (red). Scale bar = 10 μm.

3.3.5 Apoptosis and cell death. Finally, we expected the ER-GO-NPs to induce ER stress mediated apoptosis in HeLa cells. We estimated the apoptosis induced by ER-GO-NPs by flow cytometry analysis. We treated HeLa cells with ER-GO-NPs and then stained the apoptotic and

necrotic cells with Annexin V-FITC (green) and propidium iodide (PI) (red) followed by flow cytometry. We found that ER-GO-NPs triggered early and late apoptosis in 61.3% and 35.7% cells respectively (Fig. 3.11a). Since autophagy is triggered upon treatment with ER-GO-NPs, we anticipated it to help cells escape apoptosis. Hence, we performed flow cytometry study along with combination with chloroquine (CQ). We treated HeLa cells with ER-GO-NPs and 50 μM of CQ and incubated for 24 h. The flow cytometry data revealed that cotreatment of ER-GO-NPs and CQ indeed resulted in 27.5% and 60.5% cells in early and late apoptotic stages respectively (Fig. 3.11a). This flow cytometry data confirmed ER-GO-NPs triggered early apoptosis and combination treatment with autophagy inhibitor induced late apoptosis.

Finally, to evaluate the effect of apoptosis induced by ER-GO-NPs in cancer cells, we treated HeLa cells with ER-GO-NPs at different concentrations for 24 h and quantified the cell viability by MTT assay. It was observed that on treatment with ER-GO-NPs, HeLa cells exhibited cell death with IC_{50} = 5 μM (Fig. 3.11b). We also treated HeLa cells with a combination of ER-GO-NPs in a dose dependent manner with CQ at 50 μM concentration for 24 h. The cell viability assay revealed that the combination of ER-GO-NPs and CQ showed much lower IC_{50} = 1.25 μM (Fig. 3.11b). Inspired by this data, we also validated the effect of ER-GO-NPs and CQ combination in other cancer cells like A549 (human lung carcinoma), MCF-7 (human breast cancer) and MDA-MB-231 (drug resistant triple negative breast cancer) by MTT assay. At 24 h post incubation, it was found that ER-GO-NPs demonstrated IC_{50} = 5 μM, 0.8 μM and 4 μM in A549, MCF-7 and MDA-MB-231 cells respectively (Fig. 3.11b). Interestingly, in the combination treatment with CQ, the IC_{50} value reduced to 1 μM in A549 and MDA-MB-231 cells. However, the combination treatment did not change the IC_{50} value in MCF-7 cells. It is intriguing to note that ER-GO-NPs and combination treatment with CQ lead to nearly 25% of cell viability in all the cancer cell lines tested at highest concentration (50 μM). We anticipate that the cell killing ability of the ER-GO-NPs alone or in combination could be improved by either increasing the exposure time to 48h or using a more potent autophagy inhibitor Bafilomycin A1.[57] Moreover, without ER targeting dansyl moiety, doxorubicin and cisplatin containing self-assembled GO nanoparticles would localize mainly into lysosomes and release the dual drugs in acidic pH followed by nuclear DNA damage leading to direct apoptosis and improved cell killing (IC_{50} = 2 μM) in HeLa cells without autophagy.[34]

To ascertain our hypothesis that the apoptosis induced in HeLa cells by ER-GO-NPs was ER stress mediated, we treated HeLa cells with ER-GO-NPs and 4-phenyl butyric acid (4-PBA), a well-known chemical chaperone to alleviate both toxicity and proteomic alterations induced

by an ER stress inducer, by aiding in protein folding in the ER.[58,59] We co-treated HeLa cells with ER-GO-NPs along with 15 μM PBA for 24 h and then performed the cell viability assay. We observed that co-treatment with 4-PBA drastically reduced the cell death as compared to treatment with ER-GO-NPs alone (Fig. 3.11c). 4-PBA augmented protein folding and thereby helped HeLa cells survive. This proved that apoptosis induced by ER-GO-NPs in HeLa cells was indeed ER stress mediated.

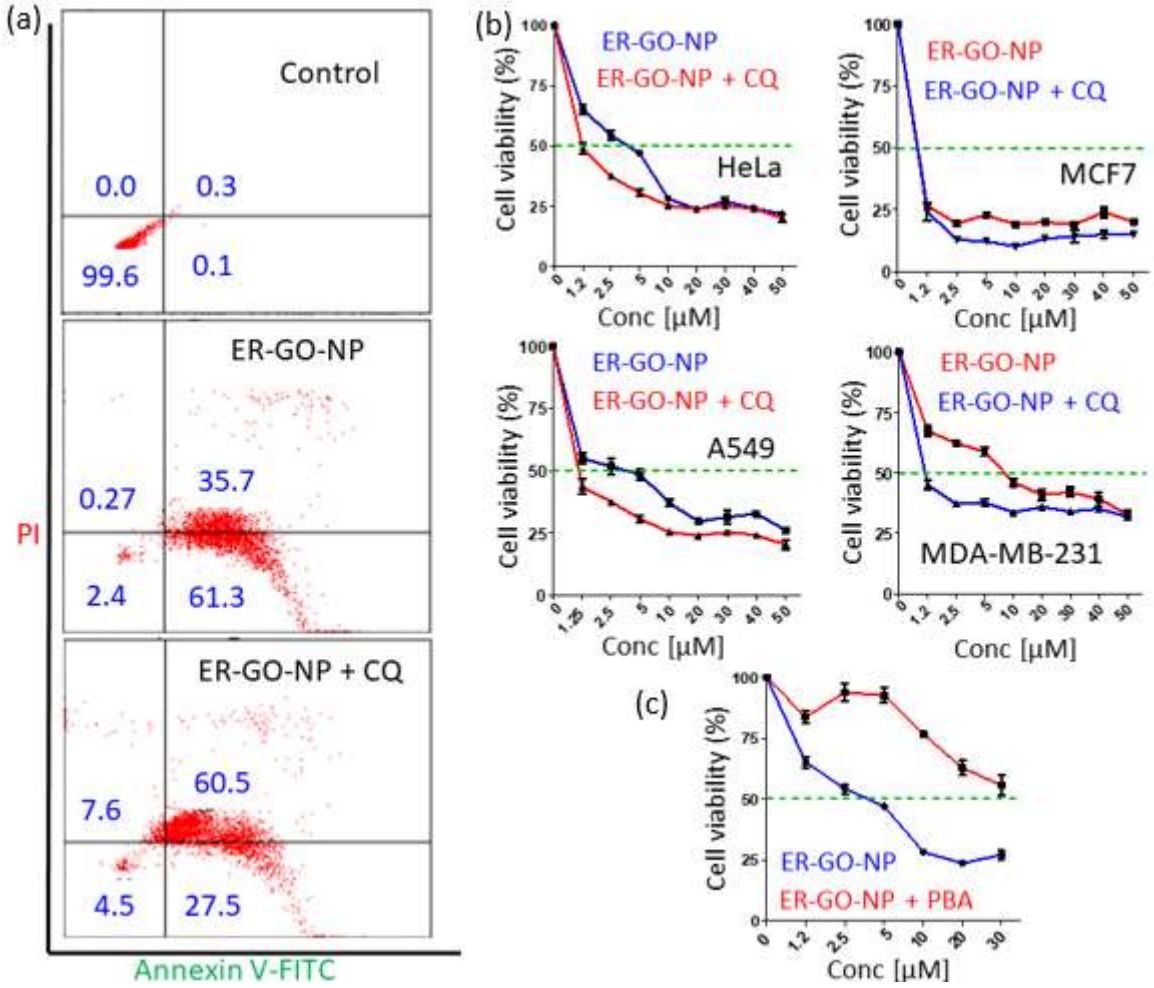

Figure 3.11: (a) Flow cytometry analysis of ER-GO-NPs and CQ in HeLa cells to evaluate the induction of apoptosis. (b) Dose dependent viability of HeLa, MDA-MB-231, MCF-7 and A549 cells after treatment with ER-GO-NPs, 24 h post incubation. (c) Cell viability of HeLa cells after co-treatment with ER-GO-NPs and 4-PBA, 24 h post incubation.

3.4 Material and Methods

3.4.1 Materials. Graphene oxide, dansyl chloride, cisplatin, Nunc® Lab-Tek® II chambered coverglass, sodium dodecyl sulfate (SDS) and silicon wafers for FESEM were purchased from

Sigma Aldrich. Doxorubicin was bought from Selleck Chemicals. Analytical thin-layer chromatography (TLC) was performed using 60 F254 pre-coated silica gel aluminium sheets bought from EMD Millipore Laboratories. UV-Visible spectra was recorded on Shimadzu. DMEM and 3-(4,5-dimethylthiazol-2-yl)-2,5-diphenyltetrazolium bromide (MTT) were purchased from HiMedia. MitoTracker® Deep Red, ER Tracker Green and LysoTracker Green DND-26 were purchased from Invitrogen. An Annexin-V-FITC staining kit was purchased from Roche. Flow cytometry analysis was performed on a BD-Accuri. Western blot analysis was performed on a Las ImageQuant 400.

3.4.2 Synthesis of *N*-(2-aminoethyl)-5-(dimethylamino) naphthalene-1-sulfonamide (2). A dansyl–ethylene diamine conjugate (**2**) was prepared according to a previously reported procedure.[26]

3.4.3 Synthesis of graphene-oxide-dansyl-doxorubicin-cisplatin nanoparticles (ER-GO-NPs). ER-GO-NPs were synthesised according to a previously reported procedure.[34] Briefly, graphene oxide (4 mg mL^{-1}) was dispersed in distilled water (1 mL) and the dansyl–ethylene diamine conjugate (**2**) was added in a 1 : 5 weight ratio in the presence of EDC as a coupling agent to obtain a GO–Dan conjugate (**3**). Doxorubicin (1 mg) dissolved in distilled water (1 mL) was then added to this GO–Dan conjugate (**3**) at room temperature. The reaction mixture was then allowed to stir for 24 h. To remove unreacted doxorubicin, the reaction mixture was dialyzed against distilled water through a dialysis membrane (MWCO = 1000 Dalton) for 6 h. Aquated cisplatin (5 mg mL^{-1}) was then added to the GO–Dan–Dox conjugate (**4**) and stirred at room temperature for 24 h. After the reaction was completed, the mixture was dialyzed again to remove excess aquated cisplatin to obtain ER-GO-NPs. The ER-GO-NPs were stored at 4 °C for further use.

3.4.4 Determination of the shape, size and morphology. The shape, size and morphology of the ER-GO-NPs were determined using dynamic light scattering (DLS) and electron microscopy techniques such as field-emission scanning electron microscopy (FESEM) and atomic force microscopy (AFM). The samples were prepared according to previously reported procedures.[34]

3.4.5 Quantification of the drug loading in the nanoparticles. The loading of doxorubicin and cisplatin in the ER-GO-NPs was determined at λ_{max}= 488 nm and 706 nm by UV-Vis spectroscopy using a previously reported method.[31] The drug loading efficiency was calculated using the formula:

$$\text{Drug Loading Efficiency (\%)} = \frac{Amount\ of\ drug\ loaded\ in\ nanoparticle}{Amount\ of\ drug\ used} X\ 100$$

3.4.6 ***In vitro*** **studies**. Confocal microscopy, cell viability assay, flow cytometry analysis and western blot analysis were performed by previously published methods.[26,27,34] Cell viability assays were performed in triplicate of triplicates (n=3) and the other assays were performed with n=2.

3.5 Conclusion

In conclusion, we have engineered dansyl (ER targeting moiety) decorated graphene oxide (GO) based nanoparticles simultaneously encompassing ER stress inducers doxorubicin and cisplatin through π–π stacking and coordinate linkage, respectively. We demonstrated specific homing of ER-GO-NPs into the subcellular ER of the HeLa cells, released their payload and induced ER stress as well as autophagy as a cellular defence mechanism. Further, ER-GO-NPs were employed to induce ER stress associated apoptosis in cervical cancer cells. Finally, these ER-GO-NPs alone and in combination with CQ showed remarkable cell killing efficacy in breast, lung and drug resistant triple negative breast cancer cells. We envision that these graphene oxide-based ER specific nanoparticles can be used as an effective tool in simultaneously impairing multiple targets in the unfolded protein response (UPR) signalling pathway in the ER thereby leading to better cancer therapeutics in the future.

3.6 Appendix-B

Treatment Time		3 h	6 h	12 h	24 h
Image Channels		C1 (red) C3 (green)	C1 (red) C3 (green)	C1 (red) C3 (green)	C1 (red) C3 (green)
Pearsons' Correlation Coeffecient		0.7264	0.8668	0.7371	0.8619
Manders Coeffecients	M1 (fraction of C1 overlapping C3)	0.9234	0.9764	0.9551	0.9776
	M2 (fraction of C3 overlapping C1)	0.9561	0.9736	0.9744	0.9791

Table B1: Quantification of co-localization of ER-GO-NPs in ER of HeLa cells at 3 h, 6 h, 12 h and 24 h from CLSM.

Treatment Time		12 h	24 h
Image Channels		C1 (red) C3 (green)	C1 (red) C3 (green)
Pearsons' Correlation Coeffecient		0.4697	0.2188
Manders Coeffecients	M1 (fraction of C1 overlapping C3)	0.3852	0.3151
	M2 (fraction of C3 overlapping C1)	0.4217	0.0225

Table B2: Quantification of co-localization of ER-GO-NPs in mitochondria of HeLa cells at 12 h and 24 h from CLSM.

Treatment Time		1 h	3 h	6 h
Image Channels		C1 (red) C3 (green)	C1 (red) C3 (green)	C1 (red) C3 (green)
Pearsons' Correlation Coeffecient		0.4132	0.8206	0.2966
Manders Coeffecients	M1 (fraction of C1 overlapping C3)	0.5733	0.9771	0.6659
	M2 (fraction of C3 overlapping C1)	0.6501	0.9674	0.7361

Table B3: Quantification of co-localization of ER-GO-NPs in lysosomes of HeLa cells at 1 h, 3 h and 6 h from CLSM.

REFERENCES

1. E. Madden, S. E. Logue, S. J. Healy, S. Manie and A. Samali. The role of the unfolded protein response in cancer progression: From oncogenesis to chemoresistance. *Biol. Cell.*, **2019**, *111*, 1-17.

2. J. R. Cubillos-Ruiz, S. E. Bettigole and L. H. Glimcher, Tumorigenic and Immunosuppressive Effects of Endoplasmic Reticulum Stress in Cancer. *Cell*, **2017**, *168*, 692-706.

3. M. Wang and R. J. Kaufman. The impact of the endoplasmic reticulum protein-folding environment on cancer development. *Nat. Rev. Cancer*, **2014**, *14*, 581-597.

4. S. S. Cao and R. J. Kaufman. Endoplasmic Reticulum Stress and Oxidative Stress in Cell Fate Decision and Human Disease. *Antioxid Redox Signal*, **2014**, *21*, *396-413.*

5. J. Miles, R. Scherz-Shouval and P. van Oosten-Hawle. Expanding the Organismal Proteostasis Network: Linking Systemic Stress Signaling with the Innate Immune Response. *Trends Biochem Sci.*, **2019**, *44*, 927-942.

6. D. Ron and H. P. Harding. Protein-Folding Homeostasis in the Endoplasmic Reticulum and Nutritional Regulation. *Cold Spring Harb Perspect Biol*, **2012**, *4*, a013177.

7. J. Lee and U. Ozcan. Unfolded Protein Response Signaling and Metabolic Diseases. *J Biol Chem.*, **2014**, *289*, 1203-1211.

8. H. J. Clarke, J. E. Chambers, E. Liniker and S.J. Marciniak, Endoplasmic Reticulum Stress in Malignancy. *Cancer Cell*, **2014**, *25*, 563-573.

9. R. Clarke, K. L. Cook, R. Hu, C. O. B. Facey, I. Tavassoly, J.L. Schwartz, W.T. Baumann, J.J. Tyson, J. Xuan, Y. Wang, A. Wärri and A.N. Shajahan. Endoplasmic Reticulum Stress, the Unfolded Protein Response, Autophagy, and the Integrated Regulation of Breast Cancer Cell Fate, *Cancer Res.*, **2012**, *72*, 1321–31.

10. A. Walczak, K. Gradzik, J. Kabzinski , K. Przybylowska-Sygut, and I. Majsterek. The Role of the ER-Induced UPR Pathway and the Efficacy of Its Inhibitors and Inducers in the Inhibition of Tumor Progression. *Oxid Med Cell Longev*. **2019**, *2019,* 5729710.

11. A. Almanza, A. Carlesso, C. Chintha, S. Creedican, D. Doultsinos, B. Leuzzi, A. Luis, N. McCarthy, L. Montibeller, S. More, A. Papaioannou, F. Püschel, M.L. Sassano, J. Skoko, P.

Agostinis, J. de Belleroche, L. A. Eriksson, S. Fulda, A. M. Gorman, S. Healy, A. Kozlov, C. Muňoz-Pinedo, M. Rehm, E. Chevet and A. Samali. Endoplasmic reticulum stress signalling – from basic mechanisms to clinical applications. *FEBS J.*, **2019**, *286*, 241-278.

12. A. H. Schönthal. Endoplasmic Reticulum Stress: Its Role in Disease and Novel Prospects for Therapy. *Scientifica*, **2012**, *2012*, 857516.

13. A. D. Garg, H. Maes, A. R. van Vliet and P. Agostinis. Targeting the hallmarks of cancer with therapy induced endoplasmic reticulum (ER) stress. *Mol Cell Oncol*., **2015**, *2*, e975089.

14. R. K. Yadav, S. W. Chae, H. R. Kim and H. J. Chae, Endoplasmic Reticulum Stress and Cancer, J Cancer Prev., **2014**, *19*, 75-88.

15. K. Shen, D. W. Johnson, D.A. Vesey, M. A. McGuckin and G. C. Gobe. Role of the unfolded protein response in determining the fate of tumor cells and the promise of multi-targeted therapies. *Cell Stress Chaperones*, **2018**, *23*, 317-334.

16. D. Xu, S. Q. Liang, H. Yang, U. Lüthi, C. Riether, S. Berezowska, T.M. Marti, S.R. R. Hall, R. Bruggmann, G.J. Kocher, R.A. Schmid and R.W. Peng. Increased sensitivity to apoptosis upon endoplasmic reticulum stress-induced activation of the unfolded protein response in chemotherapy-resistant malignant pleural mesothelioma. *Br J Cancer*, **2018**, *119*, 65-75.

17. D. H. Suh, M. K. Kim, H. S. Kim, H. H. Chung, Y. S. Song. Unfolded protein response to autophagy as a promising druggable target for anticancer therapy, Ann. N.Y. Acad. Sci., **2012**, *1271*, 20-32.

18. A.M. Martelli, F. Paganelli, F. Chiarini, C. Evangelisti and J. A. McCubrey. The Unfolded Protein Response: A Novel Therapeutic Target in Acute Leukemias. *Cancers*, **2020**, *12*, 333.

19. D. Jiang, C. Lynch, B. C. Medeiros, M. Liedtke, R. Bam, A.B. Tam, Z. Yang, M. Alagappan, P. Abidi, Q. T. Le, A. J. Giaccia, N. C. Denko, M. Niwa, and A. C. Koong, Identification of Doxorubicin as an Inhibitor of the IRE1α-XBP1 Axis of the Unfolded Protein Response. *Sci Rep*., **2016**, *6*, 33353.

20. *R. M. Cunningham and V. J. DeRose.* Platinum Binds Proteins in the Endoplasmic Reticulum of S. cerevisiae and Induces Endoplasmic Reticulum Stress. *ACS Chem. Biol.*, **2017**, *12*, 2737-2745.

21. Y. Xu, C. Wang and Z. Li. A new strategy of promoting cisplatin chemotherapeutic efficiency by targeting endoplasmic reticulum stress. *Mol Clin Oncol.*, **2014**, *2*, 3-7.

22. T. Karasawal, M. Sibrian-Vazquez, R. M. Strongin and P. S. Steyger. Identification of Cisplatin-Binding Proteins Using Agarose Conjugates of Platinum Compounds. *Plos One*, **2013**, *8*, e66220.

23. A. Mandic, J. Hansson, S. Linder and M. C. Shoshan. Cisplatin Induces Endoplasmic Reticulum Stress and Nucleus-independent Apoptotic Signaling. *J. Biol. Chem.*, **2003**, *278*, 9100-9106

24. J. L. Nitiss. Targeting DNA topoisomerase II in cancer chemotherapy. *Nat. Rev. Cancer*, **2009**, *9*, 338-350.

25. L. Kelland. The resurgence of platinum-based cancer chemotherapy. *Nat. Rev. Cancer*, **2007**, **7**, 573 —584

26. C. Ghosh, A. Nandi and S. Basu, Supramolecular self-assembly of triazine-based small molecule: targeting endoplasmic reticulum in cancer cells. *Nanoscale*, **2019**, *11*, 3326-3335.

27. C. Ghosh, A. Nandi and S. Basu. Lipid Nanoparticle-Mediated Induction of Endoplasmic Reticulum Stress in Cancer Cells. *ACS Appl. Bio Mater.*, **2019**, *2*, 3992-4001.

28. S. A. Sydlik, S. Jhunjhunwala, M. J. Webber, D. G. Anderson and R. Langer. *In Vivo* Compatibility of Graphene Oxide with Differing Oxidation States. *ACS Nano*, **2015**, *9*, 3866-3874.

29. S. Shi, F. Chen, E.B. Ehlerding and W. Cai. Surface Engineering of Graphene-Based Nanomaterials for Biomedical Applications. *Bioconjugate Chem.*, **2014**, *25*, 1609-1619.

30. L. Zhang, J. Xia, Q. Zhao, L. Liu and Z. Zhang. Functional graphene oxide as a nanocarrier for controlled loading and targeted delivery of mixed anticancer drugs. *Small*, **2010**, *6*, 537-544.

31. Z. Liu, J.T. Robinson, X. Sun and H. Dai, PEGylated nanographene oxide for delivery of water-insoluble cancer drugs. *J. Am. Chem. Soc.*, **2008**, *130*, 10876-10877.

32. H. Hong, Y. Zhang, J.W. Engle, T.R. Nayak, C.P. Theuer and R.J. Nickles, T.E. Barnhart, W. Cai, *In vivo* targeting and positron emission tomography imaging of tumor vasculature with ^{66}Ga-labeled nano-graphene. *Biomaterials*, **2012**, *33*, 4147-4156.

33. A. Mallick, A. Nandi and S. Basu. Polyethylenimine Coated Graphene Oxide Nanoparticles for Targeting Mitochondria in Cancer Cells, *ACS Appl. Bio Mater*, **2019**, *2*, 14-19.

34. A. Nandi, A. Mallick, P. More, P. Sengupta, N. Ballav and S. Basu. Cisplatin-induced self-assembly of graphene oxide sheets into spherical nanoparticles for damaging sub-cellular DNA, *Chem. Commun.*, **2017**, *53*, 1409-1412.

35. H. Xiao, C. Wu, P. Li, W. Gao, W. Zhang, W. Zhang, L. Tong and B. Tang. Ratiometric photoacoustic imaging of endoplasmic reticulum polarity in injured liver tissues of diabetic mice, *Chem. Sci.*, **2017**, *8*, 7025-7030.

36. Y. Liu, C. N. Lok, B. C. B. Ko, T. Y. T. Shum, M. K. Wong and C. M. Che. Subcellular Localization of a Fluorescent Artemisinin Derivative to Endoplasmic Reticulum. *Org. Lett.*, **2010**, *12*, 1420-1423.

37. P. Gao, W. Pan, N. Li and B. Tang. Fluorescent probes for organelle-targeted bioactive species imaging. *Chem. Sci.*, **2019**, *10*, 6035-6071.

38. Y. Matsumura and H. Maeda. A new concept for macromolecular therapeutics in cancer chemotherapy: mechanism of tumoritropic accumulation of proteins and the antitumor agent smancs. *Cancer Res.*, **1986**, *46*, 6387-6392.

39. H. Maeda, J. Wu, T. Sawa, Y. Matsumura and K. Hori. Tumor vascular permeability and the EPR effect in macromolecular therapeutics: a review. *J. Control. Release*, **2000,** *65*, 271-284.

40. A. Nandi, C. Ghosh and S. Basu. Polymer conjugated graphene-oxide nanoparticles impair nuclear DNA and Topoisomerase I in cancer. *Nanoscale Adv*, **2019,** *1*, 4965-4971.

41. W. Hakamata, S. Tamura, T. Hirano and T. Nishio. Multicolor Imaging of Endoplasmic Reticulum-Located Esterase As a Prodrug Activation Enzyme.*ACS Med. Chem. Lett.*, **2014,** *5*, 321-325.

42. S. Oyadomari and M. Mori. Roles of CHOP/GADD153 in endoplasmic reticulum stress. *Cell Death Differ.* **2004**, *11*, 381-389.

43. H. Nishitoh, Chop is a multifunctional transcription factor in the ER stress response.

J. Biochem., **2012**, *151*, 217-219.

44. H. Hu, M. Tian, C. Ding and S. Yu. The C/EBP Homologous Protein (CHOP) Transcription Factor Functions in Endoplasmic Reticulum Stress-Induced Apoptosis and

Microbial Infection. *Front. Immunol.*, **2019**, *9*, 3083.

45. M. Wang, S. Wey, Y. Zhang, R. Ye and A. S. Lee. Role of the Unfolded Protein Response Regulator GRP78/BiP in Development, Cancer, and Neurological Disorders. *Antioxid Redox Signal.*, **2009**, *11*, 2307-2316.

46. J.B. Gifford, W. Huang, A.E. Zeleniak, A. Hindoyan, H. Wu, T. R. Donahue and R. Hill. Expression of GRP78, master regulator of the unfolded protein response, increases chemoresistance in pancreatic ductal adenocarcinoma. *Mol. Cancer Ther.*, **2016**, *15*,1043-1052.

47. A. S. Lee. Glucose-regulated proteins in cancer: molecular mechanisms and therapeutic potential. *Nat. Rev. Cancer*, **2014**, *14*, 263-276.

48. Y. Yang, L. Liu, I. Naik, Z. Braunstein, J. Zhong and B. Ren. Transcription Factor C/EBP Homologous Protein in Health and Diseases. *Front. Immunol.*, **2017**, *8*,1612.

49. A. Forus, V. A. Florenes, G. M. Maelandsmo, Ø. Fodstad and O. Myklebost. The protooncogene CHOP/GADD153, involved in growth arrest and DNA damage response, is amplified in a subset of human sarcomas. *Cancer Genetics Cytogenet*, **1994**, *78*, 165-171.

50. W. S. Lee, W. H. Yoo and H. J. Chae. ER Stress and Autophagy. *Curr Mol Med*, **2015**, *15*, 735-745.

51. V. Sica, L. Galluzzi, J. M. Bravo-San Pedro, V. Izzo, M. C. Maiuri and G. Kroemer, Organelle-Specific Initiation of Autophagy, *Mol. Cell*, **2015**, *59*, 522-539.

52. I. Tanida, T. Ueno and E. Kominami, LC3 and Autophagy, *Methods Mol. Biol.*, **2008**, *445*, 77-88.

53. Z. Xie and D. J. Kilonsky. Autophagasome formation: core machinery and adaptations, *Nat. Cell Biol*., **2007**, *9*, 1102-1109.

54. Y. Cao and D. J. Klionsky. Physiological functions of Atg6/Beclin 1: a unique autophagy-related protein, *Cell Res.*, **2007**, *17*, 839-849.

55. H. Chino and N. Mizushima. ER-Phagy: Quality Control and Turnover of Endoplasmic Reticulum. *Trends Cell Biol*, **2020**, *30*, 384-398.

56. S. Wilkinson. ER-phagy: shaping up and destressing the endoplasmic reticulum. *FEBS J.*, **2019**, *286*, 2645-2663.

57. L. Galluzzi, J. M. Bravo-San Pedro, B. Levine, D. R. Green and G. Kroemer, Pharmacological modulation of autophagy: therapeutic potential and persisting obstacles. *Nat. Rev. Drug Discovery*, **2017**, *16*, 487-511

58. B. Kaur, A. Bhat, R. Chakraborty, K. Adlakha, S. Sengupta, S. Roy and K. Chakraborty, Proteomic profile of 4-PBA treated human neuronal cells during ER stress. *Mol. Omics*, **2018,** *14*, 53-63.

59. A. U. Nissar, L. Sharma, M. A. Mudasir, L. A. Nazir, S. A. Umar, P. R. Sharma, R. A. Vishwakarma and S. A. Tasduq. Chemical chaperone 4-phenyl butyric acid (4-PBA) reduces hepatocellular lipid accumulation and lipotoxicity through induction of autophagy. *J Lipid Res.*, **2017**, *58*, 1588-1868.

Chapter 4

Small Molecule-Mediated Induction of Endoplasmic Reticulum Stress in Cancer Cells

(Manuscript Under Revision)

4.1 Abstract:

Endoplasmic reticulum (ER) is one of the crucial sub-cellular organelles controlling myriads of functions including protein biosynthesis, folding/misfolding/unfolding. As a result, dysregulation of these pathways in ER is implicated in cancer development and progression. Subsequently, targeting ER in cancer emerged as interesting unorthodox strategy in next-generation anticancer therapy. However, development of small molecules to selectively target ER for cancer therapy remained elusive and unexplored. To address this, herein, we have developed a novel small molecule library of sulfonylhydrazide-hydrazone through a short and concise chemical synthetic strategy. From this library, we identified one fluorescent small molecule which localized into ER of HeLa cells within 6h followed by induction of ER stress through CHOP and IRE-1α over expression. Interestingly, this novel small molecule triggered autophagy which was subsequently inhibited by chloroquine (autophagy inhibitor) to initiate programmed cell death (apoptosis) in HeLa cells. Furthermore, this small molecule showed remarkable cancer cell killing efficacy in lung, breast and drug-resistant breast cancer cells as monotherapy as well as in combination with chloroquine. This small molecule has the potential to open up a new direction to illuminate ER-biology towards the development of novel anticancer therapeutics.

4.2 Introduction

Endoplasmic Reticulum (ER) is a vital organelle that is known to govern the synthesis, folding and processing of over a third of all the cellular proteins.[1-4]Several ER associated chaperones assist in ensuring proper folding and modification of these proteins before they traffic out of the ER.[5-7] Despite the robustness of this protein folding machinery, the success rate for optimum protein folding is low owing to the wide range of cellular disturbances that disrupt its efficiency.[8] As a result, several unfolded and misfolded proteins start accumulating inside the ER lumen leading to a state known as ER stress.[9,10] In response to this burden of unfolded proteins, a cytoprotective program known as unfolded protein response, (UPR) is launched by the cell.[11-13] Together the three mechanistically different branches of UPR regulate the expression of numerous genes that resolve this ER stress and maintain homeostasis or induce apoptotic signals in case the stress remains unmitigated.[14] Very recently, this deregulated ER homeostasis has been implicated in various pathologic states and particularly with cancer.[15,16] Baseline activity level of ER stress response system is elevated in cancer cells as compared to

normal cells. Thus, the ER stress signalling is involved in tumorigenesis and development leading it as the new Achilles heel in the development of cancer therapeutics.[17-19]

Over the last couple of decades, small molecules have emerged as important tools to illuminate myriads of biological phenomena in cancer cells leading to the development of novel anti-cancer therapies.[20,21] In this context, few small molecules have been explored that target various aspects of unfolded protein response and ER physiology. Molecules like salubrinal, GSK2606414, sunitinib are well reported to manipulate one or more arms of ER stress pathways.[22] However, due to the scarcity of the targeting moieties, the development of ER targeted therapeutics is still in its infancy and therefore the presence of such ER stress inducers and UPR inhibitors is limited. Hence, there is a serious need to develop novel small molecules that can serve as ER stress modulators. Very recently, a few molecules were demonstrated to accumulate inside the ER in cancer cells to induce ER stress or a tool to understand ER physiology.[23-27] For instance, Rochi et al reported the development of HA15 that serve as ER stress inducer and enable melanoma cells to overcome BRAF resistance.[28] On the other hand, Xiao et. al. reported the ER-H_2O_2 probe to understand the generation of hydrogen peroxide at ER during apoptosis.[29] A remarkable highlight in those small molecules is the presence of sulfonamide moieties. Furthermore, it was reported that sulphonamide moiety facilitates the internalization of small molecules in intracellular ER owing to the presence of sulphonamide receptors on ER surface. The sulphonamide part of the molecules may be interacting with the sulfonyl receptors present in the ATP sensitive K^+ channel. The sulphonamide derivatives in this way might also inhibit the protease activity of ER thereby disturbing normal cellular functions.[30,31,56] Moreover, sulphonamide-containing molecules like sulfathiazole, ripasudil, indisulam and glibenclamide showed diverse biological activities (Scheme 1a).[32-35] As a result, sulphonamide-based scaffold has emerged as one of the privileged structures in the natural and synthetic small molecules.[36]

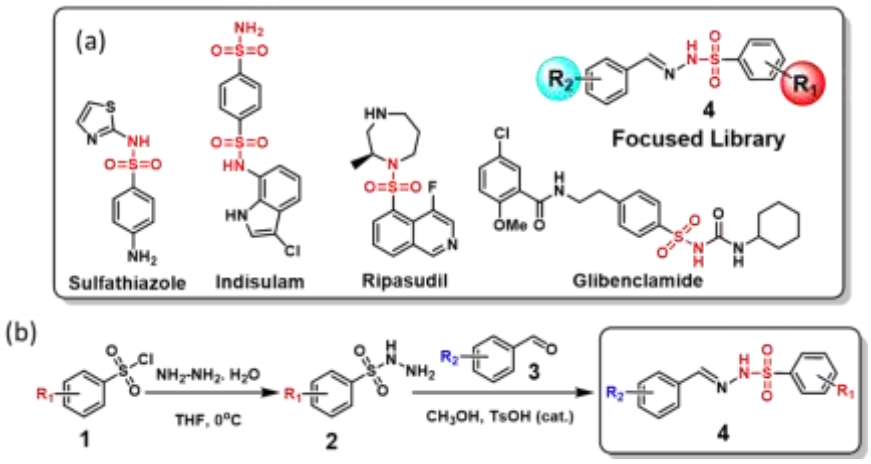

Scheme 1: (a) Biologically active sulfonohydrazide-hydrazones. (b) Synthetic route to generate a focused library of sulfonohydrazide- hydrazones.

Inspired by the scarcity of novel ER stress modulators, we hypothesise to develop a focussed library of sulfonohydrazide-hydrazone based small molecules (Scheme 1a and b) to identify novel ER stress inducers in cancer cells. To address this, herein, we report a short and concise synthesis of a library of sulfonohydrazide- hydrazone based small molecules comprising of 66 compounds. Upon screening these compounds in HeLa cell line, we identified four molecules as potential ER stress inducers. One of the four lead molecules was found to be fluorescent in nature and localized inside the subcellular ER to induced ER stress through CHOP and IRE-1α pathways (Scheme 2). Interestingly, ER stress induced by the lead molecule triggered autophagy followed by apoptosis in HeLa cells (Scheme 2). Further inhibition of autophagy by chloroquine (CQ) resulted in improved cell killing in lung and breast cancer cells including drug resistant-breast cancer cells.

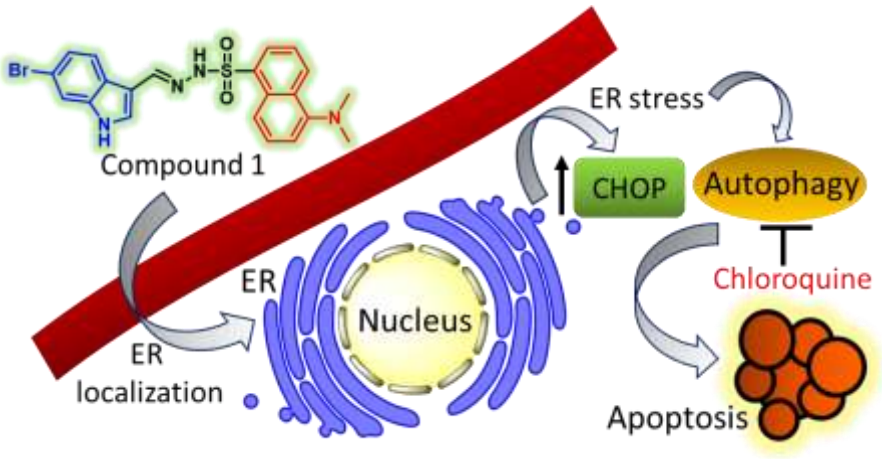

Scheme 2: Mechanism of subcellular localization and action of compound 1.

4.3 Results and Discussion

4.3.1 Synthesis of small molecule library. The synthesis of sulfonohydrazide- hydrazone molecules is illustrated in Scheme 1b. Briefly, commercially available substituted aromatic sulfonyl chlorides (1′) were reacted with hydrazine monohydrate at 0°C to obtain substituted aromatic sulfonyl hydrazides (Fig. 4.1) in 60-70 % yield. Further these aromatic sulfonyl hydrazides were reacted with different aromatic aldehydes (3′) in presence of p-toluenesulfonic acid as catalyst to afford 66 different sulfonylhydrazide-hydrazones in 50-80 % yield (Fig. 4.2).

The final products were characterized by ^{1}H, ^{13}C NMR spectroscopy and HR-MS (Fig. C1-C198).

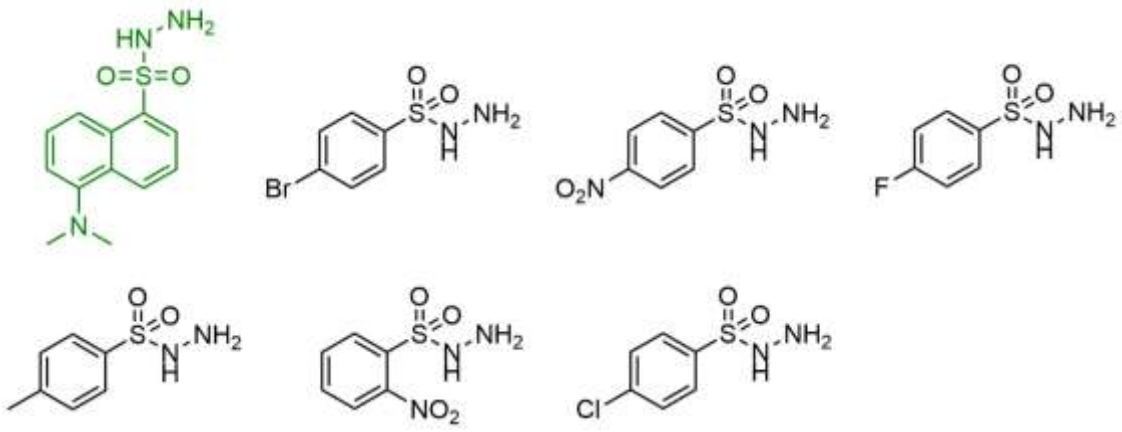

Figure 4.1: Structure of synthesised sulfonohydrazides.

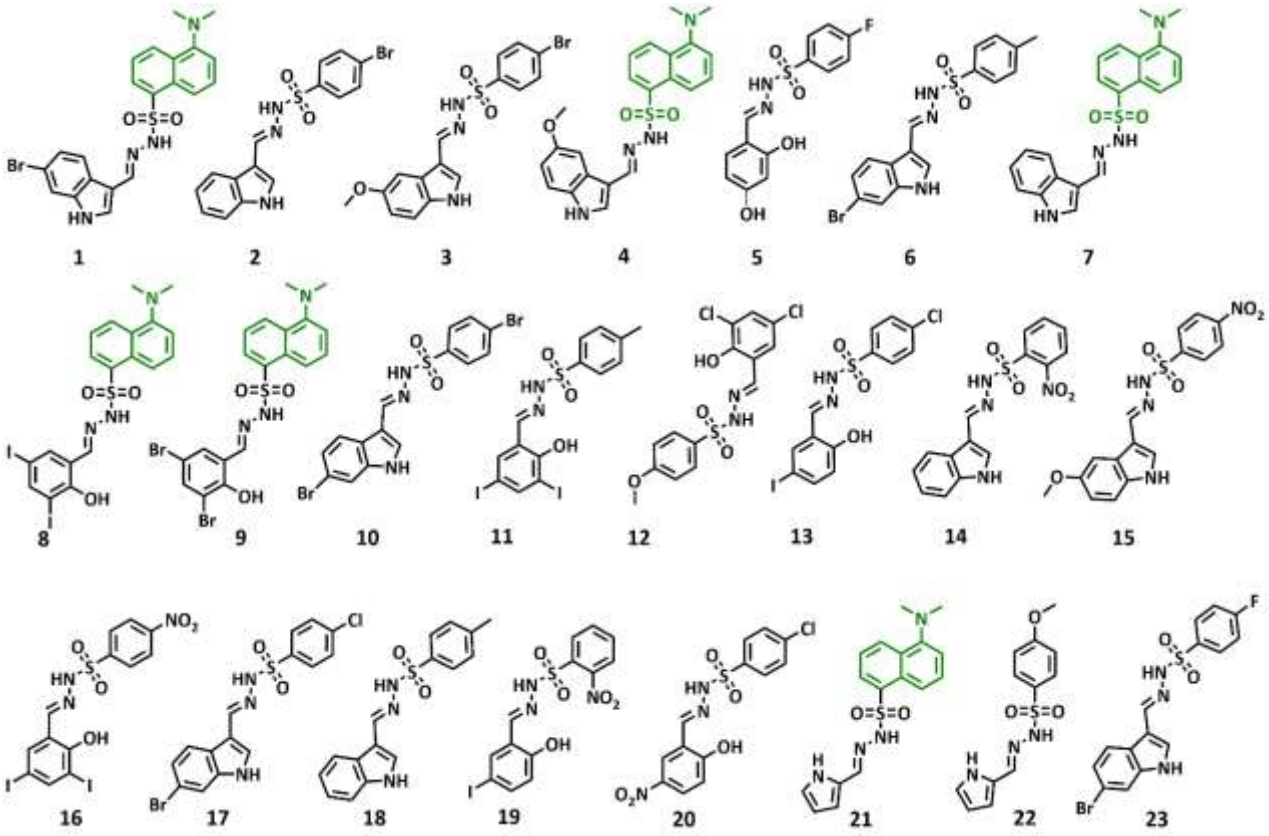

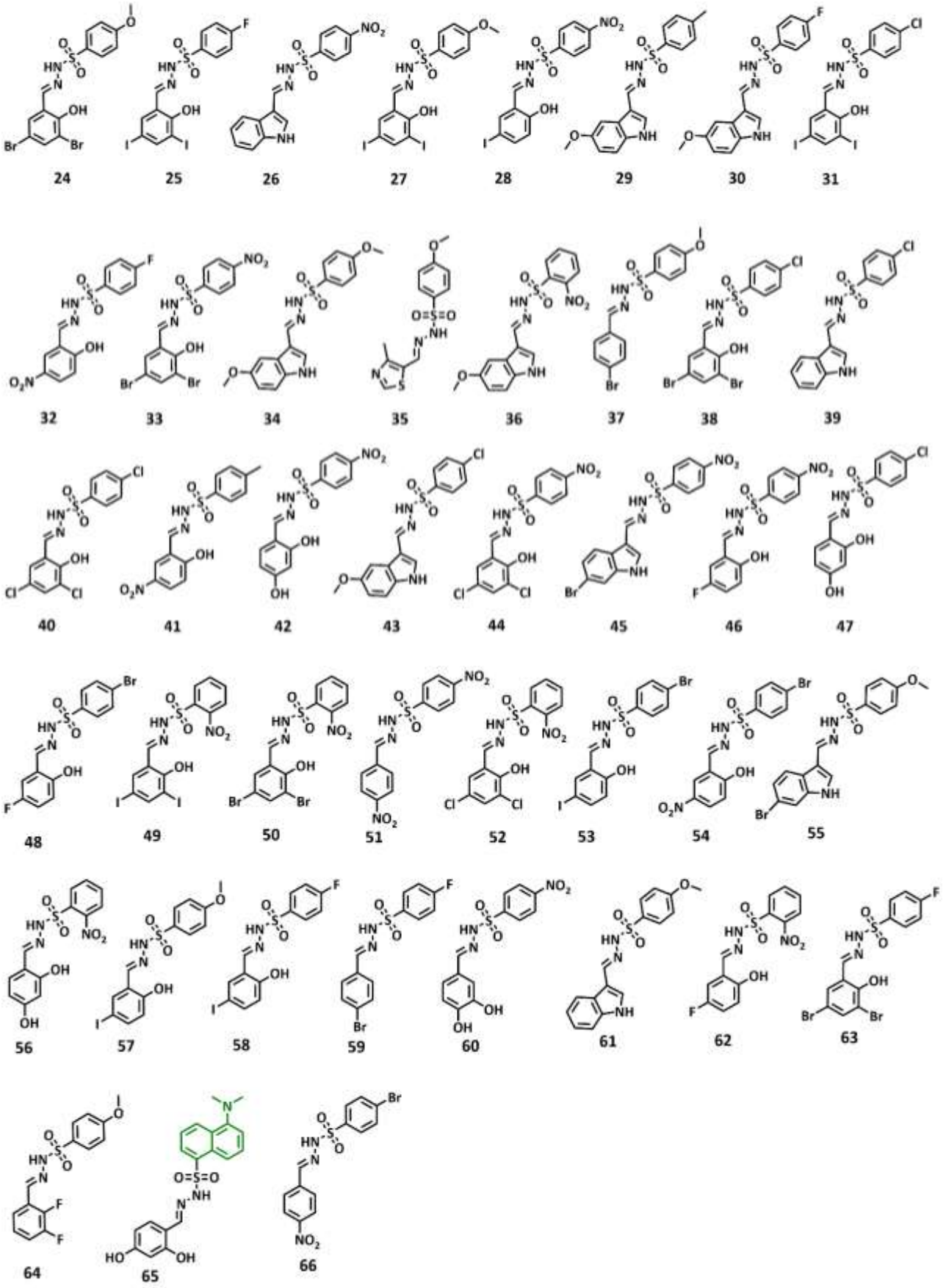

Figure 4.2: Structure of 66 sulfonohydrazide- hydrazone based small molecules.

To evaluate their cancer cell killing activity, we first incubated these library members in HeLa cervical cancer cells at a concentration of 30 μM for 24 hours. The cell viability was quantified by MTT assay. Interestingly, only four compounds (compound 1, 10, 17 and 55) were found to induce more than 60 % HeLa cell killing even at 30 μM concentration (Fig. 4.3a). After finding out the potential lead compounds, we evaluated their cancer cell killing ability in a dose dependent manner. HeLa cells were incubated with compound 1, 10, 17 and 55 for 24 h in different concentrations and the cell viability was evaluated by MTT assay. It was observed that at 24 h post incubation, compound 1, 10, 17 and 55 induced HeLa cell killing with IC_{50} value of 9 μM, 16 μM, 18 μM and 19 μM respectively (Fig. 4.3b). From this cell viability assay, it was evident that compound 1 showed best cell killing efficacy with lowest IC_{50} value. Moreover, it was found to be fluorescent with λ_{max} (emission) at 538 nm (Fig. 4.3c). This inherent fluorescence property of compound 1 will aid in its cellular tracking into endoplasmic reticulum (ER) and hence we chose to carry out further studies using compound 1.

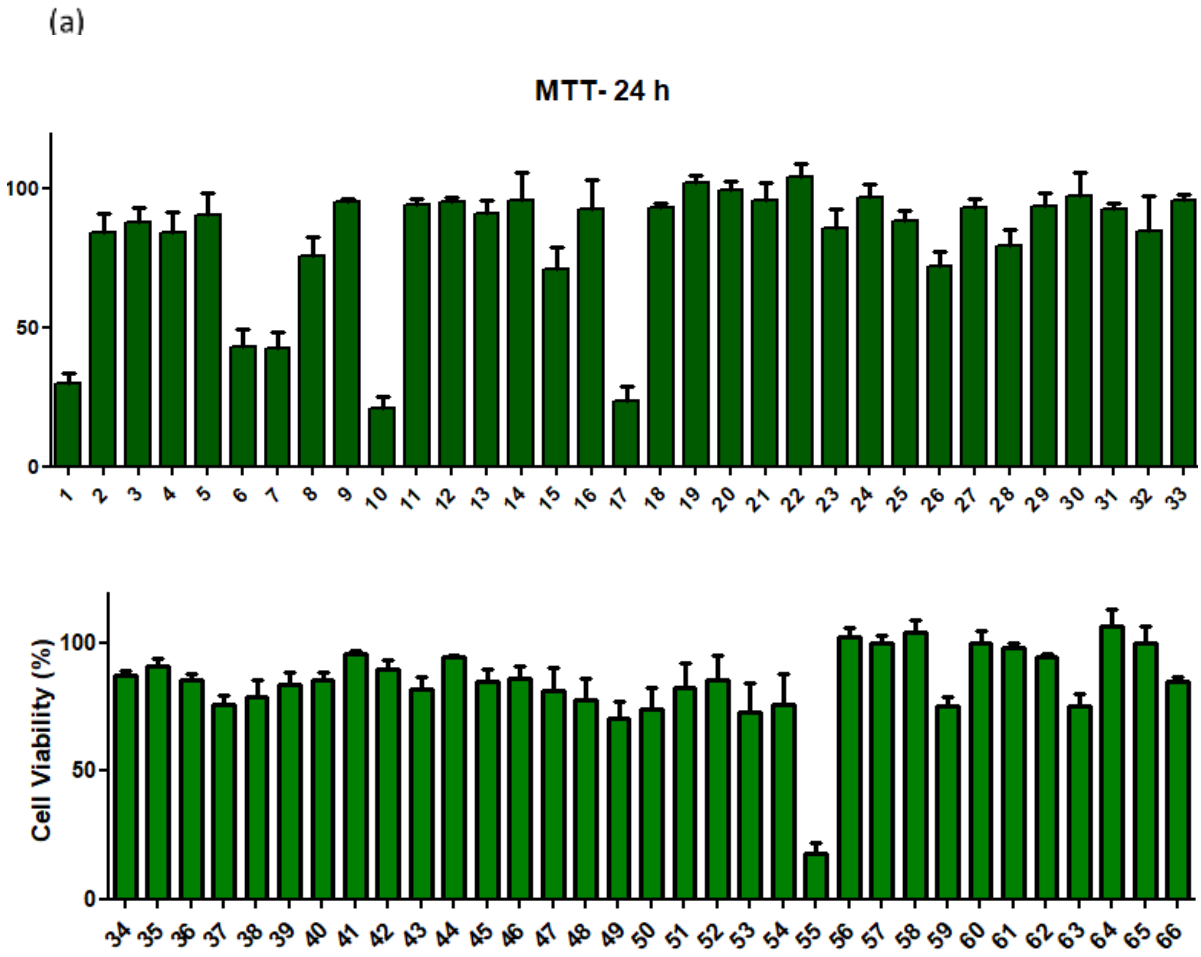

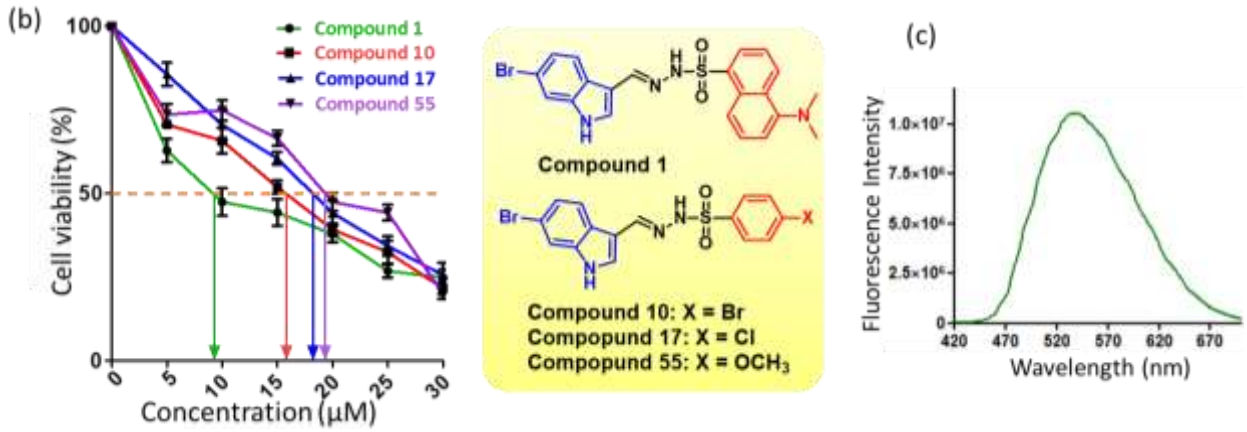

Figure 4.3: (a) Screening of 66 molecules in HeLa cell line at 30 μM for 24 h. (b) Cell viability assay for hit molecules. (c) Fluorescence spectra of compound 1 at $\lambda_{excitation}$ = 400 nm.

4.3.2 ER homing. We hypothesized that the presence of sulphonamide moiety in compound 1 will specifically navigate it and enable its localization inside the subcellular ER.[37, 38] To validate this hypothesis, we incubated the HeLa cells with compound 1 (concentration = 5 μM) (green fluorescent) for two different time points of 3 h and 6 h followed by staining the ER with ER Tracker Red. We then visualised the cells using confocal laser scanning microscopy (CLSM). It was observed that compound 1 started accumulating in the ER within 3 h and the accumulation increased at 6 h (Fig. 4.4) which was observed from the yellow fluorescence resulting from merging of red and green fluorescence. The ER localization of compound 1 was further quantified from the CLSM through Pearson's coefficients of 0.84 and 0.86 and Mander's coefficients of 0.98 and 0.97 at 3 h and 6 h respectively (Table C1, Appendix-C). These confocal images and quantification exhibited that indeed compound 1 homed into subcellular ER in HeLa cancer cells over 6 h.

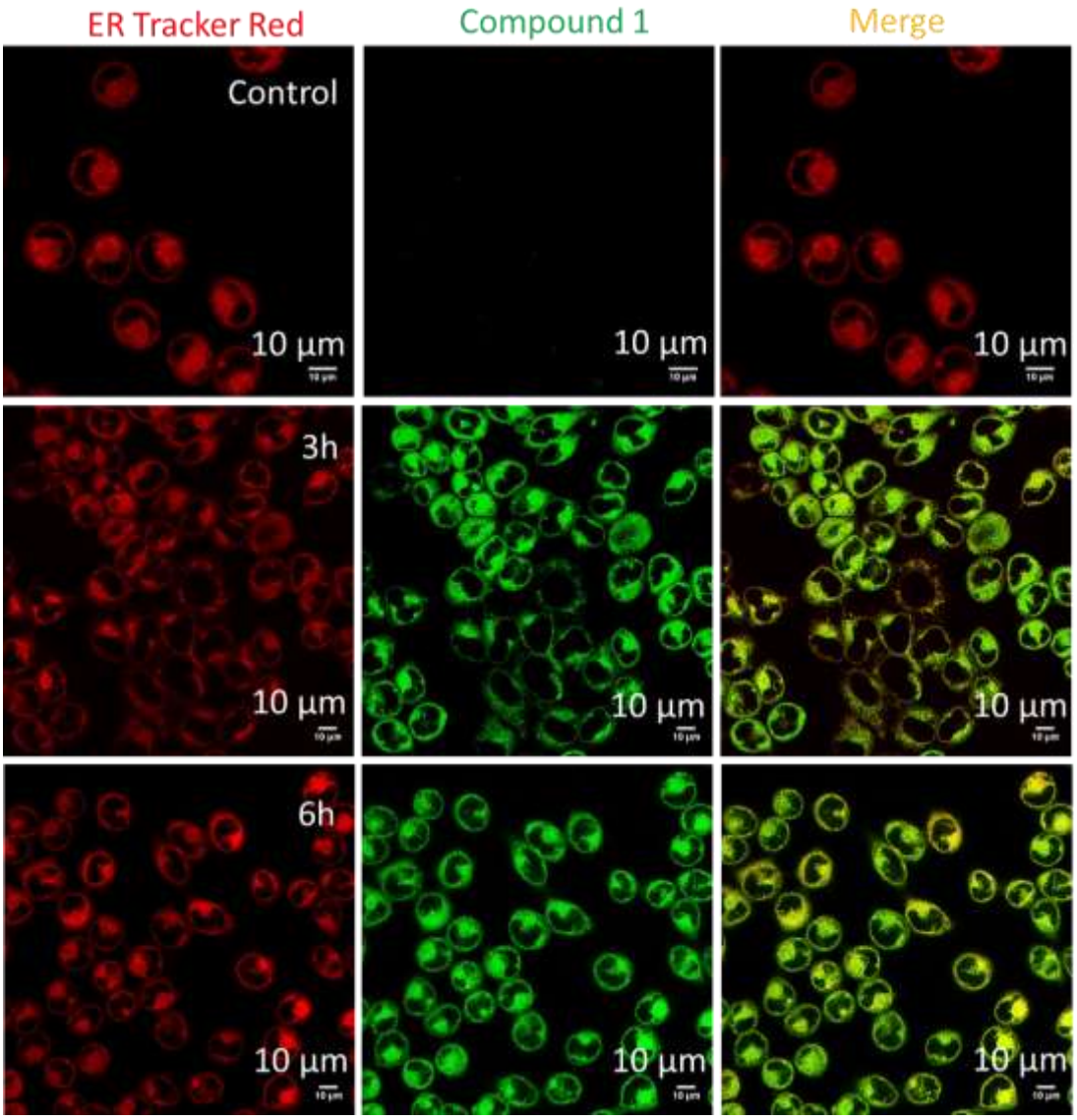

Figure 4.4: Cellular internalization of compound 1 in subcellular ER of HeLa cells.

4.3.3 ER stress. Once internalized inside the ER, compound 1 is expected to induce ER stress in the HeLa cervical cancer cells. Elevated ER stress levels lead to increment in the expression levels of protooncogene CHOP which is a marker for ER stress induced apoptosis.[39,40] To demonstrate the onset of ER stress we evaluated the levels of CHOP in HeLa cells by immunofluorescence assay. We treated HeLa cells with compound 1 for 24 h. We then incubated the cells with primary antibody specific to CHOP for 4 h followed by the incubation with Alexa-Fluor 594 (red fluorescence) tagged secondary antibody. Nucleus of the cells were stained with DAPI (blue fluorescent). We then visualized the cells with confocal microscopy. The fluorescence microscopy images showed that the control cells expressed negligible CHOP which was evident from no red fluorescence signals (Fig. 4.5a). However, the cell treated with compound 1 showed remarkably increased red fluorescence signals displaying that compound

1 increased (1.7 folds) the expression of CHOP protein in HeLa cells. Furthermore, the overlap of red and blue fluorescence to give purple fluorescence indicated the accumulation of CHOP in the nucleus which is a marker of ER stress induction.[40] We also evaluated the expression of CHOP by gel electrophoresis. We treated HeLa cells with compound 1for 24h, followed by lysis of the cells. We separated the sub-cellular proteins to perform Western blot analysis. In accordance with the confocal microscopy study, the cells after treatment with compound 1 showed a significant increase (1.6 folds) in the expression of CHOP compared to the non-treated control cells (Fig. 4.5b, c and d). To further estimate the ER stress, we evaluated the expression levels of another ER stress marker IRE1-α.[41] We found that the cells treated with compound 1 exhibited enhanced expression level of IRE1- α as compared to control cells (1.8 folds) (Fig. 4.5b, c and d). These immunofluorescence assays and gel electrophoresis revealed that compound 1 indeed induced ER stress in HeLa cells.

ER is the major site of lipid metabolism as several enzymes involved in it are compartmentalized in ER.[42] As a result, excessive ER stress is known to increase lipid accumulation inside the cell.[43] We anticipated that HeLa cells treated with compound 1 will also show enhanced lipid content in them. To validate this hypothesis, we performed Oil Red O staining experiment. We treated HeLa cells with compound 1 for 24 h followed by staining the cells with Oil-Red-O dye. Oil Red O is a lipid soluble lysochrome dye which stains the lipid droplets in the cells or frozen tissues.[44] We also stained the nucleus of the cells with blue fluorescent DAPI. We visualised the Oil-Red-O stained cells by confocal microscopy. The confocal microscopy images showed that control cells contained trace of lipid molecules as expected (Fig. 4.5e). However, compound 1 treatment remarkably increased the level of the lipids inside the cells, which was clear from the increased red fluorescence signals from Oil-Red-O dye in (Fig. 4.5e). This confocal microscopy exhibited that indeed lipidic content was increased inside the cells after treatment with compound 1 because of elevated ER stress.

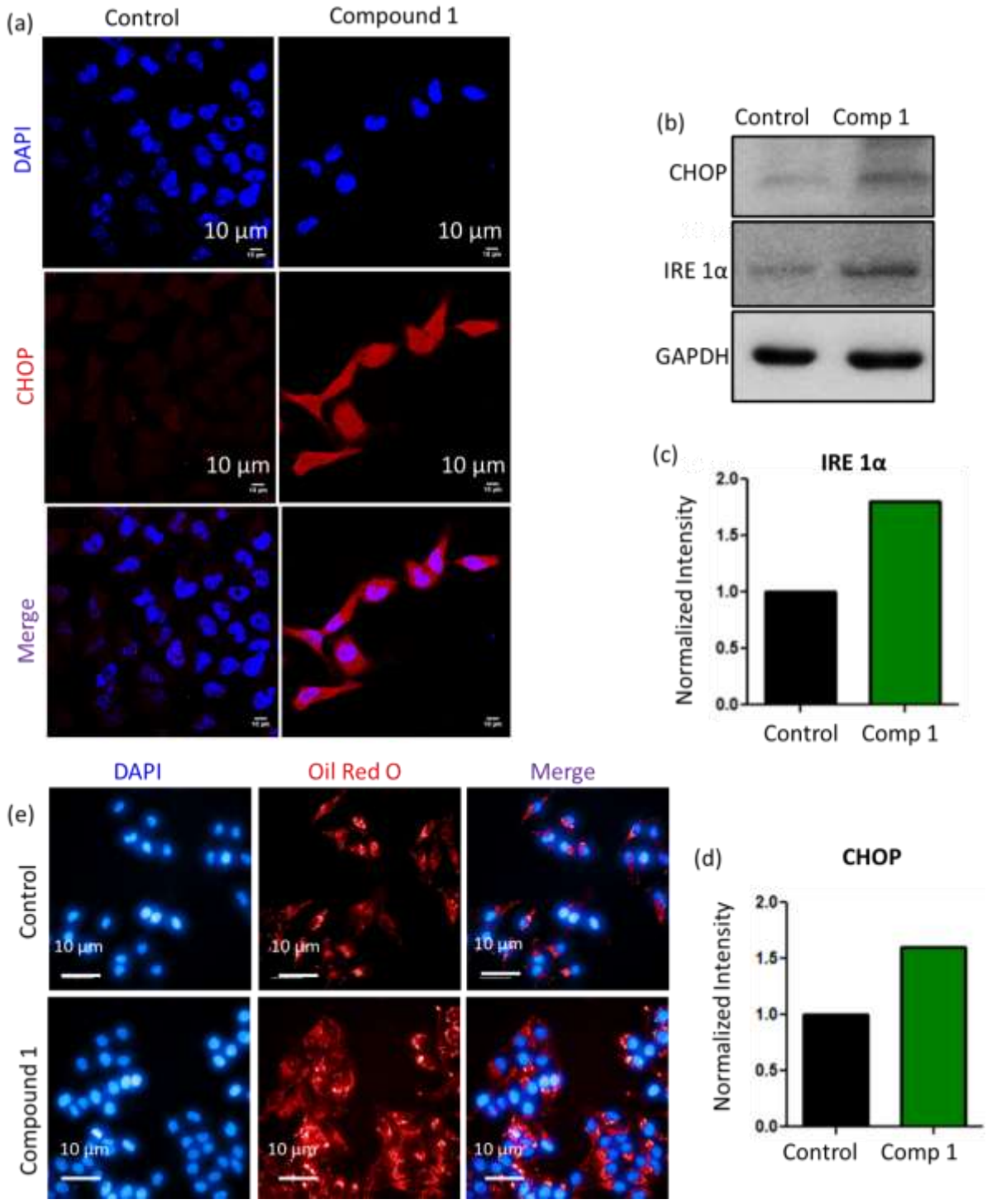

Figure 4.5: (a) Confocal microscopy illustrates increased levels of CHOP after immunofluorescence assay in HeLa cells treated with compound 1. (b) Western blot analysis to evaluate the expression of ER stress markers CHOP and IRE1- α. (c, d) Quantification of CHOP and IRE1- α from western blot analysis. (e) Confocal microscopy images of HeLa cells after treatment with compound 1. Cells were stained with Oil-Red-O dye.

4.3.4 Autophagy induction. ER stress induction acts as a potent trigger for autophagy which is primarily a cytoprotective secondary response to the excessive protein build up in the ER.[45-47] To investigate if autophagy was launched as a survival mechanism by the HeLa cells in response to treatment with compound 1, we evaluated the cellular expression level of LC3B, a key autophagy marker by immunofluorescence assay.[48] We treated HeLa cells with compound 1 for 24 h followed by incubation with primary antibody specific to LC3B for 4 h. The cells were then incubated with secondary antibody tagged with Alexa-Fluor-488 (green fluorescent). Nucleus of the cells were stained with blue fluorescent DAPI. Cells were visualised by confocal microscopy. The green fluorescence signals were hardly seen in the control cells (Fig. 4.6a). However, cells treated with compound 1 exhibited highly enhanced green fluorescence (5 folds) compared to the control cells. More interestingly, we observed the formation of autophagasomes (green puncta in the images) which is regarded as the hallmark of autophagy.[49] We also evaluated the expression level of Beclin, another autophagy marker by immunofluorescence.[50] HeLa cells were treated with compound 1 for 24 h followed by incubation with Beclin specific primary antibody. Cells were then incubated with secondary antibody tagged with Alexa-Fluor-594 (red fluorescent). Nucleus of the cells were stained with DAPI. We visualised the cells by confocal microscopy and found that an increased red fluorescence was observed in compound 1 treated cells compared to the non-treated control cells (8 folds) (Fig. 4.6b). The enhanced expression levels of LC3B and Beclin in treated cells as evaluated by immunofluorescence assay evidently demonstrated that autophagy was induced up elevation of ER stress in HeLa cells. We further validated the expression level of LC3B and Beclin by western blot analysis. We treated HeLa cells with compound 1 for 24 h followed by cell-lysis. The cellular proteins were then subjected to gel electrophoresis. The western blot analysis revealed that treatment with compound 1 resulted in increased levels of LC3B (10 folds) and Beclin (2 folds) indicating the onset of autophagy (Fig. 4.7a and b). Immunofluorescence assay and western blot analysis thus confirmed that autophagy was triggered upon ER stress induction on treatment with compound 1.

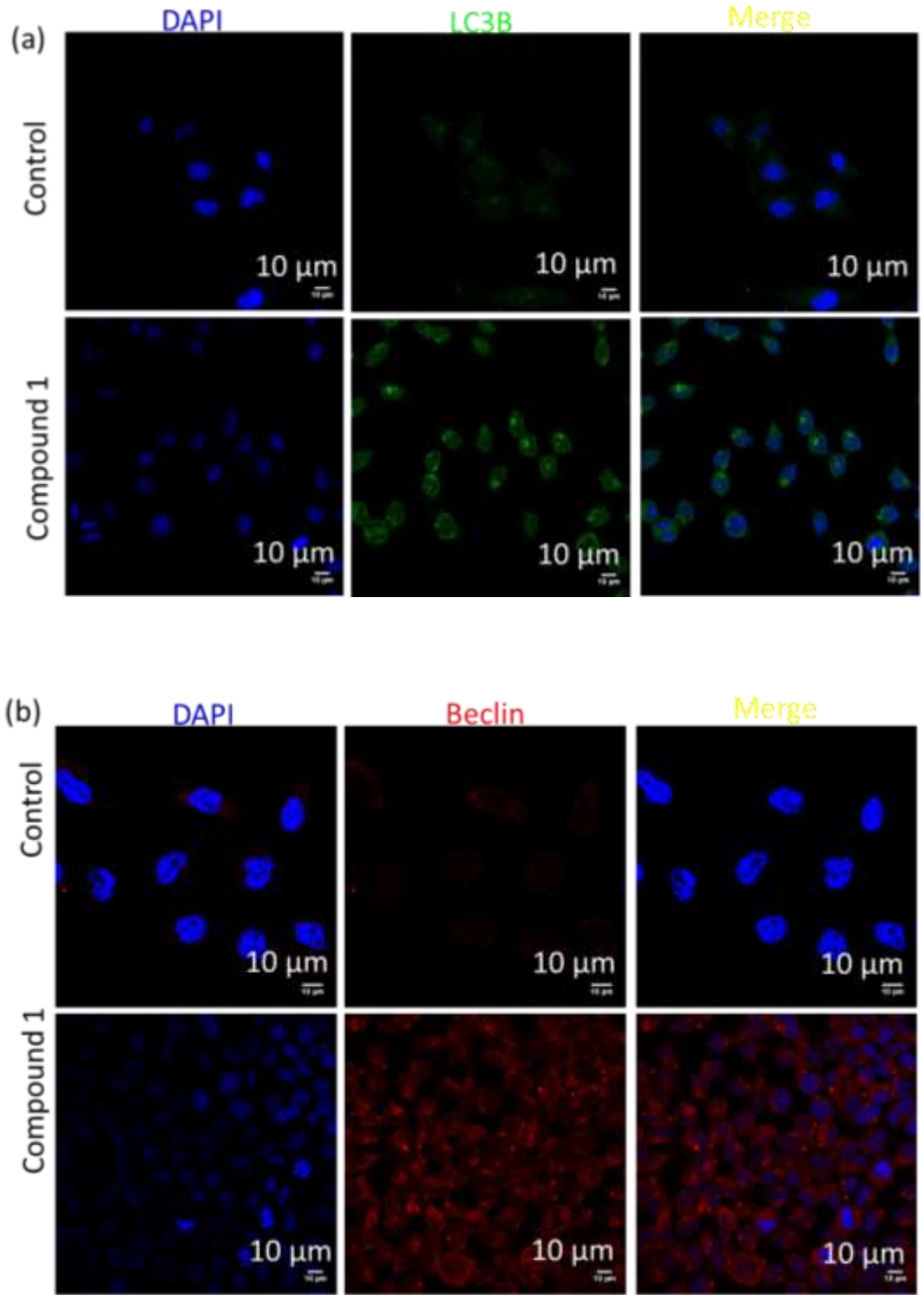

Figure 4.6: (a, b) Confocal microscopy illustrates increased levels of LC3B and Beclin after immunofluorescence assay in HeLa cells treated with compound 1.

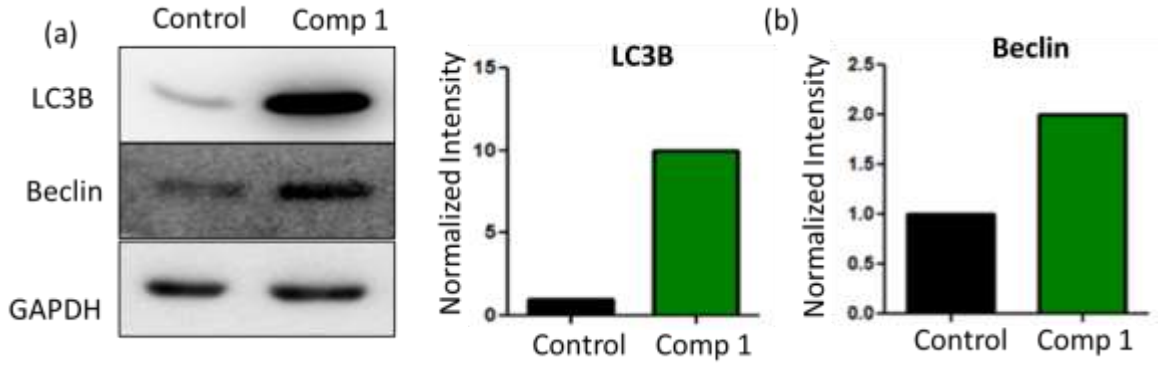

Figure 4.7: (a) Western blot analysis to evaluate the expression of ER stress markers LC3B and Beclin. (b) Quantification of LC3B and Beclin from western blot analysis.

4.3.5 Induction of apoptosis. Induction of ER stress is expected to induce apoptosis in HeLa cells. To estimate the apoptosis induced by compound 1 in HeLa cells, we performed flow cytometry assay. We treated HeLa cells with compound 1 for 24 h followed by staining the apoptotic and necrotic cells by Annexin V-FITC and propidium iodide (PI) respectively. Cells were then analysed by flow cytometry. We found that treatment with compound 1 resulted 16 % cells in early apoptotic stage and 49 % cells in late apoptotic stage compared to 0.18 % and 0.54 % in control cells respectively (Fig. 4.8a). We anticipate that, the compound 1 was not as effective to induce apoptosis due to induction of autophagy as survival mechanism. We thus hypothesized that the concomitant inhibition of autophagy will improve the apoptotic outcome in HeLa cells. To validate this hypothesis, we cotreated HeLa cells with compound 1 and 50 μM chloroquine, an autophagy inhibitor for 24 h and performed the flow cytometry assay.[51] We observed that autophagy inhibition indeed improved the apoptotic outcome with 4 % and 81 % cells in early and late apoptotic stages respectively (Fig. 4.8a). The flow cytometry data thus confirmed that compound 1 induced apoptosis in HeLa cells which further improved upon inhibition of autophagy with chloroquine.

To further investigate the effect of autophagy inhibition on the cell killing efficacy of compound 1 we performed cell viability assay. We cotreated HeLa cells with compound 1 in a dose dependent manner along with 50 μM chloroquine for 24 h. The cell viability was measured by MTT assay. We found that inhibiting autophagy improved the IC_{50} value of compound 1 from 9 μM to 4 μM in HeLa cells (Fig. 4.8b). We also evaluated the cell killing efficacy of compound 1 on three different cancer cell lines by MTT assay. We treated MCF-7 (human breast cancer), A549 (human lung carcinoma) and MDA-MB-231 (drug resistant triple

negative breast cancer) with compound 1 in a dose dependent manner for 24 h. We found that compound 1 exhibited an IC_{50} of 15 µM, 10 µM and 17 µM in MCF-7, A549 and MDA-MB-231 respectively (Fig. 4.8b). Furthermore, inhibition of autophagy by treatment with chloroquine resulted in enhanced cell killing and improved IC_{50} values of 10 µM, 5 µM and 13 µM in MCF-7, A549 and MDA-MB-231 respectively (Fig. 4.8b). Compound 1 thus efficiently induced cell killing in different cell lines which further improved upon autophagy inhibition.

We also evaluated the inhibition of autophagy along with induction of ER stress with the other lead molecules (compound 10, 17 and 55) on HeLa cells. We treated HeLa cells with CQ in combination with compound 10, 17 and 55 in a dose dependent manner for 24 h and the cell viability was measured by MTT assay. We observed that combination treatment of CQ with compound 10, 17 and 55 induced much improved HeLa cell killing with IC_{50} = 4.4 µM, 5.5 µM and 16.1 µM (Fig.4.9).

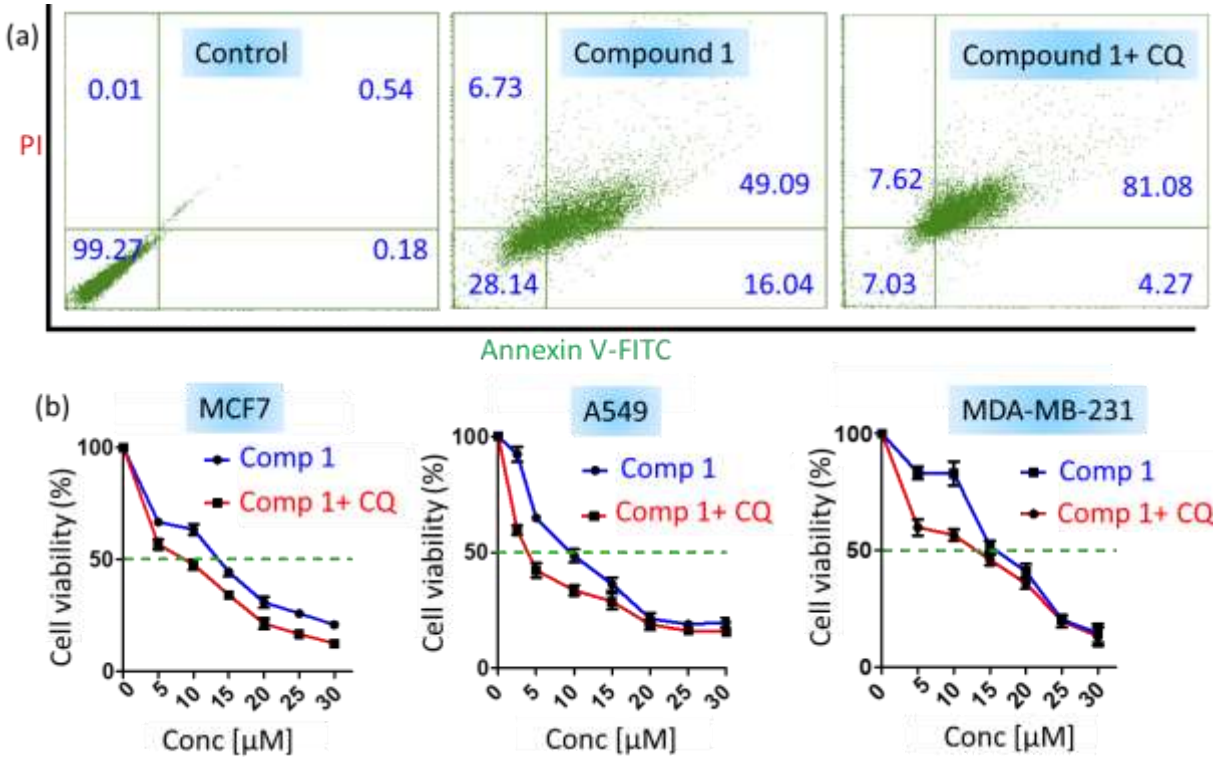

Figure 4.8: (a) Flow cytometry analysis of HeLa cells treated with compound 1 and combination of compound 1 and CQ at 24 h. (b) Cell viability assay for compound 1 and combination of compound 1 and CQ in MCF-7, A549 and MDA-MB-231 cells at 24 h.

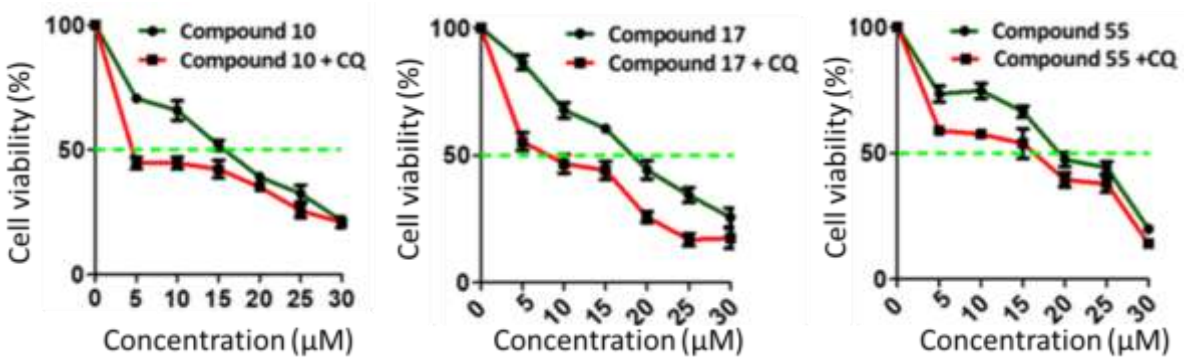

Figure 4.9: Cell viability assays of compound 10, 17 and 55 in combination with CQ in HeLa cells at 24 h.

To be successful in future cancer therapy, compound 1 should selectively induce cancer cell death without collateral damage to the non-cancerous healthy cells. To evaluate the effect of compound 1 in healthy cells, we incubated HEK293 human embryonic kidney cells with compound 1 in a dose dependent manner for 24 h and quantified the cell viability by MTT assay. To our surprise, we found that compound 1 showed only 52.8 % cell viability even in 30 μM concentration with IC_{50} = 31.7 μM, which was quite high compared to the IC_{50} value in different cancer cells (Fig. 4.10a).

Finally as the proof of concept, to confirm that ER stress induction resulted in apoptosis, we treated HeLa cells with compound 1 and 4-phenyl butyric acid (4-PBA), a chemical chaperone that alleviates both toxicity and proteomic alterations induced by an ER stress inducer, by aiding in protein folding in the ER.[52,53] We co-treated HeLa cells with compound 1 along with 15 μM PBA for 24 h and then performed the cell viability assay. We found that cotreatment with 4-PBA resulted in reduced cell killing (IC_{50} = 28 μM) in HeLa cells as compared to the treatment with compound 1 only (Fig. 4.10b). From these cell viability assays, it was evident that compound 1 triggered apoptosis after induction of autophagy. Furthermore, co-treatment of compound 1 and autophagy inhibitor would induce improved cancer cell killing without inducing significant damage to the non-cancerous cells.

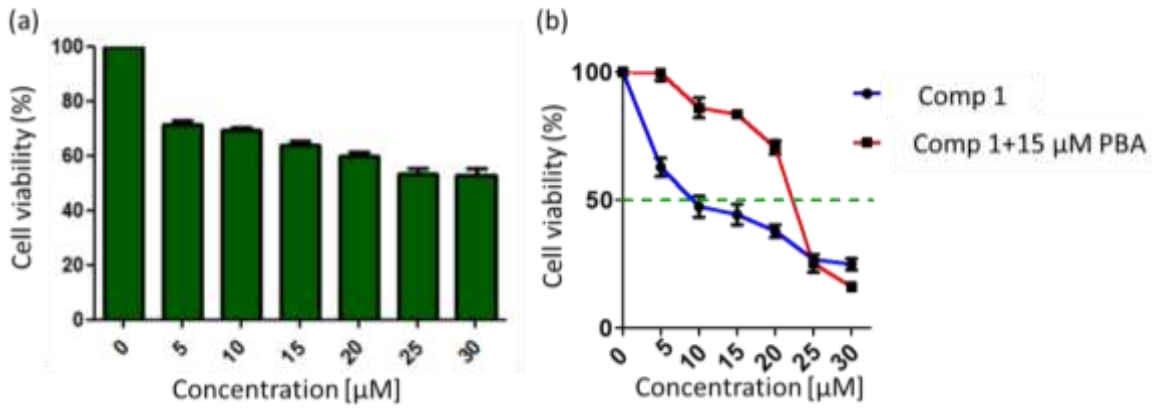

Figure 4.10: (a) Cell Viability assay for compound 1 on HEK-293 at 24 h. (b) Cell viability assay of compound 1 in combination with 4-phenyl butyric acid in HeLa cells for 24 h.

4.4 Materials and Methods

4.4.1 Materials. All the chemicals were purchased from commercial suppliers unless otherwise noted. Reactions were performed in the oven-dried glassware without inert gas. Analytical thin-layer chromatography (TLC) was performed using pre-coated silica gel aluminium sheets 60 F254 bought from EMD Millipore Laboratories. Compounds were purified by column chromatography using silica gel 100-200 mesh as the stationary phase. 1H, 13C, spectra were recorded on a Bruker Avance III HD Ascend 9.4 Tesla/400 MHz with autosampler and/or Jeol 9.4 Tesla/400 MHz with autosampler spectrometer. Chemical shifts are mentioned in parts per million (ppm) and referred to residual protons on the corresponding deuterated solvent. UV-Visible spectra was recorded on Shimadzu. DMEM media and 3-(4, 5-dimethylthiazol-2-yl)-2, 5- diphenyltetrazolium bromide (MTT) was purchased from HiMedia. Nunc® Lab-Tek® II chambered coverglass, 4-phenyl butyric acid (4-PBA), Oil-Red-O solution and Sodium dodecyl sulfate (SDS) was purchased from Sigma-Aldrich. ER Tracker Red was purchased from Invitrogen. AnnexinV- FITC and PI staining Kit was purchased from Roche. Flow Cytometry analysis was recorded on BD- Accuri. Western blot analysis was performed on Las ImageQuant 400.

4.4.2 Synthesis of sulfonohydrazides. The sulfonohydrazides were prepared according to a previous reported procedure.[54] Briefly, to a solution of sulfonyl chloride (1 eq.) in THF at -30^{o}C, hydrazine monohydrate (5 eq.) was added dropwise. The solution was then allowed to stir for about 30 minutes. Progress of reaction was monitored through TLC and after it was over ethyl acetate was added to the cold reaction mixture. It was washed multiple times with

ice cold 10% brine solution. The organic layer was collected, dried over Na2SO4 and the solvent was then evaporated using rotavap. The solid obtained was washed with pentane three times and the product was stored at 4^{o}C for further use.

4.4.3 Synthesis of sulfonohydrazide-hydrazones. To a solution of sulfonohydrazide (1 eq.) in ethanol, aldehyde was added (1 eq.) along with catalytic amount of para-toulene sulfonic acid and the reaction was allowed to stir at room temperature overnight. Extent of reaction was monitored by TLC. On completion, the solvent ethanol was evaporated, and the residue obtained was dissolved in organic solvents (DCM/ ethylacetate). The organic layer was washed with water, collected and evaporated. The residue obtained was then purified using column chromatography. The procedure was utilized to generate a library of 66 small molecules.

4.4.4 Cell Viability assay. 100 µL of 4000 HeLa cells, 4000 A549 cells, 5000 MCF-7 cells and 7000 MDA-MB-231 cells in DMEM media were seeded per well in 96-well microtiter plate and incubated for 16 h in a 5% CO_2 incubator at 37^{o}C. Cells were treated with different concentrations of the nanoparticles and incubated for 24 h. After the said time point, media was removed and 100 µL of MTT in DMEM (0.5 mg/mL) was added. After 4h, the media was carefully removed without disturbing the formazan crystals and 100 µL of DMSO was added to solubilize the formazan crystals. Absorbance was then recorded at 570 nm on Perkin Elmer Ensight. (n=3).

4.4.5 Cellular Internalization. 2 x 10^4 cells were seeded in a 8-well LabTek chamber. Cells were incubated with the Compound 1 for the mentioned time points. Cells were washed with cold PBS and costained with ER Tracker Red and incubated for 20 mins. Cells were then washed with DPBS at least three times and then visualised using Leica TCS SP8 confocal microscope.

4.4.6 Oil-Red-O staining. HeLa cells were seeded on 24 well plates and were incubated overnight. Cells were then treated with compound 1 at 9 µM concentration and were then incubated for 24 h. After 24 h prior treatment cells were washed with PBS thrice and fixed with 10% formaldehyde for 15 minutes at R.T. After fixation cells were stained with filtered Oil-Red O solution (1 part Oil Red O in 2 parts ddH_2O for 45 minutes.at R.T. Cells were then washed with PBS twice to remove unbound Oil Red O. Cells were then visualised using Perkin Elmer Operetta. (n=3)

4.4.7 Detection of CHOP, LC3B and Beclin via immunostaining. 5 x 10^4 HeLa cells were seeded for this experiment. Cells were treated with compound 1 at IC_{50} concentration and were

then incubated for 24 h followed by treatment with respective primary antibodies for 4 h. Secondary antibodies conjugated to Alexa-Fluor were then added and the cells were incubated for another 1 h. Cells were washed and then visualised by CLSM.(n=2)

4.4.8 Flow Cytometry analysis. 2 x 10^6 HeLa cells were seeded in a 6-well plate and allowed to attache in a 5% CO_2 incubator overnight. Cells were the treated with compound 1 at IC_{50} and allowed to incubate for 24 h. Cells were then trypsinized and washed with PBS. Cells were then suspended in Annexin V binding buffer and then incubated with Annexin V- FITC and PI according to the manufacturer's protocol. Apoptotic and necrotic cells were then quantified using BD FACS Caliber.

4.4.9 Western Blot analysis. 1x 10^6 cells were seeded in a 6-well plate and treated with Compound 1 for 24 h. Cells were then lysed. Sodium Dodecyl Sulphate Polyacrylamide Gel Electrophoresis (SDS-PAGE) was used to resolve the different proteins.and transferred to Proteins were then transferred to Immobilon-P Polyvinylidene Difluoride (PVDF) membrane. The blot was developed using clarity Enhanced Chemiluminescence (ECL) substrate and was visualized using ImageQuant LAS 4000. ImageJ software was used to process the blots and intensity calculations. (n=3)

4.4.10 Characterization Data. All sulfonohydrazide-hydrazone derivatives were characterized by ^{1}H-NMR, ^{13}C-NMR, HRMS as follows:

N'-((6-bromo-1H-indol-3-yl) methylene)-5-(dimethylamino) naphthalene-1-sulfonohydrazide (1)

^{1}H NMR (400 MHz, DMSO) δ 11.55 (s, 1H), 11.41 (s, 1H), 8.52 (d, *J* = 8.7 Hz, 1H), 8.47 (d, *J* = 8.5 Hz, 1H), 8.32 (dd, *J* = 7.4, 1.2 Hz, 1H), 8.05 (s, 1H), 7.70 (dd, *J* = 11.4, 5.2 Hz, 3H), 7.59 (dd, *J* = 8.6, 7.6 Hz, 1H), 7.54 (d, *J* = 1.6 Hz, 1H), 7.26 – 7.16 (m, 2H), 2.77 (s, 6H).

^{13}C NMR (100 MHz, DMSO): δ 151.27, 143.09, 137.71, 135.07, 131.03, 130.03, 130.00, 129.41, 128.96, 127.99, 123.63, 123.18, 123.16, 122.86, 119.38, 115.18, 114.40, 111.17, 45.02.

HRMS (ESI-TOF): m/z: [M + H] calculated for $C_{21}H_{19}BrN_4O_2S$ 471.0490; found 471.0489.

N'-((1H-indol-3-yl) methylene)-4-bromobenzenesulfonohydrazide (2)

^{1}H NMR (400 MHz, Acetone δ): 10.64 (s, 1H), 9.76 (s, 1H), 8.27 – 8.12 (m, 2H), 7.95 (d, *J* = 8.0 Hz, 2H), 7.79 (d, *J* = 6.7 Hz, 2H), 7.67 (s, 1H), 7.44 (d, *J* = 7.2 Hz, 1H), 7.19 (p, *J* = 7.0 Hz, 2H).

^{13}C NMR (100 MHz, Acetone δ): 146.91, 139.73, 138.23, 132.93, 130.90, 130.59, 127.83, 125.41, 123.79, 122.98, 121.71, 112.81, 112.49.

HRMS (ESI-TOF): m/z: [M + H] calculated for $C_{15}H_{12}BrN_3O_2S$ 377.9912; found: 377.9912

(4-bromo-N'-((5-methoxy-1H-indol-3-yl) methylene)benzenesulfonohydrazide (3)

^{1}H NMR (400 MHz, Acetone-d6, δ): 10.55 (s, 1H), 9.77 (s, 1H), 8.22 (s, 1H), 7.95 (d, *J* = 8.6 Hz, 2H), 7.84 – 7.77 (m, 2H), 7.67 (d, *J* = 2.4 Hz, 1H), 7.62 (d, *J* = 2.9 Hz, 1H), 7.33 (d, *J* = 8.9 Hz, 1H), 6.84 (dd, *J* = 8.8, 2.6 Hz, 1H), 3.85 (s, 3H).

^{13}C NMR (100 MHz, Acetone-d6, δ): 156.14, 147.50, 139.83, 133.00, 131.39, 130.56, 127.82, 126.05, 121.62, 114.16, 113.27, 112.59, 104.36, 55.83.

HRMS (ESI-TOF): m/z: [M + H] calculated for $C_{16}H_{14}BrN_3O_3S$ 408.0017; found 408.0020

5-(dimethylamino)-N'-((5-methoxy-1H-indol-3-yl)methylene)naphthalene-1-sulfonohydrazide (4)

^{1}H NMR (400 MHz, DMSO δ): 11.34 (d, *J* = 10.8 Hz, 2H), 8.47 (d, *J* = 8.4 Hz, 2H), 8.35 (d, *J* = 4.9 Hz, 1H), 8.07 (d, *J* = 3.6 Hz, 1H), 7.70 – 7.54 (m, 3H), 7.30 (s, 1H), 7.23 (d, *J* = 8.5 Hz, 2H), 6.75 (d, *J* = 8.8 Hz, 1H), 3.69 (s, 3H), 2.79 (s, 6H).

^{13}C NMR (100 MHz, DMSO δ): 154.24, 151.33, 143.96, 134.83, 131.73, 130.54, 130.23, 129.94, 129.25, 128.97, 127.95, 124.33, 123.51, 119.15, 115.19, 112.52, 112.40, 110.76, 103.15, 55.23, 45.22.

HRMS (ESI-TOF): m/z: [M + H] calculated for $C_{22}H_{22}N_4O_3S$ 423.1494; found 423.1496

N'-(2,4-dihydroxybenzylidene)-4-fluorobenzenesulfonohydrazide (5)

^{1}H NMR (400 MHz, DMSO δ): 11.25 (s, 1H), 10.19 (s, 1H), 9.87 (s, 1H), 8.06 (s, 1H), 7.90 (dd, *J* = 9.0, 5.2 Hz, 2H), 7.47 (t, *J* = 8.9 Hz, 2H), 7.26 (d, *J* = 8.3 Hz, 1H), 6.26 (dt, *J* = 3.7, 2.2 Hz, 2H).

^{13}C NMR (100 MHz, DMSO δ): 165.79, 163.28, 160.84, 158.42, 147.97, 135.13, 135.11, 130.34, 130.24, 129.32, 116.70, 116.47, 110.68, 107.88, 102.39.

HRMS (ESI-TOF): m/z: [M + H] calculated for $C_{13}H_{11}FN_2O_4S$ 311.0502; found 311.0495

N'-((6-bromo-1H-indol-3-yl)methylene)-4-methylbenzenesulfonohydrazide (6)

^{1}H NMR (400 MHz, DMSO δ) 11.61 (s, 1H), 10.93 (s, 1H), 8.05 (s, 1H), 7.90 (d, *J* = 8.4 Hz, 1H), 7.80 (d, *J* = 8.0 Hz, 2H), 7.74 (d, *J* = 2.6 Hz, 1H), 7.59 (s, 1H), 7.39 (d, *J* = 8.2 Hz, 2H), 7.28 (d, *J* = 8.5 Hz, 1H), 2.33 (s, 3H).

^{13}C NMR (101 MHz, DMSO δ): 144.35, 143.21, 137.77, 136.16, 131.18, 129.49, 127.37, 123.42, 123.16, 123.00, 115.24, 114.47, 111.21, 20.97.

HRMS (ESI-TOF): m/z: [M + H] calculated for $C_{16}H_{14}BrN_3O_2S$ 392.0068; found 392.0065

N'-((1H-indol-3-yl)methylene)-5-(dimethylamino)naphthalene-1-sulfonohydrazide (7)

^{1}H NMR (400 MHz, CD_3CN δ): 9.53 (s, 1H), 9.06 (s, 1H), 8.54 (dd, *J* = 8.7, 3.8 Hz, 2H), 8.43 (dd, *J* = 7.4, 1.2 Hz, 1H), 8.02 (s, 1H), 7.80 (d, *J* = 7.9 Hz, 1H), 7.63 (ddd, *J* = 17.4, 8.6, 7.6 Hz, 2H), 7.40 (dd, *J* = 14.4, 5.5 Hz, 2H), 7.24 – 7.15 (m, 2H), 7.11 – 7.08 (m, 1H), 2.79 (s, 6H).

^{13}C NMR (101 MHz, CD_3CN δ) 152.89, 145.71, 137.92, 135.44, 132.01, 131.62, 130.86, 130.77, 130.52, 129.28, 125.01, 124.44, 124.02, 122.76, 121.84, 120.31, 116.35, 112.67, 112.42, 45.66

HRMS (ESI-TOF): m/z: [M + H] calculated for $C_{21}H_{20}N_4O_2S$ 393.1385; found 393.1382.

5-(dimethylamino)-N'-(2-hydroxy-3,5-diiodobenzylidene)naphthalene-1-sulfonohydrazide (8)

^{1}H NMR (400 MHz, DMSO δ): 12.56 (s, 1H), 11.09 (s, 1H), 8.52 (d, *J* = 8.5 Hz, 1H), 8.29 (dd, *J* = 26.3, 8.0 Hz, 2H), 8.04 – 7.94 (m, 2H), 7.74 – 7.60 (m, 3H), 7.27 (d, *J* = 7.6 Hz, 1H), 2.81 (s, 6H).

^{13}C NMR (100 MHz, DMSO δ): 155.50, 151.57, 146.60, 145.59, 137.94, 133.90, 130.76, 129.81, 129.06, 128.98, 128.42, 123.80, 120.76, 118.57, 115.47, 88.17, 82.82, 45.07.

HRMS (ESI-TOF): m/z: [M + H] calculated for $C_{19}H_{17}I_2N_3O_3S$ 621.9158; found 621.9161.

N'-(3,5-dibromo-2-hydroxybenzylidene)-5-(dimethylamino)naphthalene-1-sulfonohydrazide (9)

^{1}H NMR (400 MHz, DMSO δ): 12.54 (s, 1H), 10.89 (s, 1H), 8.52 (d, *J* = 8.4 Hz, 1H), 8.31 (dd, *J* = 30.2, 7.8 Hz, 2H), 8.09 (s, 1H), 7.82 – 7.52 (m, 4H), 7.27 (d, *J* = 7.4 Hz, 1H), 2.81 (s, 6H).

^{13}C NMR (100 MHz, DMSO, δ): 152.40, 151.51, 144.52, 135.47, 134.00, 130.67, 130.57, 129.81, 129.03, 128.99, 128.30, 123.77, 121.87, 118.64, 115.40, 111.75, 110.98, 44.91.

HRMS (ESI-TOF): m/z: [M + H] calculated for $C_{19}H_{17}Br_2N_3O_3S$ 527.9415; found 527.9409.

4-bromo-N'-((6-bromo-1H-indol-3-yl)methylene)benzenesulfonohydrazide (10)

^{1}H NMR (400 MHz, Acetone δ): 10.76 (s, 1H), 9.85 (s, 1H), 8.21 (s, 1H), 8.10 (d, *J* = 8.5 Hz, 1H), 7.94 (d, *J* = 8.5 Hz, 2H), 7.81 (d, *J* = 7.7 Hz, 2H), 7.67 (d, *J* = 18.2 Hz, 2H), 7.33 (d, *J* = 8.5 Hz, 1H).

^{13}C NMR (100 MHz, Acetone δ) 146.14, 139.65, 139.05, 133.00, 131.61, 130.60, 127.93, 124.80, 124.47, 124.39, 116.82, 115.45, 112.96.

HRMS (ESI-TOF): m/z: [M + H] calculated for $C_{15}H_{11}Br_2N_3O_2S$ 457.8996; found 457.8991.

N'-((5-methoxy-1H-indol-3-yl)methylene)-2-nitrobenzenesulfonohydrazide (11)

^{1}H NMR (400 MHz, DMSO δ): 12.06 (s, 1H), 11.32 (s, 1H), 8.05 – 8.00 (m, 2H), 7.74 (ddd, *J* = 10.3, 6.7, 2.0 Hz, 3H), 7.45 (d, *J* = 8.0 Hz, 2H), 2.38 (s, 3H).

^{13}C NMR (100 MHz, DMSO) δ 155.77, 147.29, 146.82, 144.23, 138.39, 135.37, 130.11, 127.07, 120.44, 88.01, 82.77, 21.09.

HRMS (ESI-TOF): m/z: [M + H] calculated for $C_{14}H_{12}I_2N_2O_3S$ 542.8736; found 542.8740

N'-(3,5-dichloro-2-hydroxybenzylidene)-4-methoxybenzenesulfonohydrazide (12)

^{1}H NMR (400 MHz, DMSO) δ 11.91 (s, 1H), 10.98 (s, 1H), 8.13 (s, 1H), 7.79 (d, *J* = 8.9 Hz, 2H), 7.59 (s, 1H), 7.51 (d, *J* = 2.5 Hz, 1H), 7.16 (d, *J* = 8.9 Hz, 2H), 3.83 (s, 3H).

^{13}C NMR (100 MHz, DMSO) δ 162.94, 151.21, 145.48, 130.32, 129.83, 129.31, 126.93, 123.45, 121.88, 121.55, 114.72, 55.74.

HRMS (ESI-TOF): m/z: [M + H] calculated for $C_{14}H_{12}Cl_2N_2O_4S$ 374.9973; found 374.9974.

4-chloro-N'-(2-hydroxy-5-iodobenzylidene)benzenesulfonohydrazide (13)

^{1}H NMR (400 MHz, DMSO δ): 11.72 (s, 1H), 10.43 (s, 1H), 8.10 (s, 1H), 7.85 (d, *J* = 8.7 Hz, 2H), 7.72 (s, 2H), 7.70 (s, 1H), 7.51 (dd, *J* = 8.6, 2.2 Hz, 1H), 6.71 (s, 1H).

^{13}C NMR (100 MHz, DMSO δ): 156.15, 143.71, 139.55, 138.13, 137.65, 134.26, 129.56, 129.02, 122.04, 118.89, 81.58.

HRMS (ESI-TOF): m/z: [M + H] calculated for $C_{13}H_{10}ClIN_2O_3S$ 436.9223; found 436.9220.

N'-((1H-indol-3-yl)methylene)-2-nitrobenzenesulfonohydrazide (14)

^{1}H NMR (400 MHz, Acetone δ): 10.69 (s, 1H), 9.80 (s, 1H), 8.44 (s, 1H), 8.38 (dd, *J* = 8.0, 1.6 Hz, 1H), 8.14 (d, *J* = 8.4 Hz, 1H), 7.99 – 7.86 (m, 3H), 7.72 (d, *J* = 2.8 Hz, 1H), 7.44 (d, *J* = 7.7 Hz, 1H), 7.18 (ddd, *J* = 14.9, 13.5, 7.1 Hz, 2H).

^{13}C NMR (100 MHz, Acetone δ): 147.58, 138.28, 135.36, 133.32, 133.07, 132.43, 131.25, 125.51, 125.38, 123.82, 123.07, 121.73, 112.68, 112.51, 112.46.

HRMS (ESI-TOF): m/z: [M + H] calculated for $C_{15}H_{12}N_4O_4S$ 345.0657; found 345.0661

N'-((5-methoxy-1H-indol-3-yl)methylene)-4-nitrobenzenesulfonohydrazide (15)

^{1}H NMR (400 MHz, DMSO δ): 11.43 (s, 1H), 11.27 (s, 1H), 8.44 (d, *J* = 8.8 Hz, 2H), 8.21 – 8.09 (m, 3H), 7.70 (d, *J* = 2.6 Hz, 1H), 7.38 (s, 1H), 7.29 (d, *J* = 8.8 Hz, 1H), 6.80 (dd, *J* = 8.8, 2.4 Hz, 1H), 3.75 (s, 3H).

^{13}C NMR (101 MHz, DMSO) δ 154.46, 149.84, 146.87, 144.57, 131.77, 131.31, 128.87, 124.45, 112.60, 110.52, 103.03, 55.15

HRMS (ESI-TOF): m/z: [M + H] calculated for $C_{16}H_{14}N_4O_5S$ 375.0763; found 375.0765.

N'-(2-hydroxy-3,5-diiodobenzylidene)-4-nitrobenzenesulfonohydrazide (16)

^{1}H NMR (400 MHz, DMSO δ): 12.49 (s, 1H), 11.10 (s, 1H), 8.50 – 8.41 (m, 2H), 8.11 (dt, *J* = 3.5, 2.0 Hz, 3H), 8.03 (d, *J* = 2.1 Hz, 1H), 7.78 (d, *J* = 2.1 Hz, 1H).

^{13}C NMR (100 MHz, DMSO δ): 155.71, 150.21, 147.82, 147.03, 143.68, 138.02, 128.64, 124.96, 120.71, 88.43, 83.00.

HRMS (ESI-TOF): m/z: [M + H] calculated for $C_{13}H_9I_2N_3O_5S$ 573.8430; found 573.8426

N'-((6-bromo-1H-indol-3-yl)methylene)-4-chlorobenzenesulfonohydrazide (17)

^{1}H NMR (400 MHz, DMSO) δ 11.64 (s, 1H), 11.10 (s, 1H), 8.08 (d, *J* = 1.0 Hz, 1H), 7.91 (d, *J* = 8.5 Hz, 2H), 7.86 (d, *J* = 8.7 Hz, 1H), 7.77 (d, *J* = 2.7 Hz, 1H), 7.70 (d, *J* = 8.6 Hz, 2H), 7.60 (d, *J* = 1.3 Hz, 1H), 7.29 (dd, *J* = 8.5, 1.7 Hz, 1H).

^{13}C NMR (100 MHz, DMSO δ): 145.10, 137.82, 137.80, 137.78, 131.50, 129.29, 129.28, 123.54, 123.07, 122.96, 115.27, 114.51, 111.04.

HRMS (ESI-TOF): m/z: [M + H] calculated for $C_{15}H_{11}BrClN_3O_2S$ 411.9522; found 411.9519

N'-((1H-indol-3-yl)methylene)-4-methylbenzenesulfonohydrazide (18)

^{1}H NMR (400 MHz, CD_3CN δ): 9.60 (s, 1H), 8.67 (s, 1H), 8.04 (d, *J* = 7.2 Hz, 2H), 7.87 (d, *J* = 8.3 Hz, 2H), 7.50 (d, *J* = 2.8 Hz, 1H), 7.44 (d, *J* = 7.7 Hz, 1H), 7.37 (d, *J* = 8.2 Hz, 2H), 7.21 (dtd, *J* = 17.5, 7.2, 1.2 Hz, 2H), 2.36 (s, 3H).

^{13}C NMR (100 MHz, CD_3CN δ): 146.76, 145.18, 138.01, 136.84, 131.07, 130.49, 128.89, 125.12, 124.10, 122.73, 122.04, 112.71, 112.43, 21.51.

HRMS (ESI-TOF): m/z: [M + H] calculated for $C_{16}H_{15}N_3O_2S$ 314.0963; found 314.0967

N'-(2-hydroxy-5-iodobenzylidene)-2-nitrobenzenesulfonohydrazide (19)

^{1}H NMR (400 MHz, DMSO δ): 12.19 (s, 1H), 10.40 (s, 1H), 8.24 (d, *J* = 1.8 Hz, 1H), 8.03 (dd, *J* = 9.0, 4.6 Hz, 2H), 7.94 – 7.86 (m, 2H), 7.76 (s, 1H), 7.51 (dd, *J* = 8.6, 2.2 Hz, 1H), 6.71 (d, *J* = 8.6 Hz, 1H).

^{13}C NMR (100 MHz, DMSO δ): 156.21, 147.89, 143.46, 139.68, 134.92, 134.09, 132.69, 130.81, 130.35, 124.61, 122.12, 118.91, 81.62.

HRMS (ESI-TOF): m/z: [M + H] calculated for $C_{13}H_{10}IN_3O_5S$ 447.9464; found 447.9456

4-chloro-N'-(2-hydroxy-5-nitrobenzylidene)benzenesulfonohydrazide (20)

^{1}H NMR (400 MHz, DMSO δ): 11.79 (s, 2H), 8.33 (d, *J* = 2.9 Hz, 1H), 8.21 (s, 1H), 8.12 (dd, *J* = 9.1, 2.7 Hz, 1H), 7.91 – 7.83 (m, 2H), 7.71 (d, *J* = 8.5 Hz, 2H), 7.04 (d, *J* = 9.1 Hz, 1H).

^{13}C NMR (101 MHz, DMSO-D6) δ 161.84, 142.43, 139.93, 138.18, 137.69, 129.61, 129.02, 126.80, 121.78, 120.21, 116.86.

HRMS (ESI-TOF): m/z: [M + H] calculated for $C_{13}H_{10}ClN_3O_5S$ 356.0108; found 356.0109

N'-((1H-pyrrol-2-yl)methylene)-5-(dimethylamino)naphthalene-1-sulfonohydrazide (21)

^{1}H NMR (400 MHz, DMSO δ): 11.44 (s, 1H), 11.15 (s, 1H), 8.46 (t, *J* = 9.7 Hz, 2H), 8.21 (d, *J* = 7.2 Hz, 1H), 7.78 (s, 1H), 7.63 (dd, *J* = 16.1, 11.6 Hz, 2H), 7.24 (d, *J* = 7.5 Hz, 1H), 6.80 (s, 1H), 6.30 (s, 1H), 6.03 (s, 1H), 6.03 (s, 1H), 2.80 (s, 6H).

^{13}C NMR (10 MHz, DMSO δ): 151.28, 139.44, 135.25, 129.93, 129.50, 129.26, 128.96, 127.97, 126.37, 123.67, 122.17, 119.37, 115.23, 112.63, 109.08, 45.07.

HRMS (ESI-TOF): m/z: [M + H] calculated for $C_{17}H_{18}N_4O_2S$ 343.1228; found 343.1228

N'-((1H-pyrrol-2-yl)methylene)-4-methoxybenzenesulfonohydrazide (22)

^{1}H NMR (400 MHz, DMSO δ): 11.26 (s, 1H), 10.84 (s, 1H), 7.85 – 7.80 (m, 2H), 7.73 (s, 1H), 7.09 (d, *J* = 9.0 Hz, 2H), 6.84 (dd, *J* = 4.1, 2.7 Hz, 1H), 6.37 – 6.33 (m, 1H), 6.06 (dd, *J* = 5.9, 2.4 Hz, 1H), 3.81 (s, 3H).

^{13}C NMR (100 MHz, DMSO δ): 162.46, 140.43, 130.81, 129.45, 126.50, 122.23, 114.23, 112.95, 109.08, 55.64.

HRMS (ESI-TOF): m/z: [M + H] calculated for $C_{12}H_{13}N_3O_3S$ 280.0756; found 280.0761

N'-((6-bromo-1H-indol-3-yl)methylene)-4-fluorobenzenesulfonohydrazide (23)

^{1}H NMR (400 MHz, Acetone, δ): 10.76 (s, 1H), 9.80 (s, 1H), 8.20 (s, 1H), 8.15 – 8.03 (m, 3H), 7.70 (d, *J* = 2.5 Hz, 1H), 7.65 (s, 1H), 7.43 – 7.29 (m, 3H).

^{13}C NMR (100 MHz, Acetone, δ): 167.19, 164.69, 145.97, 139.05, 136.70, 136.67, 131.51, 124.70, 124.45, 124.37, 116.93, 116.74, 116.70, 115.42, 112.95.

HRMS (ESI-TOF): m/z: [M + H] calculated for $C_{15}H_{11}BrFN_3O_2S$ 395.9818 found 395.9813

N'-(3,5-dibromo-2-hydroxybenzylidene)-4-methoxybenzenesulfonohydrazide (24)

^{1}H NMR (400 MHz, DMSO δ): 11.97 (s, 1H), 11.15 (s, 1H), 8.11 (s, 1H), 7.82 – 7.76 (m, 3H), 7.67 (d, *J* = 2.2 Hz, 1H), 7.17 (t, *J* = 5.9 Hz, 2H), 3.83 (s, 3H).

^{13}C NMR (100 MHz, DMSO δ): 162.98, 152.67, 146.23, 135.69, 131.11, 129.74, 129.29, 121.45, 114.76, 111.59, 110.96, 55.75.

HRMS (ESI-TOF): m/z: [M + H] calculated for $C_{14}H_{12}Br_2N_2O_4S$ 464.8942: found 464.8939.

4-fluoro-N'-(2-hydroxy-3,5-diiodobenzylidene)benzenesulfonohydrazide (25)

^{1}H NMR (400 MHz, Acetone δ): 11.51 (s, 1H), 10.87 (s, 1H), 8.12 (s, 1H), 8.08 – 7.99 (m, 3H), 7.69 (d, *J* = 2.0 Hz, 1H), 7.44 (t, *J* = 8.8 Hz, 2H).

^{13}C NMR (100 MHz, Acetone δ) 167.68, 165.16, 157.61, 149.55, 148.53, 140.45, 135.72, 135.69, 131.51, 131.42, 120.57, 117.69, 117.46, 86.85, 81.38.

HRMS (ESI-TOF): m/z: [M + H] calculated for $C_{13}H_9FI_2N_2O_3S$ 546.8486; found 546.8491.

N'-((1H-indol-3-yl)methylene)-4-nitrobenzenesulfonohydrazide (26)

^{1}H NMR (400 MHz, DMSO δ): 11.56 (s, 1H), 11.30 (s, 1H), 8.44 (d, *J* = 8.6 Hz, 2H), 8.23 – 8.04 (m, 3H), 7.93 (d, *J* = 7.5 Hz, 1H), 7.75 (d, *J* = 2.7 Hz, 1H), 7.40 (d, *J* = 7.8 Hz, 1H), 7.23 – 7.01 (m, 2H).

^{13}C NMR (100 MHz, DMSO δ): 149.84, 146.27, 144.50, 136.92, 130.98, 128.93, 124.43, 123.96, 122.65, 121.48, 120.71, 111.86, 110.78.

HRMS (ESI-TOF): m/z: [M + H] calculated for $C_{15}H_{12}N_4O_4S$ 345.0657; found 345.0659.

N'-(2-hydroxy-3,5-diiodobenzylidene)-4-methoxybenzenesulfonohydrazide (27)

^{1}H NMR (400 MHz, DMSO δ): 11.98 (s, 1H), 11.37 (s, 1H), 8.02 (d, *J* = 5.6 Hz, 2H), 7.78 (d, *J* = 8.1 Hz, 3H), 7.16 (d, *J* = 7.6 Hz, 2H), 3.83 (s, 3H).

^{13}C NMR (100 MHz, DMSO δ): 163.00, 155.74, 147.10, 146.72, 138.35, 129.70, 129.26, 120.41, 114.79, 87.94, 82.72, 55.77.

HRMS (ESI-TOF): m/z: [M + H] calculated for $C_{14}H_{12}I_2N_2O_4S$ 558.8685; found 558.8687.

N'-(2-hydroxy-5-iodobenzylidene)-4-nitrobenzenesulfonohydrazide (28)

^{1}H NMR (400 MHz, DMSO δ): 11.96 (s, 1H), 10.41 (s, 1H), 8.44 (d, *J* = 8.6 Hz, 2H), 8.12 (s, 2H), 8.10 (s, 1H), 7.75 (s, 1H), 7.51 (d, *J* = 8.5 Hz, 1H), 6.69 (s, 1H).

^{13}C NMR (100 MHz, DMSO δ): 156.18, 150.01, 144.17, 143.98, 139.71, 134.04, 128.70, 124.74, 122.02, 118.88, 81.61.

HRMS (ESI-TOF): m/z: [M + H] calculated for $C_{13}H_{10}IN_3O_5S$ 447.9464; found 447.9461.

N'-((5-methoxy-1H-indol-3-yl)methylene)-4-methylbenzenesulfonohydrazide (29)

^{1}H NMR (400 MHz, DMSO δ): 11.38 (s, 1H), 10.84 (s, 1H), 8.07 (d, *J* = 2.9 Hz, 1H), 7.81 (dd, *J* = 8.2, 2.1 Hz, 2H), 7.69 – 7.63 (m, 1H), 7.45 (s, 1H), 7.39 (d, *J* = 8.1 Hz, 2H), 7.28 (dd, *J* = 8.8, 2.0 Hz, 1H), 6.79 (dt, *J* = 8.8, 2.0 Hz, 1H), 3.76 (s, 3H), 2.34 (s, 3H).

^{13}C NMR (100 MHz, DMSO δ): 154.39, 145.57, 143.20, 136.31, 131.76, 130.80, 129.47, 127.39, 124.49, 112.66, 112.53, 110.86, 103.13, 55.15, 39.52, 20.96.

HRMS (ESI-TOF): m/z: [M + H] calculated for $C_{17}H_{17}N_3O_3S$ 344.1069; found 344.1068.

4-fluoro-N'-((5-methoxy-1H-indol-3-yl)methylene)benzenesulfonohydrazide (30)

^{1}H NMR (400 MHz, DMSO δ): 11.41 (s, 1H), 10.95 (s, 1H), 8.10 (d, *J* = 2.3 Hz, 1H), 7.97 (ddd, *J* = 7.3, 5.1, 1.9 Hz, 2H), 7.68 (d, *J* = 1.5 Hz, 1H), 7.45 (dd, *J* = 18.2, 9.4 Hz, 3H), 7.29 (dd, *J* = 8.8, 1.1 Hz, 1H), 6.80 (d, *J* = 8.9 Hz, 1H), 3.74 (d, *J* = 0.9 Hz, 3H).

^{13}C NMR (100 MHz, DMSO δ): 165.61, 163.11, 154.41, 146.20, 135.56, 135.53, 131.79, 131.03, 130.36, 130.26, 124.47, 116.40, 116.17, 112.63, 112.55, 110.70, 103.03, 55.15.

HRMS (ESI-TOF): m/z: [M + H] calculated for $C_{16}H_{14}FN_3O_3S$ 348.0818; found 348.0822.

4-chloro-N'-(2-hydroxy-3,5-diiodobenzylidene)benzenesulfonohydrazide (31)

^{1}H NMR (400 MHz, DMSO δ): 12.23 (s, 1H), 11.20 (s, 1H), 8.06 (s, 1H), 8.02 (s, 1H), 7.85 (d, *J* = 8.6 Hz, 2H), 7.78 (d, *J* = 1.7 Hz, 1H), 7.74 (d, *J* = 8.6 Hz, 2H).

^{13}C NMR (100 MHz, DMSO δ): 155.76, 147.65, 146.95, 138.59, 138.26, 137.13, 129.86, 128.97, 120.55, 88.24, 82.92, 39.52.

HRMS (ESI-TOF): m/z: [M + H] calculated for $C_{13}H_9ClI_2N_2O_3S$ 562.8190; found 562.8184.

4-fluoro-N'-(2-hydroxy-5-nitrobenzylidene) benzenesulfonohydrazide (32)

^{1}H NMR (400 MHz, Acetone δ): 11.30 (s, 2H), 8.39 (s, 1H), 8.35 (d, *J* = 2.8 Hz, 1H), 8.19 (dd, *J* = 9.1, 2.8 Hz, 1H), 8.04 (dd, *J* = 9.0, 5.1 Hz, 2H), 7.44 (t, *J* = 8.8 Hz, 2H), 7.11 (d, *J* = 9.1 Hz, 1H).

^{13}C NMR (100 MHz, Acetone δ): 167.61, 165.09, 163.56, 148.79, 141.52, 135.79, 131.55, 131.45, 127.60, 126.94, 119.08, 118.28, 117.58, 117.35.

HRMS (ESI-TOF): m/z: [M + H] calculated for $C_{13}H_{10}FN_3O_5S$ 340.0403; found 340.0403.

N'-(3,5-dibromo-2-hydroxybenzylidene)-4-nitrobenzenesulfonohydrazide (33)

^{1}H NMR (400 MHz, DMSO δ): 12.44 (s, 1H), 10.88 (s, 1H), 8.45 (d, *J* = 8.8 Hz, 2H), 8.17 (s, 1H), 8.12 (d, *J* = 8.8 Hz, 2H), 7.80 (s, 1H), 7.67 (d, *J* = 2.1 Hz, 1H).

^{13}C NMR (100 MHz, DMSO) δ 152.60, 150.17, 146.60, 143.75, 135.96, 130.47, 128.66, 124.90, 121.96, 112.05, 111.19.

HRMS (ESI-TOF): m/z: [M + H] calculated for $C_{13}H_9Br_2N_3O_5S$ 479.8687; found 479.8684.

4-methoxy-N'-((5-methoxy-1H-indol-3-yl)methylene)benzenesulfonohydrazide (34)

^{1}H NMR (400 MHz, DMSO δ): 11.37 (s, 1H), 10.75 (s, 1H), 8.07 (s, 1H), 7.85 (d, *J* = 8.6 Hz, 2H), 7.66 (d, *J* = 2.6 Hz, 1H), 7.45 (s, 1H), 7.28 (d, *J* = 8.8 Hz, 1H), 7.10 (d, *J* = 8.9 Hz, 2H), 6.79 (dd, *J* = 8.8, 2.0 Hz, 1H), 3.80 (s, 3H), 3.75 (s, 3H).

^{13}C NMR (100 MHz, DMSO) δ 205.95, 162.43, 154.35, 145.46, 131.78, 130.84, 130.73, 129.48, 124.48, 114.19, 112.59, 112.48, 110.85, 103.12, 55.63, 55.15.

HRMS (ESI-TOF): m/z: [M + H] calculated for $C_{17}H_{17}N_3O_4S$ 360.1018; found 360.1014.

4-methoxy-N'-((4-methylthiazol-5-yl)methylene)benzenesulfonohydrazide (35)

^{1}H NMR (400 MHz, DMSO δ): 11.36 (s, 1H), 8.99 (s, 1H), 8.13 (s, 1H), 7.76 (d, *J* = 7.7 Hz, 2H), 7.12 (d, *J* = 8.9 Hz, 2H), 3.82 (s, 3H), 2.39 (s, 3H).

^{13}C NMR (100 MHz, DMSO δ): 162.67, 154.72, 153.76, 139.87, 130.32, 129.39, 126.84, 114.38, 55.68, 15.26.

HRMS (ESI-TOF): m/z: [M + H] calculated for $C_{12}H_{13}N_3O_3S_2$ 312.0477; found 312.0481.

N'-((5-methoxy-1H-indol-3-yl)methylene)-2-nitrobenzenesulfonohydrazide (36)

^{1}H NMR (400 MHz, Acetone, δ): 10.60 (s, 1H), 9.81 (s, 1H), 8.43 (s, 1H), 8.38 – 8.33 (m, 1H), 7.97 – 7.88 (m, 2H), 7.66 (dd, *J* = 14.7, 2.7 Hz, 2H), 7.33 (d, *J* = 8.9 Hz, 1H), 6.83 (dd, *J* = 8.8, 2.5 Hz, 1H), 3.84 (s, 3H).

^{13}C NMR (100 MHz, Acetone, δ) 156.17, 149.46, 148.02, 135.38, 133.13, 133.09, 132.49, 131.65, 125.90, 125.63, 114.17, 113.24, 112.43, 104.30, 55.85.

HRMS (ESI-TOF): m/z: [M + H] calculated for $C_{16}H_{14}N_4O_5S$ 375.0763; found 375.0758.

N'-(4-bromobenzylidene)-4-methoxybenzenesulfonohydrazide (37)

^{1}H NMR (400 MHz, DMSO δ): 11.47 (s, 1H), 7.88 (s, 1H), 7.80 (d, *J* = 8.6 Hz, 2H), 7.59 (d, *J* = 8.5 Hz, 2H), 7.50 (d, *J* = 8.6 Hz, 2H), 7.12 (d, *J* = 9.0 Hz, 2H), 3.81 (s, 3H).

^{13}C NMR (101 MHz, DMSO δ): 162.62, 145.57, 132.98, 131.78, 130.52, 129.38, 128.58, 123.25, 114.40, 55.66.

HRMS (ESI-TOF): m/z: [M + H] calculated for $C_{14}H_{13}BrN_2O_3S$ 368.9908; found 368.9909.

4-chloro-N'-(3,5-dibromo-2-hydroxybenzylidene)benzenesulfonohydrazide (38)

^{1}H NMR (400 MHz, DMSO δ): 12.22 (s, 1H), 10.99 (s, 1H), 8.14 (s, 1H), 7.86 (d, *J* = 8.6 Hz, 2H), 7.80 (s, 1H), 7.74 (d, *J* = 8.6 Hz, 2H), 7.66 (s, 1H).

^{13}C NMR (100 MHz, DMSO δ): 152.68, 146.60, 138.56, 137.19, 135.92, 130.85, 129.83, 129.02, 121.72, 111.88, 111.14.

HRMS (ESI-TOF): m/z: [M + H] calculated for $C_{13}H_9Br_2ClN_2O_3S$ 468.8447; found 468.8436

N'-((1H-indol-3-yl)methylene)-4-chlorobenzenesulfonohydrazide (39)

^{1}H NMR (400 MHz, DMSO δ): 11.53 (s, 1H), 11.01 (s, 1H), 8.10 (s, 1H), 7.92 (d, *J* = 8.5 Hz, 3H), 7.71 (dd, *J* = 14.0, 5.7 Hz, 3H), 7.40 (d, *J* = 7.9 Hz, 1H), 7.20 – 7.09 (m, 2H).

^{13}C NMR (100 MHz, DMSO δ) 145.73, 137.95, 137.73, 136.91, 130.71, 129.27, 129.22, 123.94, 122.60, 121.47, 120.59, 111.84, 110.90.

HRMS (ESI-TOF): m/z: [M + H] calculated for $C_{15}H_{12}ClN_3O_2S$ 334.0417; found 334.0418.

4-chloro-N'-(3,5-dichloro-2-hydroxybenzylidene)benzenesulfonohydrazide (40)

^{1}H NMR (400 MHz, DMSO) δ 12.13 (s, 1H), 10.83 (s, 1H), 8.17 (s, 1H), 7.87 (d, *J* = 8.6 Hz, 2H), 7.73 (d, *J* = 8.6 Hz, 2H), 7.59 (s, 1H), 7.50 (s, 1H).

^{13}C NMR (100 MHz, DMSO) δ 151.17, 145.69, 138.43, 137.25, 130.47, 129.74, 129.00, 126.53, 123.56, 122.10, 121.81.

HRMS (ESI-TOF): m/z: [M + H] calculated for $C_{13}H_9Cl_3N_2O_3S$ 378.9477; found 378.9477.

N'-(2-hydroxy-5-nitrobenzylidene)-4-methylbenzenesulfonohydrazide (41)

^{1}H NMR (400 MHz, DMSO δ): 11.74 (s, 1H), 11.68 (s, 1H), 8.33 (d, *J* = 2.9 Hz, 1H), 8.19 (s, 1H), 8.12 (dd, *J* = 9.1, 2.9 Hz, 1H), 7.75 (d, *J* = 8.3 Hz, 2H), 7.43 (d, *J* = 8.0 Hz, 2H), 7.04 (d, *J* = 9.1 Hz, 1H), 2.37 (s, 3H).

^{13}C NMR (100 MHz, DMSO δ): 161.81, 143.77, 142.05, 139.95, 135.95, 129.88, 127.14, 126.72, 121.91, 120.29, 116.88, 21.04.

HRMS (ESI-TOF): m/z: [M + H] calculated for $C_{14}H_{13}N_3O_5S$ 336.0654; found 336.0657

N'-(2,4-dihydroxybenzylidene)-4-nitrobenzenesulfonohydrazide (42)

^{1}H NMR (400 MHz, DMSO δ): 11.54 (s, 1H), 10.12 (s, 1H), 9.88 (s, 1H), 8.47 – 8.40 (m, 2H), 8.11 – 8.07 (m, 3H), 7.30 (d, *J* = 8.9 Hz, 1H), 6.31 – 6.22 (m, 2H).

^{13}C NMR (101 MHz, DMSO δ): 160.94, 158.34, 149.96, 147.82, 144.21, 128.79, 124.65, 110.69, 107.90, 102.31.

HRMS (ESI-TOF): m/z: [M + H] calculated for $C_{13}H_{11}N_3O_6S$ 338.0447; found 338.0445

4-chloro-N'-((5-methoxy-1H-indol-3-yl)methylene)benzenesulfonohydrazide (43)

^{1}H NMR (400 MHz, DMSO δ): 11.43 (s, 1H), 11.02 (s, 1H), 8.10 (s, 1H), 7.91 (d, *J* = 8.5 Hz, 2H), 7.70 (d, *J* = 8.6 Hz, 3H), 7.39 (s, 1H), 7.29 (d, *J* = 8.8 Hz, 1H), 6.80 (dd, *J* = 8.8, 2.4 Hz, 1H), 3.73 (s, 3H).

^{13}C NMR (100 MHz, DMSO δ): 154.44, 146.42, 138.00, 137.80, 131.81, 131.16, 129.30, 129.28, 124.47, 112.69, 112.62, 110.67, 102.97, 55.15.

HRMS (ESI-TOF): m/z: [M + H] calculated for $C_{16}H_{14}ClN_3O_3S$ 364.0522; found 364.0521

N'-(3,5-dichloro-2-hydroxybenzylidene)-4-nitrobenzenesulfonohydrazide (44)

^{1}H NMR (400 MHz, DMSO δ): 12.35 (s, 1H), 10.74 (s, 1H), 8.48 – 8.42 (m, 2H), 8.19 (s, 1H), 8.15 – 8.09 (m, 2H), 7.59 (d, *J* = 2.6 Hz, 1H), 7.51 (d, *J* = 2.5 Hz, 1H).

^{13}C NMR (100 MHz, DMSO δ) 151.14, 150.14, 145.70, 143.81, 130.56, 128.70, 126.16, 124.87, 123.65, 122.26, 122.08

HRMS (ESI-TOF): m/z: [M + H] calculated for $C_{13}H_9Cl_2N_3O_5S$ 389.9718; found 389.9719

N'-((6-bromo-1H-indol-3-yl)methylene)-4-nitrobenzenesulfonohydrazide (45)

^{1}H NMR (400 MHz, DMSO δ): 11.65 (s, 1H), 11.36 (s, 1H), 8.44 (d, *J* = 8.8 Hz, 2H), 8.21 – 8.09 (m, 3H), 7.87 (d, *J* = 8.5 Hz, 1H), 7.78 (d, *J* = 2.7 Hz, 1H), 7.60 (d, *J* = 1.3 Hz, 1H), 7.30 (dd, *J* = 8.5, 1.7 Hz, 1H).

^{13}C NMR (100 MHz, DMSO δ): 149.88, 145.64, 144.33, 137.77, 131.75, 128.92, 124.46, 123.66, 123.08, 122.92, 115.29, 114.51, 110.90.

HRMS (ESI-TOF): m/z: [M + H] calculated for $C_{15}H_{11}BrN_4O_4S$ 422.9763; found 422.9766

N'-(5-fluoro-2-hydroxybenzylidene)-4-nitrobenzenesulfonohydrazide (46)

^{1}H NMR (400 MHz, DMSO δ): 11.93 (s, 1H), 10.13 (s, 1H), 8.46 – 8.41 (m, 2H), 8.17 (s, 1H), 8.15 – 8.10 (m, 2H), 7.26 (dd, *J* = 9.4, 3.2 Hz, 1H), 7.09 (td, *J* = 8.6, 3.2 Hz, 1H), 6.85 (dd, *J* = 9.0, 4.7 Hz, 1H).

^{13}C NMR (100 MHz, DMSO δ): 156.58, 154.24, 152.81, 150.03, 144.32, 144.09, 128.82, 124.73, 120.26, 120.19, 118.54, 118.31, 117.61, 117.53, 111.44, 111.20.

HRMS (ESI-TOF): m/z: [M + H] calculated for $C_{13}H_{10}FN_3O_5S$ 340.0403; found 340.0401.

4-chloro-N'-(2,4-dihydroxybenzylidene)benzenesulfonohydrazide (47)

^{1}H NMR (400 MHz, DMSO δ): 11.30 (s, 1H), 10.17 (s, 1H), 9.88 (s, 1H), 8.07 (s, 1H), 7.84 (d, *J* = 8.6 Hz, 2H), 7.70 (d, *J* = 8.7 Hz, 2H), 7.27 (d, *J* = 8.3 Hz, 1H), 6.30 – 6.23 (m, 2H).

^{13}C NMR (100 MHz, DMSO δ): 160.85, 158.38, 148.03, 138.05, 137.57, 129.49, 129.25, 129.11, 110.63, 107.87, 102.37.

HRMS (ESI-TOF): m/z: [M + H] calculated for $C_{13}H_{11}ClN_2O_4S$ 327.0206; found 327.0209.

4-bromo-N'-(5-fluoro-2-hydroxybenzylidene)benzenesulfonohydrazide (48)

^{1}H NMR (400 MHz, DMSO, δ): 11.68 (s, 1H), 10.12 (s, 1H), 8.15 (s, 1H), 7.82 (dd, *J* = 26.1, 8.6 Hz, 4H), 7.23 (dd, *J* = 9.4, 3.2 Hz, 1H), 7.08 (td, *J* = 8.6, 3.2 Hz, 1H), 6.86 (dd, *J* = 9.0, 4.7 Hz, 1H).

^{13}C NMR (100 MHz, DMSO, δ): 156.55, 154.21, 152.75, 152.74, 144.10, 137.99, 132.47, 129.15, 127.16, 120.24, 120.17, 118.36, 118.12, 117.59, 117.51, 111.61, 111.37.
HRMS (ESI-TOF): m/z: [M + H] calculated for $C_{13}H_{11}BrFN_2O_3S$ 372.9658; found 372.9658.

N'-(2-hydroxy-3,5-diiodobenzylidene)-2-nitrobenzenesulfonohydrazide (49)

^{1}H NMR (400 MHz, CD_3CN δ):11.17 (s, 1H), 9.93 (s, 1H), 8.17 – 8.12 (m, 1H), 8.07 (d, *J* = 2.1 Hz, 1H), 8.04 (s, 1H), 7.91 (ddd, *J* = 6.3, 3.6, 2.1 Hz, 1H), 7.88 – 7.82 (m, 2H), 7.65 (d, *J* = 2.1 Hz, 1H).

^{13}C NMR (100 MHz, CD3CN δ): 157.57, 150.82, 148.98, 140.92, 136.46, 134.12, 132.36, 131.41, 126.33, 120.30, 86.88, 81.58.

HRMS (ESI-TOF): m/z: [M + H] calculated for $C_{13}H_9I_2N_3O_5S$ 573.8431; found 573.8429.

N'-(3,5-dibromo-2-hydroxybenzylidene)-2-nitrobenzenesulfonohydrazide (50)

^{1}H NMR (400 MHz, DMSO δ): 12.65 (s, 1H), 10.76 (s, 1H), 8.26 (s, 1H), 8.10 – 8.01 (m, 2H), 7.96 – 7.88 (m, 2H), 7.80 (d, *J* = 2.3 Hz, 1H), 7.69 (d, *J* = 2.4 Hz, 1H).

^{13}C NMR (100 MHz, DMSO δ): 152.55, 147.82, 145.99, 135.93, 135.17, 132.92, 130.59, 130.47, 130.24, 124.77, 122.14, 112.12, 111.22.

HRMS (ESI-TOF): m/z: [M + H] calculated for $C_{13}H_9Br_2N_3O_5S$ 479.8687; found 479.8680.

4-nitro-N'-(4-nitrobenzylidene)benzenesulfonohydrazide (51)

^{1}H NMR (400 MHz, DMSO δ): 12.32 (s, 1H), 8.46 – 8.41 (m, 2H), 8.23 (d, *J* = 8.6 Hz, 2H), 8.18 – 8.13 (m, 2H), 8.08 (s, 1H), 7.88 – 7.83 (m, 2H).

^{13}C NMR (101 MHz, DMSO δ): 150.07, 148.04, 145.79, 144.04, 139.47, 128.81, 127.95, 124.73, 124.02.

HRMS (ESI-TOF): m/z: [M + H] calculated for $C_{13}H_{10}N_4O_6S$ 351.0399; found 351.0398

N'-(3,5-dichloro-2-hydroxybenzylidene)-2-nitrobenzenesulfonohydrazide (52)

^{1}H NMR (400 MHz, DMSO δ): 12.58 (s, 1H), 10.66 (s, 1H), 8.29 (s, 1H), 8.05 (ddd, *J* = 9.3, 4.7, 2.2 Hz, 2H), 7.97 – 7.86 (m, 2H), 7.55 (dd, *J* = 29.4, 2.5 Hz, 2H).

^{13}C NMR (100 MHz, DMSO δ): 151.09, 147.80, 145.12, 135.11, 132.85, 130.58, 130.49, 130.33, 126.14, 124.70, 123.63, 122.29, 122.21.

HRMS (ESI-TOF): m/z: [M + H] calculated for $C_{13}H_9Cl_2N_3O_5S$ 389.9718; found 389.9718.

***4-bromo-N'-(2-hydroxy-5-iodobenzylidene)benzenesulfonohydrazide (53*)**

^{1}H NMR (400 MHz, DMSO δ): 11.72 (s, 1H), 10.42 (s, 1H), 8.10 (s, 1H), 7.85 (d, *J* = 8.4 Hz, 2H), 7.77 (d, *J* = 8.6 Hz, 2H), 7.74 (d, *J* = 2.0 Hz, 1H), 7.51 (dd, *J* = 8.6, 2.2 Hz, 1H), 6.70 (d, *J* = 8.6 Hz, 1H).

^{13}C NMR (100 MHz, DMSO δ): 156.17, 143.75, 139.58, 138.06, 134.27, 132.52, 129.09, 127.18, 122.04, 118.90, 81.59.

HRMS (ESI-TOF): m/z: [M + H] calculated for $C_{13}H_{10}BrIN_2O_3S$ 480.8718; found 480.8718.

4-bromo-N'-(2-hydroxy-5-nitrobenzylidene)benzenesulfonohydrazide (54)

^{1}H NMR (400 MHz, DMSO δ) 11.80 (d, *J* = 73.7 Hz, 2H), 8.33 (d, *J* = 2.9 Hz, 1H), 8.21 (s, 1H), 8.13 (dd, *J* = 9.0, 2.9 Hz, 1H), 7.89 – 7.75 (m, 4H), 7.04 (d, *J* = 9.1 Hz, 1H).

^{13}C NMR (100 MHz, DMSO δ): 161.83, 142.45, 139.94, 138.06, 132.57, 129.09, 127.24, 126.83, 121.77, 120.21, 116.87.

HRMS (ESI-TOF): m/z: [M + H] calculated for $C_{13}H_{10}BrN_3O_5S$ 399.9603; found 399.9600

N'-((6-bromo-1H-indol-3-yl)methylene)-4-methoxybenzenesulfonohydrazide (55)

^{1}H NMR (400 MHz, DMSO δ): 11.60 (s, 1H), 10.85 (s, 1H), 8.05 (d, *J* = 2.0 Hz, 1H), 7.87 (ddd, *J* = 24.4, 8.7, 2.0 Hz, 3H), 7.74 (d, *J* = 2.3 Hz, 1H), 7.59 (s, 1H), 7.31 – 7.26 (m, 1H), 7.12 (dd, *J* = 6.9, 5.0 Hz, 2H), 3.79 (s, 3H).

^{13}C NMR (100 MHz, DMSO δ): 162.49, 144.27, 137.77, 131.14, 130.69, 129.52, 123.43, 123.19, 123.02, 115.24, 114.46, 114.24, 111.24, 55.64.

HRMS (ESI-TOF): m/z: [M + H] calculated for $C_{16}H_{14}BrN_3O_3S$ 408.0017; found 408.0030

N'-(2,4-dihydroxybenzylidene)-2-nitrobenzenesulfonohydrazide (56)

^{1}H NMR (400 MHz, DMSO δ): 11.78 (s, 1H), 10.05 (s, 1H), 9.87 (s, 1H), 8.21 (s, 1H), 8.04 – 7.98 (m, 1H), 7.91 – 7.86 (m, 1H), 7.30 – 7.25 (m, 1H), 6.28 – 6.23 (m, 1H).

^{13}C NMR (100 MHz, DMSO δ): 160.95, 158.35, 148.00, 147.56, 134.74, 132.59, 130.85, 130.35, 128.94, 110.68, 107.91, 102.35.

HRMS (ESI-TOF): m/z: [M + H] calculated for $C_{13}H_{11}N_3O_6S$ 338.0447; found 338.0453

N'-(2-hydroxy-5-iodobenzylidene)-4-methoxybenzenesulfonohydrazide (57)

^{1}H NMR (400 MHz, DMSO, δ): 11.49 (s, 1H), 10.43 (s, 1H), 8.07 (s, 1H), 7.79 – 7.75 (m, 2H), 7.73 (d, *J* = 2.3 Hz, 1H), 7.50 (dd, *J* = 8.6, 2.3 Hz, 1H), 7.16 – 7.11 (m, 2H), 6.69 (d, *J* = 8.6 Hz, 1H), 3.82 (s, 3H).

^{13}C NMR (101 MHz, DMSO δ): 162.73, 156.12, 143.43, 139.37, 134.59, 130.30, 129.31, 122.09, 118.88, 114.53, 81.53, 55.70

HRMS (ESI-TOF): m/z: [M + H] calculated for $C_{14}H_{13}IN_2O_4S$ 432.9719; found 432.9724.

4-fluoro-N'-(2-hydroxy-5-iodobenzylidene)benzenesulfonohydrazide (58)

^{1}H NMR (400 MHz, CD_3CN δ): 10.30 (s, 1H), 9.80 (s, 1H), 7.98 – 7.91 (m, 3H), 7.65 – 7.51 (m, 2H), 7.41 – 7.22 (m, 2H), 6.71 (d, *J* = 8.7 Hz, 1H).

^{13}C NMR (100 MHz, CD_3CN δ): 158.49, 156.36, 150.83, 141.20, 140.07, 135.20, 131.70, 131.64, 131.57, 120.95, 120.11, 120.07, 117.76, 117.51, 117.50, 80.96.

HRMS (ESI-TOF): m/z: [M + H] calculated for $C_{13}H_{10}FIN_2O_3S$ 420.9519; found 420.9521

N'-(4-bromobenzylidene)-4-fluorobenzenesulfonohydrazide (59)

^{1}H NMR (400 MHz, DMSO δ): 11.65 (s, 1H), 7.93 (ddd, *J* = 8.4, 5.2, 2.7 Hz, 3H), 7.64 – 7.56 (m, 2H), 7.55 – 7.49 (m, 2H), 7.49 – 7.41 (m, 2H).

^{13}C NMR (100 MHz, DMSO) δ 165.74, 163.24, 146.30, 135.26, 135.23, 133.40, 132.80, 132.08, 131.81, 130.32, 130.22, 128.68, 123.45, 116.62, 116.40.

HRMS (ESI-TOF): m/z: [M + H] calculated for $C_{13}H_{10}BrFN_2O_2S$ 356.9708; found 356.9708.

N'-(3, 4-dihydroxybenzylidene)-4-nitrobenzenesulfonohydrazide (60)

^{1}H NMR (400 MHz, DMSO δ): 11.52 (s, 1H), 9.42 (s, 1H), 9.19 (s, 1H), 8.50 – 8.38 (m, 2H), 8.17 – 8.04 (m, 2H), 7.77 (s, 1H), 7.02 (d, *J* = 1.9 Hz, 1H), 6.89 – 6.64 (m, 2H).

^{13}C NMR (10 MHz, DMSO δ): 150.00, 149.15, 148.24, 145.69, 144.51, 128.82, 124.83, 124.60, 120.52, 115.53, 112.65.

HRMS (ESI-TOF): m/z: [M + H] calculated for $C_{13}H_{11}N_3O_6S$ 338.0447; found 338.0454.

N'-((1H-indol-3-yl)methylene)-4-methoxybenzenesulfonohydrazide (61)

^{1}H NMR (400 MHz, DMSO δ): 11.49 (s, 1H), 10.76 (s, 1H), 8.08 (s, 1H), 7.97 (d, *J* = 7.6 Hz, 1H), 7.85 (d, *J* = 9.0 Hz, 2H), 7.70 (d, *J* = 2.8 Hz, 1H), 7.39 (d, *J* = 7.8 Hz, 1H), 7.13 (ddd, *J* = 10.3, 9.0, 4.5 Hz, 4H), 3.79 (s, 3H).

^{13}C NMR (100 MHz, DMSO δ): 162.44, 144.93, 136.90, 130.84, 130.35, 129.49, 124.01, 122.56, 121.59, 120.49, 114.19, 111.79, 111.11, 55.62.

HRMS (ESI-TOF): m/z: [M + H] calculated for $C_{16}H_{15}N_3O_3S$ 330.0912; found 330.0911.

N'-(5-fluoro-2-hydroxybenzylidene)-2-nitrobenzenesulfonohydrazide (62)

^{1}H NMR (400 MHz, DMSO δ): 12.27 – 12.02 (m, 1H), 10.11 (s, 1H), 8.29 (d, *J* = 1.5 Hz, 1H), 8.14 – 7.97 (m, 2H), 7.95 – 7.83 (m, 2H), 7.23 (dd, *J* = 9.4, 3.2 Hz, 1H), 7.08 (td, *J* = 8.6, 3.2 Hz, 1H), 6.86 (dd, *J* = 9.0, 4.7 Hz, 1H).

^{13}C NMR (100 MHz, DMSO δ): 156.57, 154.23, 152.83, 147.88, 143.92, 134.91, 132.66, 130.71, 130.56, 124.53, 120.34, 120.26, 118.47, 118.24, 117.64, 117.55, 111.44, 111.20.

HRMS (ESI-TOF): m/z: [M + H] calculated for $C_{13}H_{10}FN_3O_5S$ 340.0403; found 340.0410

N'-(3,5-dibromo-2-hydroxybenzylidene)-4-fluorobenzenesulfonohydrazide (63)

^{1}H NMR (400 MHz, DMSO δ): 12.15 (s, 1H), 11.01 (s, 1H), 8.14 (s, 1H), 7.93 (dd, *J* = 8.8, 5.1 Hz, 2H), 7.79 (s, 1H), 7.67 (d, *J* = 2.1 Hz, 1H), 7.50 (t, *J* = 8.8 Hz, 2H).

^{13}C NMR (100 MHz, DMSO δ): 165.98, 163.47, 152.65, 146.49, 135.84, 134.70, 134.68, 130.87, 130.24, 130.14, 121.66, 116.99, 116.76, 111.80, 111.08.

HRMS (ESI-TOF): m/z: [M + H] calculated for $C_{13}H_9Br_2FN_2O_3S$ 450.8763; found 450.8761

N'-(2,3-difluorobenzylidene)-4-methoxybenzenesulfonohydrazide (64)

^{1}H NMR (400 MHz, DMSO δ): 11.70 (s, 1H), 8.06 (s, 1H), 7.81 (d, *J* = 8.6 Hz, 2H), 7.52 – 7.40 (m, 2H), 7.23 (dd, *J* = 13.0, 6.8 Hz, 1H), 7.13 (d, *J* = 8.8 Hz, 2H), 3.82 (s, 3H).

^{13}C NMR (100 MHz, DMSO δ): 162.80, 151.20, 151.08, 149.59, 149.45, 148.76, 148.64, 147.08, 146.94, 138.51, 130.38, 129.46, 125.30, 125.25, 125.23, 125.18, 123.62, 123.55, 121.52, 121.50, 118.67, 118.51, 114.55, 55.74.

HRMS (ESI-TOF): m/z: [M + H] calculated for $C_{14}H_{12}F_2N_2O_3S$ 327.0615; found 327.0620

N'-(2,4-dihydroxybenzylidene)-5-(dimethylamino)naphthalene-1-sulfonohydrazide (65)

^{1}H NMR (400 MHz, DMSO δ): 11.66 (s, 1H), 10.08 (t, *J* = 1.5 Hz, 1H), 9.82 (s, 1H), 8.49 (d, *J* = 8.5 Hz, 1H), 8.39 (d, *J* = 8.7 Hz, 1H), 8.26 – 8.17 (m, 1H), 8.04 (s, 1H), 7.71 – 7.58 (m, 2H), 7.25 (d, *J* = 7.5 Hz, 1H), 7.17 (d, *J* = 8.4 Hz, 1H), 6.25 – 6.17 (m, 2H), 2.80 (s, 6H).

^{13}C NMR (100 MHz, DMSO δ): 160.57, 158.18, 151.40, 146.28, 134.53, 130.25, 129.81, 129.23, 129.18, 129.01, 128.10, 123.71, 119.00, 115.31, 110.66, 107.76, 102.34, 45.07.

HRMS (ESI-TOF): m/z: [M + H] calculated for $C_{19}H_{19}N_3O_4S$ 386.1174; found 386.1169

4-bromo-N'-(4-nitrobenzylidene)benzenesulfonohydrazide (66)

^{1}H NMR (400 MHz, CD_3CN, δ): 9.53 (s, 1H), 9.53 (s, 1H), 9.53 (s, 1H), 8.20 (d, *J* = 8.8 Hz, 2H), 7.93 (s, 1H), 7.86 – 7.82 (m, 2H), 7.80 – 7.72 (m, 4H).

^{13}C NMR (101 MHz, CD_3CN, δ): 149.69, 146.70, 140.56, 138.74, 133.44, 130.46, 128.81, 124.94.

HRMS (ESI-TOF): m/z: [M + H] calculated for $C_{13}H_{10}BrN_3O_4S$ 383.9653; found 383.9656

4.5 Conclusion

In conclusion, we synthesised a library comprising of 66 small molecules based on sulfonohydrazide hydrazone through short and concise synthetic steps. Upon screening, we identified four molecules as potential ER stress inducers. Further studies with the dansyl based sulfonohydrazide hydrazone (compound 1) revealed its accumulation in ER within 3 h in HeLa cervical cancer cells. The identified small molecule efficiently induced ER stress mediated apoptosis and autophagy in HeLa cells. It also induced ER stress associated apoptosis in lung,

breast and drug resistant breast cancer cell lines. Finally, the treatment in combination with autophagy inhibitor, chloroquine remarkably improved the cell killing efficacy of the small molecule in the cancer cell lines. We envision that these small molecules can be employed in understanding the ER biology and functions in cancer and pave way for development of novel ER stress inducers thereby improving the cancer therapeutics.

4.6 Appendix-C

Characterization of Compounds

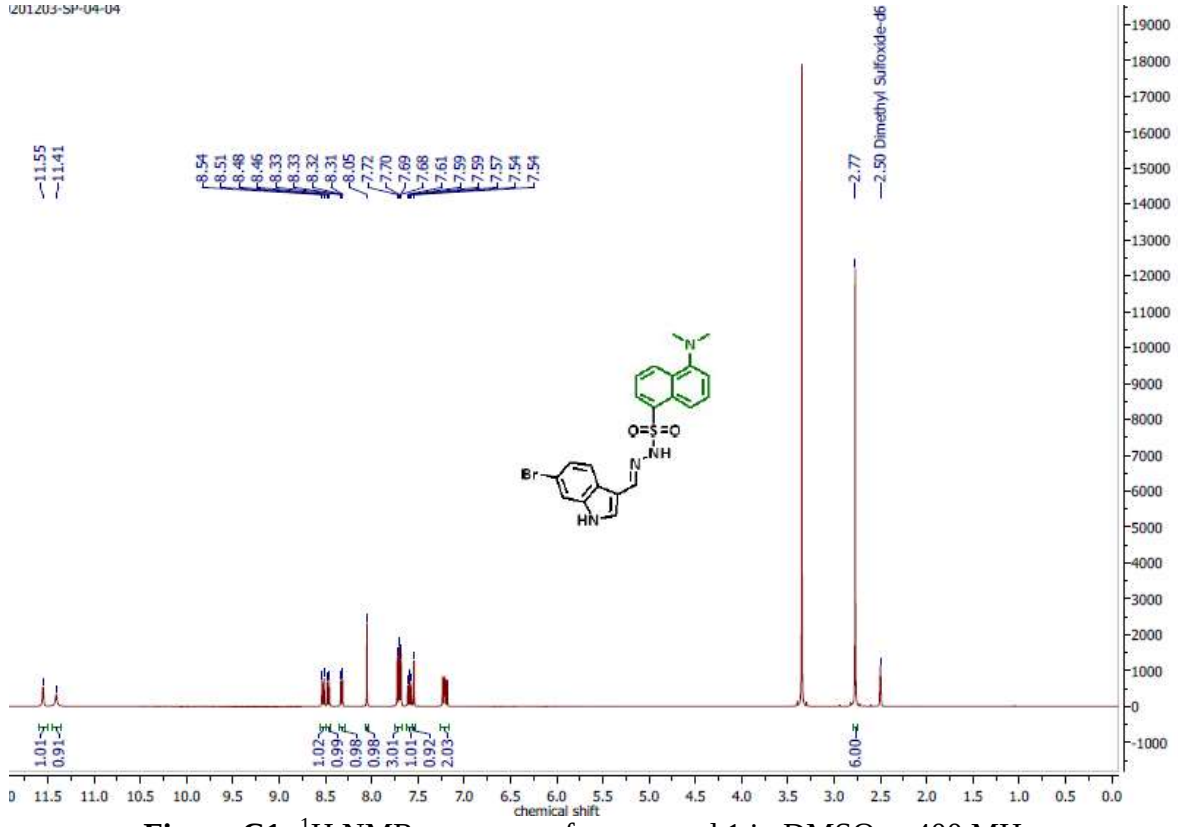

Figure C1: ^{1}H NMR spectrum of compound 1 in DMSO at 400 MHz.

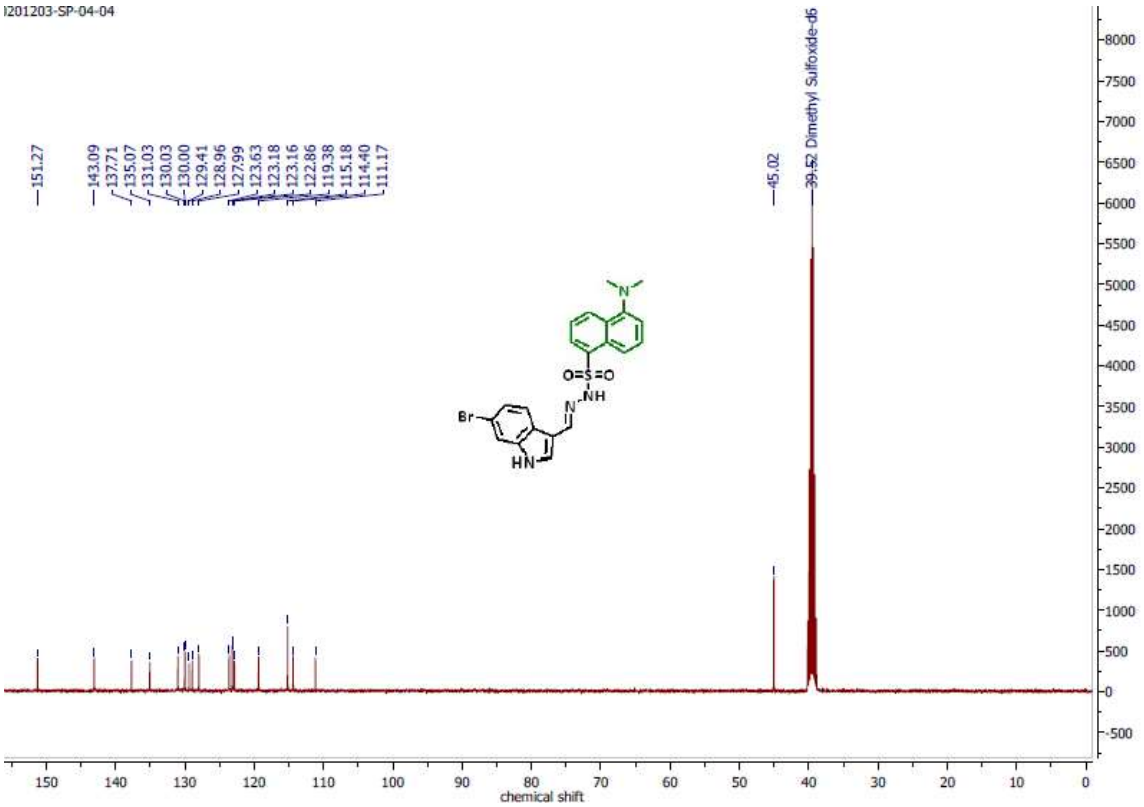

Figure C2: ^{13}CNMR spectrum of compound 1 in DMSO at 100 MHz.

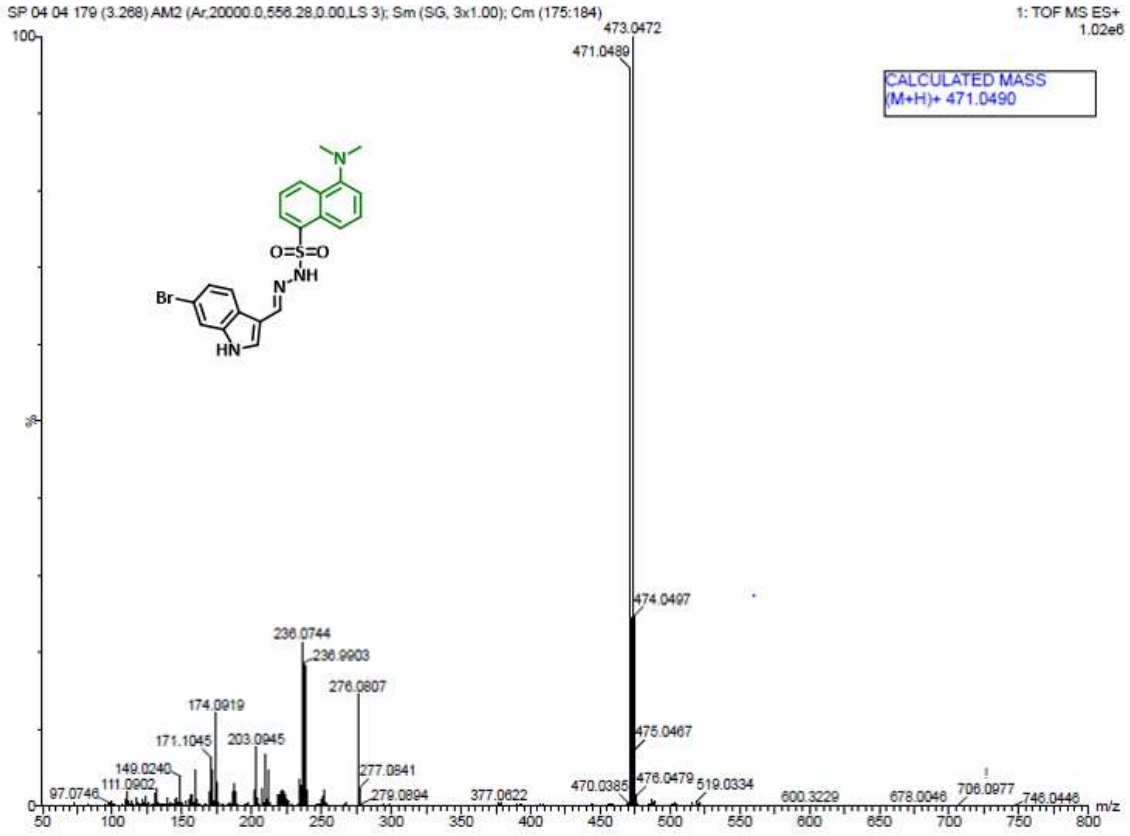

Figure C3: HRMS spectrum of compound 1

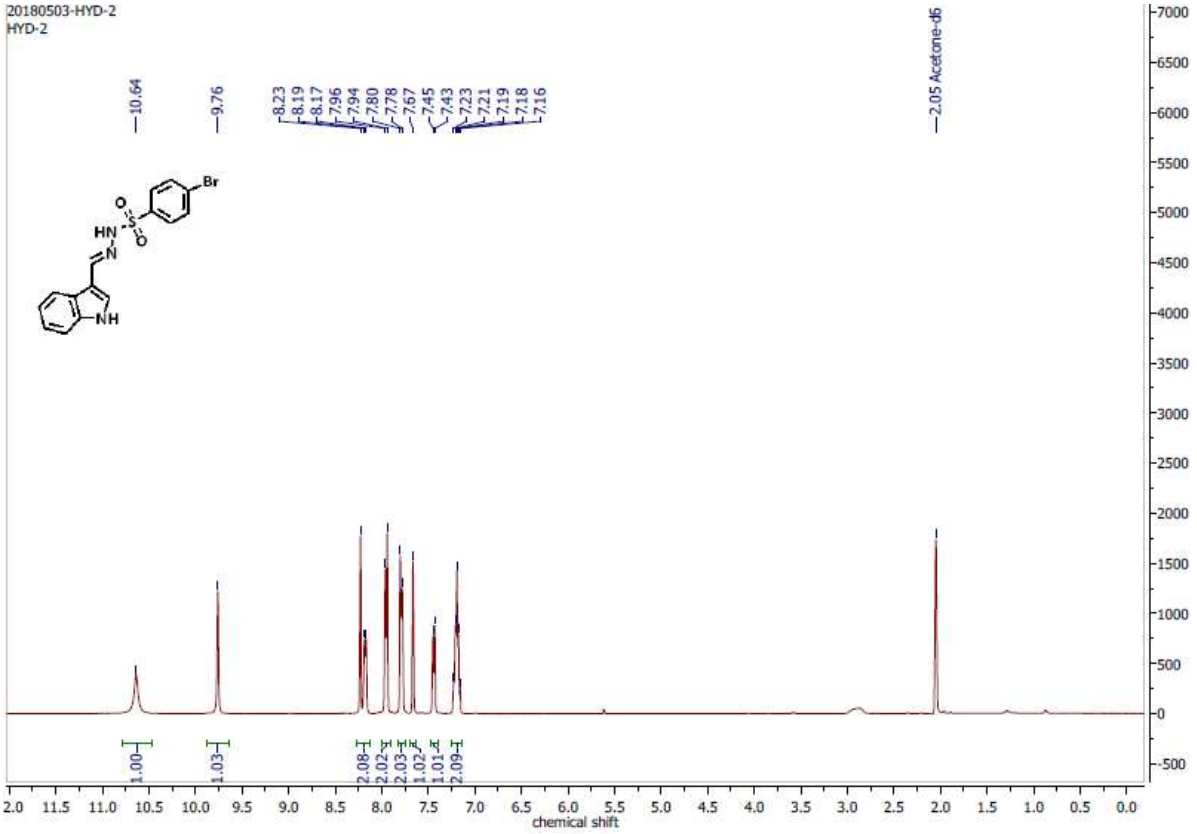

Figure C4: ^{1}H NMR spectrum of compound 2 in Acetone at 400 MHz.

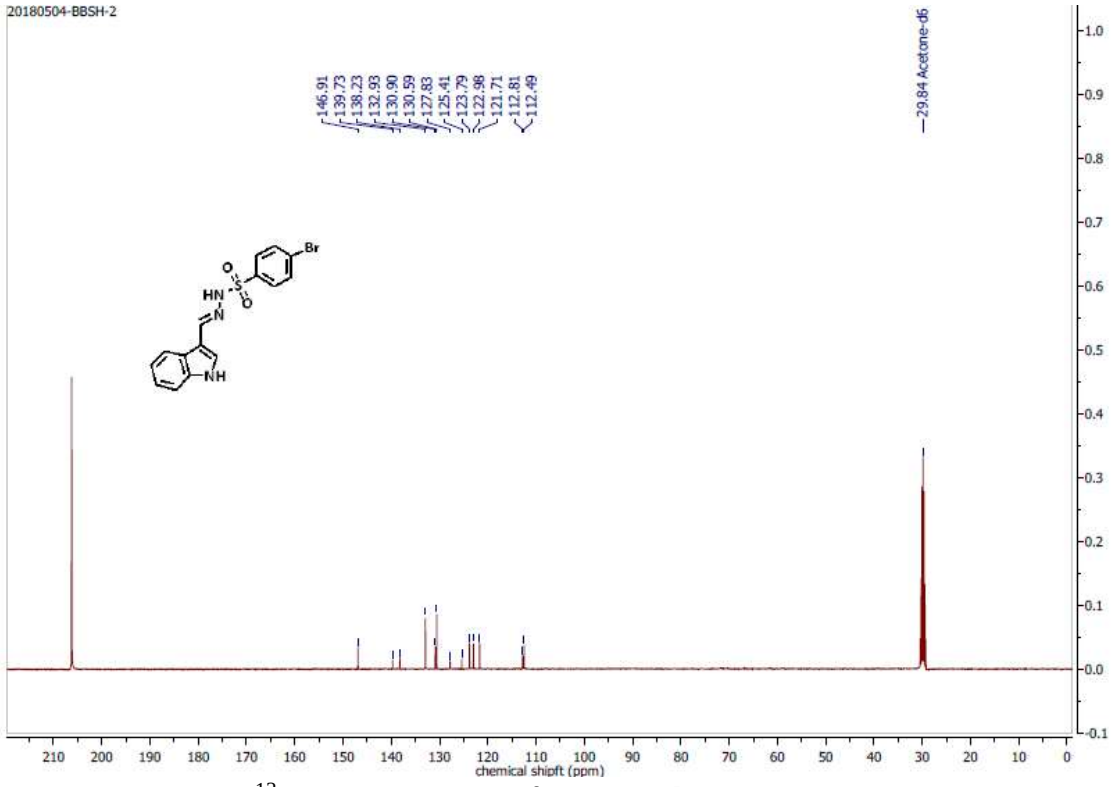

Figure C5: ^{13}C NMR spectrum of compound 2 in Acetone at 100 MHz.

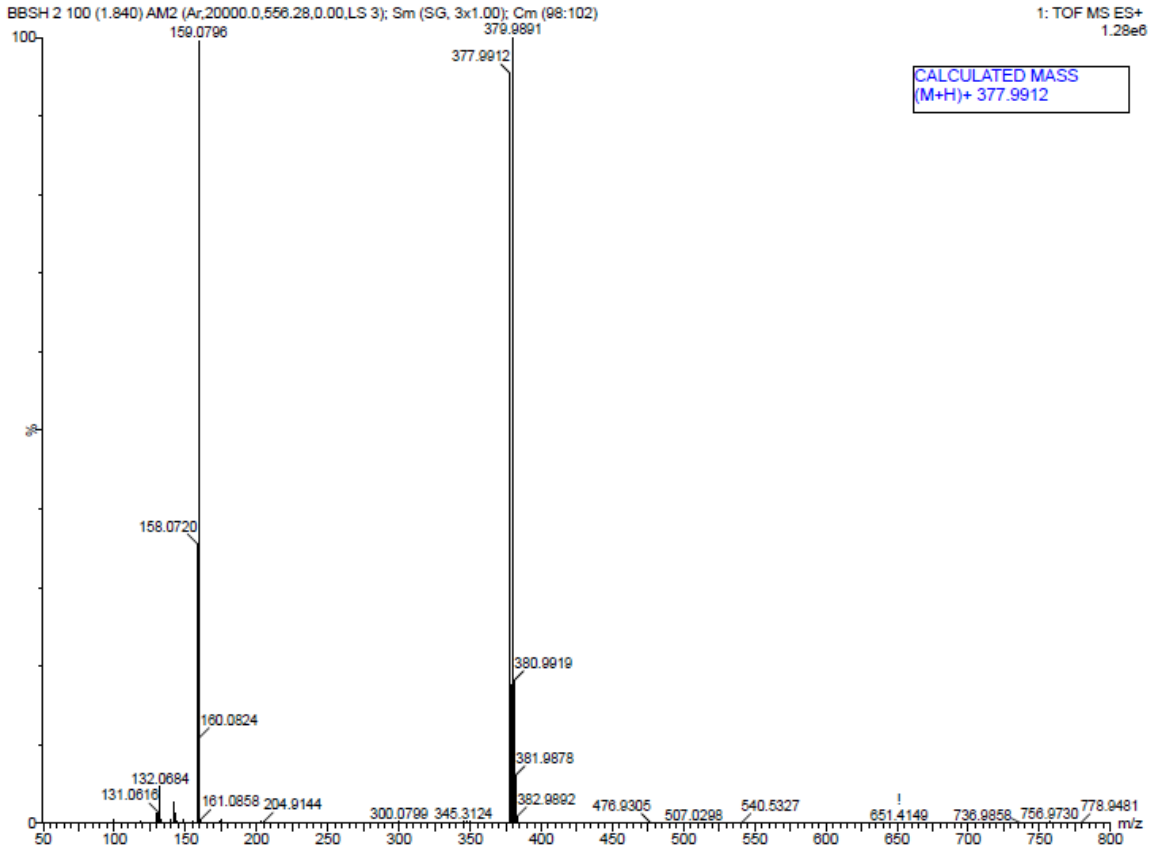

Figure A6: HRMS spectrum of compound 2.

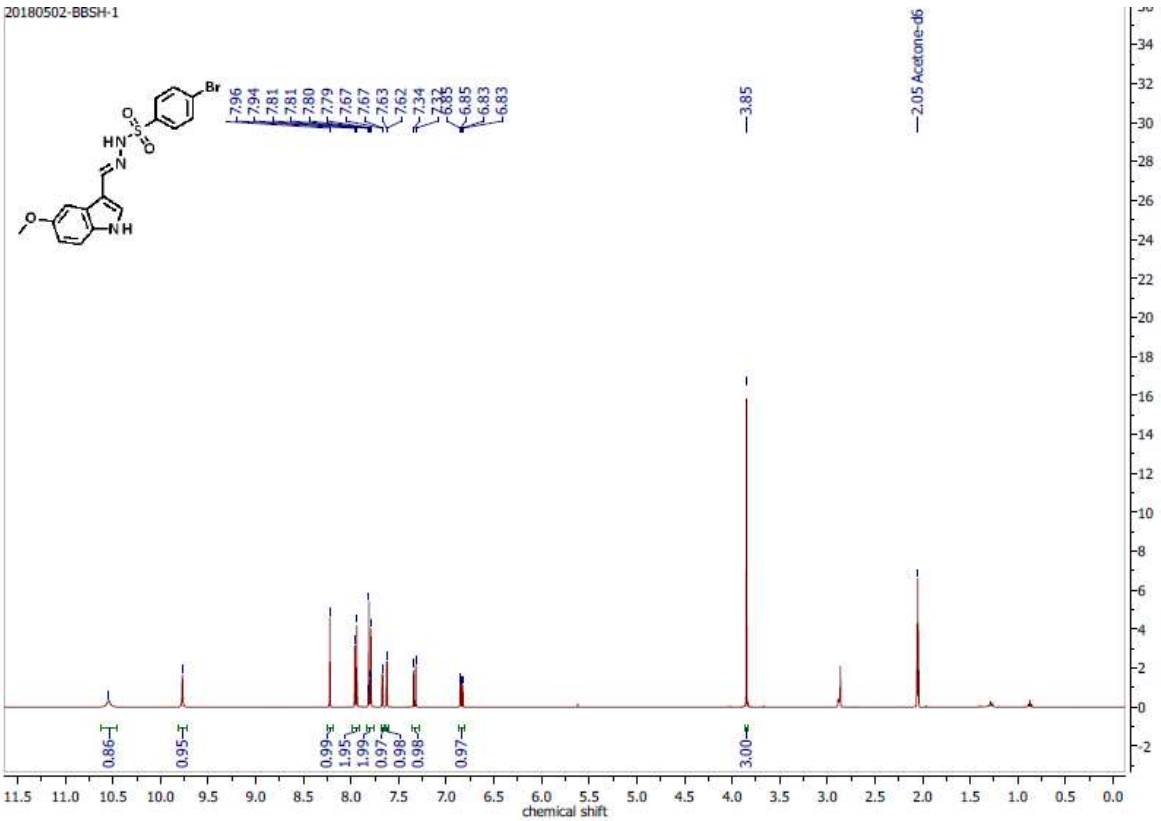

Figure C7: ^{1}H NMR spectrum of compound 3 in Acetone at 400 MHz.

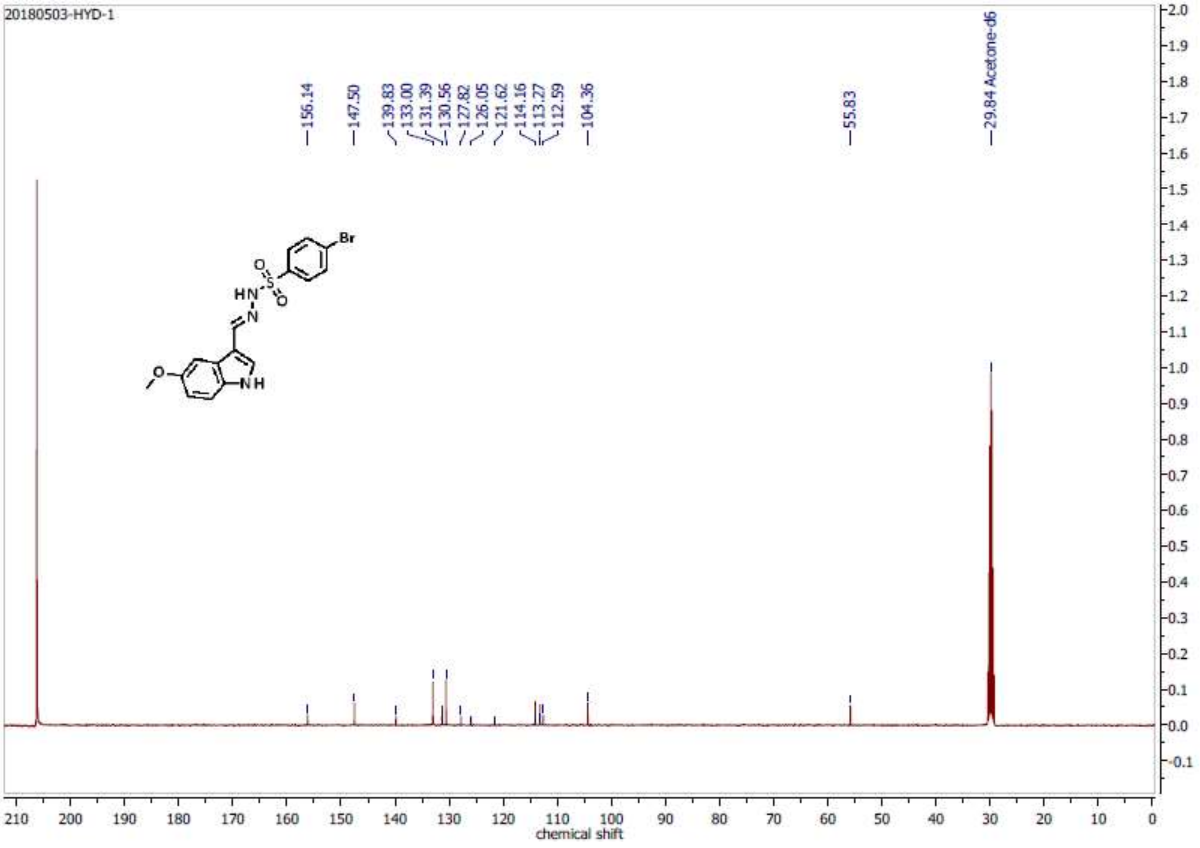

Figure C8: ^{13}C NMR spectrum of compound 3 in Acetone at 100 MHz.

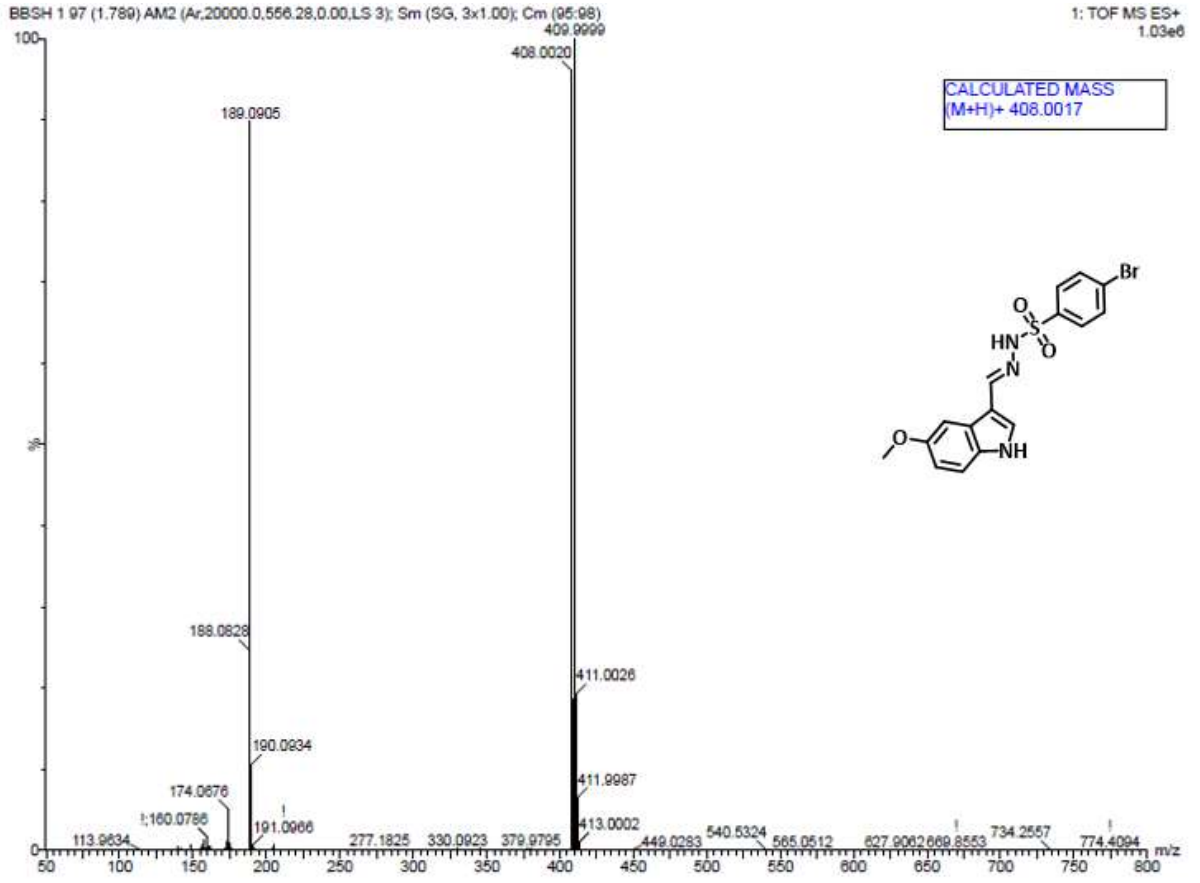

Figure C9: HRMS spectrum of compound 3.

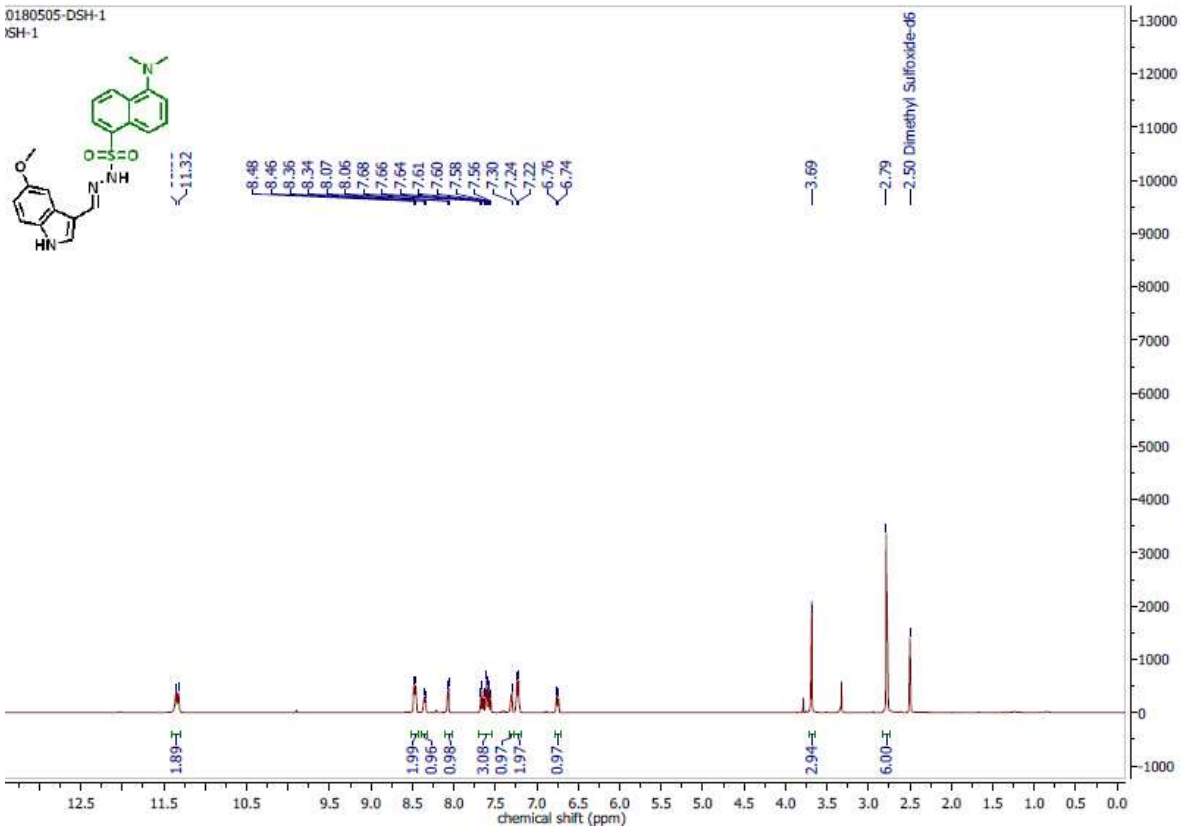

Figure C10: ^{1}H NMR spectrum of compound 4 in DMSO at 400 MHz.

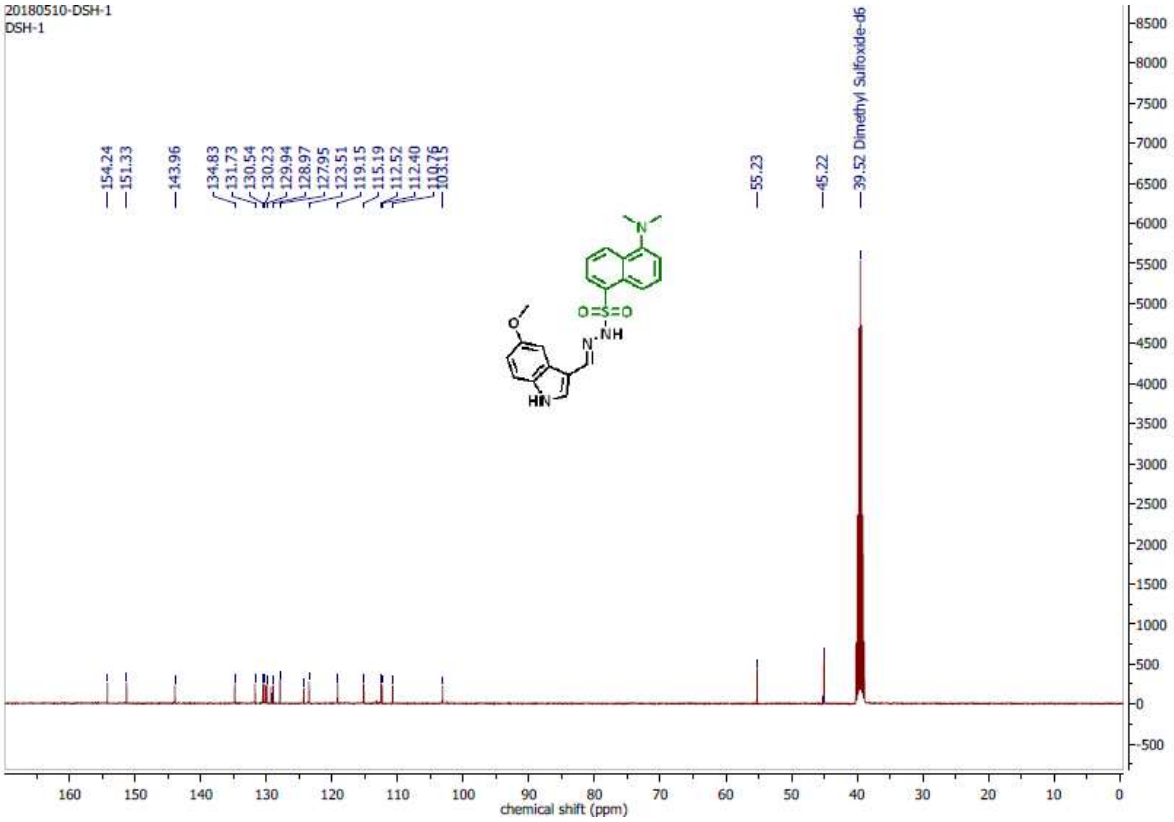

Figure C11: ^{13}C NMR spectrum of compound 4 in DMSO at 100 MHz.

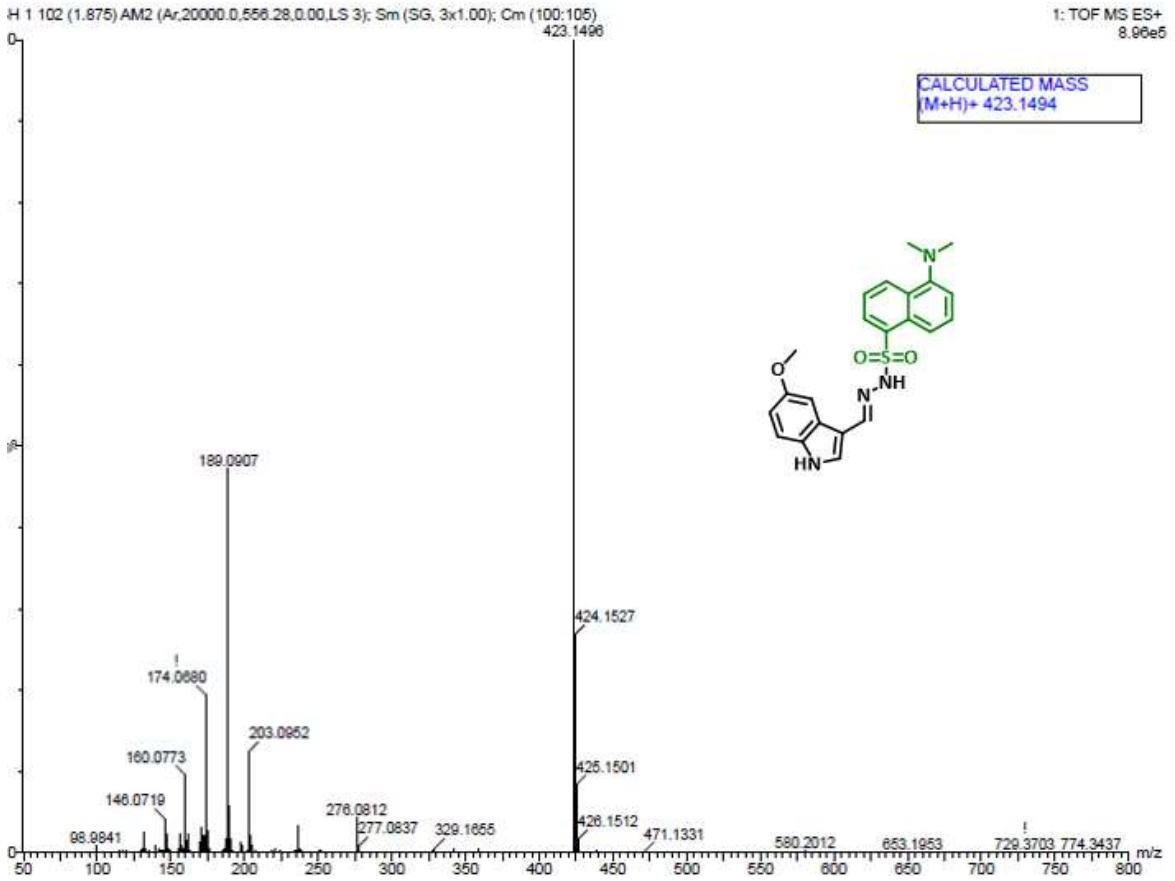

Figure C12: HRMS spectrum of compound 4.

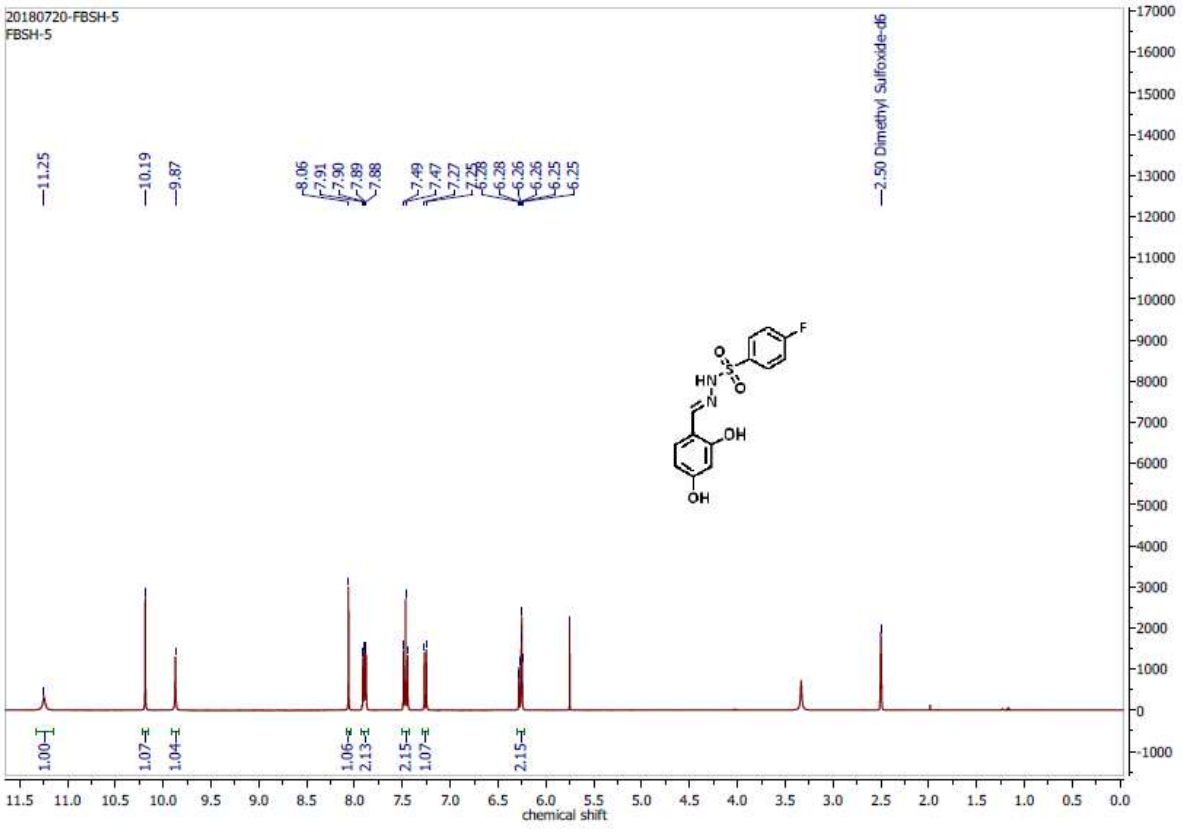

Figure C13: ^{1}H NMR spectrum of compound 5 in DMSO at 400 MHz.

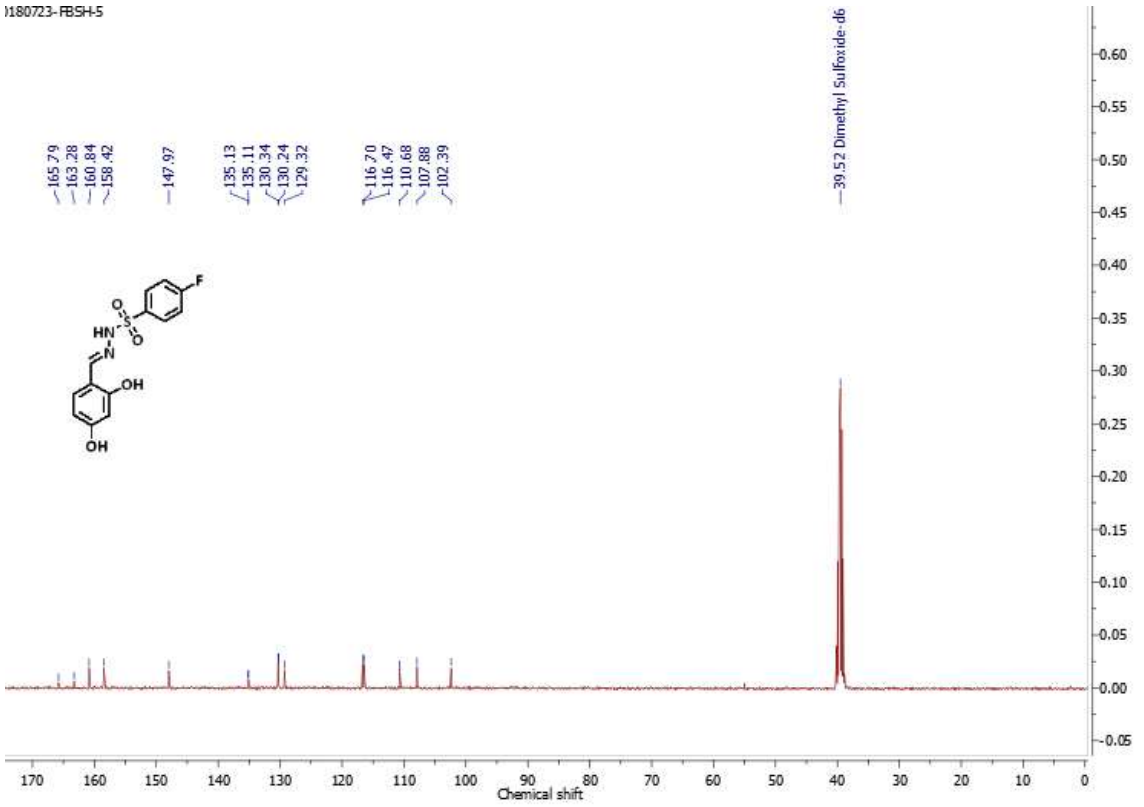

Figure C14: ^{13}C NMR spectrum of compound 5 in DMSO at 100 MHz.

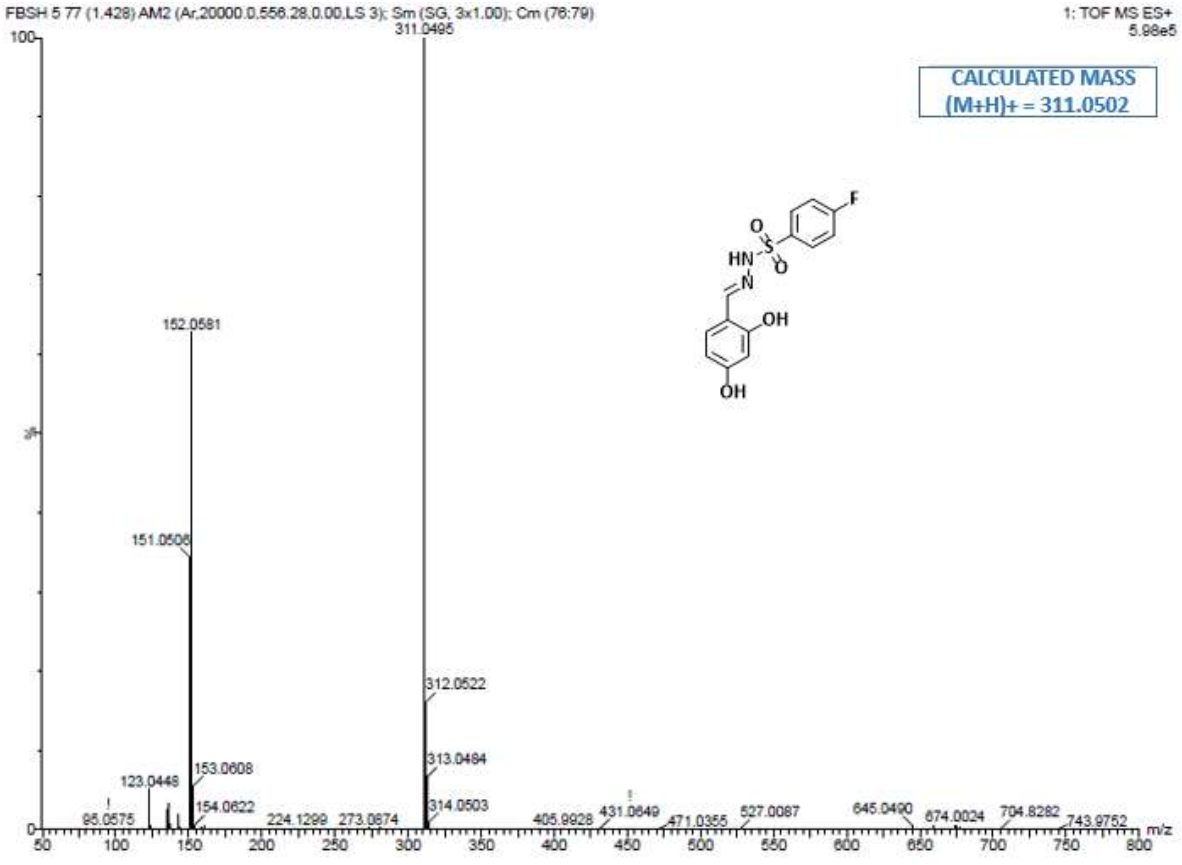

Figure C15: HRMS spectrum of compound 5.

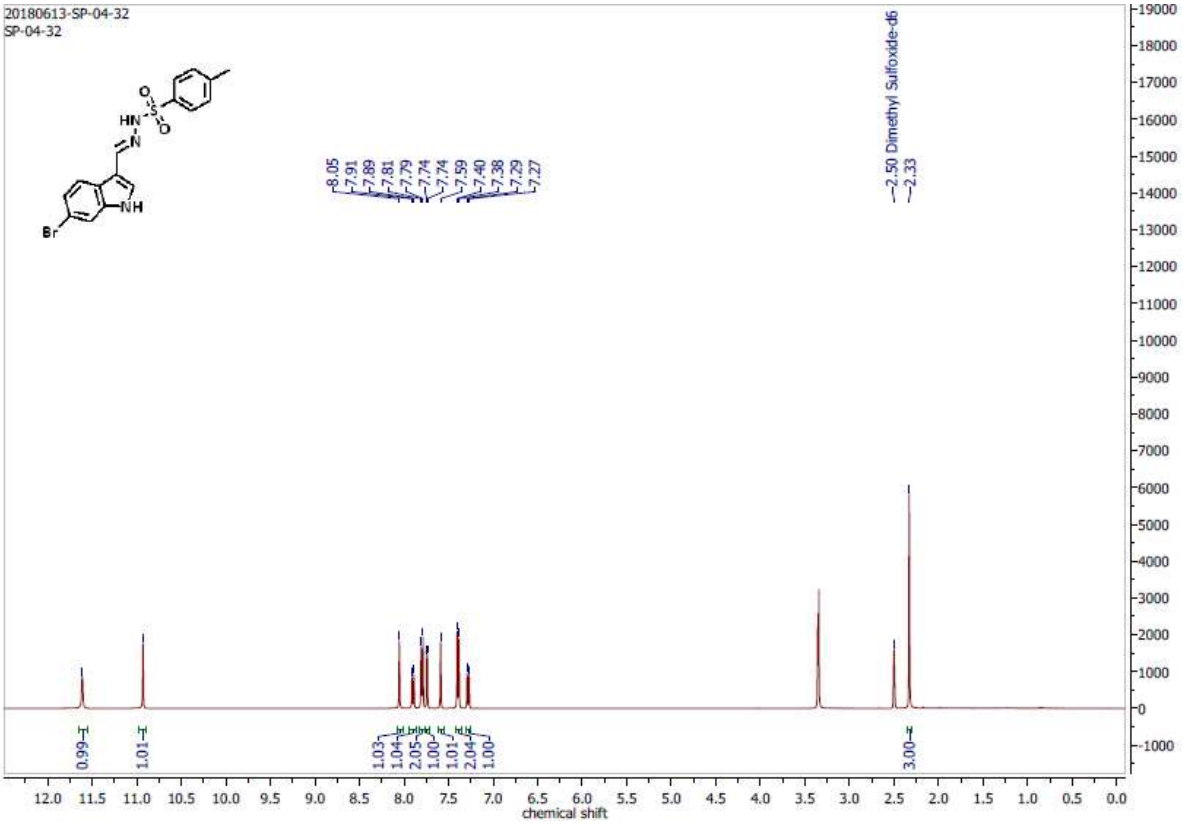

Figure C16: ^{1}H NMR spectrum of compound 6 in DMSO at 400 MHz.

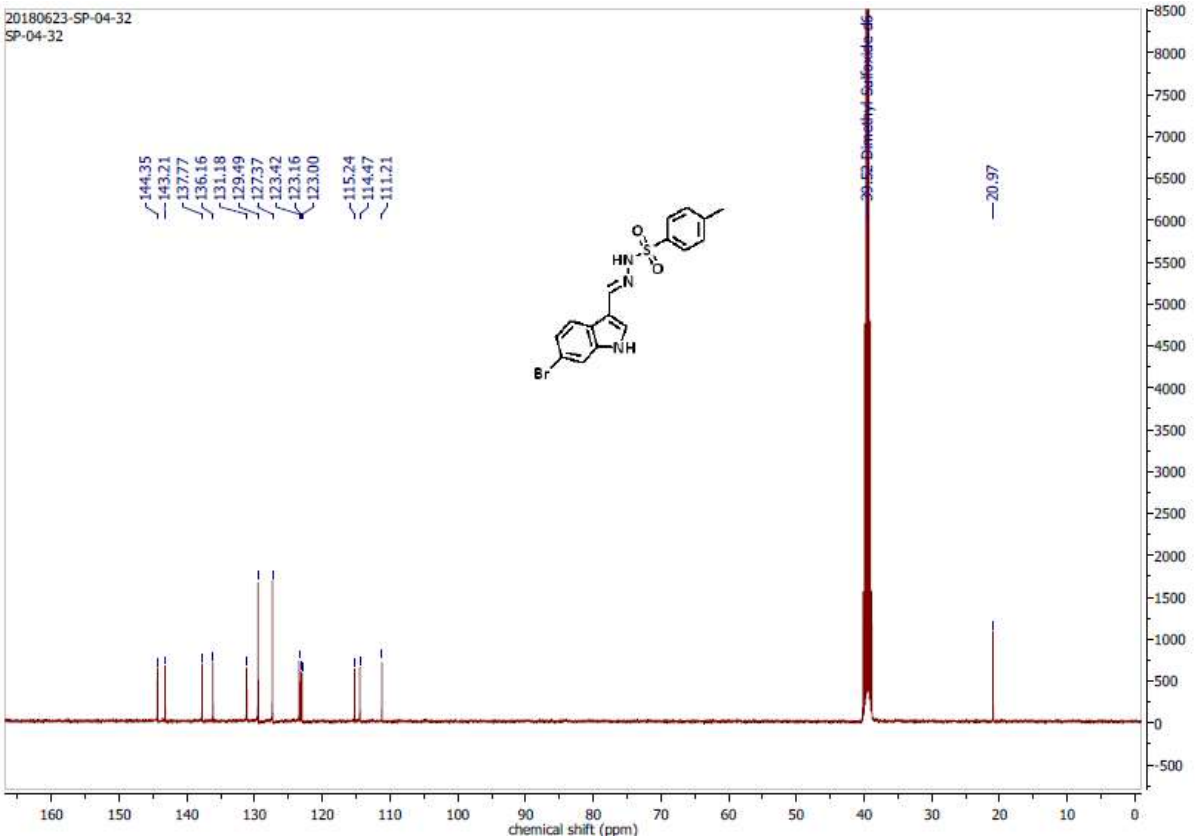

Figure C17: ^{13}C NMR spectrum of compound 6 in DMSO at 100 MHz.

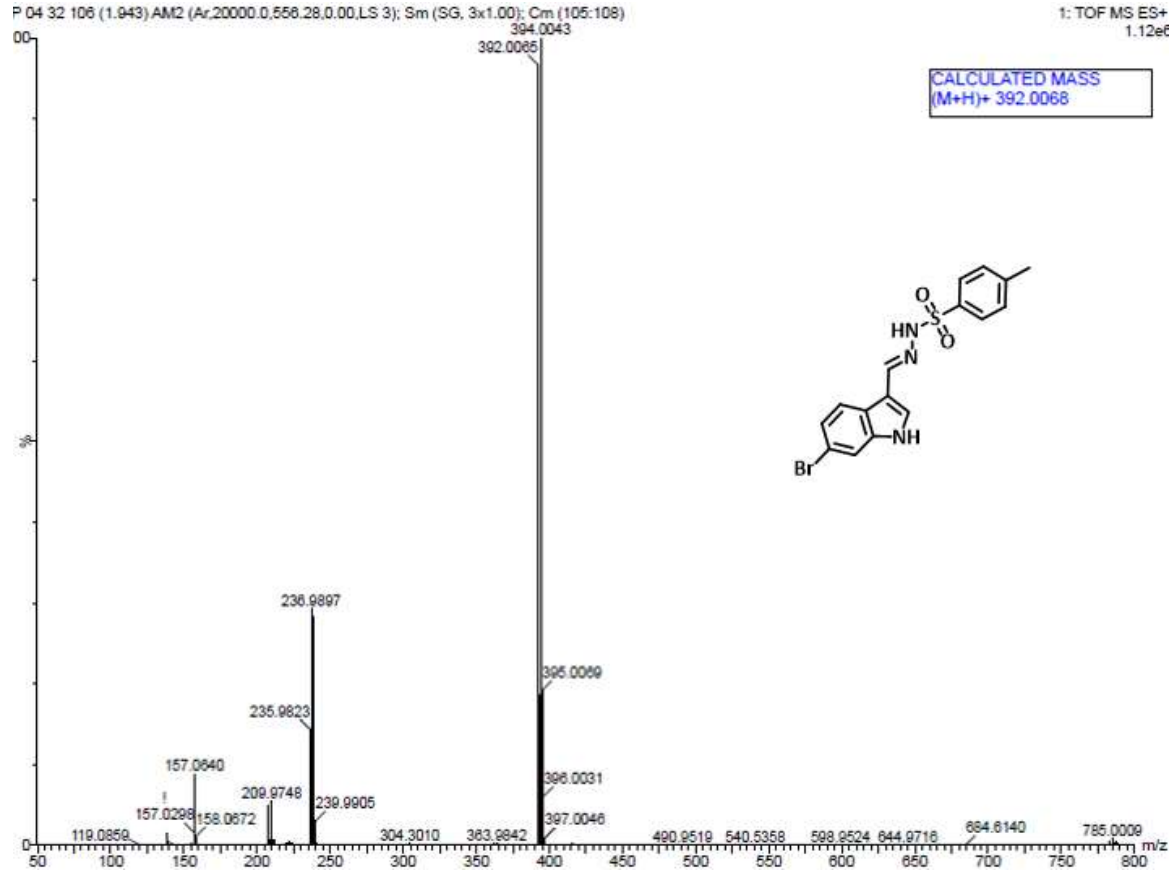

Figure C18: HRMS spectrum of compound 6.

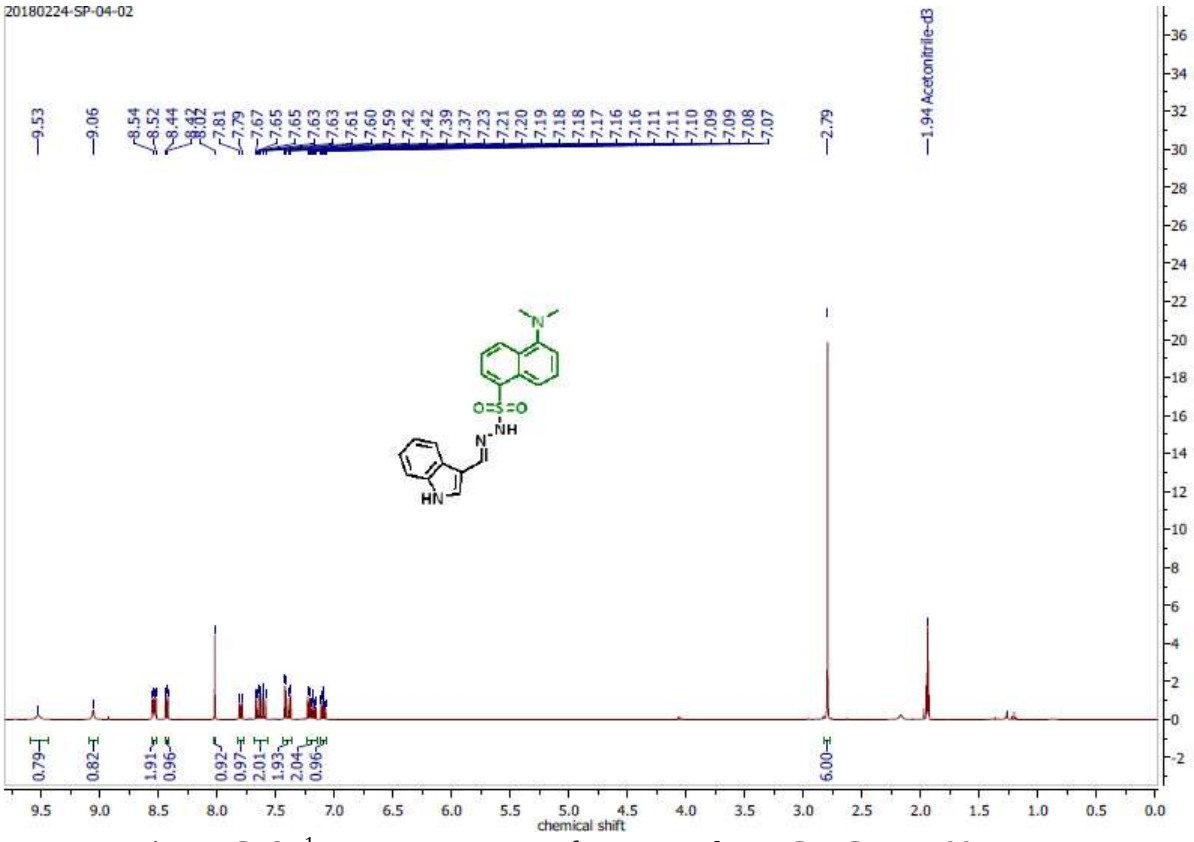

Figure C19: ^{1}H NMR spectrum of compound 7 in CD_3CN at 400 MHz.

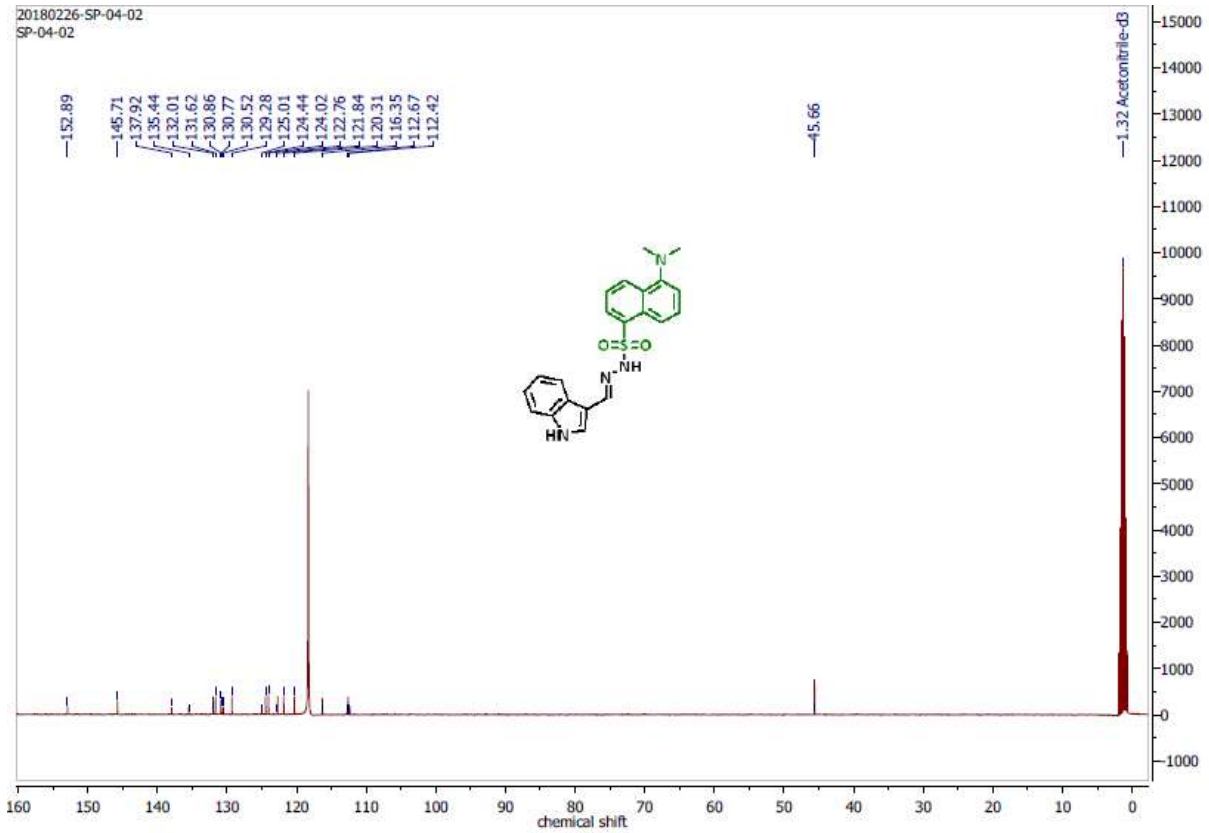

Figure C20: ^{13}C NMR spectrum of compound 7 in CD_3CN at 100 MHz.

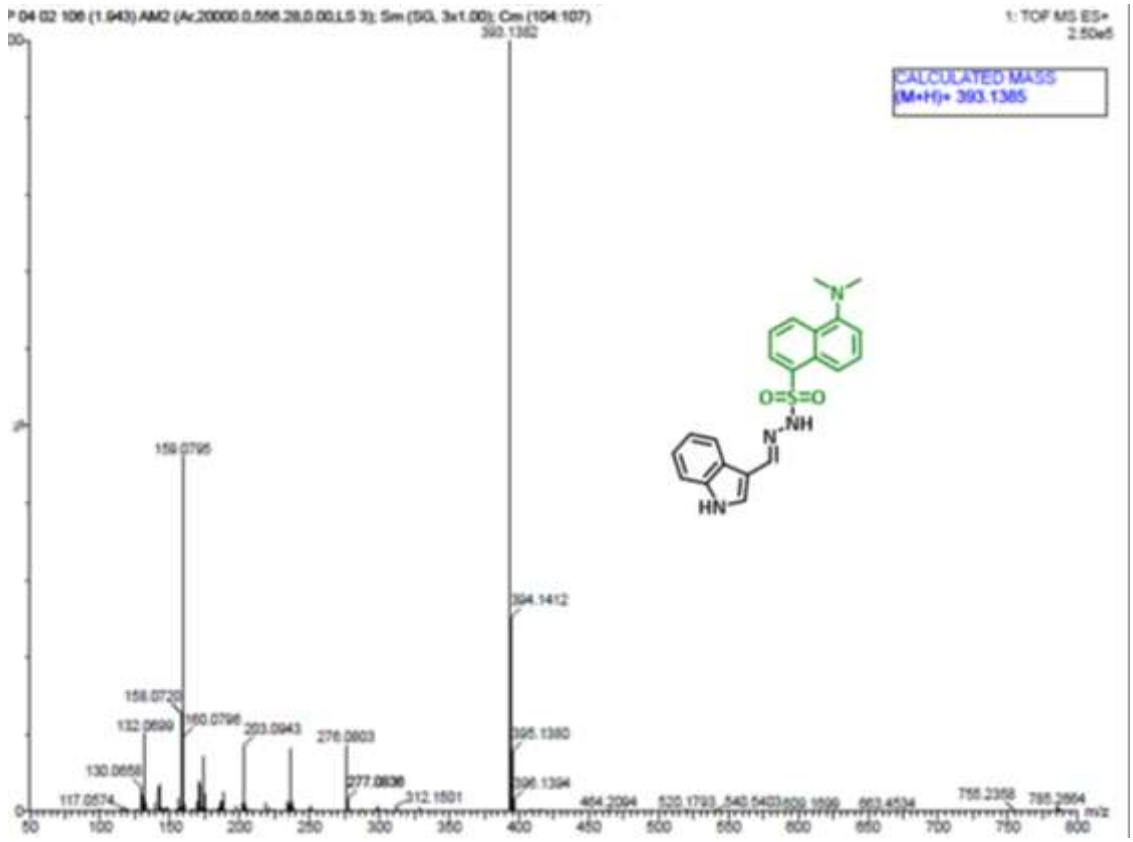

Figure C21: HRMS spectrum of compound 7.

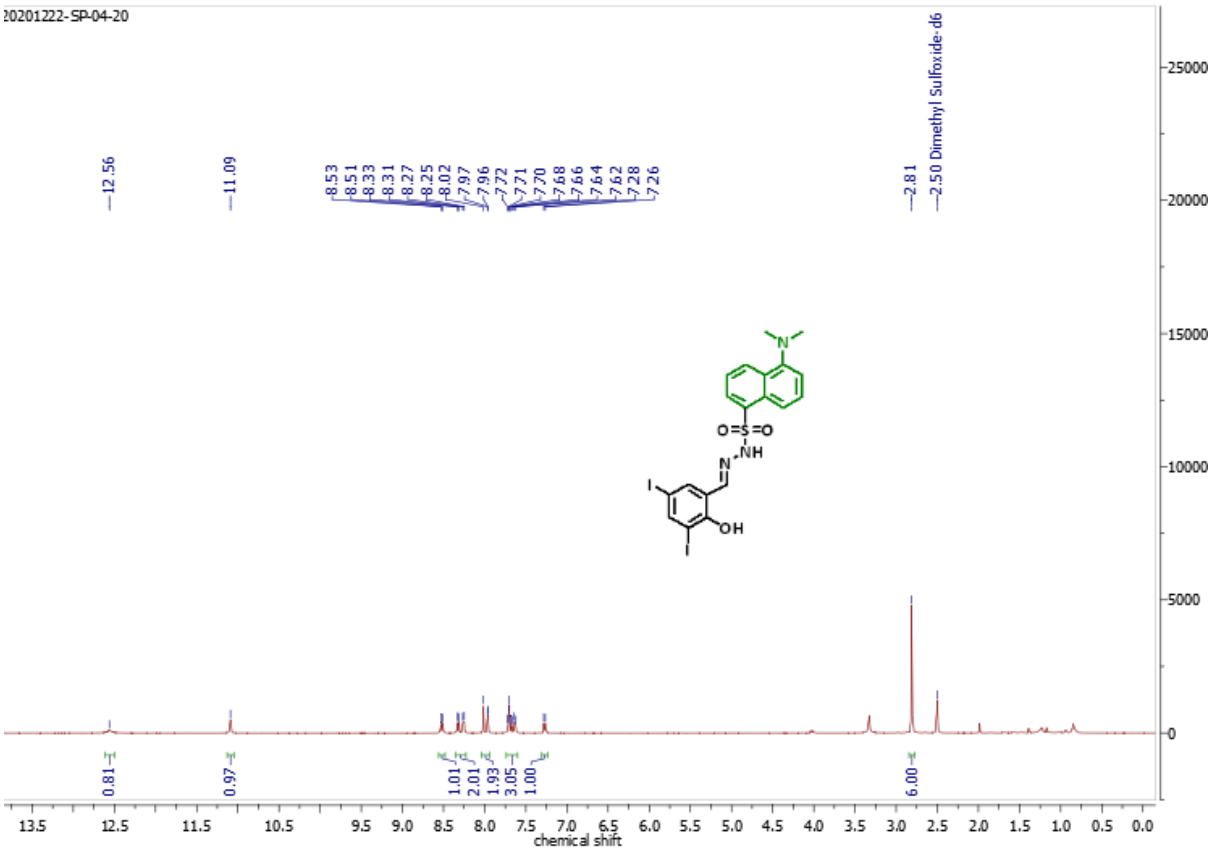

Figure C22: ^{1}H NMR spectrum of compound 8 in DMSO at 400 MHz.

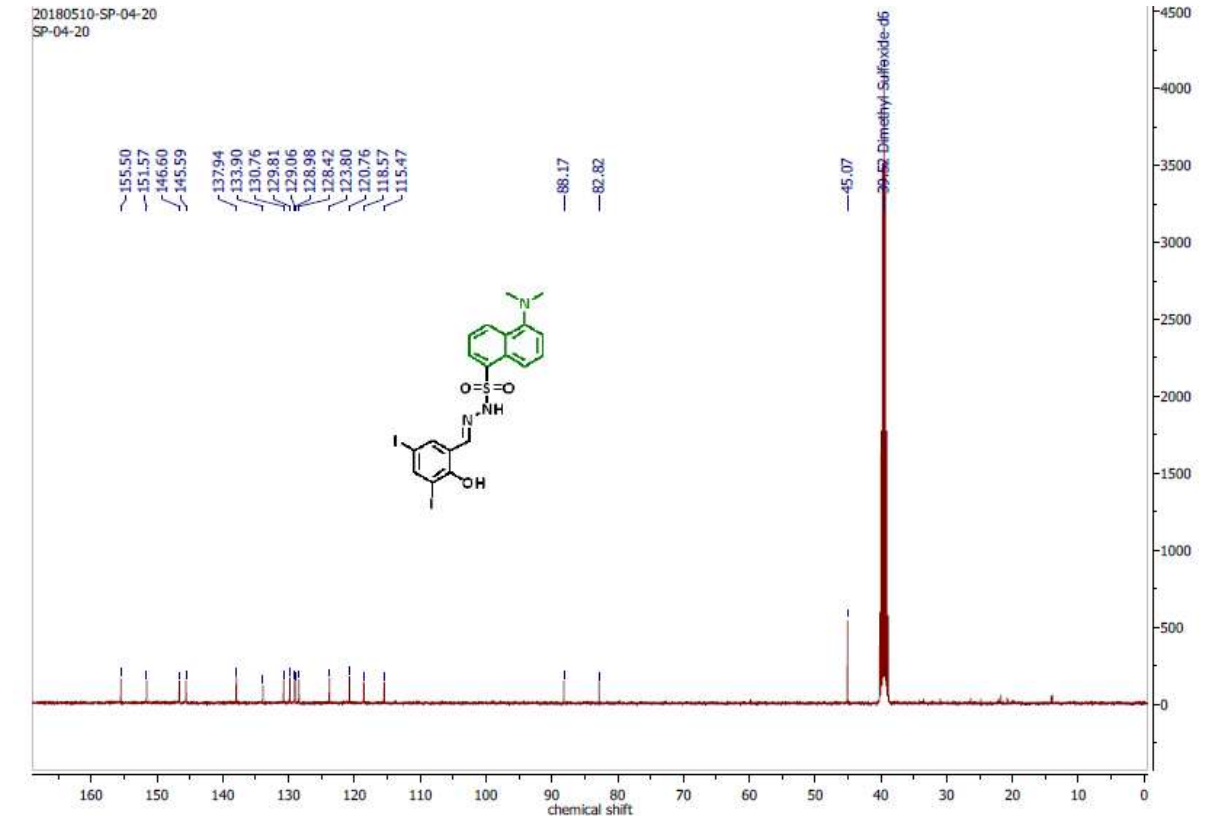

Figure C23: ^{13}C NMR spectrum of compound 8 in DMSO at 100 MHz

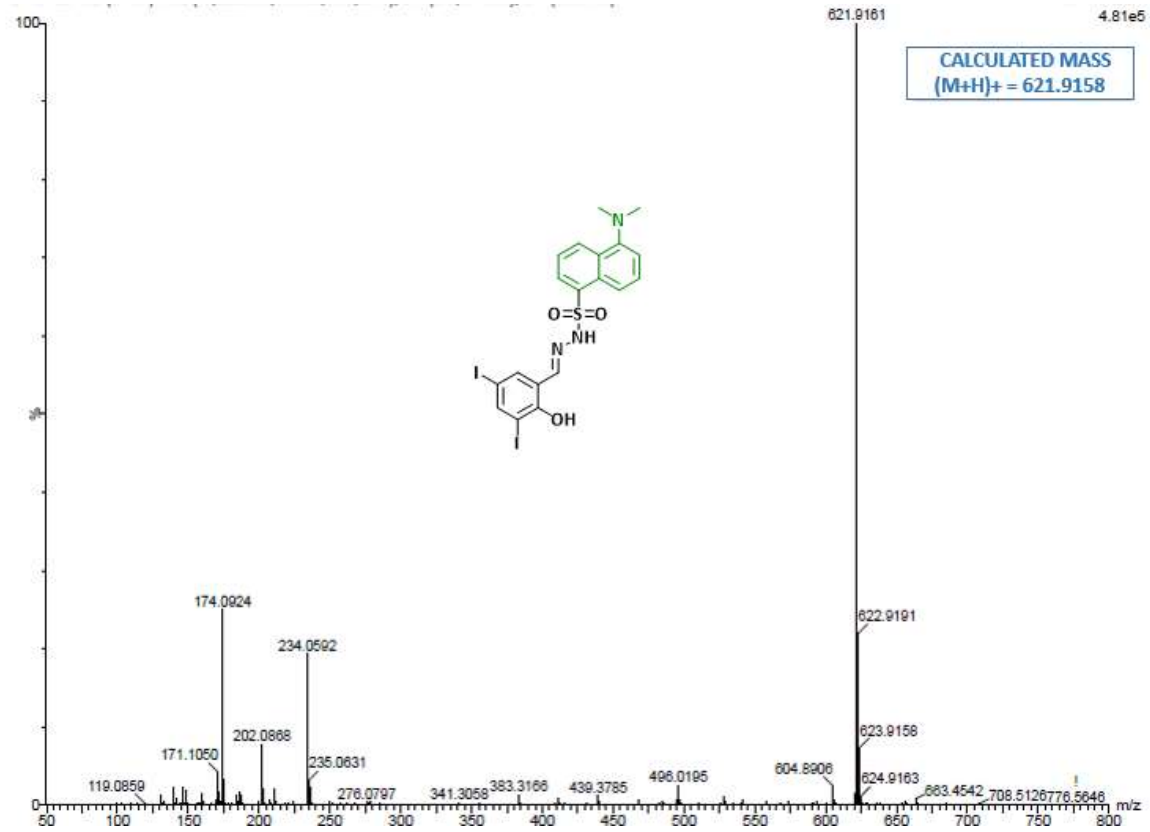

Figure C24: HRMS spectrum of compound 8.

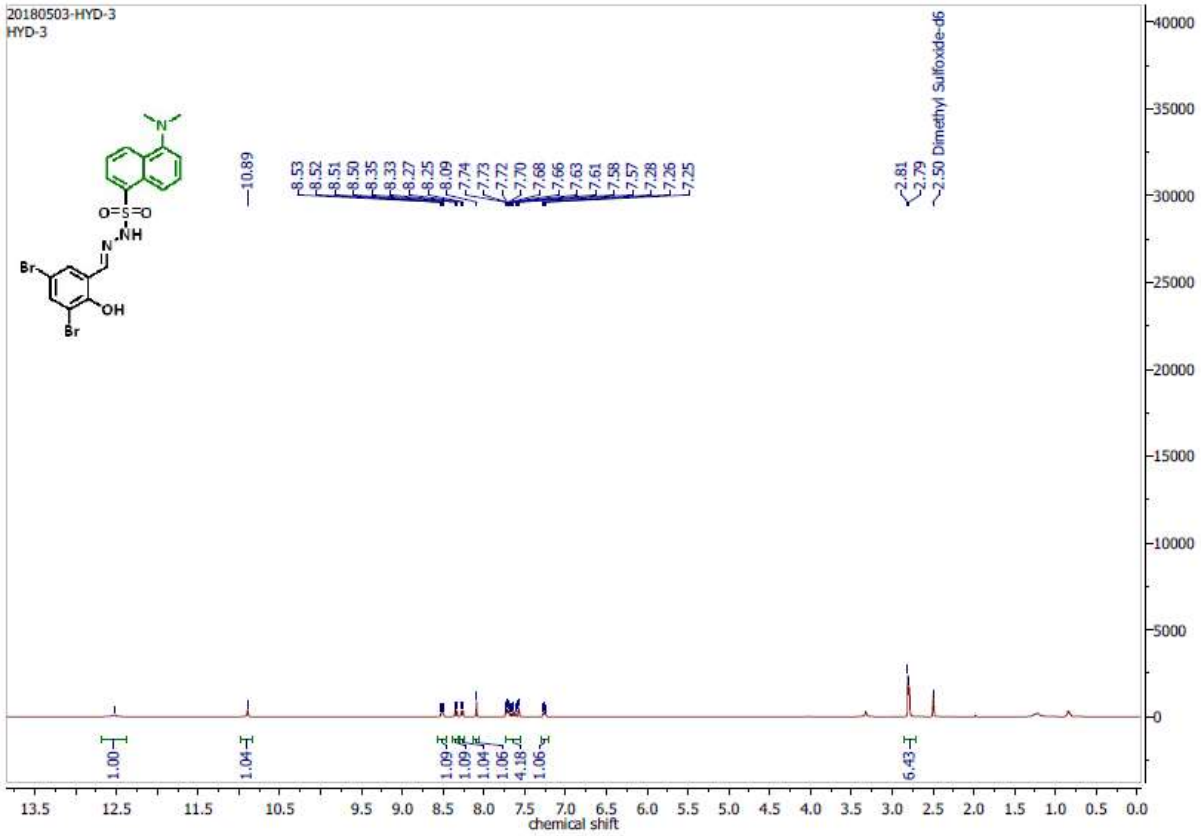

Figure C25: ^{1}H NMR spectrum of compound 9 in DMSO at 400 MHz.

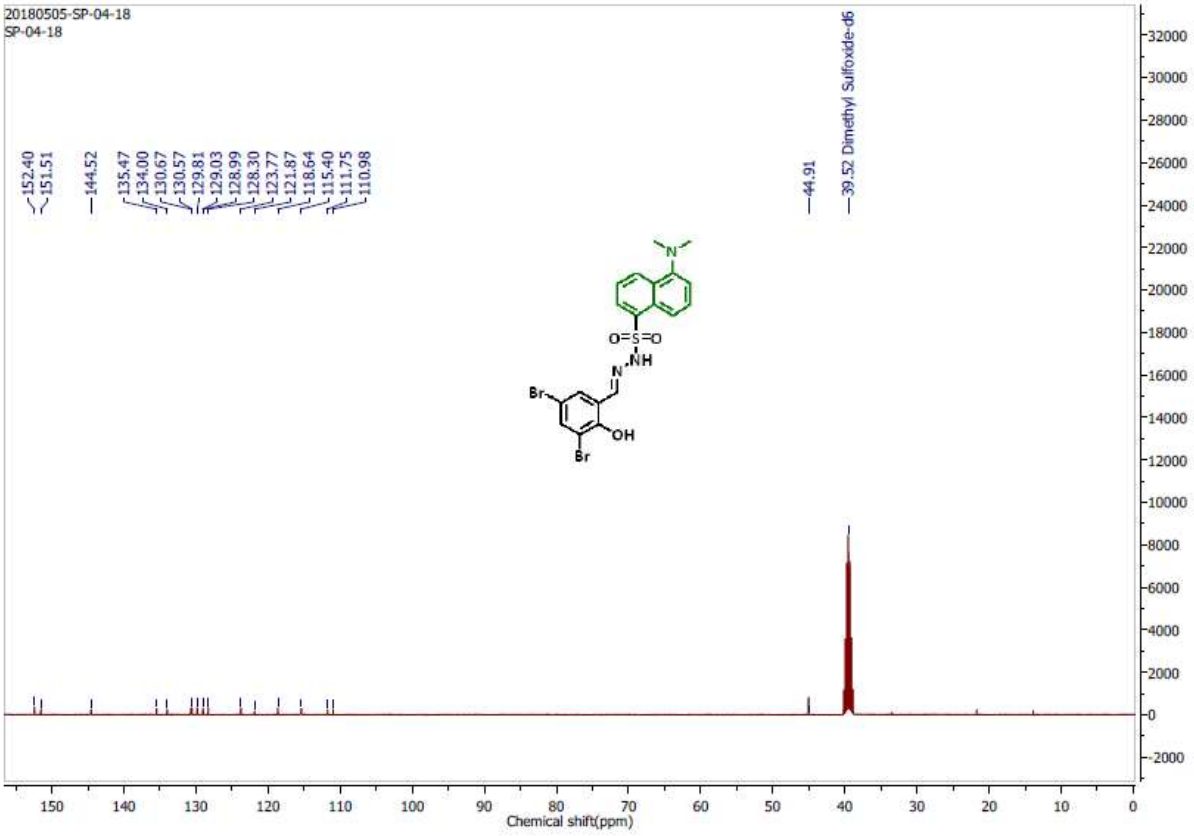

Figure C26: ^{13}C NMR spectrum of compound 9 in DMSO at 100 MHz.

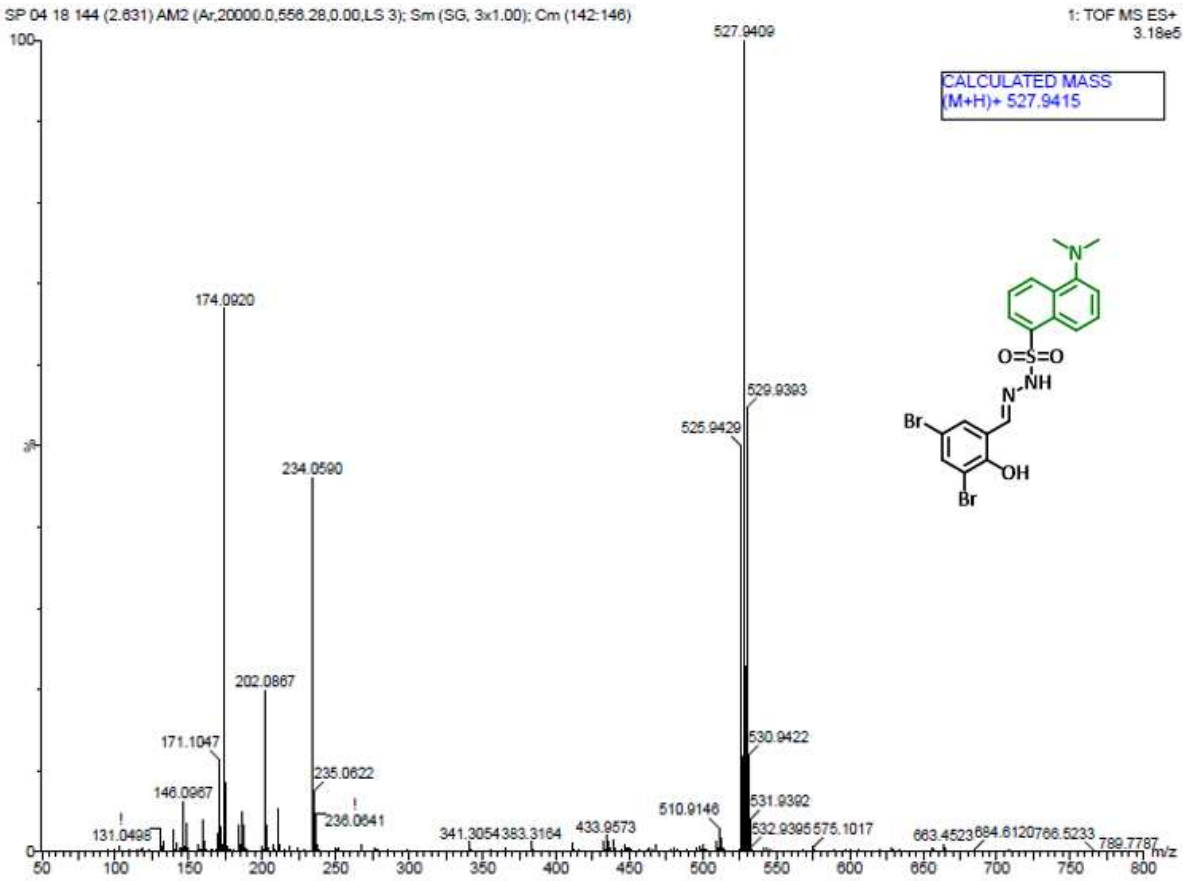

Figure C27: HRMS spectrum of compound 9.

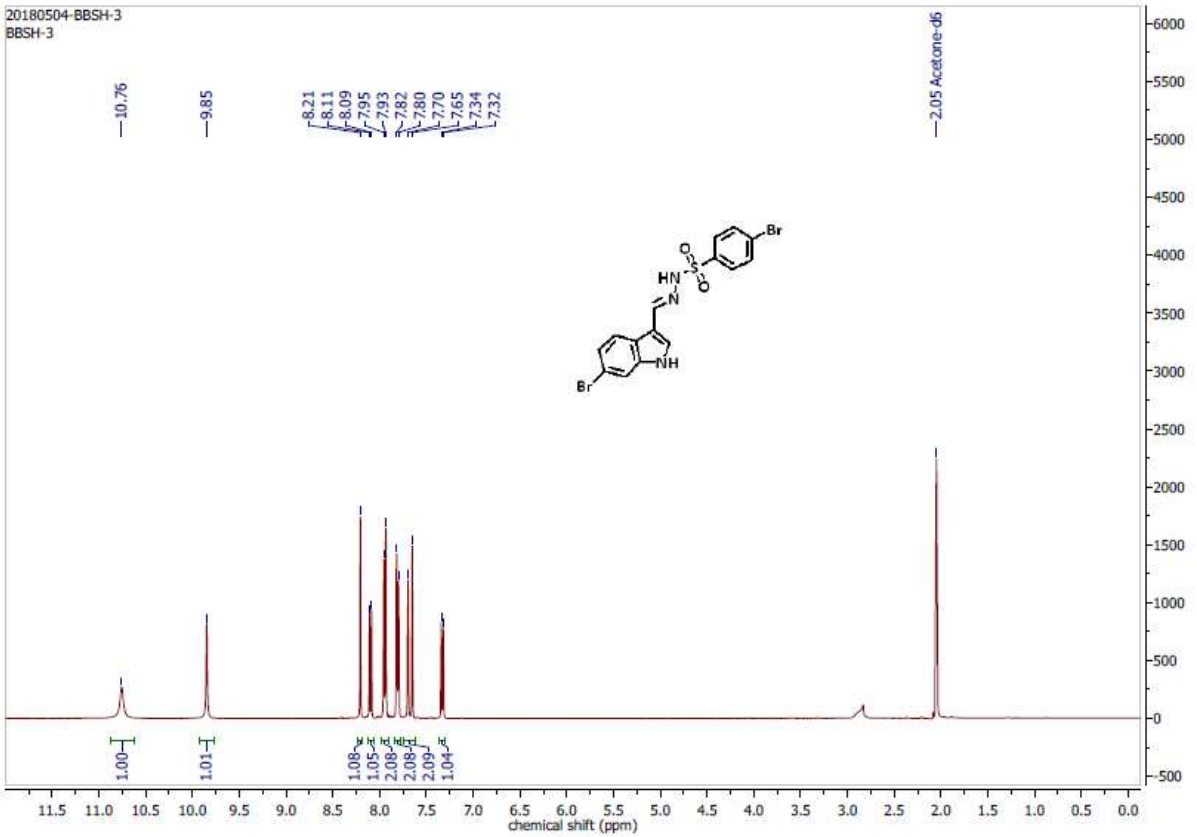

Figure C28: ^{1}H NMR spectrum of compound 10 in Acetone at 400 MHz.

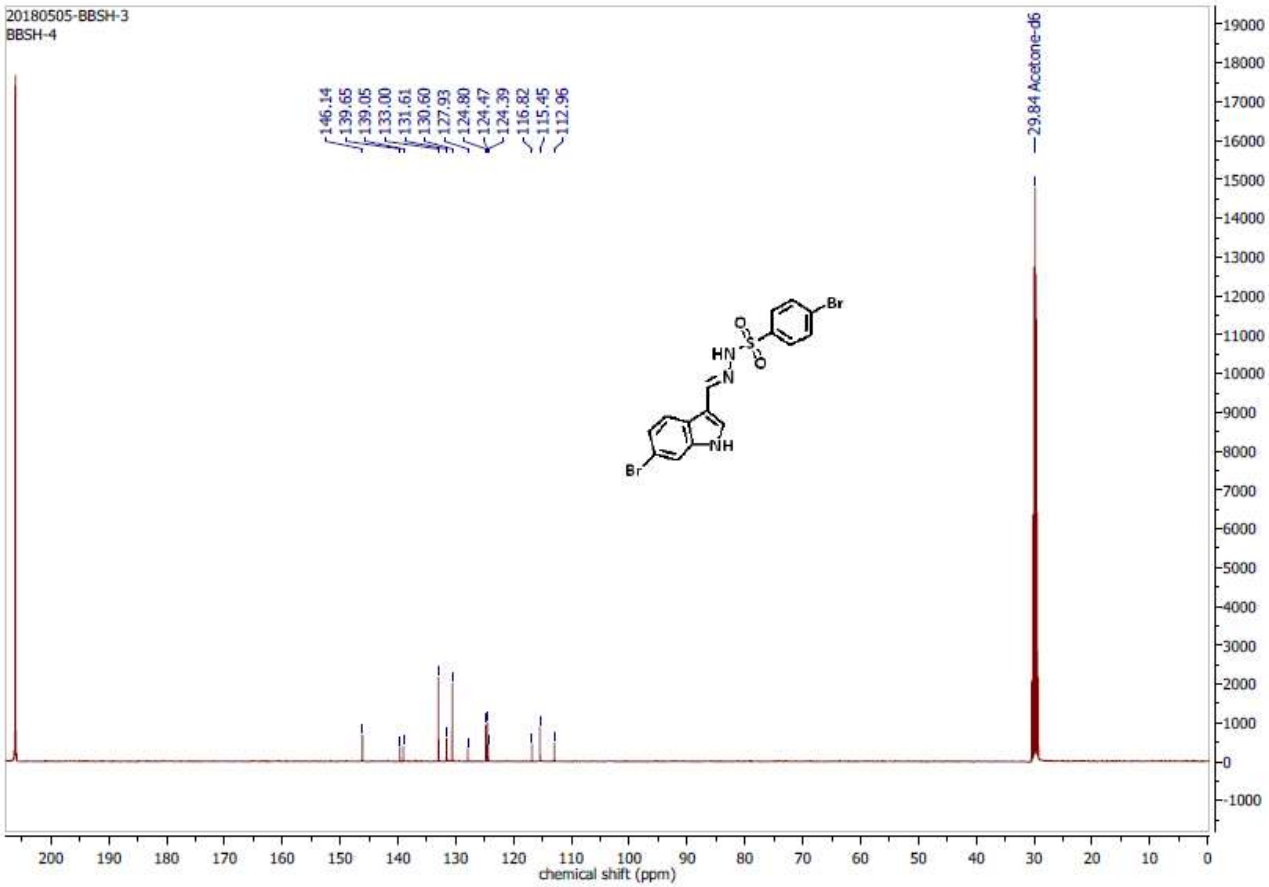

Figure C29: ^{13}C NMR spectrum of compound 10 in Acetone at 100 MHz.

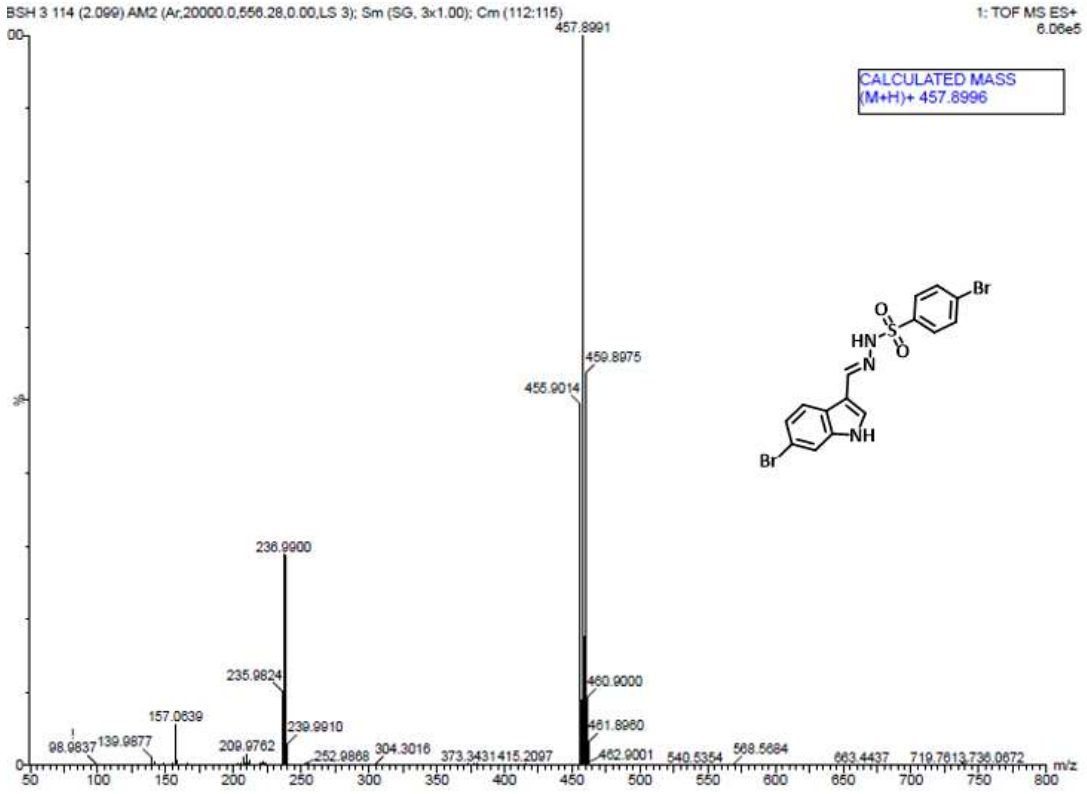

Figure C30: HRMS spectrum of compound 10.

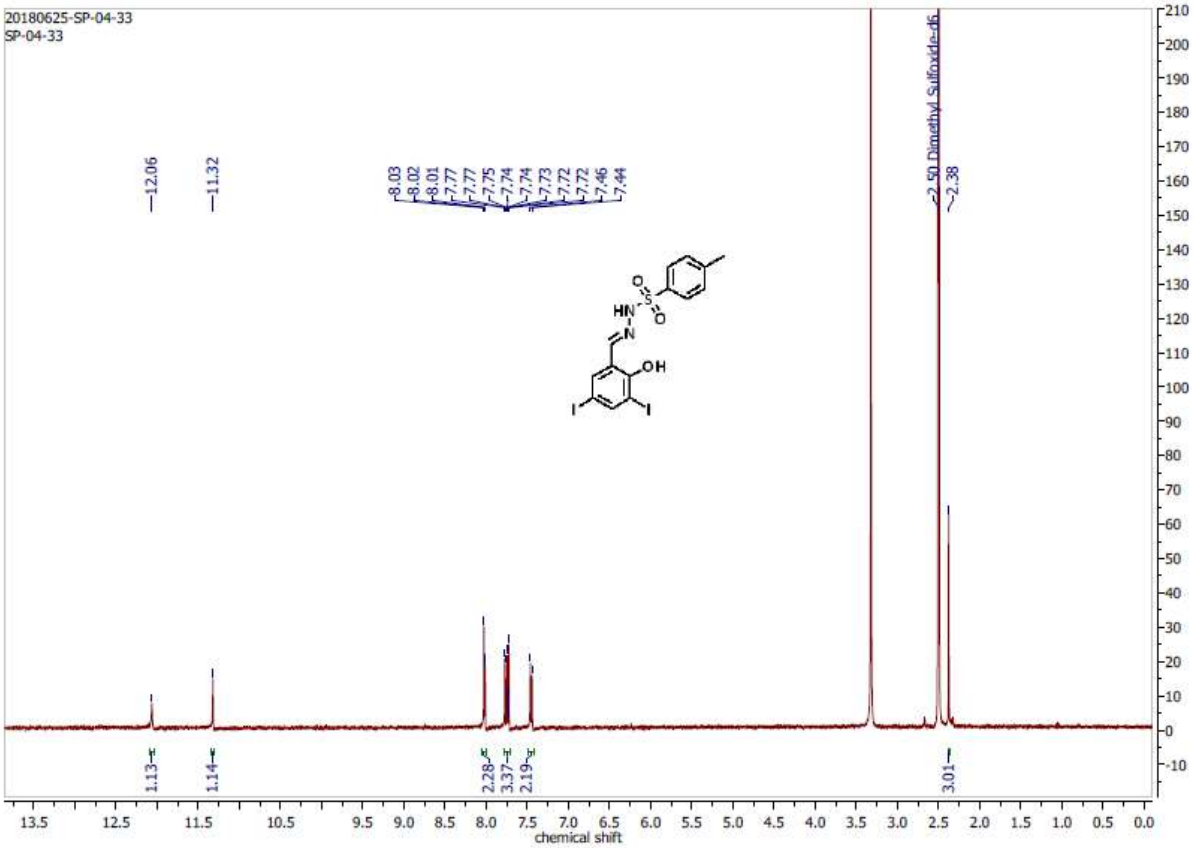

Figure C31: ^{1}H NMR spectrum of compound 11 in DMSO at 400 MHz.

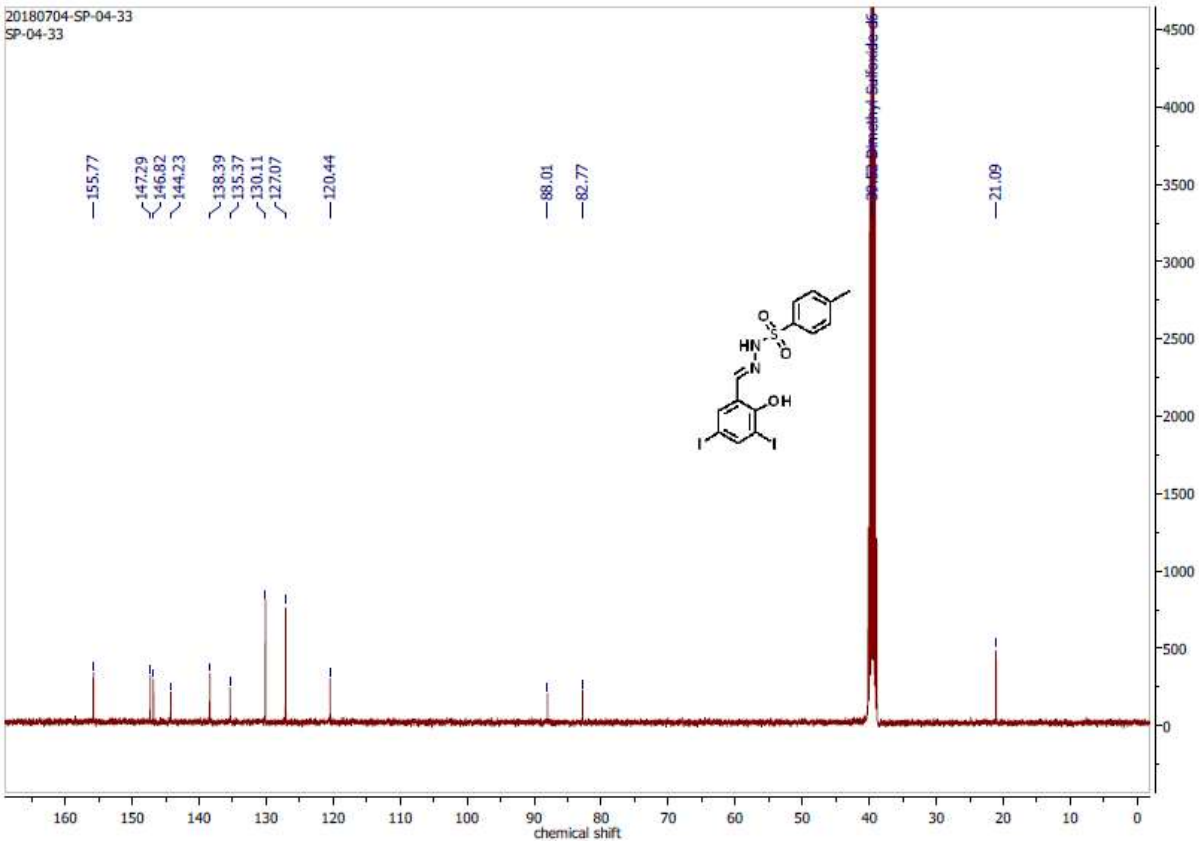

Figure C32: ^{13}C NMR spectrum of compound 11 in DMSO at 100 MHz.

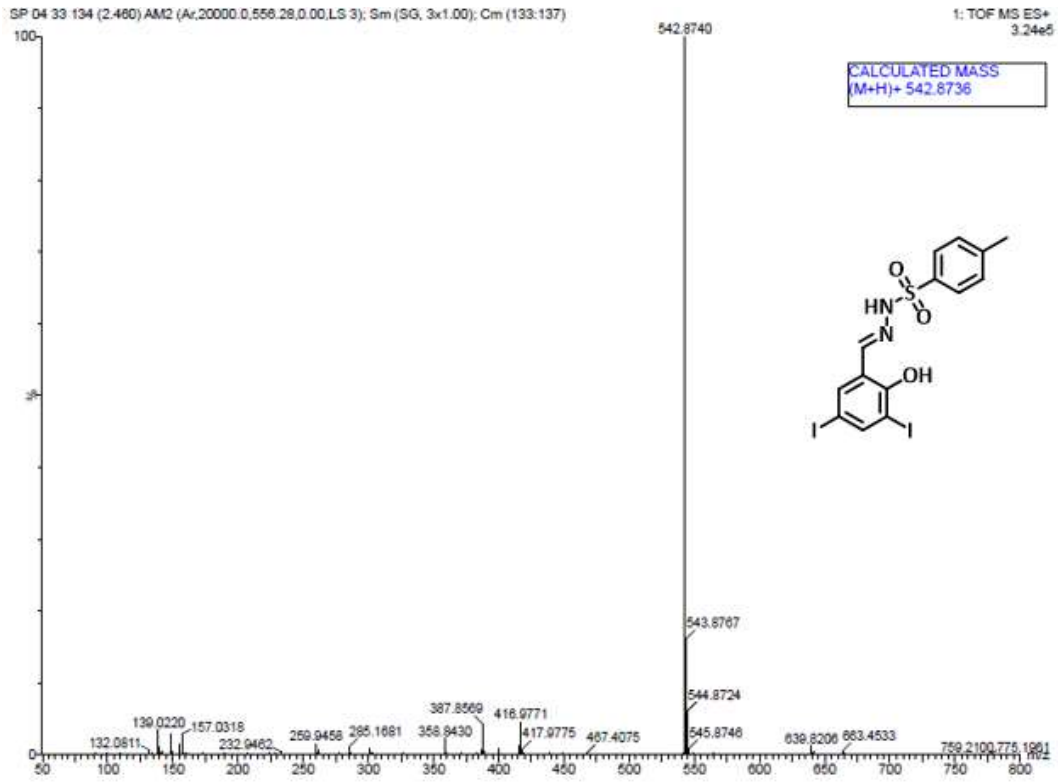

Figure C33: HRMS spectrum of compound 11.

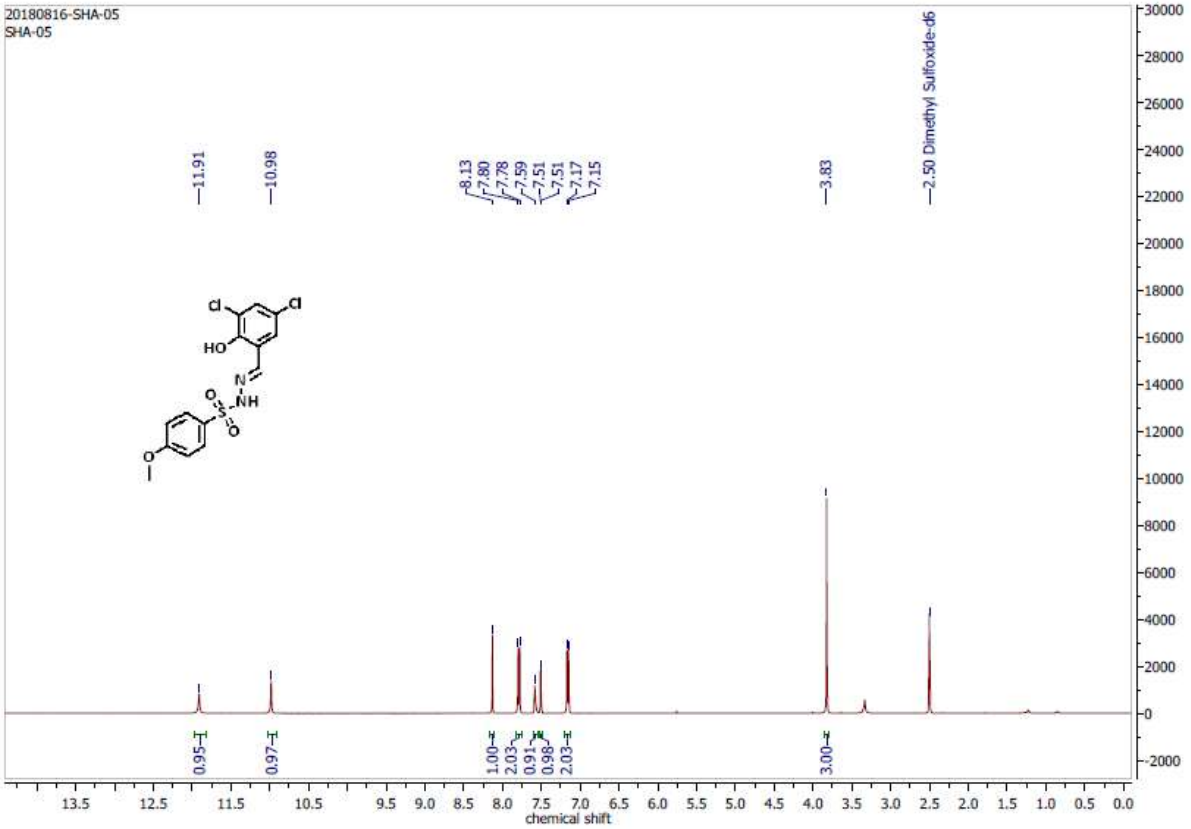

Figure C34: ^{1}H NMR spectrum of compound 12 in DMSO at 400 MHz.

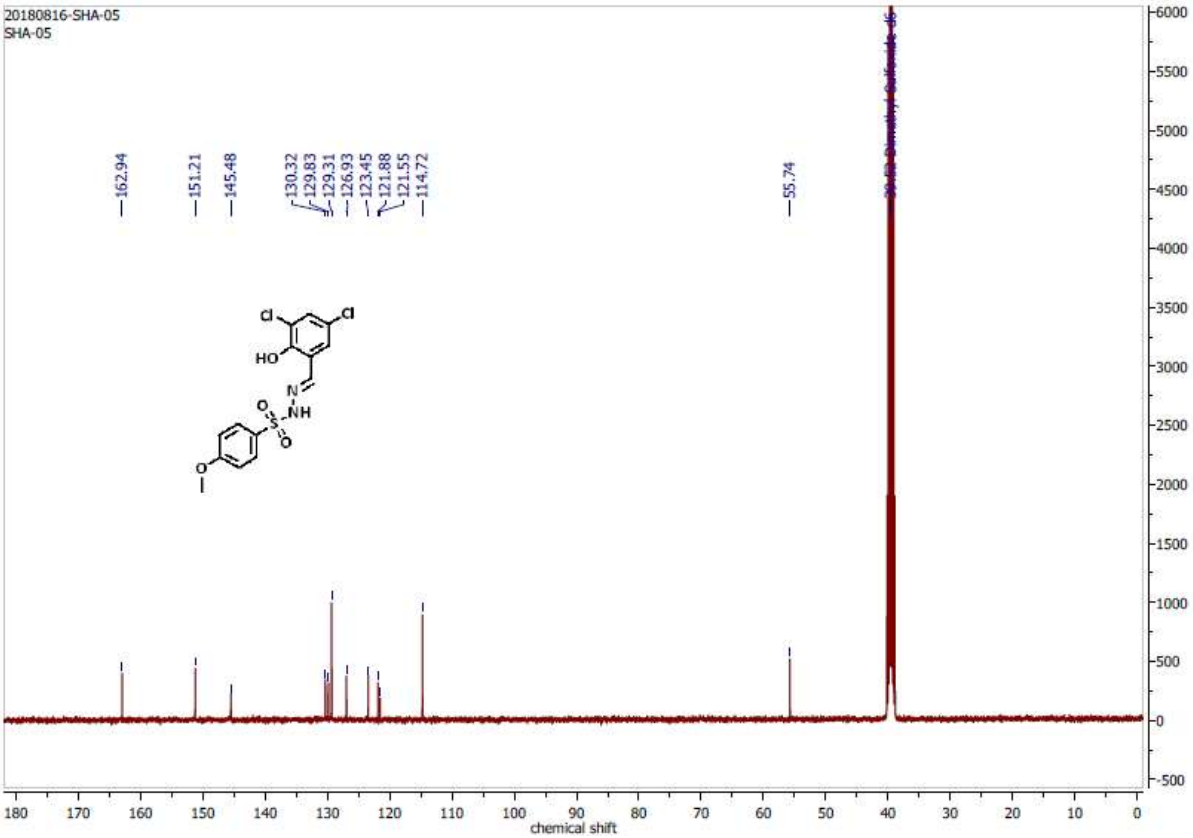

Figure C35: ^{13}C NMR spectrum of compound 12 in DMSO at 100 MHz.

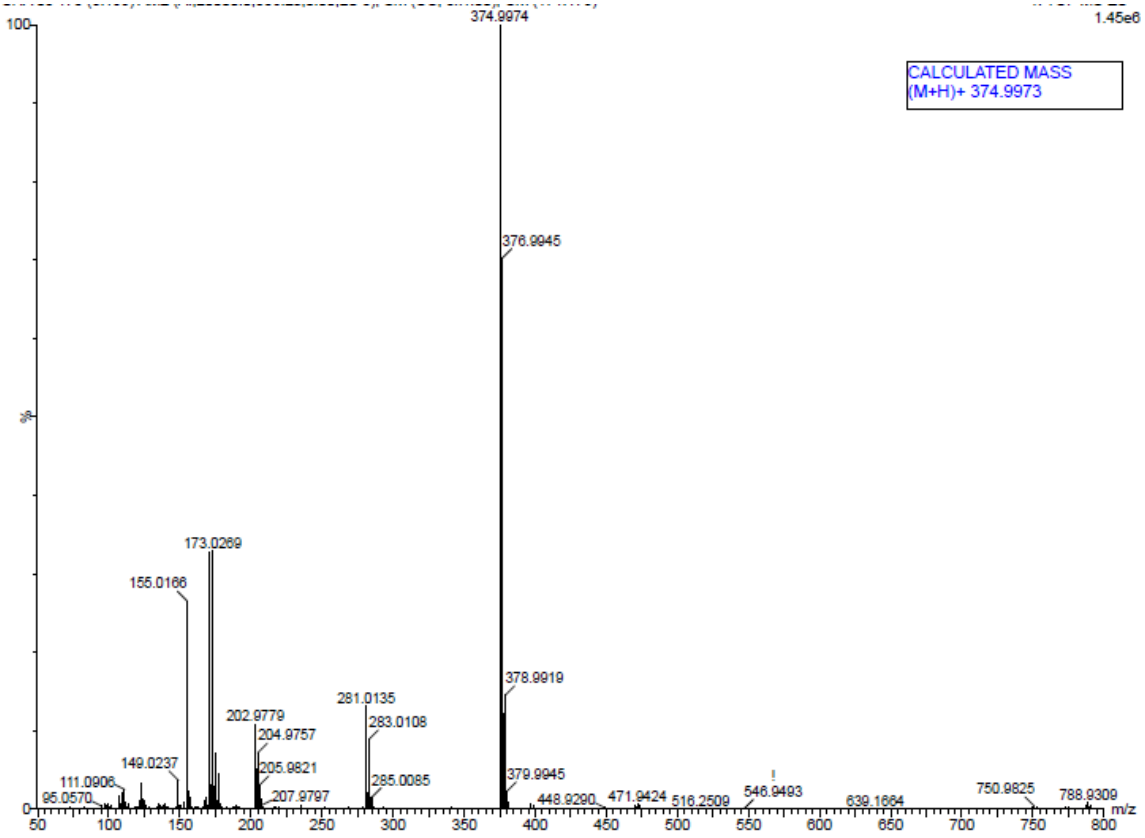

Figure C36: HRMS spectrum of compound 12.

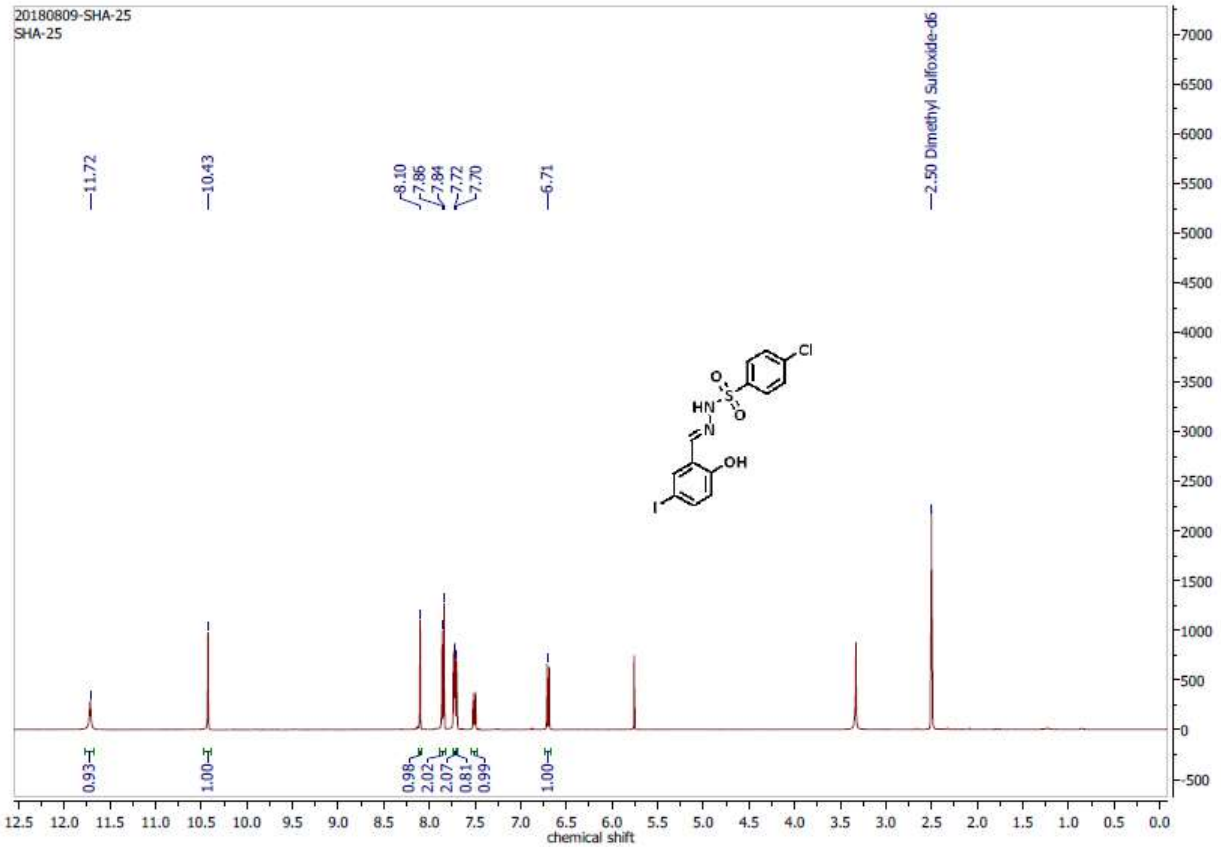

Figure C37: ^{1}H NMR spectrum of compound 13 in DMSO at 400 MHz.

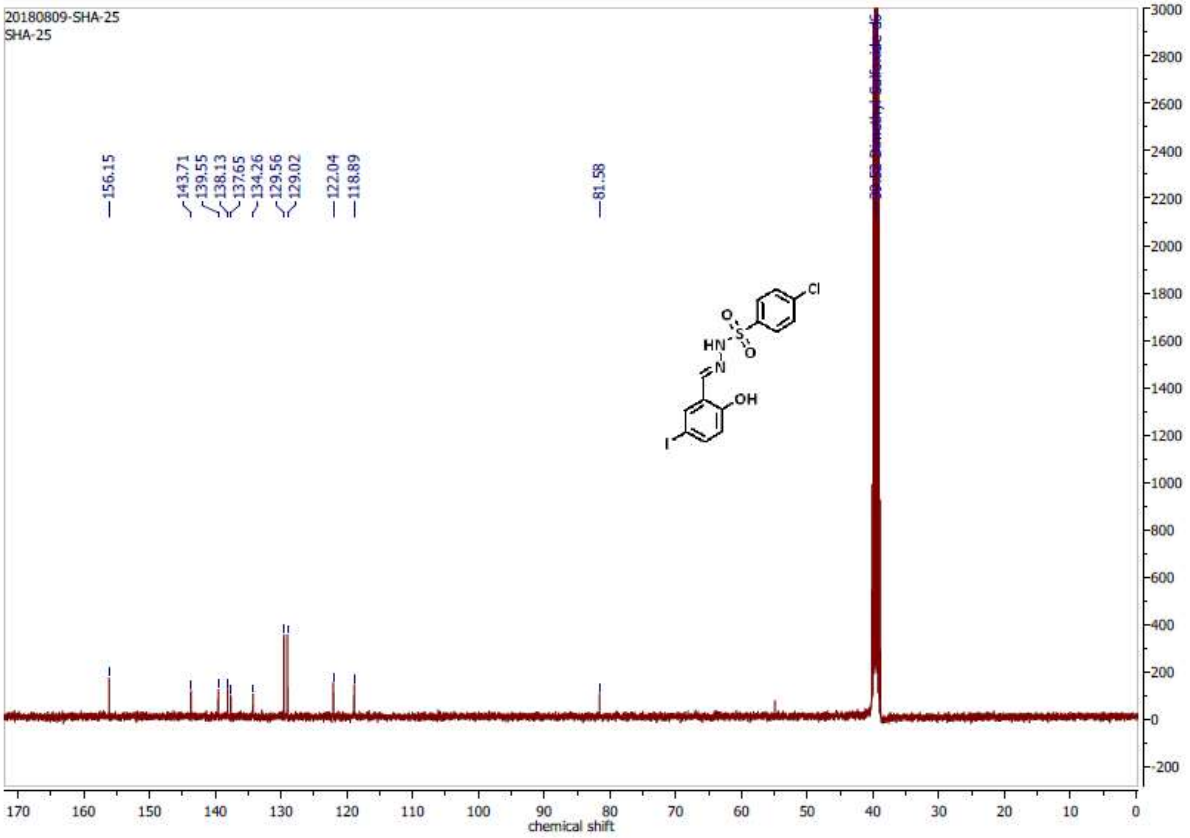

Figure C38: ^{13}C NMR spectrum of compound 13 in DMSO at 100 MHz.

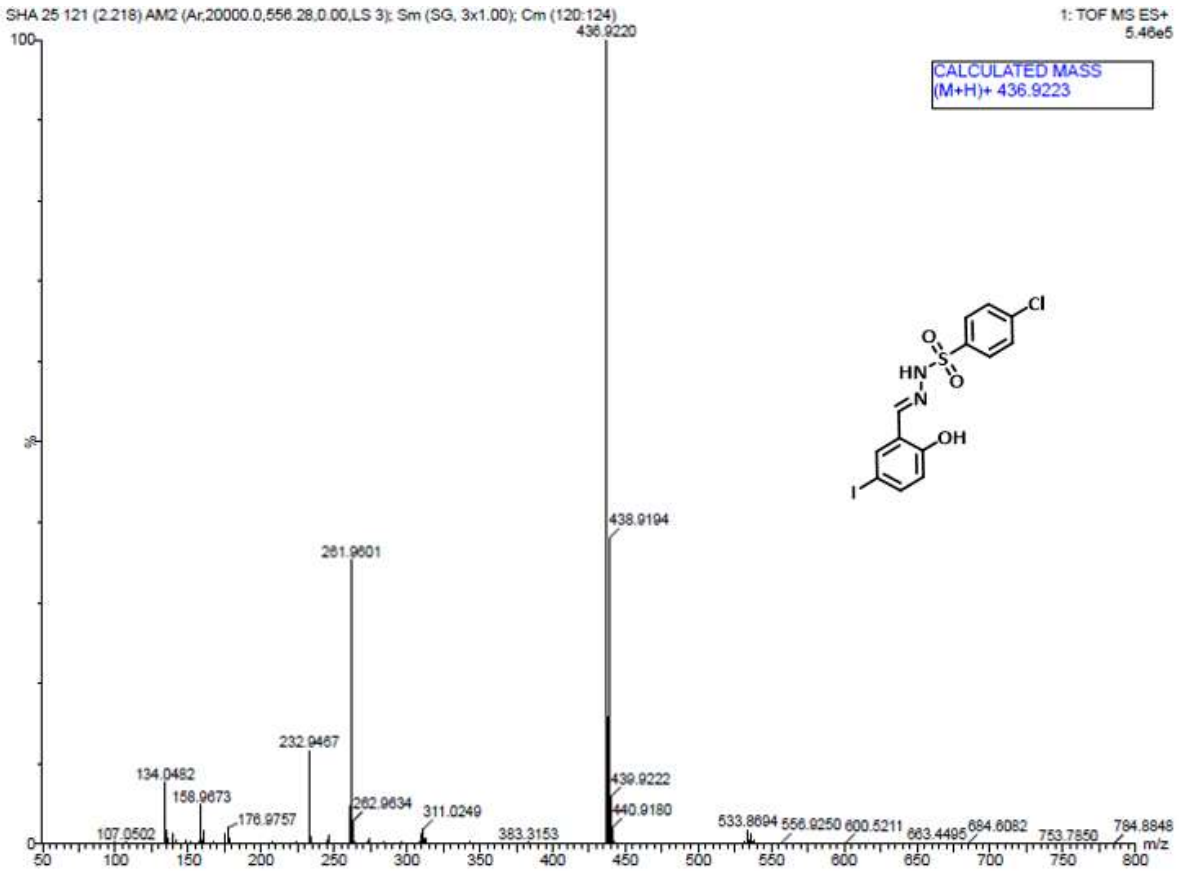

Figure C39: HRMS spectrum of compound 13.

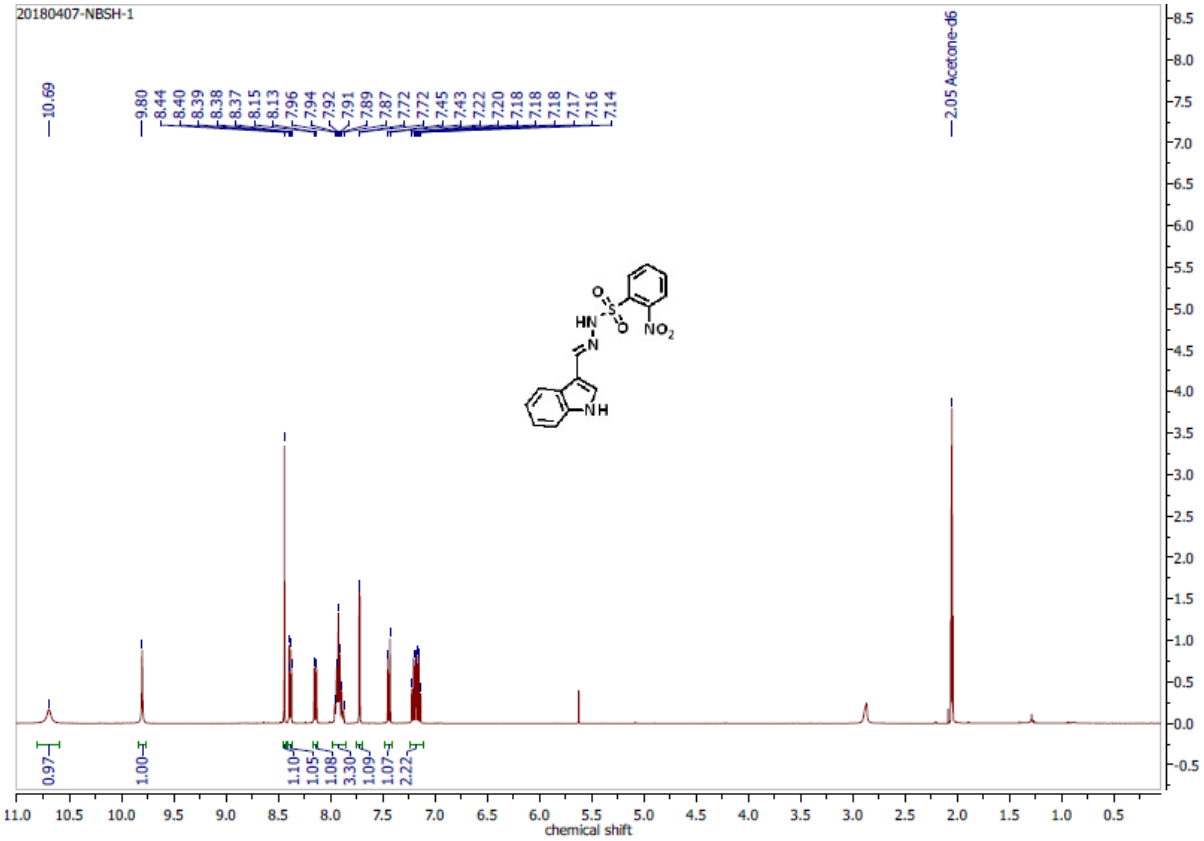

Figure C40: ^{1}H NMR spectrum of compound 14 in Acetone at 400 MHz.

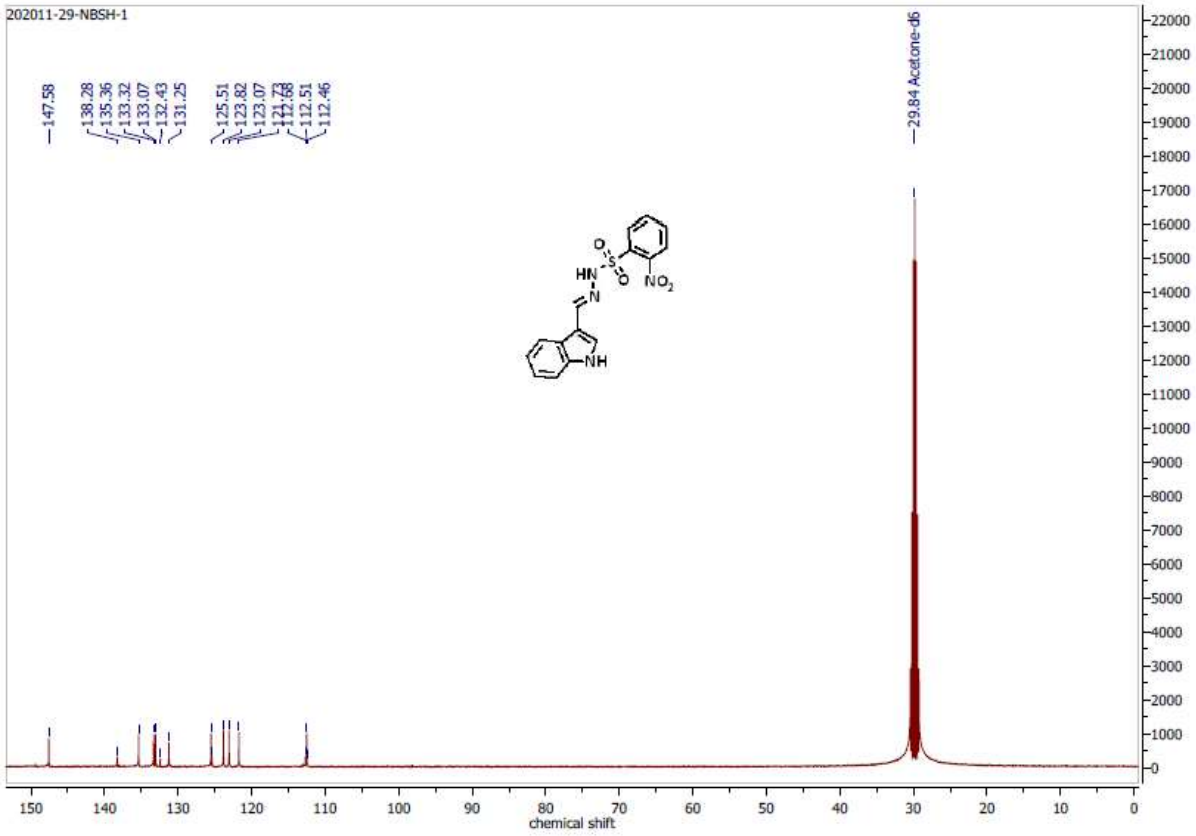

Figure C41: ^{13}C NMR spectrum of compound 14 in Acetone at 100 MHz.

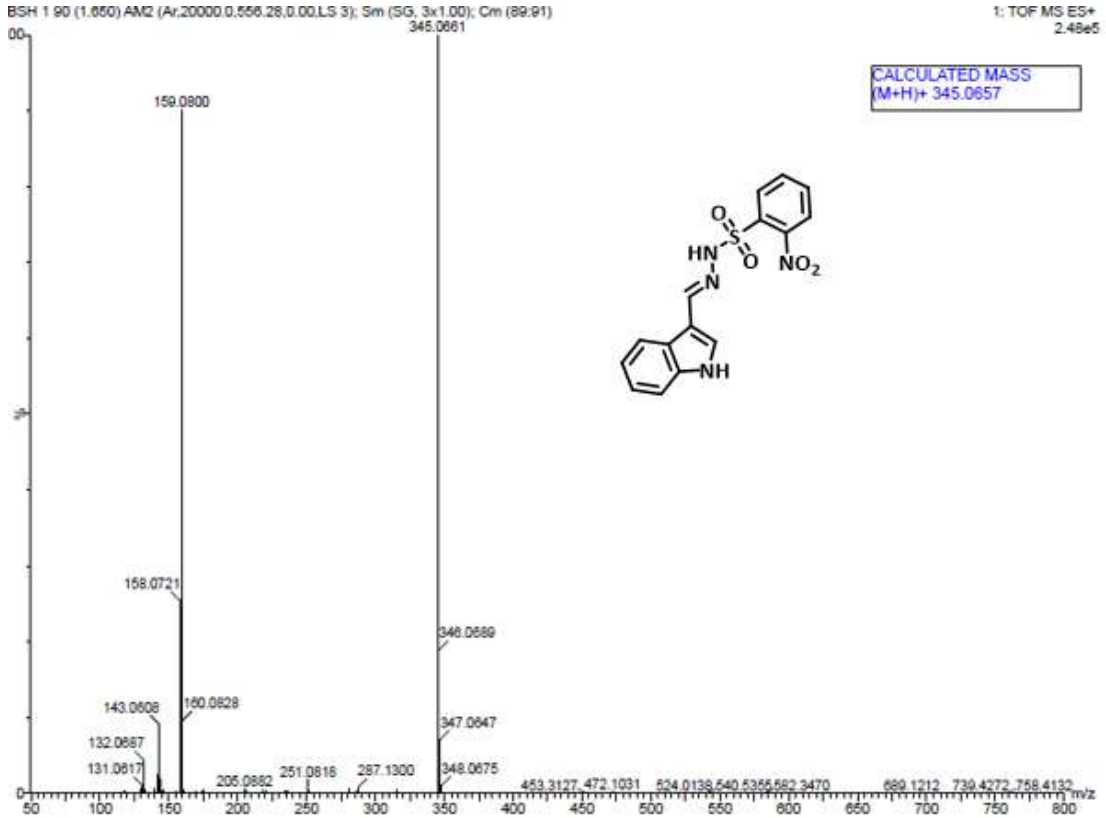

Figure C42: HRMS spectrum of compound 14.

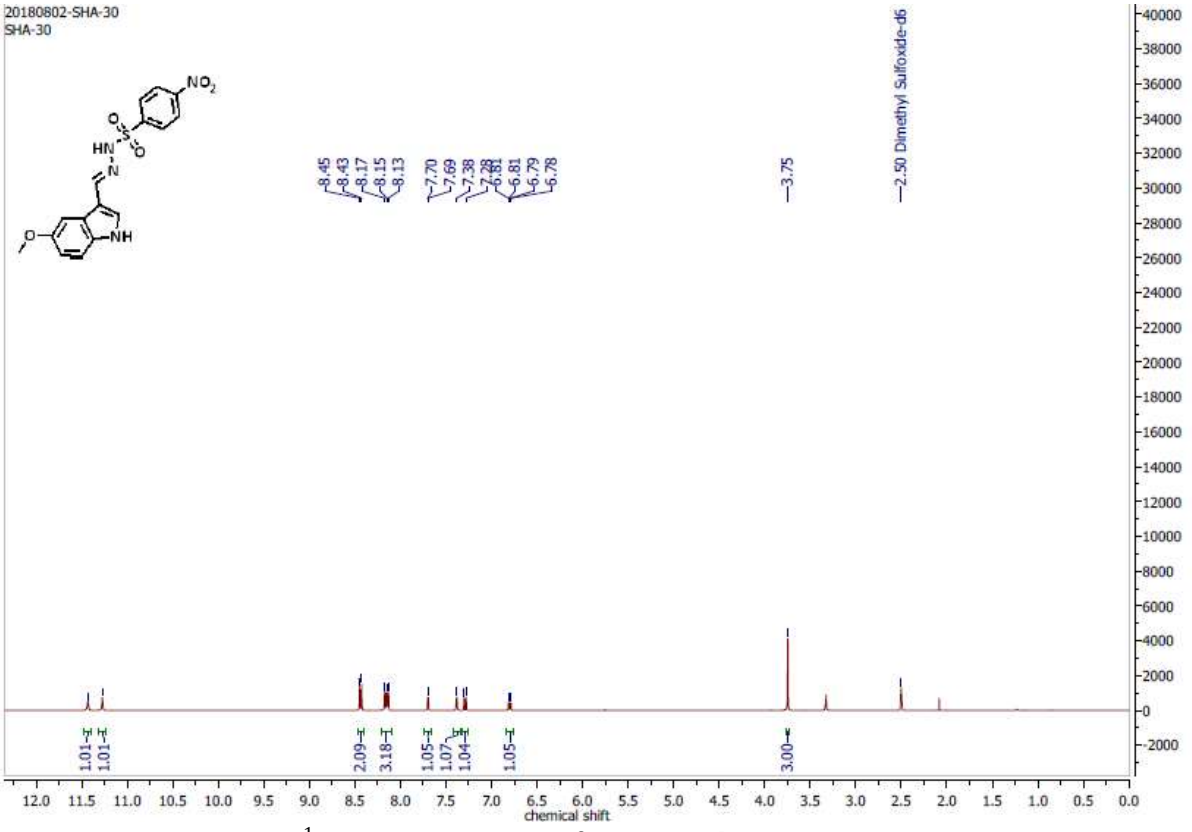

Figure C43: [1] H NMR spectrum of compound 15 in DMSO at 400 MHz.

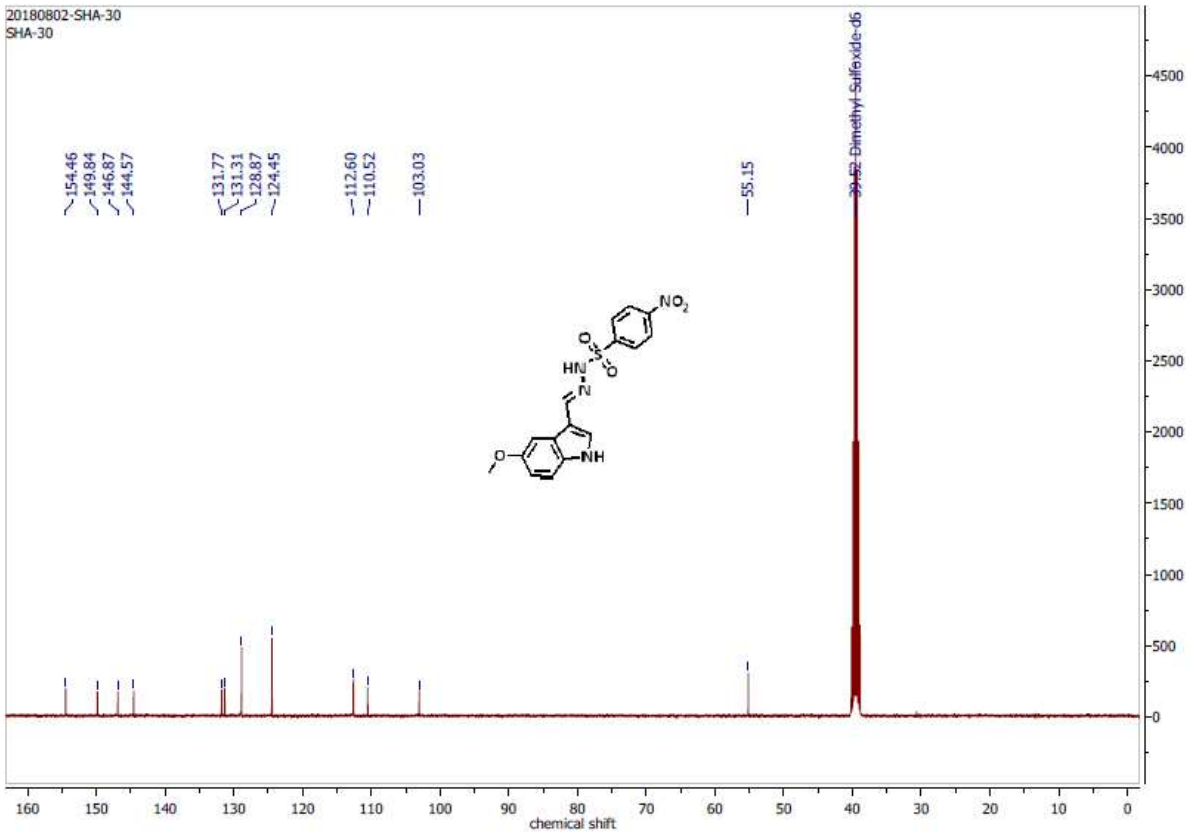

Figure C44: ^{13}C NMR spectrum of compound 15 in DMSO at 100 MHz.

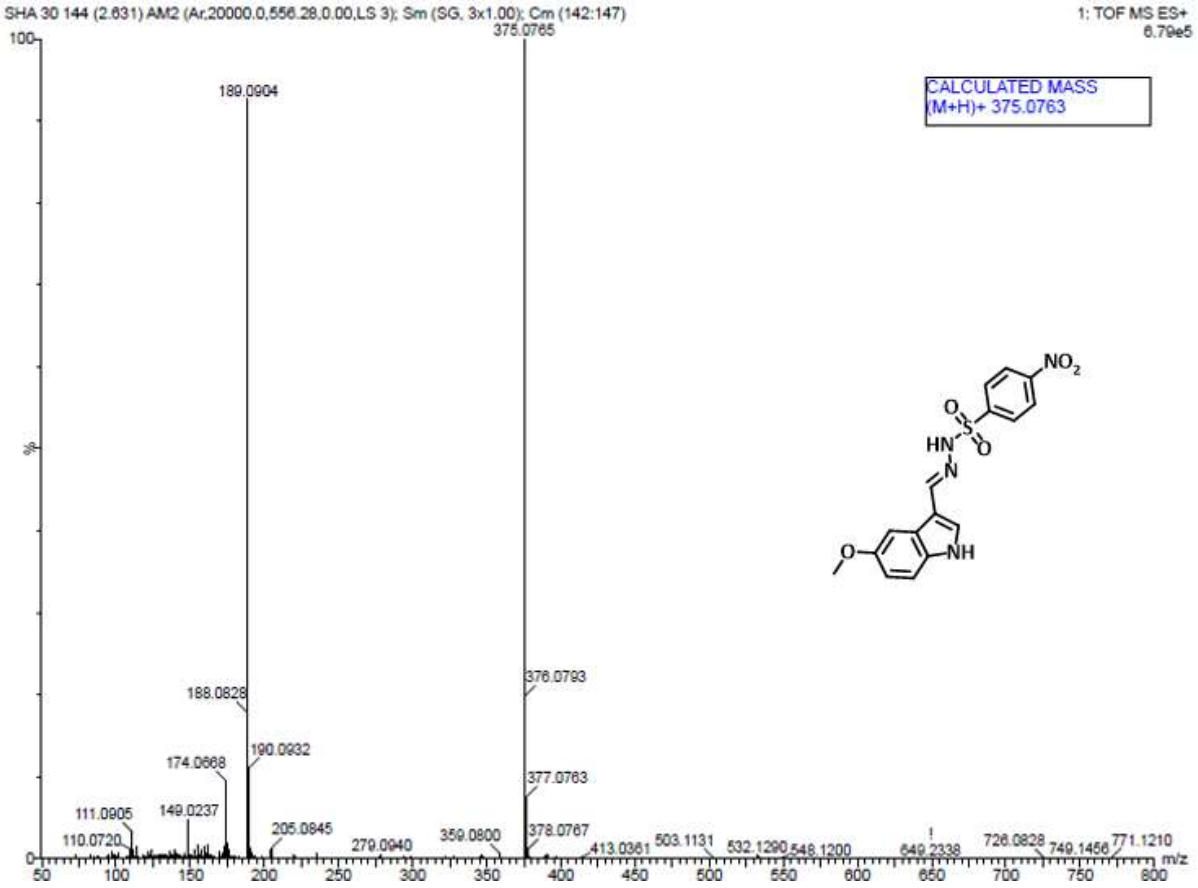

Figure C45: HRMS spectrum of compound 15

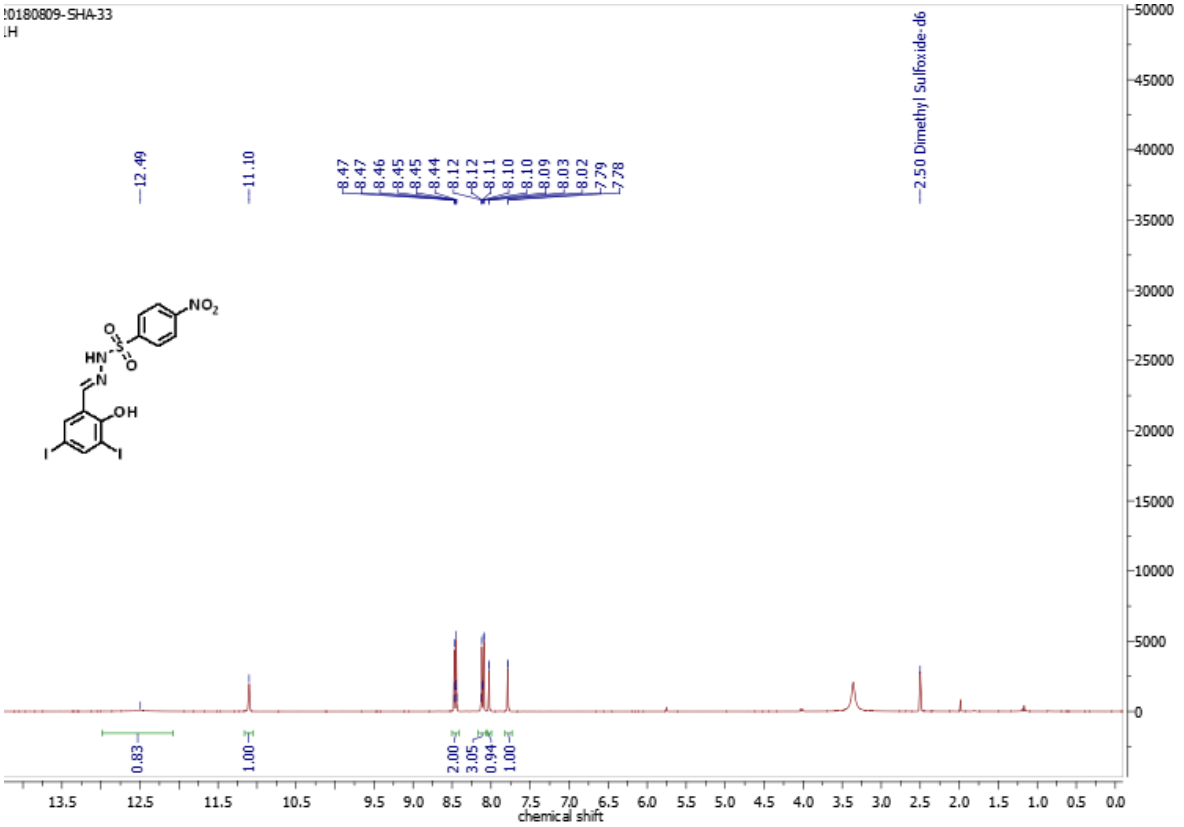

Figure C46: ^{1}H NMR spectrum of compound 16 in DMSO at 400 MHz.

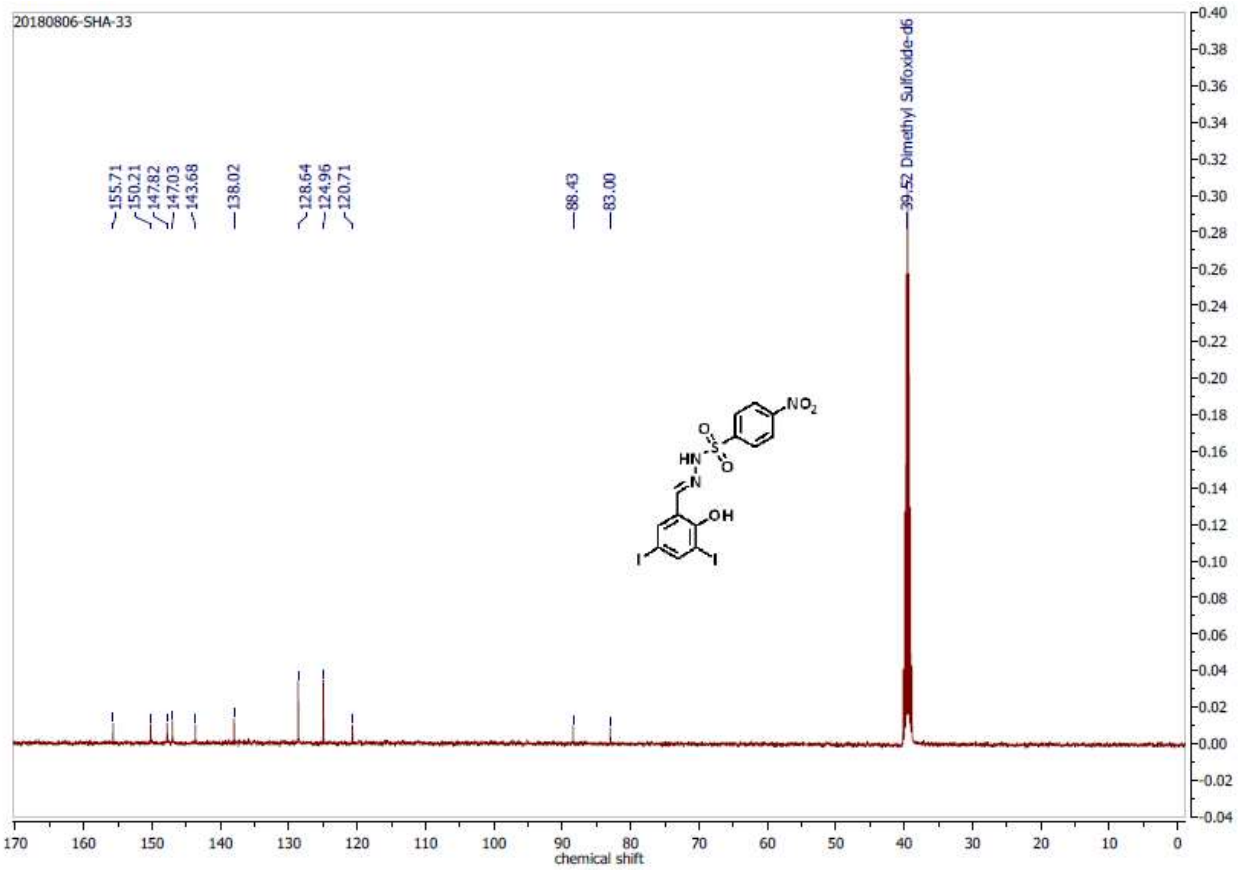

Figure C47: ^{13}C NMR spectrum of compound 16 in DMSO at 100 MHz.

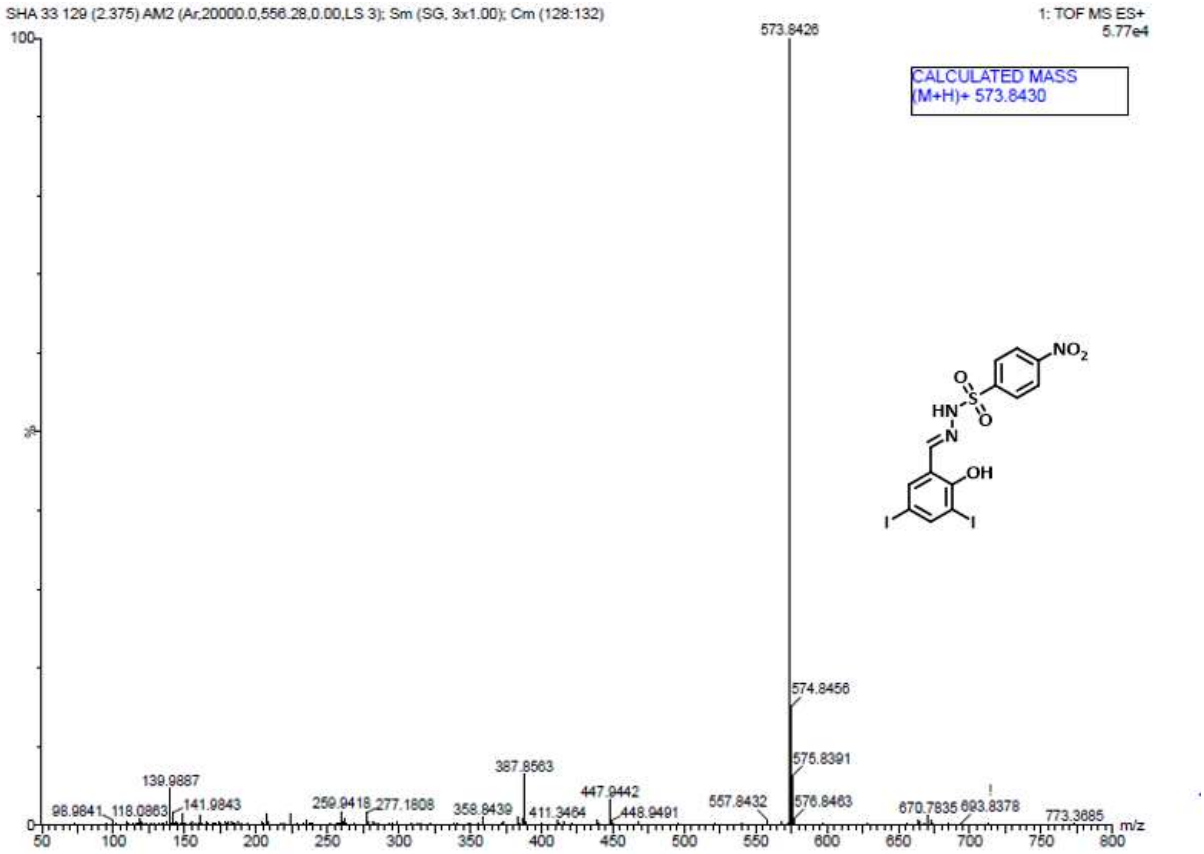

Figure C48: HRMS spectrum of compound 16.

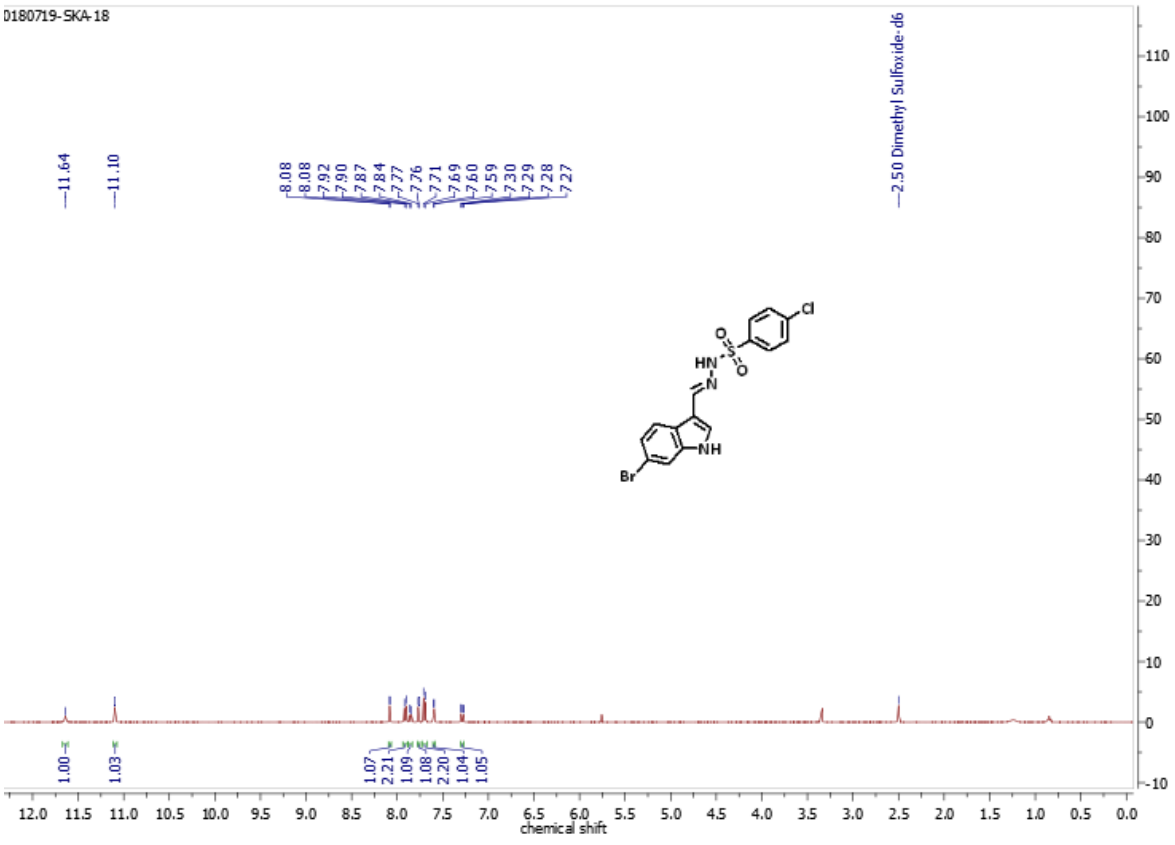

Figure C49: ^{1}H NMR spectrum of compound 17 in DMSO at 400 MHz.

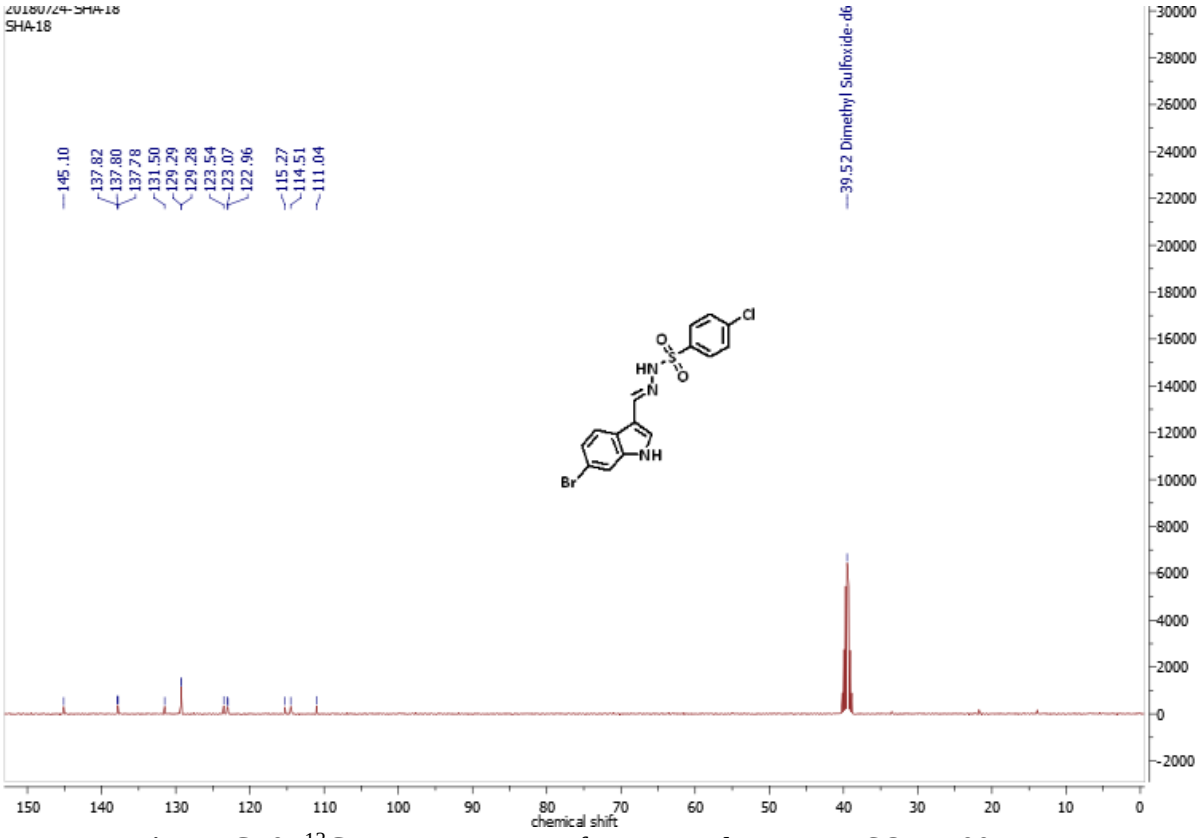

Figure C50: ^{13}C NMR spectrum of compound 17 in DMSO at 100 MHz

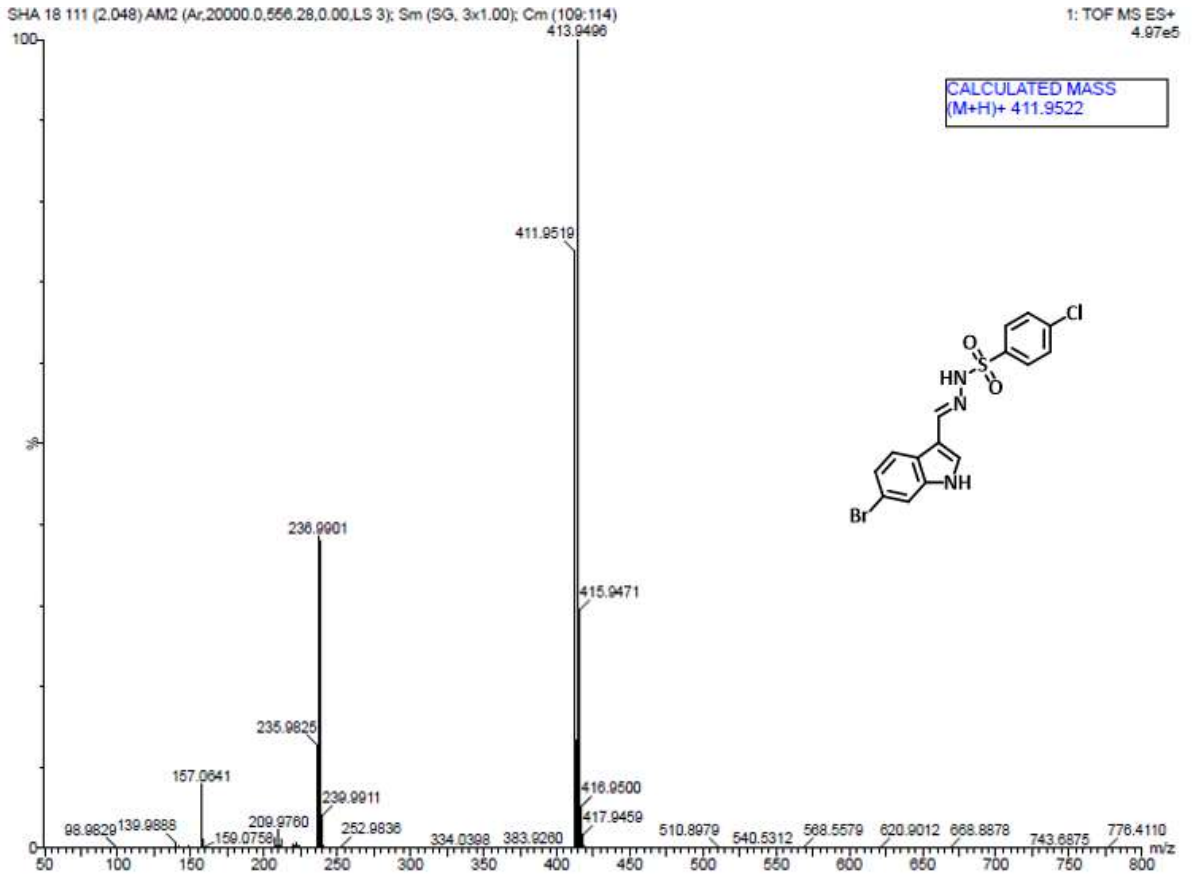

Figure C51: HRMS spectrum of compound 17.

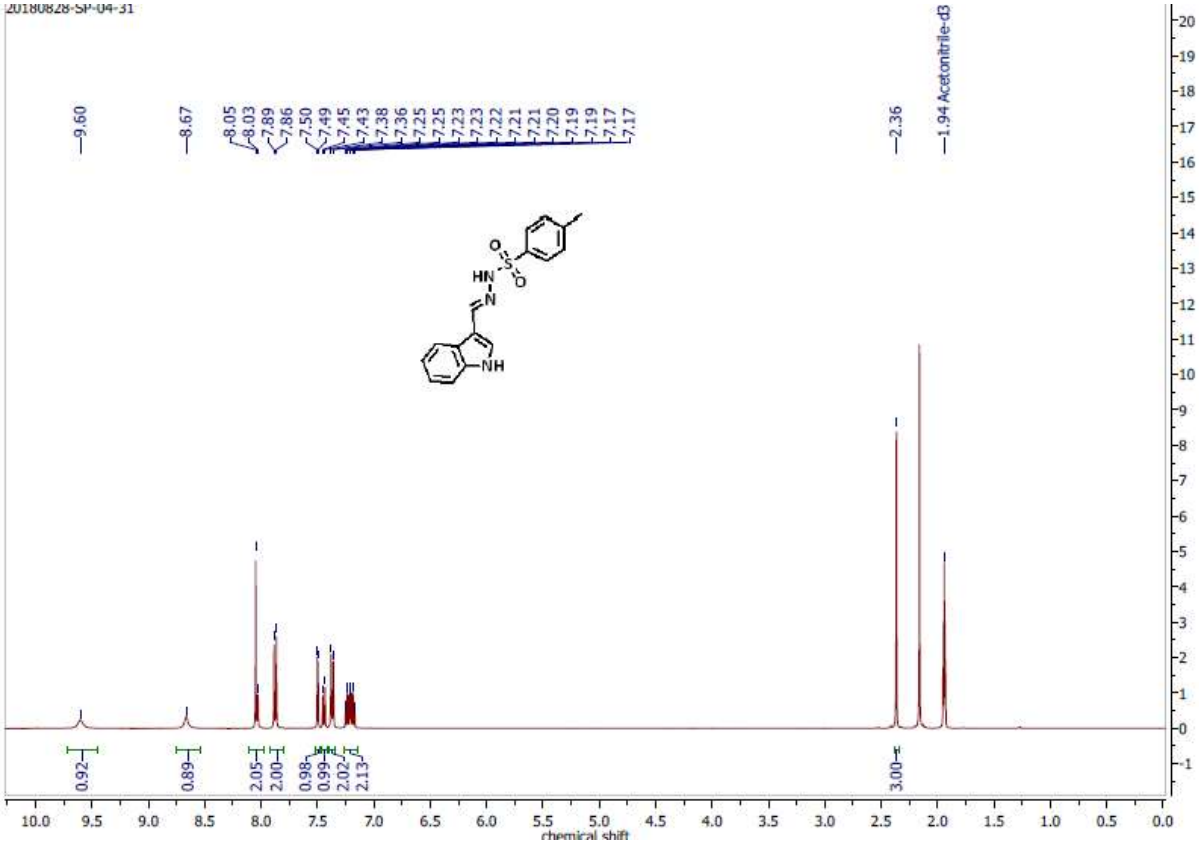

Figure C52: ^{1}H NMR spectrum of compound 18 in CD_3CN at 400 MHz.

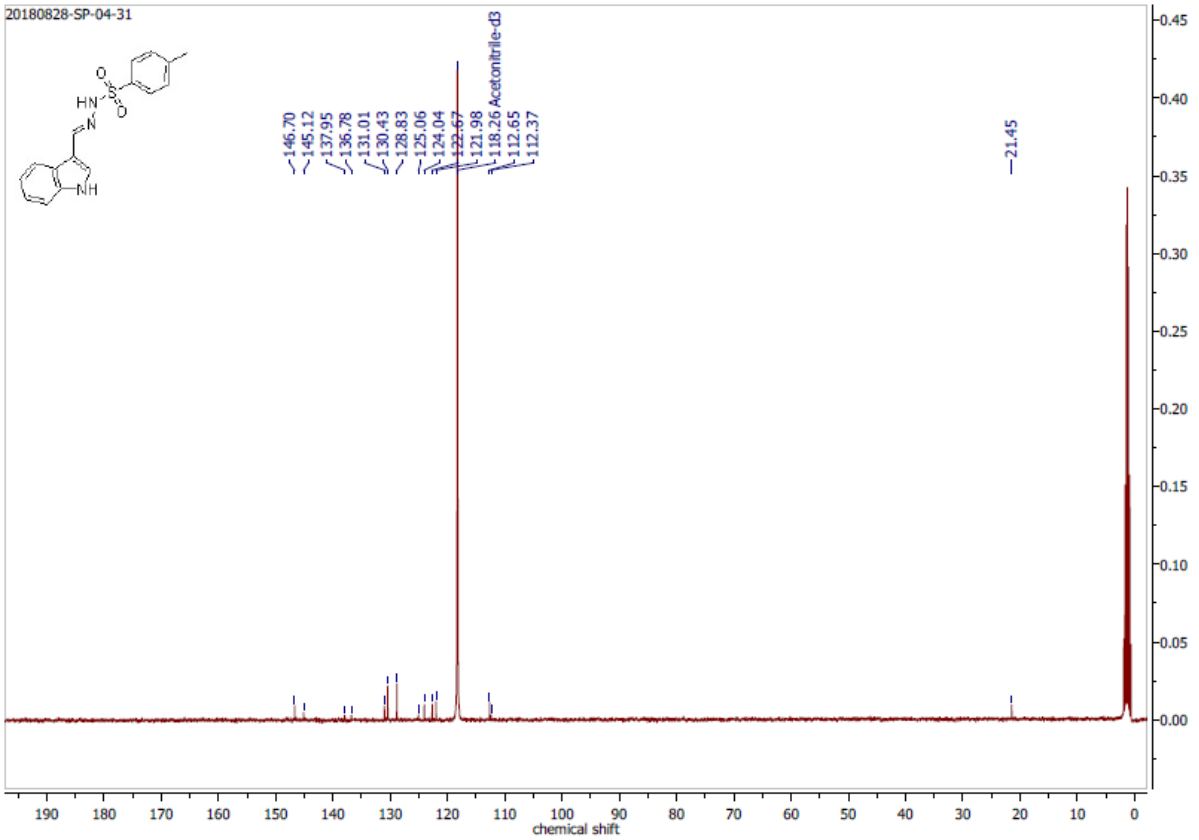

Figure C53: ^{13}C NMR spectrum of compound 18 in CD_3CN at 100 MHz.

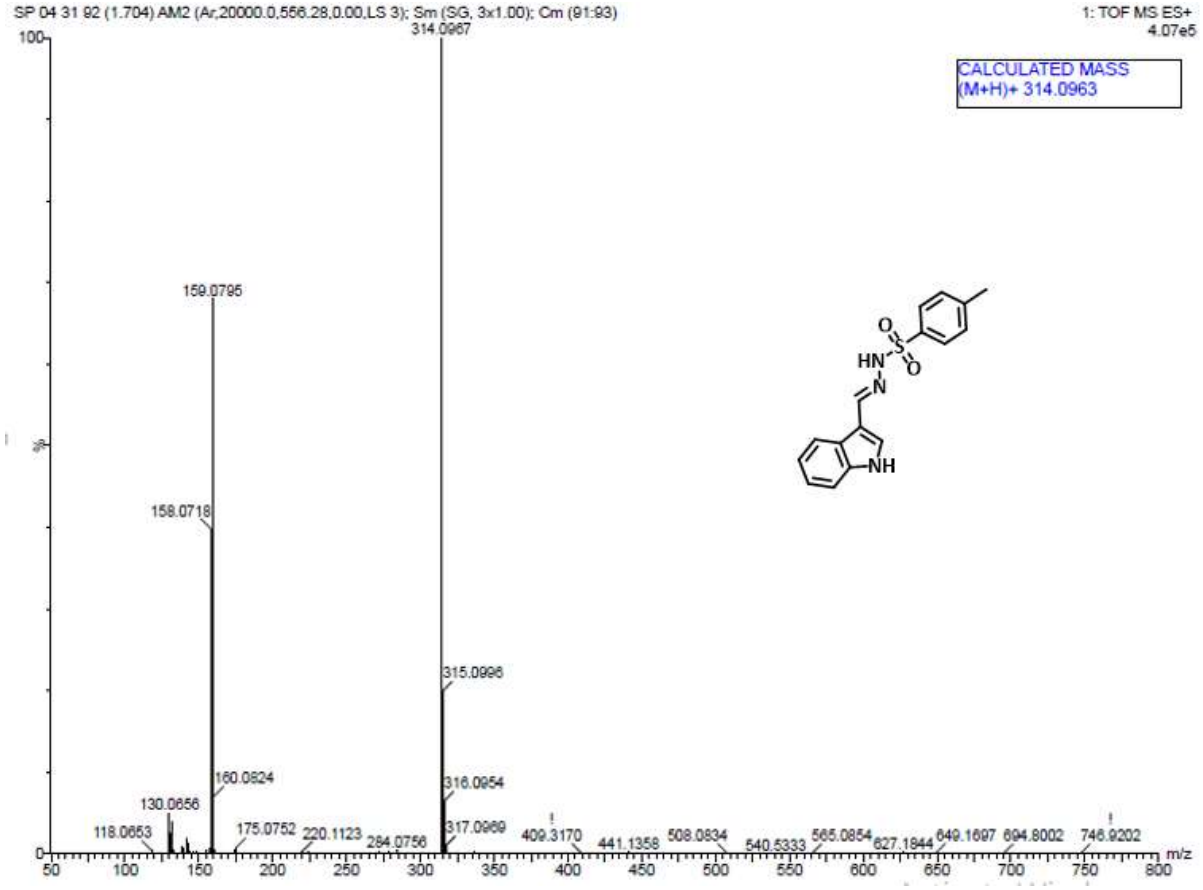

Figure C54: HRMS spectrum of compound 18.

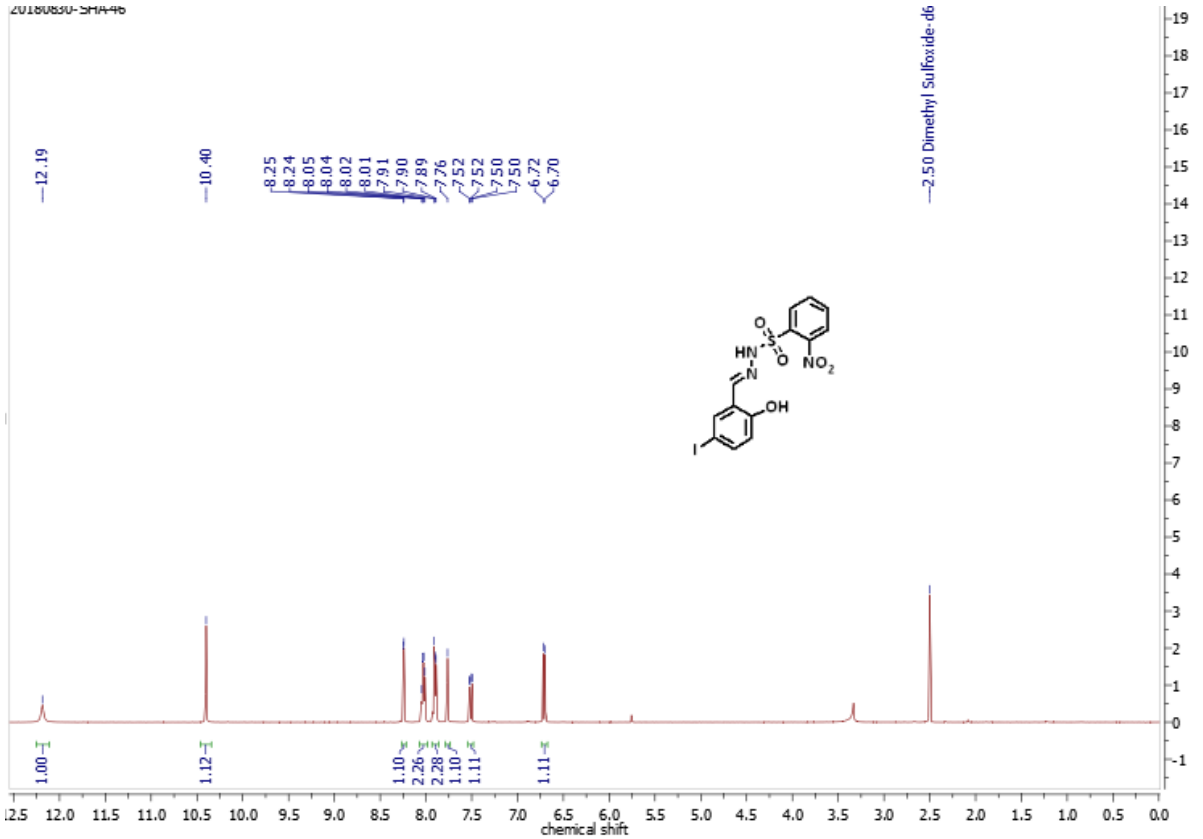

Figure C55: ^{1}H NMR spectrum of compound 19 in DMSO at 400 MHz.

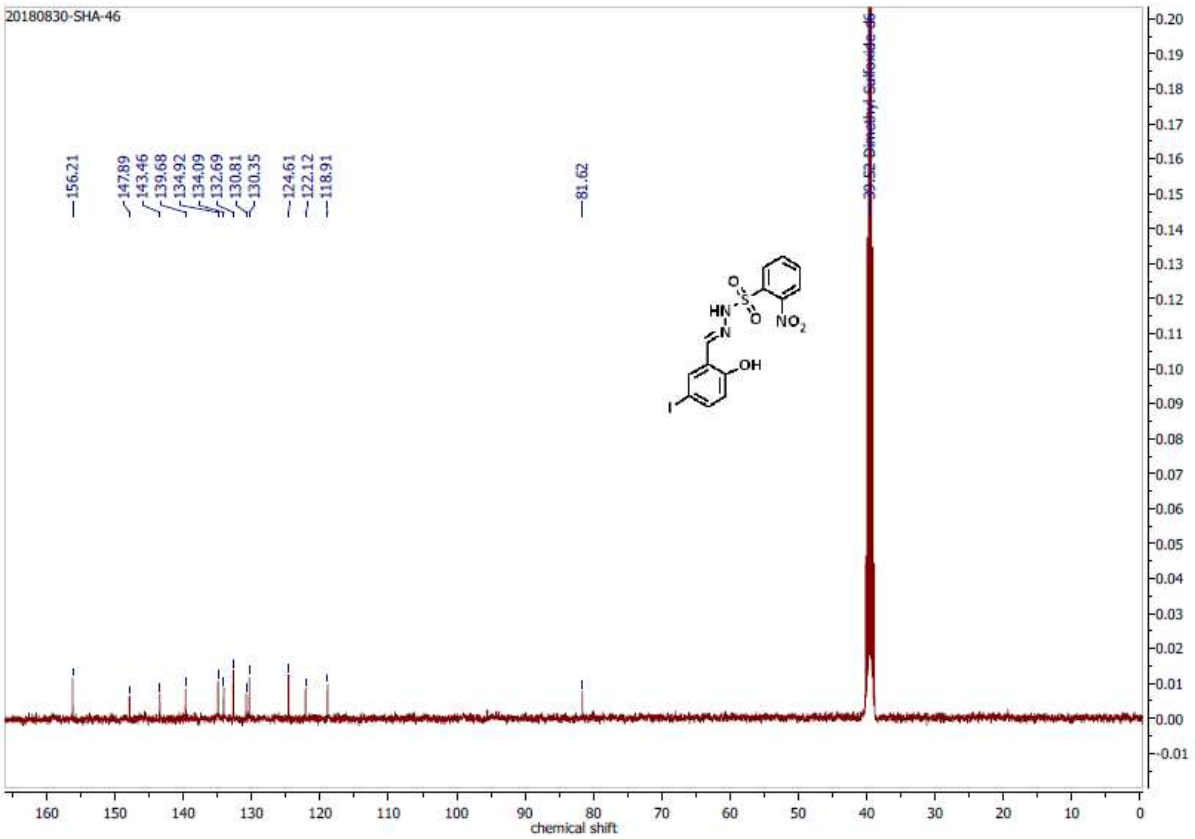

Figure C56: ^{13}C NMR spectrum of compound 19 in DMSO at 100 MHz.

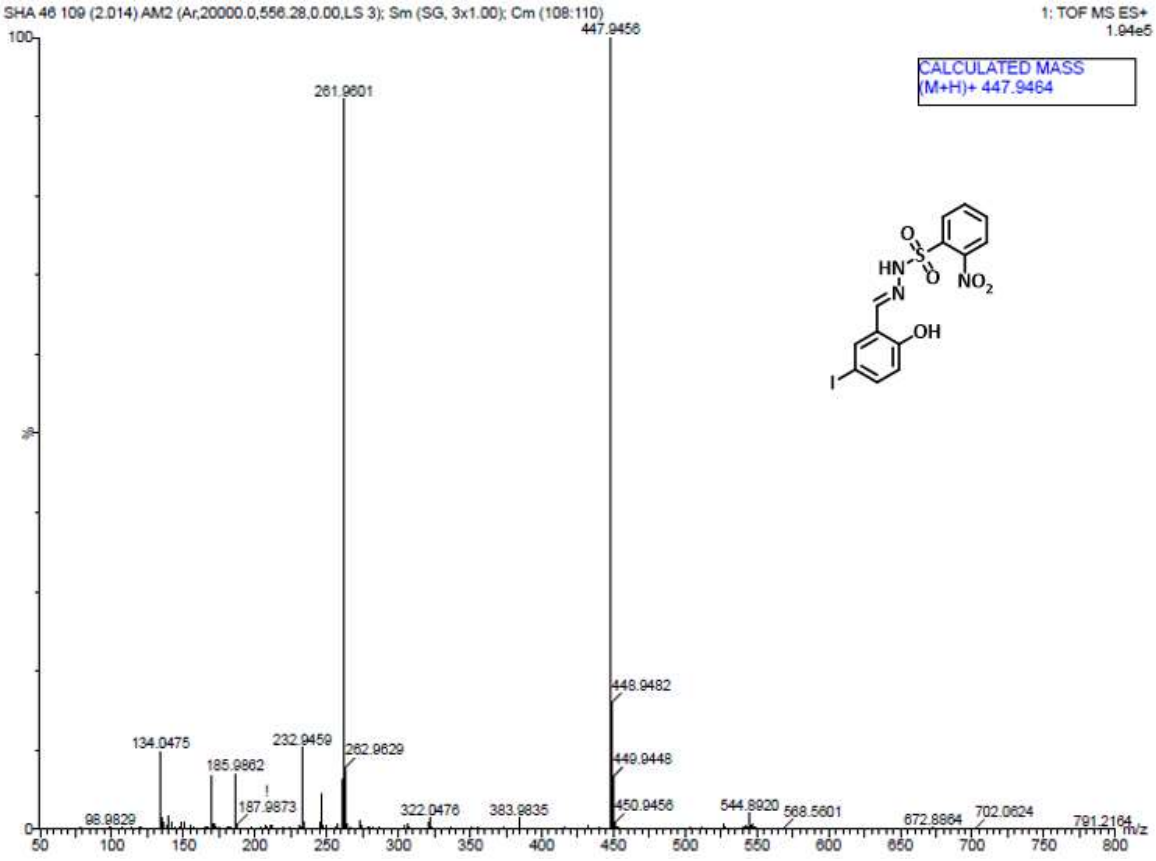

Figure C57: HRMS spectrum of compound 19.

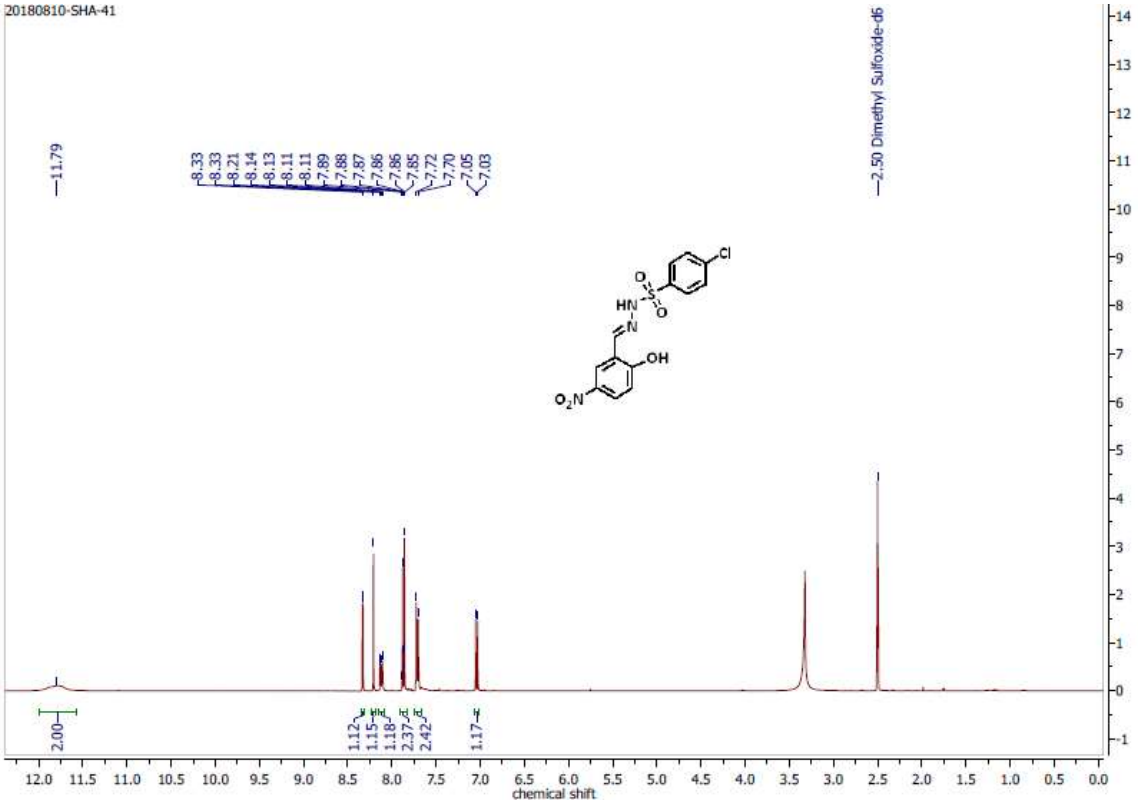

Figure C58: ^{1}H NMR spectrum of compound 20 in DMSO at 400 MHz.

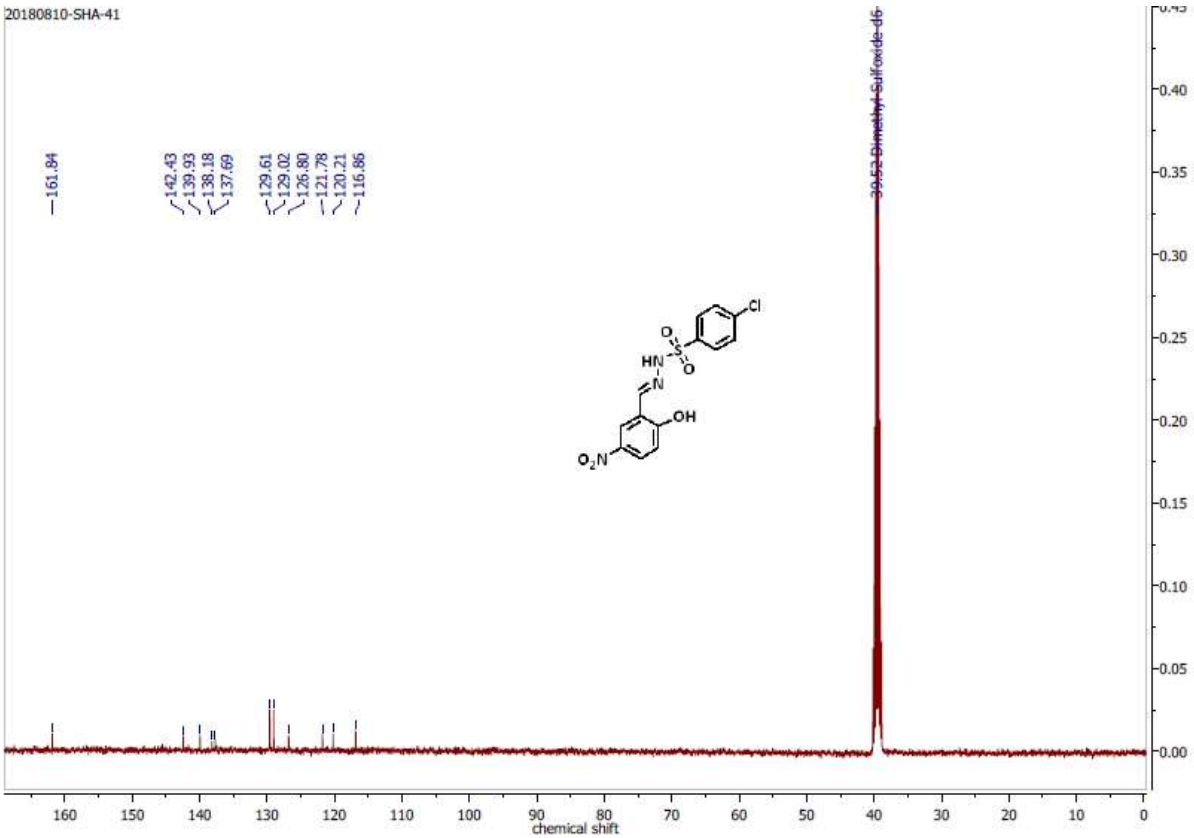

Figure C59: ^{13}C NMR spectrum of compound 20 in DMSO at 100 MHz.

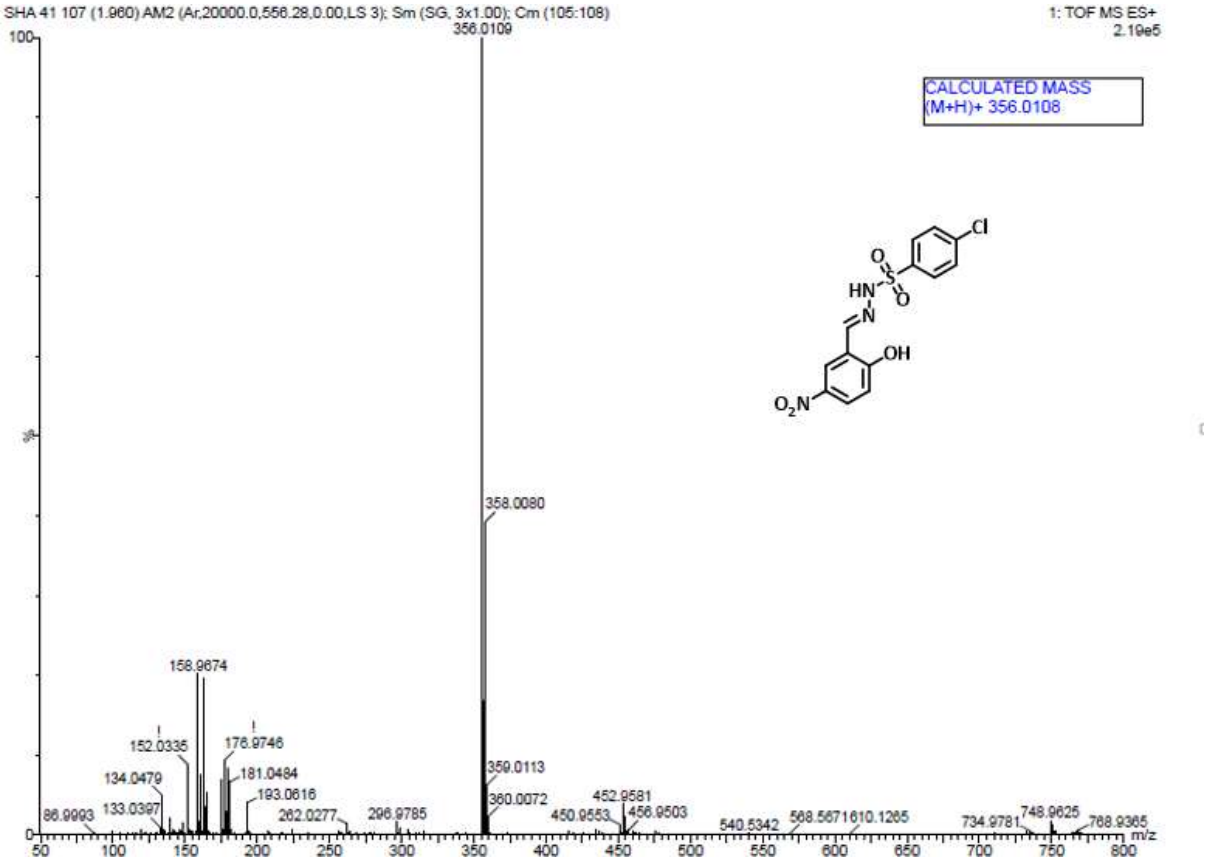

Figure C60: HRMS spectrum of compound 20.

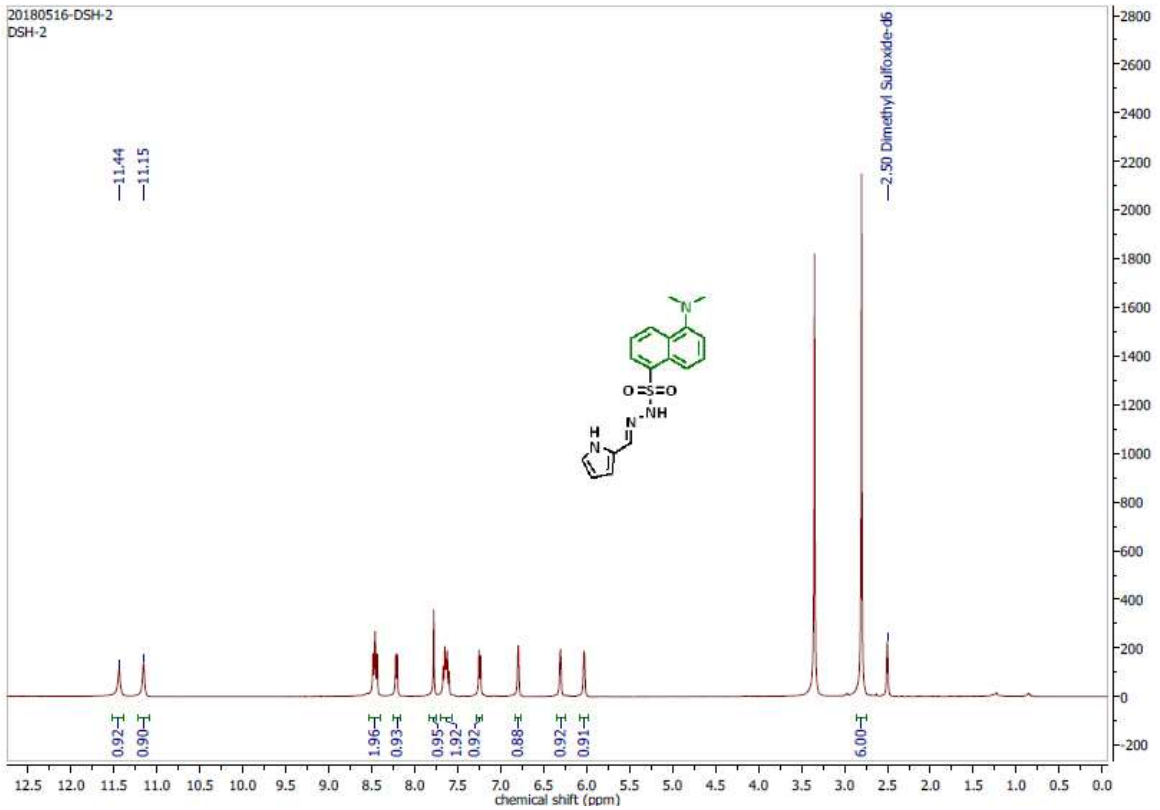

Figure C61: ^{1}H NMR spectrum of compound 21 in DMSO at 400 MHz.

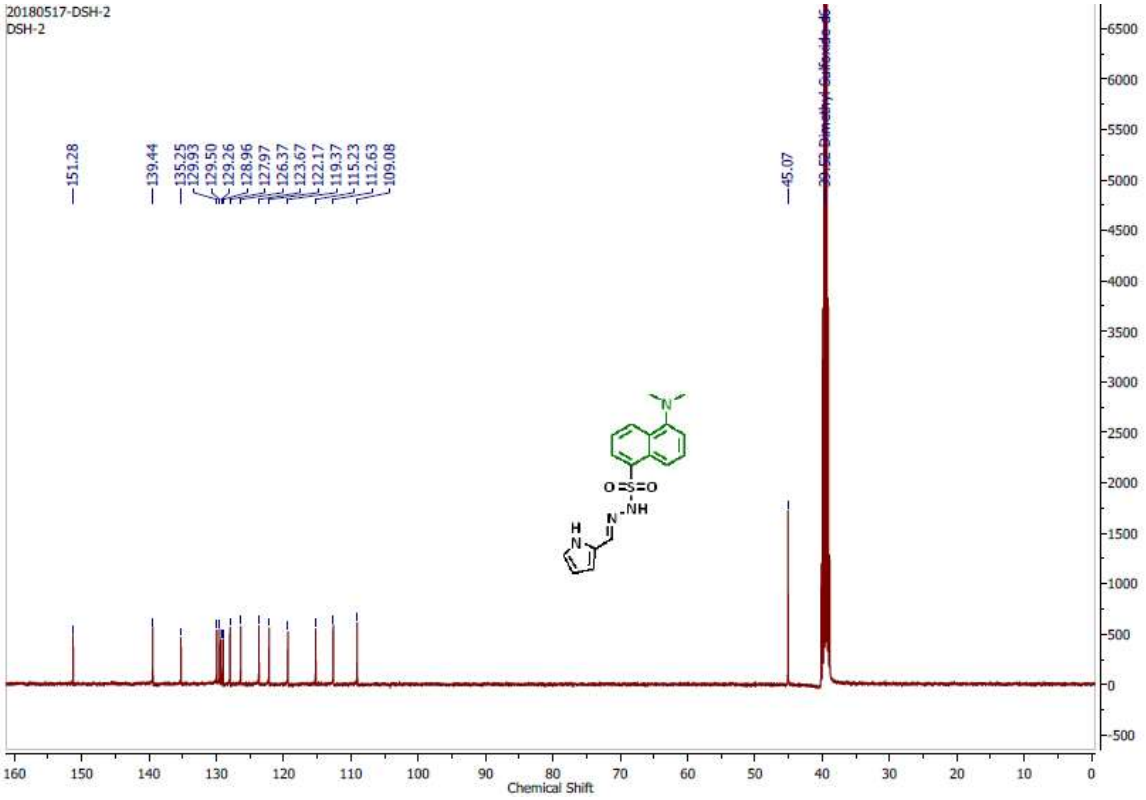

Figure C62: ^{13}C NMR spectrum of compound 21 in DMSO at 100 MHz.

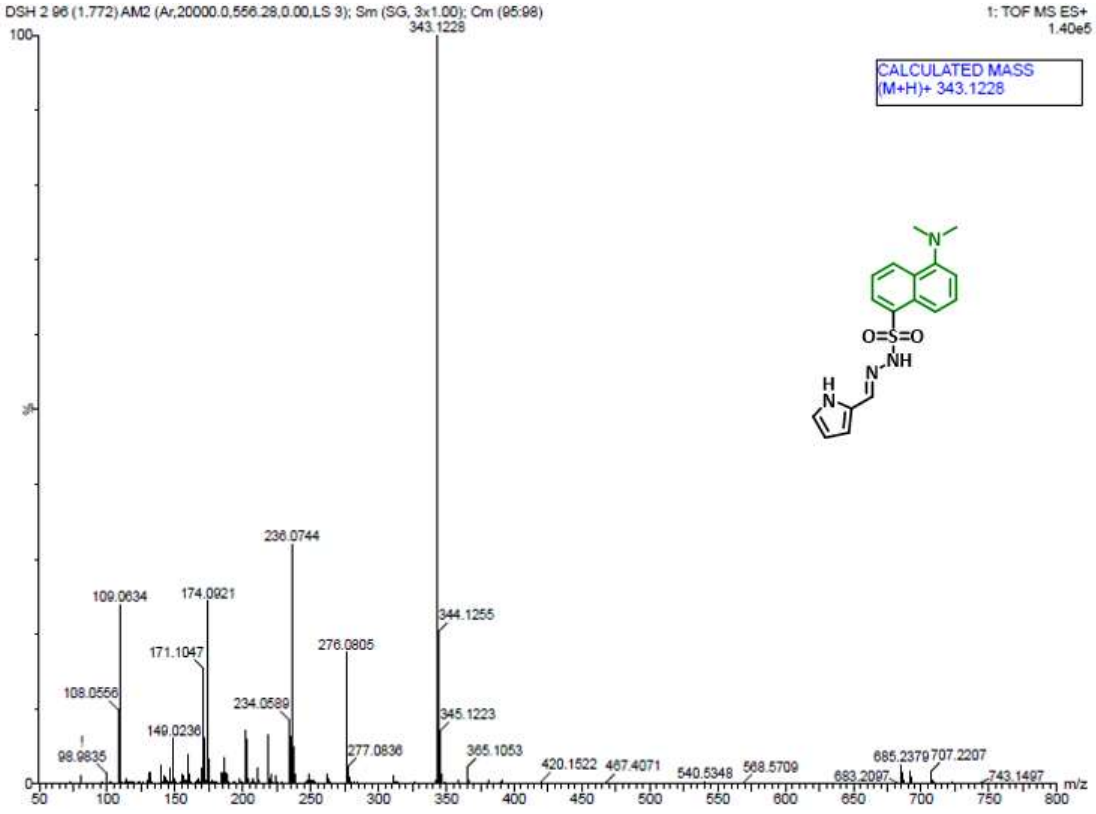

Figure C63: HRMS spectrum of compound 21.

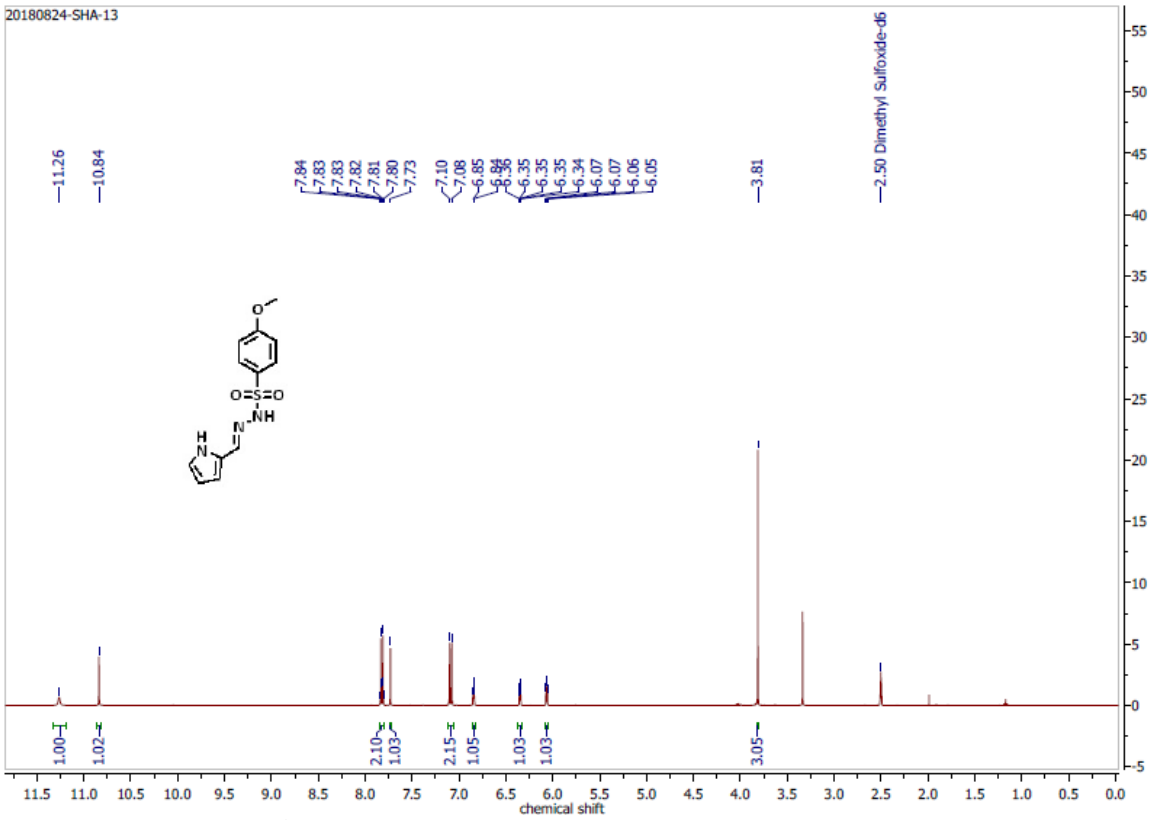

Figure C64: ^{1}H NMR spectrum of compound 22 in DMSO at 400 MHz.

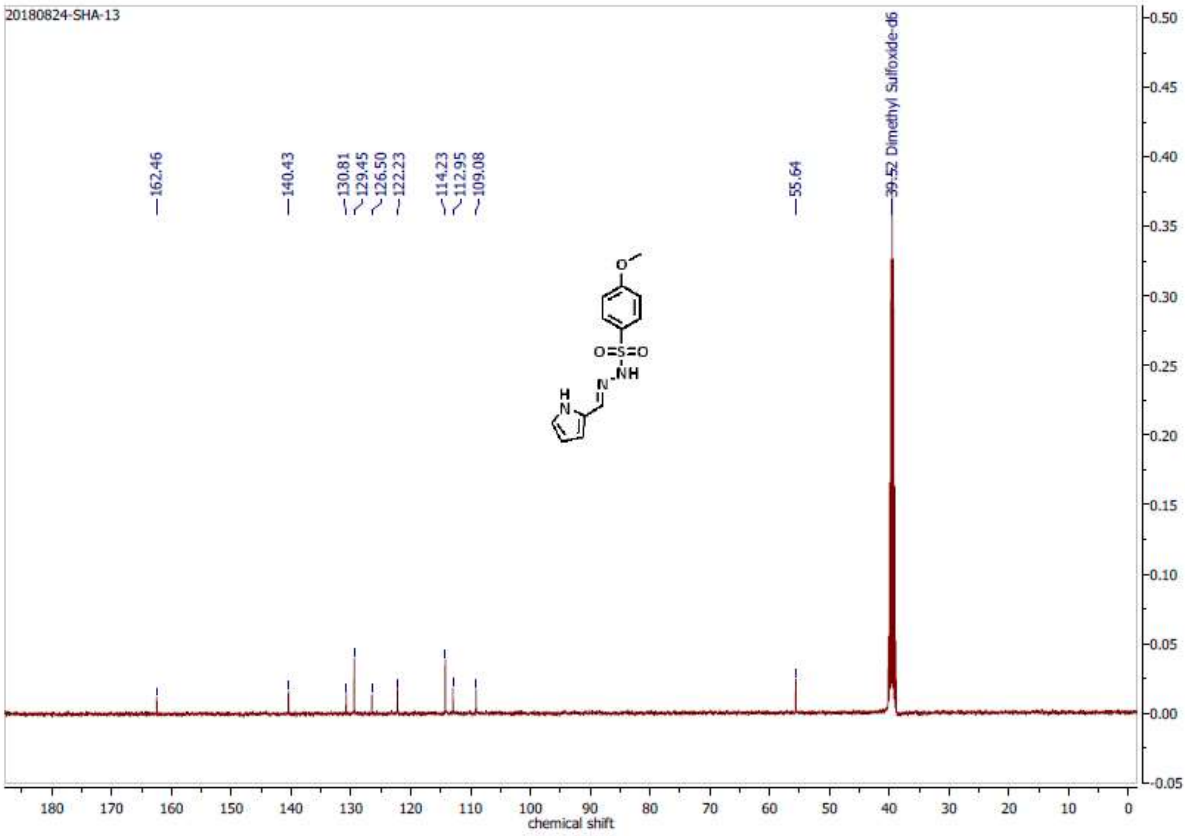

Figure C65: ^{13}C NMR spectrum of compound 22 in DMSO at 100 MHz.

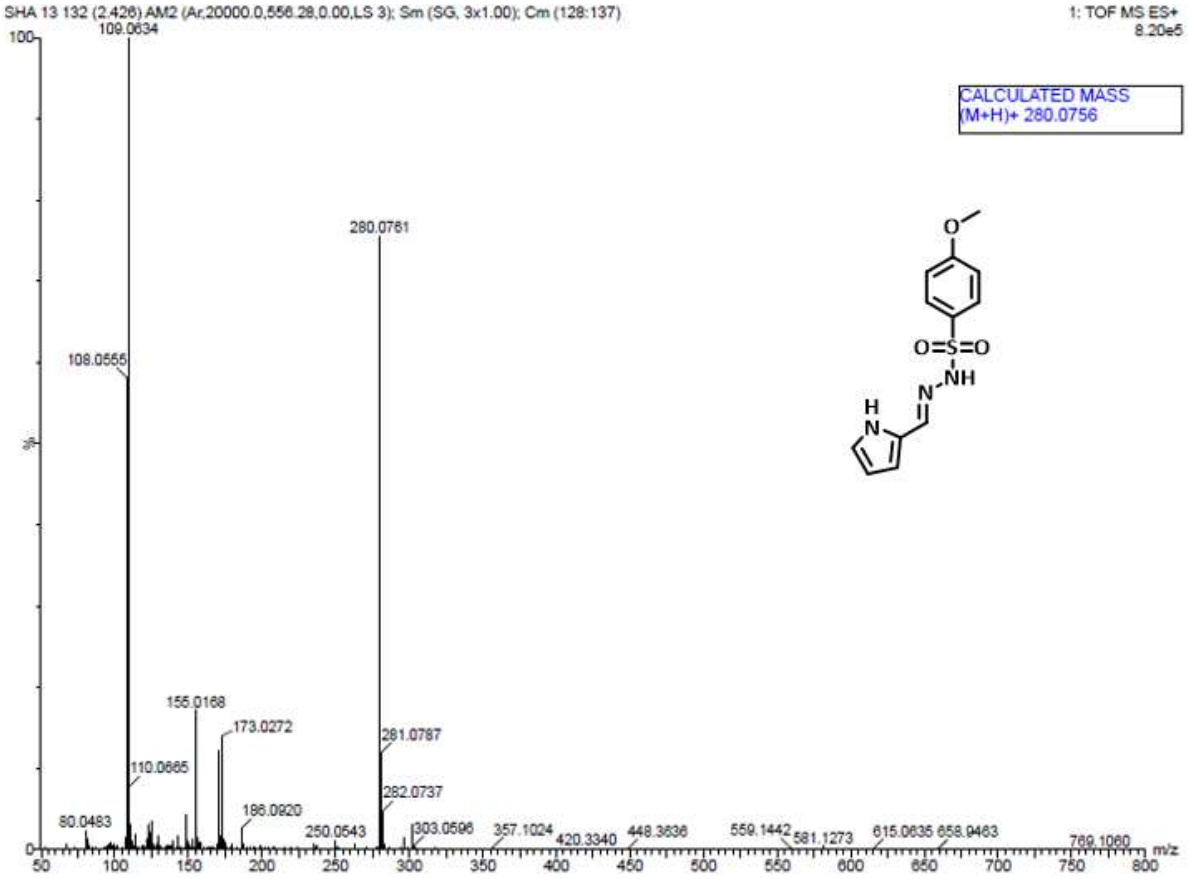

Figure C66: HRMS spectrum of compound 22.

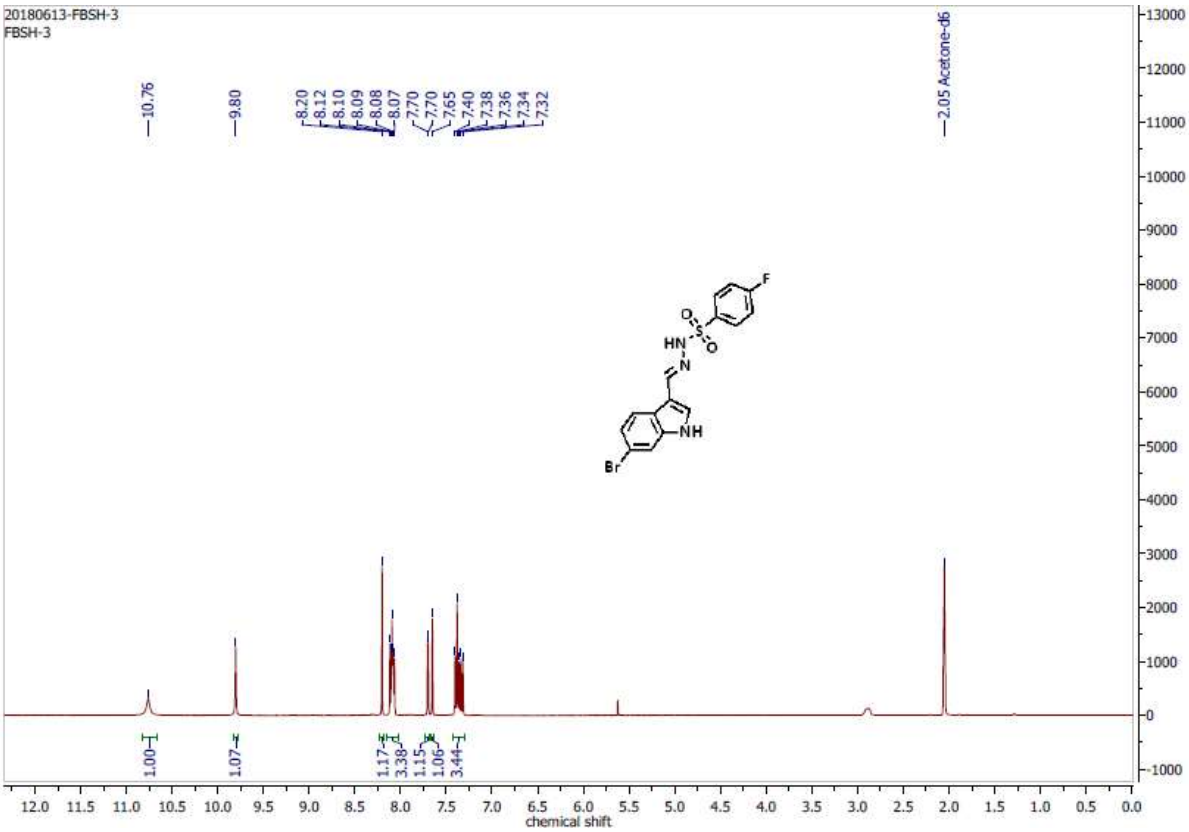

Figure C67: [1] H NMR spectrum of compound 23 in DMSO at 400 MHz.

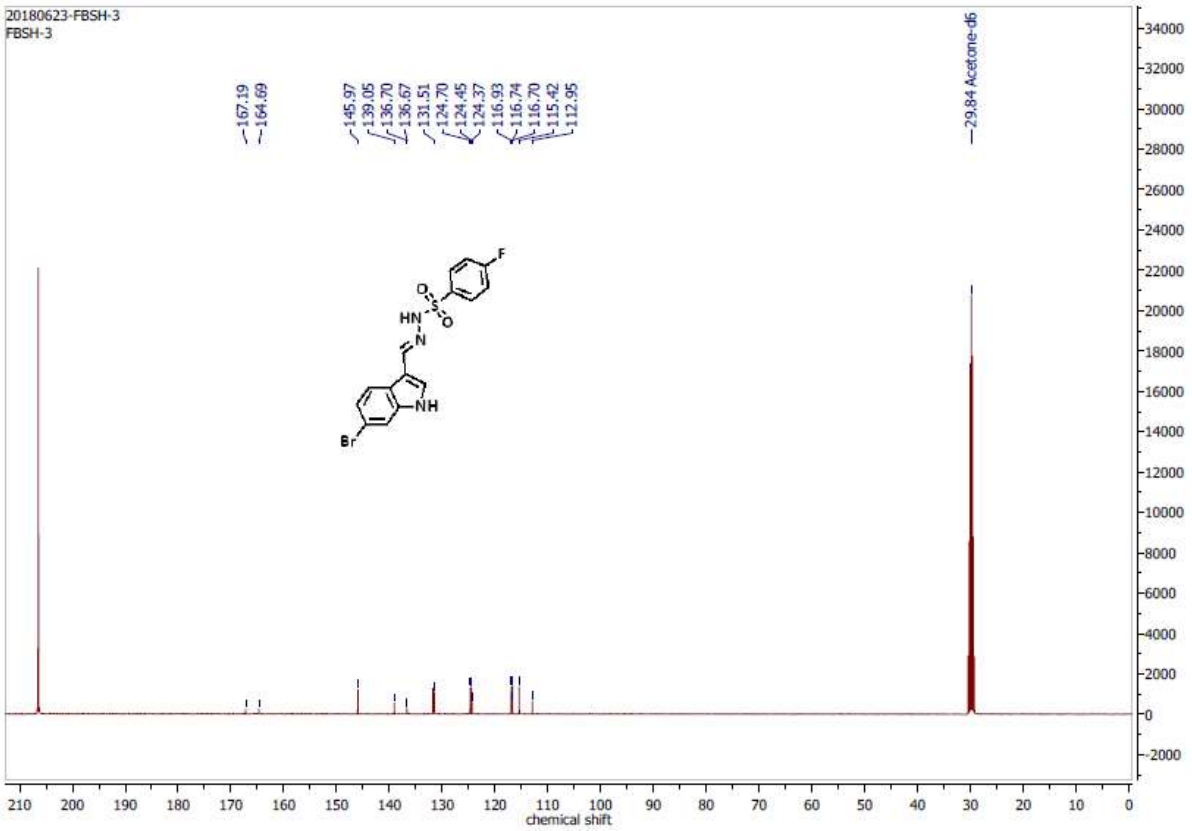

Figure C68: ^{13}C NMR spectrum of compound 23 in DMSO at 100 MHz.

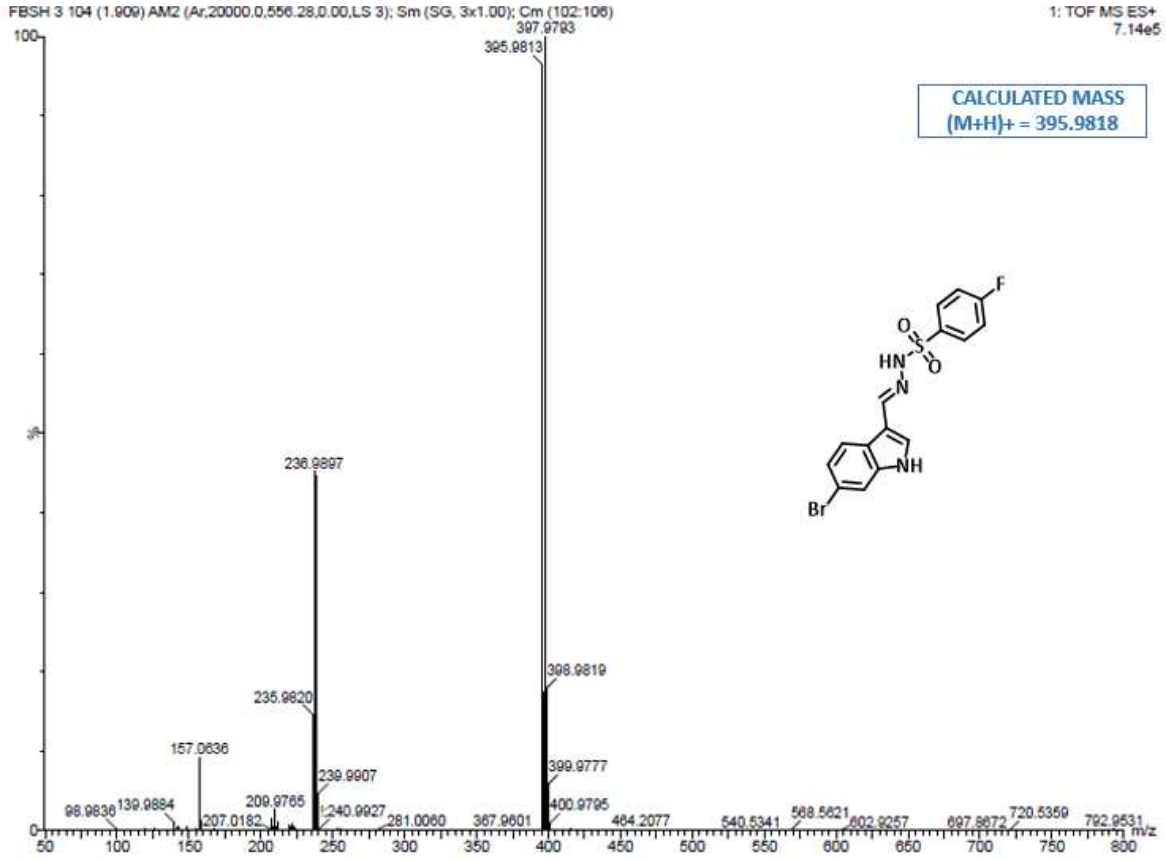

Figure C69: HRMS spectrum of compound 23.

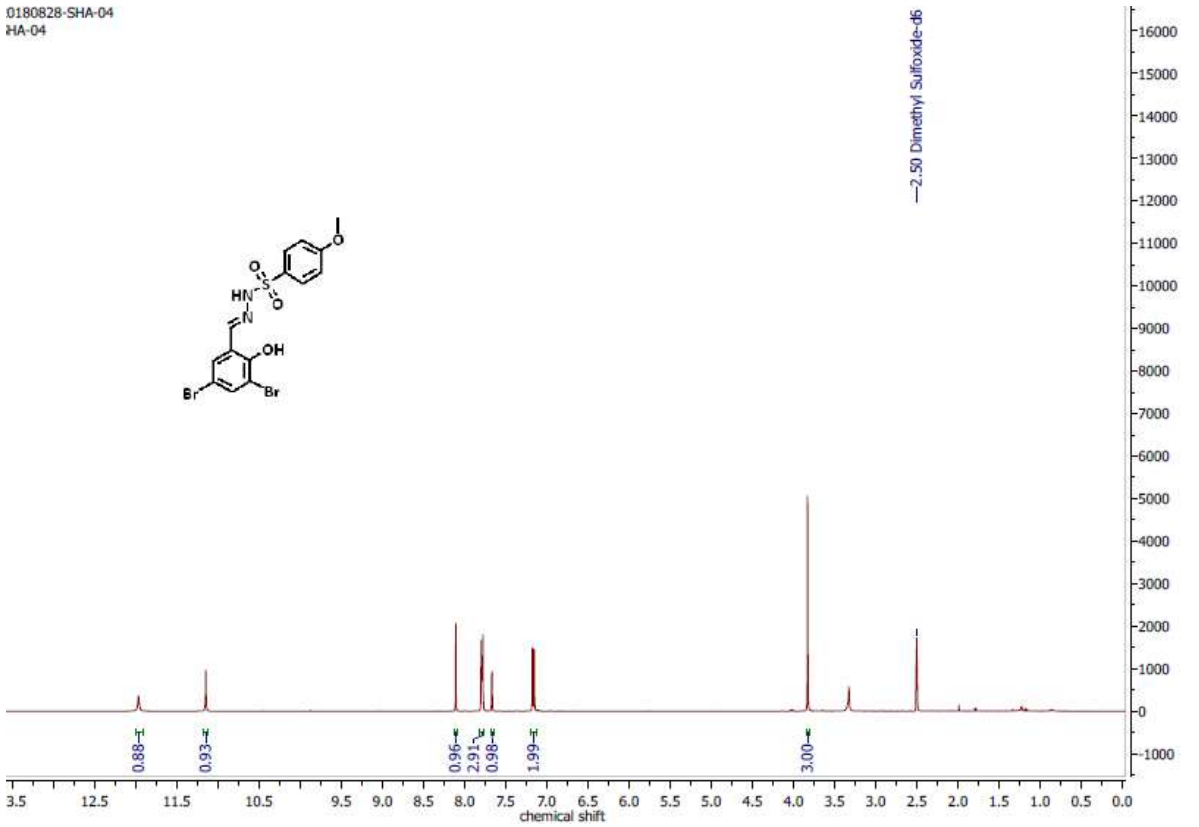

Figure C70: [1] H NMR spectrum of compound 24 in DMSO at 400 MHz.

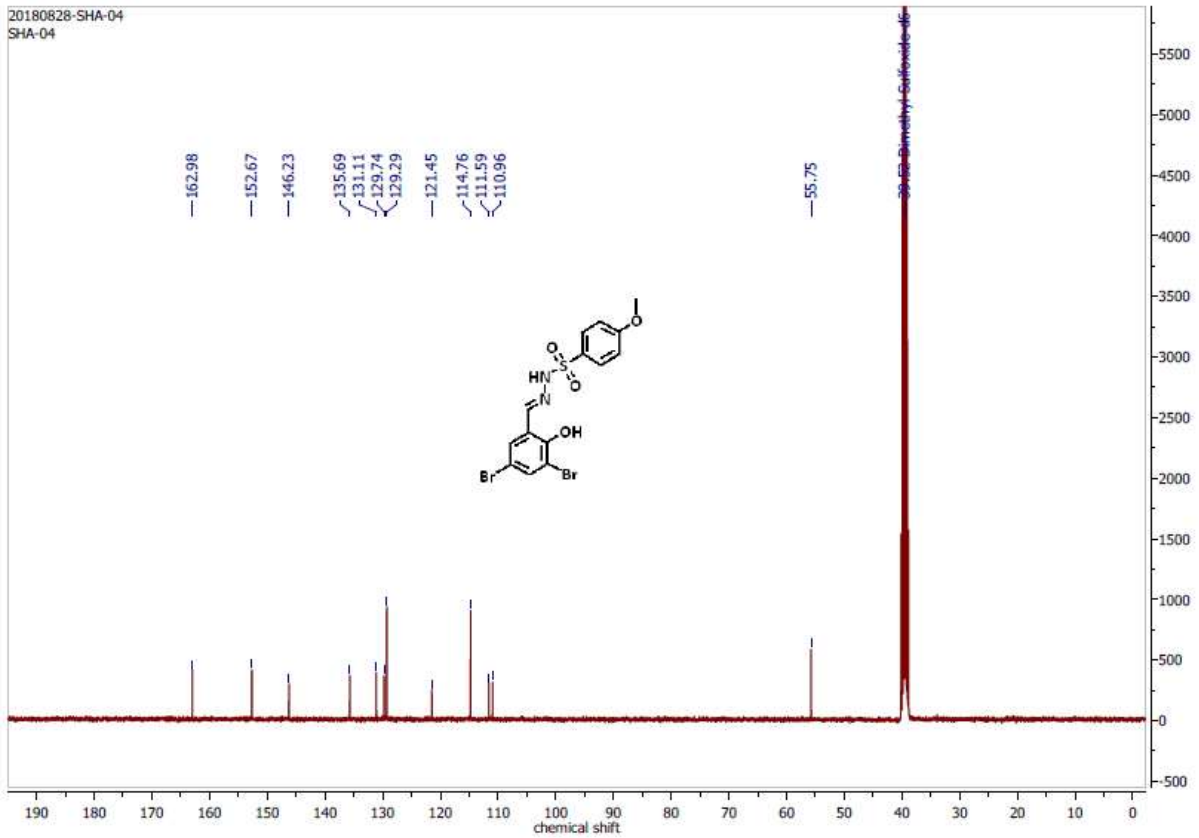

Figure C71: [13]C NMR spectrum of compound 24 in DMSO at 100 MHz.

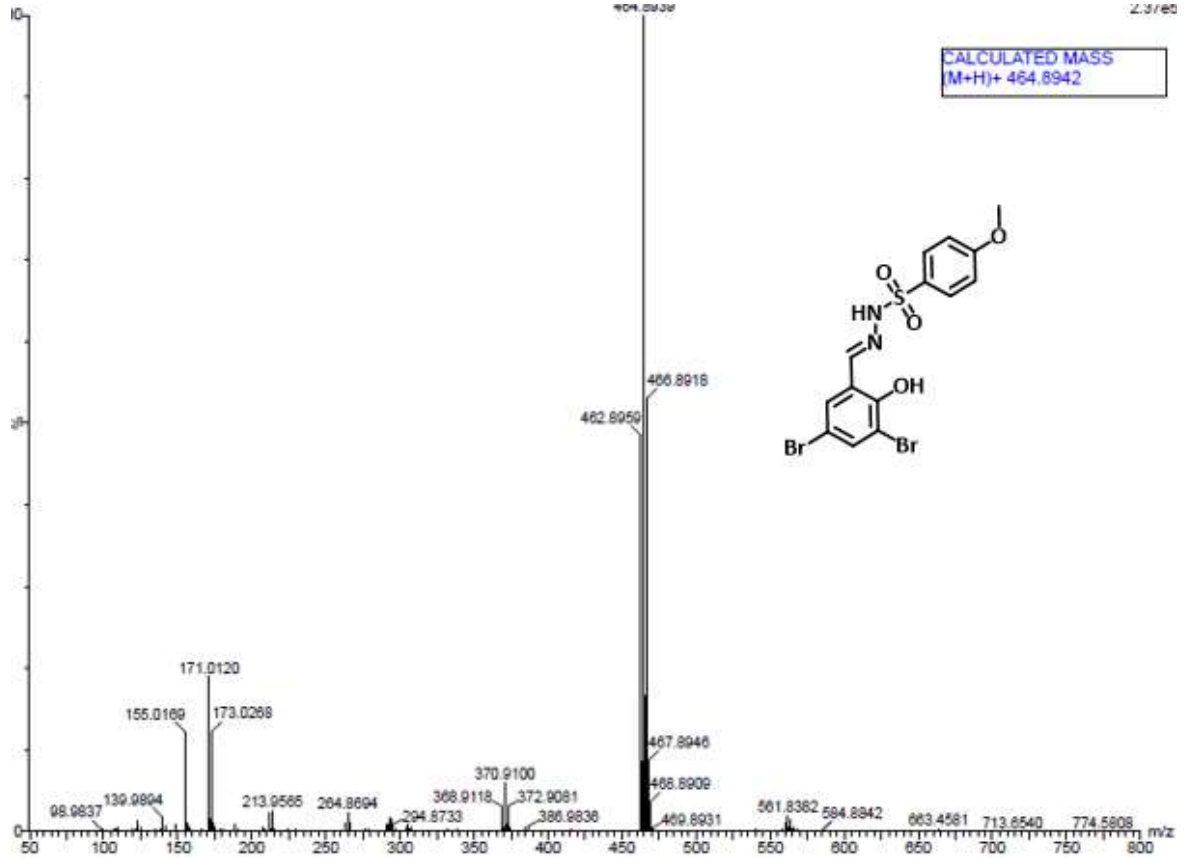

Figure C72: HRMS spectrum of compound 24.

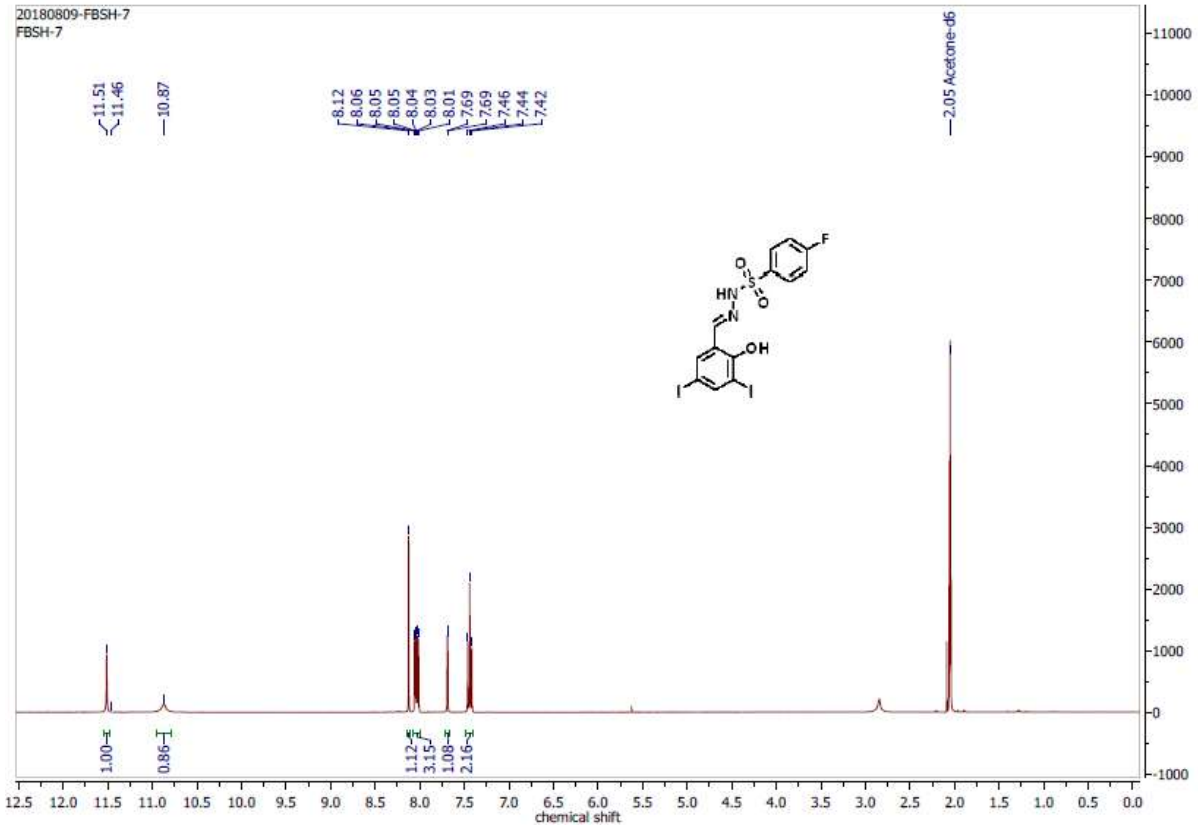

Figure C73: ^{1}H NMR spectrum of compound 25 in Acetone at 400 MHz.

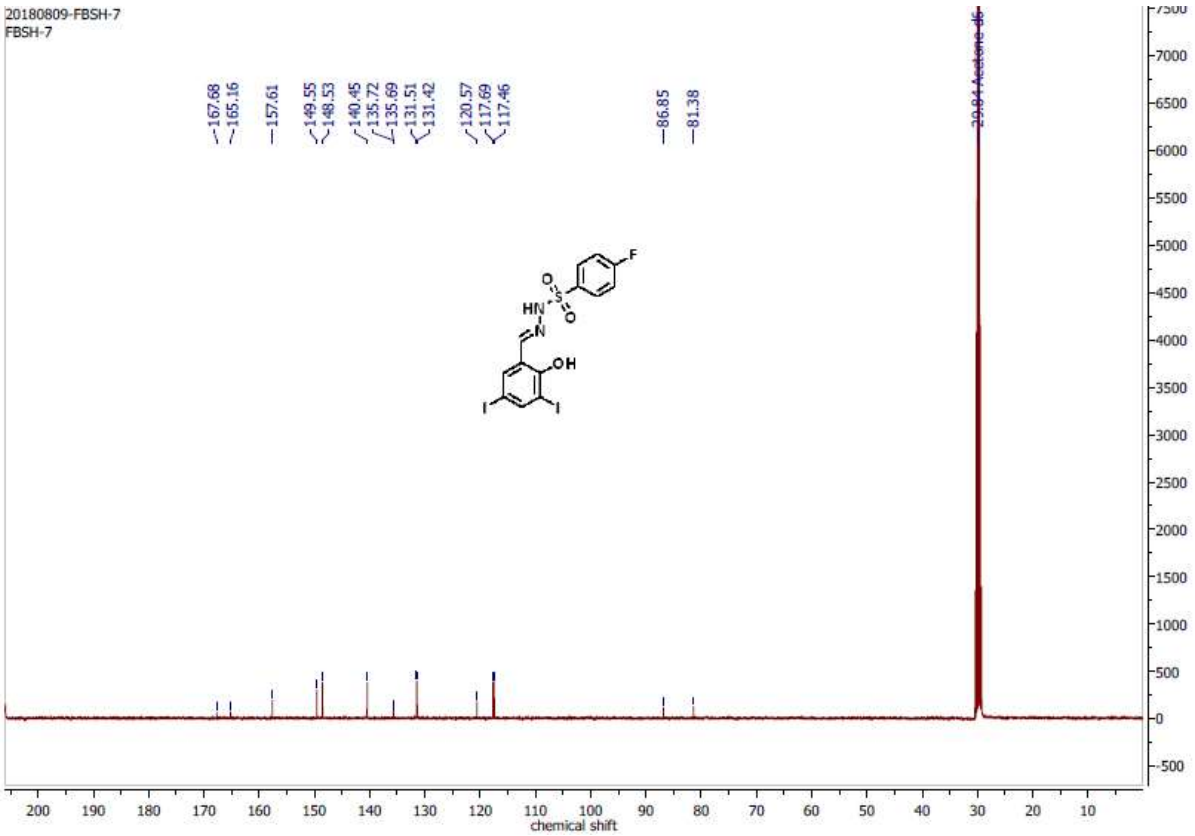

Figure C74: ^{13}C NMR spectrum of compound 25 in Acetone at 100 MHz.

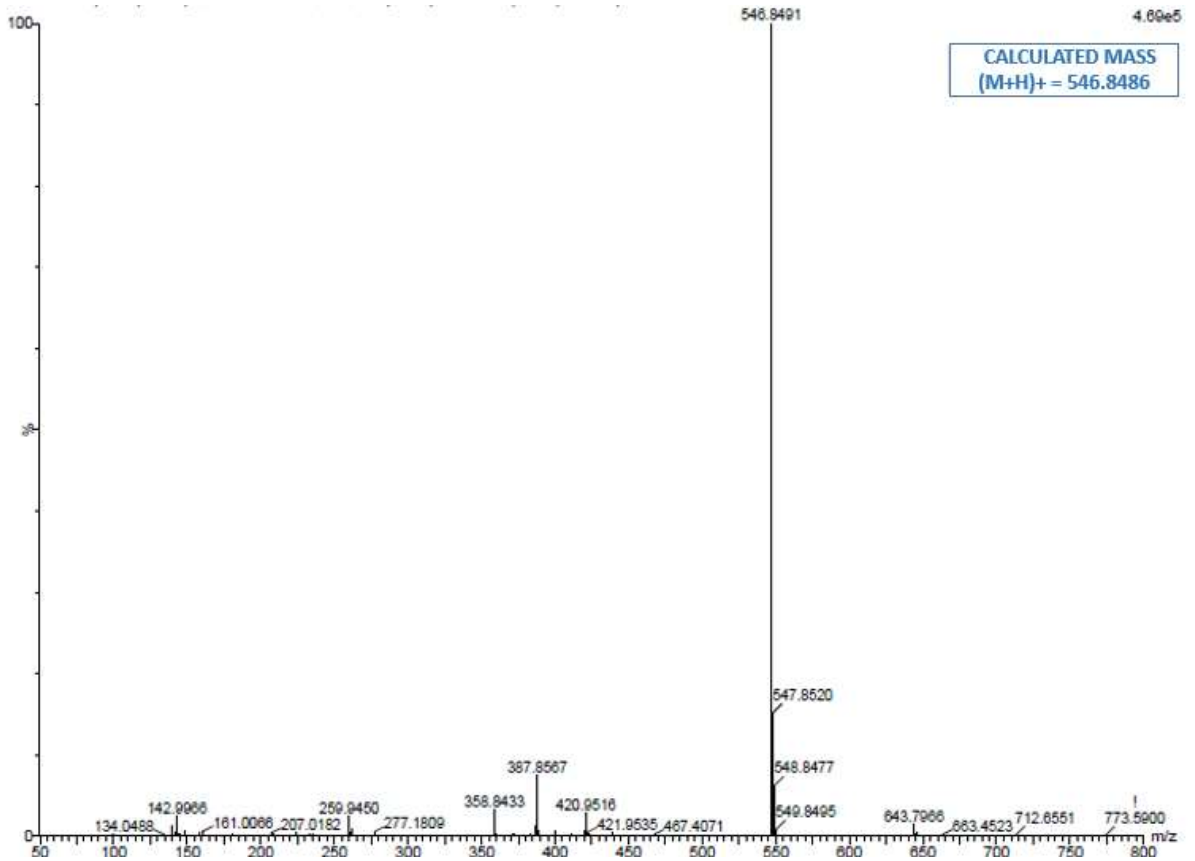

Figure C75: HRMS spectrum of compound 25.

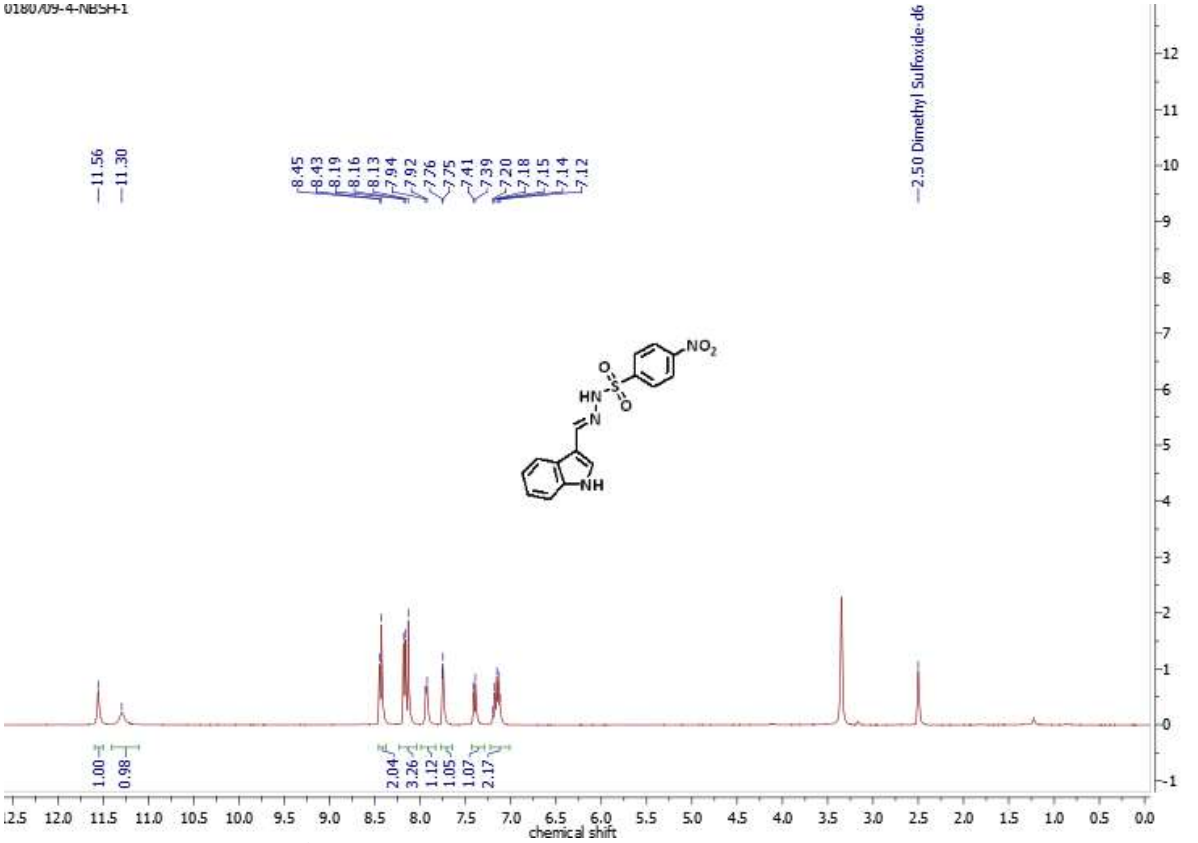

Figure C76: [1] H NMR spectrum of compound 26 in DMSO at 400 MHz.

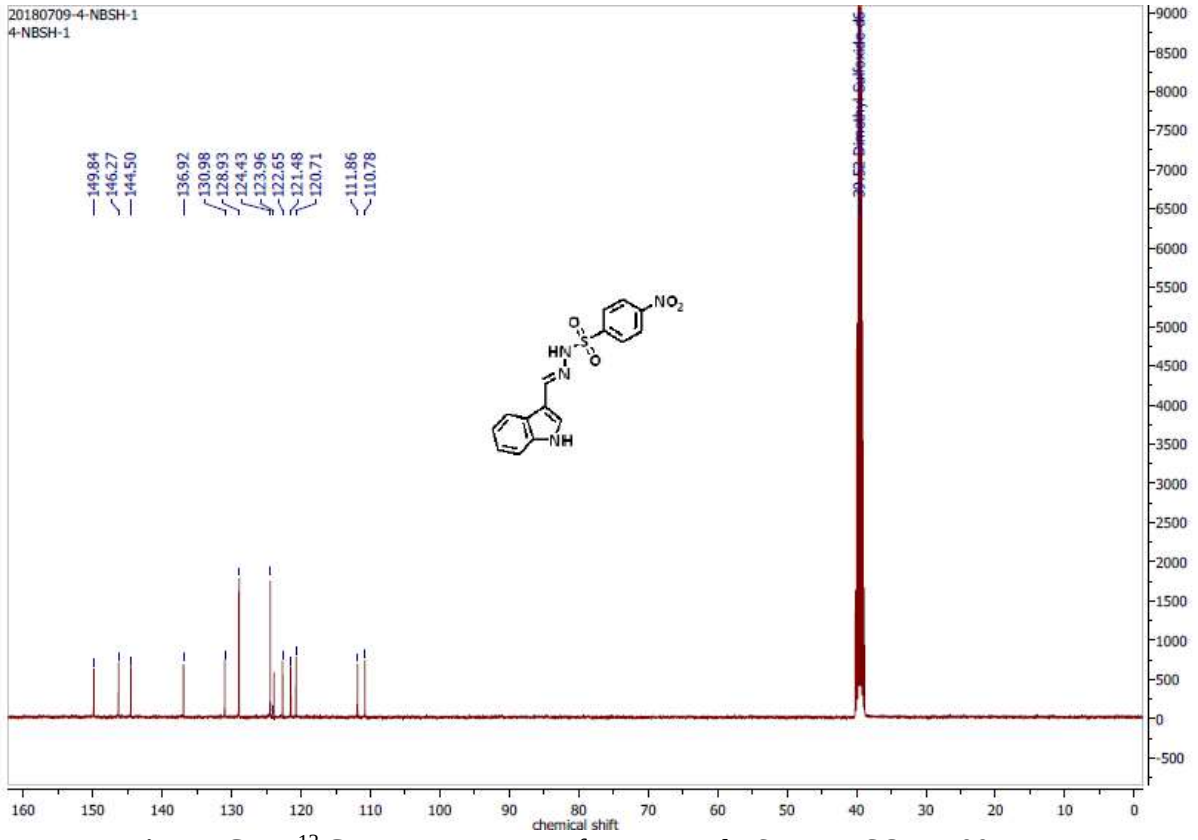

Figure C77: [13] C NMR spectrum of compound 26 in DMSO at 100 MHz.

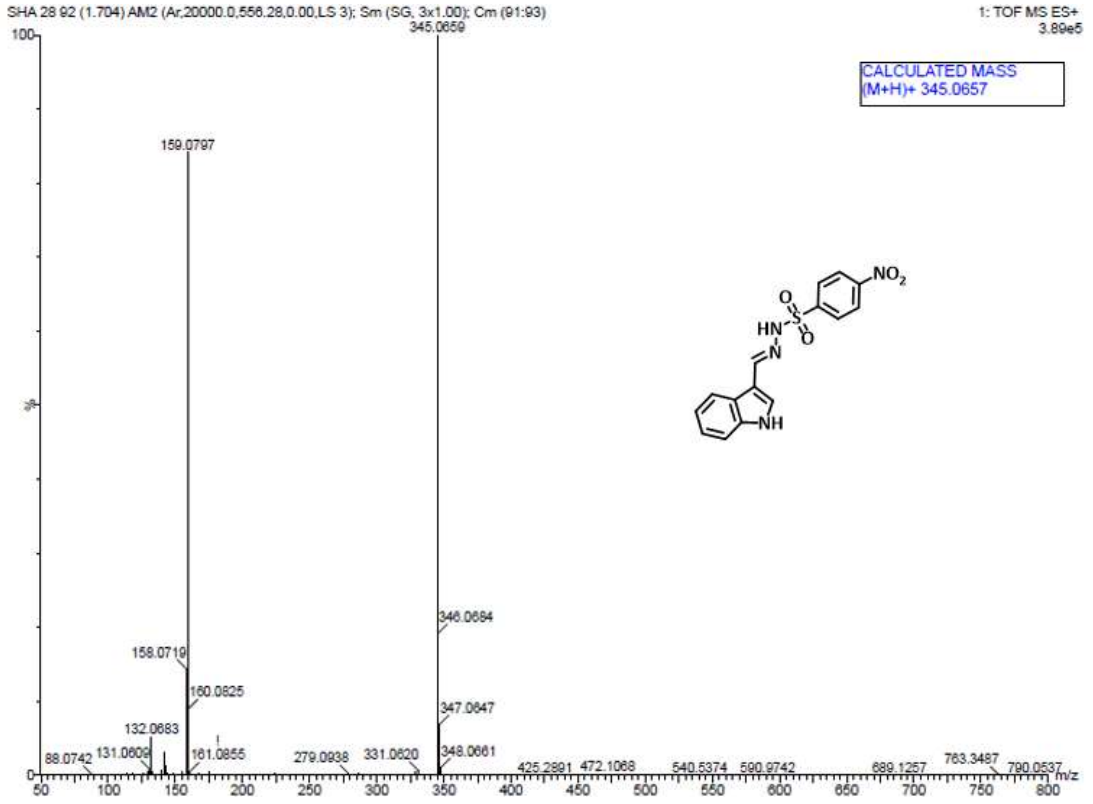

Figure C78: HRMS spectrum of compound 26.

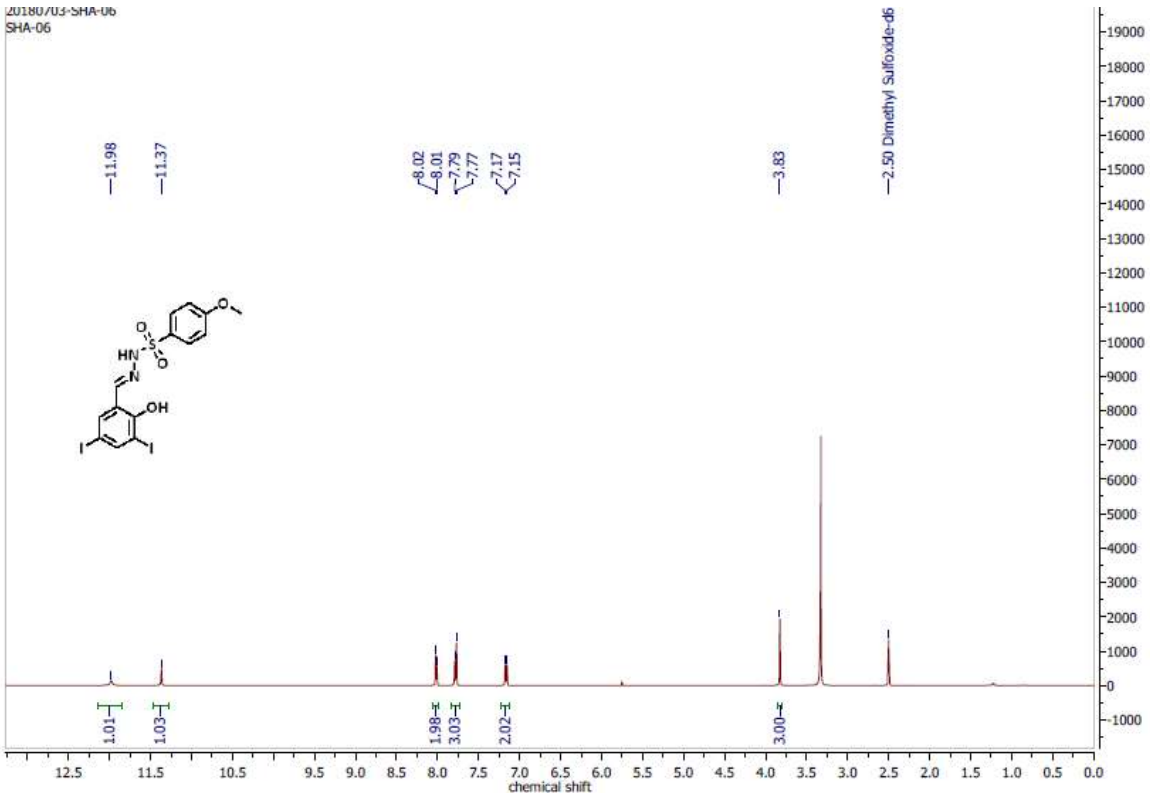

Figure C79: [1] H NMR spectrum of compound 27 in DMSO at 400 MHz.

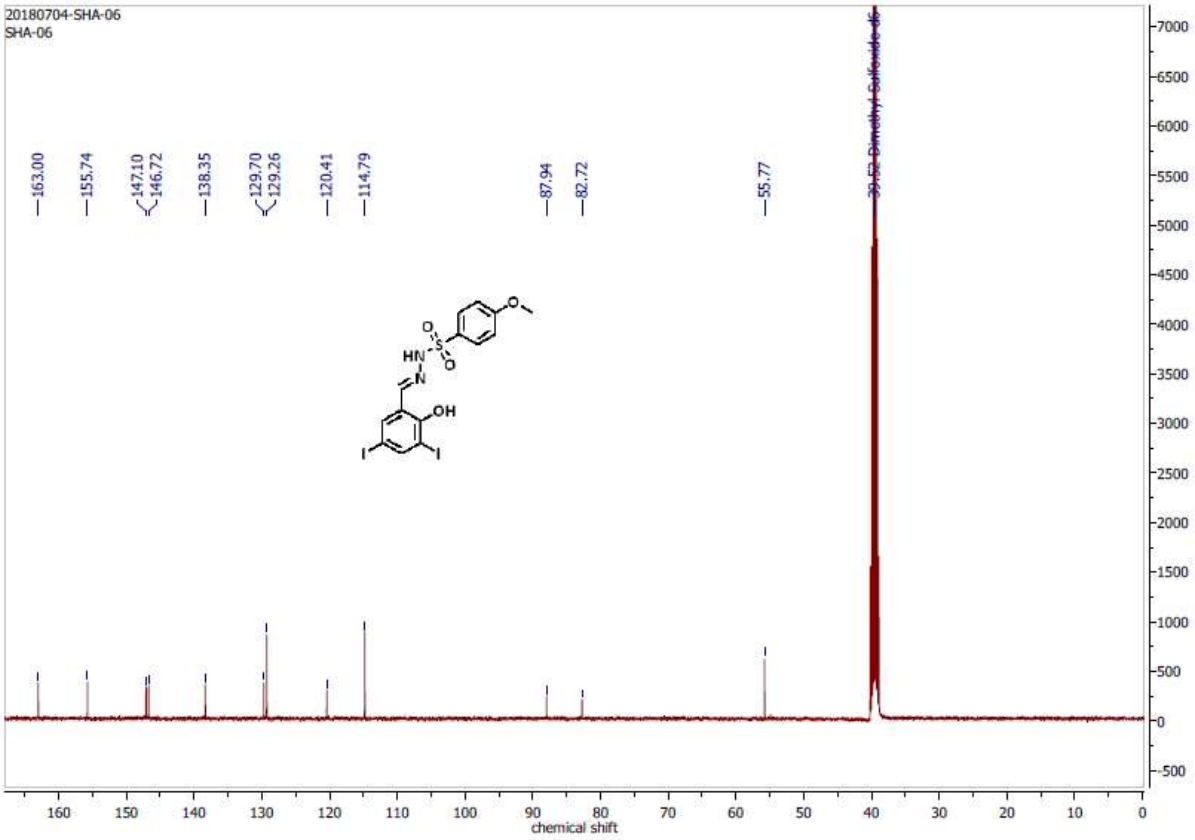

Figure C80: [13] CNMR spectrum of compound 27 in DMSO at 100 MHz.

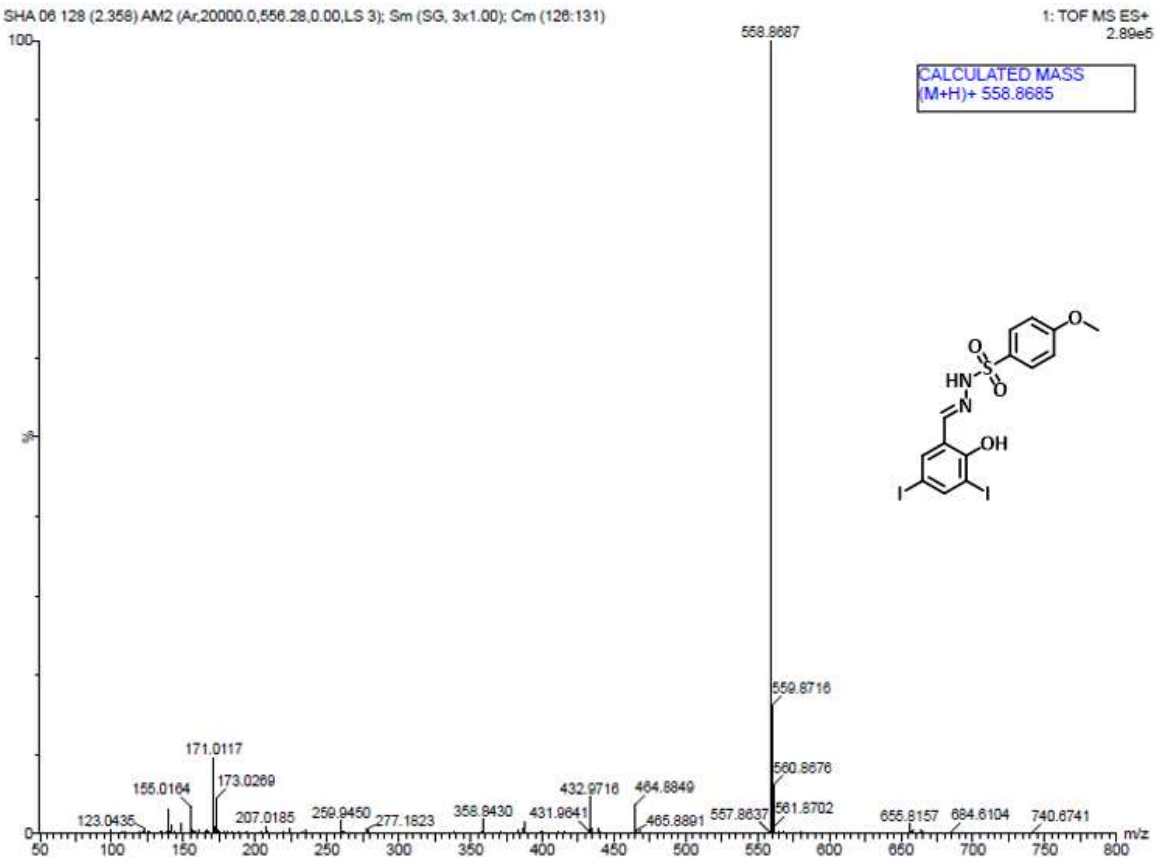

Figure C81: HRMS spectrum of compound 27.

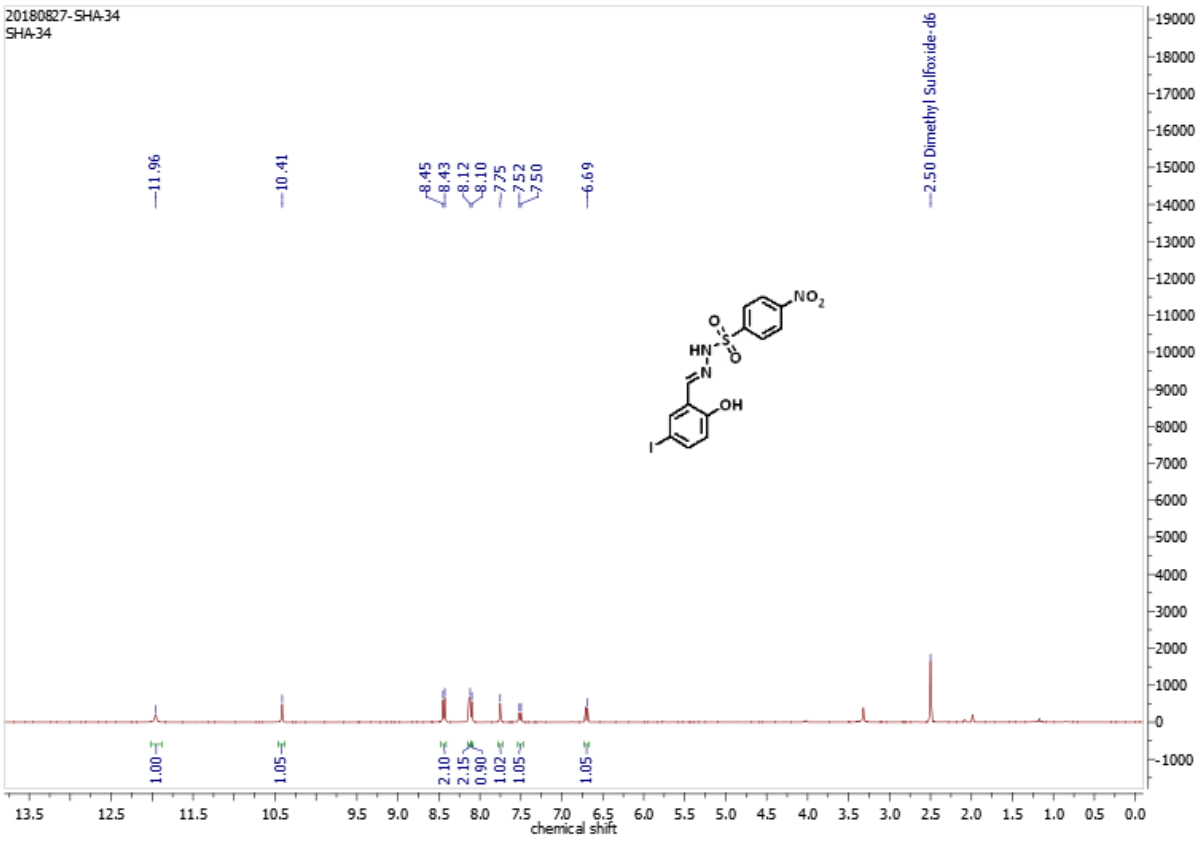

Figure C82: [1] H NMR spectrum of compound 28 in DMSO at 400 MHz.

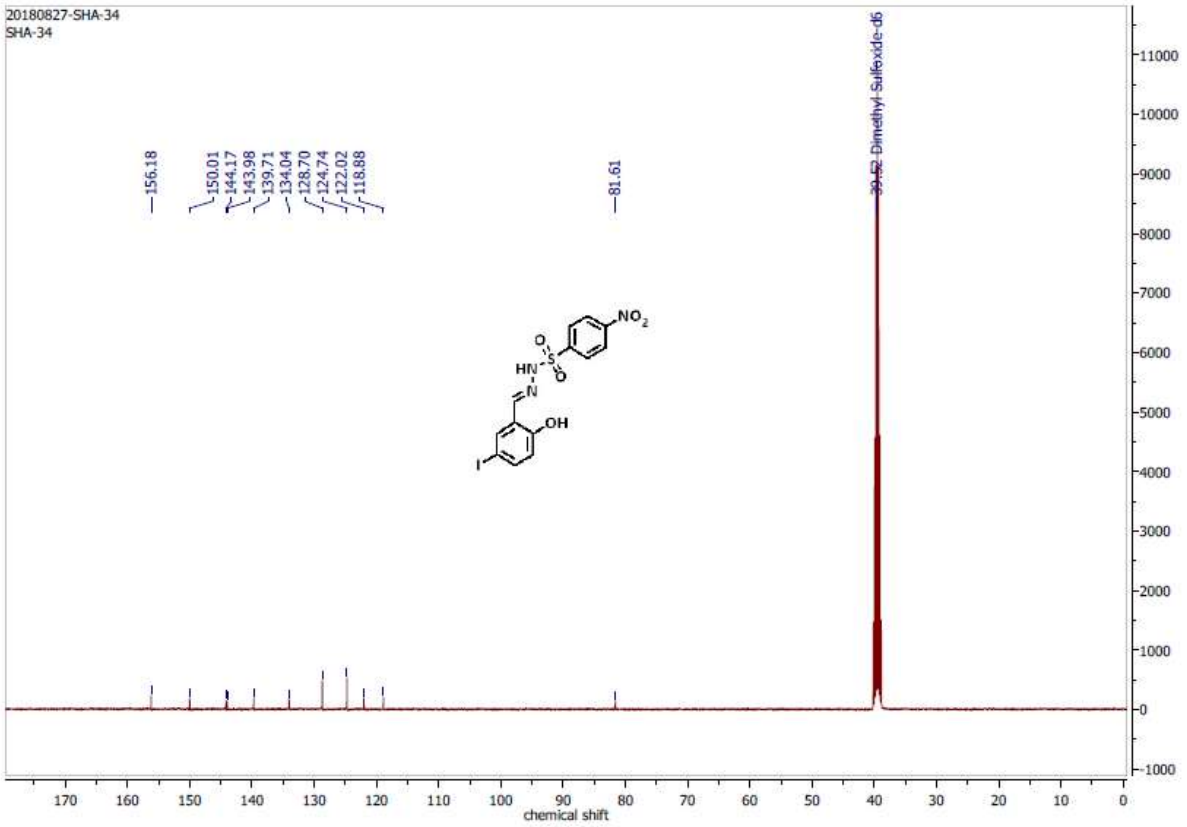

Figure C83: [13] C NMR spectrum of compound 28 in DMSO at 100 MHz.

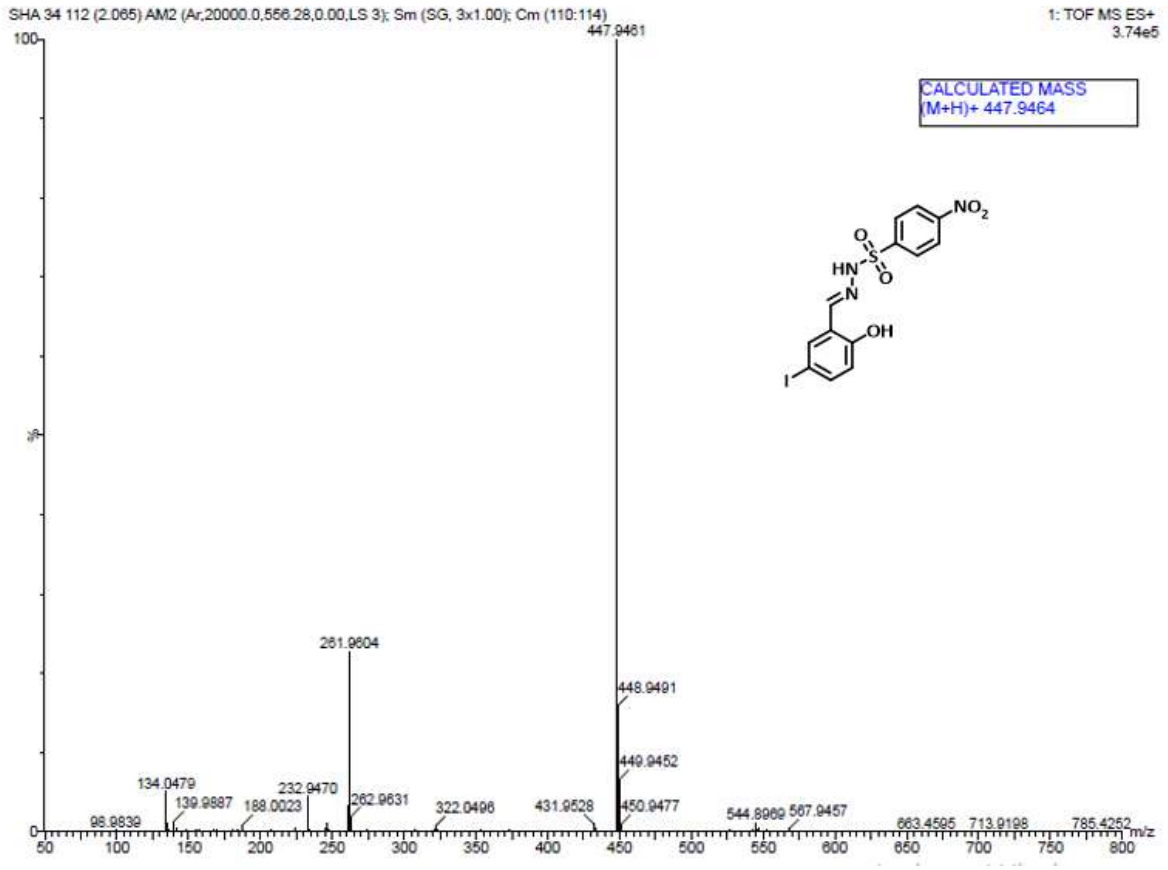

Figure C84: HRMS spectrum of compound 28.

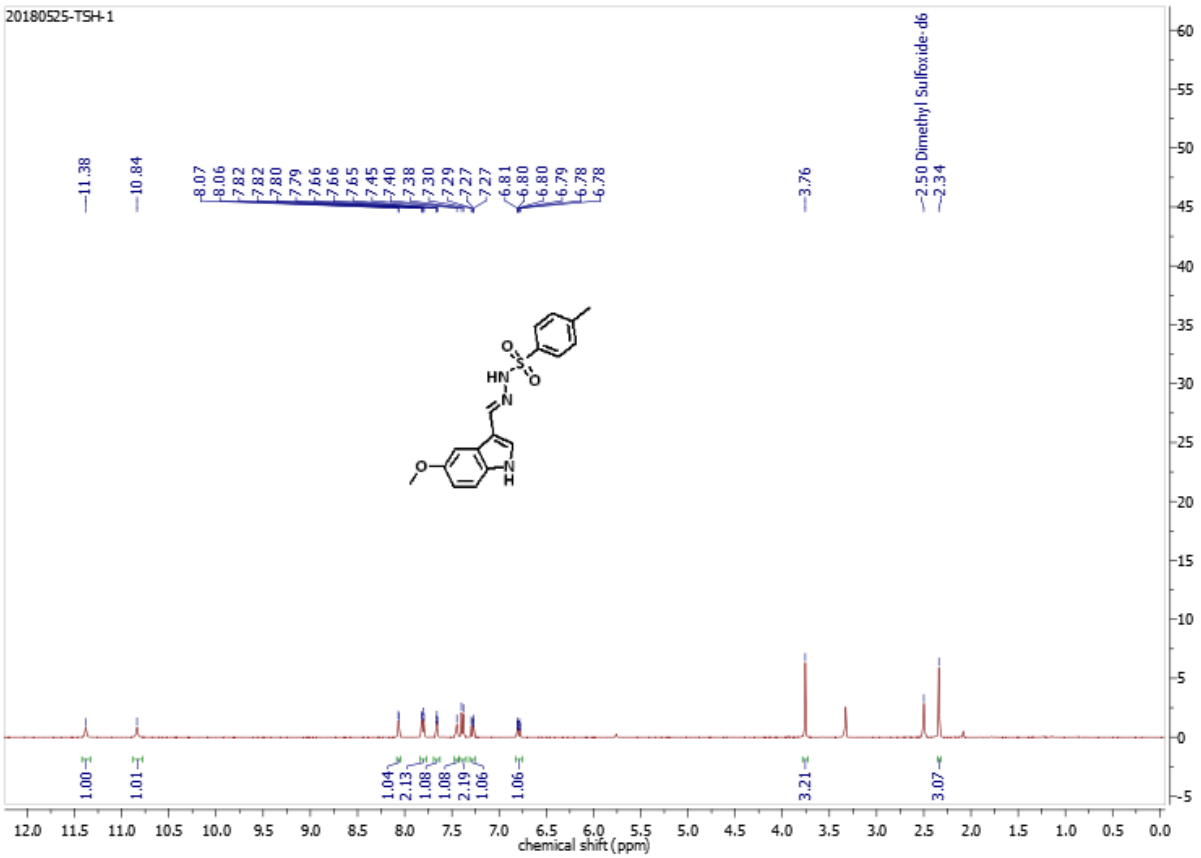

Figure C85: [1] H NMR spectrum of compound 29 in DMSO at 400 MHz.

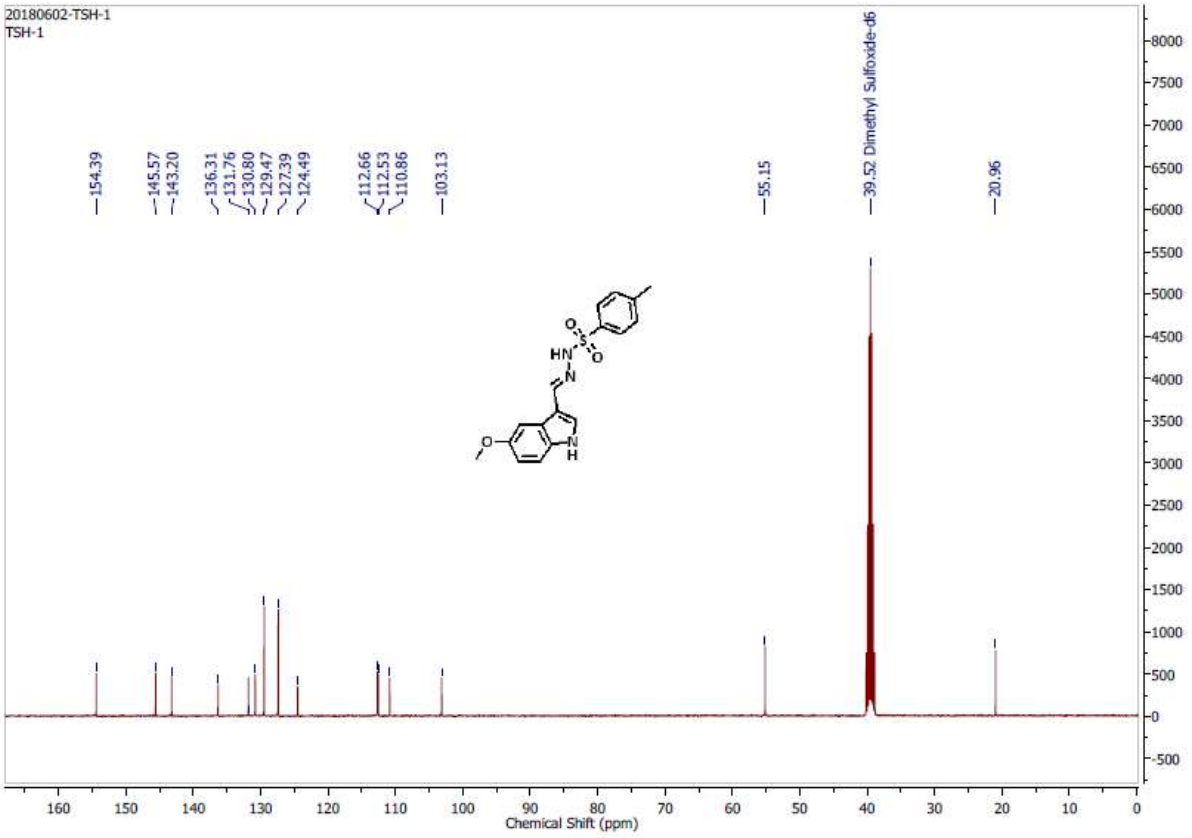

Figure C86: ^{13}C NMR spectrum of compound 29 in DMSO at 100 MHz.

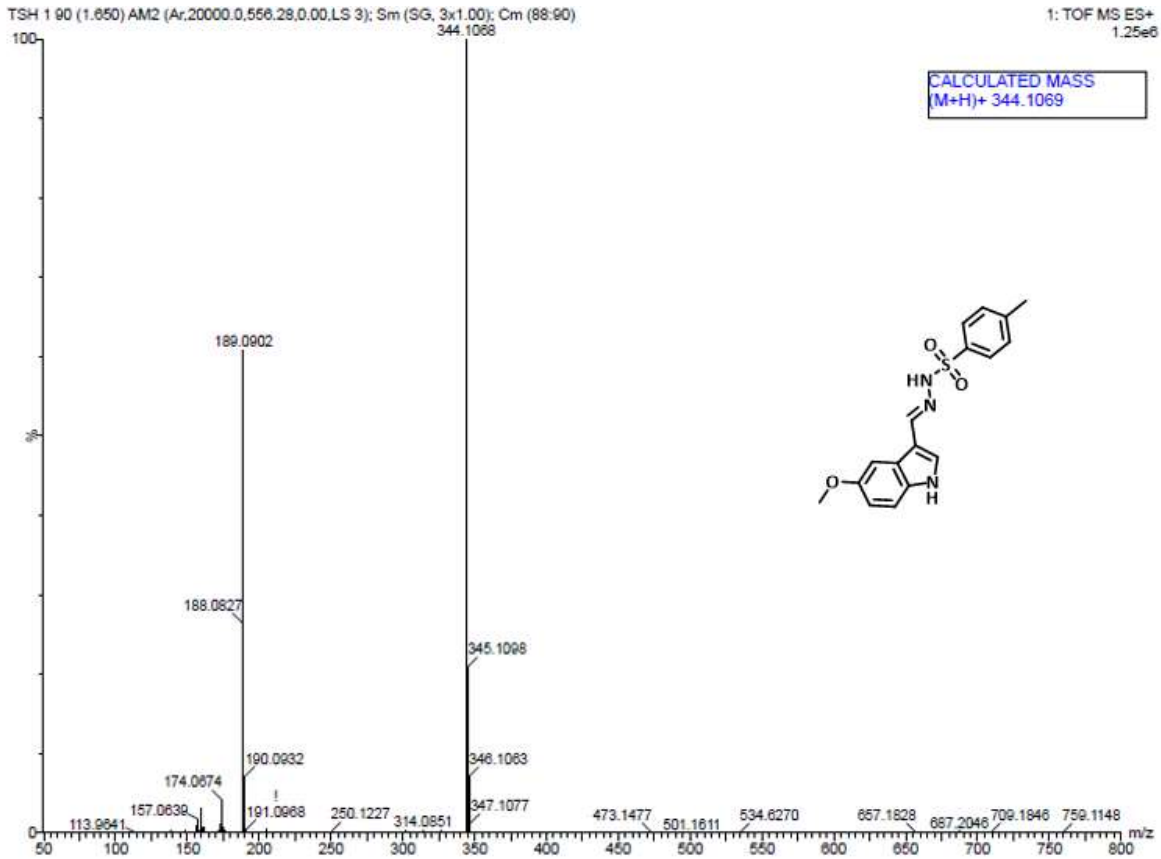

Figure C87: HRMS spectrum of compound 29.

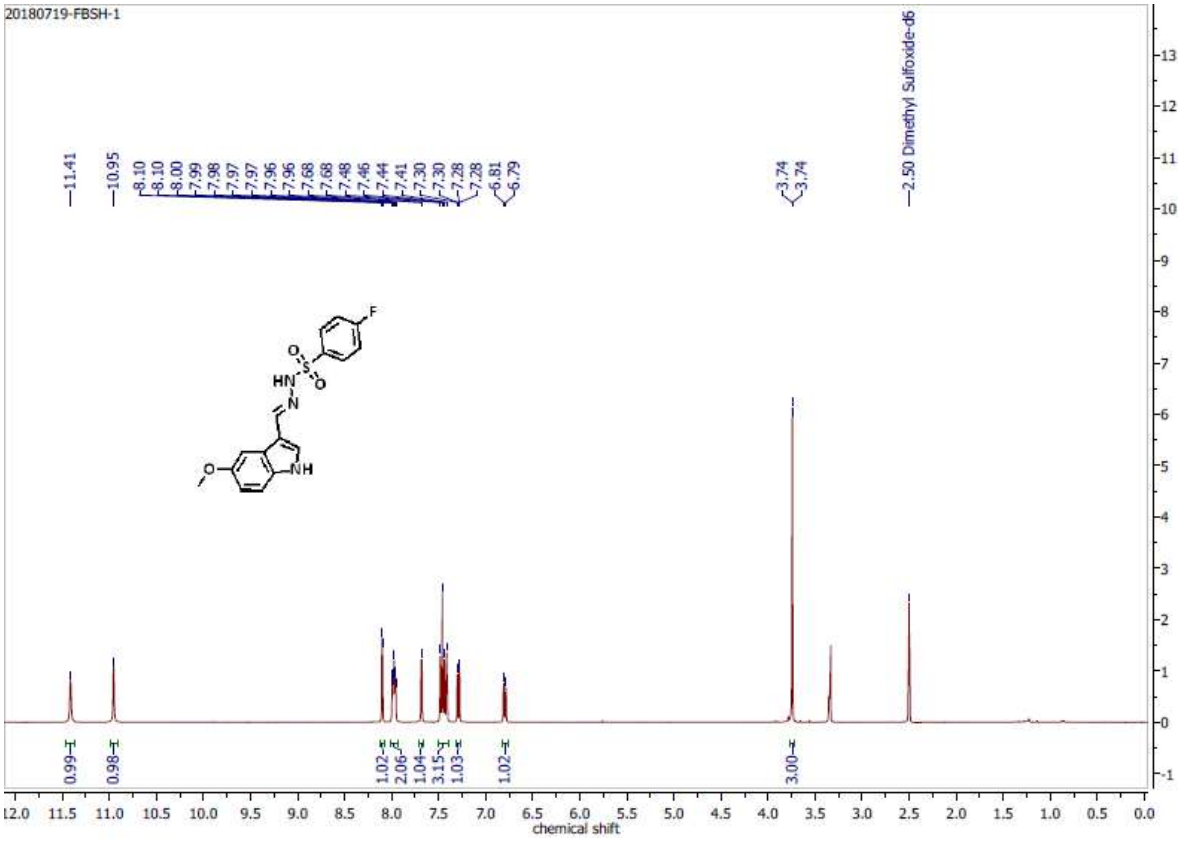

Figure C88: [1] H NMR spectrum of compound 30 in DMSO at 400 MHz.

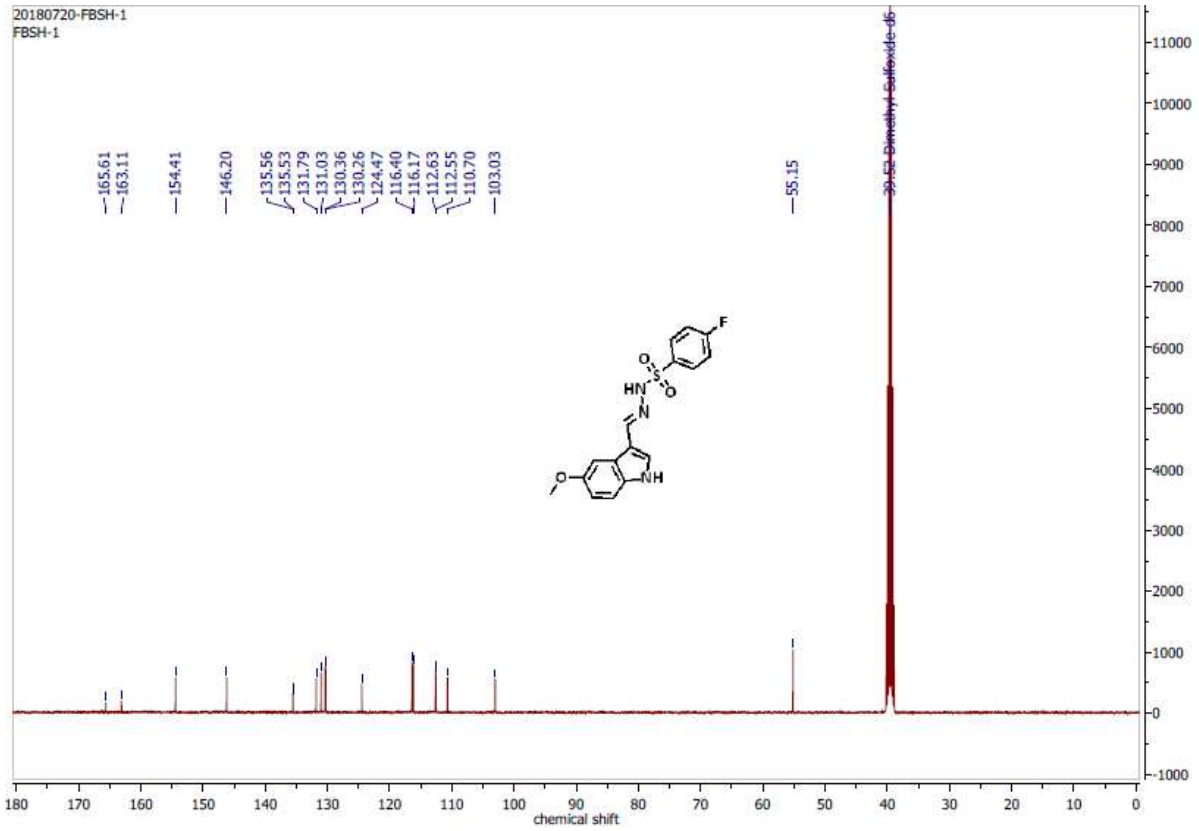

Figure C89: [13] C NMR spectrum of compound 30 in DMSO at 100 MHz.

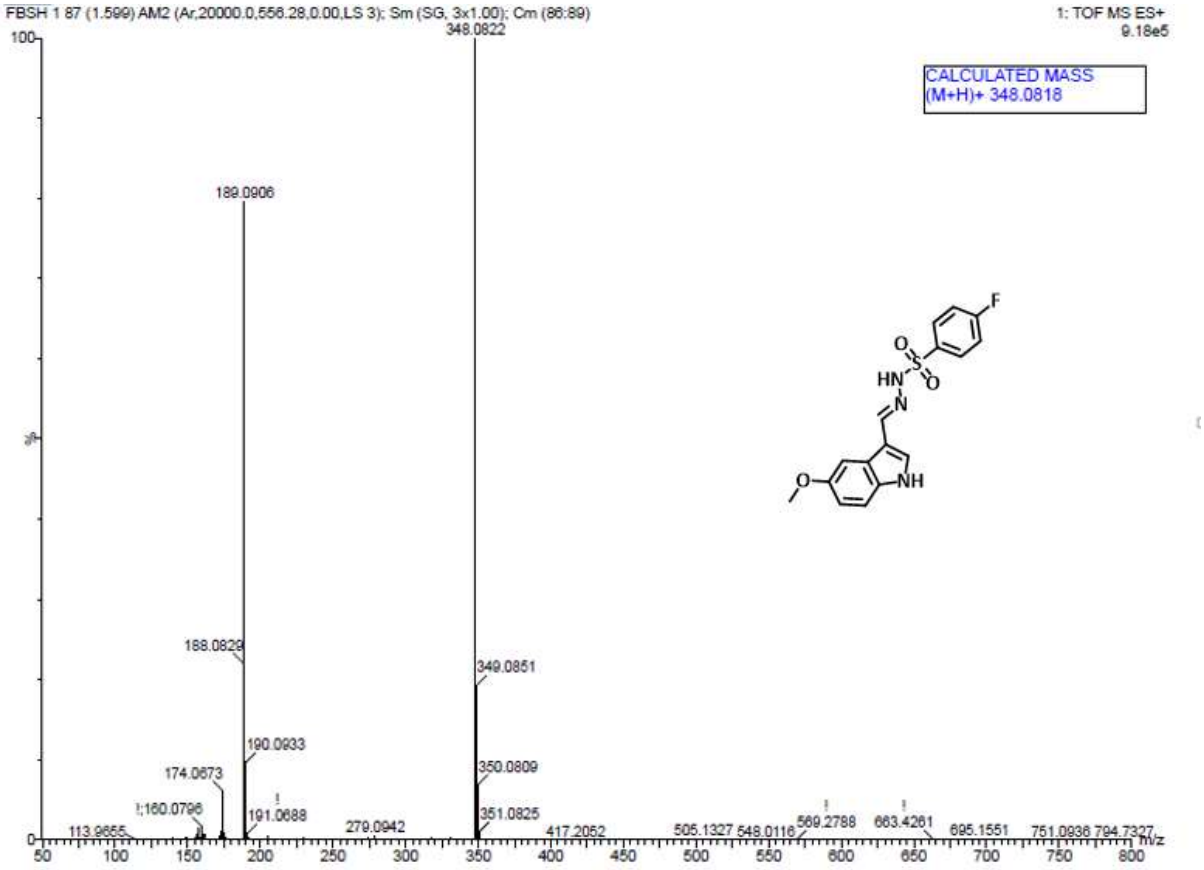

Figure C90: HRMS spectrum of compound 30.

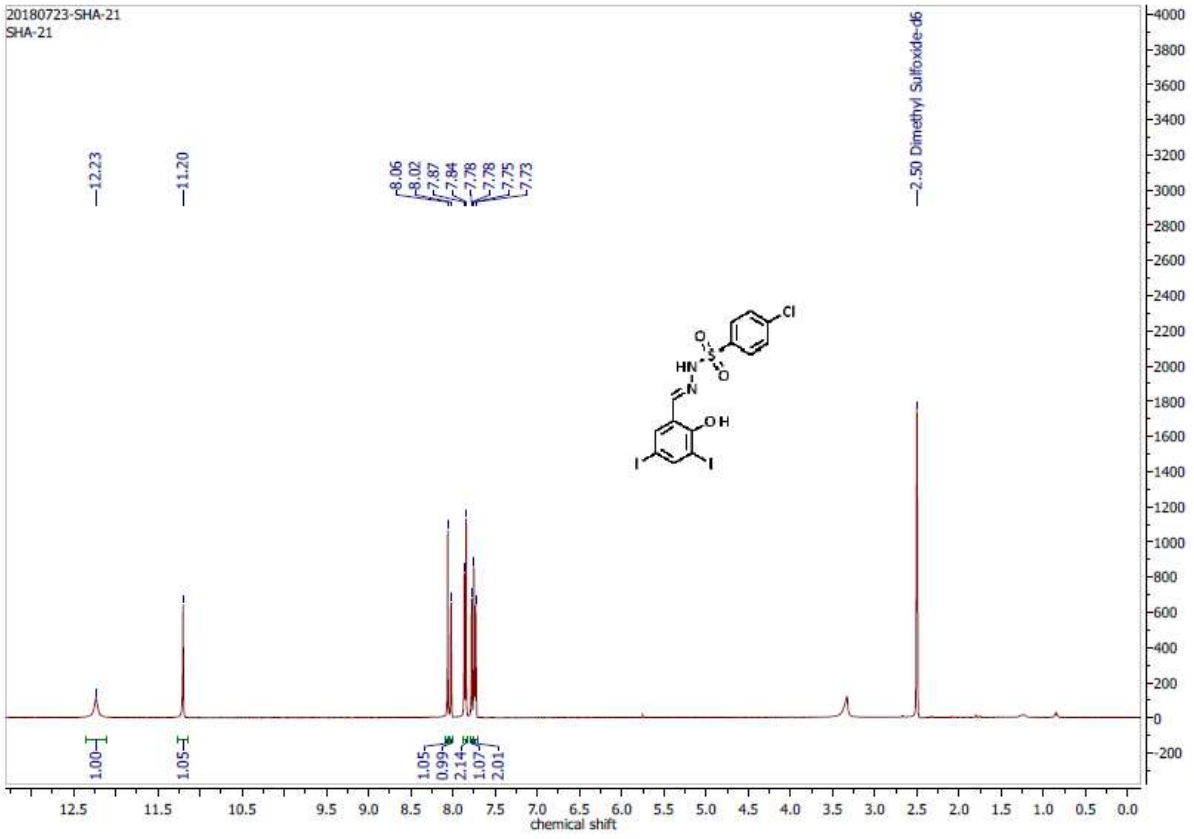

Figure C91: [1] H NMR spectrum of compound 31 in DMSO at 400 MHz.

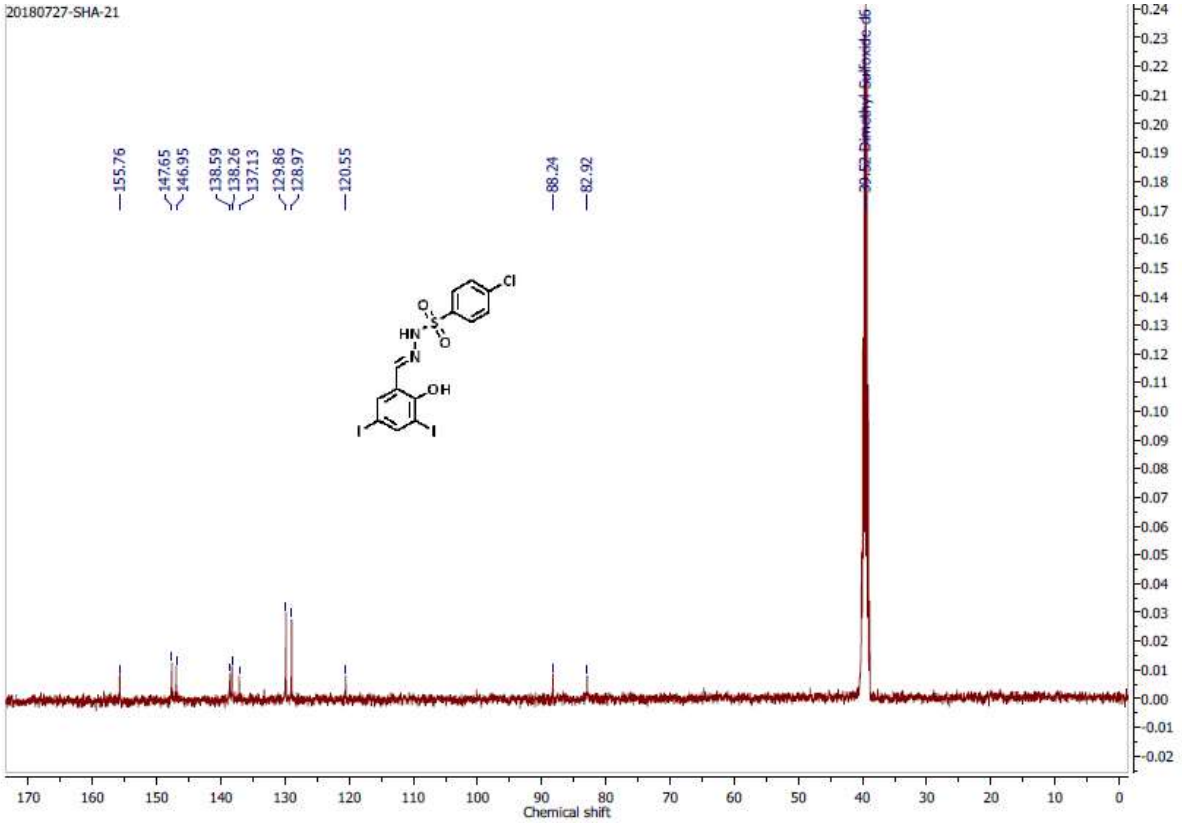

Figure C92: ^{13}C NMR spectrum of compound 31 in DMSO at 100 MHz.

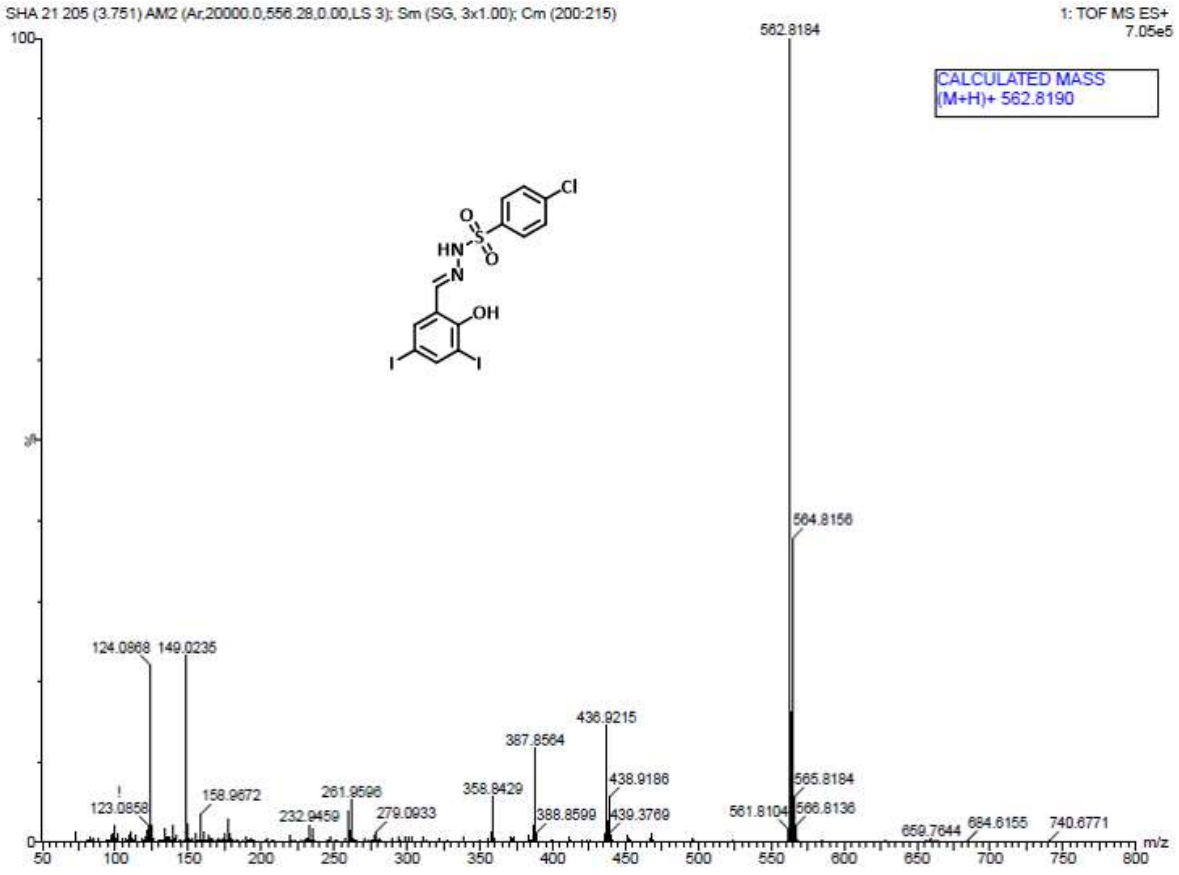

Figure C93: HRMS spectrum of compound 31.

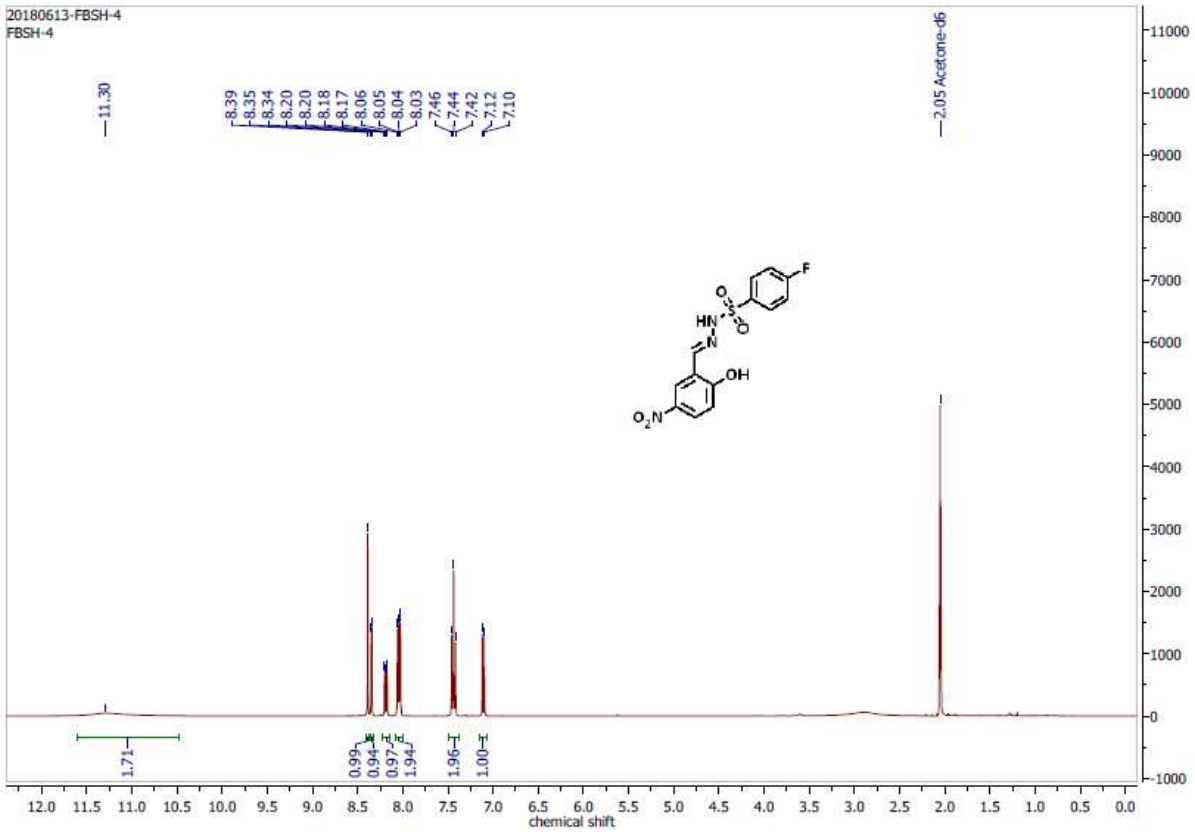

Figure C94: [1] H NMR spectrum of compound 32 in DMSO at 400 MHz.

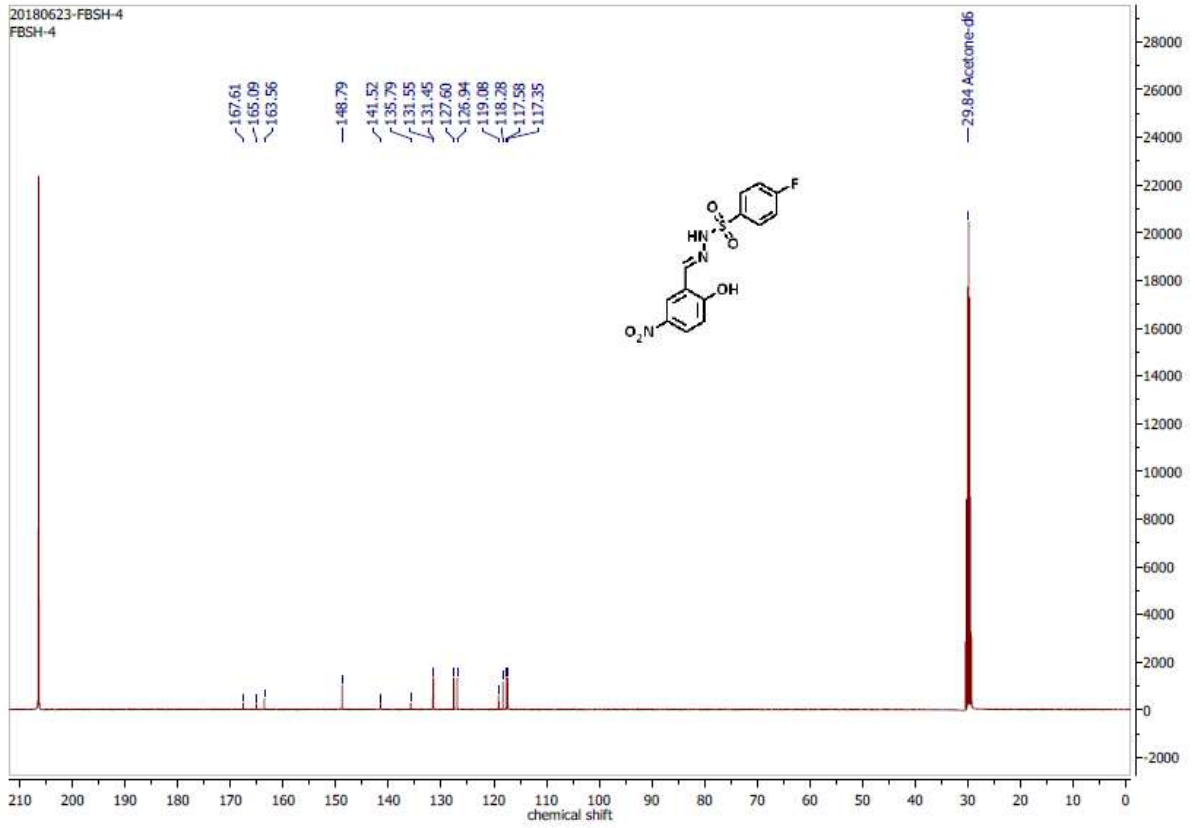

Figure C95: [13] C NMR spectrum of compound 32 in DMSO at 100 MHz.

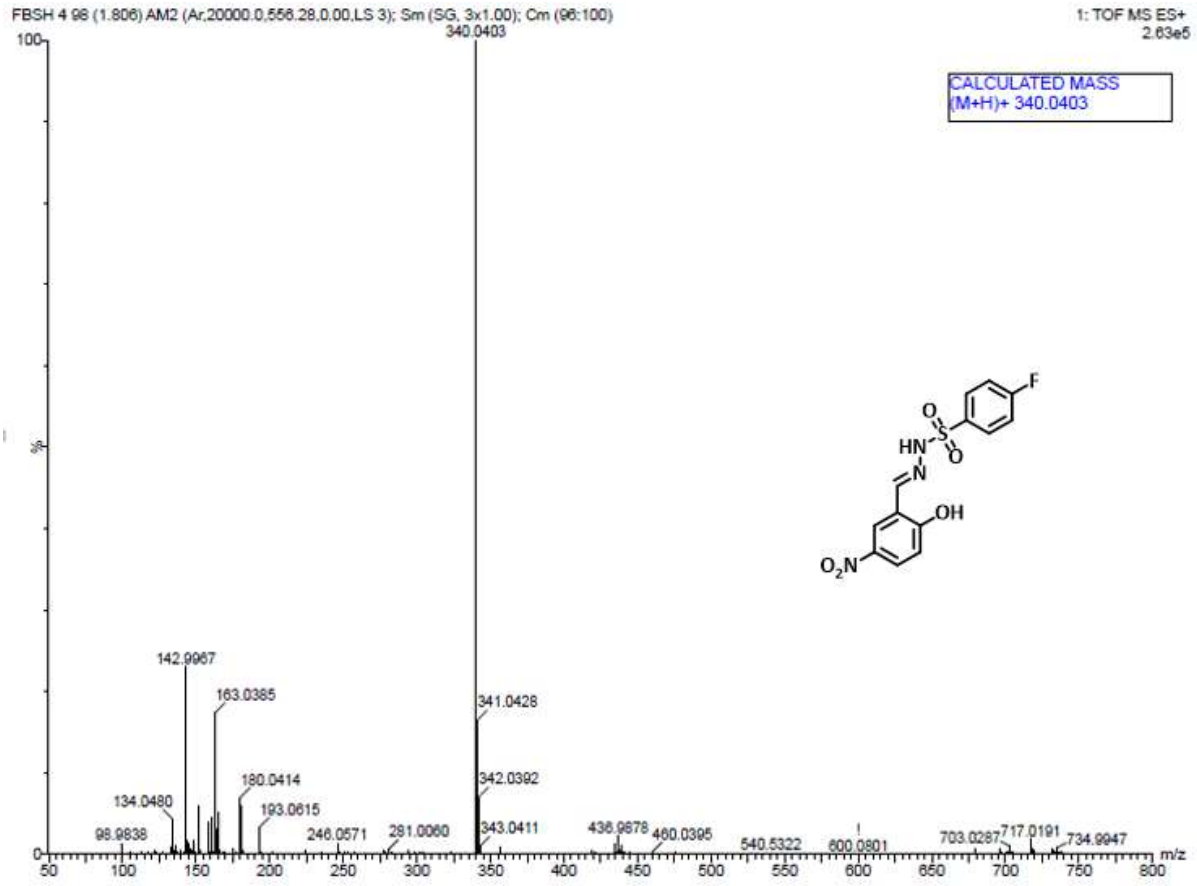

Figure C96: HRMS spectrum of compound 32.

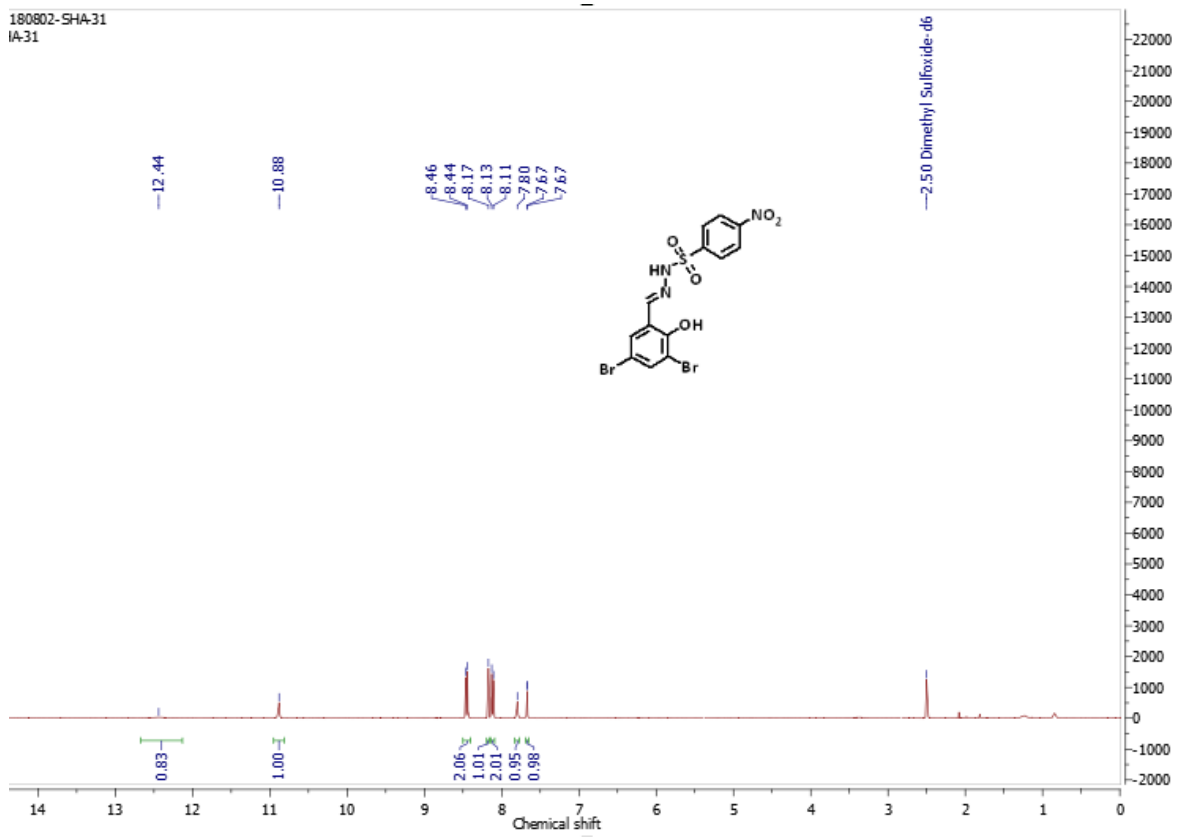

Figure C97: [1] H NMR spectrum of compound 33 in DMSO at 400 MHz.

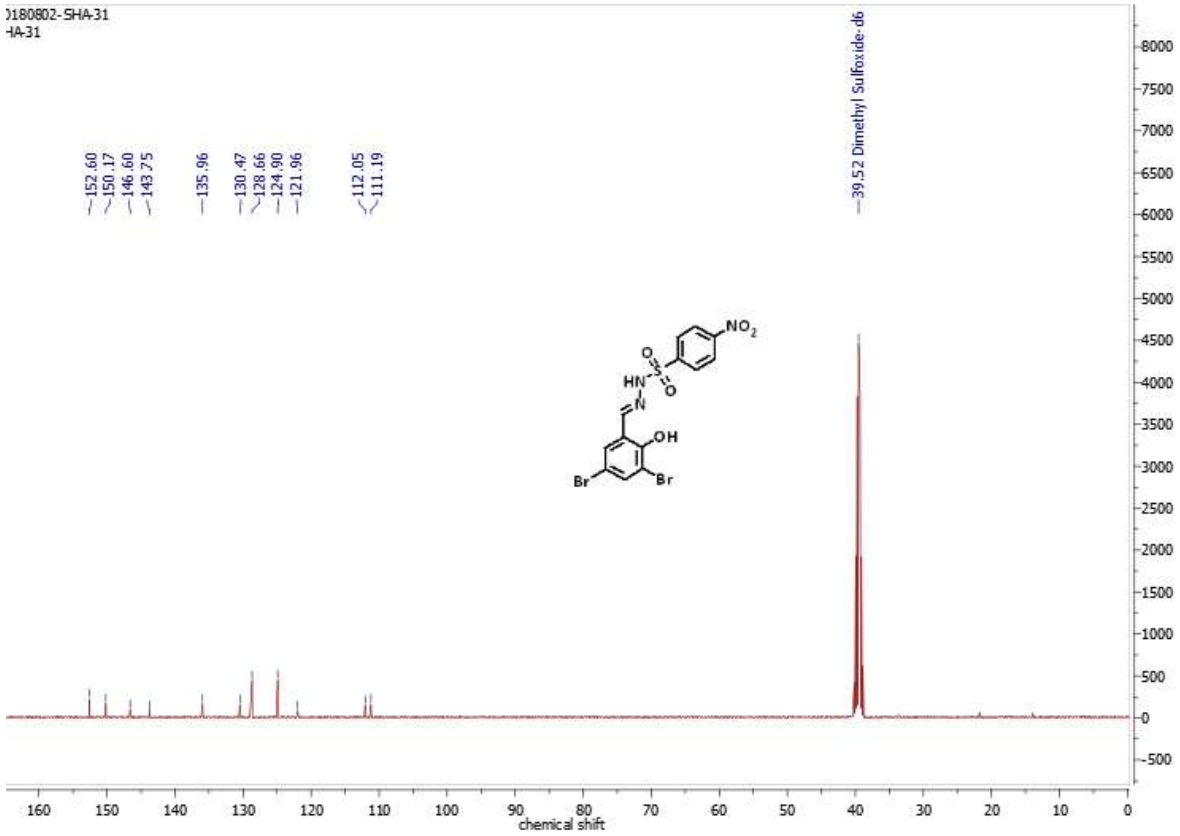

Figure C98: ^{13}C NMR spectrum of compound 33 in DMSO at 100 MHz.

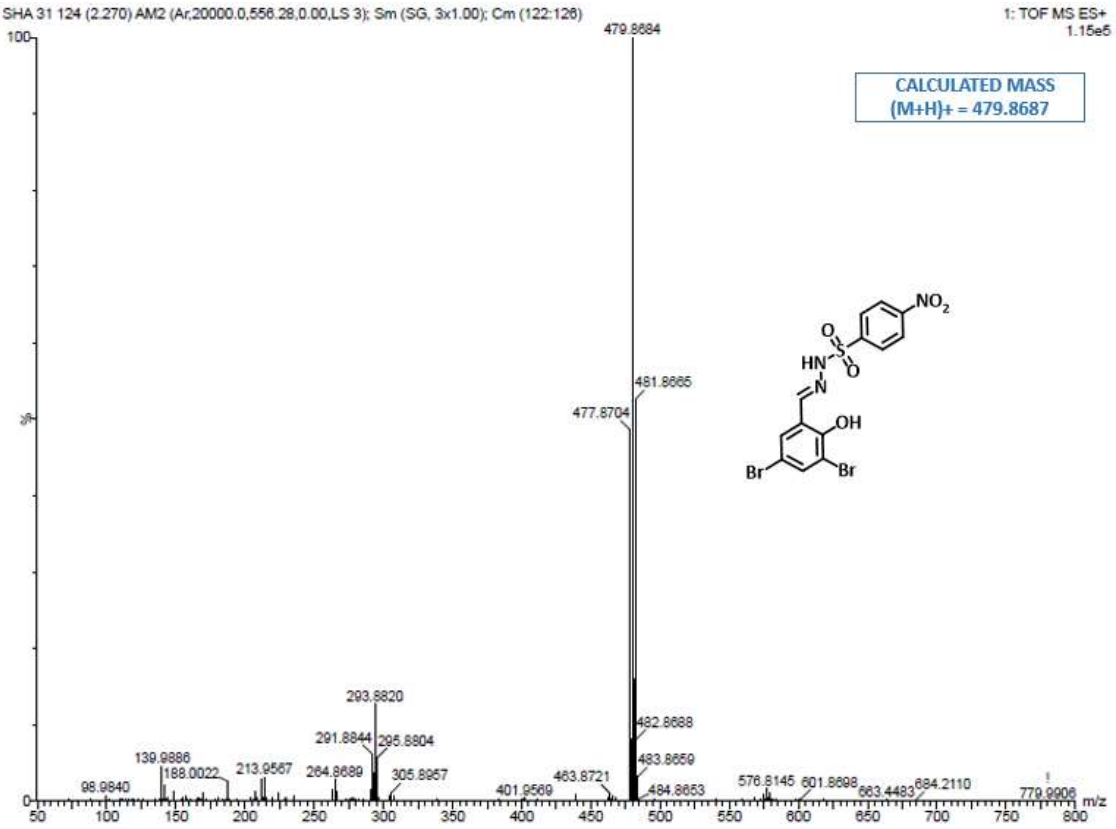

Figure C99: HRMS spectrum of compound 33.

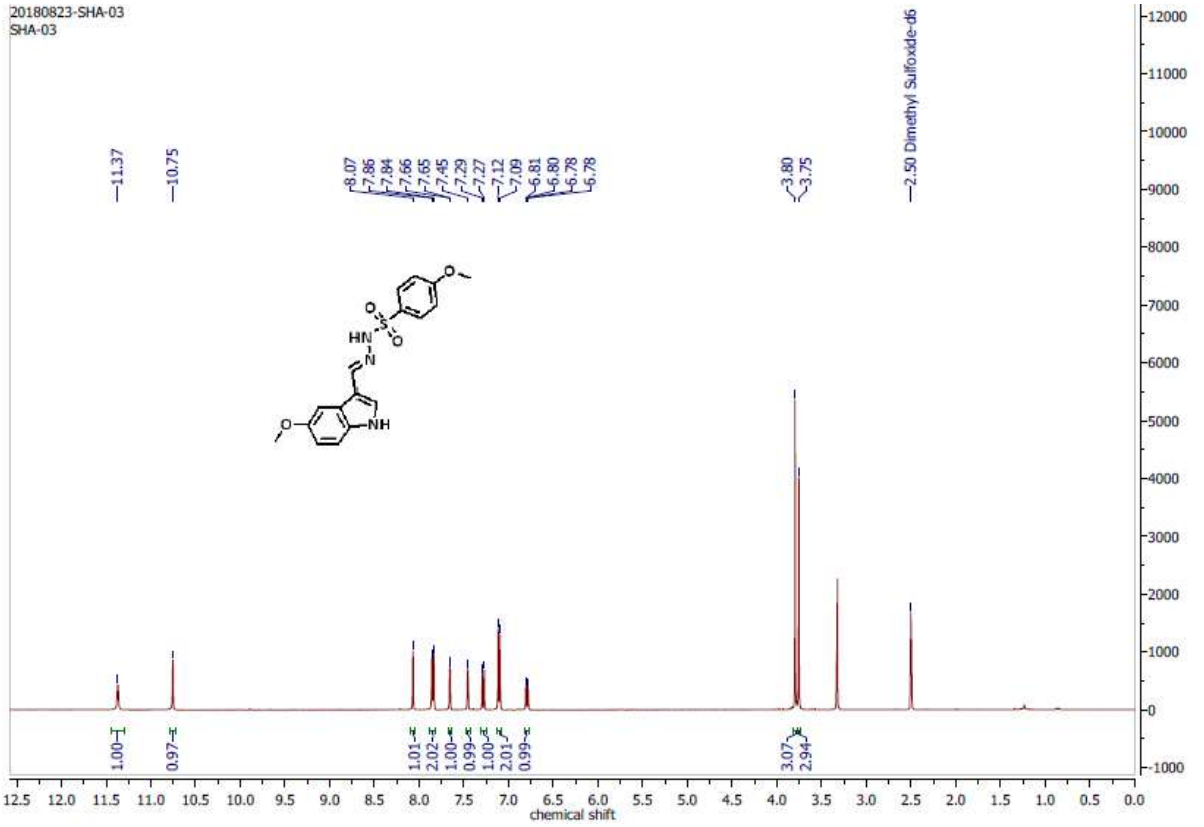

Figure C100: [1] H NMR spectrum of compound 34 in DMSO at 400 MHz.

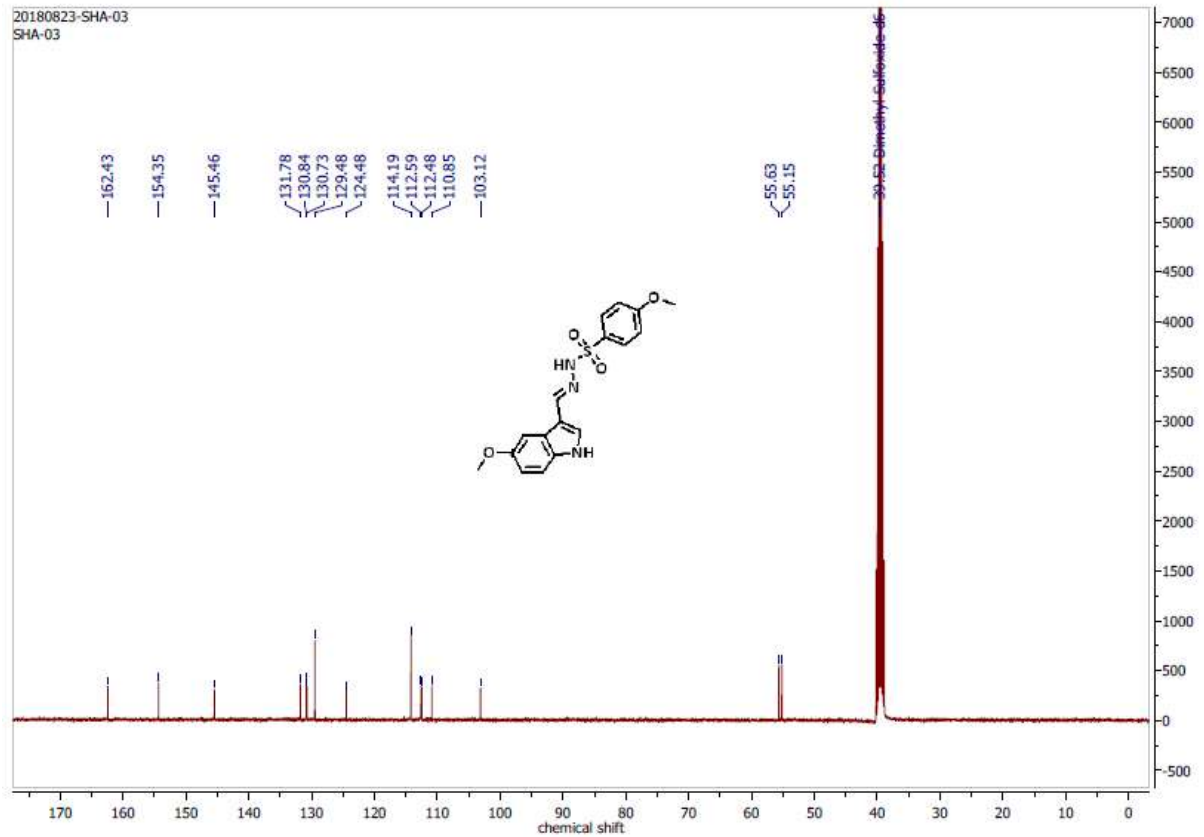

Figure C101: [13] C NMR spectrum of compound 34 in DMSO at 100 MHz.

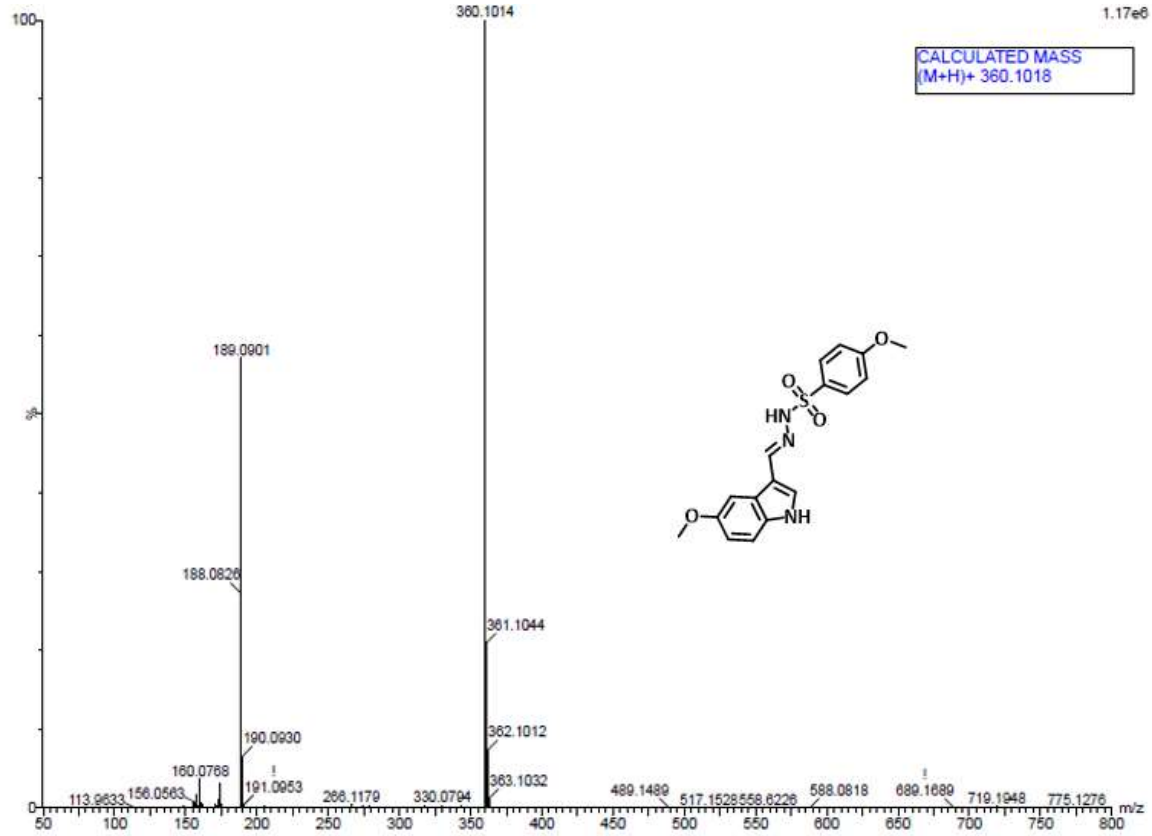

Figure C102: HRMS spectrum of compound 34.

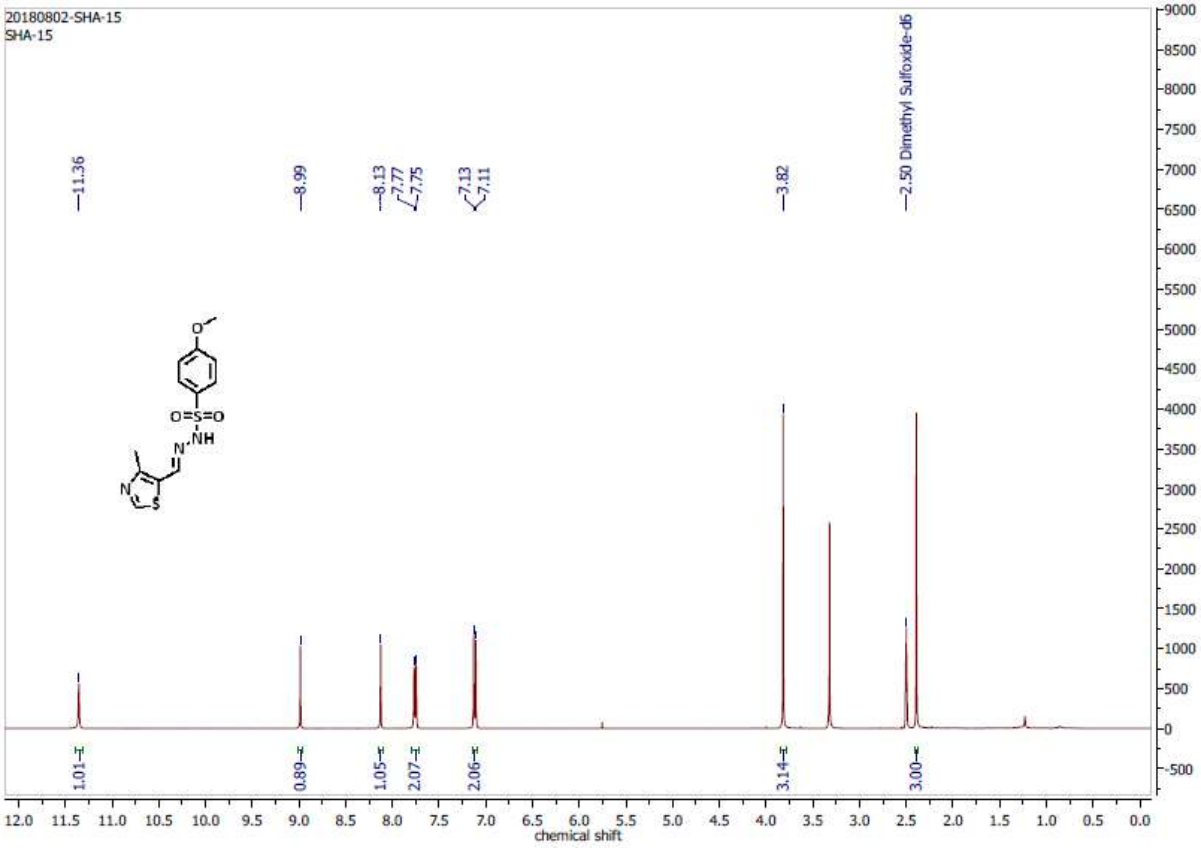

Figure C103: [1] H NMR spectrum of compound 35 in DMSO at 400 MHz.

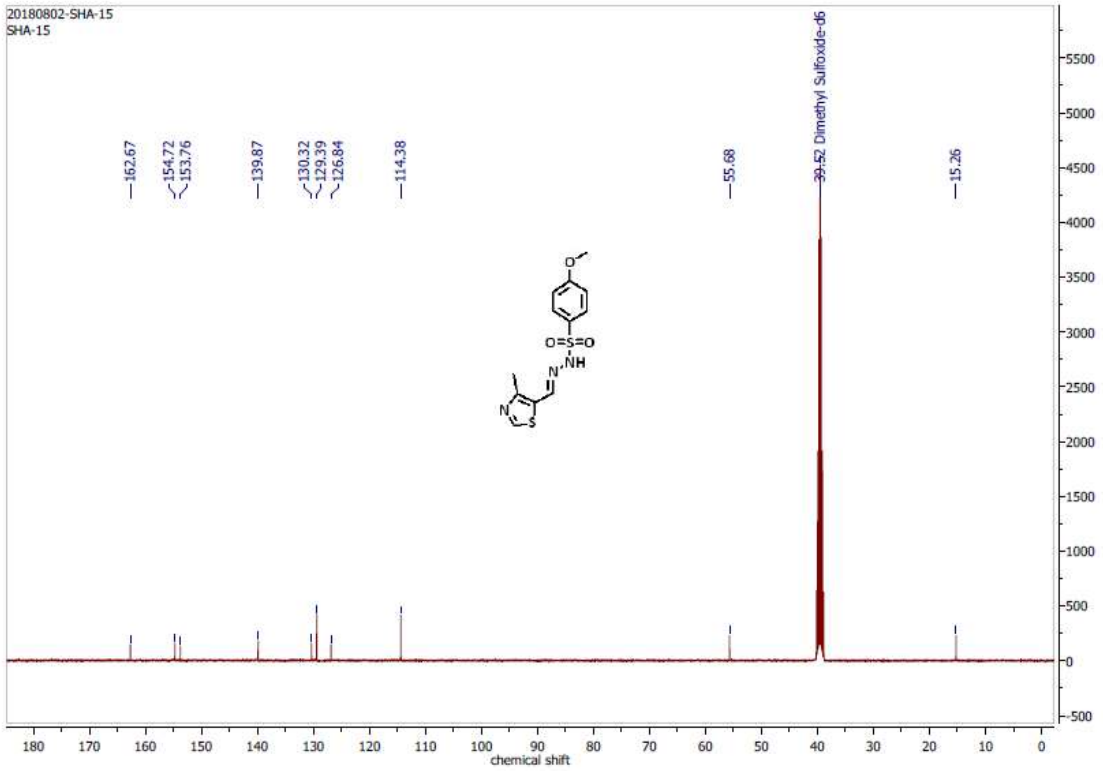

Figure C104: ^{13}C NMR spectrum of compound 35 in DMSO at 100 MHz.

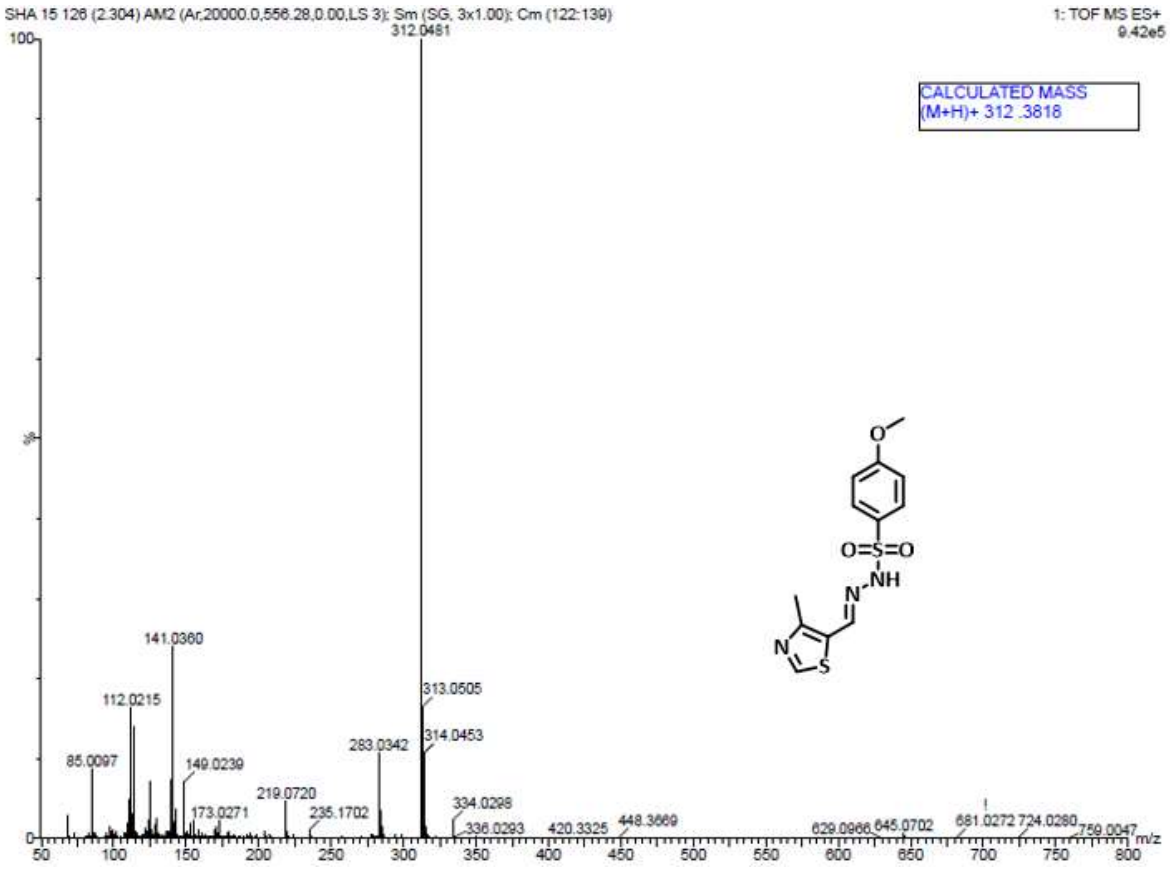

Figure C105: HRMS spectrum of compound 35.

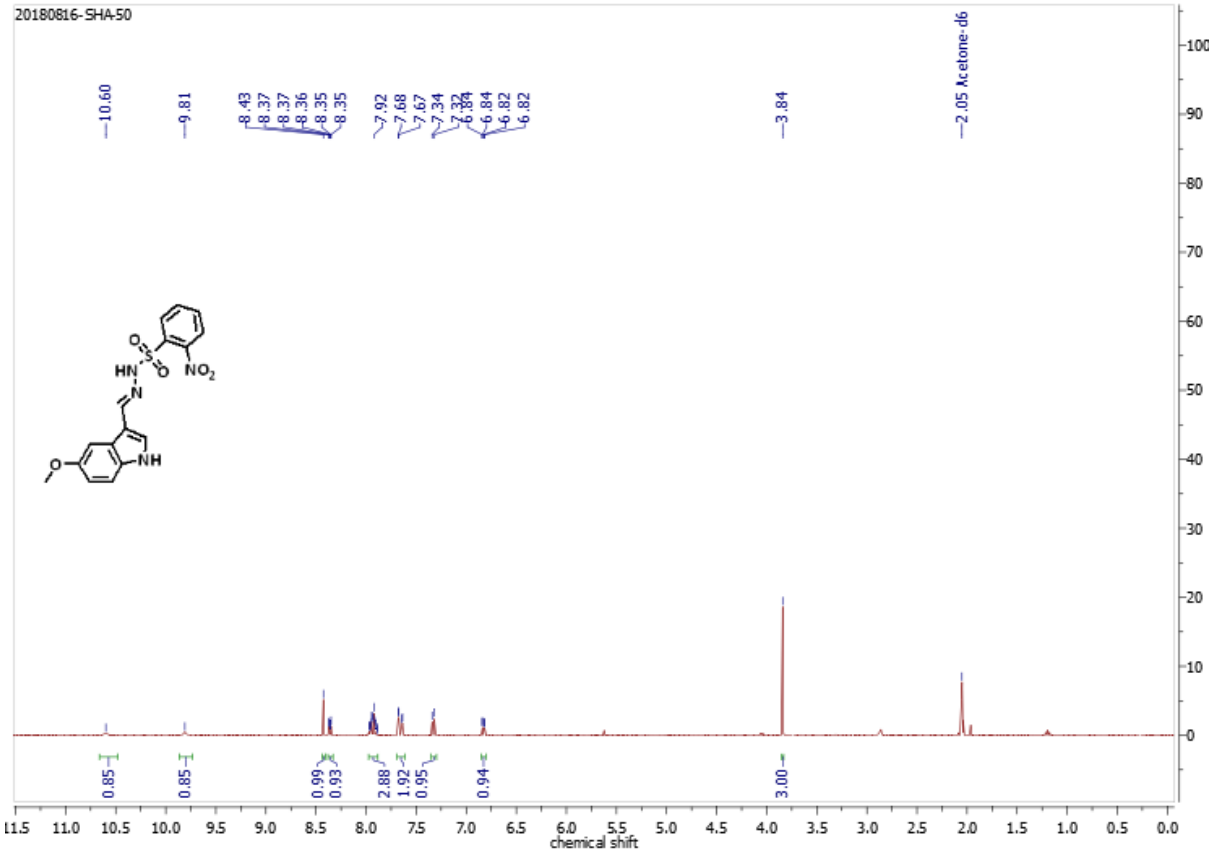

Figure C106: [1] H NMR spectrum of compound 36 in Acetone at 400 MHz.

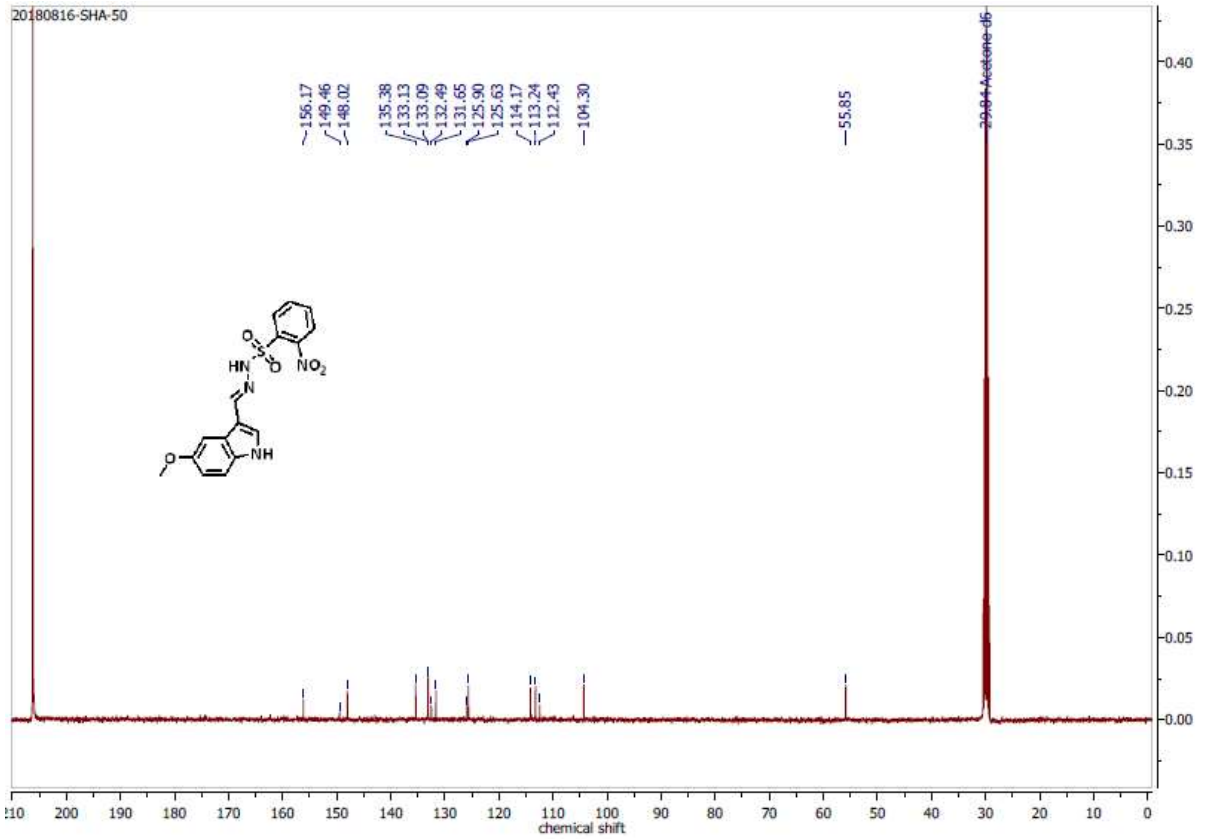

Figure C107: [13] C NMR spectrum of compound 36 in Acetone at 100 MHz.

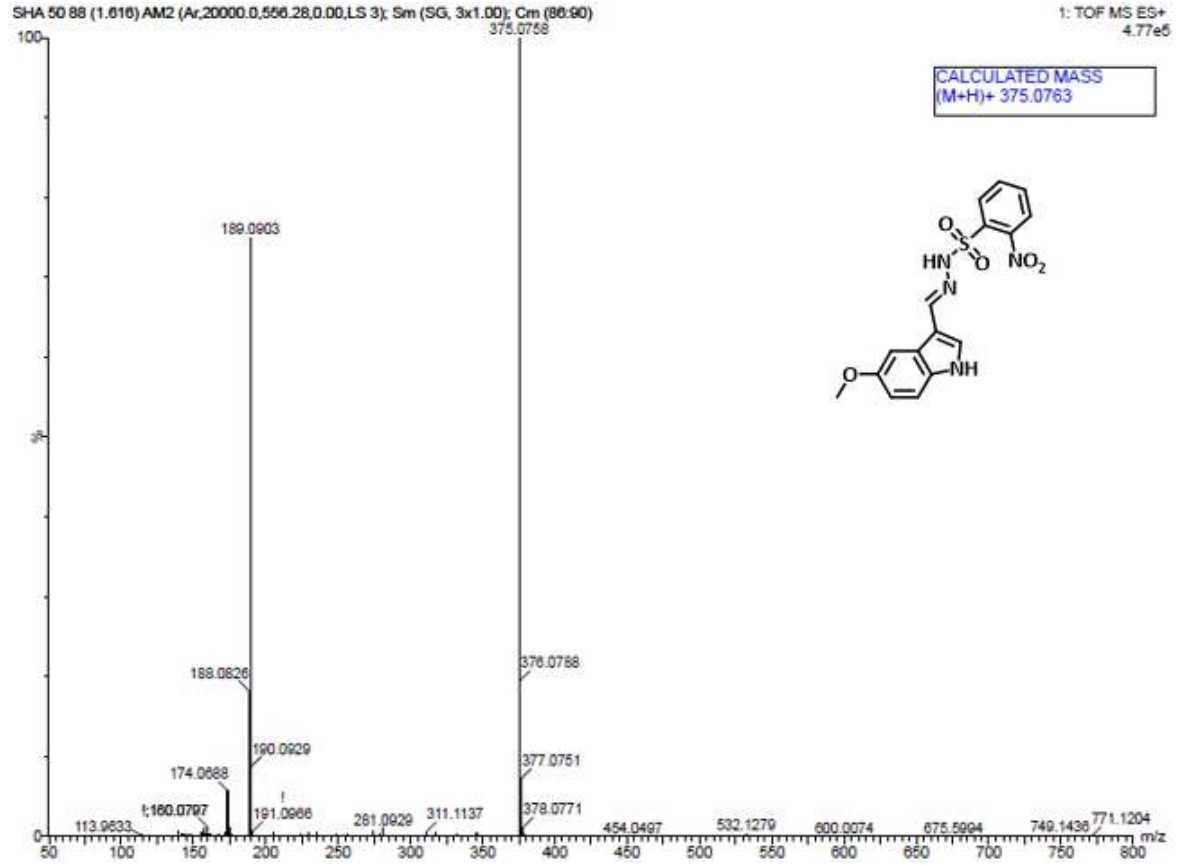

Figure C108: HRMS spectrum of compound 36.

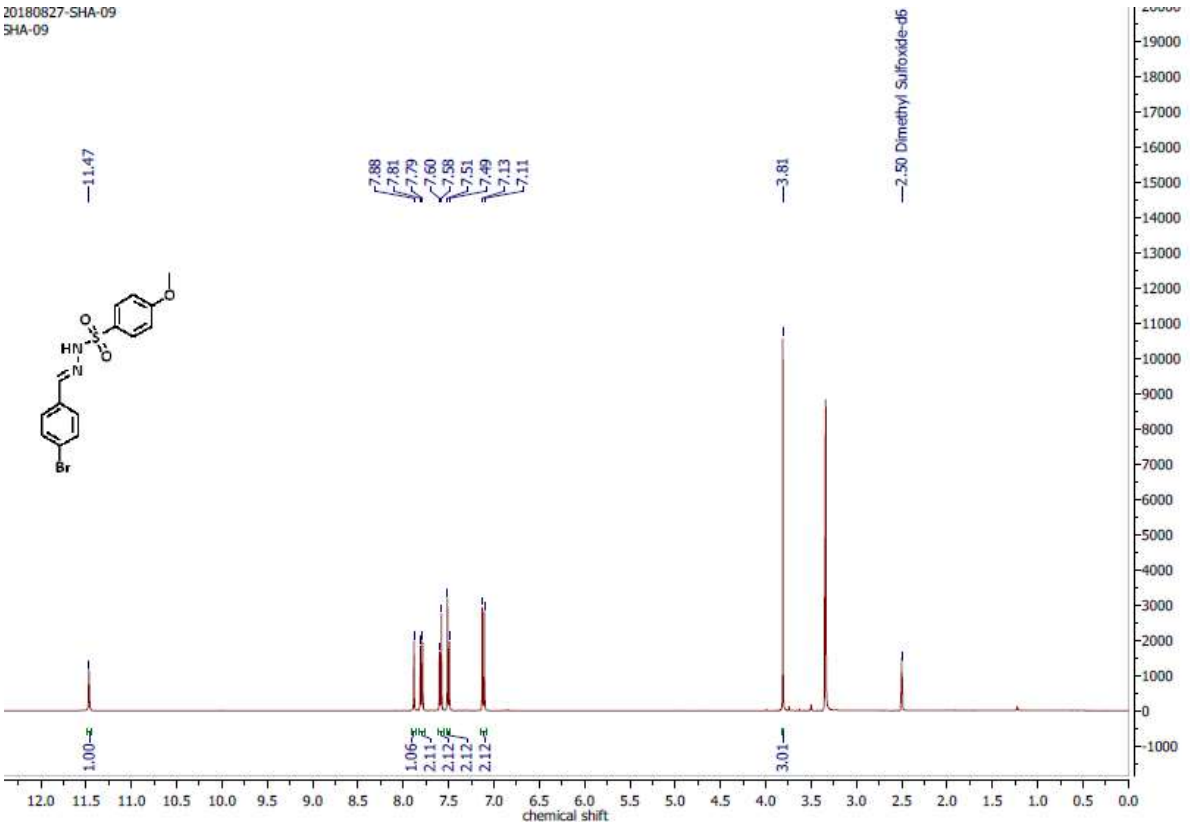

Figure C109: [1] H NMR spectrum of compound 37 in DMSO at 400 MHz.

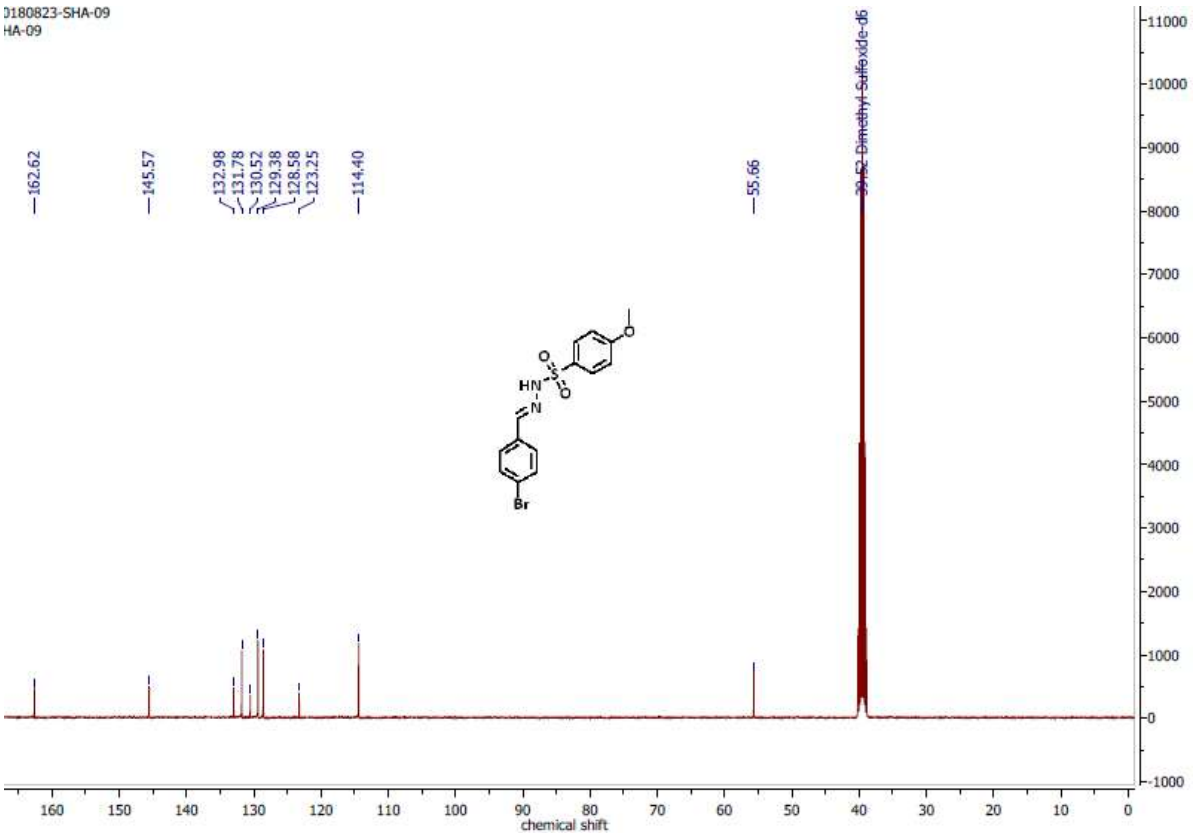

Figure C110: ^{13}C NMR spectrum of compound 37 in DMSO at 100 MHz.

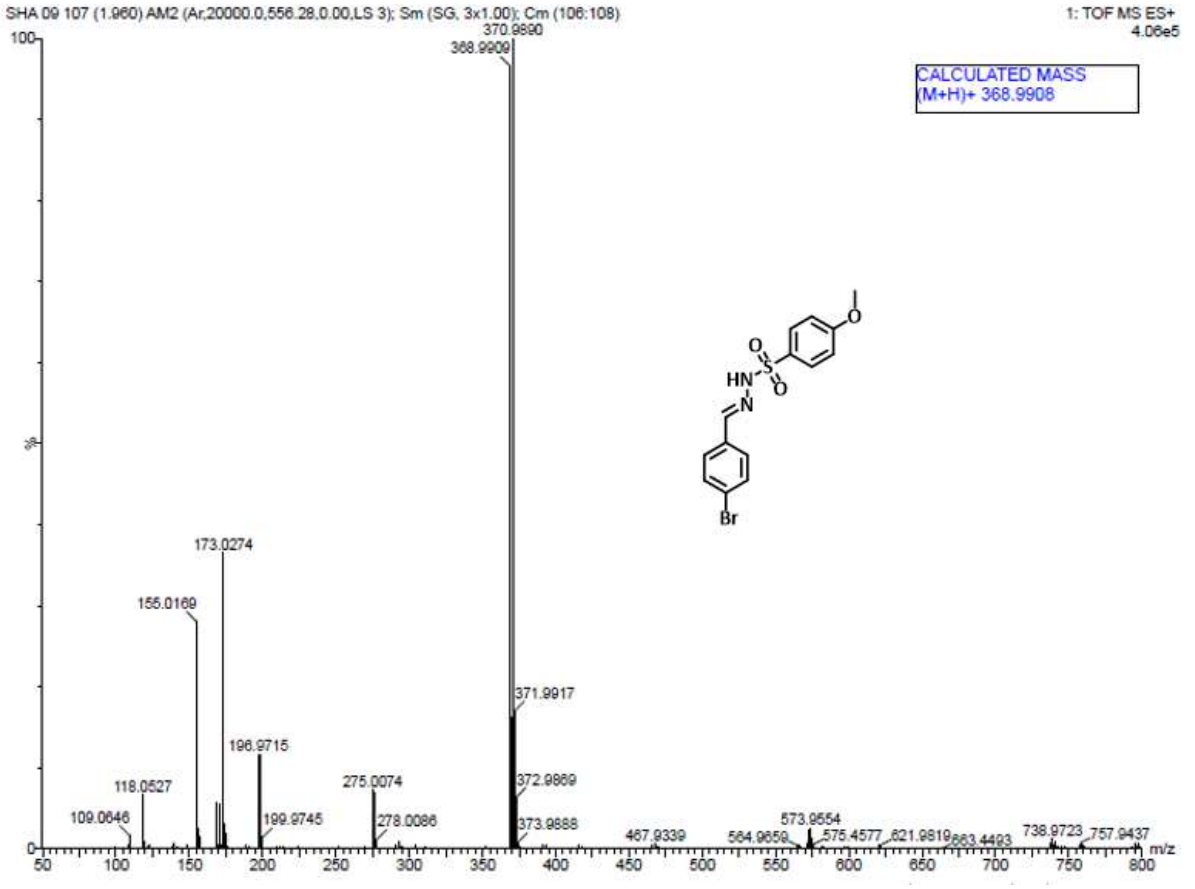

Figure C111: HRMS spectrum of compound 37.

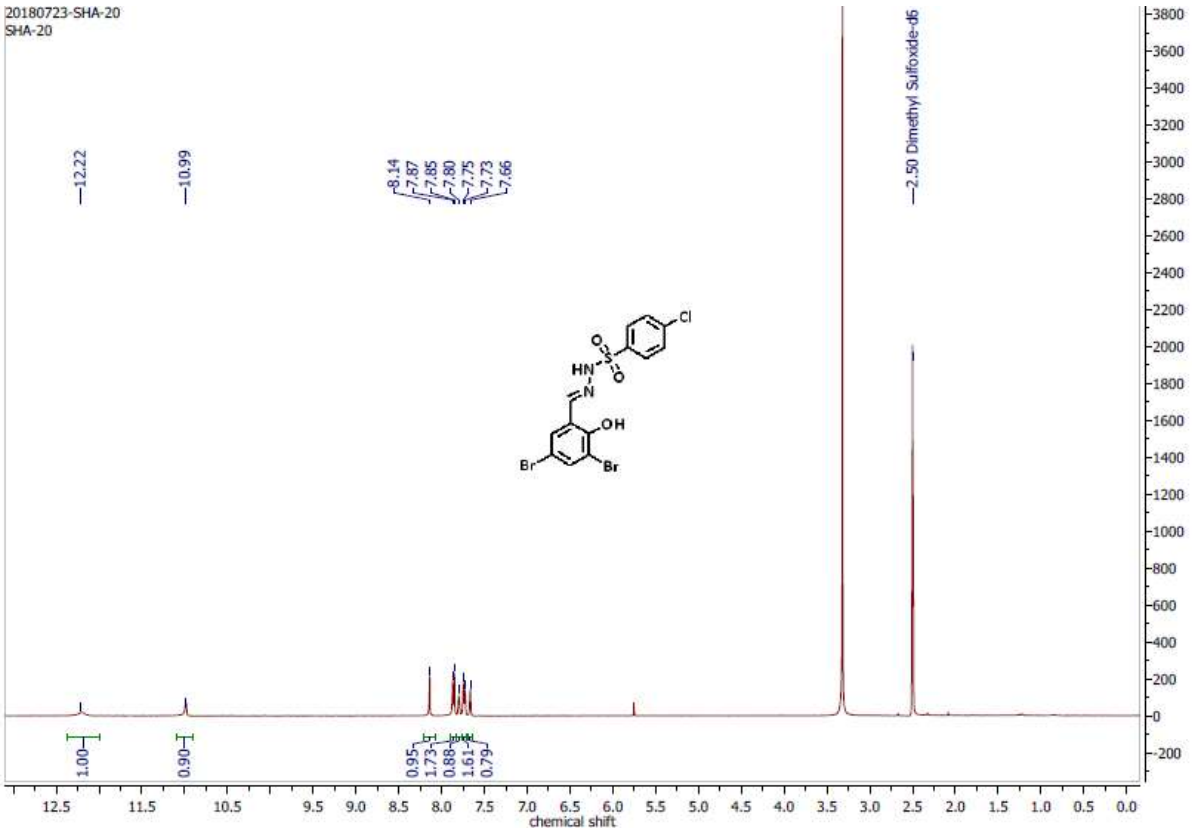

Figure C112: [1] H NMR spectrum of compound 38 in DMSO at 400 MHz.

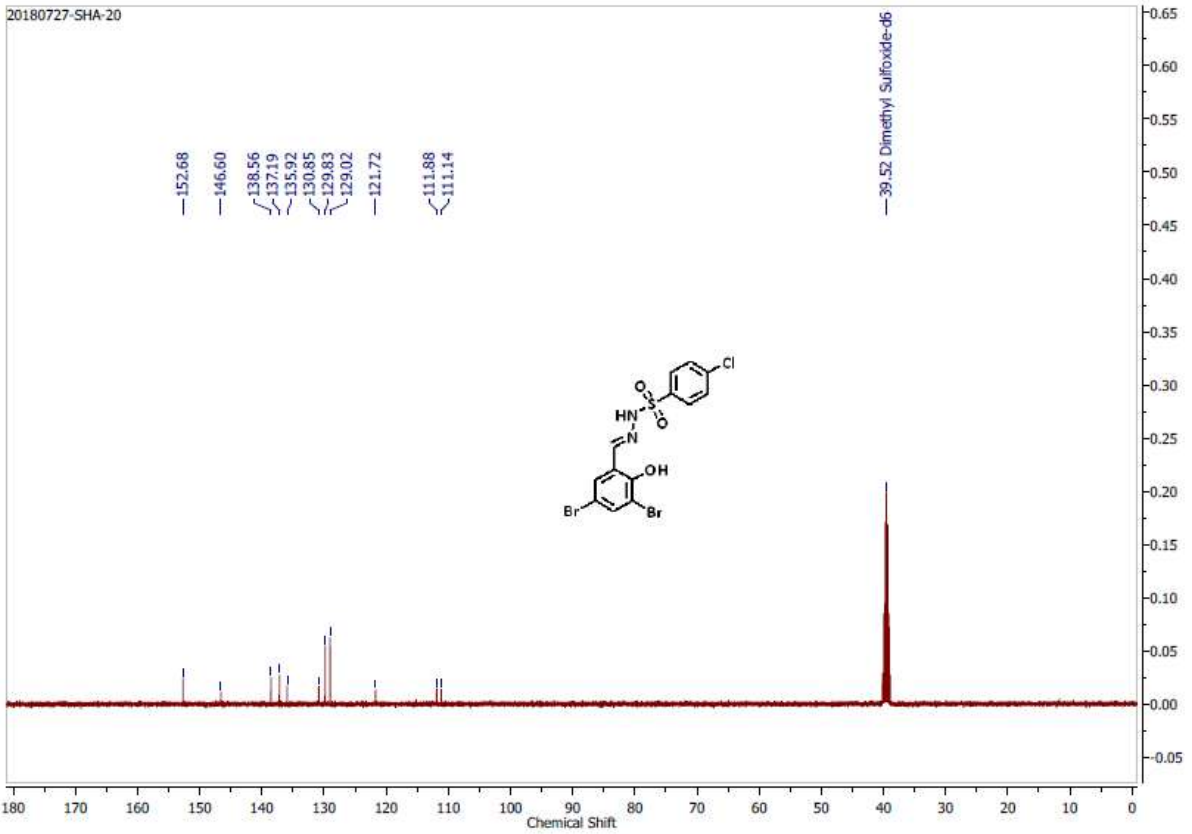

Figure C113: [13] C NMR spectrum of compound 38 in DMSO at 100 MHz.

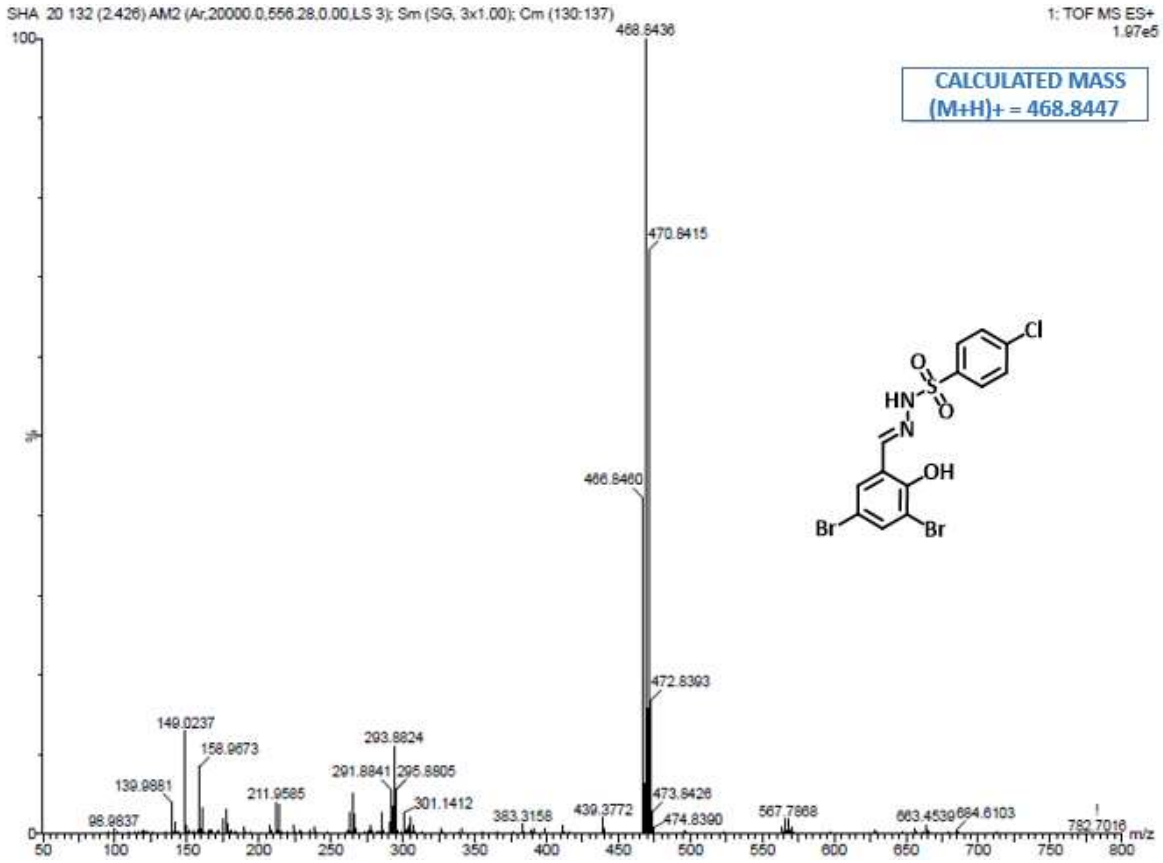

Figure C114: HRMS spectrum of compound 38.

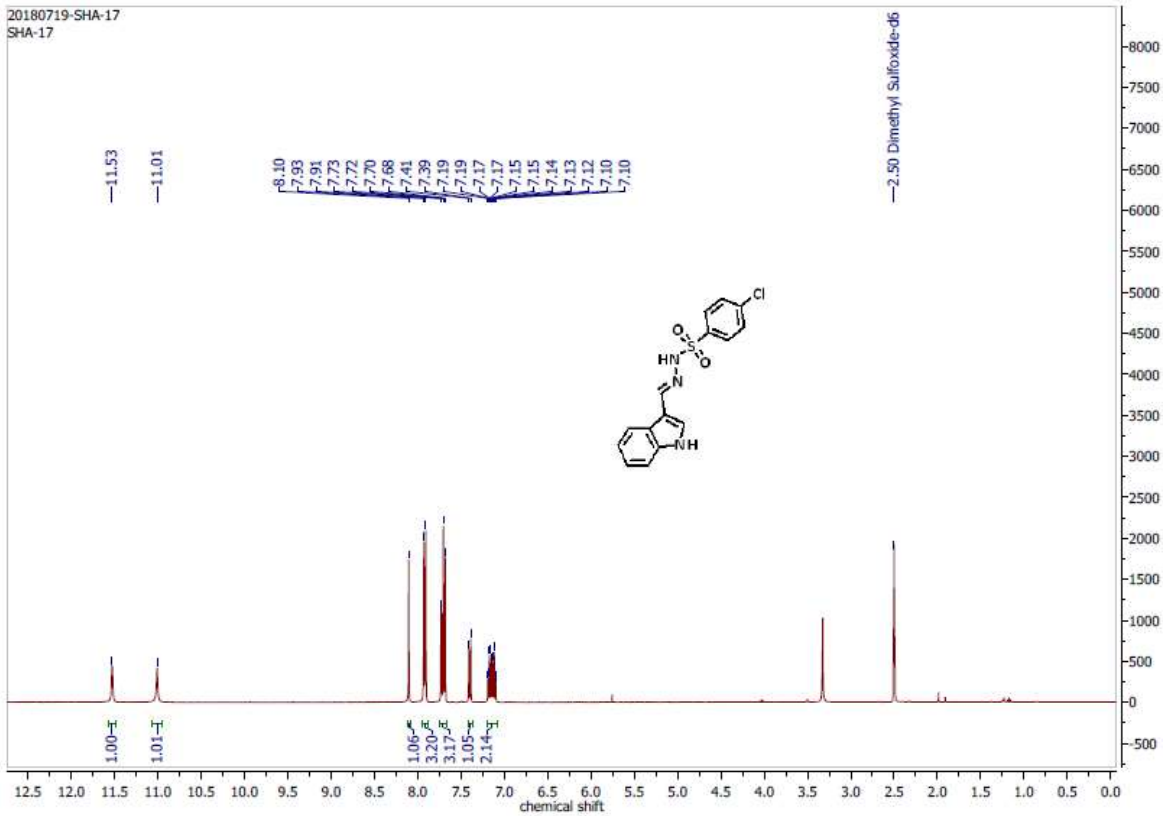

Figure C115: [1] H NMR spectrum of compound 39 in DMSO at 400 MHz.

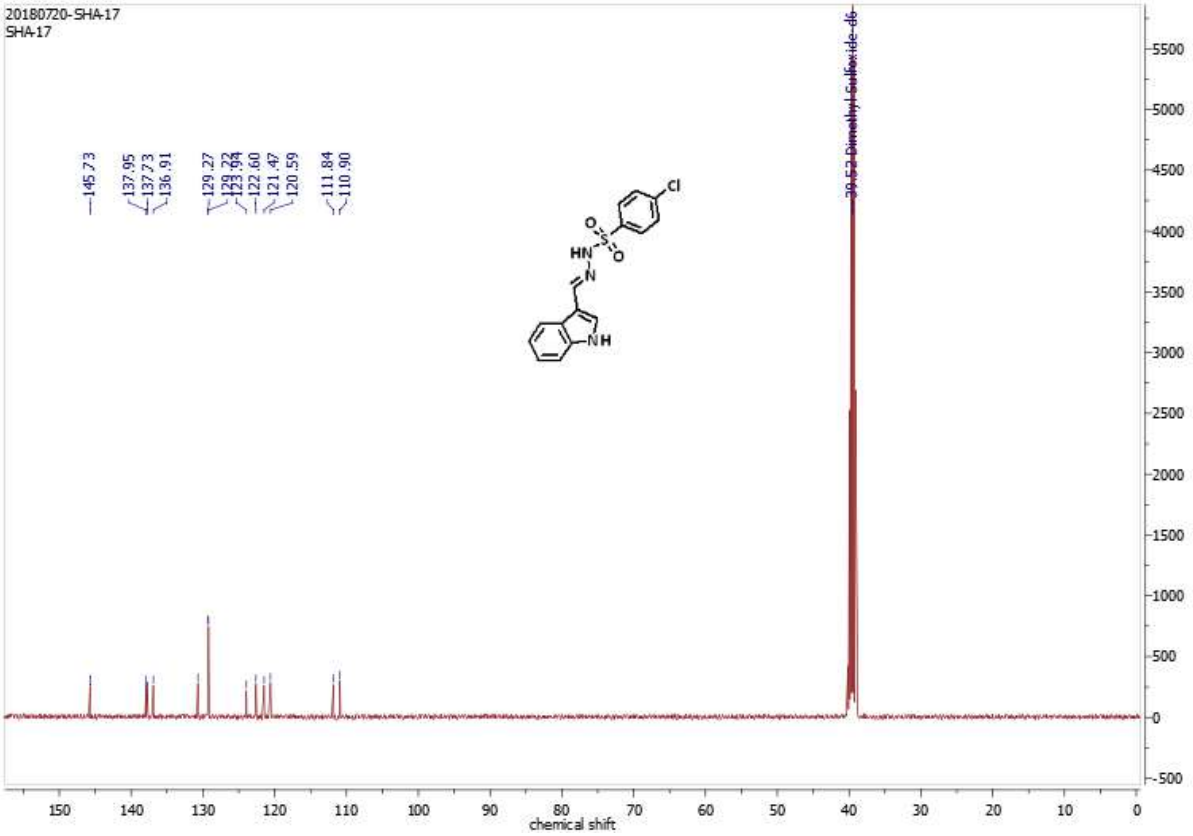

Figure C116: ^{13}C NMR spectrum of compound 39 in DMSO at 100 MHz.

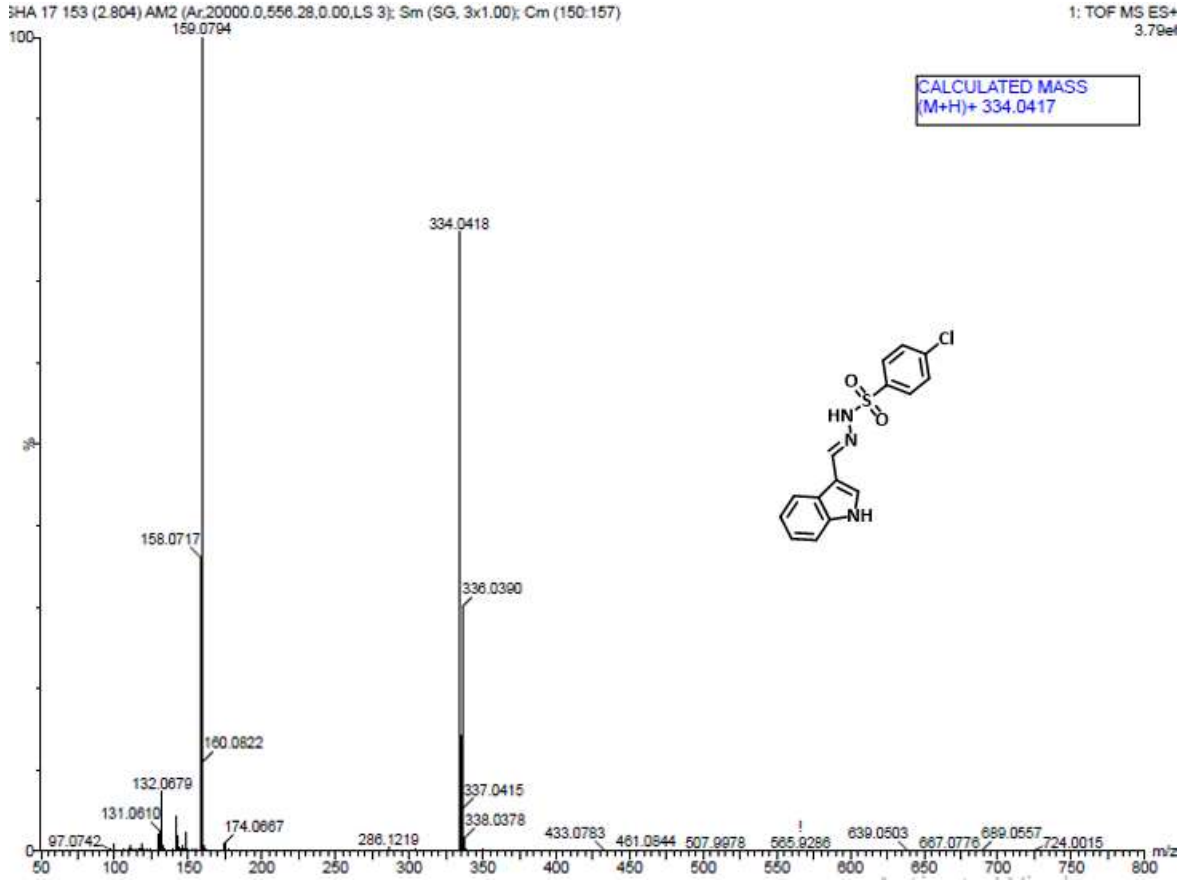

Figure C117: HRMS spectrum of compound 39.

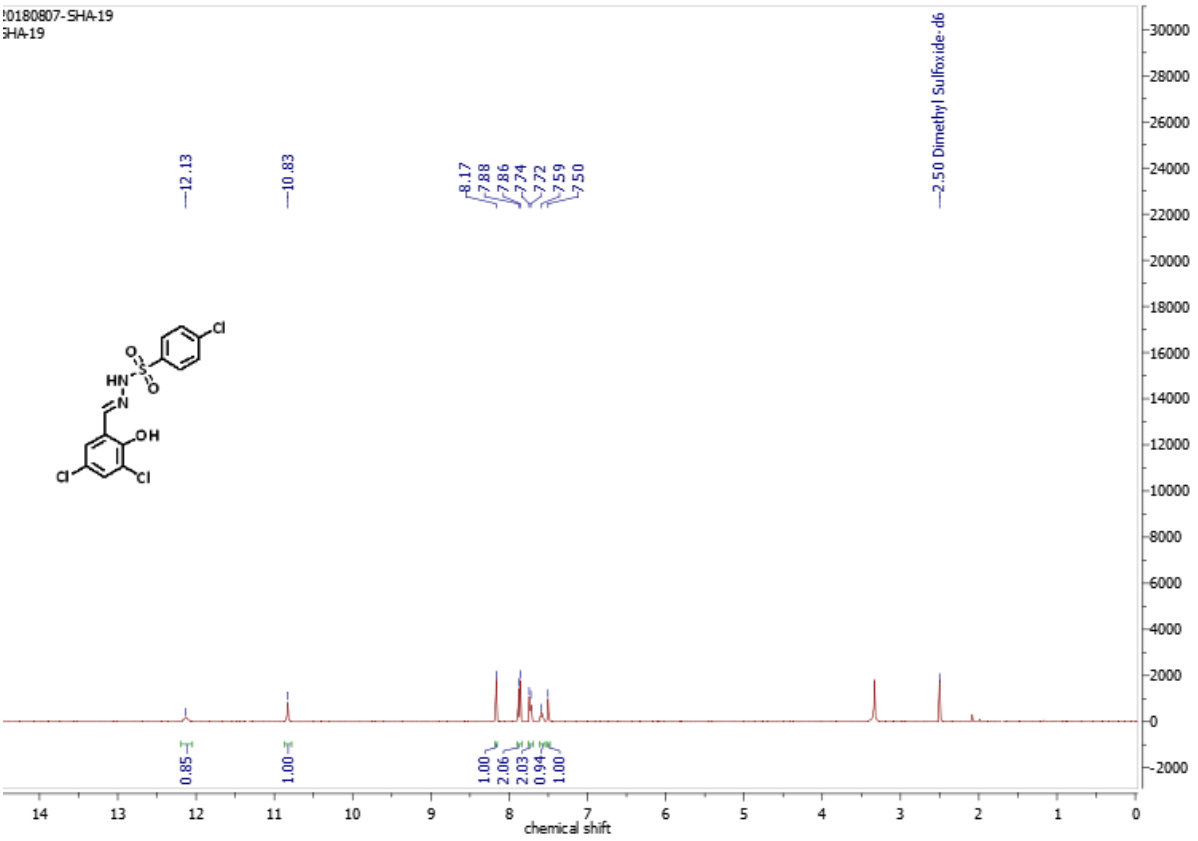

Figure C118: ^{1}H NMR spectrum of compound 40 in DMSO at 400 MHz.

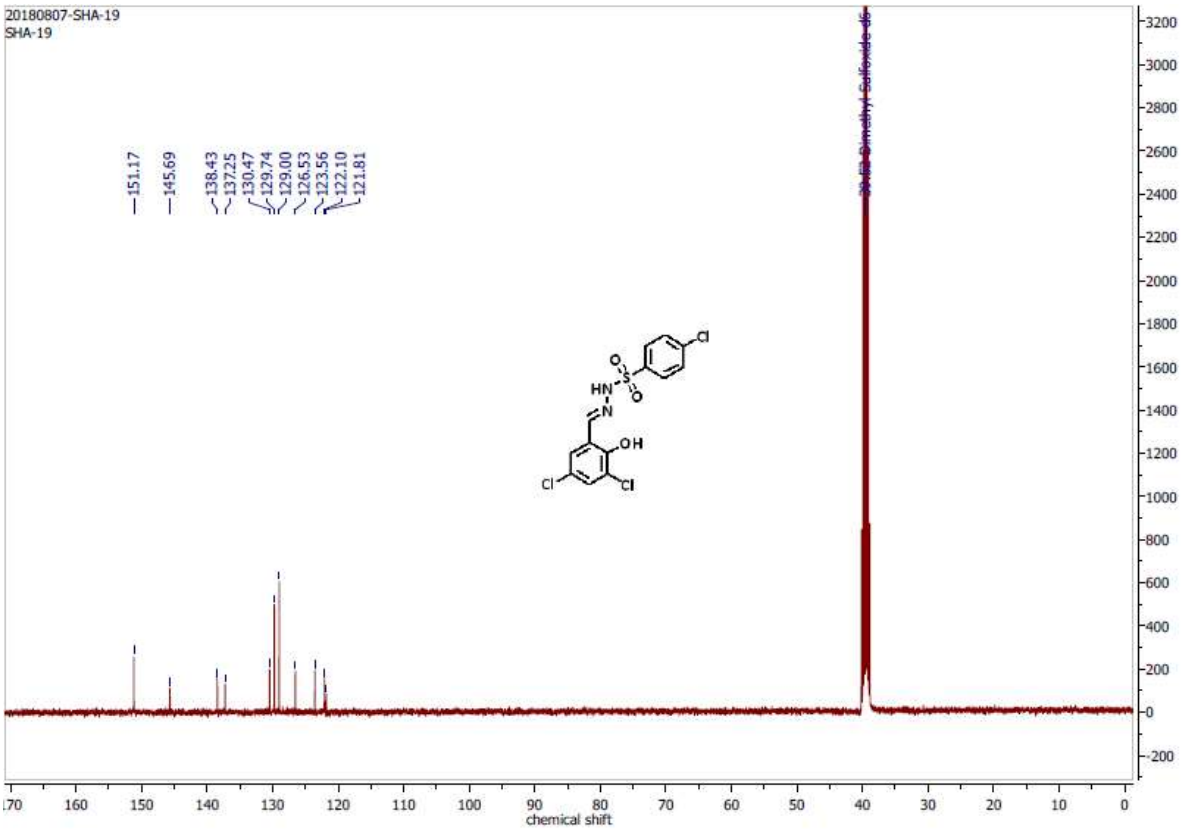

Figure C119: ^{13}C NMR spectrum of compound 40 in DMSO at 100 MHz.

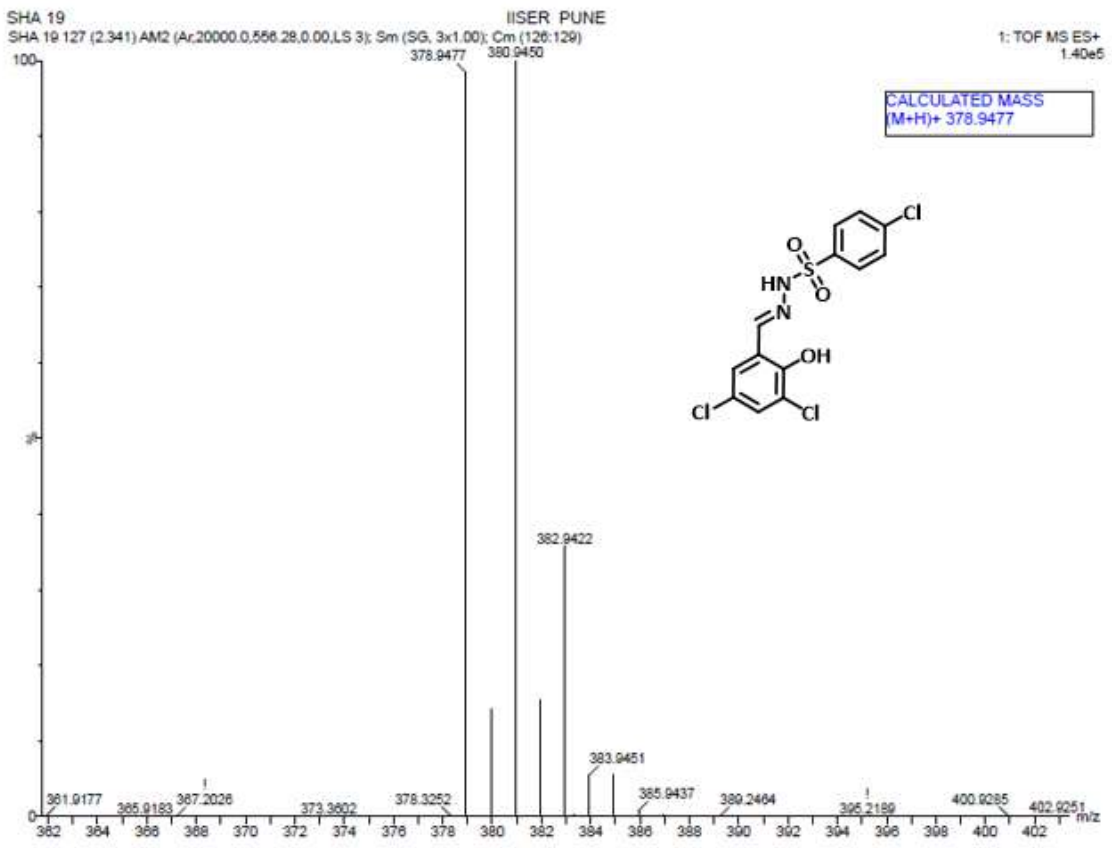

Figure C120: HRMS spectrum of compound 40.

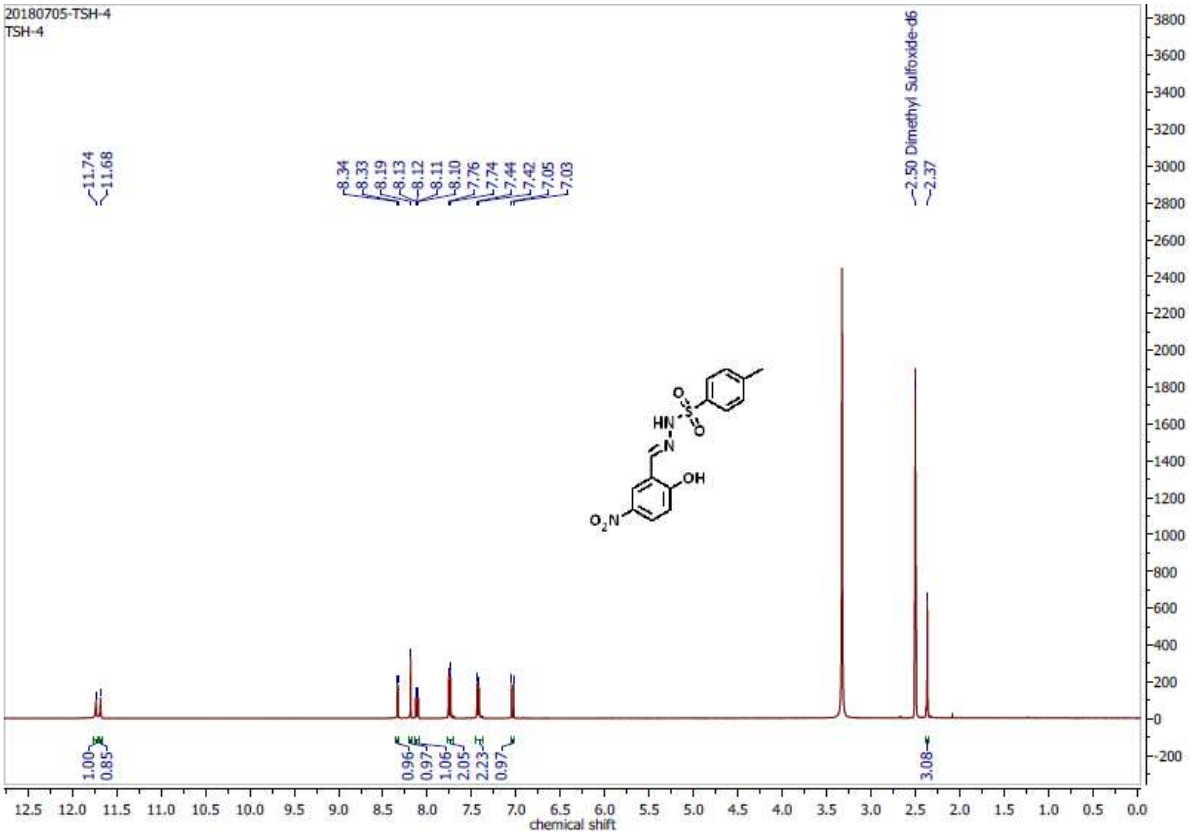

Figure C121: [1] H NMR spectrum of compound 41 in DMSO at 400 MHz.

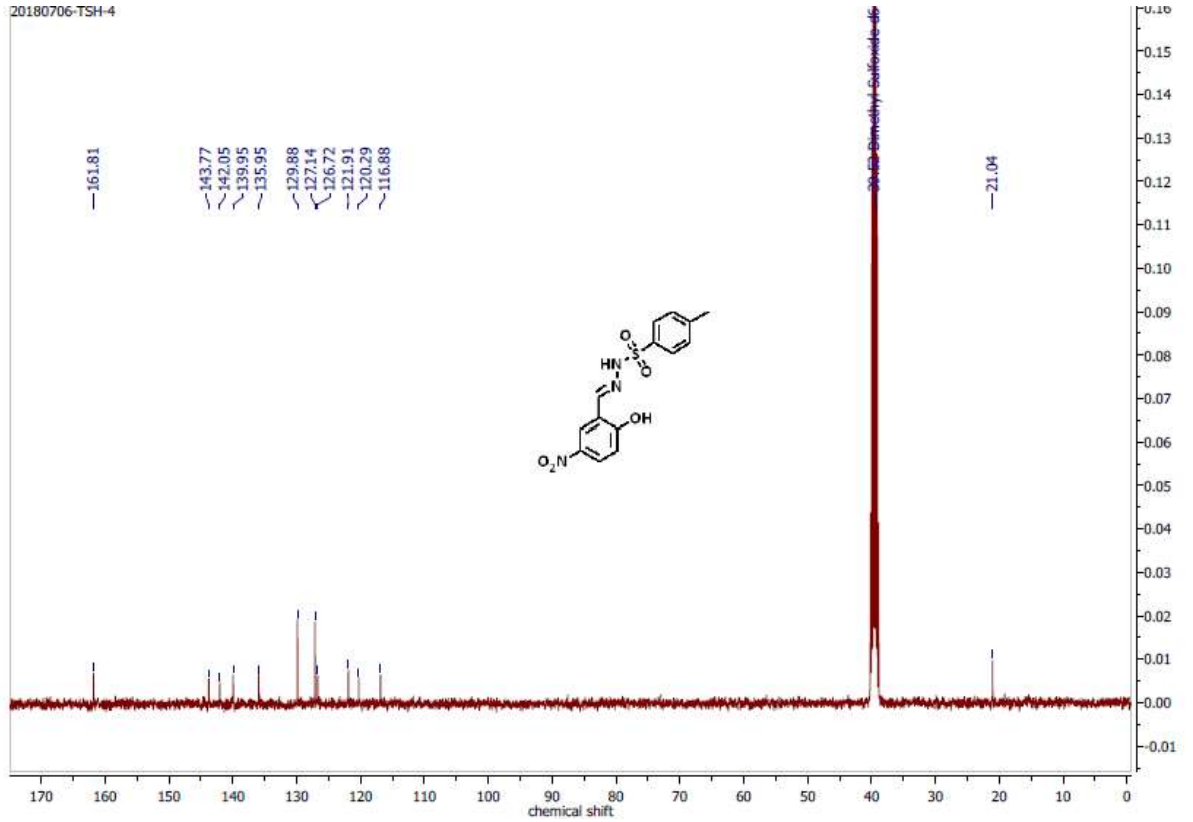

Figure C122: ^{13}C NMR spectrum of compound 41 in DMSO at 100 MHz.

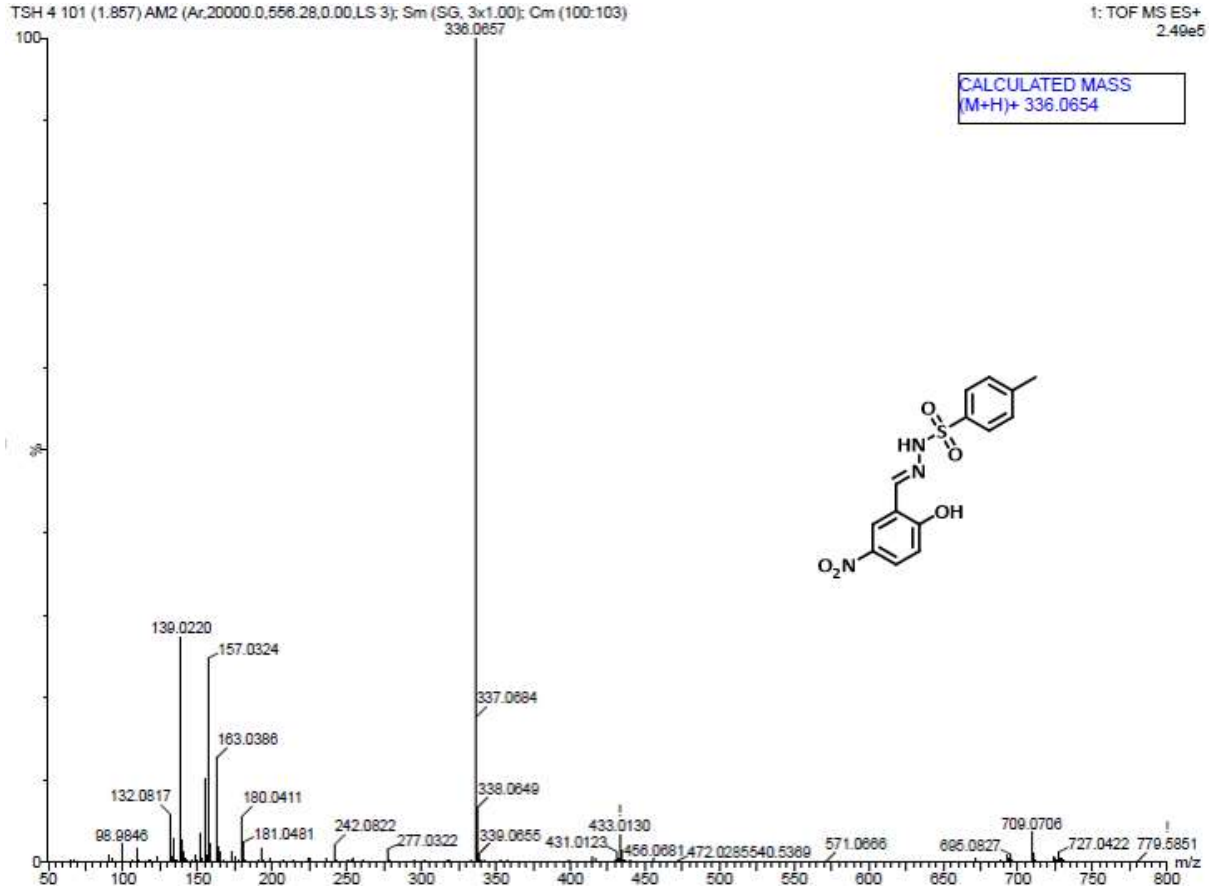

Figure C123: HRMS spectrum of compound 41.

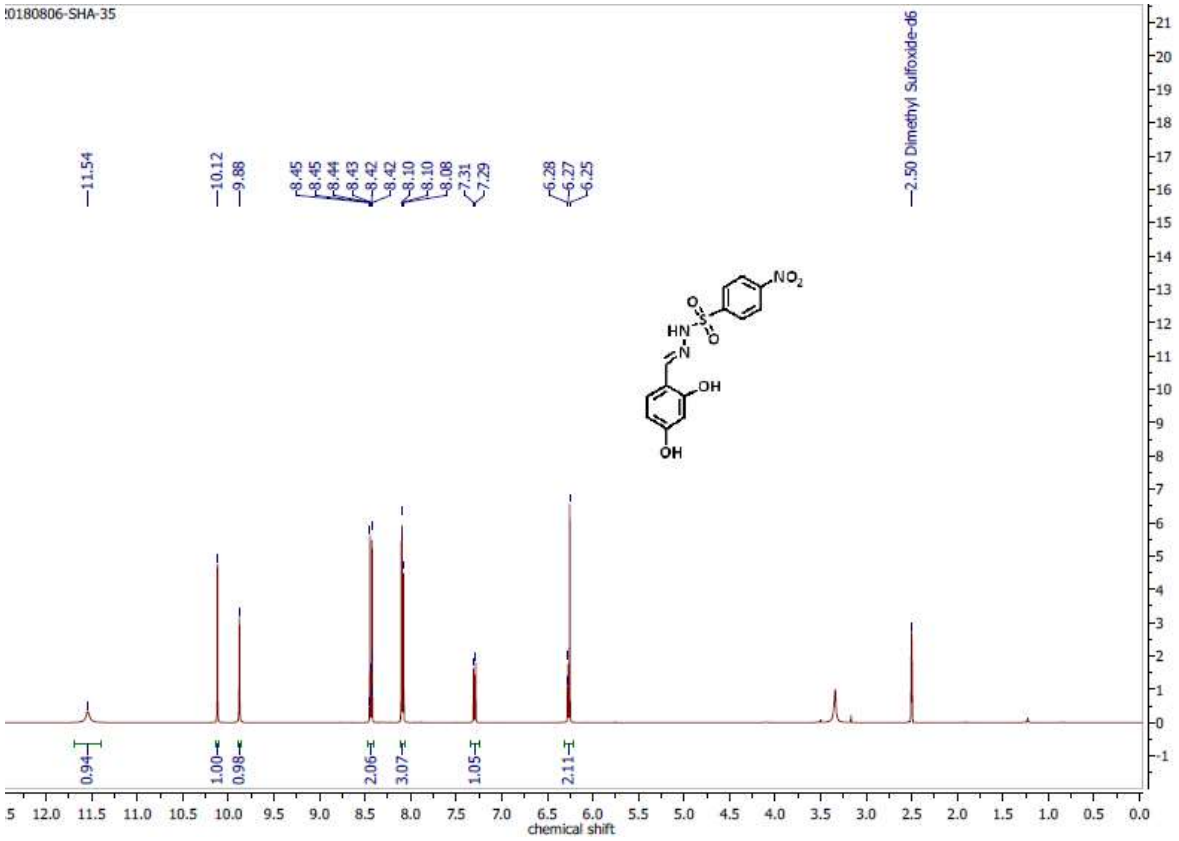

Figure C124: [1] H NMR spectrum of compound 42 in DMSO at 400 MHz.

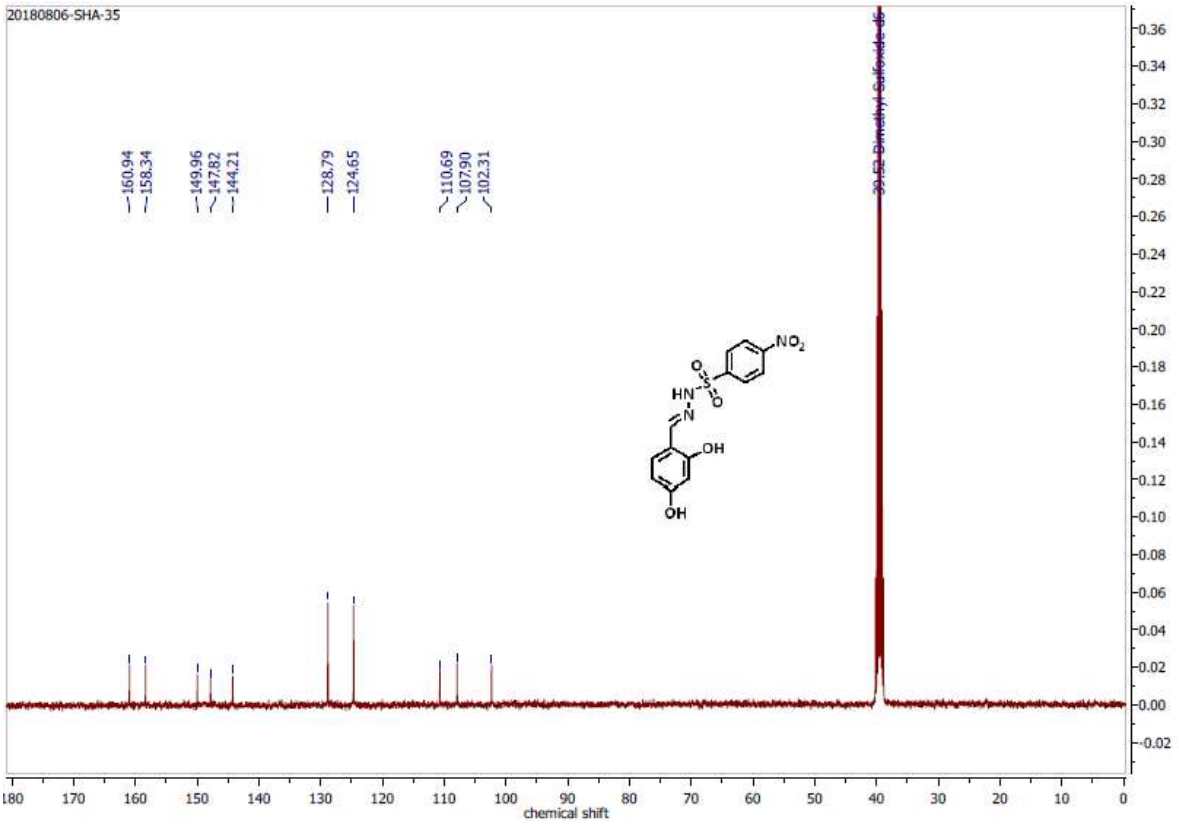

Figure C125: [13] C NMR spectrum of compound 42 in DMSO at 100 MHz.

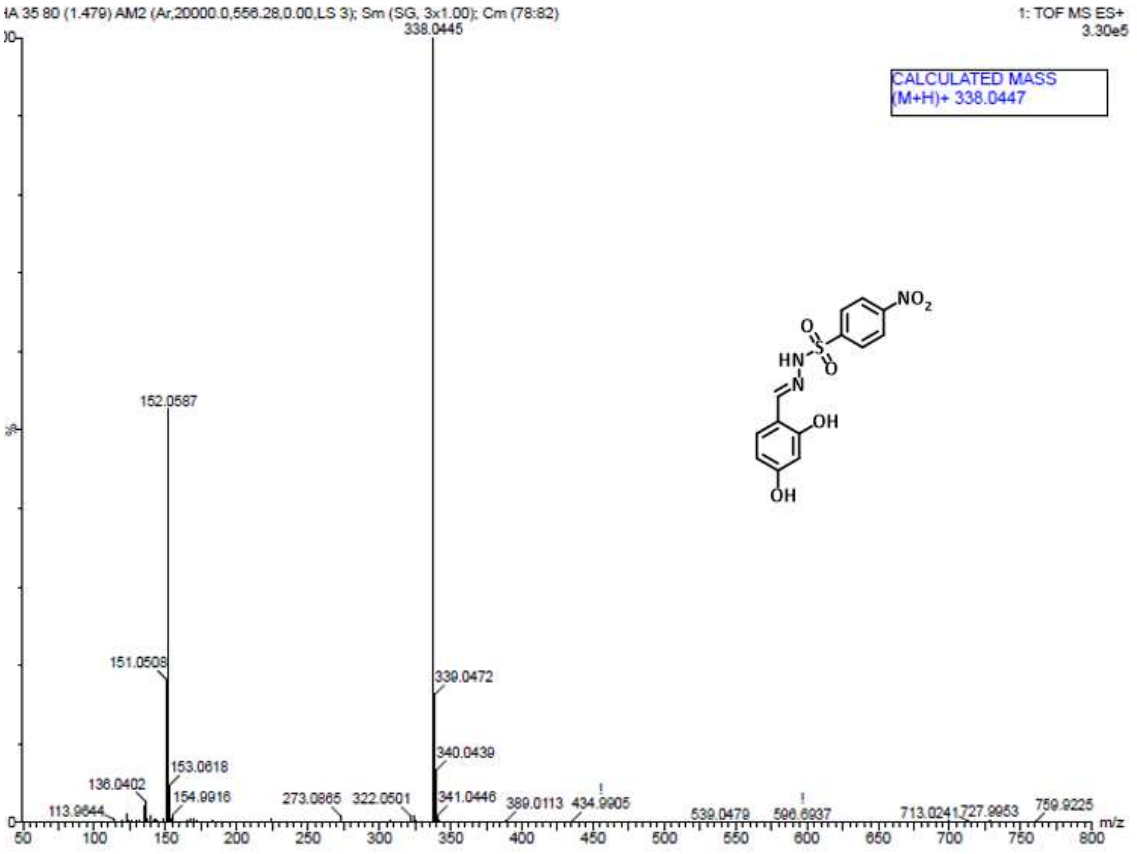

Figure C126: HRMS spectrum of compound 42.

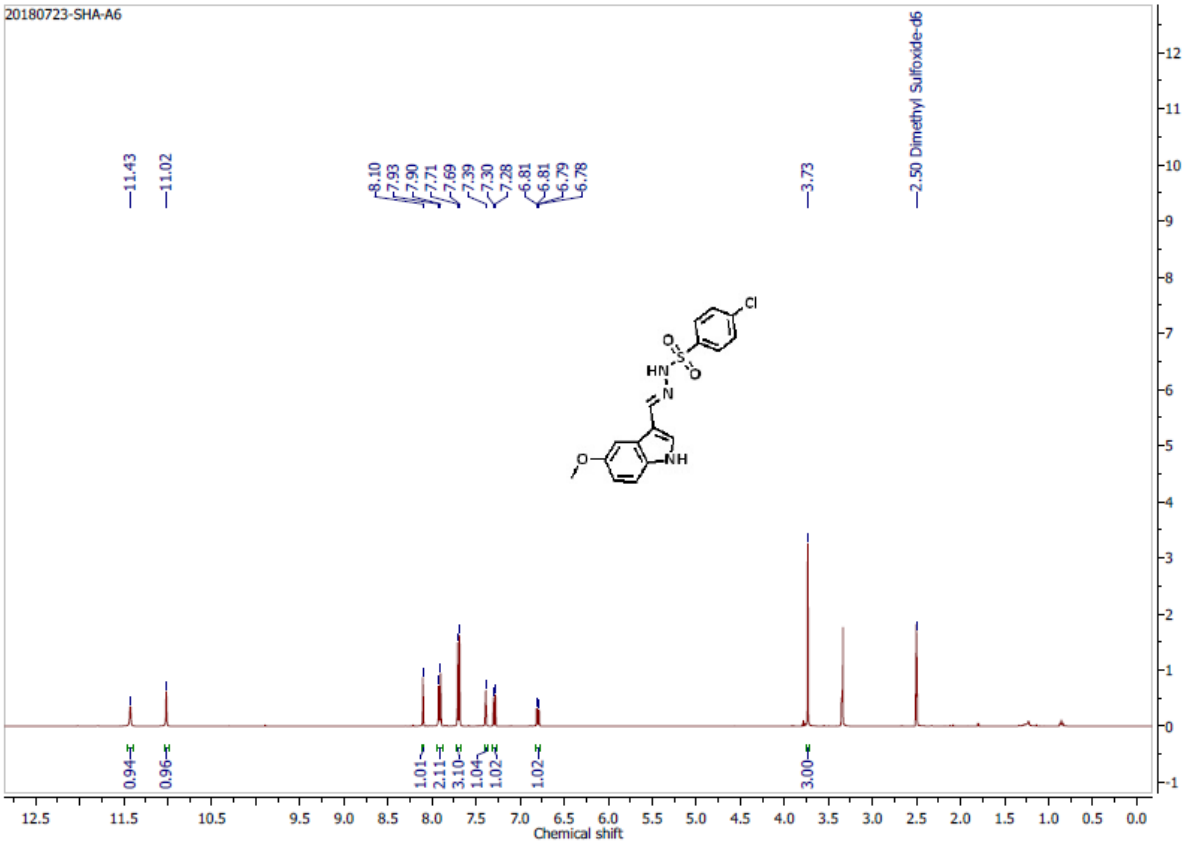

Figure C127: [1] H NMR spectrum of compound 43 in DMSO at 400 MHz.

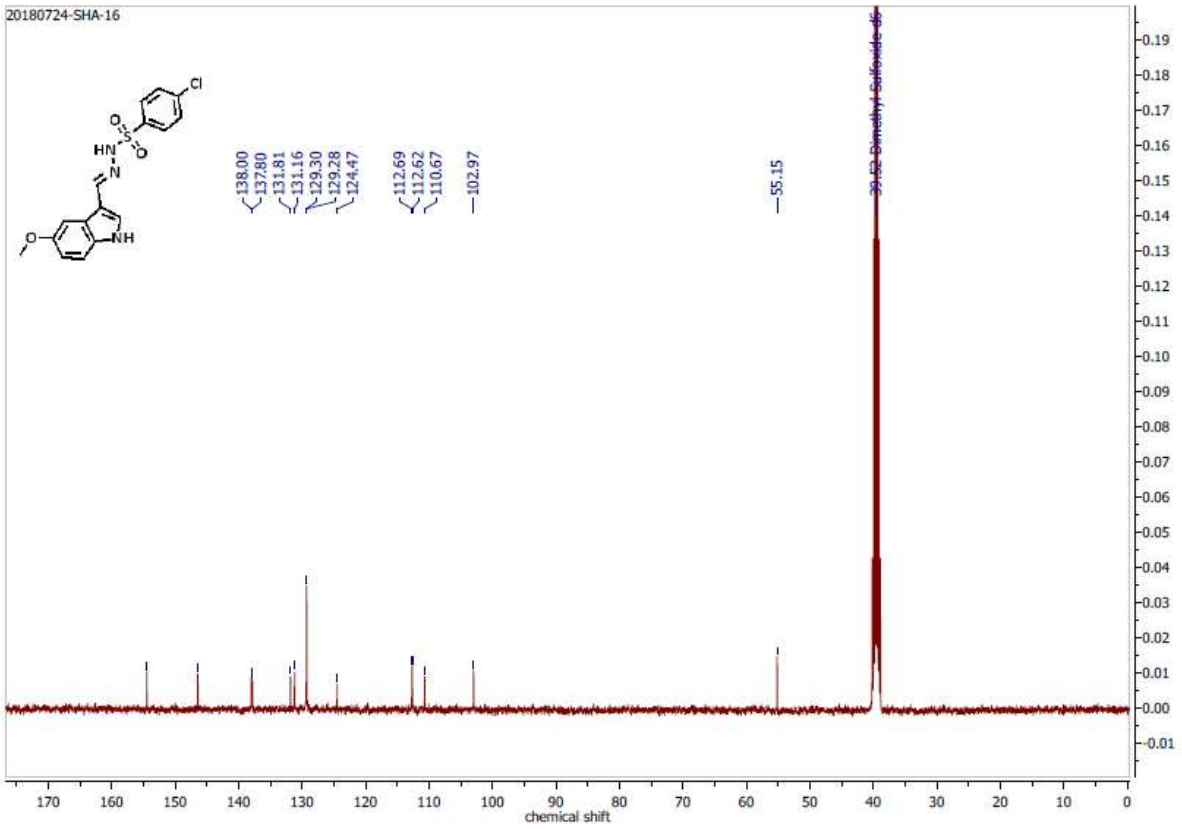

Figure C128: ^{13}C NMR spectrum of compound 43 in DMSO at 100 MHz.

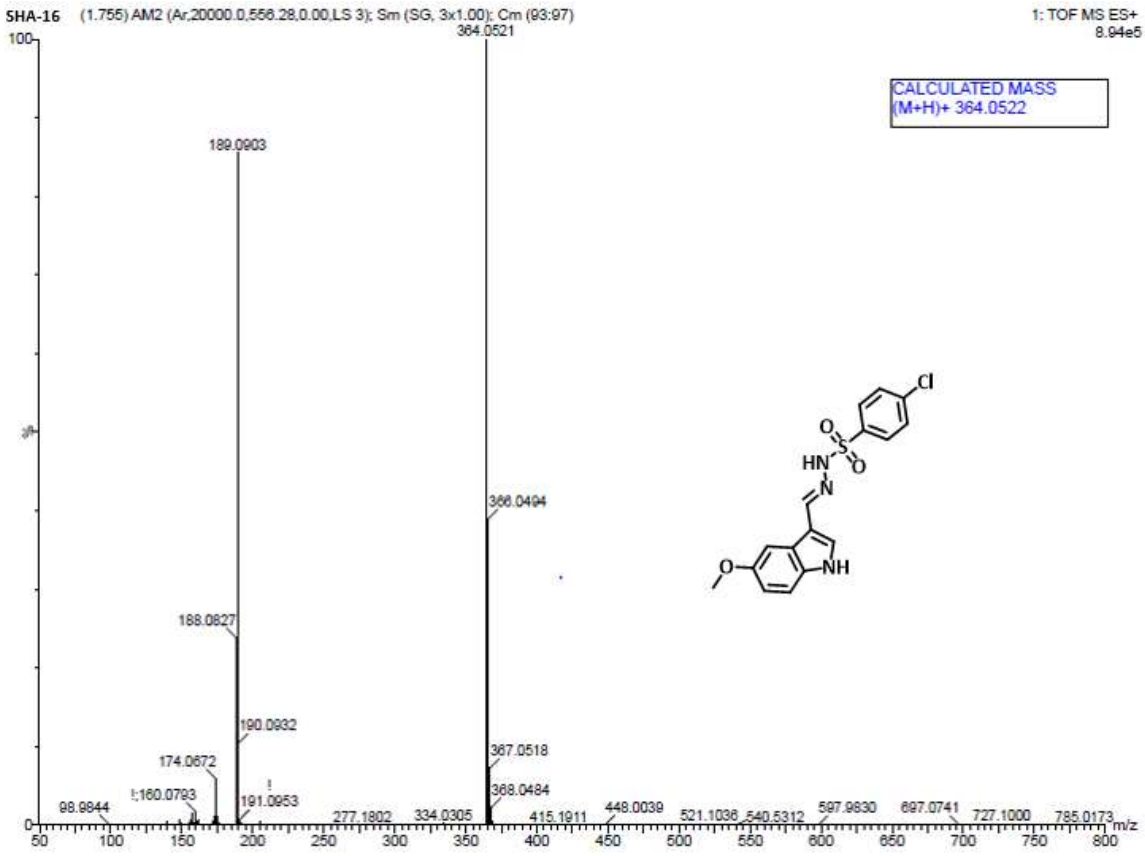

Figure C129: HRMS spectrum of compound 43.

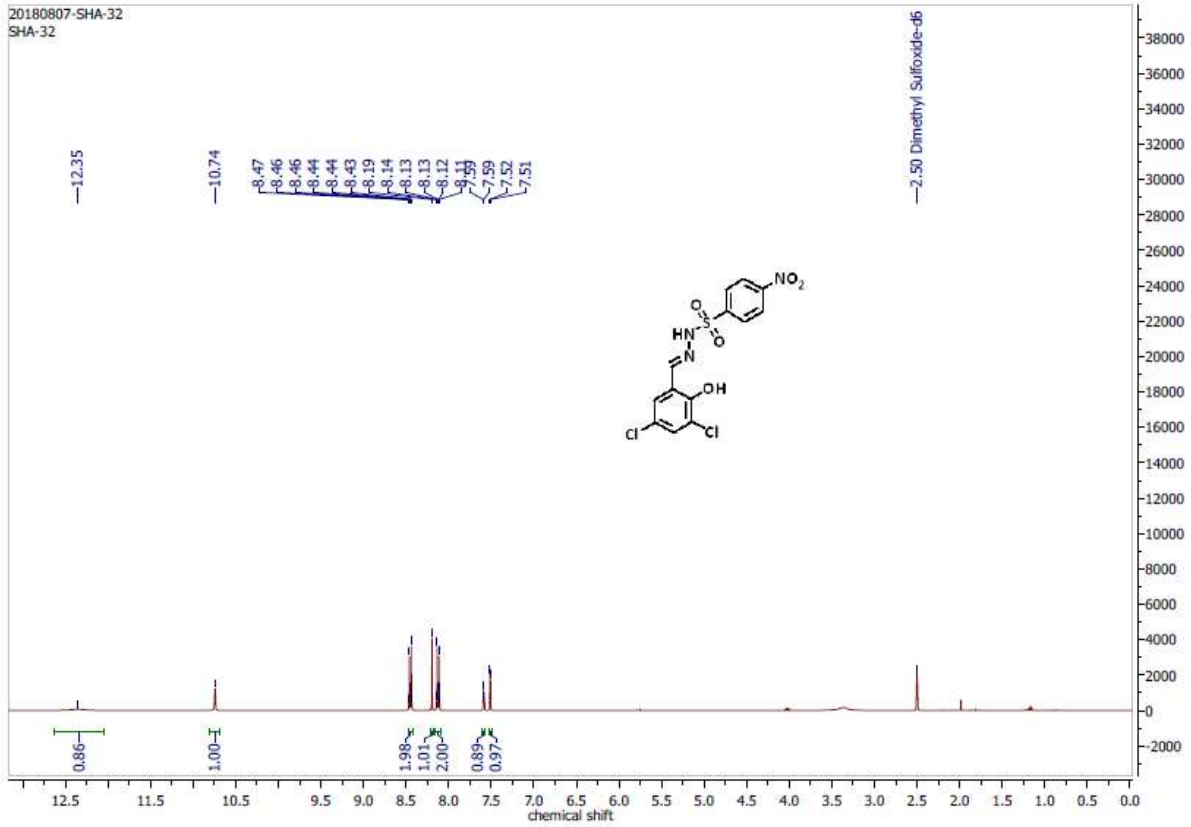

Figure C130: [1] H NMR spectrum of compound 44 in DMSO at 400 MHz.

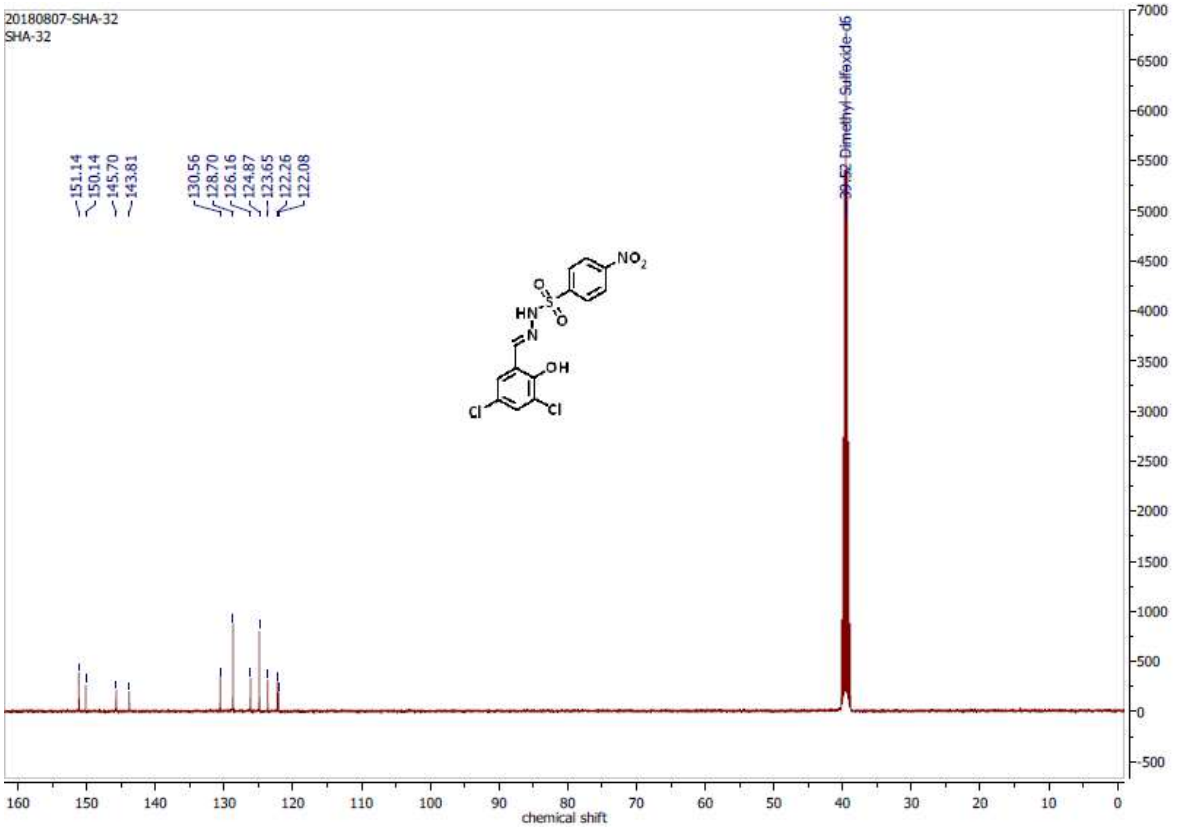

Figure C131: [13] C NMR spectrum of compound 44 in DMSO at 100 MHz.

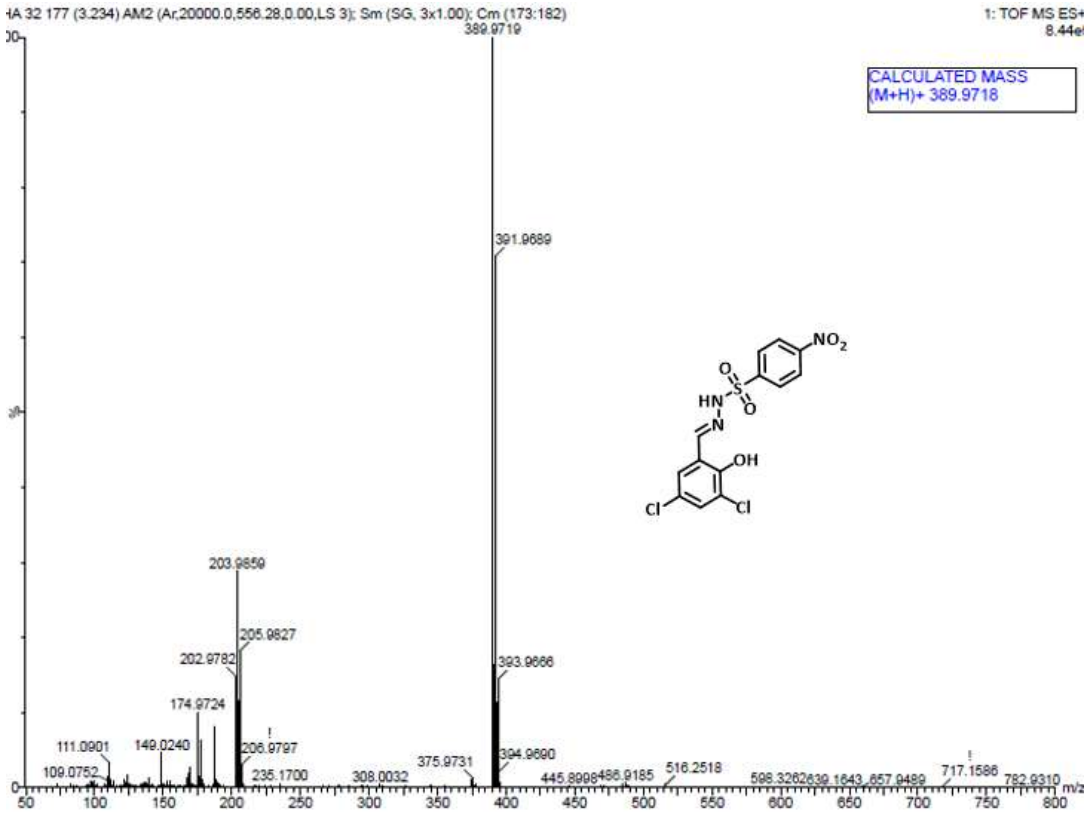

Figure C132: HRMS spectrum of compound 44.

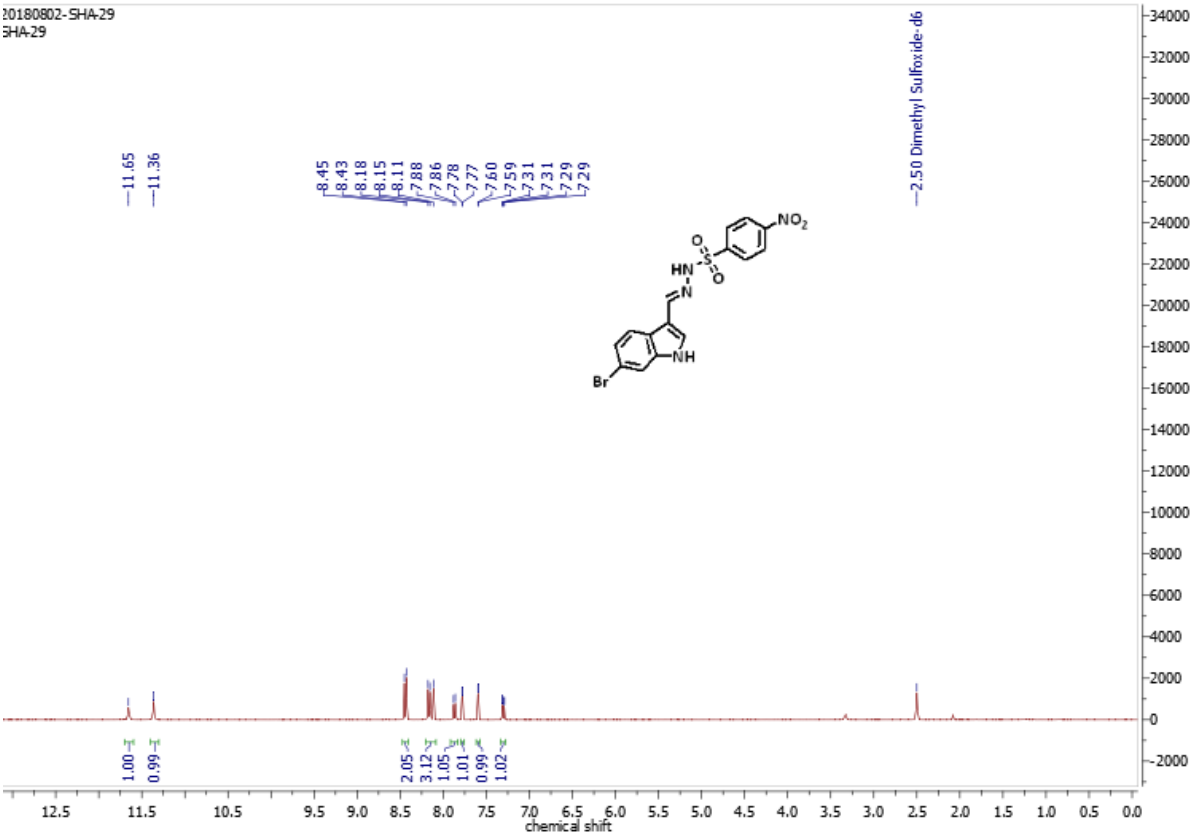

Figure C133: [1] H NMR spectrum of compound 45 in DMSO at 400 MHz.

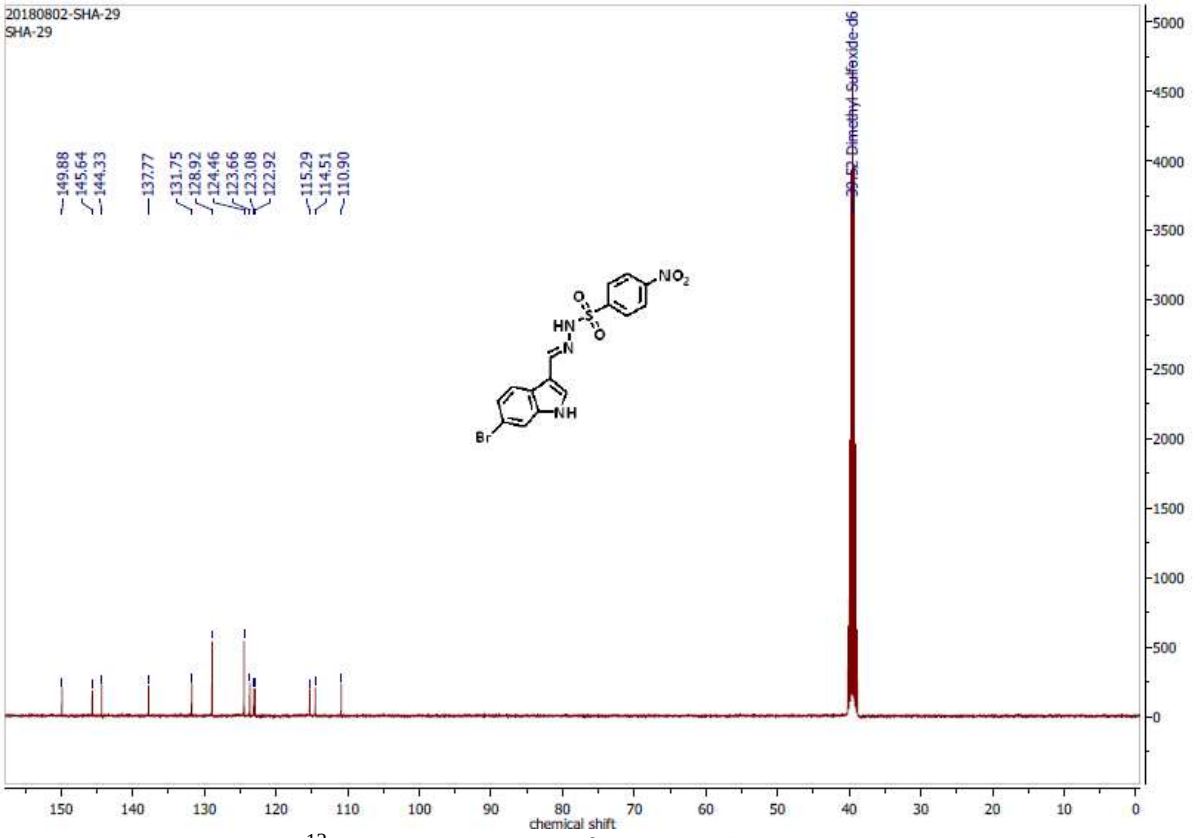

Figure C134: ^{13}C NMR spectrum of compound 45 in DMSO at 100 MHz.

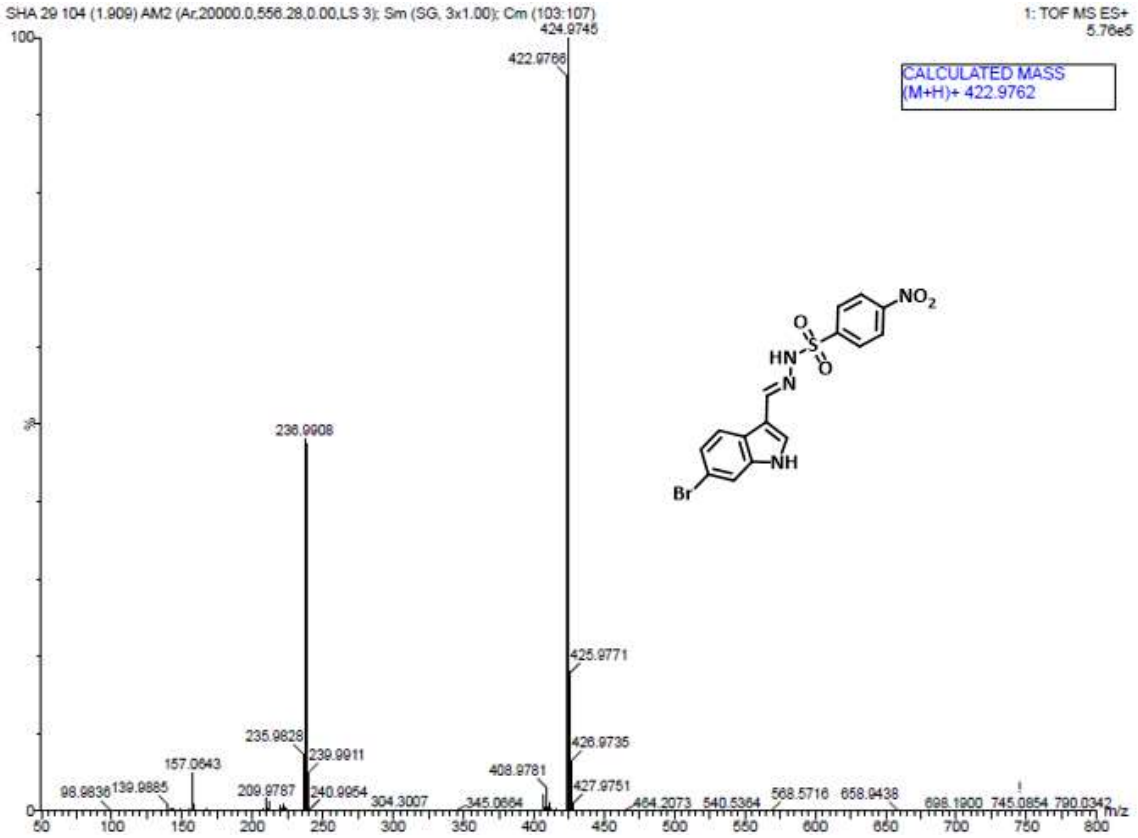

Figure C135: HRMS spectrum of compound 45.

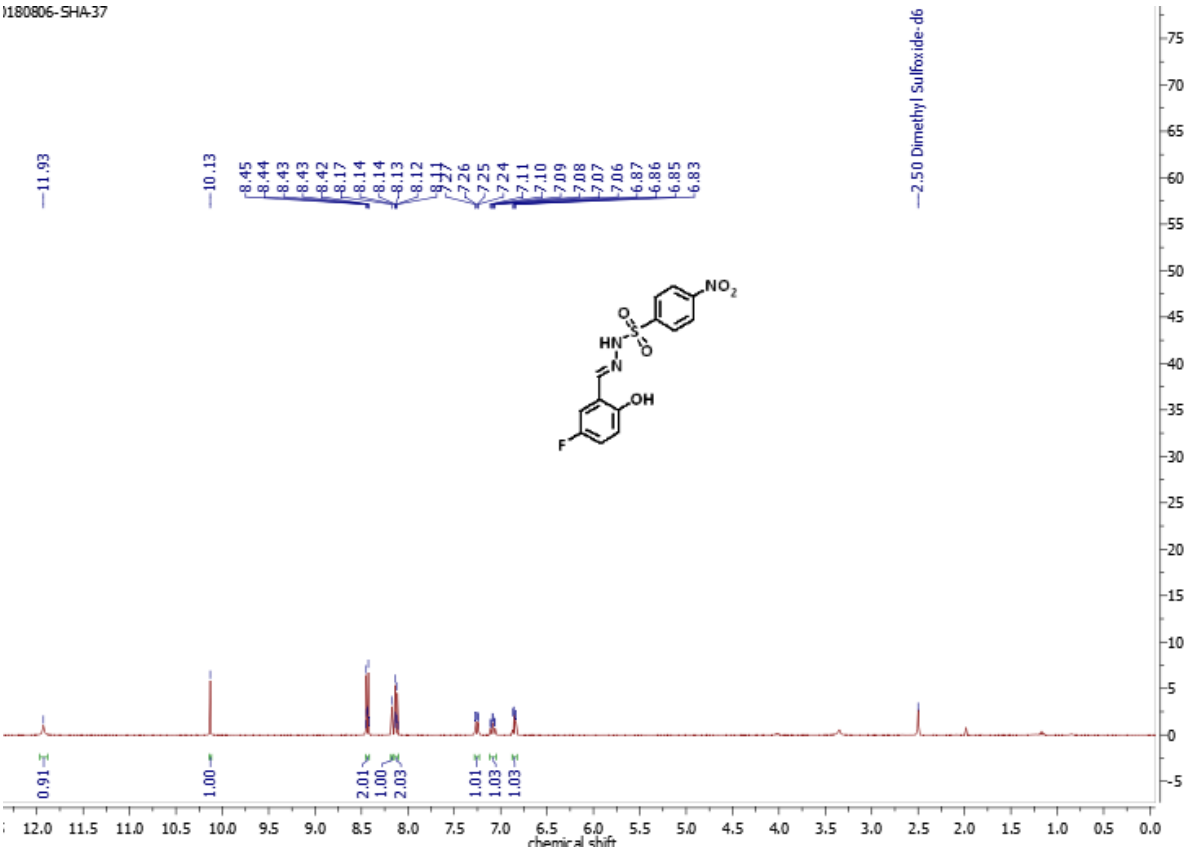

Figure C136: [1] H NMR spectrum of compound 46 in DMSO at 400 MHz.

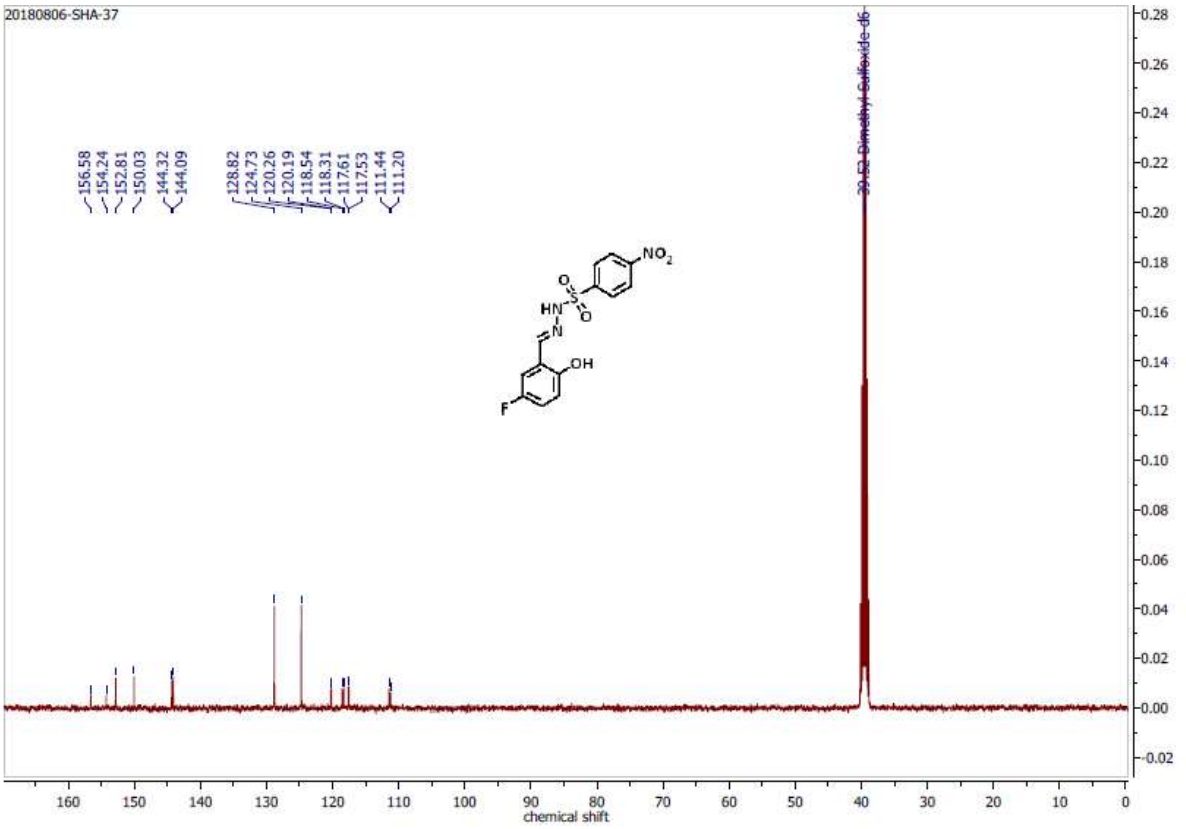

Figure C137: [13] C NMR spectrum of compound 46 in DMSO at 100 MHz.

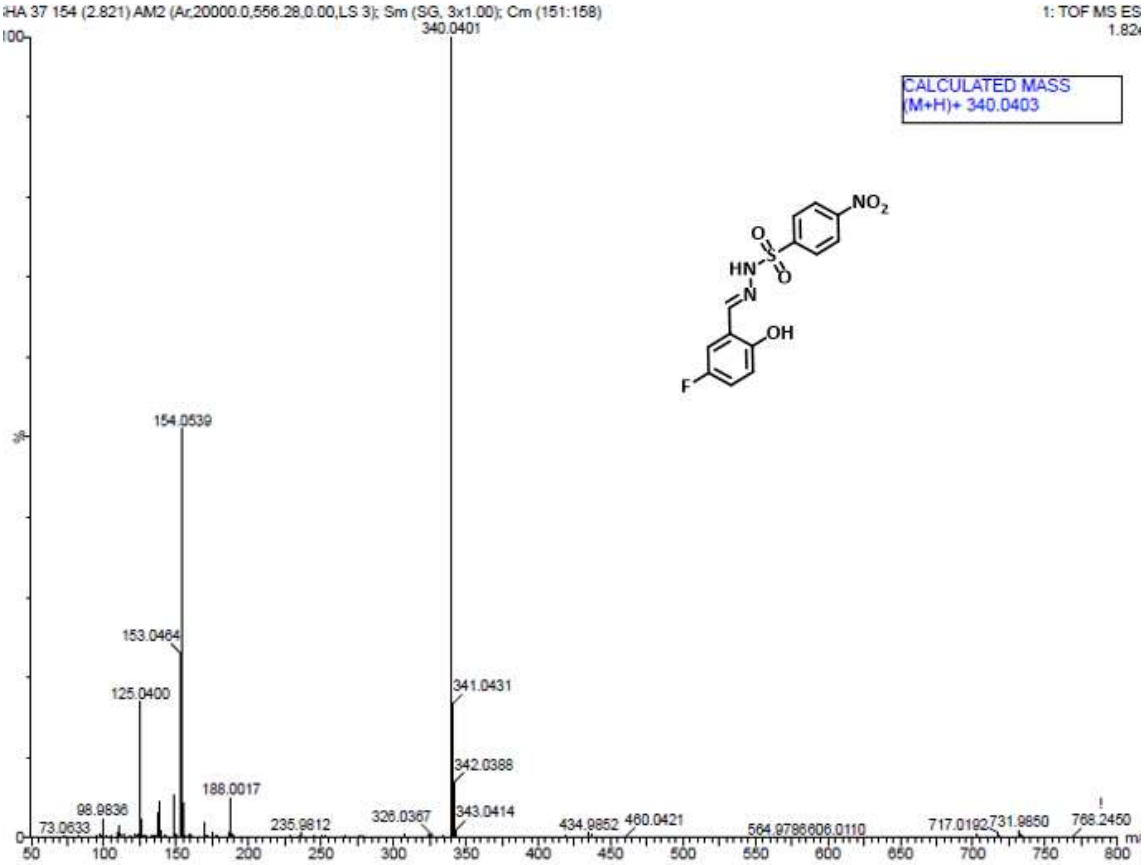

Figure C138: HRMS spectrum of compound 46.

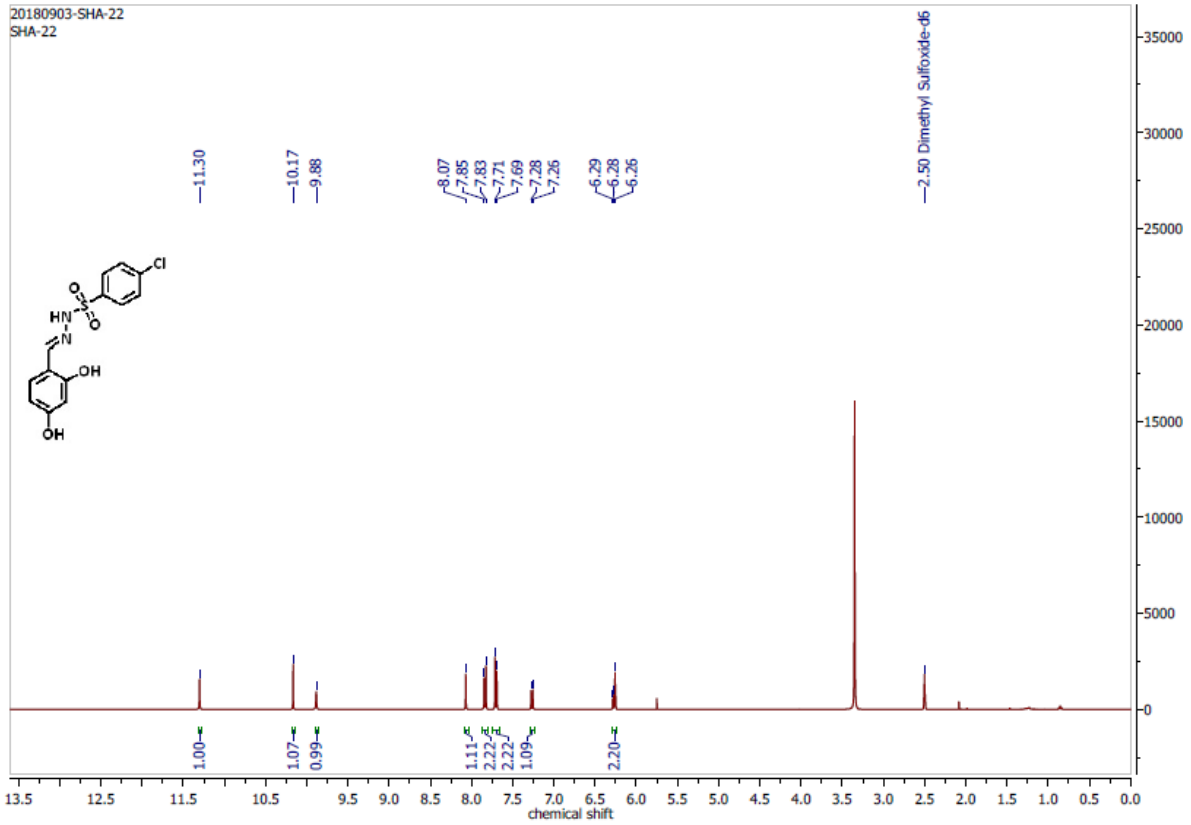

Figure C139: [1] H NMR spectrum of compound 47 in DMSO at 400 MHz.

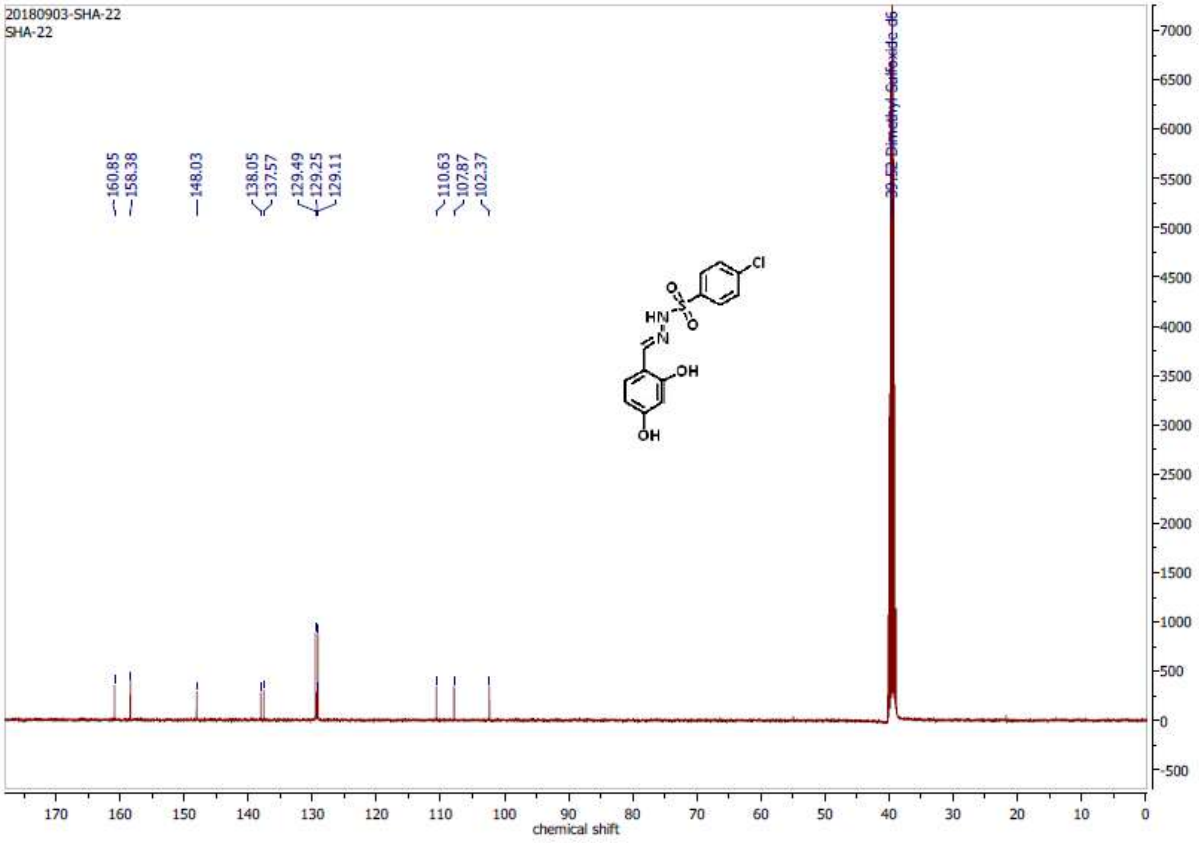

Figure C140: ^{13}C NMR spectrum of compound 47 in DMSO at 100 MHz.

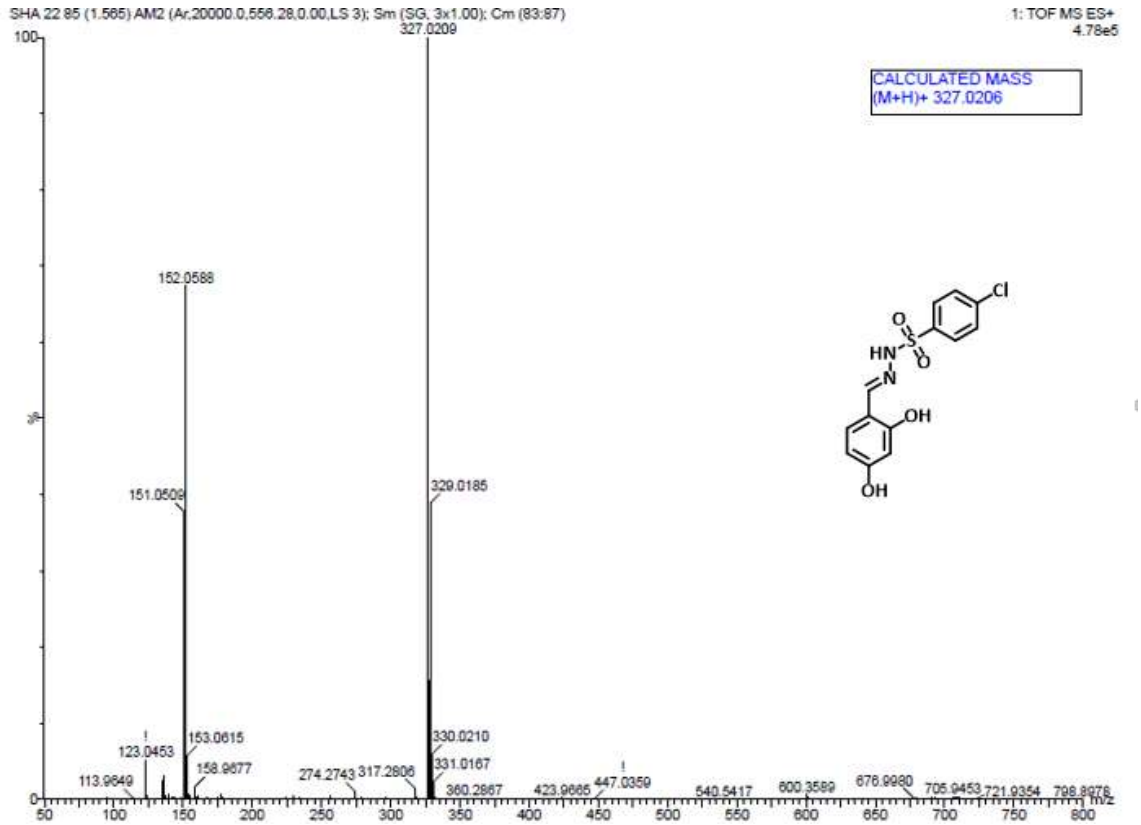

Figure C141: HRMS spectrum of compound 47.

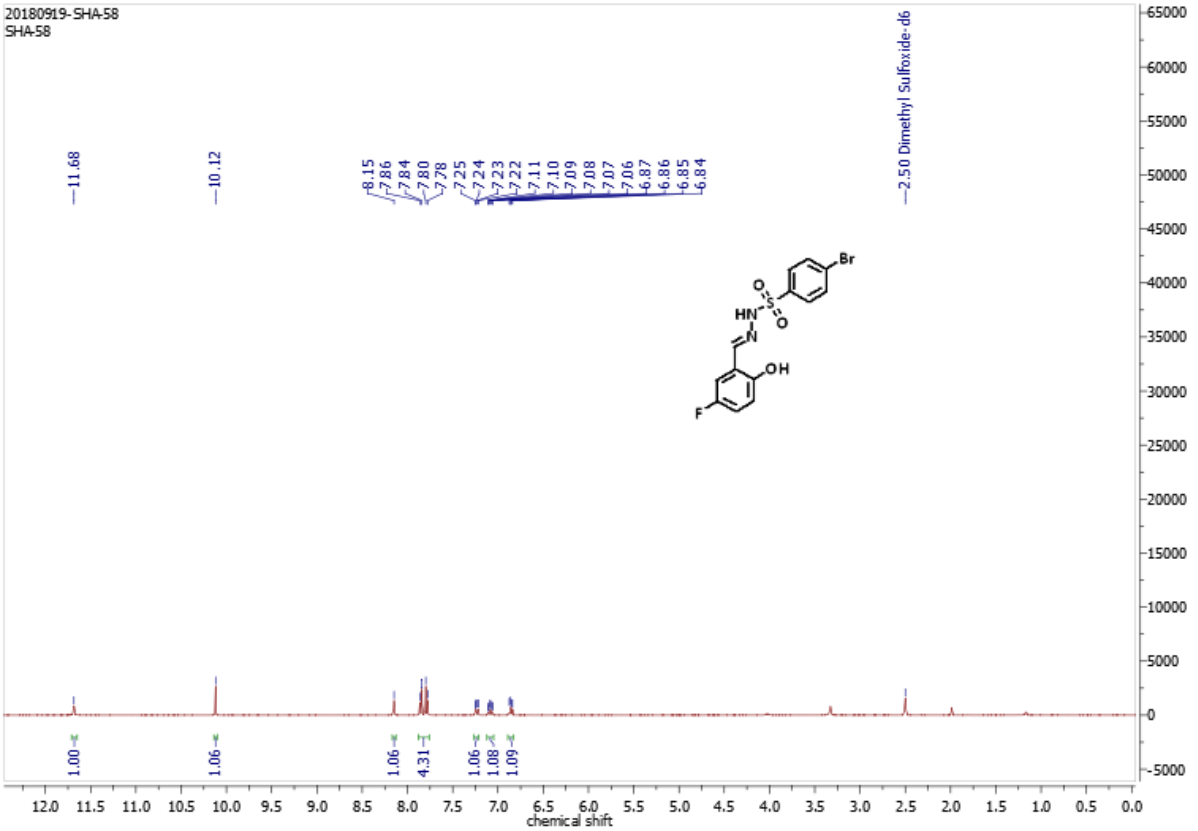

Figure C142: [1] H NMR spectrum of compound 48 in DMSO at 400 MHz.

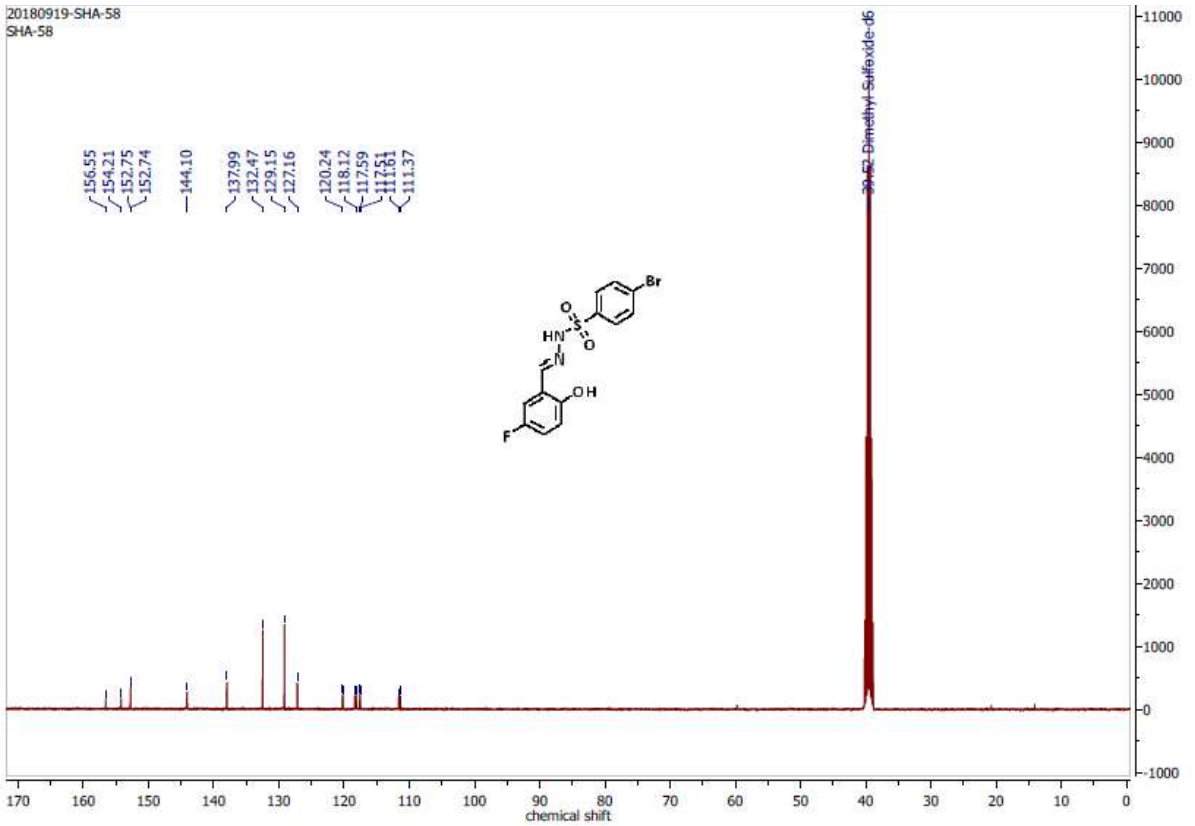

Figure C143: [13] C NMR spectrum of compound 48 in DMSO at 100 MHz.

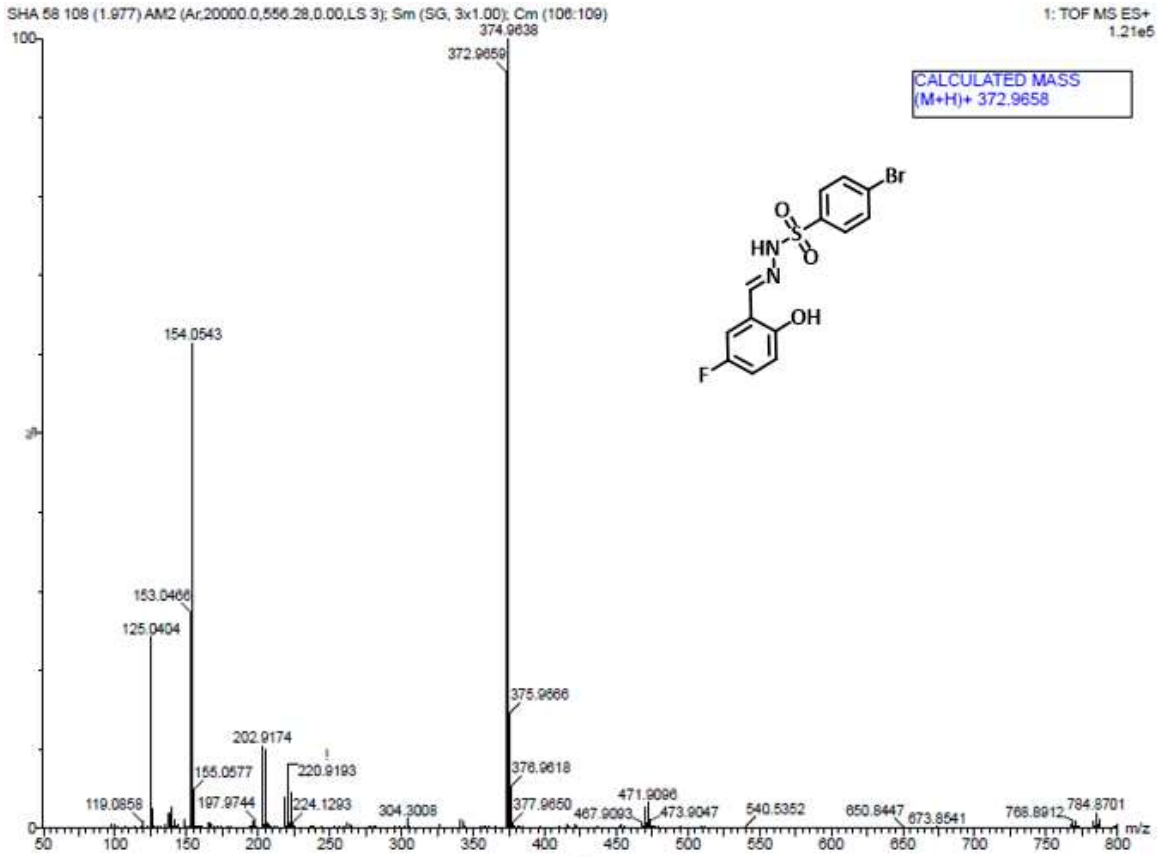

Figure C144: HRMS spectrum of compound 48.

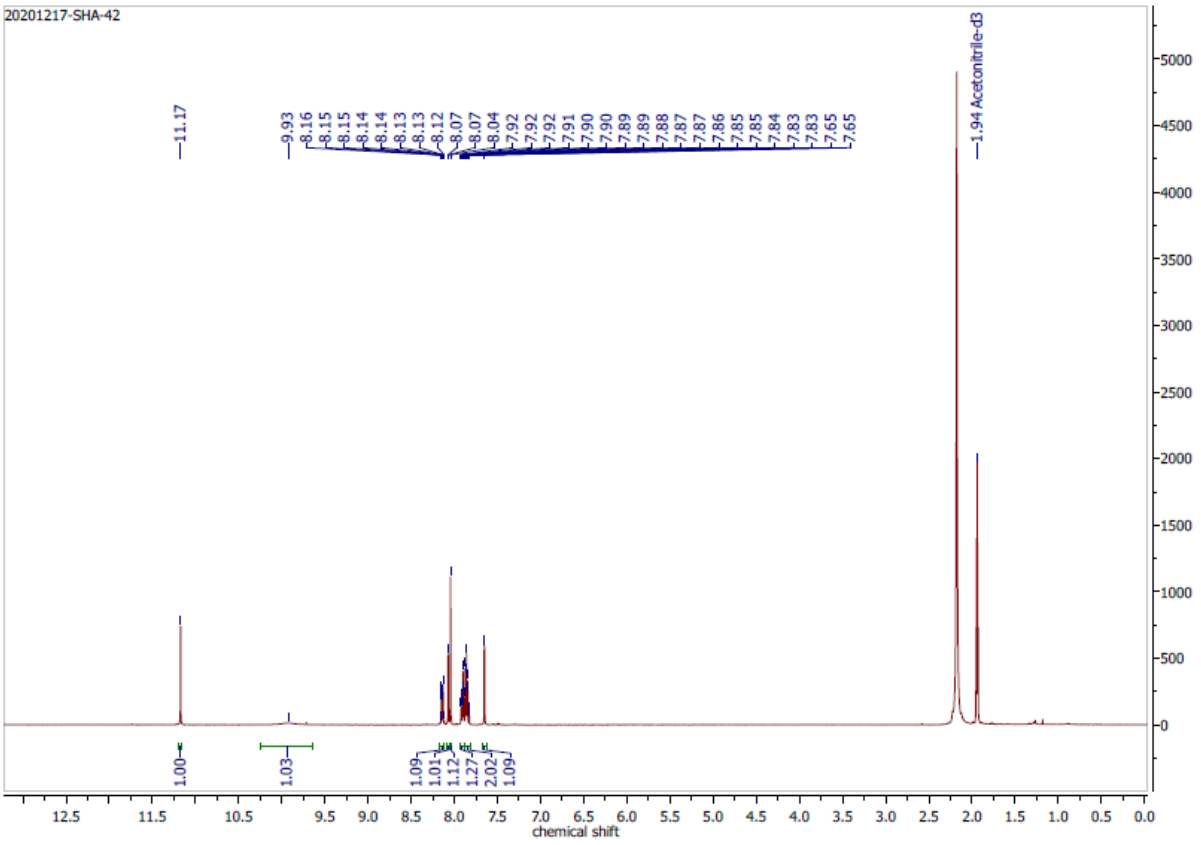

Figure C145: [1] H NMR spectrum of compound 49 in CD_3CN at 400 MHz.

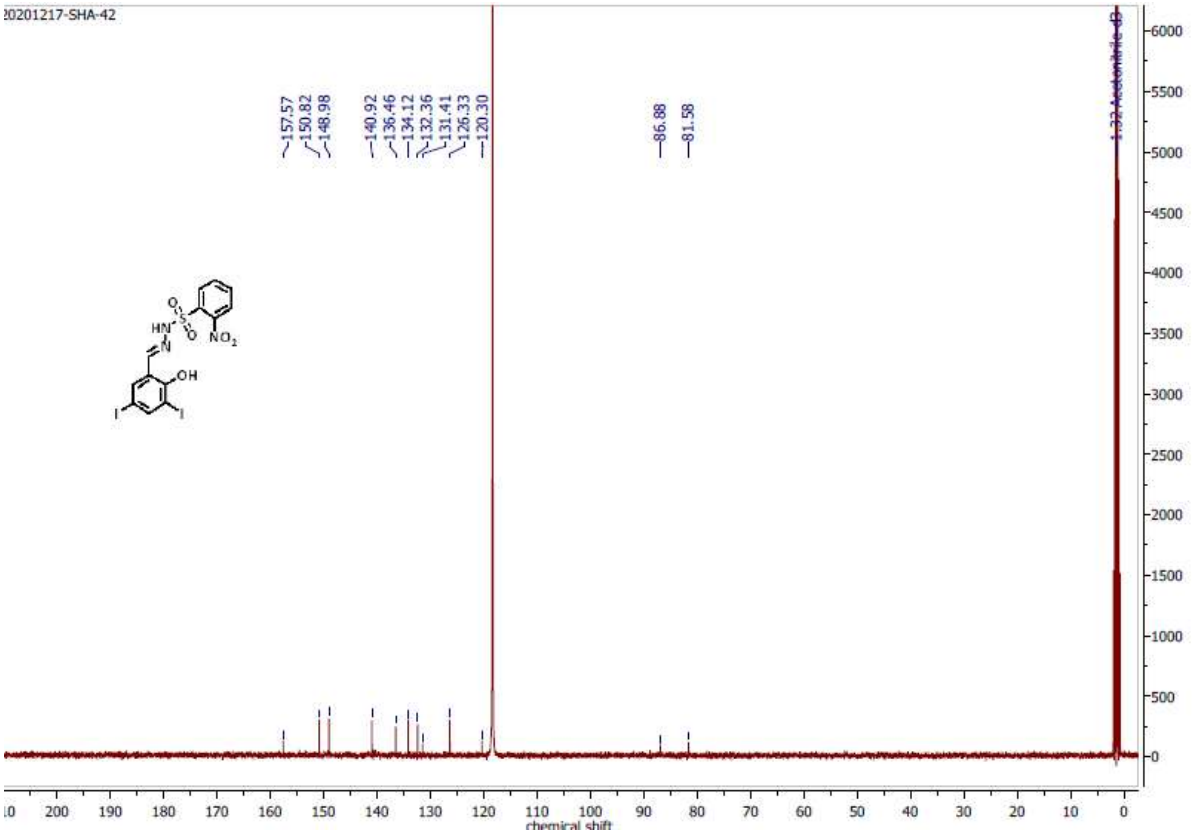

Figure C146: ^{13} C NMR spectrum of compound 49 in CD_3CN at 100 MHz.

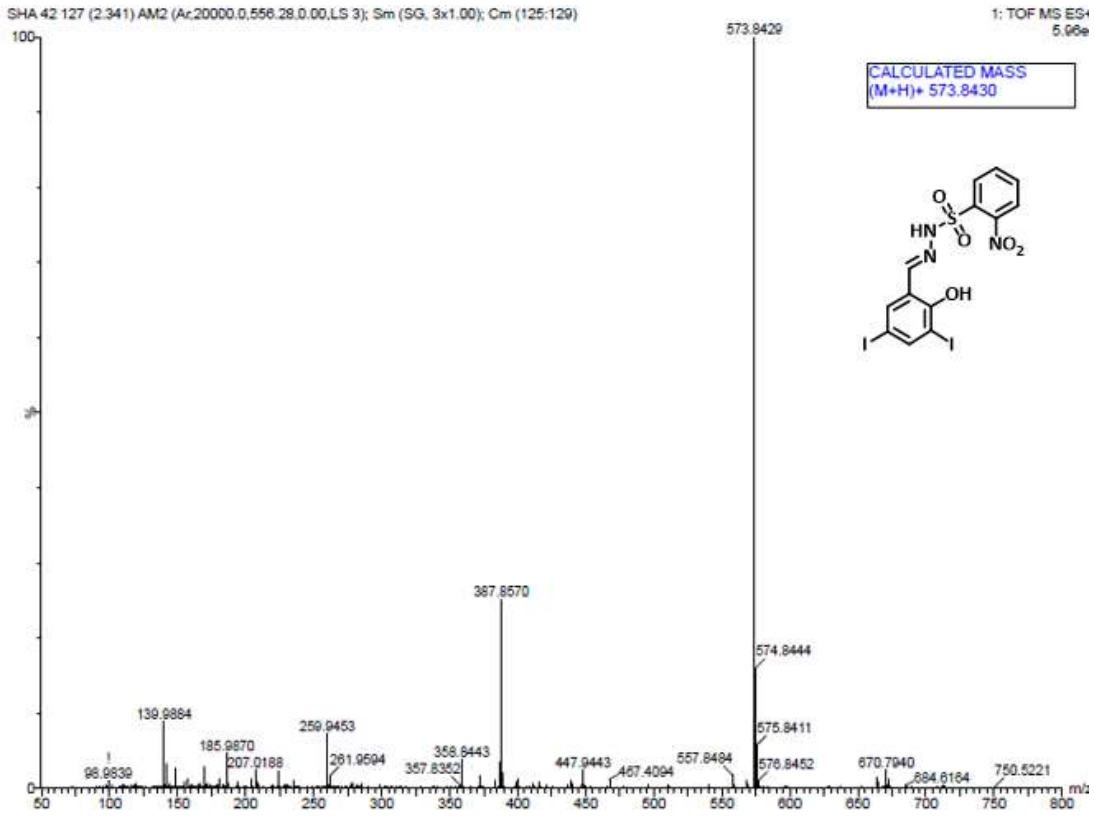

Figure C147: HRMS spectrum of compound 49.

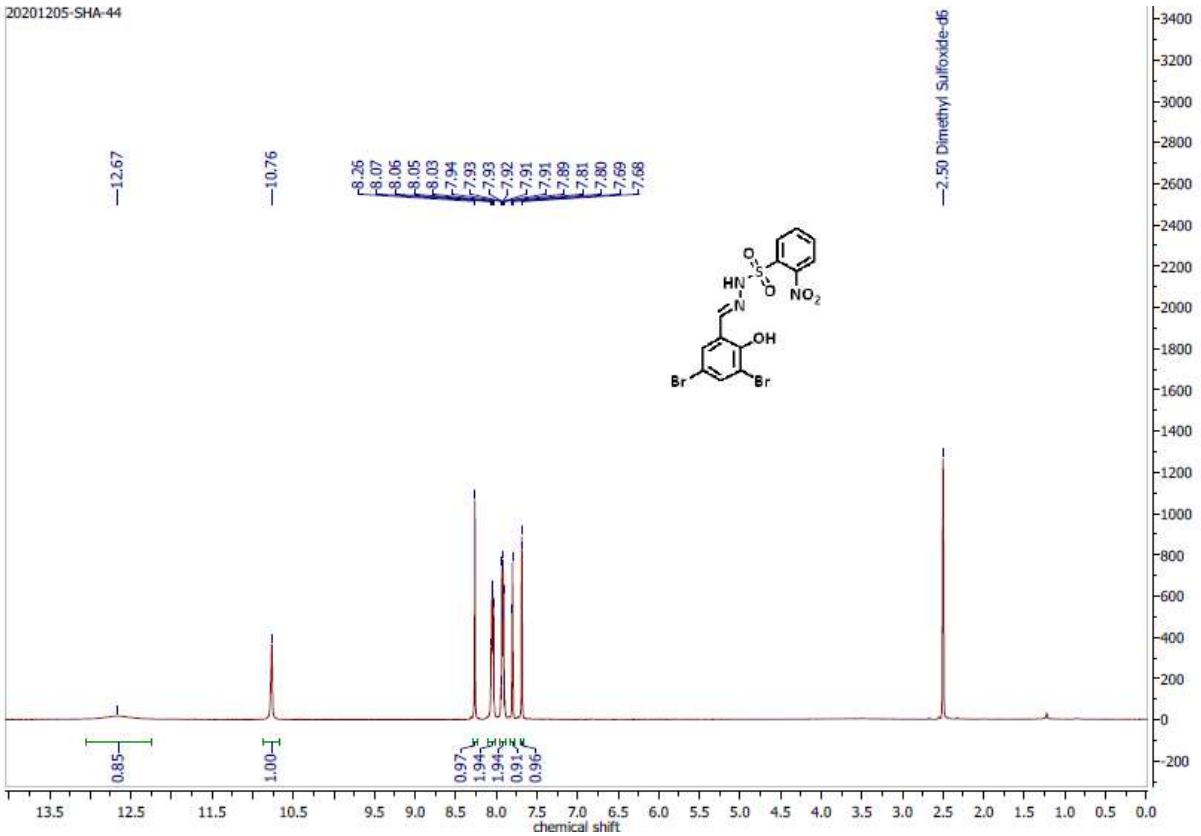

Figure C148: [1] H NMR spectrum of compound 50 in DMSO at 400 MHz.

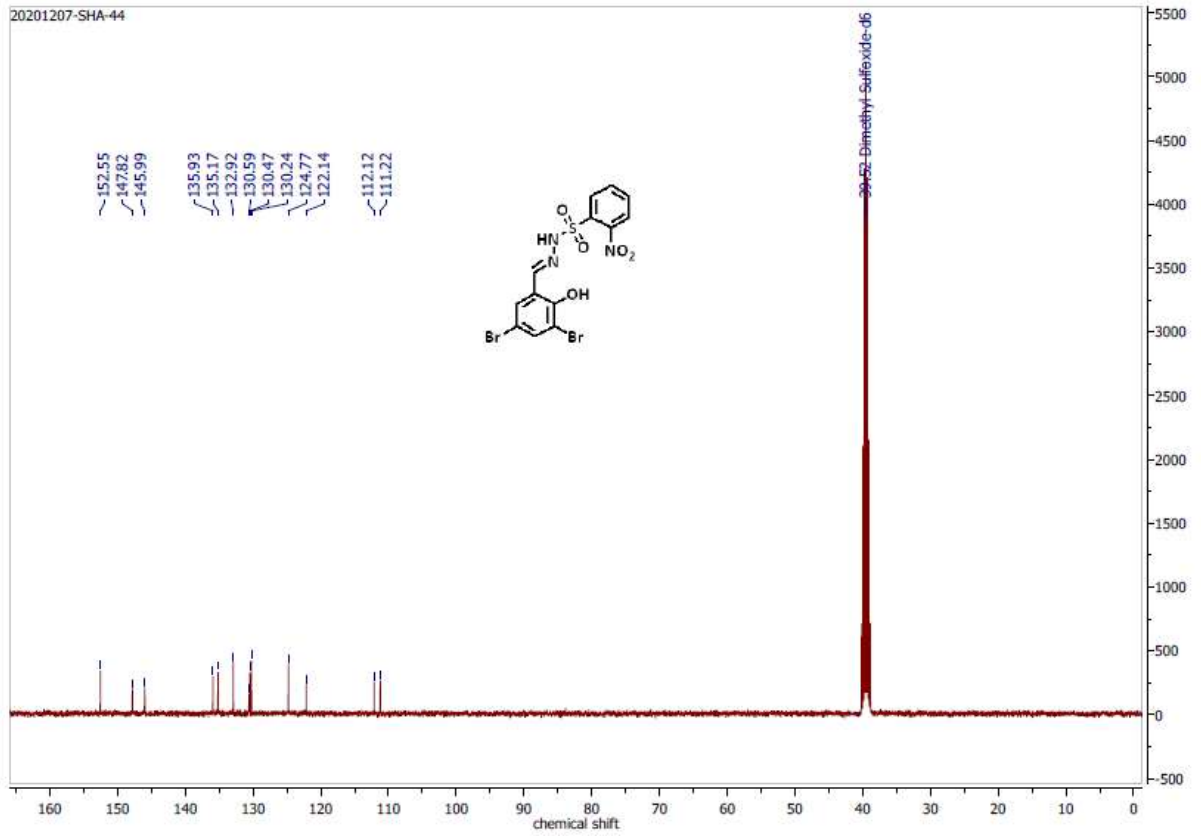

Figure C149: [13] C NMR spectrum of compound 50 in DMSO at 100 MHz.

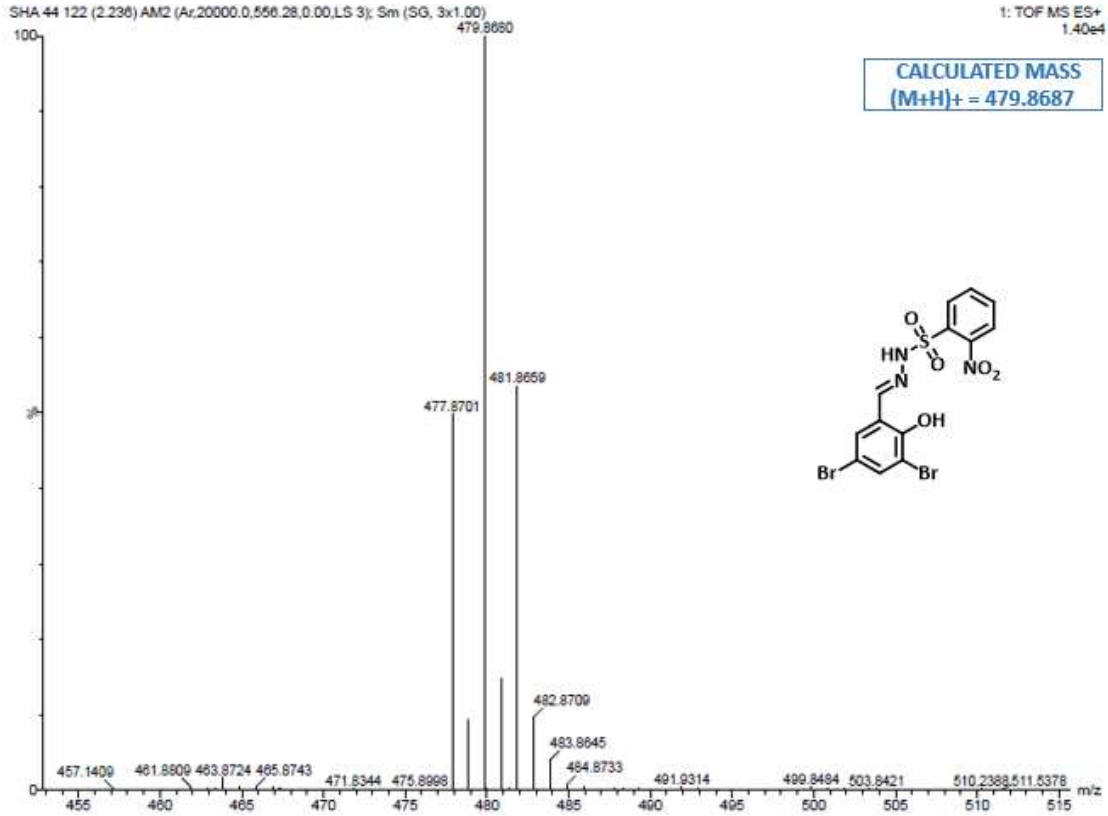

Figure C150: HRMS spectrum of compound 50.

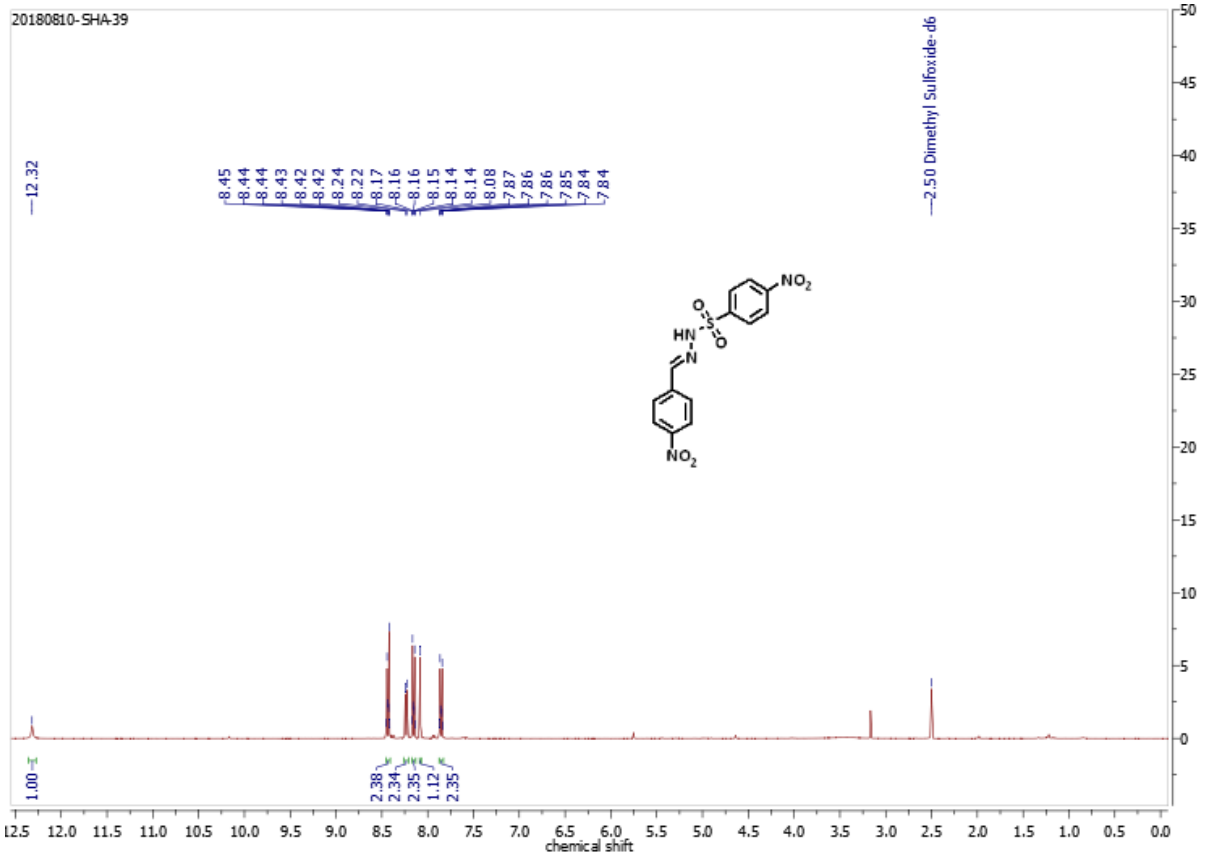

Figure C151: [1] H NMR spectrum of compound 51 in DMSO at 400 MHz.

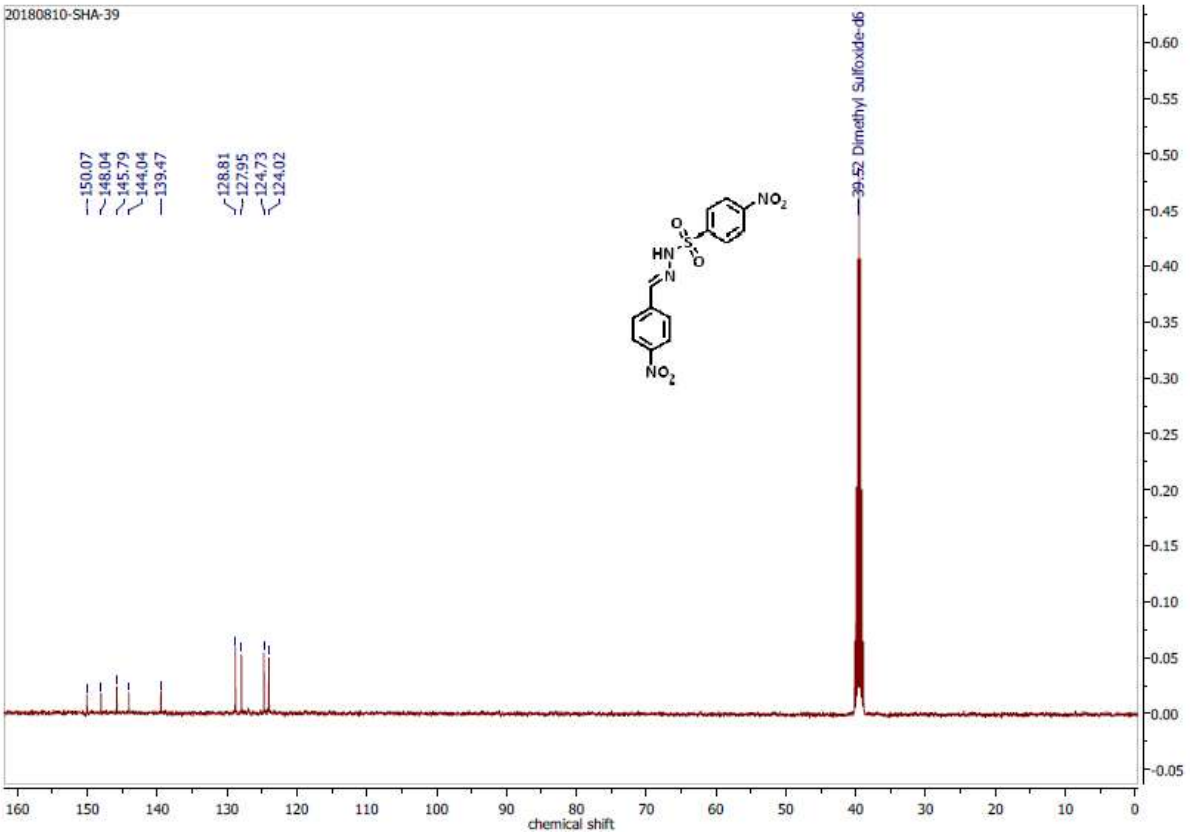

Figure C152: ^{13}C NMR spectrum of compound 51 in DMSO at 100 MHz.

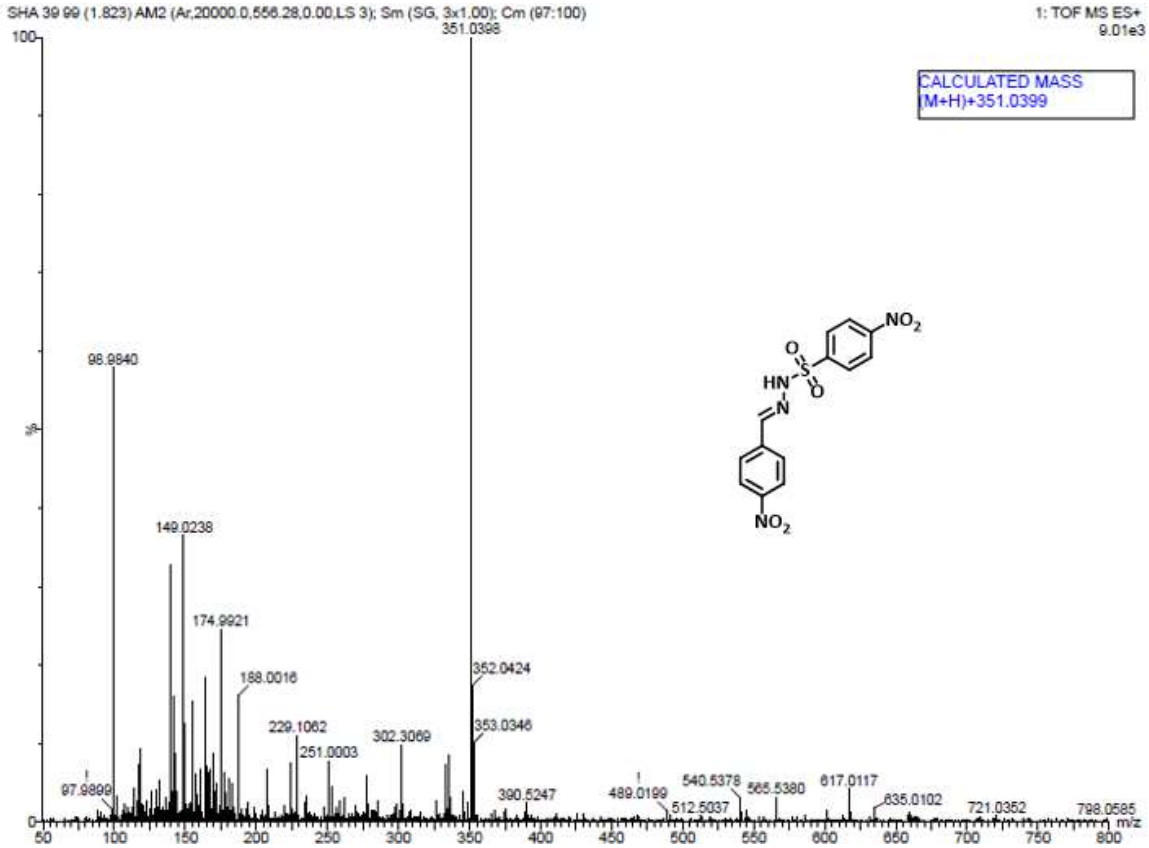

Figure C153: HRMS spectrum of compound 51.

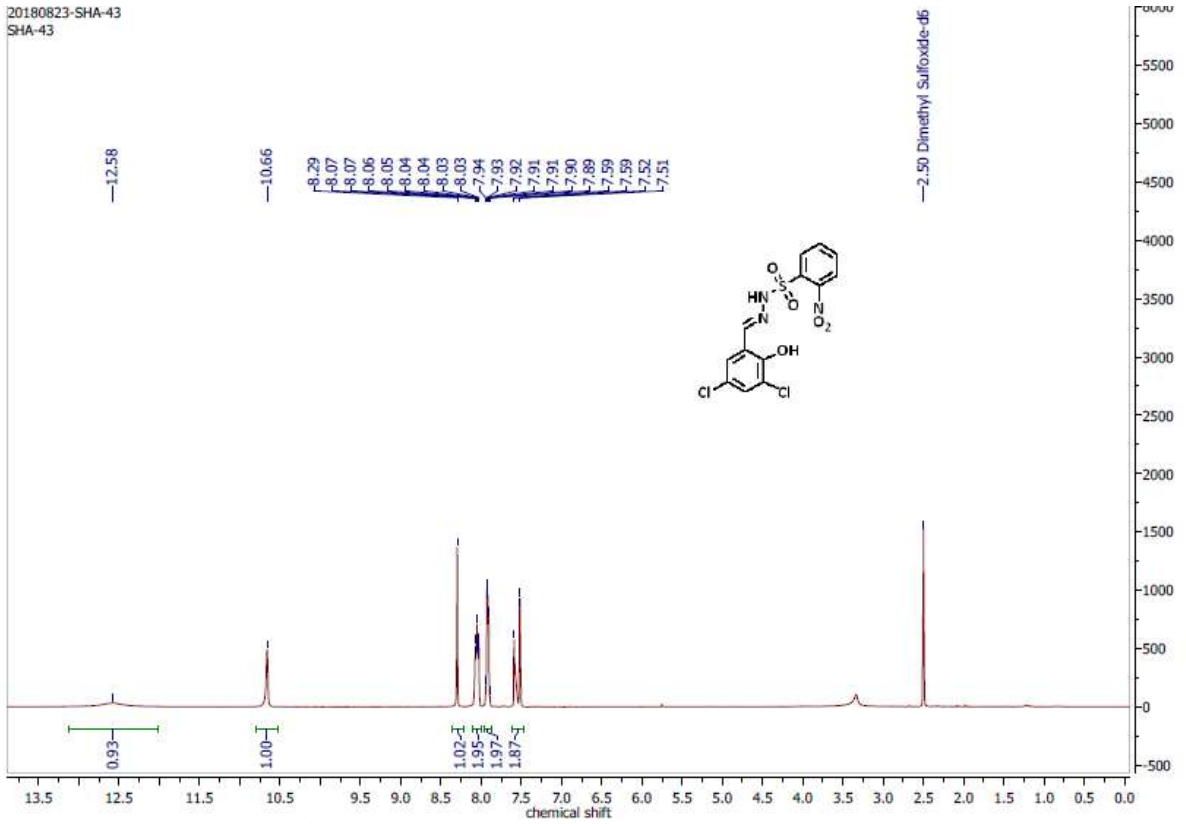

Figure C154: [1] H NMR spectrum of compound 52 in DMSO at 400 MHz.

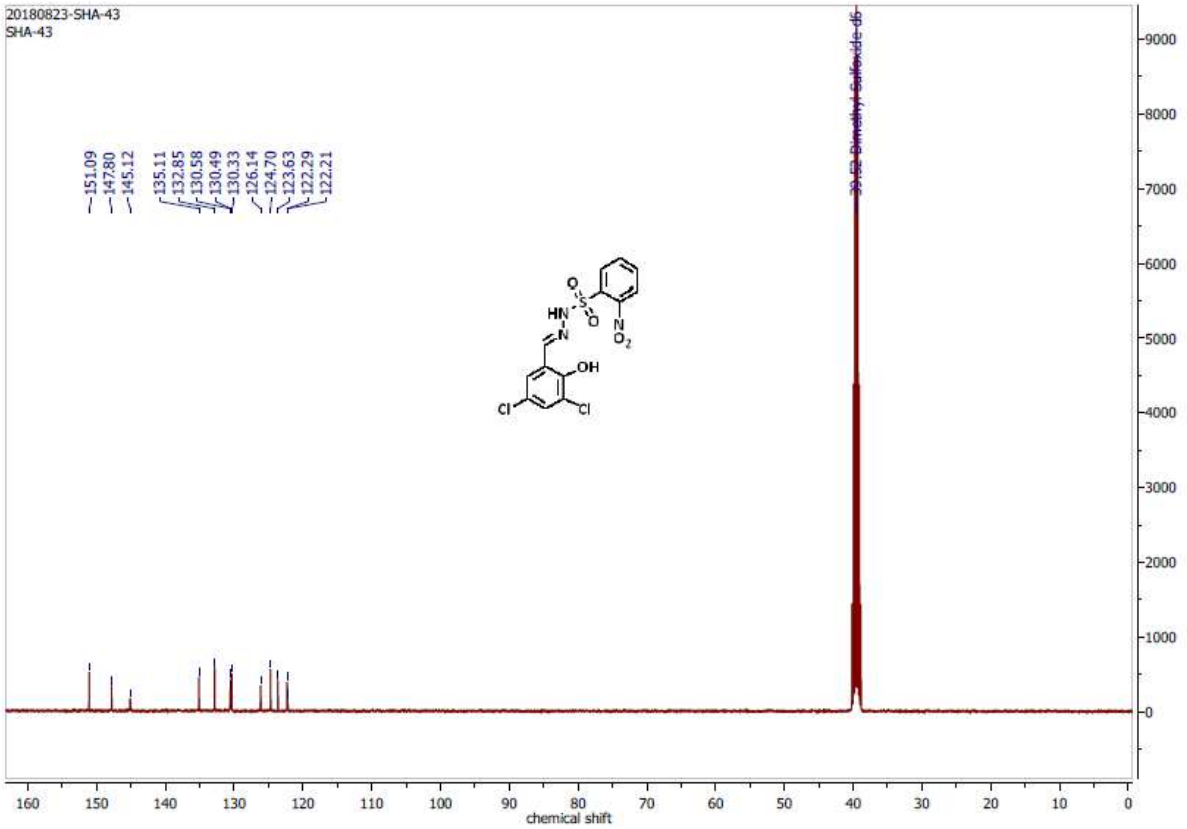

Figure C155: ^{13}C NMR spectrum of compound 52 in DMSO at 100 MHz.

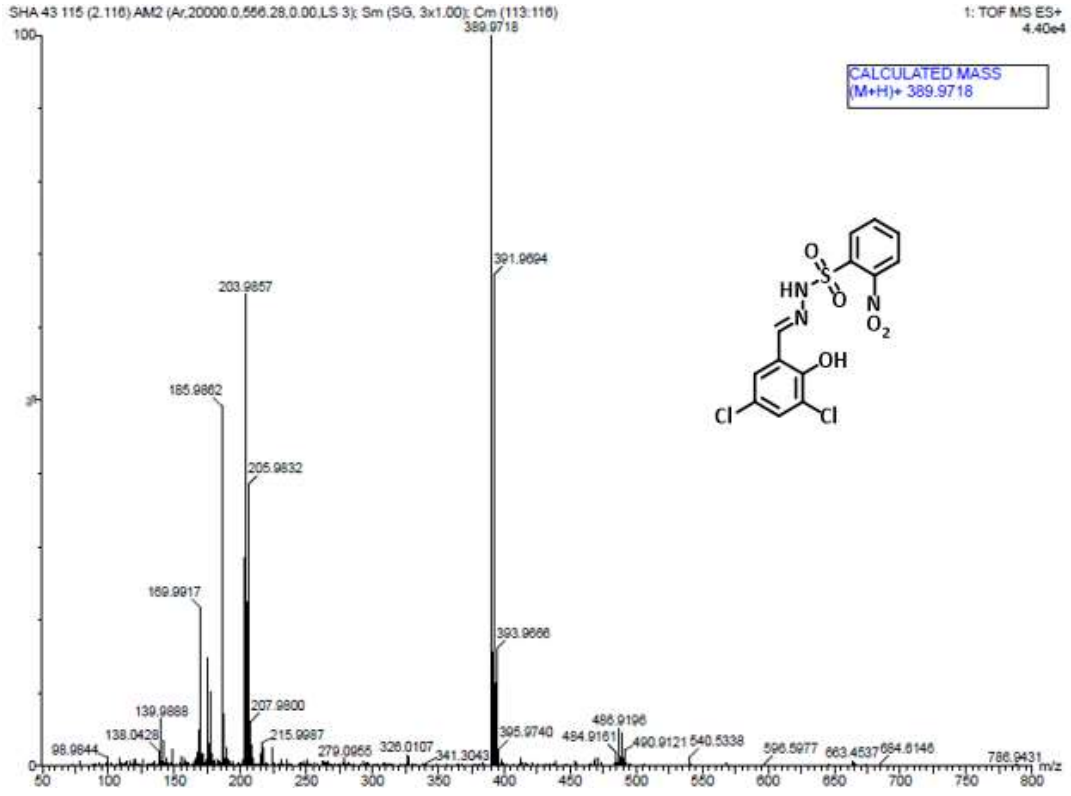

Figure C156: HRMS spectrum of compound 52.

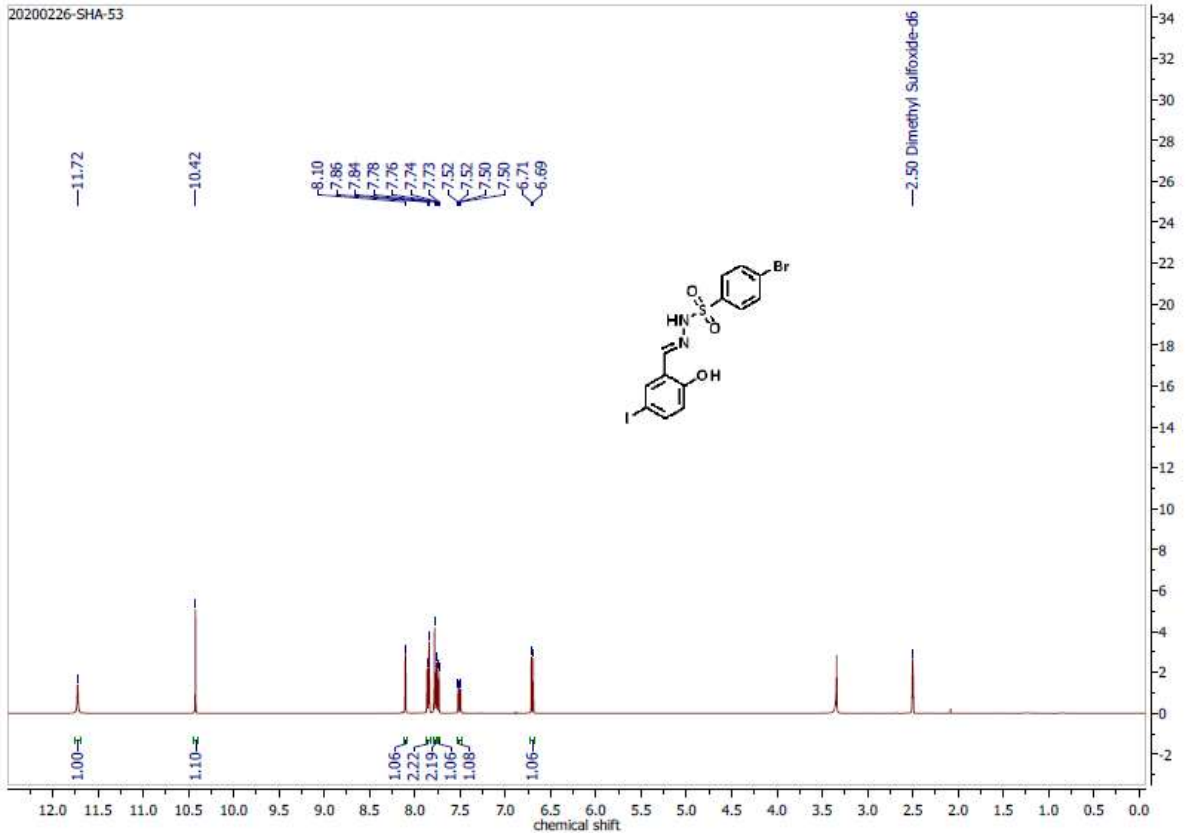

Figure C157: [1] H NMR spectrum of compound 53 in DMSO at 400 MHz.

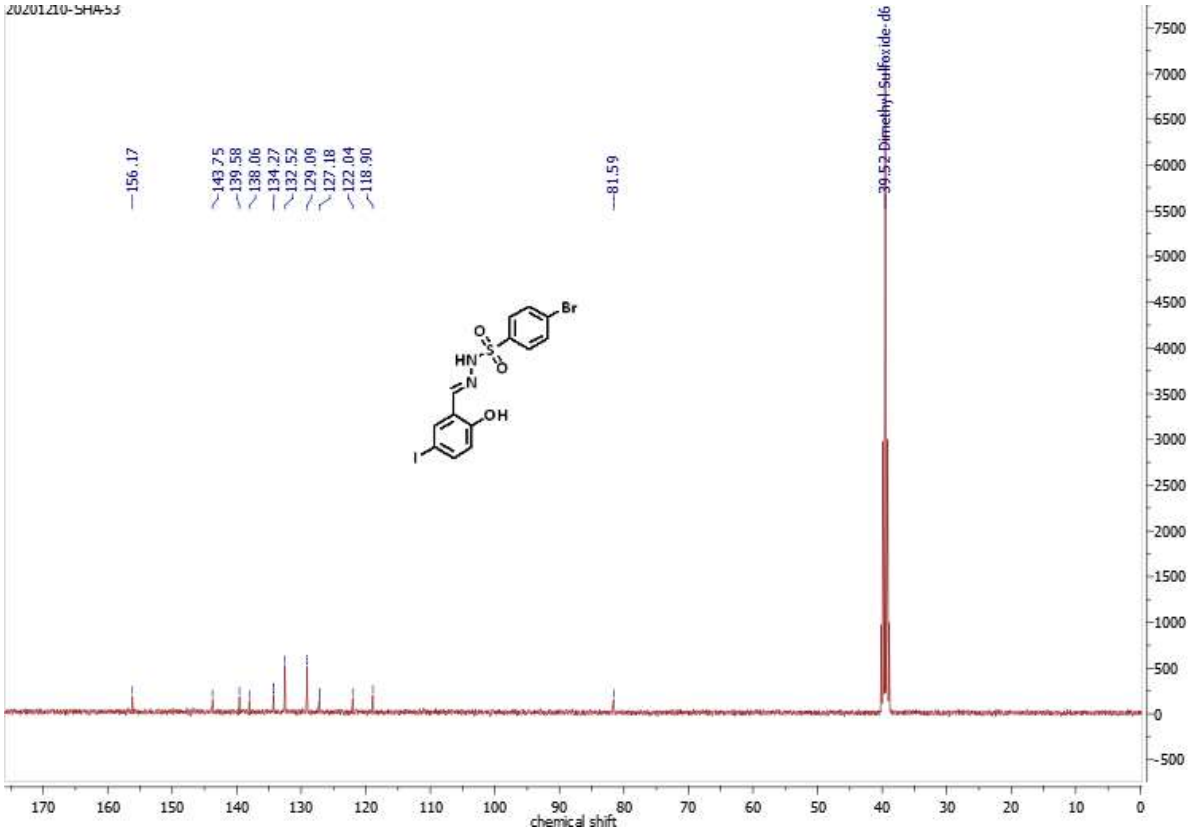

Figure C158: [13] C NMR spectrum of compound 53 in DMSO at 100 MHz.

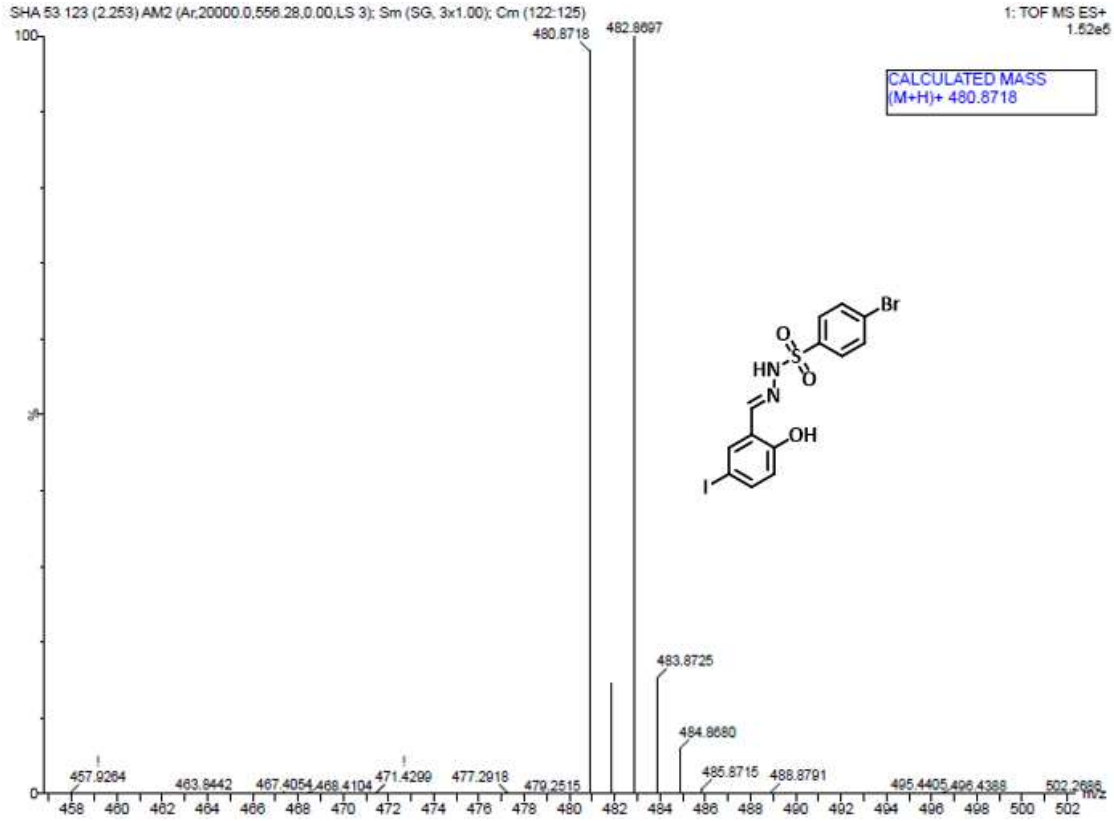

Figure C159: HRMS spectrum of compound 53.

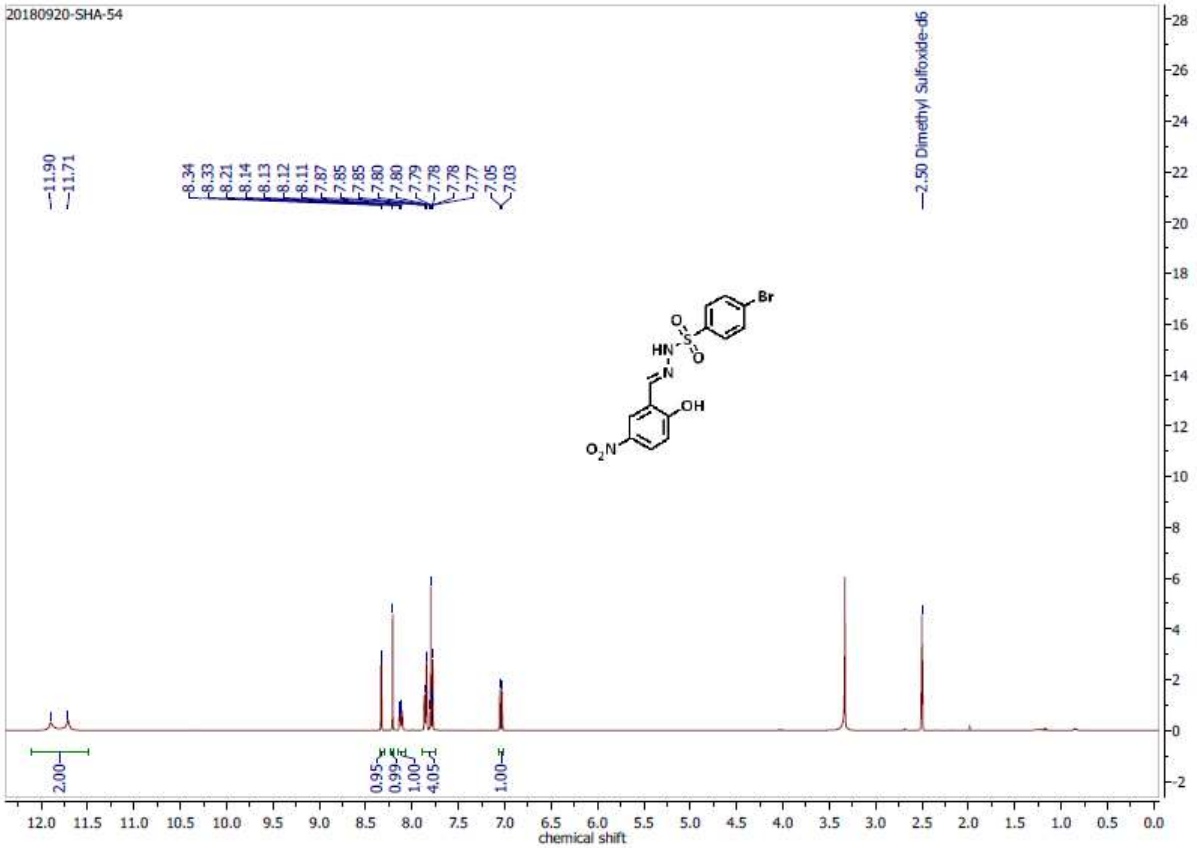

Figure C160: [1] H NMR spectrum of compound 54 in DMSO at 400 MHz.

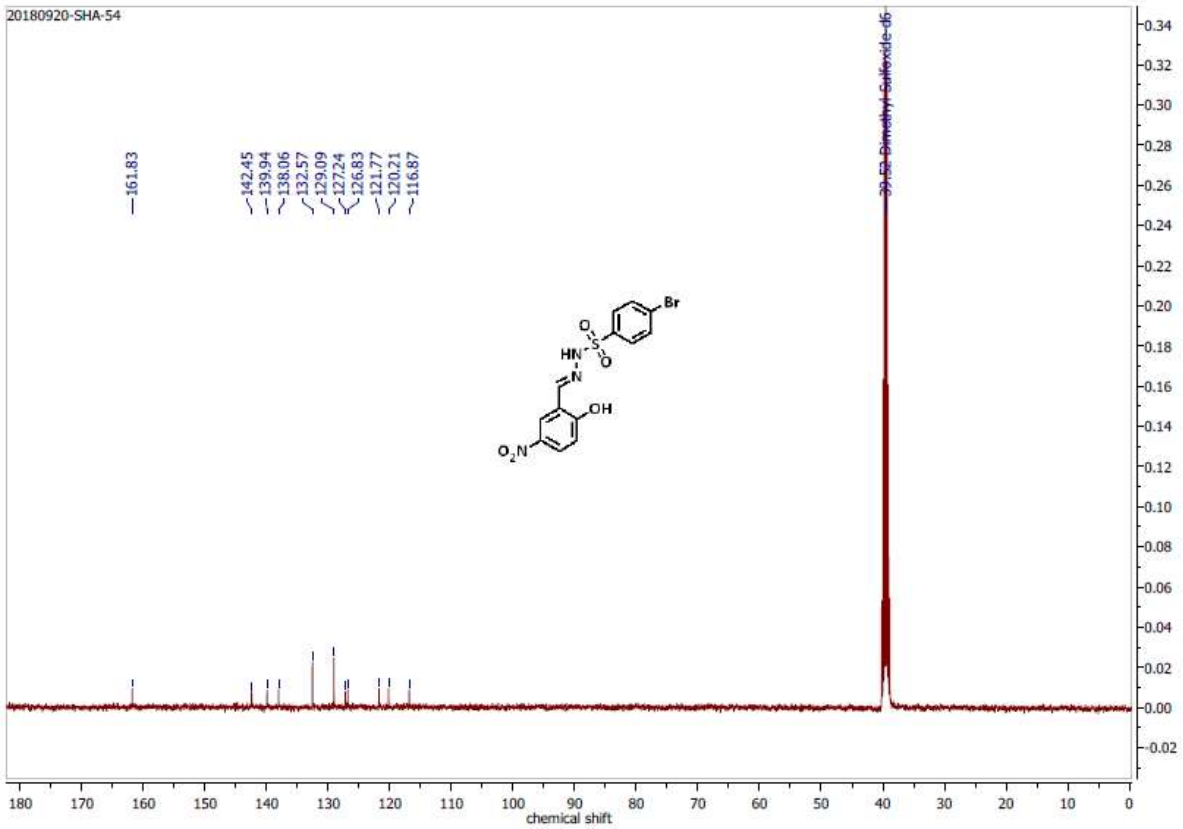

Figure C161: ^{13}C NMR spectrum of compound 54 in DMSO at 100 MHz.

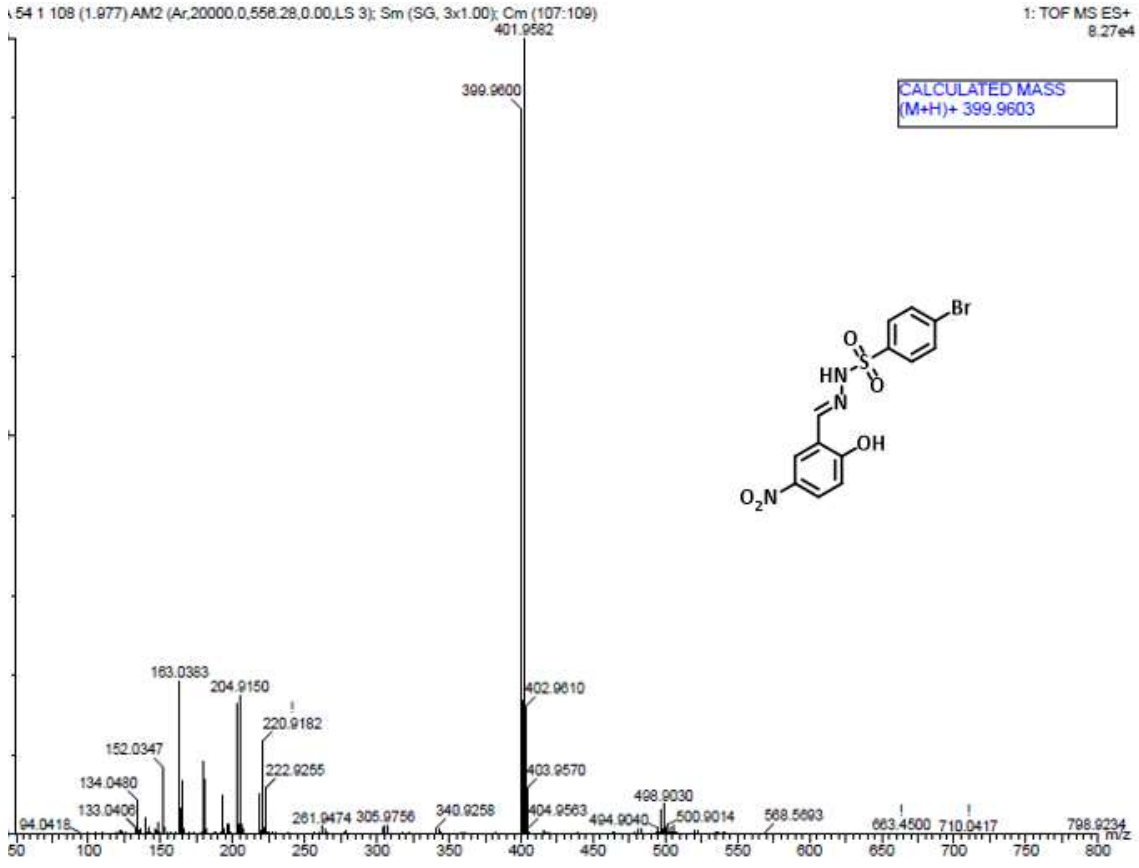

Figure C162: HRMS spectrum of compound 54.

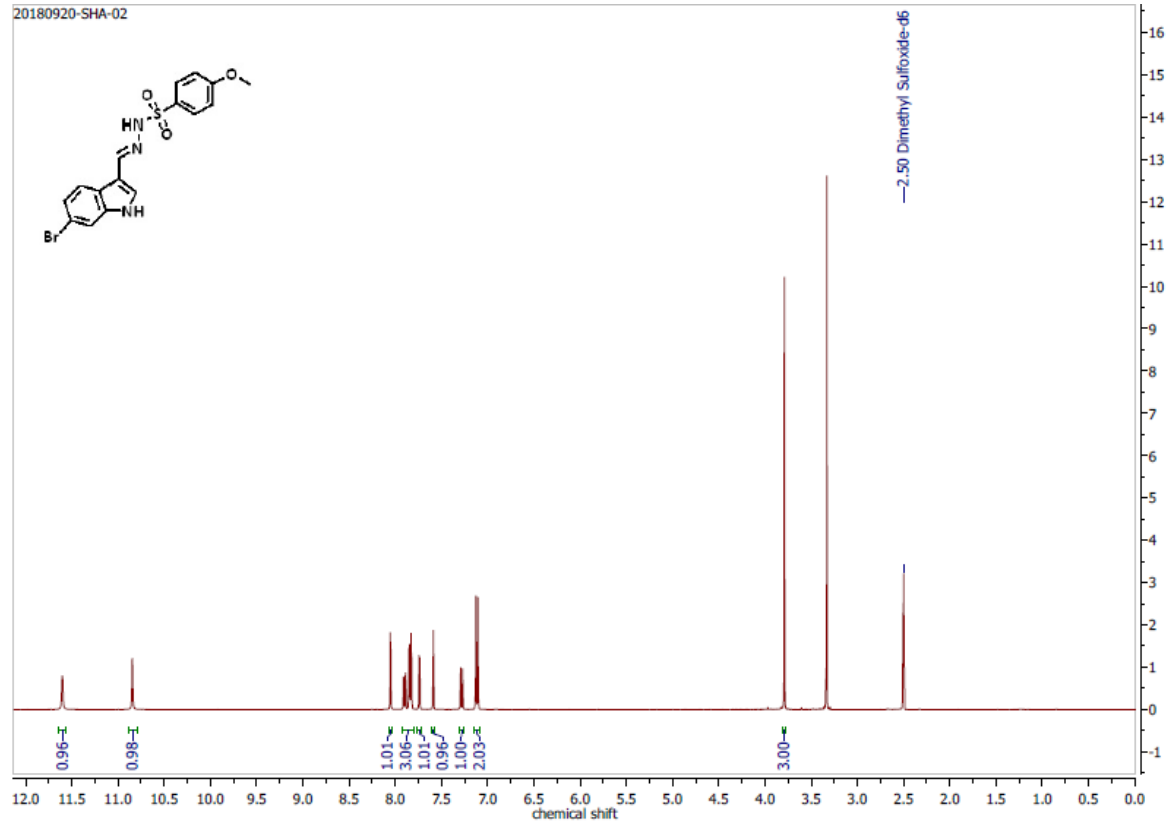

Figure C163: [1] H NMR spectrum of compound 55 in DMSO at 400 MHz.

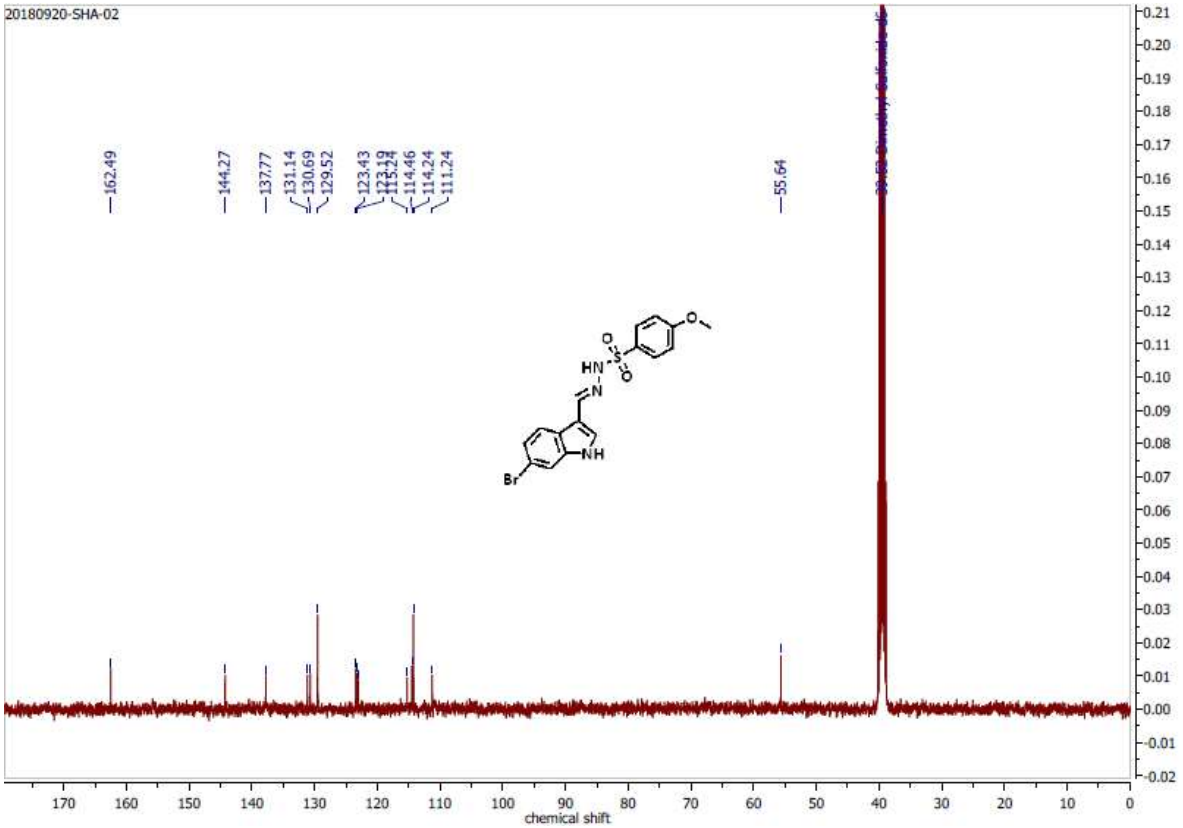

Figure C164: [13] C NMR spectrum of compound 55 in DMSO at 100 MHz.

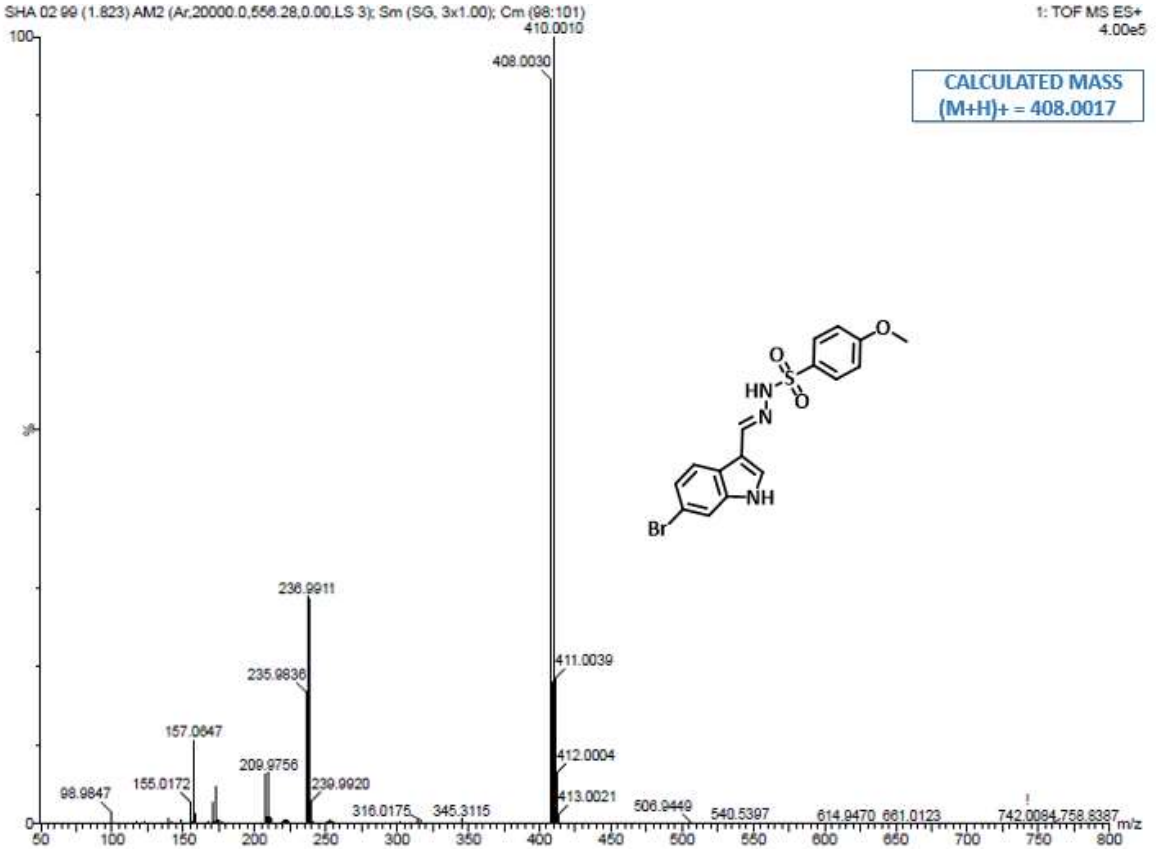

Figure C165: HRMS spectrum of compound 55.

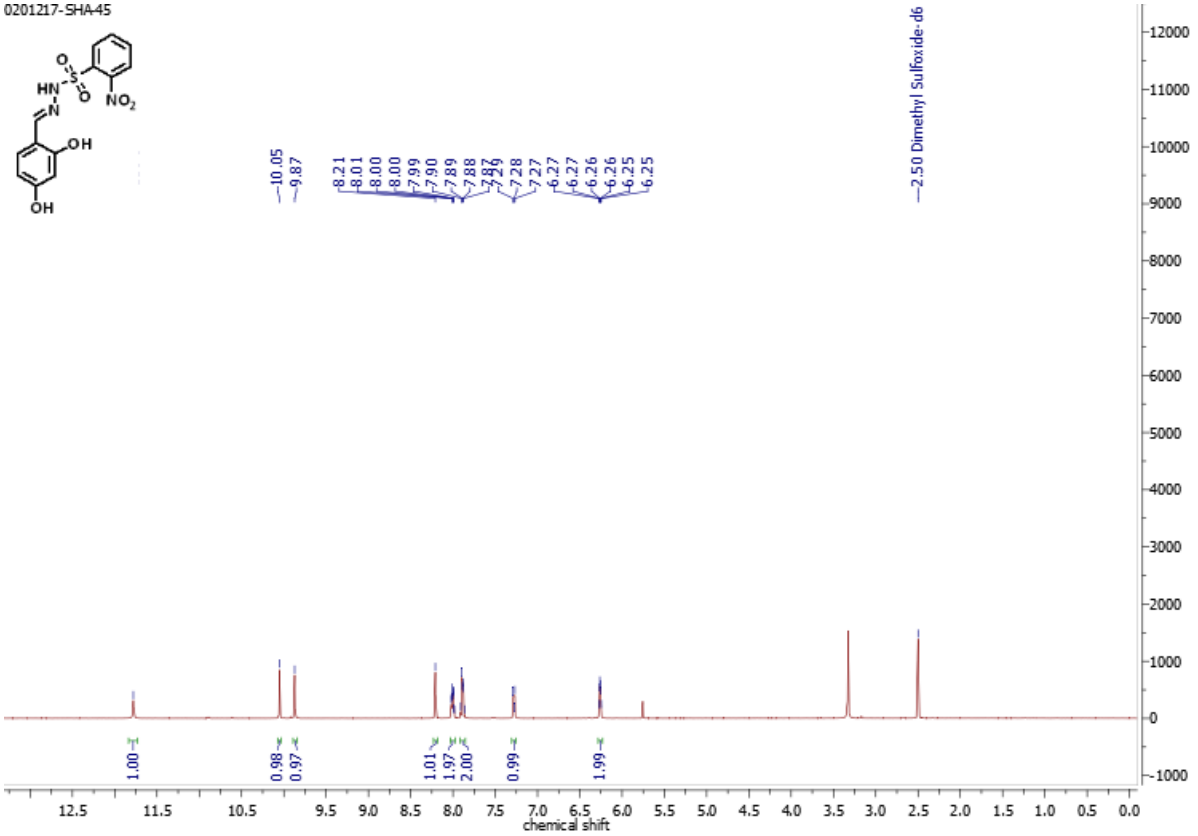

Figure C166: [1] H NMR spectrum of compound 56 in DMSO at 400 MHz.

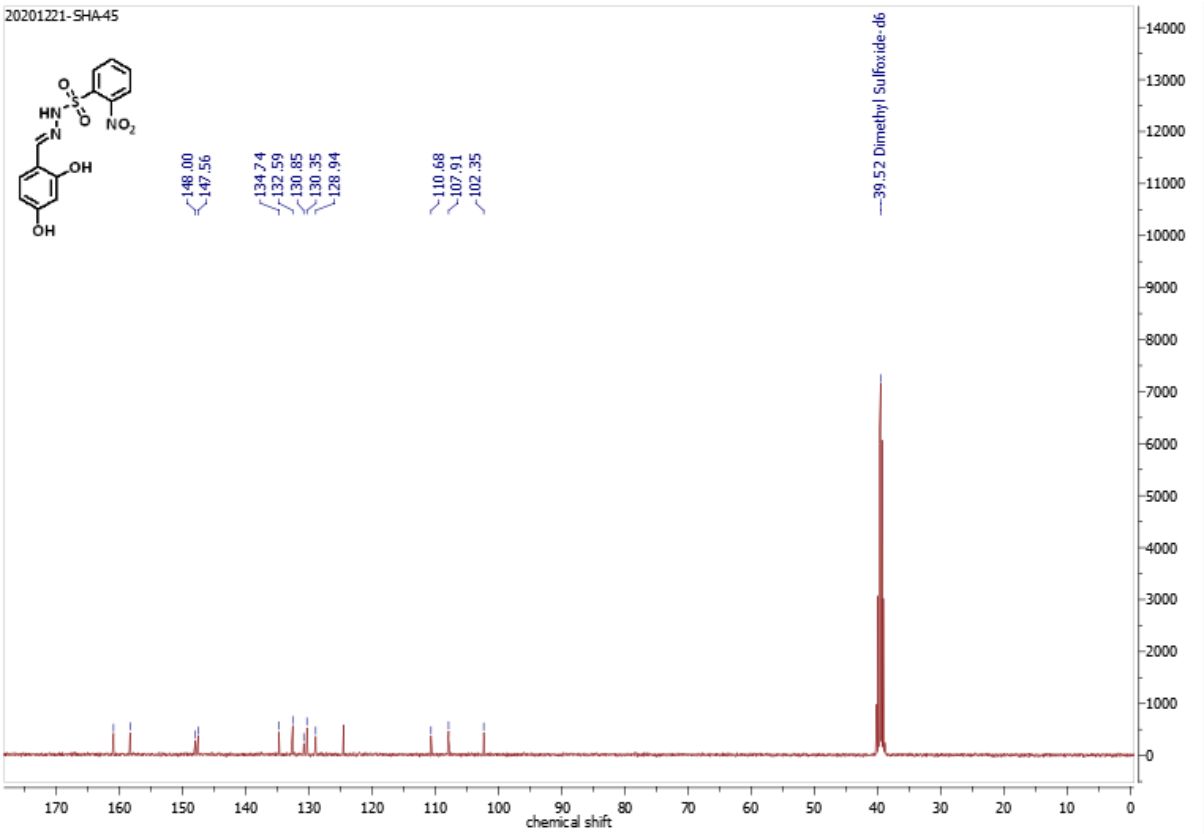

Figure C167: ^{13}C NMR spectrum of compound 56 in DMSO at 100 MHz.

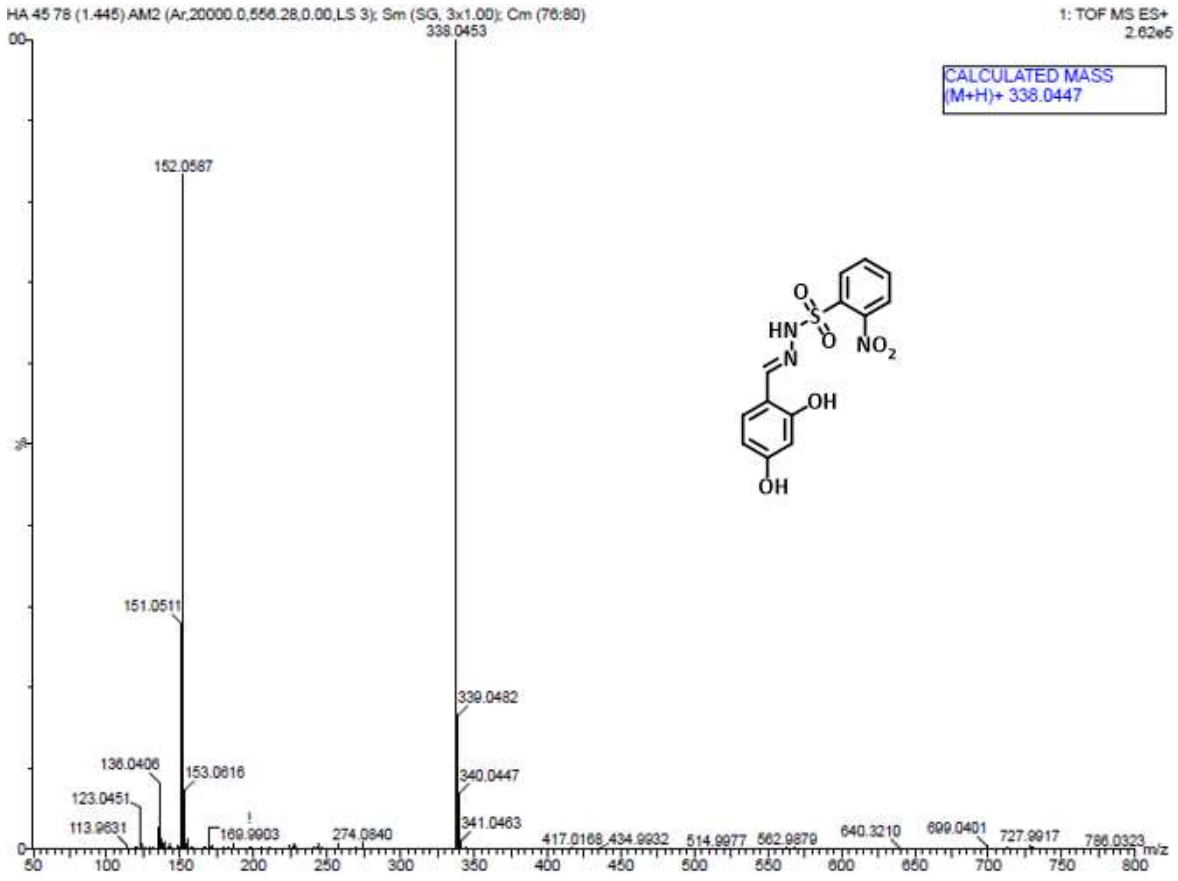

Figure C168: HRMS spectrum of compound 56.

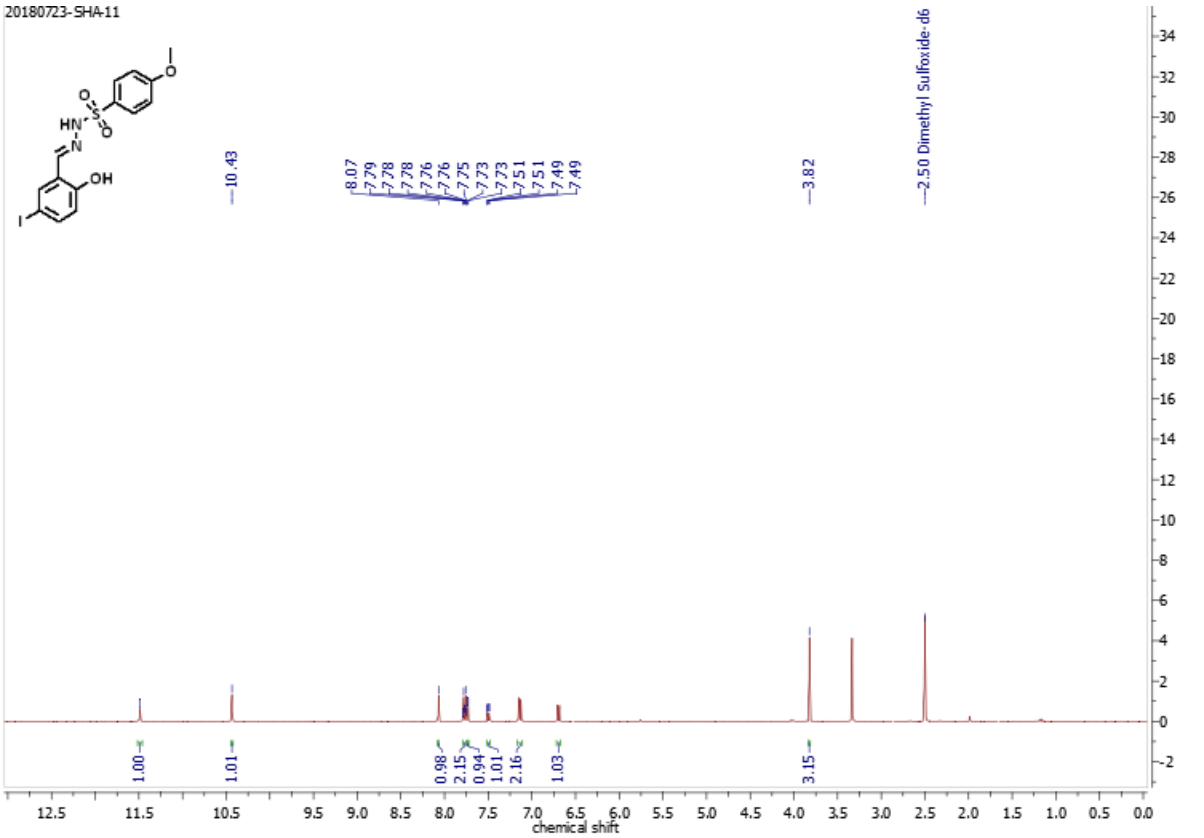

Figure C169: [1] H NMR spectrum of compound 57 in DMSO at 400 MHz.

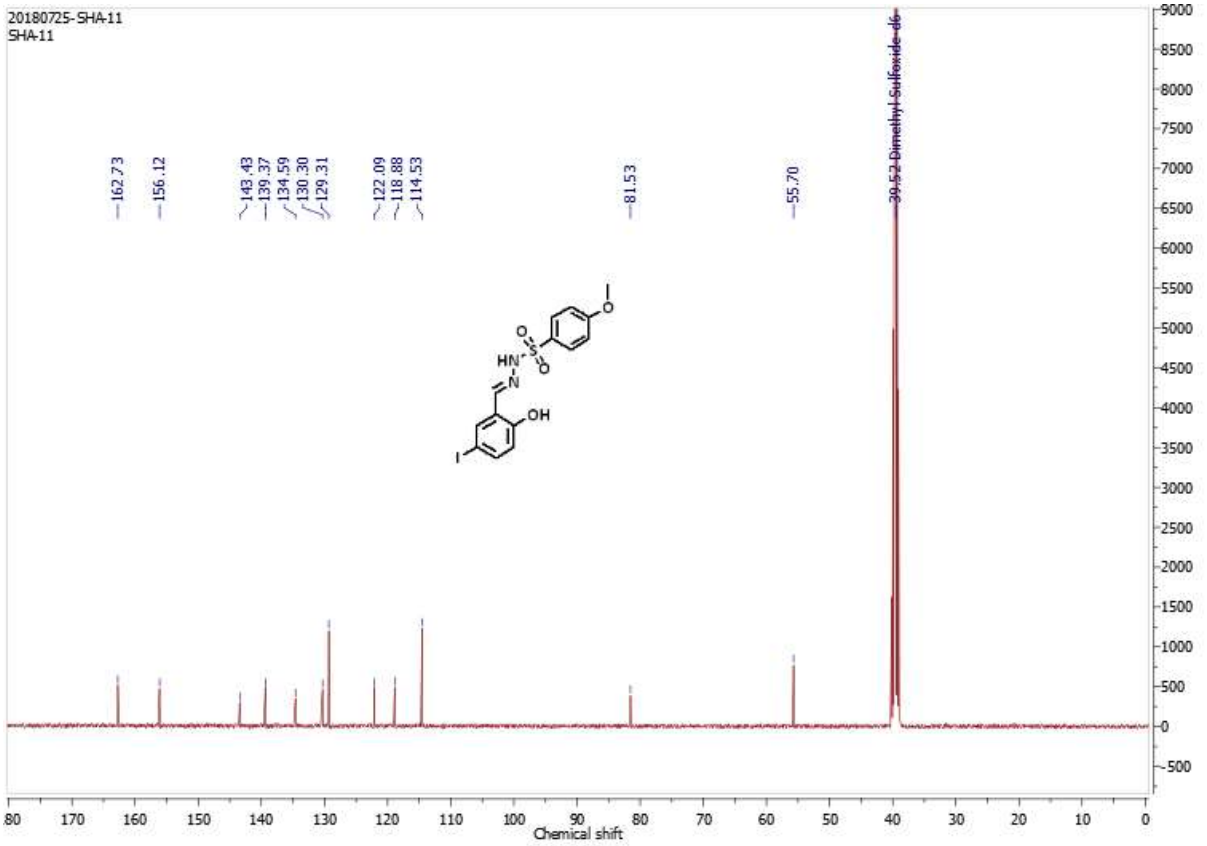

Figure C170: [13] C NMR spectrum of compound 57 in DMSO at 100 MHz.

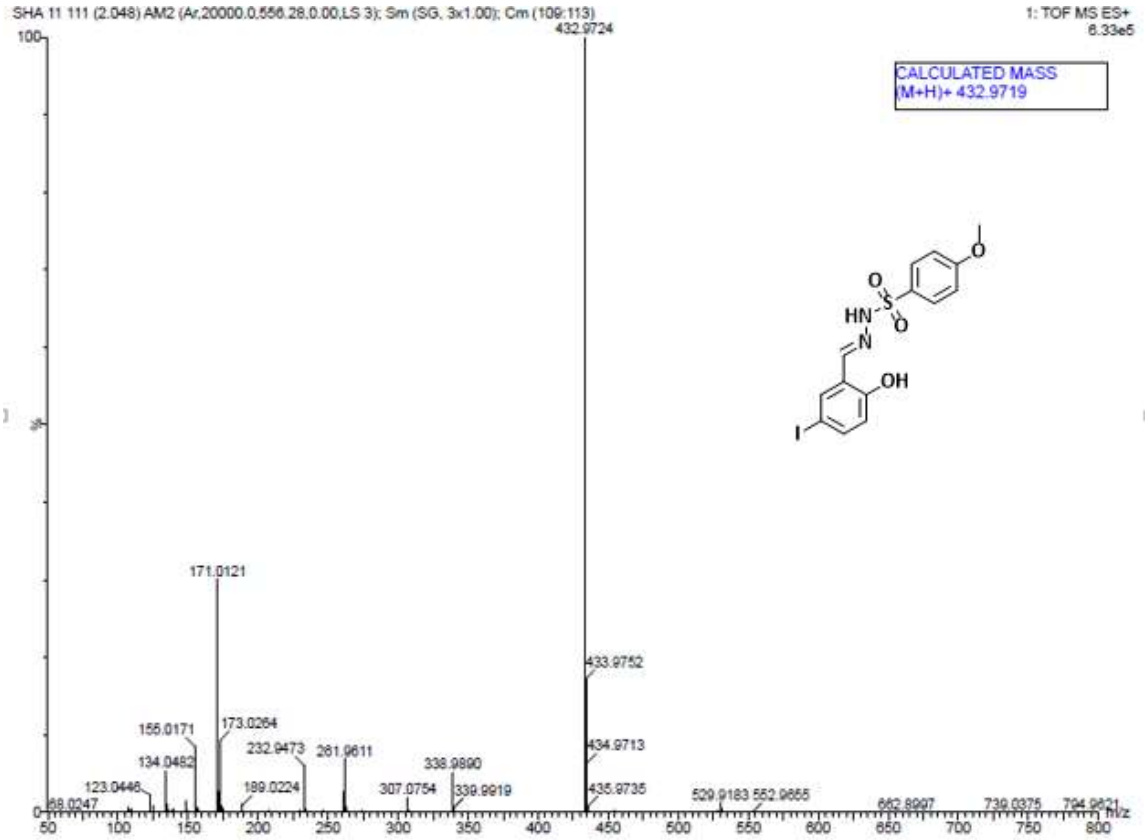

Figure C171: HRMS spectrum of compound 57.

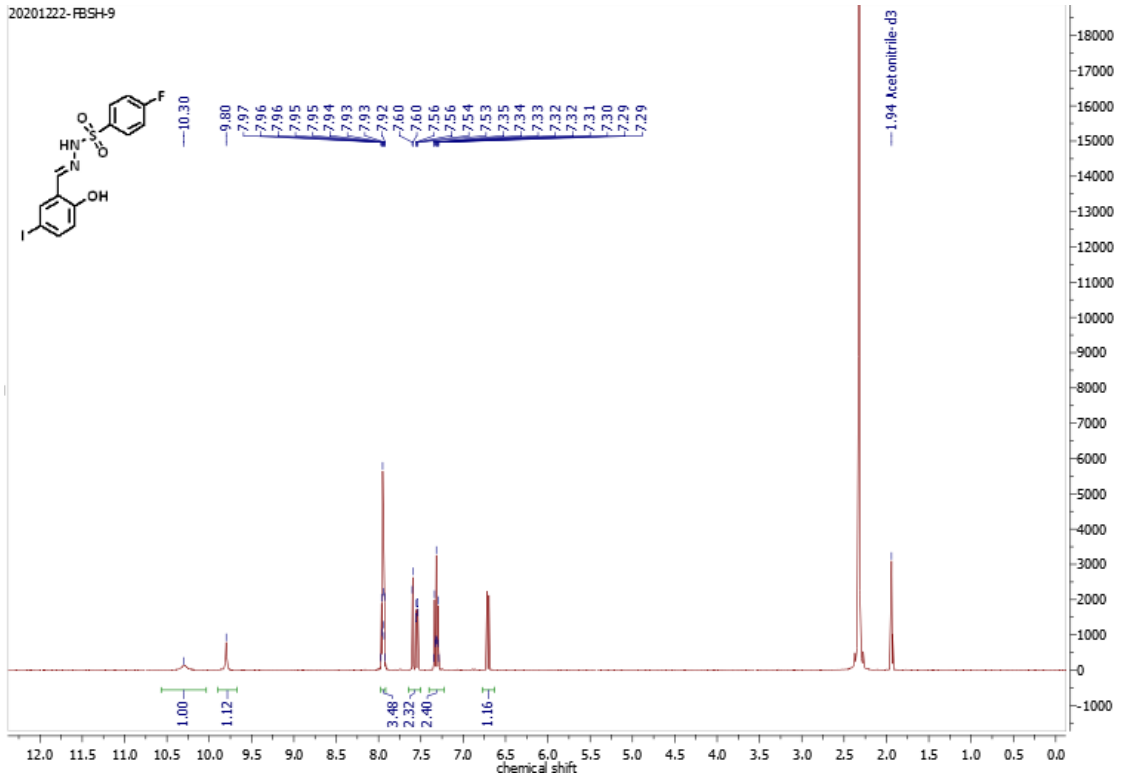

Figure C172: [1] H NMR spectrum of compound 58 in CD_3CN at 400 MHz.

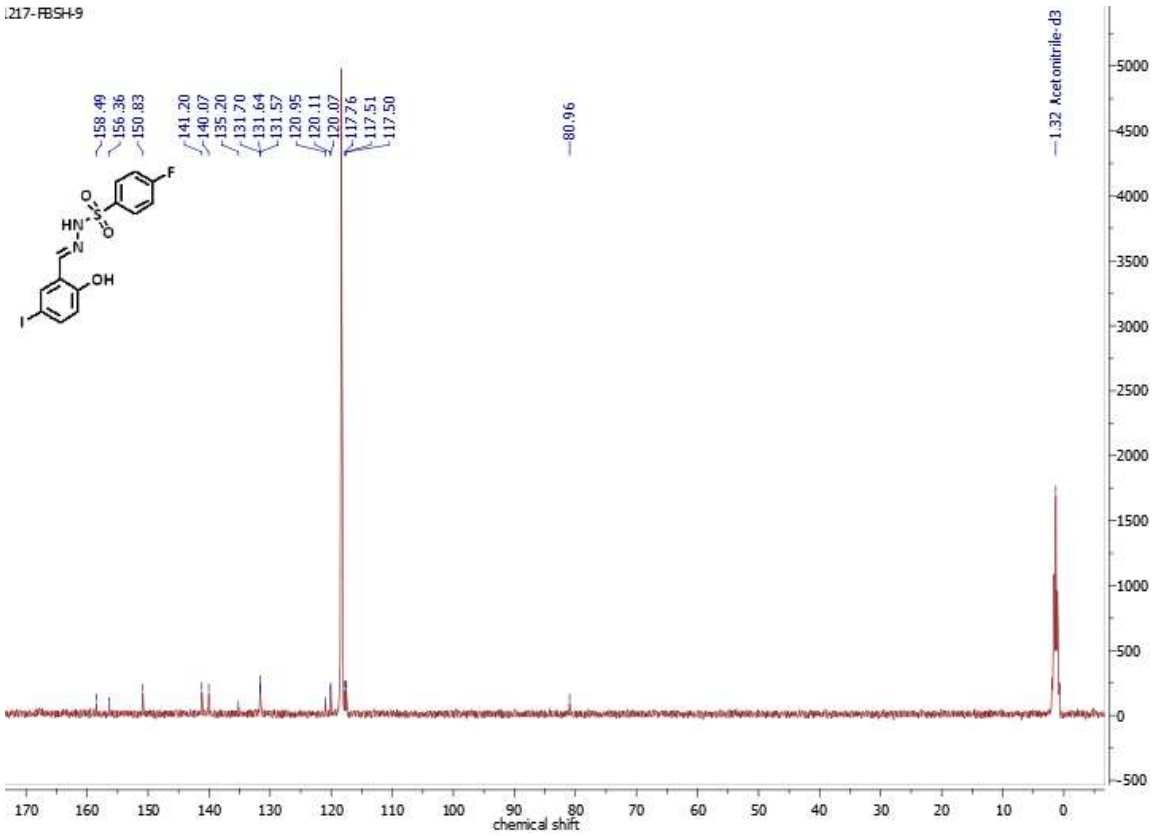

Figure C173: ^{13}C NMR spectrum of compound 58 in CD_3CN at 100 MHz.

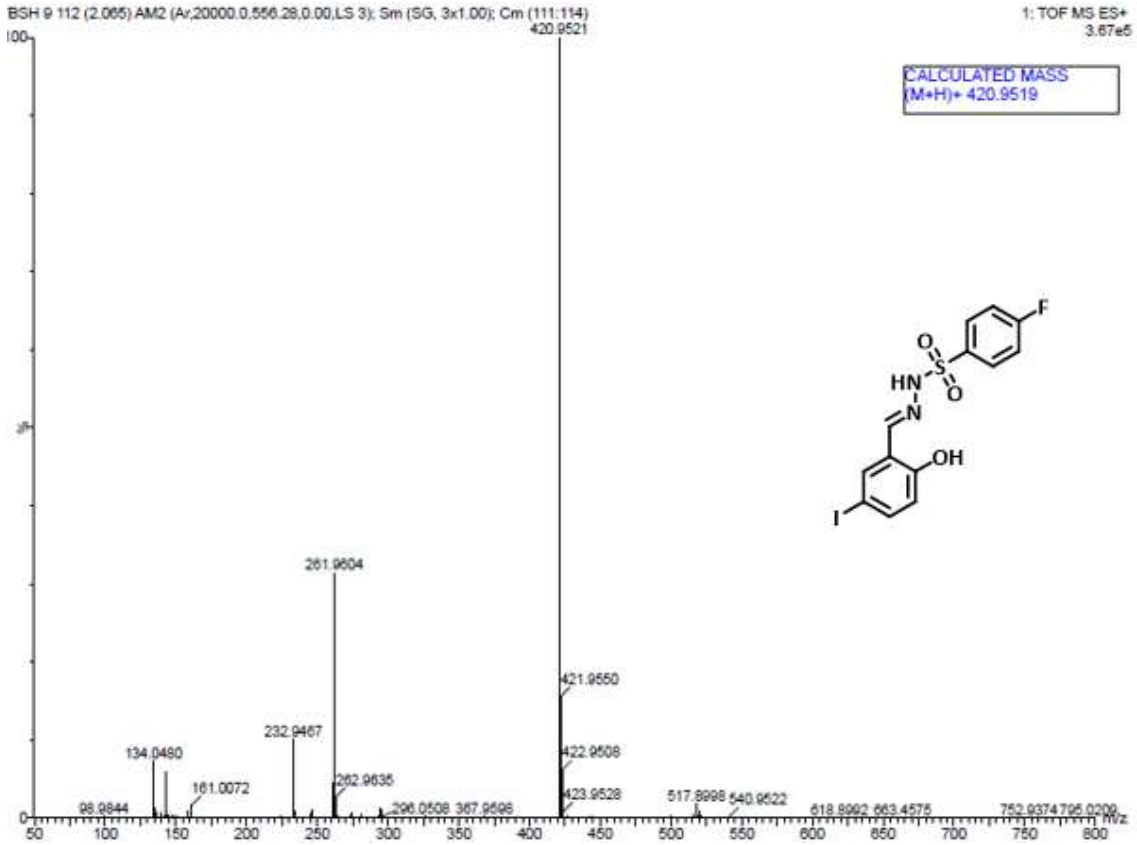

Figure C174: HRMS spectrum of compound 58.

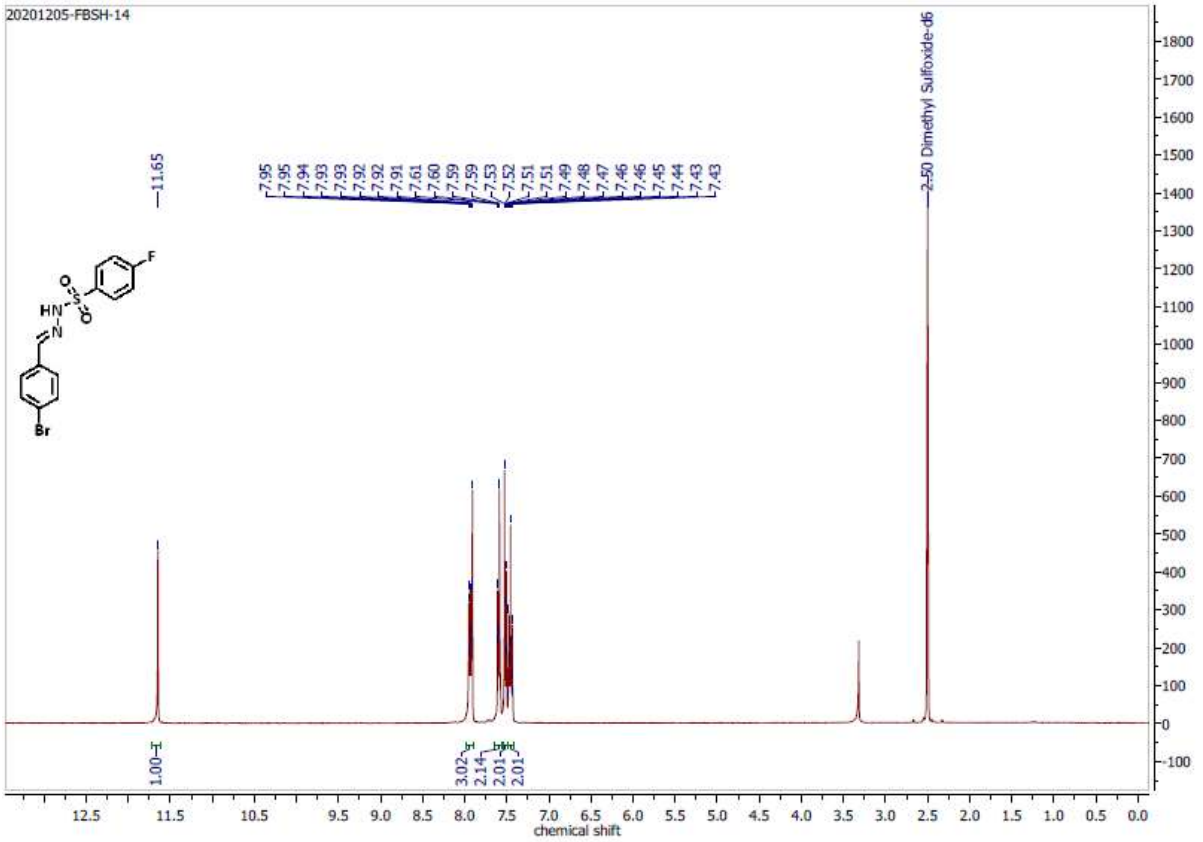

Figure C175: [1] H NMR spectrum of compound 59 in DMSO at 400 MHz.

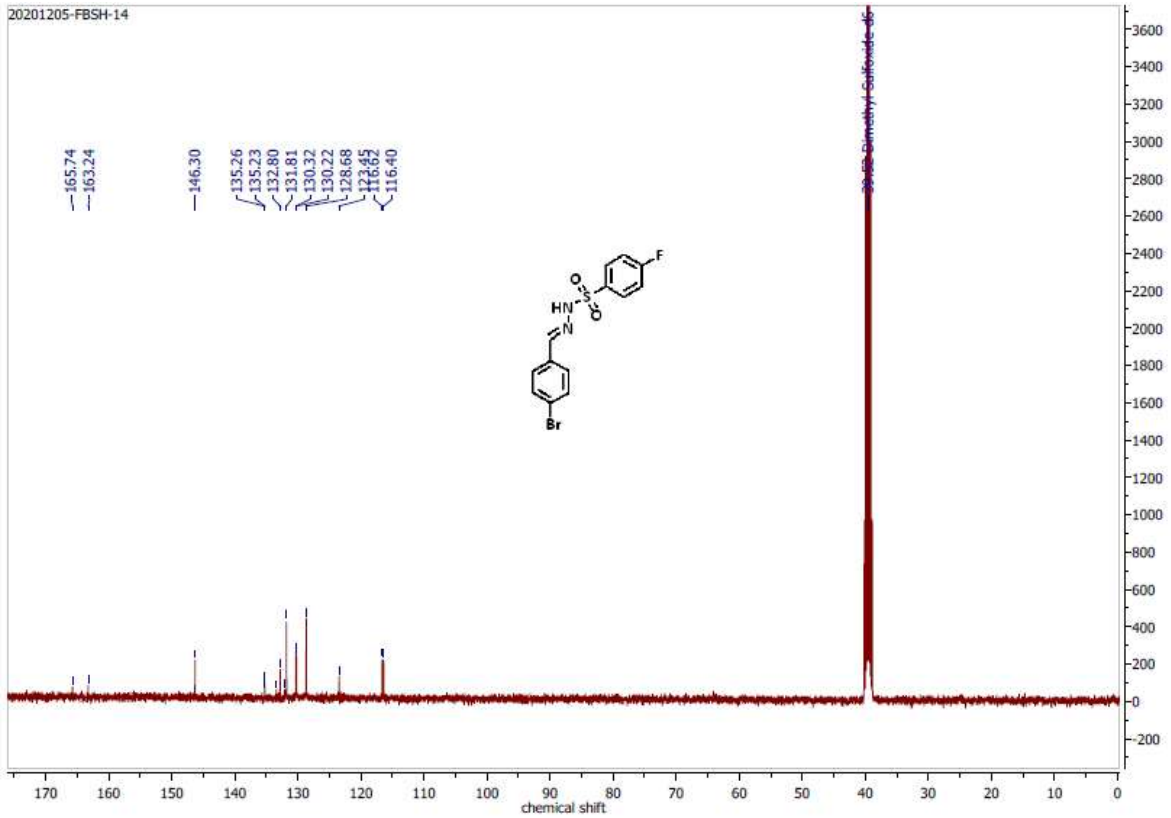

Figure C176: [13] C NMR spectrum of compound 59 in DMSO at 100 MHz.

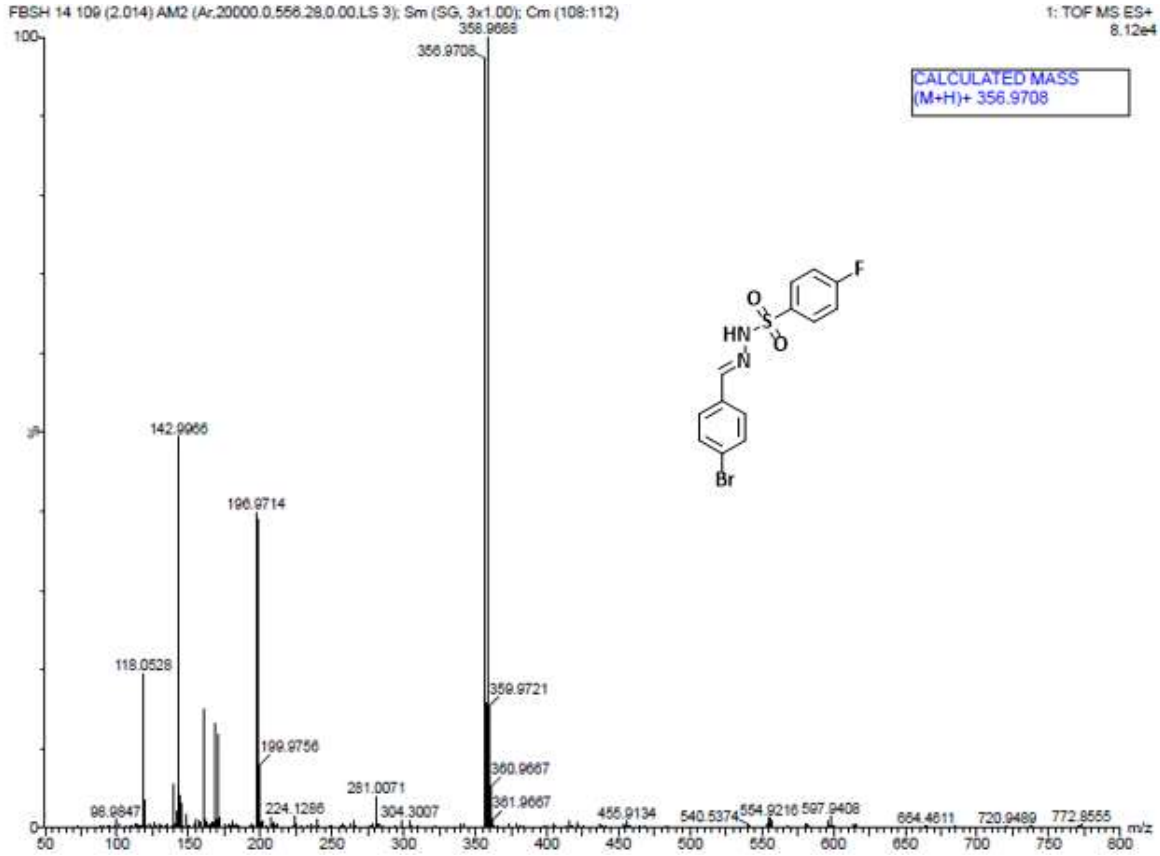

Figure C177: HRMS spectrum of compound 59

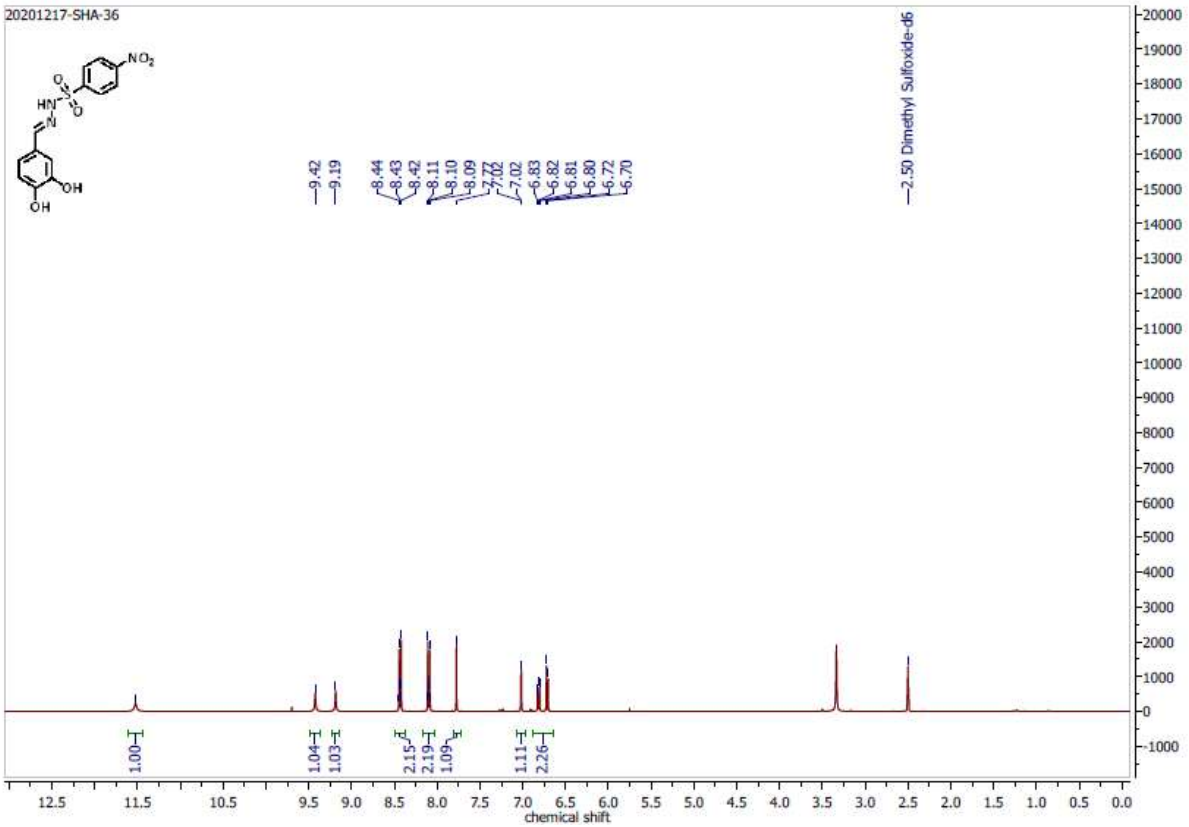

Figure C178: [1] H NMR spectrum of compound 60 in DMSO at 400 MHz.

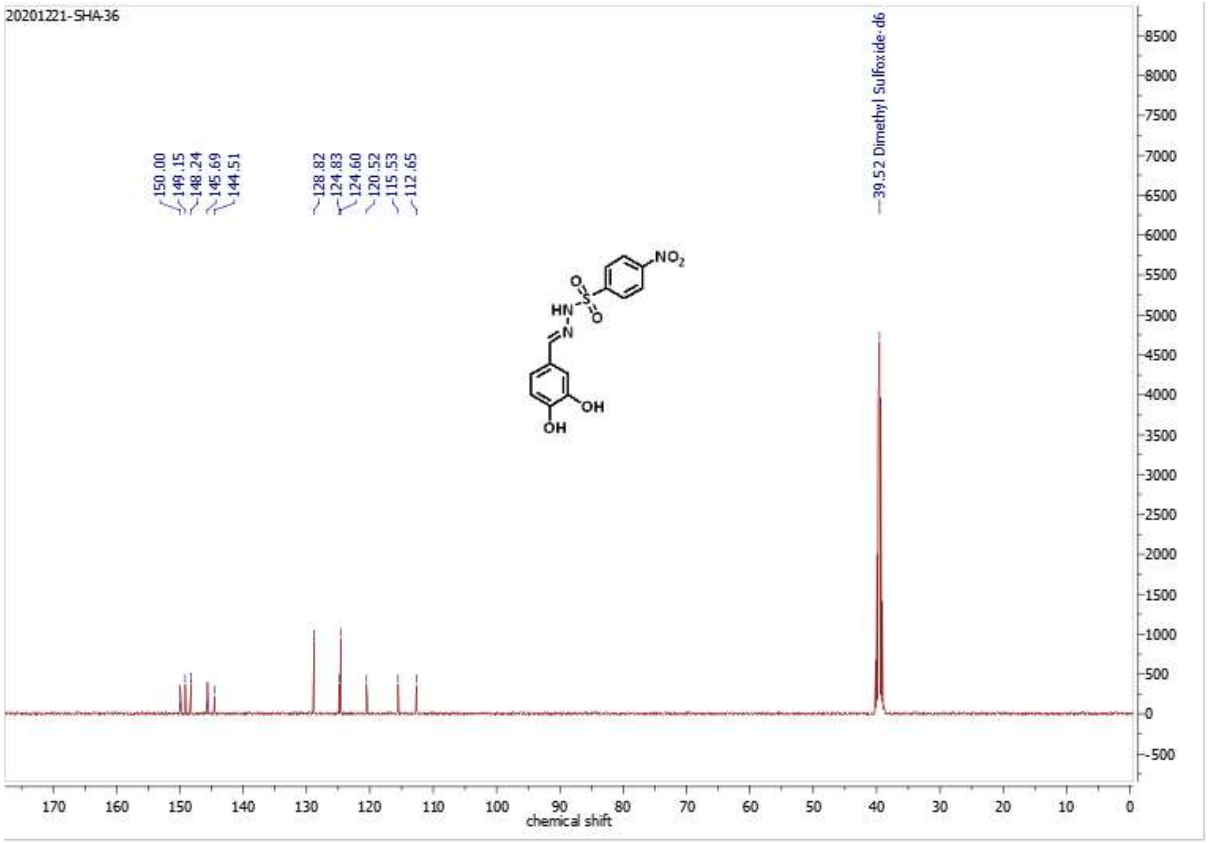

Figure C179: ^{13}C NMR spectrum of compound 60 in DMSO at 100 MHz.

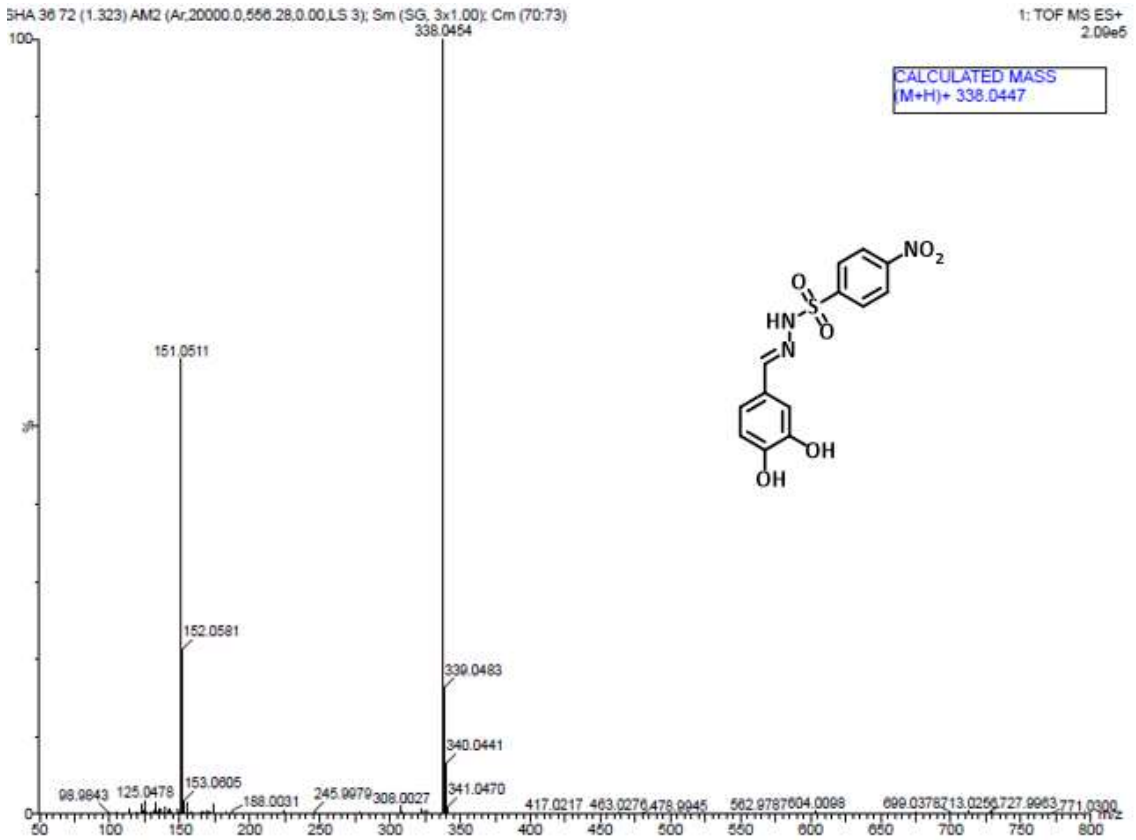

Figure C180: HRMS spectrum of compound 60

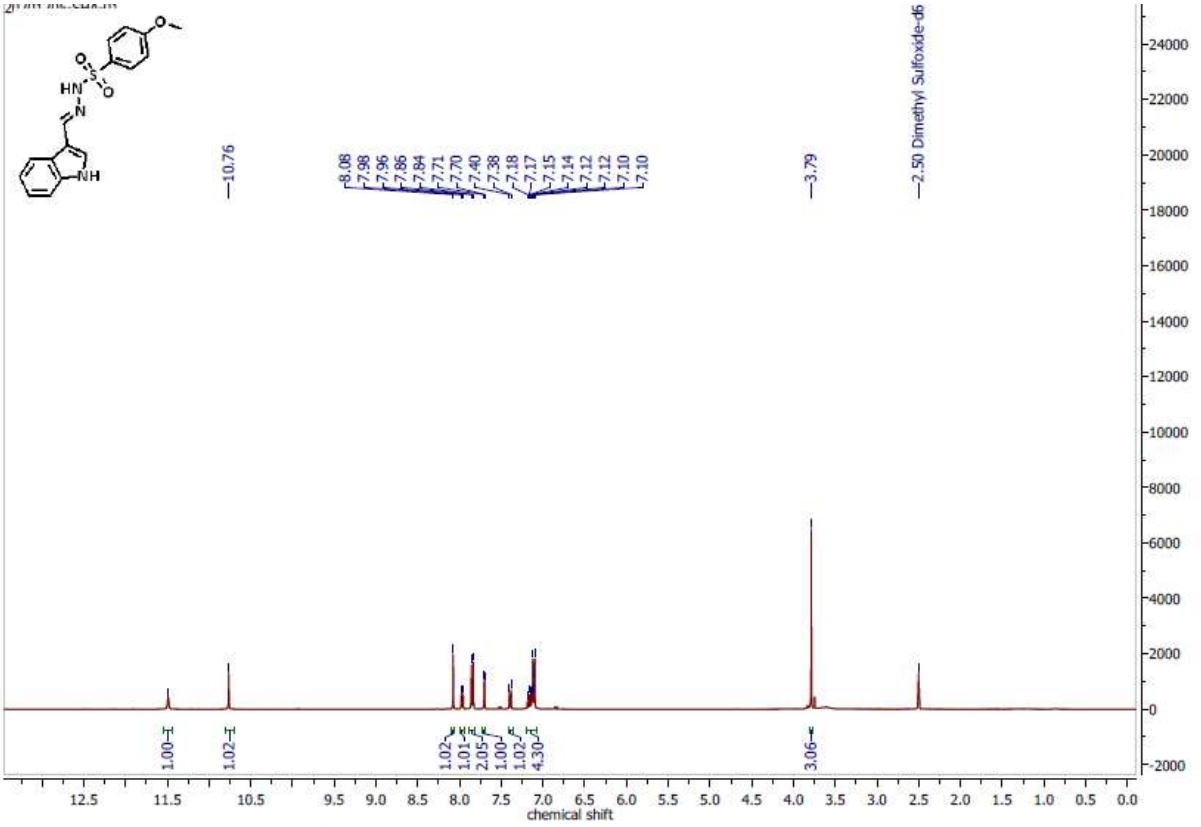

Figure C181: [1] H NMR spectrum of compound 61 in DMSO at 400 MHz

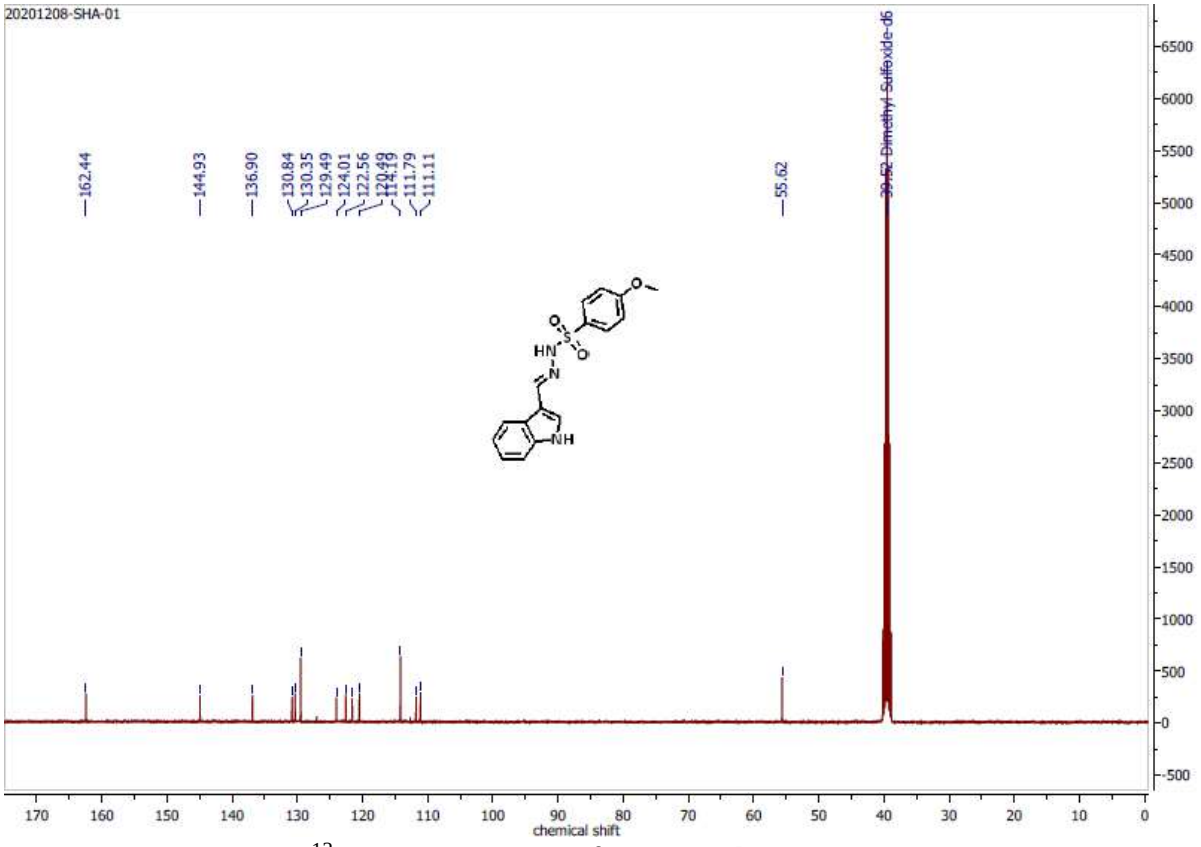

Figure C182: [13] C NMR spectrum of compound 61 in DMSO at 100 MHz

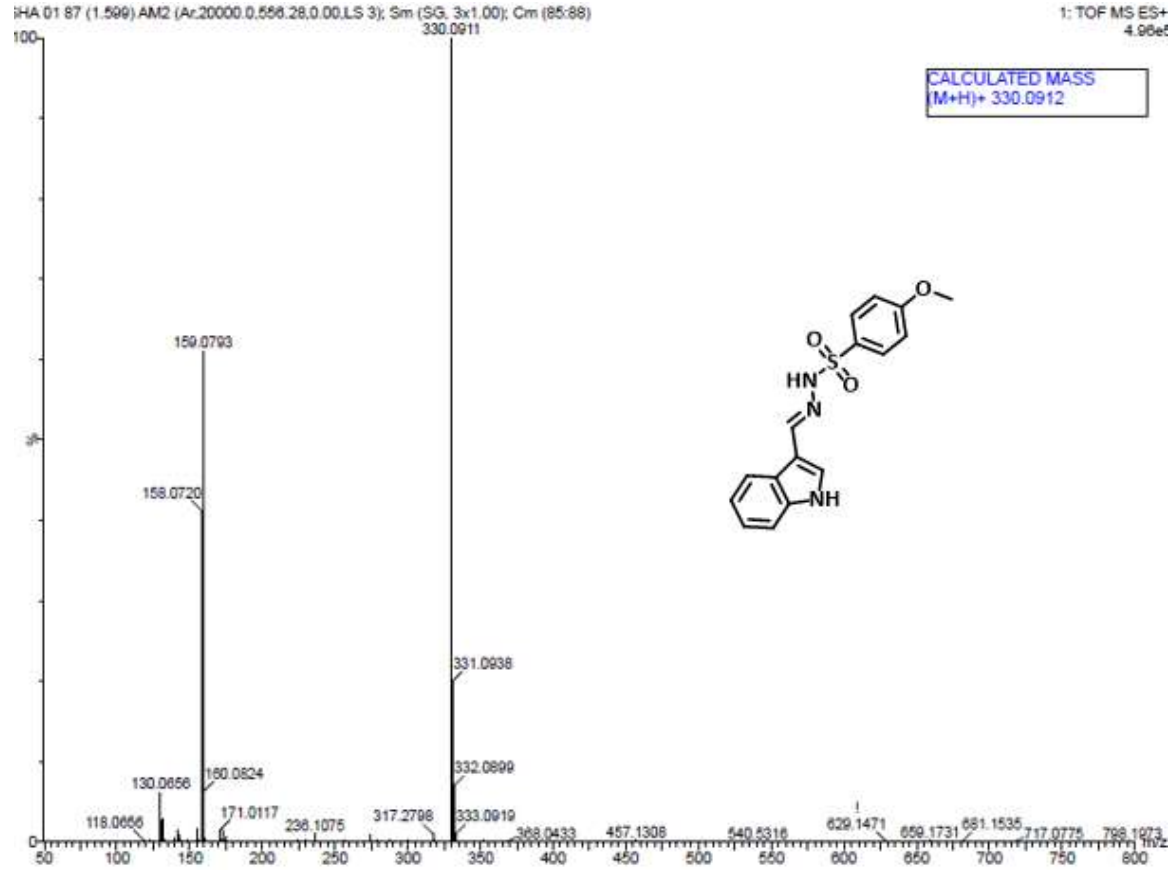

Figure C183: HRMS spectrum of compound 61

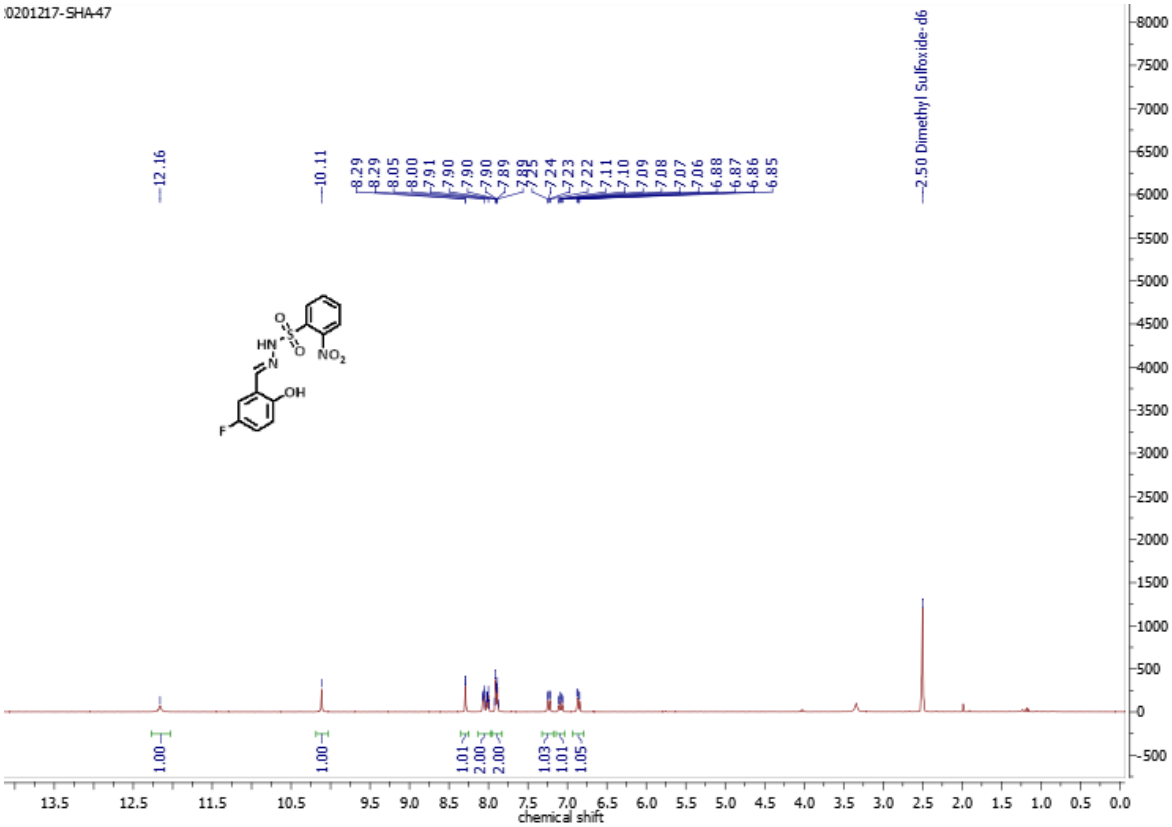

Figure C184: [1] H NMR spectrum of compound 62 in DMSO at 400 MHz

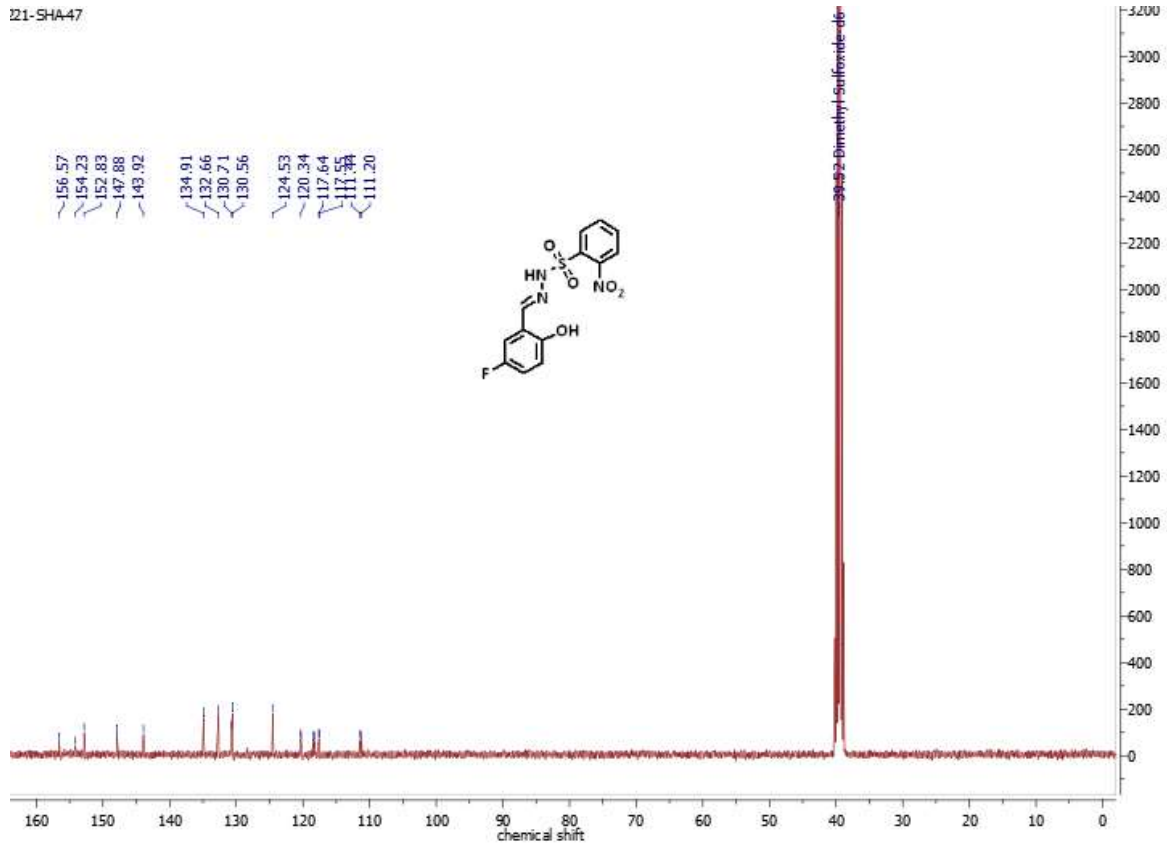

Figure C185: ^{13}C NMR spectrum of compound 62 in DMSO at 100 MHz

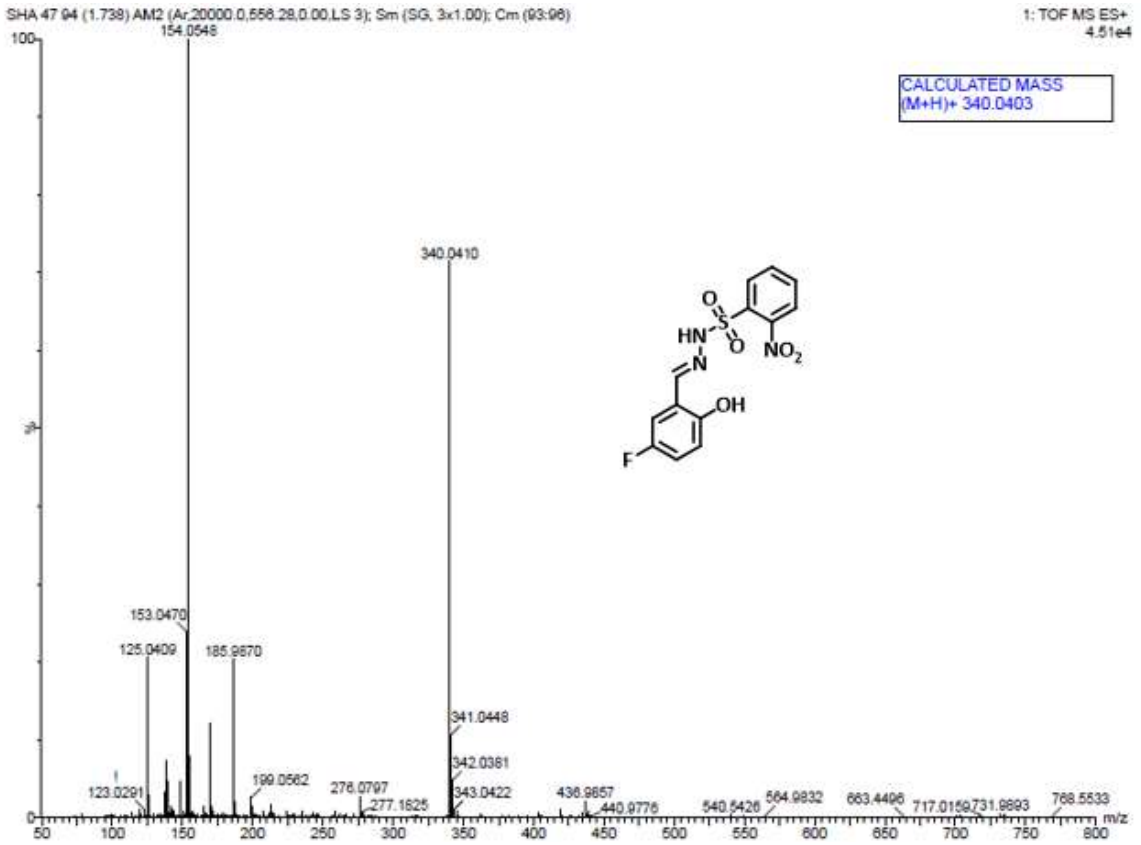

Figure C186: HRMS spectrum of compound 62

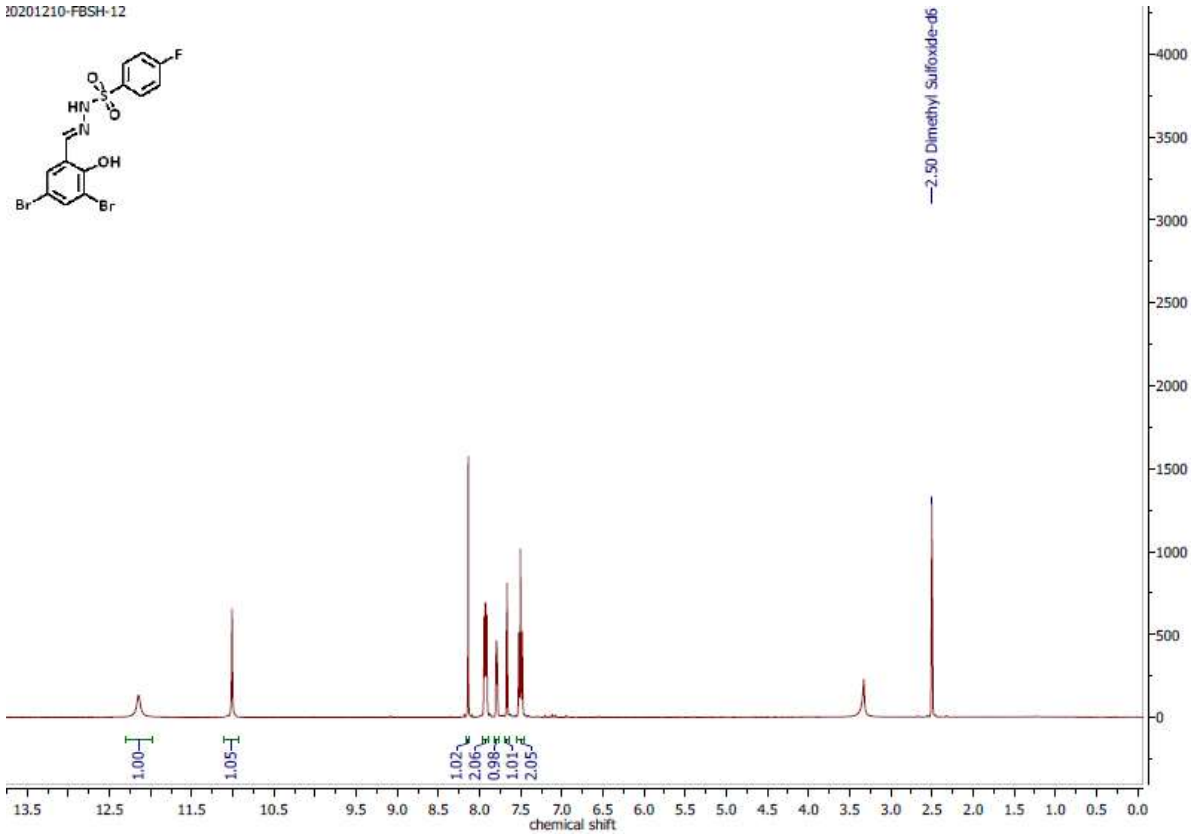

Figure C187: [1] H NMR spectrum of compound 63 in DMSO at 400 MHz

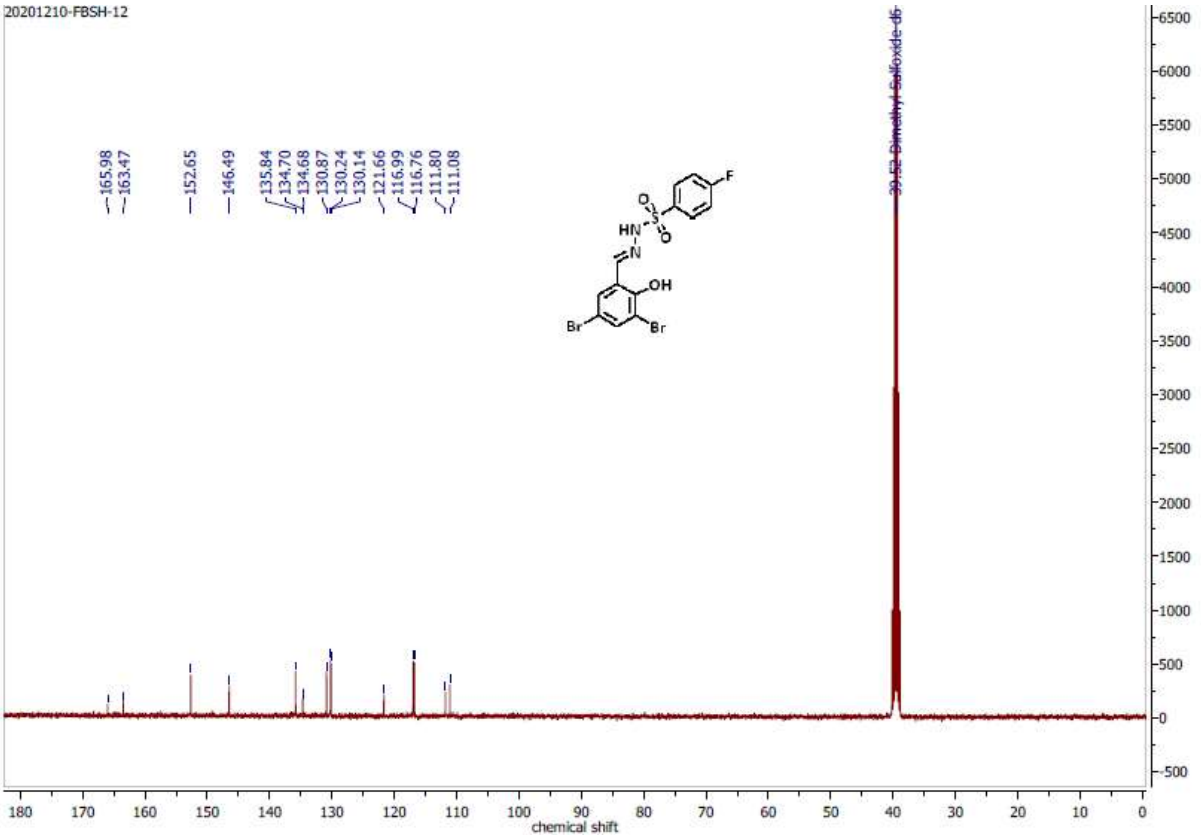

Figure C188: [13] C NMR spectrum of compound 63 in DMSO at 100 MHz

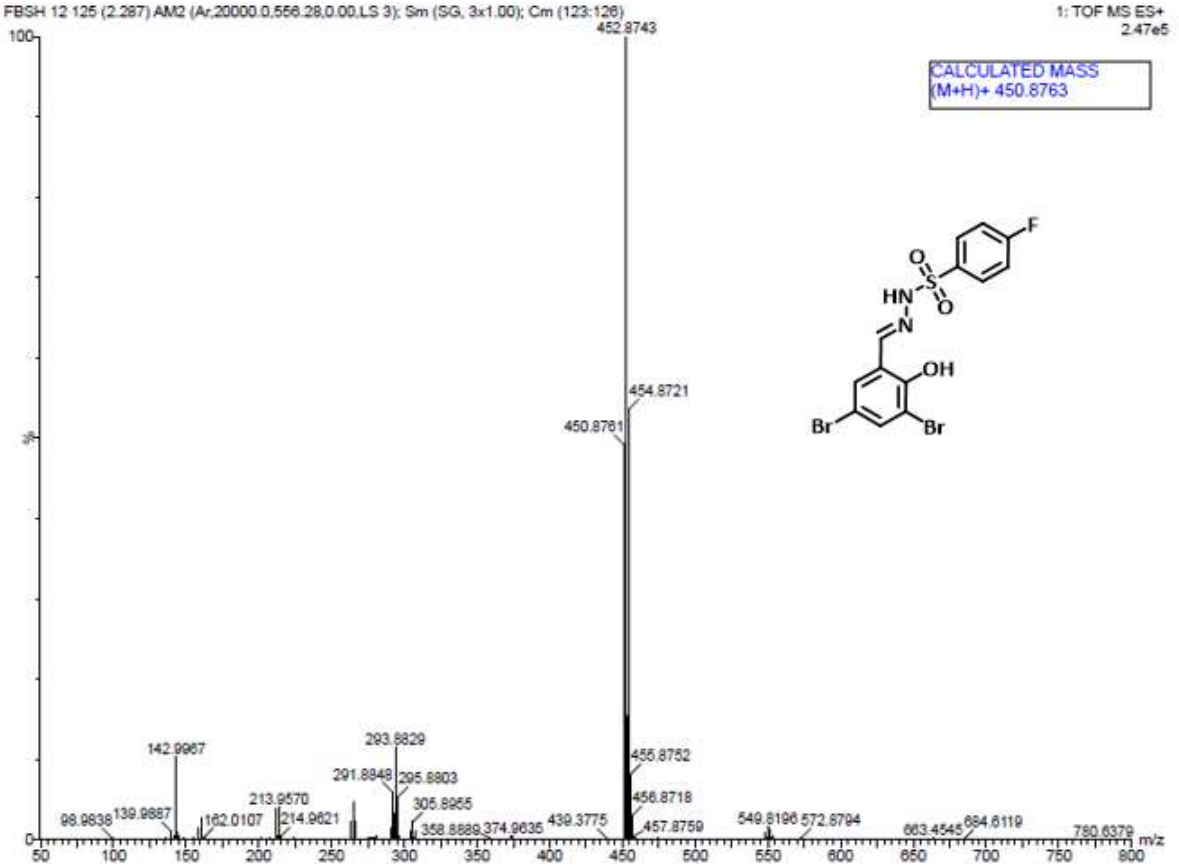

Figure C189: HRMS spectrum of compound 63

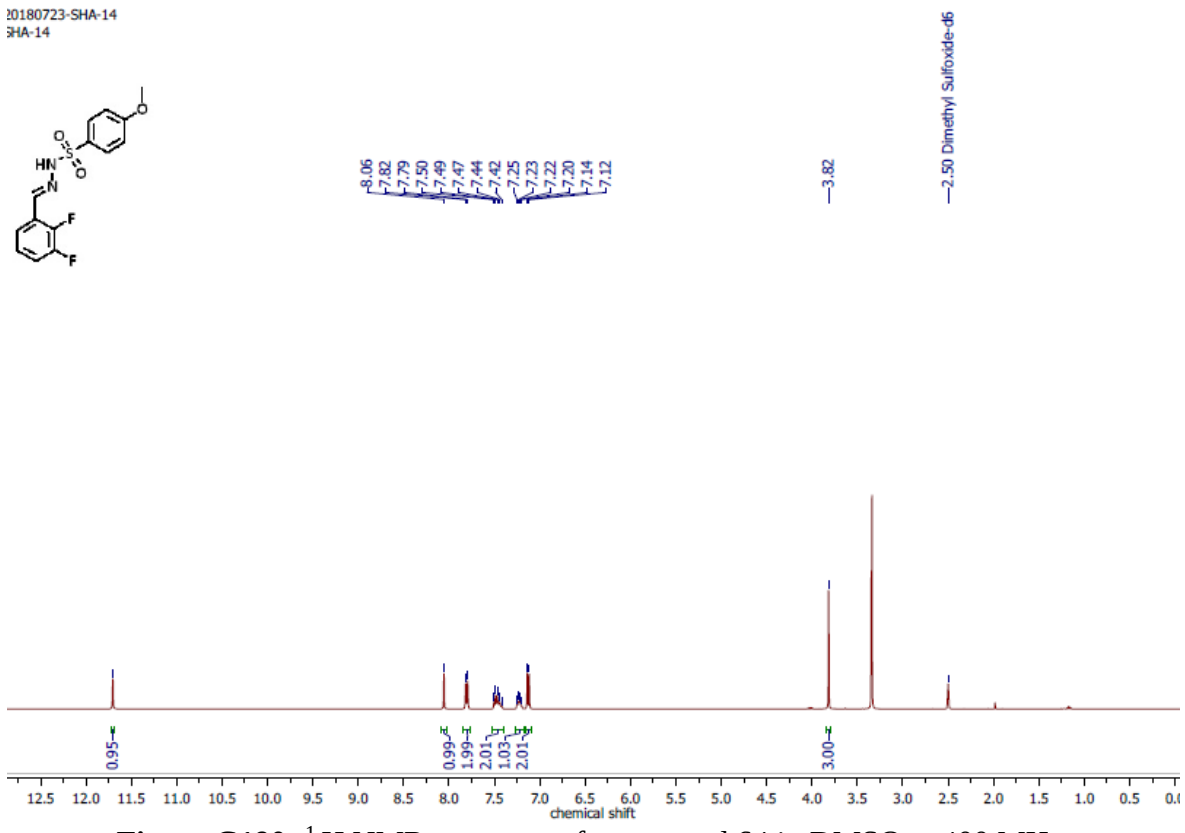

Figure C190: [1] H NMR spectrum of compound 64 in DMSO at 400 MHz.

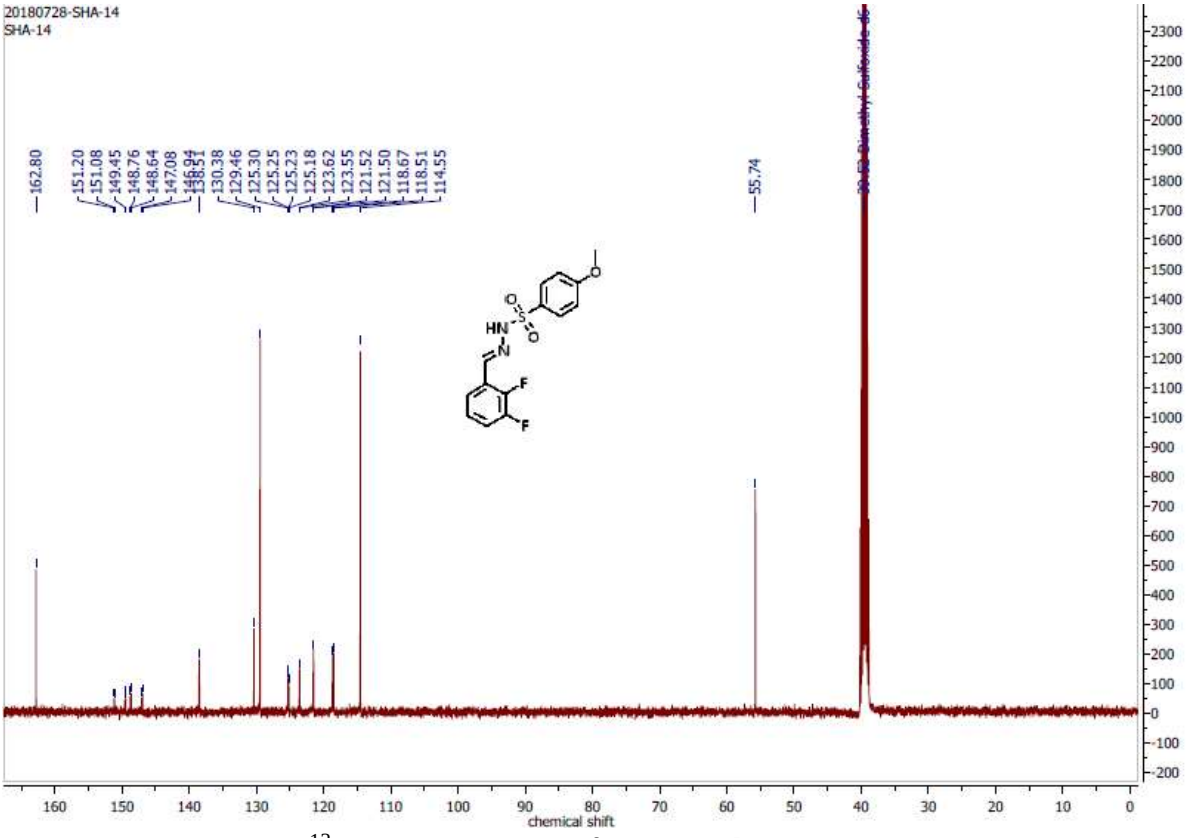

Figure C191: ^{13}C NMR spectrum of compound 64 in DMSO at 100 MHz

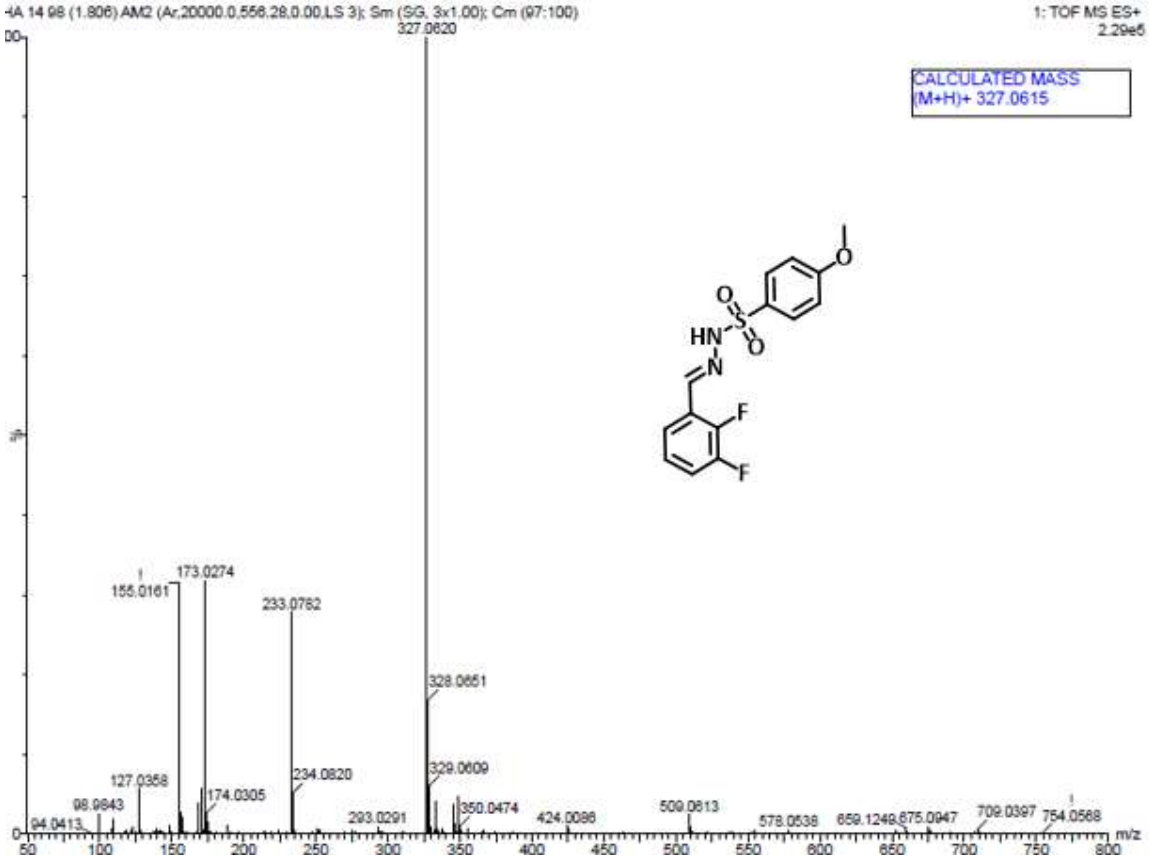

Figure C192: HR-MS spectrum of compound 64

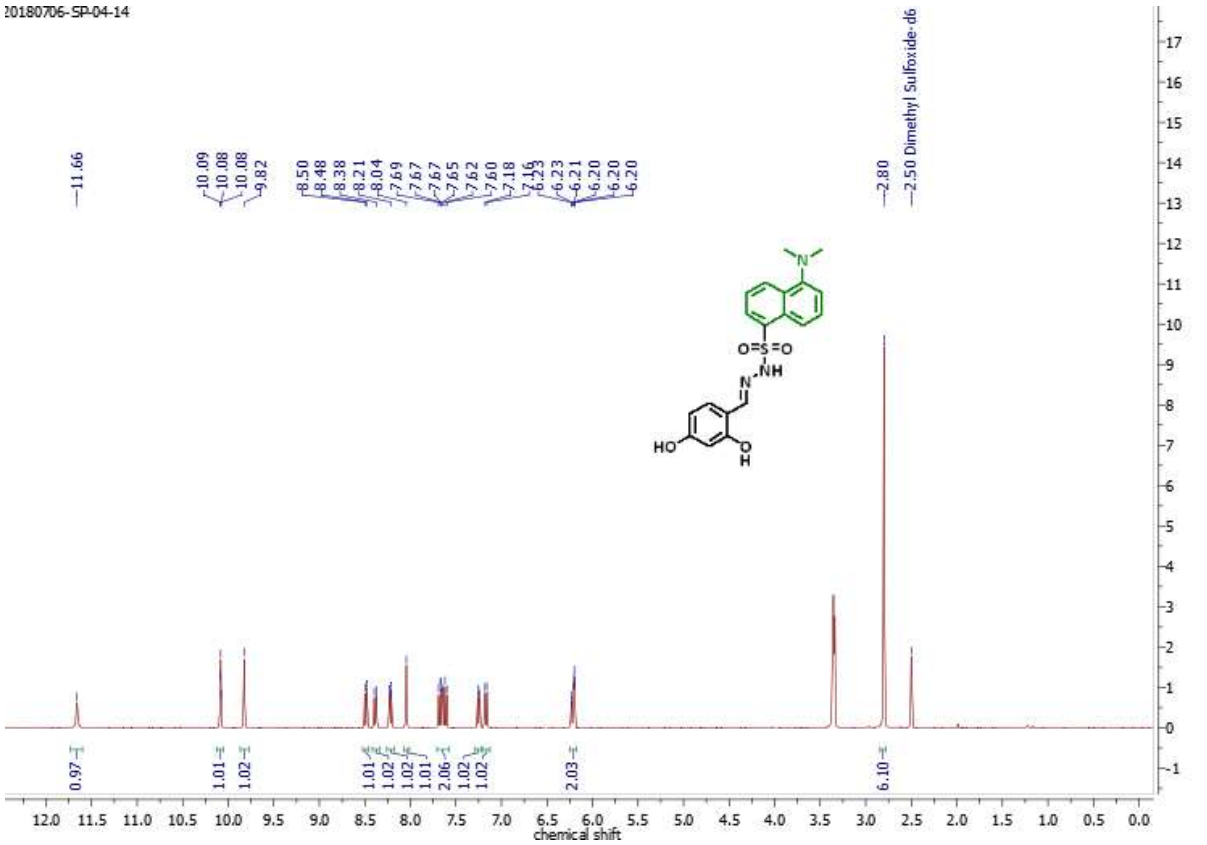

Figure C193: [1] H NMR spectrum of compound 65 in DMSO at 400 MHz

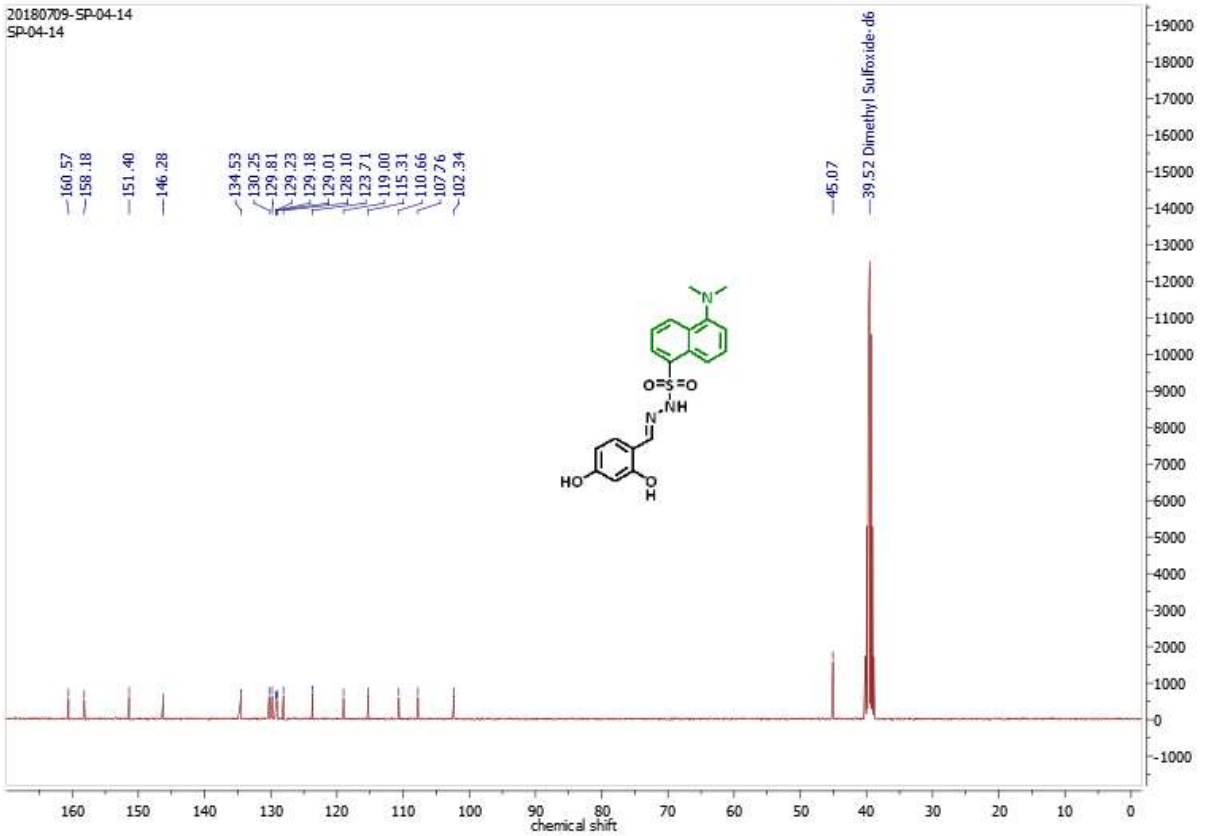

Figure C194: [13] C NMR spectrum of compound 65 in DMSO at 100 MHz

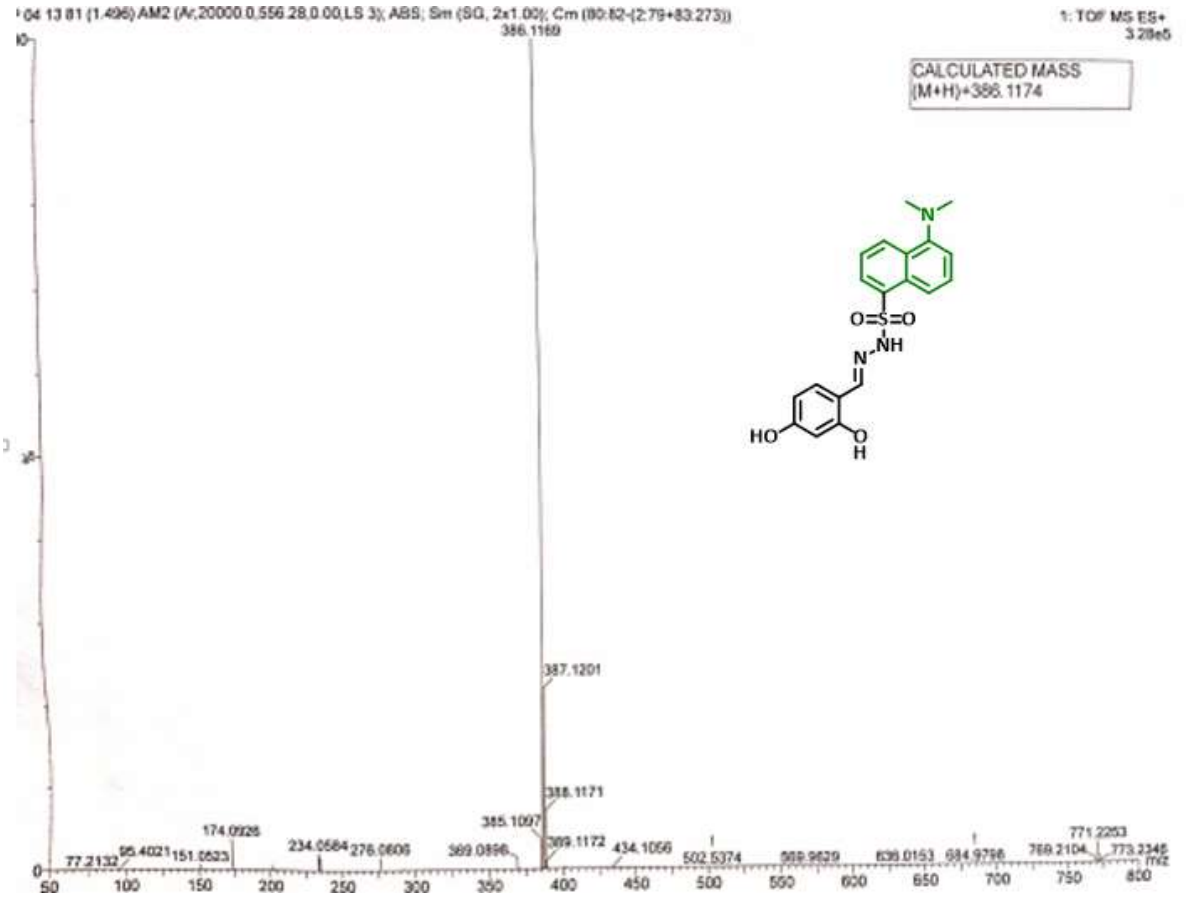

Figure C195: HR-MS spectrum of compound 65

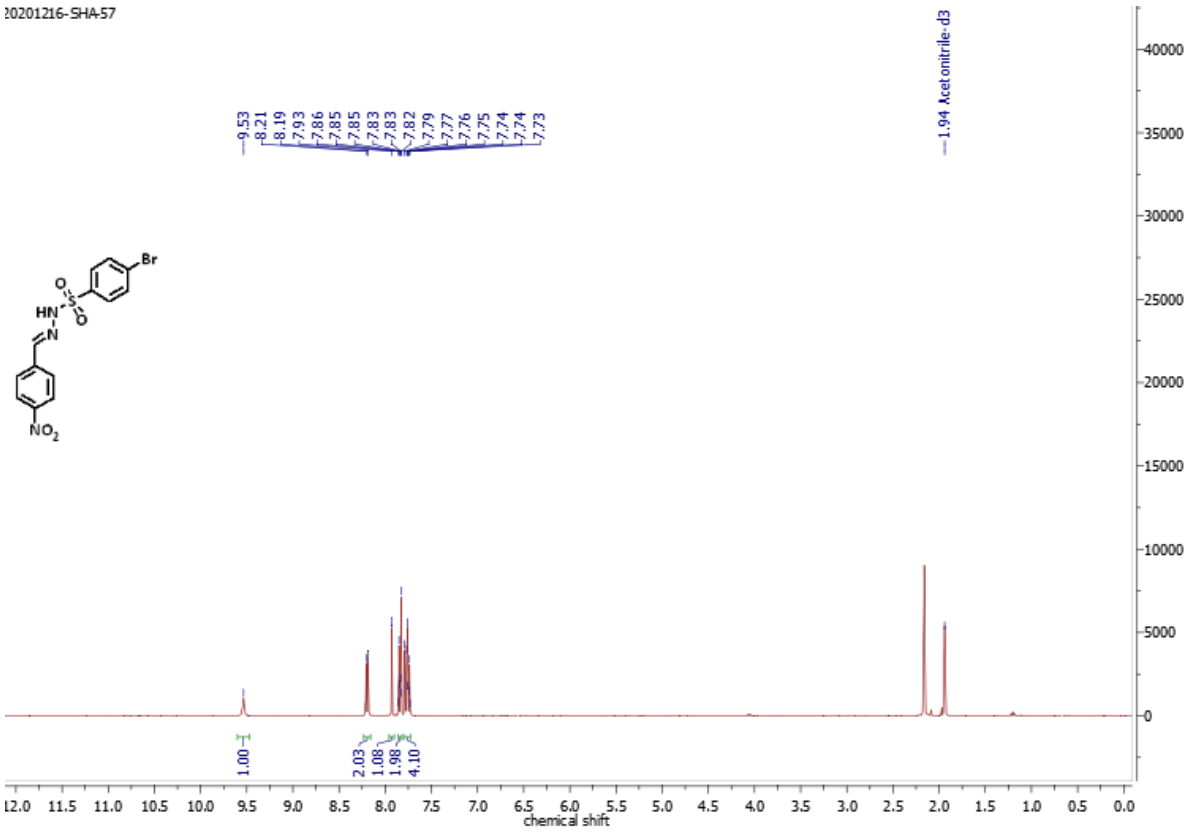

Figure C196: [1] H NMR spectrum of compound 66 in CD_3CN at 400 MHz.

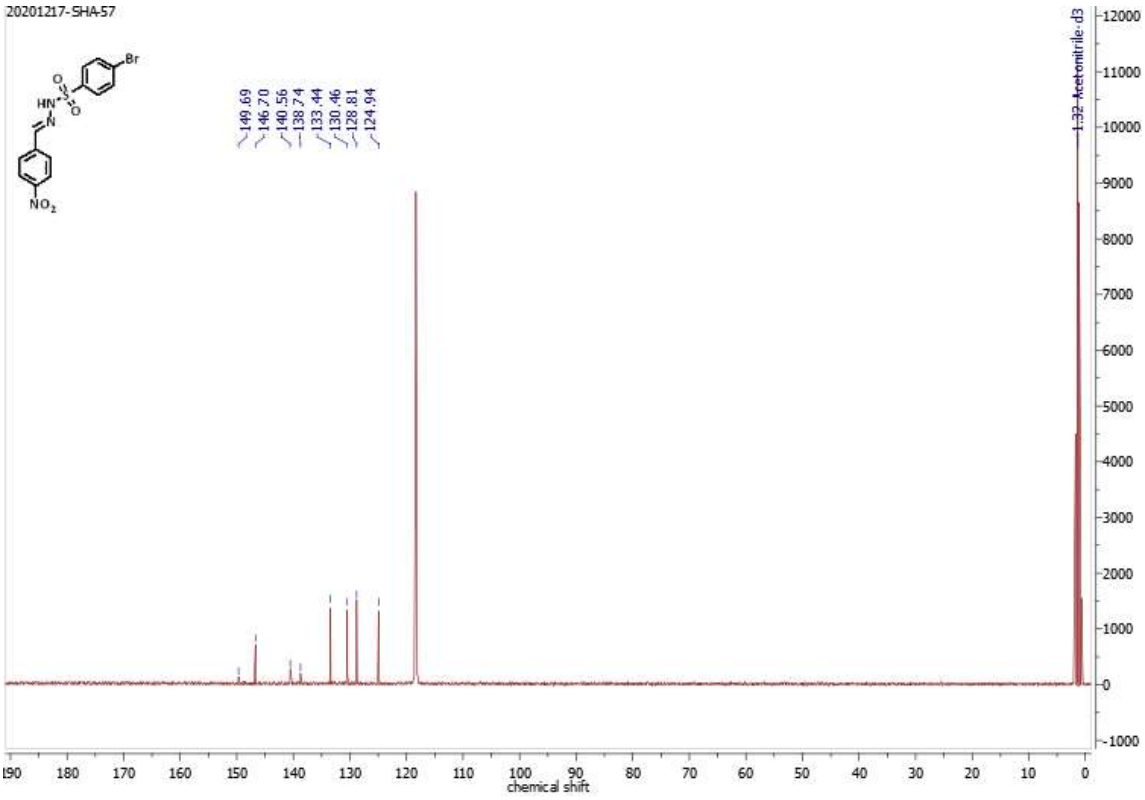

Figure C197: ^{13}C NMR spectrum of compound 66 in CD_3CN at 100 MHz.

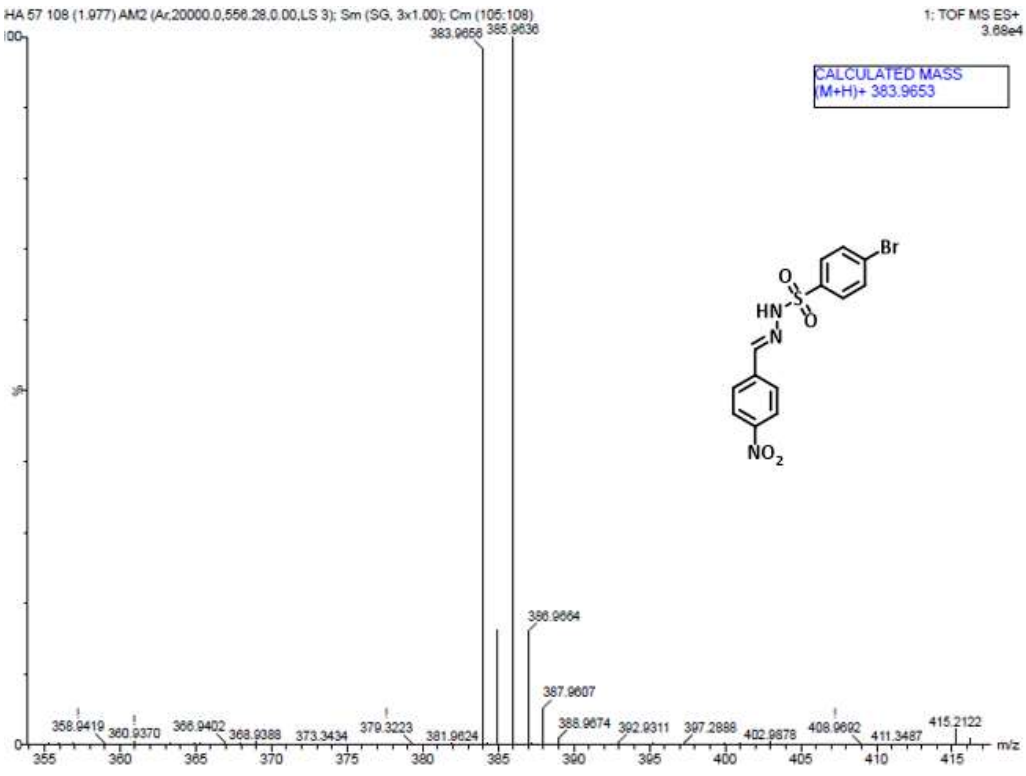

Figure C198: HRMS spectrum of compound 66

Treatment Time		3 h	6 h
Image Channels		C1 (red) C2 (green)	C1 (red) C2 (green)
Pearsons' Correlation Coeffecient		0.8497	0.8666
Manders Coeffecients	M1 (fraction of C1 overlapping C2)	0.9830	0.9763
	M2 (fraction of C2 overlapping C1)	1	0.9866

Table C1: Quantification of co-localization of Compound 1 in ER of HeLa cells at 3 h and 6 h from CLSM.

REFERENCES

1. M. Wang and R. Kaufman. Protein misfolding in the endoplasmic reticulum as a conduit to human disease. *Nature*, **2016**, *529*, 326–335.

2. P. Pizzo and T. Pozzan. Mitochondria-endoplasmic reticulum choreography: structure and signaling dynamics. *Trends Cell Biol*., **2007**, *17*, 511-517.

3. T. Anelli and R. Sitia. Protein quality control in the early secretory pathway. *EMBO. J*., **2008**, *27*, 315-327.

4. T. Avril, E. Vauleon, and E. Chevet. Endoplasmic reticulum stress signaling and chemotherapy resistance in solid cancers. *Oncogenesis*, **2017**, *6*, e373.

5. S. A. Houck, S.Singh, and D. M. Cyr. Cellular responses to misfolded proteins and protein aggregates. *Methods Mol Biol.*, **2012**, *832*, 455-461.

6. I. Braakman and D. N. Hebert. Protein folding in the endoplasmic reticulum. *Cold Spring Harb Perspect Biol*., **2013**, *5*, a013201.

7. J. Miles, R. S. Shouval and P. van Oosten-Hawle. Expanding the Organismal Proteostasis Network: Linking Systemic Stress Signaling with the Innate Immune Response *Trends Biochem Sci.*, **2019**, *44*, 927-942.

8. C. Hetz and F.R. Papa. The Unfolded Protein Response and Cell Fate Control. *Mol Cell*, **2018**, *69*, 169-181.

9. H. Urra, E. Dufey, T. Avril, E. Chevet and C. Hetz. Endoplasmic Reticulum Stress and the Hallmarks of Cancer. *Trends Cancer.* **2016**, *2*, 252-262.

10. H. J. Clarke, J.E. Chambers, E. Liniker and S.J. Marciniak. Endoplasmic reticulum stress in malignancy. *Cancer Cell*, **2014**, *25*, 563-573.

11. M. H. Smith, H. L. Ploegh and J. S. Weissman. Road to ruin: targeting proteins for degradation in the endoplasmic reticulum. *Science*, **2011**, *334*, 1086-1090.

12. R. Bravo, V. Parra, D. Gatica, A. E. Rodriguez, N. Torrealba, F. Paredes, Z. V. Wang, A. Zorzano, J. A. Hill, E. Jaimovich, A. F. Quest and S. Lavandero. Endoplasmic reticulum and the unfolded protein response: dynamics and metabolic integration. *Int Rev Cell Mol Biol.* **2013**, *301*, 215-90.

13. C. Y. Liu and R. J. Kaufman. The unfolded protein response. *J. Cell Sci.,* **2003**, *116,* 1861-1862.

14. P. Walter and D. Ron. The Unfolded Protein Response: From Stress Pathway to Homeostatic Regulation. *Science*, **2011**, *334*, 1081-1086.

15. S.S. Cao and R.J. Kaufman. *Endoplasmic Reticulum Stress and Oxidative Stress in Cell Fate Decision and Human Disease*. *Antioxid Redox Signal*, **2014**, *21, 396-413.*

16. J. Lee and U. Ozcan. Unfolded Protein Response Signaling and Metabolic Diseases. *J Biol Chem.*, **2014**, *289*, 1203-1211.

17. A. H. Schönthal. , Endoplasmic Reticulum Stress: Its Role in Disease and Novel Prospects for Therapy. *Scientifica*, **2012**, *2012*, 857516.

18. A.H. Schonthal. Targeting endoplasmic reticulum stress for cancer therapy *Front Biosci.,* **2012**, *4*, 412-431.

19. R. K. Yadav, S. W Chae, H. R. Kim and H. J. Chae. Endoplasmic Reticulum Stress and Cancer. *J. Cancer Prev.* **2014**, *19*, 75-88.

20. A. R. Sekhar, B. Mallik, V. Kumar and J. Sankar. A cell-permeant small molecule for the super-resolution imaging of the endoplasmic reticulum in live cells. *Org. Biomol. Chem.***, 2019**, *17***,** 3732-3736.

21. L. Wang, M. S. Frei, A. Salim and K. Johnsson. Small-Molecule Fluorescent Probes for Live-Cell Super-Resolution Microscopy *J. Am. Chem. Soc.* **2019**, *141*, 2770-2781.

22. C. Hetz, E. Chevet and H. P. Harding. Targeting the unfolded protein response in disease. *Nat Rev Drug Discov.*, **2013**, *12*, 703-719.

23. Y. Liu, C. N. Lok, B. C. Ko, T. Y. Shum, M. K. Wong and C. M. Che. Subcellular Localization of a Fluorescent Artemisinin Derivative to Endoplasmic Reticulum *Org. Lett.*, **2010**, *12*, 1420-1423.

24. S. Louzoun-Zada, Q. Z. Jaber and M. Fridman. Guiding Drugs to Target-Harboring Organelles: Stretching Drug-Delivery to a Higher Level of Resolution. *Angew. Chem. Int. Ed.***, 2019,** *58*, 15584.

25. J.-T. Hou , H. S. Kim , C. Duan , M. S. Ji , S. Wang , L. Zeng , W. X. Ren and J. S. Kim. A ratiometric fluorescent probe for detecting hypochlorite in the endoplasmic reticulum. *Chem. Commun.*, **2019**, *55*, 2533-2536.

26. S. J. Li, D. Y. Zhou, Y. Li, H. W. Liu, P. Wu, J. Ou-Yang , W. L. Jiang and C. Y. Li. Efficient Two-Photon Fluorescent Probe for Imaging of Nitric Oxide during Endoplasmic Reticulum Stress. *ACS Sens.*, **2018**, ***3***, 2311-2319.

27. H. Xiao, C. Wu, P. Li, W. Gao, W. Zhang, W. Zhang, L. Tong and B. Tang. , Ratiometric photoacoustic imaging of endoplasmic reticulum polarity in injured liver tissues of diabetic mice *Chem. Sci.* **2017**, *8*, 7025-7030.

28. M. Cerezo, A. Lehraiki, A. Millet, F. Rouaud, M. Plaisant, E. Jaune, T. Botton, C. Ronco, P. Abbe, H. Amdouni, T. Passeron, V. Hofman, B. Mograbi, A.S. Dabert-Gay, D. Debayle, D. Alcor, N. Rabhi, J.S. Annicotte, L. Héliot, M. Gonzalez-Pisfil, C. Robert, S. Moréra, A. Vigouroux, P. Gual, M. M. U. Ali, C. Bertolotto, P. Hofman, R. Ballotti, R. Benhida and S. Rocchi. Compounds Triggering ER Stress Exert Anti-Melanoma Effects and Overcome BRAF Inhibitor Resistance. *Cancer Cell*, **2016**, *29*, 805-819.

29. H. Xiao, P. Li, X. Hu, X. Shi, W. Zhang and B. Tang. Simultaneous fluorescence imaging of hydrogen peroxide in mitochondria and endoplasmic reticulum during apoptosis. *Chem. Sci*.**, 2016**, ***7***, 6153-6159.

30. I. Johnson and M. T. Z. Spence, *The molecular probes handbook*. Life Technologies Corporation, Carlsbad, 11th Edn, **2010**.

31. B. K. McMahon, R. Pal and D. Parker. A bright and responsive europium probe for determination of pH change within the endoplasmic reticulum of living cells. *Chem. Commun.*, **2013**, *49*, 5363-5365.

32. K.M. Bailey, J.W. Wojtkowiak, A.I. Hashim and R.J. Gillies. Bailey KM, Wojtkowiak JW, Hashim AI, Gillies RJ. Targeting the metabolic microenvironment of tumors. *Adv Pharmacol.* **2012**, *65*, 63-107.

33. C. T. Supuran. Indisulam: an anticancer sulfonamide in clinical development. *Expert Opin Investig Drugs.*, **2003**, *12*, 283-287.

34. C. Dittrich, A. S. Zandvliet, M. Gneist, A. D. R. Huitema, A. A. J. King and J. Wanders. A phase I and pharmacokinetic study of indisulam in combination with carboplatin. *Br J Cancer*, **2007**, *96*, 559-566.

35. V. Rambiritch, B. Maharaj, P. Naidoo. Glibenclamide in patients with poorly controlled type 2 diabetes: a 12-week, prospective, single-center, open-label, dose-escalation study. *Clin. Pharmacol*. **2014**, *6*, 63-69.

36. C. Zhao, K. P. Rakesh, L. Ravidar, W.Y. Fang and H. L. Qin. Pharmaceutical and medicinal significance of sulfur (S^{VI})-Containing motifs for drug discovery: A critical review. *Eur. J. Med. Chem*. **2019**, *162*, 679-734.

37. C. Ghosh, A. Nandi and S. Basu. Supramolecular self-assembly of triazine-based small molecule: targeting endoplasmic reticulum in cancer cells. *Nanoscale*, **2019**, *11*, 3326-3335.

38. S. Pandey, S. Patil, N. Ballav and S. Basu. Spatial targeting of Bcl-2 on endoplasmic reticulum and mitochondria in cancer cells by lipid nanoparticles. .*J. Mater. Chem. B***, 2020**, *8*, 4259-4266.

39. H. Nishitoh. Chop is a multifunctional transcription factor in the ER stress response *J. Biochem.*, **2012**, *151*, 217-219.

40. S. Oyadomari and M. Mori. Roles of CHOP/GADD153 in endoplasmic reticulum stress *Cell Death Differ.,* **2004,** *11*, 381-389.

41. Y. Chen and F. Brandizzi. ER stress signaling requires RHD3, a functionally conserved ER-shaping GTPase. *Cell Biol.*, **2013**, *23*, 1-9.

42. G. van Meer, D. Voelker, and G. Feigenson. Membrane lipids: where they are and how they behave. *Nat. Rev. Mol. Cell Biol.,* **2008**, *9*, 112-124.

43. J. Wang, X. Fang and W. Liang. Pegylated Phospholipid Micelles Induce Endoplasmic Reticulum-Dependent Apoptosis of Cancer Cells but not Normal Cells. *ACS Nano*, **2012**, *6*, 5018–5030.

44. A. Mehlem, C. E. Hagberg, L. Muhl, U. Eriksson and A. Falkevall. Imaging of neutral lipids by oil red O for analyzing the metabolic status in health and disease. *Nat Protoc.*, **2013**, *8*, 1149–1154.

45. V. Sica, L. Galluzzi, J. M. Bravo-San Pedro, V. Izzo, M. C. Maiuri and G. Kroemer. Organelle-Specific Initiation of Autophagy. *Mol. Cell*, **2015**, *59*, 522–539.

46. W. S. Lee, W. H. Yoo and H. J. Chae. ER Stress and Autophagy. *Curr. Mol. Med.,* **2015**, *15*, 735-745.

47. K. R. Parzych and D.J. Klionsky. An overview of autophagy: morphology, mechanism, and regulation. *Antioxid Redox Signal*. **2014**, *20*, 460-473.

48. I. Tanida, T. Ueno and E. Kominami. LC3 and Autophagy. *Methods Mol. Biol.,* **2008**, *445*, 77-88.

49. Z. Xie and D. J. Kilonsky. Autophagasome formation: core machinery and adaptations *Nat. Cell Biol.*, **2007**, *9*, 1102-1109.

50. Y. Cao and D. J. Klionsky. Physiological functions of Atg6/Beclin 1: a unique autophagy-related protein *Cell Res.*, **2007**, *17*, 839-849.

51. M. Mauthe, I. Orhon, C. Rocchi, X. Zhou, M. Luhr, K. J. Hijlkema, R. P. Coppes, N. Engedal, M. Mari and F. Reggiori. Chloroquine inhibits autophagic flux by decreasing autophagosome-lysosome fusion. *Autophagy*, **2018**, *14*, 1435-1455.

52. A. U. Nissar, L. Sharma, M. A. Mudasir, L. A. Nazir, S. A. Umar, P. R. Sharma, R. A. Vishwakarma and S. A. Tasduq Chemical chaperone 4-phenyl butyric acid (4-PBA) reduces

hepatocellular lipid accumulation and lipotoxicity through induction of autophagy *J. Lipid Res.*, **2017**, *58*, 1588-1868.

53. B. Kaur, A. Bhat, R. Chakraborty, K. Adlakha, S. Sengupta, S. Roy and K. Chakraborty. Proteomic profile of 4-PBA treated human neuronal cells during ER stress. *Mol. Omics*, **2018**, *14*, 53-63.

55. A. G. Myers, B. Zheng and M. Movassaghi. Preparation of the Reagent *o*-Nitrobenzenesulfonylhydrazide. *J. Org. Chem.* **1997**, *62*, 7507.

56. Ji-W. Choi, S.-Hye Choi, S. T. Hong, M. S. Kim, S. S. Ryu, Y. U. Yoon, K. C. Paik, M. S. Han, T. Sim and B. R. Cho. Two-photon probes for the endoplasmic reticulum: its detection in a live tissue by two-photon microscopy *Chem. Commun.*, **2020**, *56*, 3657-3660